AD-A051 514 AUBURN UNIV ALA SCHOOL OF ENGINEERING F/G 5/2
1977 USAF-ASEE SUMMER FACULTY RESEARCH PROGRAM. VOLUME II.(U)
SEP 77 J F O'BRIEN F44620-75-C-0031
UNCLASSIFIED AFOSR-TR-78-0349 NL

1 OF 6
AD A051514



AFOSR-TR- 78-0349

AD A051514

1977 USAF-ASEE SUMMER FACULTY RESEARCH PROGRAM

Research Reports

Volume II of II

AD No.
DDC FILE COPY

DDC
RECEIVED
MAR 20 1978
A

Conducted by:
SCHOOL OF ENGINEERING
AUBURN UNIVERSITY
Auburn, Alabama
September, 1977

Approved for public release;
distribution unlimited.

REPORT DOCUMENTATION PAGE	READ INSTRUCTIONS BEFORE COMPLETING FORM
1. REPORT NUMBER: AFOSR-TR-78-0349	2. GOVT ACCESSION NO. / 3. RECIPIENT'S CATALOG NUMBER
4. TITLE (and Subtitle): 1977 USAF-ASEE SUMMER FACULTY RESEARCH PROGRAM. VOLUME II.	5. TYPE OF REPORT & PERIOD COVERED: INTERIM rept.
	6. PERFORMING ORG. REPORT NUMBER
7. AUTHOR(s): ALFRED O'BRIEN, JR	8. CONTRACT OR GRANT NUMBER(s): F44620-75-C-0031
9. PERFORMING ORGANIZATION NAME AND ADDRESS: AUBURN UNIVERSITY, ENGINEERING EXTENSION SERVICE, AUBURN, ALABAMA 30830	10. PROGRAM ELEMENT, PROJECT, TASK AREA & WORK UNIT NUMBERS: 2307D3, 61102F
11. CONTROLLING OFFICE NAME AND ADDRESS: AIR FORCE OFFICE OF SCIENTIFIC RESEARCH/NA, BLDG 410, BOLLING AIR FORCE BASE, D C 20332	11. REPORT DATE: Sep 77
	12. NUMBER OF PAGES: 1134 (551 pp.)
14. MONITORING AGENCY NAME & ADDRESS (if different from Controlling Office)	15. SECURITY CLASS. (of this report): UNCLASSIFIED
	15a. DECLASSIFICATION/DOWNGRADING SCHEDULE

16. DISTRIBUTION STATEMENT (of this Report)

Approved for public release; distribution unlimited.

17. DISTRIBUTION STATEMENT (of the abstract entered in Block 20, if different from Report)

18. SUPPLEMENTARY NOTES

19. KEY WORDS (Continue on reverse side if necessary and identify by block number)

SUMMER FACULTY RESEARCH PROGRAM

20. ABSTRACT (Continue on reverse side if necessary and identify by block number)

This report represents the third years effort of an annual 10 week summer research program conducted by university faculty members at selected USAF System Command Laboratories. Program objectives are 1) To provide scientific and technological benefits to the USAF while enhancing the research interests and capabilities of engineering educators. 2) To stimulate continuing relations among participating faculty members and their professional peers at the AFSC laboratories. 3) To form the basis for continuing research of interest to the Air Force at the participant's institution. 4) To sponsor research in areas of mutual interest to the USAF, the faculty member, and his institution.

DD FORM 1 JAN 73 1473 EDITION OF 1 NOV 65 IS OBSOLETE

UNCLASSIFIED.

SECURITY CLASSIFICATION OF THIS PAGE (When Data Entered)

390 276

1977 USAF/ASEE Summer Faculty
RESEARCH PROGRAM

Conducted by
Auburn University
with Assistance from
Ohio State University
and
Other Installations
under
USAF Contract Grant F 44620-75-C-0031

PARTICIPANT'S RESEARCH REPORTS

VOLUME II of II

Submitted to
Air Force Office of Scientific Research
Bolling Air Force Base
Washington, D. C.

by
J. Fred O'Brien, Jr., University Project Director
Associate Director, Engineering Extension Service
Auburn University

September 1977

AIR FORCE OFFICE OF SCIENTIFIC RESEARCH (AFSC)
NOTICE OF TRANSMITTAL TO DDC
This technical report has been reviewed and is
approved for publ c release IAW AFR 190-12 (7b).
Distribution is unlimited.
A. D. BLOSE
Technical Information Officer

RESEARCH REPORTS

1977 USAF/ASEE SUMMER FACULTY RESEARCH PROGRAM

VOLUME I

Report No.	Title	Research Associates
1	Livability as Applied to Air Force Bases	Dr. Harry H. Caldwell
2	Nondestructive Pavement Evaluations	Dr. Braja Mohan Das
3	Effect of Cooling Water Spray on Turbine Engine Test Cell Emissions	Dr. Charles Springer
4	A Study of Reliability of Deep Well Anodes for Cathodic Protection	Dr. John A. Stevens
5	Tactical Shelter Hardening	Dr. Alvin M. Strauss
6	The Status of Bishop Pine on Vandenberg Air Force Base and Recommendations for Its Management	Dr. Paul H. Zedler
7	Nonlinear Guidance for Air-to-Air Missiles	Dr. J. Frederick Andrus
8	Spread Spectrum ECCM Performance CW Jamming Signal Reduction in Spread Spectrum Receivers	Dr. Maurice J. Bouvier, Jr.
9	An Analysis of Aerodynamic Force and Moment Models for Asymmetric Munitions	Dr. Robert W. Courter
10	Reducing the Volume of Computation in Monte Carlo Missile Flight Simulation	Dr. Carl G. Looney
11	Flush Mounted Aircraft Antennas for Satellite Communication. A Study of Multipath Performance	Dr. Vaughn P. Cable
12	A Multimode Fiber-Optic Coupler with Low Insertion Loss	Dr. Marvin M. Drake
13	Analysis of a Discrepancy in Trapped Proton Fluxes in the South Atlantic Anomaly	Dr. Thomas E. Morgan
14	A Study of the Particle Spectrum of the Continuous Aurora and Associated E-Region Ionization Before and After a Magnetic Storm	Dr. James R. Sharber

RESEARCH REPORTS (Continued)

Report No.	Title	Research Associates
15	Directionally Solidified Eutectic Materials for Electronic, Magnetic, and Optical Applications	Dr. Richard D. Sisson, Jr.
16	Synthesis and Characterization of Novel Nitroaliphatic Materials	Dr. Melvin L. Druelinger
17	Optimal Weapon Assignment in a Tiered Aimpoint System	Dr. Jerren Gould
18	Electrochemical and Luminescence Studies with Special Emphasis on Molten Salt Media	Dr. Csaba P. Keszthelyi
19	Test of Two Hypotheses Concerning the Optical Properties of Cryodeposited Gases	Dr. William B. Newbolt
20	Rocket Exhaust Gas Dynamics	Dr. Peter C. Sukanek
21	Simulation of Turbulent Flow Velocity	Dr. John W. Weatherly, III
VOLUME II		
22	Nitronium Salt Synthesis	Dr. Alton J. Banks
23	Synthesis of Fluorodinitroethylnitramines	Dr. Catherine H. Banks
24	Submicron Particle Size Measurements in Acetylene-Oxygen and Aluminum-Oxygen Flames	Dr. James F. Driscoll
25	Solid Teflon Propulsion Contamination Investigation	Dr. James K. Hartman
26	Infrared, Raman, Mass Spectroscopy and Gas Chromatography of Selected Fluorodinitro Plasticizers	Dr. Steven Riethmiller
27	Rotational and Mean Flow Effects on Motor Stability	Dr. Wm. K. Van Moorhem
28	Investigation of Raman Microwave Emission from Plasmas	Dr. Tse-Wen Hsu
29	Automatic Speech Processing-Speech Enhancement	Dr. Russell J. Niederjohn
30	Design of System Diagnostic and Fault Isolation Procedures	Dr. Theodore J. Sheskin

RESEARCH REPORTS (Continued)

Report No.	Title	Research Associates
31	Maximum Entrophy Spectral Demodulator Investigation	Dr. Robert G. Van Meter
32	Software Design Validation and Artificial Intelligence	Dr. Ralph M. Weischedel
33	Engineering Analysis of the Dynamics and Control of the Human Centrifuge	Dr. Thomas J. Jones
34	Investigation of Ultrashort 1060 NM Laser Pulse Induced Intensity Dependent Damage Processes and Development of an On-Line Pulse Width Measuring Technique	Dr. Demetrius D. Venable
35	Application of a Specialized Statistical Computer Program, Alphaf, To a Visual Evoked Response Data Analysis System	Dr. James M. Verlander
36	Fixed Capacity Measurement of Attentional Load Using Dual-Task Performance Operating Curves	Dr. Herbert A. Colle
37	Simulator for Air-to-Air Combat Platform Motion System Investigation	Dr. John A. Seevers
38	The Radiative Lifetime and Quenching Cross Sections of the $A^2\Sigma$ State of GeF	Dr. Richard A. Anderson
39	Transient Fields From a Vertically Polarized Dipole Radiator With a Ramp-Function Input Voltage	Dr. Martin D. Bradshaw
40	Liquefaction Potential of Soils Under Blast Loads	Dr. Wayne A. Charlie
41	Double Resonance Apparatus for Relaxation Studies of HF in High Vibrational States	Dr. Richard L. Redington
42	Electron-Ion Recombination in Laser Gas Mixes	Dr. Harold D. Southward
43	The Nature and Prediction of Secondary Calcium Carbonate Cementation (Caliche) in Alluvial Basins of the Southwestern United States	Dr. Stephen G. Wells
APPENDIX	Listing of 1975 Research Reports Listing of 1976 Research Reports	

PARTICIPANT LABORATORY ASSIGNMENT

1977 USAF/ASEE SUMMER FACULTY RESEARCH PROGRAM

AFCEC — AIR FORCE CIVIL ENGINEERING CENTER (TYNDALL AIR FORCE BASE)
1. Harry H. Caldwell - University of Idaho
2. Braja M. Das - South Dakota State University
3. John A. Stevens - Youngstown State University

AFCEEDO — AIR FORCE CIVIL AND ENVIRONMENTAL ENGINEERING DEVELOPMENT OFFICE (TYNDALL AIR FORCE BASE)
1. Charles Springer - University of Arkansas
2. Alvin M. Strauss - University of Cincinnati
3. Paul H. Zedler - San Diego State University

AFATL — AIR FORCE ARMAMENT LABORATORY (EGLIN AIR FORCE BASE)
1. Jan F. Andrus - University of New Orleans
2. Maurice J. Bouvier - Louisiana State University
3. Robert W. Courter - Louisiana State University
4. Carl Grant Looney - University of Toledo

DET — ROME AIR DEVELOPMENT LABORATORY (HANSCOM AIR FORCE BASE)
1. Vaughn P. Cable - California State University
2. Richard Dean Sisson, Jr. - Worcester Polytechnic Institute

ESD — ELECTRONICS SYSTEMS DIVISION (HANSCOM AIR FORCE BASE)
1. Marvin D. Drake - Florida Institute of Technology

AFGL — AIR FORCE GEOPHYSICS LABORATORY (HANSCOM AIR FORCE BASE)
1. Thomas E. Morgan - State University of New York
2. James R. Sharber - Florida Institute of Technology

FJSRL — FRANK J. SEILER RESEARCH LABORATORY (AIR FORCE ACADEMY)
1. Melvin L. Druelinger - Indiana State University
2. Jerren Gould - Claremont Graduate School
3. Csaba Peter Keszthelyi - Louisiana State University

AEDC — ARNOLD ENGINEERING DEVELOPMENT CENTER (ARNOLD AIR FORCE BASE)
1. William B. Newbolt - Washington & Lee University
2. Peter Sukanek - Clarkson College of Technology
3. John Weatherly III - Louisiana State University

AFRPL — AIR FORCE ROCKET PROPULSION LABORATORY (EDWARDS AIR FORCE BASE)
1. Alton J. Banks - Texas A & M University
2. Catherine H. Banks - Texas A & M University
3. James F. Driscoll - University of Michigan
4. J. Keith Hartman - Canisius College
5. Steven Riethmiller - Virginia Military Institute
6. William K. Van Moorhem - University of Utah

ACCESSION for
NTIS White Section
DDC Buff Section
UNANNOUNCED
JUSTIFICATION
BY
DISTRIBUTION/AVAILABILITY CODES
Dist. AVAIL. and/or SPECIAL

PARTICIPANT LABORATORY ASSIGNMENT Continued

RADC — ROME AIR DEVELOPMENT CENTER (GRIFFISS AIR FORCE BASE)
1. Tse-Wen Hsu - Villanova University
2. Russell J. Niederjohn - Marquett University
3. Theodore J. Sheskin - Cleveland State University
4. Robert G. Van Meter - State University College
5. Ralph M. Weischedel - University of Delaware

SAM — SCHOOL OF AEROSPACE MEDICINE (BROOKS AIR FORCE BASE)
1. Thomas J. Jones - Trinity University
2. Demetrius D. Venable - St. Paul's College
3. James M. Verlander - Texas A & M University

AFHRL-FT — AIR FORCE HUMAN RESOURCES LABORATORY (WILLIAMS AIR FORCE BASE)
1. Herbert A. Colle - Wright State University

AFHRL-FT — AIR FORCE HUMAN RESOURCES LABORATORY (LUKE AIR FORCE BASE)
1. John A. Seevers - Washington State University

AFWL — AIR FORCE WEAPONS LABORATORY (KIRTLAND AIR FORCE BASE)
1. Richard A. Anderson - University of Missouri-Rolla
2. Martin D. Bradshaw - University of New Mexico
3. Wayne A. Charlie - Colorado State University
4. Richard L. Redington - Texas Tech University
5. Harold D. Southward - University of New Mexico
6. Stephen G. Wells - University of New Mexico

LIST OF PARTICIPANTS

1977 USAF/ASEE SUMMER FACULTY RESEARCH PROGRAM

AFCEC/CEEDO (Tyndall)	DEGREE, SPECIALTY & LAB ASSIGNMENT
Dr. Harry H. Caldwell Department of Geography University of Idaho Moscow, ID 83843	Degree: Ph.D., Geography Specialty: Livability Meas Systems Assigned: AFCEC Colleague: Mr. Charles Lewis
Dr. Braja Mohan Das Associate Professor Civil Engineering Department South Dakota State University Brookings, SD 57006	Degree: Ph.D., Soil Mech & Foundations Specialty: Soils and Foundations Assigned: AFCEC Colleague: Major James I. Clark
Dr. Charles Springer Professor, Chemical Engineering Dept 332 Engineering Building University of Arkansas Fayetteville, AR 72701	Degree: Ph.D., Chemical Engineering Specialty: Mass Transfer Assigned: DET I (CEEDO) HdQtrs. ADTC Colleague: Major Peter Daley
Dr. John Augustus Stevens Associate Professor Chemical Engineer & Material Science Dept The Rayen School of Engineering Youngstown State University Youngstown, OH 44555	Degree: Ph.D., Physical Chemistry Specialty: Corrosion and Materials Assigned: AFCEC Colleague: Mr. Harold Stevens Mr. Tom Lewicki
Dr. Alvin M. Strauss Engineering Science Department University of Cincinnati Cincinnati, OH 45221	Degree: Ph.D., Theor. & Appld. Mech. Specialty: Mechanics, Applied Math Assigned: DET I (CEEDO) HDQTRS ADTC Colleague: Capt. Monte H. Callen
Dr. Paul H. Zedler Department of Biology San Diego State University San Diego, CA 92182	Degree: Ph.D., Botony Specialty: Plant Ecology Assigned: DET I (CEEDO) HDQTRS. ADTC Colleague: Major R. C. Wooten
AFATL (Eglin)	
Dr. Jan Frederick Andrus Associate Professor, Dept of Math University of New Orleans New Orleans, LA 70122	Degree: Ph.D., Math Specialty: Numerical Analysis Assigned: AFATL Colleague: Mr. Mike Caluda
Dr. Maurice J. Bouvier Electrical Engineering Department Louisiana State University Baton Rouge, LA 70803	Degree: Ph.D., Elec Engineering Specialty: Communications Systems Assigned: AFATL Colleague: Major Dave DePriest

AFATL (Eglin) Continued

Dr. Robert W. Courter
Associate Professor, Mech Engineering
Louisiana State University
Baton Rouge, LA 70803

Degree: Ph.D., Psychology
Specialty: Aerodynamics, Flight Dyn
Assigned: AFATL
Colleague: Mr. Ken Cobb

Dr. Carl Grant Looney
Assistant Professor
Mathematics Department
University of Toledo
Toledo, OH 43603

Degree: Ph.D., Mathematics
Specialty: Computational Mathematics
Assigned: AFATL
Colleague: Mr. Aaron Brinson

DET/ESD/AFGL (Hanscom)

Dr. Vaughn Paul Cable
Assistant Professor
Dept of Electrical & Electronics Engineering
California State University

Degree: Ph.D., Electromagnetic Theory
Specialty: Electromagnetic Theory
Assigned: DET
Colleague: Dr. R. J. Mailloux

Dr. Marvin D. Drake
Assistant Professor, Dept of Elec Engr.
Florida Institute of Technology
P. O. Box 1150
Melbourne, FL 32901

Degree: Ph.D., Electrical Engineering
Specialty: Electro-optic, Mat'ls & divices
Assigned: ESD(DP)
Colleague: Dr. Donald B. Brick

Dr. Thomas E. Morgan
Acting Chairman
Department of Earth Sciences
Oswego, NY 13126

Degree: Ph.D., Astrophysics
Specialty: Solar & Stellar Atmos
Assigned: AFGL
Colleague: Mr. Charles Dubs

Dr. James Randall Sharber
Physics and Space Science Deparmtnet
Florida Institute of Technology
Melbourne, FL 32901

Degree: Ph.D., Physics
Specialty: Near-earth space physics
Assigned: AFGL
Colleague: Dr. James A. Whalen

Dr. Richard Dean Sisson, Jr.
Assistant Professor
Mechanical Engineering Materials Division
Worcester Polytechnic Institute
Worcester, MA 01609

Degree: Ph.D., Materials Engineering
Specialty: Materials Engineering
Assigned: DET
Colleague: Mr. Alton Armington

FJSRL (AF Academy)

Dr. Melvin Leroy Druelinger
Associate Professor
Chemistry Department
Indiana State University
Terre Haute, In. 47809

Degree: Ph.D., Organic Chemistry
Specialty: Organic Chemistry
Assigned: FJSRL
Colleague: Capt. Scott Shackleford

FJSRL (AF Academy) Continued

Dr. Jerren Gould
Mathematics
Claremont Graduate School
Claremont, CA 91711

Degree: Ph.D. Statistics
Specialty: Statistical Theory, O'n's Res.
Assigned: FJSRL
Colleague: Capt. S. J. Monaco

Dr. Csaba Peter Kexzthelyi
Assistant Professor
Chemistry Department
Louisiana State University
Baton Rouge, LA 70803

Degree: Ph.D., Electrochemistry
Specialty: Non-Aqueous Systems
Assigned: FJSRL
Colleague: Capt. C. L. Hussey
Capt. L. Davis

AEDC (Arnold)

Dr. William Barlow Newbolt
Professor of Physics
Washington and Lee University
Lexington, VA 24450

Degree: Ph.D., Physics
Specialty: Nuclear Spectroscopy
Assigned: AEDC
Colleague: Mr. J. A. Roux

Dr. Peter Sukanek
Clarkson College of Technology
Potsdam, NY 13676

Degree: Ph.D., Chemical Engineering
Specialty: Fluid Mechanics
Assigned: AEDC
Colleague: Mr. R. Rholes

Dr. John Wilson Weatherly III
Associate Professor
Mechanical & Ind. Engineering Dept
Louisiana State University
Baton Rouge, LA 70803

Degree: Ph.D., Mechanical Engineering
Specialty: Thermal Sciences
Assigned: AEDC
Colleague: Dr. Don Barnett

AFRPL (Edwards)

Dr. Alton Joseph Banks
Department of Chemistry
Texas A & M
Texas Avenue
College Station, TX 77843

Degree: Ph.D., Chemistry
Specialty: Inorganic Chemistry
Assigned: AFRPL
Colleague: Dr. Claude Merrill

Dr. Catherine Hamrick Banks
Department of Chemistry
Texas A & M
Texas Avenue
College Station, TX 77843

Degree: Ph.D., Organic Chemistry
Specialty: Organo-Sulfur Compounds
Assigned: AFRPL
Colleague: Dr. Claud Merrill

AFRPL (Edwards) Continued

Dr. James Francis Driscoll
Assistant Professor
Department of Aerospace Engineering
209 Aerospace Engineering Building
The University of Michigan
Ann Arbor, MI 48105

Degree: Ph.D., Aerospace & Mech Scien
Specialty: Laser Meas tech. Gasdynamics
Assigned: AFRPL
Colleague: Dr. David Mann

Dr. James Keith Hartman
Physics Department
Canisius College
Buffalo, NY 14208

Degree: Ph.D., Applied Physics
Specialty: Modeling of Physical Systems
Assigned: AFRPL
Colleague: Lt. Sharon Pruitt

Dr. Steven Riethmiller
Associate Professor
V.M.I. Chemistry Department
Lexington, VA 24450

Degree: Ph.D., Chemistry
Specialty: Molecular Spectroscopy
Assigned: AFRPL
Colleague: Mr. Louis Dee

Dr. William K. Van Moorhem
Mechanical Engineering Department
University of Utah
Salt Lake City, UT 84112

Degree: Ph.D., Aerospace Engineering
Specialty: Fluid Mechanics, Acoustics
Assigned: AFRPL
Colleague: Mr. Jay Levine

RADC (Griffiss)

Dr. Tse-Wen Hsu
Electrical Engineering Department
Assistant Professor
Villanova University
Villanova, Pennsylvania 19085

Degree: Ph.D., Microwave Electronics
Specialty: Microwave Electronics
Assigned: RADC
Colleague: Mr. R. H. Chilton

Dr. Russell James Niederjohn
Associate Professor
Electrical Engineering Department
Marquett University
1515 W. Wisconsin Avenue
Milwaukee, Wisconsin 53233

Degree: Ph.D., Electrical Engineering
Specialty: Speech Processing
Assigned: RADC
Colleague: Capt Robert Curtis

Dr. Theodore Jerome Sheskin
Assistant Professor of Industrial Engineering
Cleveland State University
Cleveland, OH 44115

Degree: Ph.D., Industrial Engineering
Specialty: Operations Research
Assigned: RADC
Colleague: Mr. Jerry Klion

RADC (Griffiss) Continued

Dr. Robert Guy Van Meter
Department of Mathematical Sciences
State University College
Oneonta, NY 13861

Degree: Ph.D., Mathematics (Algebra)
Specialty: Finite fields
Assigned: RADC
Colleague: Capt Kenneth E. Wilson

Dr. Ralph M. Weischedel
Assistant Professor
Stat & Computer Science
University of Delaware
Newark, DE 19711

Degree: Ph.D., Computer Science
Specialty: Artificial Intelligence
Assigned: RADC
Colleague: Mr. William E. Rzepka

SAM (Brooks)

Dr. Thomas Jefferson Jones
Associate Professor
Engineering Department
Trinity University
San Antonio, TX 78284

Degree: Sc.D., Electrical Engineering
Specialty: Electronic Control Systems
Assigned: SAM
Colleague: Mr. Kent Gillingham

Dr. Demetrius Dante Venable
Assistant Professor Of Physics
Saint Paul's College
Lawrenceville, VA 23868

Degree: Ph.D., Physics
Specialty: Physics
Assigned: SAM
Colleague: Dr. John Toboada

Dr. James Milton Verlander, Lecturer
Department of Biology
Texas A & M University
College Station, TX 77843

Degree: Ph.D., Physiology
Specialty: Elect Activity of Brain
Assigned: SAM
Colleague: Major Gibbons

AFHRL-FT (Williams)

Dr. Hergert Anthony Colle
Department of Psychology
Wright State University
Dayton, OH 45431

Degree: Ph.D., Psychology
Specialty: Psych; Human Performance
Assigned: AFHRL-FT
Colleague: Mr. James Smith

AFHRL-FT (Luke)

Dr. John Altman Seevers
Department of Mechanical Engineering
Washington State University
Pullman, Washington 99163

Degree: Ph.D., Engineering
Specialty: Dynamic Systems Analysis
Assigned: AFHRL-FT (Luke)
Colleague: Mr. Bill Hopkins

AFWL (Kirtland)

Dr. Richard Alan Anderson
Professor of Physics
Physics Department
University of MO-Rolla
Rolla, MO 65401

Degree: Ph.D., Physics
Specialty: Physics and Spectroscopy
Assigned: AFWL
Colleague: Mr. Steve Davis

Dr. Martin D. Bradshaw
EECS Department
University of New Mexico
Albuquerque, NM 87131

Degree: Ph.D., Elec Engineering
Specialty: Electromagnetic Fields
Assigned: AFWL
Colleague: Dr. J. Phillip Castillo

Dr. Wayne Alexander Charlie
Department of Civil Engineering
Colorado State University
Fort Collins, CO 80523

Degree: Ph.D., Civil Engineering
Specialty: Geotechnical Engineering
Assigned: AFWL
Colleague:

Dr. Richard Lee Redington
Professor of Chemistry
Texas Tech University
Lubbock, TX 79409

Degree: Ph.D., Physical Chemistry
Specialty: Molecular Structure
Assigned: AFWL
Colleague: Mr. Leroy Wilson

Dr. Harold D. Southward
Professor, Electrical Engineering Dept
University of New Mexico
Albuquerque, NM 87131

Degree: Ph.D., Physics
Specialty: Solid State Physics & Devices
Assigned: AFWL
Colleague: Lt Col Peter D. Tannen

Dr. Stephen Gene Wells
Department of Geology
University of New Mexico
Albuquerque, NM 87131

Degree: Ph.D., Geology
Specialty: Geomorphology/Surficial Pro.
Assigned: AFWL
Colleague: Capt Alber R. Schenker, Jr.

1977 USAF-ASEE SUMMER FACULTY RESEARCH PROGRAM

SPONSORED BY

THE AIR FORCE OFFICE SCIENTIFIC RESEARCH

CONDUCTED BY

AUBURN UNIVERSITY AND OHIO STATE UNIVERSITY

PARTICIPANT'S FINAL REPORT

NITRONIUM SALT SYNTHESIS

PREPARED BY:	Alton J. Banks, Ph.D.
ACADEMIC RANK:	Lecturer
DEPARTMENT and UNIVERSITY:	Department of Chemistry Texas A & M University
ASSIGNMENT:	
(Air Force Base)	Edwards AFB
(Laboratory)	Rocket Propulsion Laboratory
(Division)	Solid Rocket Propellant (MK)
(Branch)	Propellant Formulation (PA)
USAF Research Colleague	Claude Merrill, Ph. D.
DATE:	19 August 1977
CONTRACT NO:	F 44620-75-C-0031

NITRONIUM SALT SYNTHESIS

by

Alton J. Banks

ABSTRACT

The preparation of nitronium salts and the efficiency of these salts as nitrating agents has been investigated. In addition, other nitrating agents have been examined. The efficiency of these agents has been compared utilizing two model systems: nitrobenzene and α-fluoroacetophenone.

The nitration of nitrobenzene was accomplished in 94% yield using the nitronium and nitrosonium fluorosulfonate salts under very mild conditions. The degradative nitration of α-fluoroacetophenone was accomplished but in much lower yields.

ACKNOWLEDGMENT

The author is grateful to the AFOSR for support of the summer Research Program and to ASEE and Auburn University for administration of the program. A special note of thanks is extended to Mr. Fred O'Brien for his efficient administration. His efforts have made the program both enjoyable and productive.

The author is sincerely appreciative of the assistance and friendship of Dr. Claude Merrill. The personnel at the Chemistry Branch/EAFB also deserve many thanks for their efficient assistance. The author would also like to express thanks to Dr. Richard Weiss and Dr. Lawrence Quinn whose hospitality has made the stay here enjoyable.

LIST OF TABLES

1. Nitration Efficiency for Nitrobenzene

2. Nitration Efficiency for α-fluoroacetophenone

INTRODUCTION

The use of nitro compounds in propellants requires an efficient synthetic method for their production. Since nitration is commonly thought to occur via the nitronium ion (NO_2^+)[1], substances either containing or capable of producing the nitronium ion have been used as nitrating agents. The most common nitrating system in use is the mixed acid (HNO_3/H_2SO_4) system, which gives the nitronium ion in a medium of high dielectric constant. Nitronium salts, particularly those with fluoroanions, have also been used in a variety of conditions as nitrating agents. The major drawback in the use of the nitronium salts is the high cost of the source of the fluoroanion.

The objectives of this project are, therefore, twofold: (1) devise a method for synthesis of nitronium salts which is more cost-effective and; (2) determine the nitration efficiency of these salts under various conditions. As models for nitration efficiency two systems were chosen: nitrobenzene and α-fluoroacetophenone.

EXPERIMENTAL

A Preparation:

1. Anhydrous nitric acid - To 133 ml of nitric acid (90% reagent) 69 ml of oleum (65%) was added dropwise. This mixture was distilled under vacuum (~150 mm) and the fraction boiling between 40-50°C was collected.

2. Nitronium Fluorosulfonate - Vials containing nitrogen tetroxide (N_2O_4) and peroxydisulfuryldifluoride ($F_2S_2O_6$) were connected to a vacuum line. Nitrogen tetroxide was warmed slightly and allowed to pass into the vial containing the $F_2S_2O_6$. A white solid formed immediately upon contact. After a sufficient quantity of nitronium fluorosulfonate was formed, the non-condensible gases were evacuated. The solid was characterized by melting point, IR and Raman spectra. The melting point (196-199° decomp) compares well with the previously published m.p. (200° decomp).[2] IR bands (2350, 1660, 1420, 1380, 1170, 1070, 950, 760, 590, and 560 cm^{-1}) and Raman bands (2320, 1400, 1300, 1280, 1170, 760, 740, 410, 400 cm^{-1}) also agree with published data.[3]

3. Nitronium Fluorosulfonate & Nitrosonium Fluorosulfonate (mixture)

Into 6.8 ml of FSO_3H (11.8g - 0.12 mole) chilled in an ice/water bath N_2O_4 (3.6g - 0.04 mole) was bubbled with rapid stirring. The addition occurred over a period of ~20 minutes. As the addition of N_2O_4 nears completion, a white solid forms. The solid is filtered (with vacuum) while nitrogen is blown over the filtration funnel. As the contents of the flask solidify completely, the filtration step was

dispensed with in later preparations with no apparent effects in the reaction.

In an attempt to increase the ease of formation of the salt, the fluorosulfonic acid was poured into 100 ml of distilled acetonitrile, and N_2O_4 was bubbled into the solution which was chilled in an ice/water bath. Although no immediate decomposition was apparent, when the stoppered flask was stored in the refrigerator overnight, a noticeable darkening of the solid was observed. Storage of the solution for an additional 24 hours resulted in a reddish solid and a red-brown solution. The decomposition products were not characterized and all subsequent preparations were carried out with no solvents present.

The melting point (73-74° decomp) indicates that the solid is indeed a mixture (NO_2SO_3F + $NOSO_3F$, literature melting point for NO_2SO_3F 200°C[2]).

The white solid is very hygroscopic, and reacts with nujol, even in a glove bag. Infrared spectra are therefore taken using the solid pressed between silver chloride plates. The hygroscopic nature of the salts precluded the use of KBr plates or KBr discs as reaction with these materials occurs almost immediately upon contact. IR bands of the mixture agree with published bands for the nitronium and nitrosonium fluorosulfonate.[3] No attempt was made to separate the two salts.

4. Nitronium Methanesulfonate - Into 7.8 ml (0.12 mole) of CH_3SO_3H, placed in an ice/water bath, was bubbled 3.6g of N_2O_4 (0.04 mole) with vigorous stirring. Crystals were not observed until the ice/water bath

had been removed and the temperature of the flask approached ambient temperature (~27°). The flask was allowed to remain at room temperature for approximately two hours and refrigerated (5°C) overnight. The cold mixture was vacuum filtered under nitrogen with a fritted-glass funnel. The solid decomposed with evolution of NO_2 as filtration proceeded. No further attempts were made to synthesize this compound.

B. Nitrations with Nitrobenzene:

1. Reactions without solvent

To 15.8g of mixed fluorosulfonate salt (.08 moles total) was added nitrobenzene (4.8g - .04 mole). The mixture was stirred at room temperature for 24 hours, poured over ice, and extracted with methylene chloride. The CH_2Cl_2 layer was dried with anhydrous magnesium sulfate and evaporated till crystals formed. The product, m-dinitrobenzene, was obtained in 65% yield (4.2g). The reaction was carried out at 50°, using the same molar ratios, for periods of 8 hours - with a yield of 90% of the theoretical - and a period of 24 hours - with a theoretical yield of 85%. Reaction workup and isolation using these variations was carried out as described above.

2. Reactions in methylene chloride

a. To 25 ml of CH_2Cl_2 was added 2.4g of nitrobenzene (0.02 mole) and 5.6g of nitronium fluorosulfonate (0.04 mole). The solution was chilled in an ice/water bath as the nitrobenzene was added, warmed to room temperature and heated to reflux (37°C) for 24 hours. The reaction workup proceeded as described in the previous section. The product, m-dinitrobenzene, was obtained in 94% of the theoretical yield, (3.1g) and

characterized by melting point, IR spectrum, and liquid chromatography.

b. The reaction was repeated replacing the nitronium salt with the mixed salt (15.8g - .08 moles total). All other conditions were identical. Product was obtained in 94% of theoretical yield (3.1g).

c. A mixture of 2.1 ml (.04 mole) of concentrated sulfuric acid and 1.8 ml (.04 mole) of concentrated nitric acid was added to a solution of 2.4g of nitrobenzene in 25 ml of CH_2Cl_2. The reaction was carried out under identical conditions to those described above. The yield obtained was 88% of theoretical.

d. Dinitrobenzene (3.3g - .02 mole) was dissolved in 10 ml CH_2Cl_2, and NO_2SO_3F (5.6g - .04 mole) was slurried in 20 ml CH_2Cl_2. The dinitrobenzene was added over a period of 5 minutes to the nitronium salt slurry. The mixture was heated at CH_2Cl_2 reflux (37°C) for 24 hours. Dinitrobenzene was recovered unchanged. No trace of trinitrobenzene was found.

3. Reactions in Fluorosulfonic Acid

a. Nitrobenzene (4.8g) was added dropwise to a solution of NO_2SO_3F (5.6g) in 30 ml of FSO_3H which had been chilled in an ice/water bath. After the mixture warmed to room temperature, it was heated for three hours at 90-100°C. Dinitrobenzene (5.7g) was obtained in 87% of theoretical yield.

b. Anhydrous HNO_3 (7.4g) was added dropwise to fluorosulfonic acid (6.8 ml). The flask was chilled in an ice bath, and nitrobenzene (7.8g) was added dropwise with stirring. Fluorosulfonic acid (13.6 ml)

was added and the mixture heated to 90-100°C for one hour. Product was obtained in 90% of the theoretical yield (9.7g).

Workup for both these reactions followed the procedure outlined in section B1.

C. Nitrations with α-Fluoroacetophenone:

α-Fluoroacetophenone was obtained from Aerojet Solid Propulsion Company and used without further purification.

1. Reactions in methylene chloride

a. Anhydrous nitric acid (3.3g - .05 moles) was added to 20 ml of CH_2Cl_2. To this mixture, cooled in an ice/water bath, FSO_3H(3 ml - .05 moles) was added, whereupon the white solid, NO_2SO_3F formed. A solution of α-fluoroacetophenone (1.44g - .01 moles) in 10 ml of CH_2Cl_2 was added dropwise over a period of 10 minutes. The mixture was heated at reflux (37°C) for 1 hour, cooled, and then quenched by pouring over ice. The mixture was extracted three times with 30 ml portions of CH_2Cl_2. The CH_2Cl_2 layer was extracted three times with 30 ml portions of a saturated sodium bicarbonate solution, and evaporated to dryness. The solid which resulted was identified as nitro-α-fluoroacetophenone (m.p. 91-92°C, lit. m.p. 95°C.[4] Elemental analysis for $C_8H_6NO_3F$ % calc: C 52.46, H 3.28, N 7.65; %obs: C 53.18, H 3.34, N 7.74) and was obtained in 53% of theoretical yield.

b. To fuming nitric acid (90% - 76.1g), which had been chilled in an ice/water bath, was added a solution of α-fluoroacetophenone (5g - .04 mole) in 15 ml CH_2Cl_2. The mixture was rapidly heated to reflux (37°C) and maintained at that temperature for 24 hours. The reaction was then quenched by pouring over ice and the workup carried out as described in the previous section. Nitro -α-fluoroacetophenone was isolated in 56% yield (3.7g).

c. α-fluoroacetophenone (3g - .02 moles) was dissolved in 10 ml of CH_2Cl_2 and added dropwise to 9.45g of NO_2SO_3F slurried in 25 ml of CH_2Cl_2. The mixture was heated to 37° for 24 hours. The solution was decanted off an orange-yellow solid which formed during the course of the reaction. As some unreacted nitronium salt had been occluded by the orange-yellow solid, treatment of the solid mass with acetone resulted in the rapid decomposition of the nitronium salt and tarring of the solid. No attempt was made to characterize the tar. The decanted solution was neutralized with $NaHCO_3$ (saturated solution), extracted twice with CH_2Cl_2 (25 ml portions), and acidified with HNO_3 to pH4. Two extractions with CH_2Cl_2 yielded 1.3g of yellow solid identified as nitrobenzoic acid (IR bands: 2600-3100, 1700, 1610, 1530, 1475, 1350 cm^{-1}). Only a crude melting point was obtained (130° - lit. value for 2-nitrobenzoic acid 140°). The nitrobenzoic acid was obtained in 36% yield.

2. Reactions in fluorosulfonic acid

Anhydrous nitric acid (3.5g - .05 mole) was poured into FSO_3H (15 ml) and cooled in an ice/water bath. α-fluoroacetophenone (1.5g - .01 mole) was dissolved in 15 ml of CH_2Cl_2 and added dropwise over a period of 10-15 minutes. The mixture was then heated slowly to a temperature of 70°C and maintained at that temperature for 3 hours. The workup was identical to that described in section 1a. Nitro-α-fluoroacetophenone (0.57g) was obtained in 28% yield.

3. Reactions in nitric acid (90%)

α-fluoroacetophenone (2.0g) was added to 20 ml of nitric acid (90%) and heated to 90°C for 30 minutes. The reaction was quenched by pouring over ice and placed in refrigeration overnight. A solid formed and was filtered off. The solid, identified by IR spectrum, melting point and mass spectrum as nitro-α-fluoroacetophenone, was obtained in 52% yield (1.4g).

DISCUSSION

Nitronium salts have been used for several years as nitrating agents with a wide variety of solvents.[5] A major problem with nitrations using these salts is the cost of the salts. The low yields associated with many of these reactions add an additional hindrance. The synthesis of such salts usually includes reaction of a nitrogen oxide (preferably N_2O_5) with a strong acid (e.g. FSO_3H).

$$N_2O_5 + 3HSO_3F \longrightarrow 2NO_2^+SO_3F + H_3O^+ + SO_3F^- \quad (1)$$

Other methods for generating these salts have been investigated and their nitrating efficacy has been checked using two model systems: nitrobenzene and α-fluoroacetophenone. The synthesis of nitronium salts has followed two paths:

$$N_2O_4 + F_2S_2O_6 \longrightarrow 2NO_2^+SO_3F^- \quad (2)$$

$$N_2O_4 + 3HSO_3X \longrightarrow NO^+ + NO_2^+ + H_3O^+ + 3SO_3X^- \quad (3)$$

(where X = F-, CH_3-)

The preparation of nitronium salts by the first method (Reaction 2) is desirable as separation from other products is averted, while the higher cost and unavailability of peroxydisulfuryl difluoride renders the second method (Reaction 3) more desirable. Separation of the nitronium and nitrosonium salts will be difficult and has not been attempted in this study - although the separation should prove worthwhile. In the nitration of nitrobenzene with the mixed salt, the yield of dinitrobenzene was identical to that obtained using the nitronium salt prepared by Reaction 2.

The reaction utilizing the mixed salt appeared to go much faster than the reaction using the nitronium salt - although a kinetic study has not been done.

The ionic nature of these nitronium salts was confirmed spectroscopically by Ingold et. al..[6] The necessity for a strong electron-withdrawing moiety on the acid (Reaction 3) is indicated by the stability of the nitronium fluorosulfonate towards dissociation while the nitronium methanesulfonate decomposes during isolation. Replacement of fluorine with chlorine to form nitronium chlorosulfonate (Reaction 1) led rather to the formation of nitryl chloride and SO_3^2.

Two model systems were investigated to compare the efficiencies of these nitrating species. In the first model system, nitrobenzene was chosen as the moiety to be nitrated. Since the aromatic ring is deactivated by the nitro group, an increase in the yield of dinitrobenzene should indicate favorable nitrating conditions. A wide variety of reaction conditions was tested and the yields of dinitrobenzene calculated (See Table 1). One notes that in experiments 4 and 5 yields of 94% were obtained. This is an appreciable increase over the mixed acid (HNO_3/H_2SO_4) under the same conditions. These conditions are also less drastic than those used in the production of dinitrobenzene from nitrobenzene (95° with fuming $HNO_3$and concentrated H_2SO_4)[7] and the mole ratios of nitrating agent to nitrobenzene are much lower. An attempt to synthesize trinitrobenzene from dinitrobenzene with NO_2SO_3F was unsuccessful.

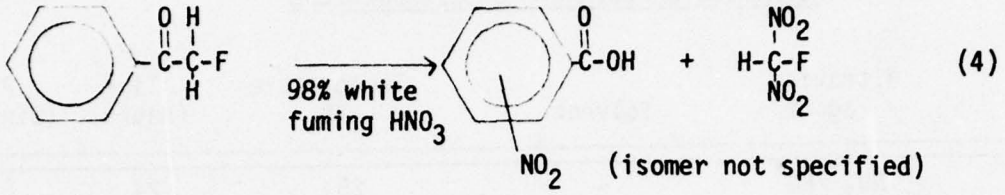
The second model system undertaken was the nitration of α-fluoroacetophenone. The nitration of α-fluoroacetophenone has been reported to

TABLE 1

NITRATION EFFICIENCY FOR NITROBENZENE

Experiment Number	Nitrating agent	Solvent	Temperature °C	Time (Hours)	Percent Yield (Dinitrobenzene)
1	NO_2^+/NO^+ (mixed salt)	-	25	24	65
2	(mixed salt)	-	50	8	90
3	(mixed salt)	-	50	24	85
4	(mixed salt)	CH_2Cl_2	37	24	94
5	(mixed salt)	CH_2Cl_2	37	24	94
6	HNO_3/H_2SO_4	CH_2Cl_2	37	24	88
7	NO_2SO_3F	FSO_3H	90-100	3	87
8	Anhydrous HNO_3	FSO_3H	90-100	1	90

produce nitrobenzoic acid and fluorodinitromethane (FDNM) according to reaction (4).[8]



(4)

Our original intention was to monitor the amount of fluorodinitromethane produced as a measure of nitration efficiency. Table 2 presents a summary of reaction conditions. Attempts were made to isolate the FDNM from all layers in every reaction. As the report cited indicated decomposition of the FDNM with time, it is possible that trace amounts may have been formed; however, attempts to find FDNM by IR and UV spectra, thin layer and liquid chromatography or separation by fractional distillation were unsuccessful. The report also indicated maximum yields of FDNM (16%) occurred at 120°C, 15 psi pressure with a reaction time of 31 minutes. The major product of the nitration under the conditions in this project was nitro-α-fluoroacetophenone, with nitrobenzoic acid also being produced. This nitration has been previously reported, using HNO_3/H_2SO_4 as nitrating agent, with the major product, m-nitro-α-fluoroacetophenone, obtained in 66% yield.[4]

As can be seen from Table 2, the production of nitro-α-fluoroacetophenone can be accomplished in medium yields under mild conditions. When very strong conditions (Experiment No. 4) are used a low yield is obtained, probably due to decomposition of the α-fluoroacetophenone. As tarring

TABLE 2

NITRATION EFFICIENCY FOR α-FLUOROACETOPHENONE

Experiment Number	Nitrating Agent	Solvent	Temperature (°C)	Time (Hours)	Percent Yield (Nitro-α-fluoroacetophenone)
1	Anhydrous HNO_3	CH_2Cl_2	37	1	53
2	90% HNO_3	CH_2Cl_2	37	24	56
3	NO_2SO_3F	CH_2Cl_2	37	24	*
4	Anhy. HNO_3	FSO_3H	70	3	28
5	90% HNO_3	90% HNO_3	90	0.5	52

* 36% (for nitrobenzoic acid)

occurred when α-fluoroacetophenone was placed in contact with concentrated sulfuric acid this decomposition appears feasible.

Future efforts should include duplication of the reaction conditions cited in the report (reference 8) to assure the presence of FDNM. Also, the synthesis of nitronium trifluoromethanesulfonate should give further information regarding stability of these nitronium salts. The separation of the nitronium and nitrosonium salts should also prove enlightening.

REFERENCES

1. C. K. Ingold, Structure and Mechanism in Organic Chemistry, Cornell University Press, Ithaca, N. Y., (1953).

2. D. R. Goddard, E. D. Hughes, and C. K. Ingold, J. Chem. Soc., (1950), 2569.

3. M. DePorcq-Stratmains, and P. Vast, J. Chem. Phys. Physicochim. Biol., (1970), 67(5), 1002

4. F. Bergmann, A. Kalmus, and E. Breuer, J. Amer. Chem. Soc., 79, 4178, (1957).

5. G. A. Olah and S. J. Kuhn in Friedel-Crafts and Related Reactions, Vol. III, part 2, Interscience Publishers, New York,(1964).

6. C. K. Ingold, D. J. Millen, and C. Poole, Nature, 158, 480, (1946).

7. L. F. Fieser and M. Fieser, Advanced Organic Chemistry, p. 676 Reinhold Publishers, New York, (1961).

8. Aerojet Solid Propulsion Company, Report LAK-M-9.

1977 USAF-ASEE SUMMER FACULTY RESEARCH PROGRAM

SPONSORED BY

THE AIR FORCE OFFICE SCIENTIFIC RESEARCH

CONDUCTED BY

AUBURN UNIVERSITY AND OHIO STATE UNIVERSITY

PARTICIPANT'S FINAL REPORT

SYNTHESIS OF FLUORODINITROETHYLNITRAMINES

PREPARED BY:	Catherine H. Banks, Ph.D
ACADEMIC RANK:	Research Associate
DEPARTMENT AND UNIVERSITY:	Department of Chemistry Texas A & M University
ASSIGNMENT:	
(Air Force Base)	Edwards AFB
(Laboratory)	Rocket Propulsion Laboratory
(Division)	Solid Rocket Division (MK)
(Branch)	Propellant Formulation(PA)
USAF Research Colleague:	Claude Merrill, Ph.D
DATE:	August 19, 1977
CONTRACT NO:	F44620-75-5031

SYNTHESIS OF FLUORODINITROETHYLNITRAMINES

by

Catherine H. Banks, Ph.D.

ABSTRACT

When presently used propellants are burned, they create a great deal of smoke. This is due to the perchlorates that are used in the fuel mixtures. Research is in progress at this time to find compounds to replace the perchlorates and thus, hopefully, reduce or eliminate the smoke problem. This project deals with the synthesis of fluorodinitroethylnitramines which will be used in the fuels with the hope of averting the problem. One nitramine, N,N'-bis(fluorodinitroethyl)-N,N'-dinitroethylenediamine, was successfully synthesized, characterized, and prepared in large quantity. Synthesis of other nitramines were investigated.

ACKNOWLEDGMENT

The author wishes to thank Dr. Claude Merrill for his time and assistance during the project. The personnel of the Chemistry Laboratory also are due thanks for their assistance throughout the summer.

INTRODUCTION

Due to the smoking of the presently used propellants, the Air Force has undertaken a research program to find alternate compounds. Perchlorates, presently used as part of the fuel mixture in the rockets cause the smoking problem. A new compound in theory would need to give little or no smoking. Elimination of chlorine and a large percentage of oxygen would give a highly energetic compound, which would have less chance of producing smoke upon combustion. For these reasons, the class of nitramines was chosen for study. Condensation of fluorodinitroethanol (FDNE) with the amines would increase the energetics of the molecule by the very nature of the side chain. The compounds investigated in this project were, therefore, fluorodinitroethylnitramines.

DISCUSSION

Several fluorodinitroethylnitramines were of interest in this project. The first one studied was N,N'-bis(fluorodinitroethyl)-N,N'-dinitroethylenediamine (1). This nitramine has been previously prepared by Frankel and co-workers.[1]

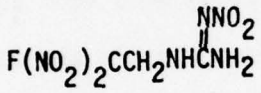
The procedure used is rather straight forward and an overall yield of 76% was obtained.

$$F(NO_2)_2CCH_2OH + H_2NCH_2CH_2NH_2 \rightarrow F(NO_2)_2CCH_2NCH_2CH_2NCH_2C(NO_2)_2F \xrightarrow{HNO_3/H_2SO_4} F(NO_2)_2CCH_2\underset{\underset{NO_2}{|}}{N}CH_2CH_2\underset{\underset{NO_2}{|}}{N}CH_2C(NO_2)_2F$$

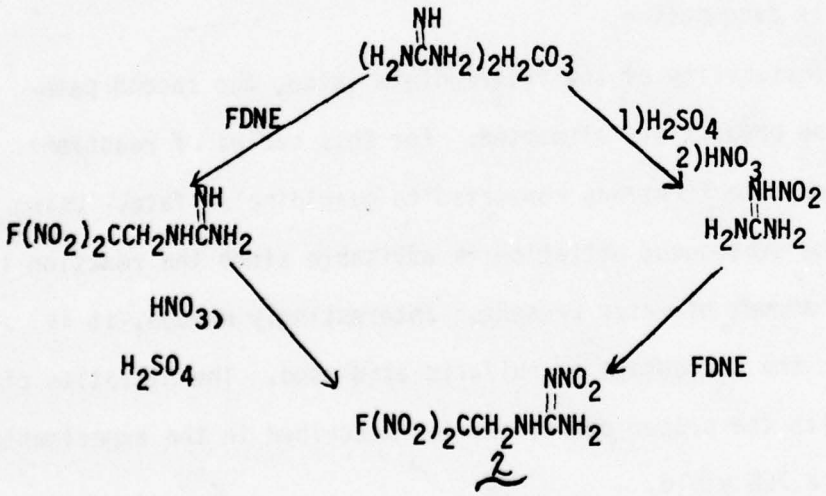
(1)

Mass spectra, infrared spectra, melting point, and elemental analysis confirmed the identity and purity of compound 1. This nitramine seems to be quite stable. It appears not to be impact or shock sensitive and has a rather high melting point (148-149°C). Approximately 100g was prepared for future testing by the permanent research personnel. If the testing seems favorable, the synthetic yield and mild reaction conditions would enhance the compounds desirability for use on a large scale.

The second nitramine which was investigated was derived from guanidine. One such derivative has been synthesized from guanidine at the present time:



No details of the synthetic route are available at this time. Therefore, the problem was approached as if no work had been done with these compounds. Two avenues of approach were investigated:



The nitramine 2 is a compound which might feasibly be obtained by

either route shown. It is not, although, the only compound which can be prepared or be useful. In the first route, the condensation of FDNE and guanidine can yield products other than the monoalkylated one shown, eg:

$$F(NO_2)_2CCH_2NHC(=NH)-NHCH_2C(NO_2)_2F$$

$$F(NO_2)_2CCH_2NH-C(=NCH_2C(NO)_2F)-NHCH_2C(NO_2)_2F$$

Maximum alkylation would yield five fluorodinitroethyl groups on the guanidine's nitrogens, i.e. replacement of all amine protons. The condensation product obtained was an amber oil. The solubility properties (insoluble in CH_2Cl_2, soluble in EtOH) were such as to suggest that a condensation did occur. The infrared spectra showed the presence of $-NO_2$, and -F. After isolation, the oil began to evolve a gas which was not identified. Mass spectrum observed is not that of FDNE or guanidine, but is compatible with their condensation product. The compound was shown to be slowly decomposing.

Due to the instability of the intermediate amine, the second pathway to the desired product was attempted. For this series of reactions, the guanidine carbonate first was converted to guanidine sulfate. Using the sulfate in the subsequent nitration is advisable since the reaction is sensitive to the amount of water present. Interestingly enough, it is also sensitive to the percentage of sulfuric acid used. The nitration did proceed nicely with the proper conditions (as described in the experimental section) to give a 76% yield.

The structure of nitroguanidine has been debated for many years.[2] The position of the nitro group and the possibility of a dimer remain subjects of study. The structure used here is one which is chosen for convenience and not proposed as the actual structure.

The nitroguanidine previously prepared was allowed to react with FDNE, hopefully, to afford the desired nitramine 2. Several reaction conditions were tried, as can be seen in the experimental section. All of them showed no reaction to have occurred.

Addition of base to the reaction mixture was tried in hope of facilitating the reaction. In theory, the base should remove a proton from the nitroguanidine, and that the resultant anion would then attack the FDNE to form the condensation product. Pyridine was first base used, but no condensation products were obtained. Due to the time limitation of this project, no further work could be done. The fluorodinitroethylguanidinenitramines seem to be promising compounds, but the synthesis will take repeated attempts with various conditions.

EXPERIMENTAL

GENERAL: All starting materials were commercially available and used as received. Infrared spectra were taken on Beckman IR 4240 spectrophotometer. Elemental analyses and mass spectra were run within the laboratory. Melting points are uncorrected.

N,N'-bis(fluorodinitroethyl)-ethylenediamine: The procedure used was that of M. Frankel and co-workers.[1] Ethylenediamine (4ml,5.8g,9.6×10^{-2} moles) was added to 100 ml HOH. Addition of 84 ml (114g, 0.192 moles FDNE) of a 26% solution (in CH_2Cl_2) of fluorodinitroethanol then followed. The two mixture was stirred with maximum phase contact for 1 hour. At the end of this time the phases were separated. The HOH layer was extracted with 30 ml CH_2Cl_2. This extraction was added to the CH_2Cl_2 layer and in turn was extracted with 2 x 40 ml of HOH. It was then dried over $MgSO_4$ and solvent evaporated to afford 30.5g (96% yield) of desired amine as an amber oil. Yields of the amine varied from 98-80% during various preparations. IR bands showed the presence of the $-NO_2$ and -F groups: 1600, 1310, 1080, 850, and 800 cm^{-1}. The oil was used without further purification.

N,N'-(Bisfluorodinitroethyl)-N,N'-dinitroethylenediamine (1):

The procedure used was essentially that of M. Frankel.[1] N,N'-(Bisfluorodinitroethyl)-ethylenediamine (15g, 4.1×10^{-2} moles) was added dropwise at 0°-10° to a solution of 90% HNO_3 (75 ml), conc. H_2SO_4 (60 ml), and 65% oleum (15 ml). The mixture then was heated to 45-50° for 1 hour. At the end of this time, the solution was cooled and poured over ice. The

desired product separated as a white powder, was collected and then washed repeatedly with water. The crude material was recrystallized from methanol/water and gave 15g (78.2% yield) of pure 1, mp 148-149°. IR bands at 1595, 1310, and 1160 cm^{-1} confirmed the presence of the nitramine linkages and fluorine. The mass spectrum of the compound confirmed its structure with m/e: 211, 166, 119, 90, 80, 72, 64, 60, 46, 42, 30, 28. Elemental analysis showed the compound to be pure,% calc: for $C_6H_8F_2N_8O_{12}$: C, 17.06; H, 1.89; N, 26.54; found: C, 17.04; H, 1.86; N, 26.49.

Attempted Preparation of Fluorodinitroethyl guanidines:

METHOD A: In order to explore the condensation reaction between guanidine and fluorodinitroethanol, the first attempt employed very mild reaction conditions. Guanidine carbonate (1.0g, 5.5×10^{-3} moles) and fluorodinitro- (7.2 ml, 1.66×10^{-2} moles) were allowed to react using the reaction procedure designed for the preparation of N,N'-bis(fluorodinitroethyl)-ethylenediamine. Upon workup, no condensation product was found.

METHOD B: Guanidine carbonate (1g, 5.5×10^{-3} moles was dissolved in 50 ml of water. To this solution was added 7.2 ml (1.66×10^{-2} moles) of a 26% CH_2Cl_2 solution of FDNE. The mixture was stirred vigorously and formalin (1.34 ml, 1.66×10^{-2} mole) was added. The two phase reaction then was heated to 40°C for 3 hours. At the end of this time, the solution was cooled to room temperature and then extracted with CH_2Cl_2 (2 x 30 ml). The aqueous layer was evaporated and the residue again extracted with $CHCl_2$ (2 x 30 ml). The remaining oil was treated with 95% ethanol. A precipitate (unreacted guanidine) formed and was removed. The ethanolic solution was evaporated

To yield an amber oil (1.5g). This oil seemed to decompose upon standing. Infrared of the oil showed the presence of $-NO_2$ (1560 cm^{-1}, 1350 cm^{-1}) and -F (1080 cm^{-1}). The mass spectrum showed no weight over 153. The fragmentation pattern indicated the decomposition of a condensation product and not merely a mixture of reactants. This reaction also was run using a 1:5 ratio of amine: FDNE with the same results (formation of an unstable product).

Preparation of Nitroguanidine:

The procedures used are based on two known preparations of this compound:[3,4] Guanidine carbonate (18g, 0.1 mole) was slowly added to conc. H_2SO_4 (10 ml. 0.2 moles). After the evolution of CO_2 had ceased, the wet salt was dried leaving guanidine sulfate (31.4g, 0.2 mole).

The prepared guanidine sulfate (1g, 6.36×10^{-3} moles) then was added slowly to a cooled (0-10°) mixture of 5 ml HNO_3 (90%) and 2 ml of 65% oleum. The reaction mixture was kept below 20° during the addition and then allowed to warm to room temperature. The reaction mixture was stirred for 2 hours and then poured onto cracked ice. The desired product precipitated and was isolated by filtration. Recrystallization from water gave 0.5g (76%) of pure product, mp 248-9°C(lit mp 235-257°, depending on rate of heating[2,3]).

Condensation Reaction With Nitroguanidine

METHOD A: This procedure is similar to the condensation with guanidine carbonate. Nitroguanidine (0.25g, 2.4×10^{-3} moles) was added to 15 ml of 95% ethanol, and the resultant slurry was stirred rapidly. To this mixture 2.7 ml of a 26% CH_2Cl_2 solution of FDNE and 1 ml of formalin was added.

The reaction mixture was heated to 45° for 2 hours, cooled to R. T. and then stirred 36 hours. At this point, the unreacted nitroguanidine was removed by filtration and the solvent removed to afford unreacted fluorodinitroethanol and additional nitroguanidine. No product was obtained. Recovery of nitroguanidine was quantitative.

METHOD B: This procedure follows Method A in stoichiometry and mode of addition. The solvent used was CH_2Cl_2 and the reaction mixture was stirred for 36 hours. Work-up followed that of Method A to yield only the starting materials. Nitroguanidine was recovered quantitatively.

METHOD C: This procedure followed Method A in stoichiometry and mode of addition. The solvent used was anhydrous methanol. Pyridine (1 ml) was added to the reaction mixture to afford a base initiation of the reaction. After stirring at room temperature for 36 hours, the mixture quenched and analyzed as in Method A. Nitroguanidine was recovered quantitatively, and thus no reaction product was obtained.

REFERENCES

1. E. F. Witucki, G. L. Rowley, N. N. Ogimachi, and M. B. Frankel, Jr. Chem. Eng. Data, 16, 373 (1971).

2. "The Chemistry of the Nitro and Nitroso Groups", part 1, ed. Henry Feuer, (1970).

3. "Organic Synthesis", Coll. Vol. 1, p.399.

4. P. Auberstein, Mein Pourdres, 30, 143-57 (1948), C.A., 45:8250C.

1977 USAF-ASEE SUMMER FACULTY RESEARCH PROGRAM
sponsored by
THE AIR FORCE OFFICE SCIENTIFIC RESEARCH
conducted by
AUBURN UNIVERSITY AND OHIO STATE UNIVERSITY

PARTICIPANT'S FINAL REPORT

SUBMICRON PARTICLE SIZE MEASUREMENTS IN ACETYLENE-OXYGEN AND ALUMINUM-OXYGEN FLAMES

Prepared by:	James F. Driscoll Ph D
Academic Rank:	Assistant Professor
Department and University:	Department of Aerospace Engineering University of Michigan
Assignment:	Edwards AFB Rocket Propulsion Laboratory Technology Division Supporting Technology
USAF Research Colleague:	David Mann Ph D
Date:	August 26, 1977
Contract No.:	F44620-75-C-0031

SUBMICRON PARTICLE SIZE MEASUREMENTS IN ACETYLENE-OXYGEN AND ALUMINUM-OXYGEN FLAMES

by
James F. Driscoll

ABSTRACT

A new technique for making in situ measurements of aerosol particles in the submicron size range has been investigated. Making use of the broadening of a monochromatic laser line produced by random particle motion the technique has been shown to be suitable for application to measurements in high temperature environments at pressures from 20 torr to 1 atmosphere.

Particle diameters were measured in acetylene/oxygen and aluminum/oxygen flames. Particle size was determined as a function of mixture ratio and height above a flat-flame burner which was operated as a premixed acetylene/oxygen/nitrogen flame. Sizes were found to vary from 40 to 250 nm as height above the burner varied from 0.5 to 3.0 cm. Little variation was found as a result of mixture ratio changes. The flame was found to have large gradients in particle size on a scale comparable with the measurement volume (1 mm^3). Sizes measured from electron microscope photographs of soot particles collected from the flame showed reasonable agreement with those calculated from scattering measurements. Size determinations in an aluminum/oxygen flame were made for the first time using this technique. A mean diameter of 280 nm was found 40 cm downstream of the primary reaction zone at 20 torr pressure.

The results of this study have demonstrated the utility of the technique for determination of mean, submicron particle sizes and have pointed the way toward methods for improvements to yield particle size distributions, as well.

ACKNOWLEDGMENT

This summer research project has been an especially gratifying research experience due in large part to the effort and time spent by Dr. Dave Mann, the AFRPL research colleague on the project, and by Dr. Wheeler McGregor. Technical discussions with Dr. McGregor and assistance in obtaining a flat flame burner are appreciated. The author is indebted to Dr. Richard Weiss, Chief Scientist at AFRPL, for information and assistance in making this summer research visit possible. Technical assistance was provided by Mr. Mel Abrego during the burner setup and by Mr. Thomas Owens, who made the electron microscope photographs. Dr. Larry Quinn and Mr. Fred O'Brien deserve special recognition for their efforts that resulted in excellent coordination between participants and AFRPL.

INTRODUCTION

The formation of particulates in solid rocket motors is important from two standpoints: in the combustion zone particulates can alter propellant burning rates and radiative heat transfer which have a direct effect on combustor design; in the exhaust plume particulates are a primary cause of nozzle radiative heating, two-phase flow energy losses, and plume visibility. In order to develop improved smokeless propellants, fundamental research has been initiated by the Air Force Rocket Propulsion Laboratory to determine the physical mechanisms that occur in condensation processes. The occurrence of alumina ($A\ell_2O_3$) condensation in rocket motors, in particular, cannot yet be adequately predicted. To experimentally study the $A\ell_2O_3$ condensation processes, there is a direct need to develop and apply diagnostic techniques for measurement of particulates in the early stages of formation, i.e. sub-micron sizes.

Historically, sampling probes have been used to collect particles of interest which are viewed using electron microscopes. Results can be ambiguous because the collection process promotes particle agglomeration due to electrostatic charges of the particles. In order to study the nucleation and agglomeration processes, in situ sizing techniques are required. In this research program, a new optical diagnostic technique, laser Doppler spectroscopy[1], is used to perform in situ size measurements of submicron particulates.

RESEARCH OBJECTIVES

The goal of this research program has been to make in situ measurements of mean particle diameters in the 1.0-100 nm size range in flowing, high temperature gases. These measurements are in direct support of an AFRPL in-house experimental study of alumina particle condensation. The diagnostic technique selected for this program was laser Doppler spectroscopy (LDS). The LDS technique is independent of particulate properties and provides local submillimeter spatial resolution. Hinds and Reist' have demonstrated the feasibility of using LDS for submicron spherical particle size measurements. Penner, Bernard and Jerskey[2] first applied the LDS technique to flowing gases for the case of an ethylene-oxygen flame.

A secondary goal of this program was to create solid particulate aerosols with specific properties to be used in the validation of the experimental measurement technique. The aerosol had to be as monodisperse as possible, with particle mean diameter in the .001 to 0.1μm range. The aerosol should be uniformly distributed in a steady, high temperature (500°K-2500°K) gas flow. The above conditions are difficult to achieve and have been most closely realized by using specially designed laboratory flames[3]. Two types of flames were used to produce aerosols. An acetylene-oxygen flat flame burner provided carbon particles in the desired size range. An aluminum-oxygen flame was later used to provide alumina particles.

Validity of the LDS results was to be investigated by performing the following: (a) Scattering angle was to be varied and results compared to LDS theory. (b) Measurement location in the flame was to be varied to see if particle size increased with height above the burner. (c) Electron microscope photographs of sampled particulates were to be used to determine if LDS results were reasonable.

LASER DOPPLER SPECTROSCOPY-THEORY

The use of the LDS technique for particle size measurements is now described. Hinds and Reist[1] first demonstrated the feasibility of LDS for use in stationary aerosols. Using concepts first proposed by Benedek[4], they developed a theory for monodisperse aerosols and described effects of aerosol polydispersity. Good agreement between LDS experimental results, theory and electron microscope measurements were found for controlled monodisperse aerosols of latex spheres in the range 500 to 1,100 nm. Penner, Bernard and Jerskey[2] later included theoretical effects of gas flow velocity and demonstrated the feasibility of LDS application to an ethylene-oxygen flame.

When laser light is scattered by submicron aerosol particles, the Brownian motion gives rise to frequency fluctuations of the scattered light. The broadening of the scattered line profile can be measured, from which the particle diffusion coefficient can be inferred. Mean particle diameter is determined from the Stokes-Einstein diffusion relation, modified for large Knudson number effects. Small particles undergoing rapid Brownian motion cause greater broadening than large particles, thus the measured power spectrum of light fluctuations may be related to a mean particle diameter.

A schematic of a laser scattering system and the resulting power spectrum is shown in Figure 1. Consider two particles that are travelling through the focused submillimeter laser beam with equal average directed velocities U, but with opposite instantaneous components of random velocity. In general, radiation scattered from moving particles will be Doppler shifted by an amount Δf given by:

$$\frac{\Delta f}{f} = \frac{\bar{V}}{c} \cdot (\bar{e}_s - \bar{e}_i) \qquad (1)$$

where unit vectors $\bar{e}_s$ and $\bar{e}_i$ are in the scattered and incident radiation directions, respectively, vector $\bar{V}$ is the particle velocity, c is the velocity of light, and f is the laser frequency (on the order of 10^{14} Hz). The homodyne power spectrum (cf Figure 1b) resulting from many scattering centers simultaneously passing through the focal volume has been shown to have a Lorentzian profile[1]. The halfwidth (HW) of the power spectrum for the case of a stationary, monodisperse aerosol whose size is much greater than the molecular mean free path is given by:

$$HW = \frac{16\pi D}{\lambda^2} \sin^2 \left(\frac{\theta}{2}\right) \qquad (2)$$

where θ is the scattering angle, λ the wavelength and D the particle diffusion coefficient, describing the mean squared length travelled by a particle per unit time. For the case of Reynolds number based on particle diameter approaching zero, the Stokes-Einstein diffusion coefficient is given by

$$D = kT\,(1 + 1.648\ell/d)/3\pi\mu d \qquad (3)$$

which is valid for molecular mean free path ℓ less than particle size d or, as

is more typically the case, greater than d. Thus, homodyne power spectrum halfwidth is given by:

$$HW = \left(\frac{4\pi}{\lambda} \sin \frac{\theta}{2}\right)^2 \frac{kT}{3\pi^2 \mu d} \left(1 + 1.648 \frac{\ell}{d}\right). \quad (4)$$

The measurement of the homodyne spectral halfwidth, combined with knowledge of local gas temperature T and viscosity μ, yields a unique value of particle size in a stationary, monodisperse aerosol. For polydisperse aerosols the particle size given by Equation 4 is some mean size.

Turbulence that occurs on a scale less than the focal volume dimension can also broaden the homodyne spectrum. Larger scale turbulence causes a time varying Doppler shift of the optical spectrum, but has no effect on the measured homodyne spectrum. The homodyne spectrum is affected only by velocity variations simultaneously detected within the focal volume. The particle sizing technique is thus insensitive to turbulence and mean flow gradients providing that the focal volume is significantly smaller than the scale of local velocity variations.

In addition to the homodyne spectrum also shown in Figure 1b is the heterodyne spectrum centered in the megahertz range which can be produced by optical mixing of two coherent laser beams at the focal point. The heterodyne spectrum arises from the doppler shift due to the mean flow velocity and is employed in laser doppler velocimetry techniques. Thus the average flow velocity, average Brownian motion velocity and mean particle size can be measured by simultaneously recording the homodyne and heterodyne spectra.

APPARATUS AND DATA REDUCTION

Two separate facilities were employed in this study to produce submicron sized particulates in high temperature flowing gases. Initially, soot particulates were produced in an acetylene-oxygen flat flame. During the latter part of the program, alumina particles were produced in a low pressure aluminum-oxygen diffusion flame and identical diagnostics were employed.

A photograph of the acetylene-oxygen flame is shown in Figure 2. A flat flame burner provided a relatively uniform and stable premixed flat flame. The burner surface consisted of bundled copper rods between which the premixed acetylene ($C_2 H_2$), nitrogen and oxygen flowed. The 1-1/8 inch diameter burner surface was surrounded by an annular flow of nitrogen to stabilize the flame. The entire apparatus was water cooled. Gas flowrates were regulated and measured.

The aluminum-oxygen flame apparatus was designed and assembled at AFRPL. Aluminum vapor is produced by heating aluminum pellets in an alumina crucible to 1600°K at a pressure of 20 torr. The aluminum vapor is mixed with inert argon gas which flows upward. Oxygen is introduced above the crucible. Reaction occurs between the aluminum vapor and oxygen yielding a bluish flame. Light scattering from alumina particles is observed visually at a location 40 cm above the crucible, using a laser light source.

The light source was 100 milliwatt He Ne laser beam which was split into two beams and focused to intersect at the focal volume, allowing scattering to be

observed at 25° and 60° from the incident beam. A collecting lens of 15.2 cm focal length was used to focus the enlarged (3X) image of the focal volume on the surface of an RCA 4832 photo-multiplier tube. An interference filter centered at 632.8 nm with a measured halfwidth of 1.65 nm was used to block flame emission. Photomultiplier current was passed to ground through a 0.1MΩ resistor, providing a frequency response of 50 KHz. The amplified signal was observed on a Tektronix 465 oscilloscope and 315 Spectrum Analyzer, and was recorded as FM on analog tape at 60 inches per second (ips).

Recorded data were analyzed using a digital spectrum analyzer (Spectral Dynamics 360-35), which displayed the real time power spectrum, allowing time variations in the spectrum to be observed. Data were replayed at 15 ips, high pass filtered at 1 KHz (real time) and sampled at a 16 KHz sample rate. Each computed power spectrum was determined from 2.5 X 10^5 data points. Bandwidth of the entire data acquisition system was 25 KHz. Prior to data reduction for each run, system accuracy was checked using a calibration square wave, whose power spectrum consists of peaks at odd multiples of the square wave frequency, with an f^{-2} rolloff.

RESULTS AND DISCUSSION

The laser scattering system was assembled and applied first to the acetylene-oxygen flame. Carbon aerosol measurements were attempted first because soot formation in such flames is well documented[5]. Production of a relatively steady and monodisperse submicron aerosol is a difficult task and cannot be fully achieved with an acetylene flame. However, the LDS technique could be tested by: (a) varying the scattering angle and comparing results with theory, (b) varying measurement location in the flame and (c) comparing results with electron microscope photographs of carbon sampled from the flame.

Photographs of the laser scattering apparatus with the acetylene flame are shown in Figures 2 and 3. In this flame, flame emission was so intense that proper alignment of the optical system was crucial to obtaining sufficient scattering signal-to-noise. The 28 milliwatt laser power used in this study provided a typical signal to flame emission ratio of 25 and signal to shot noise ratio of 40. Within 0.5 cm of the burner surface, however, the scattered signal barely exceeded flame emission, making measurement of the smallest particles difficult.

Proper focussing was found to be critical for optimal scattering signal to flame emission signal. A thin sheet of plexiglass was placed in the attenuated laser beam and focused visually. A 0.5 mm pinhole was drilled in the back side of the phototube mount, allowing a direct visual line of sight down the optical collection axis when the phototube is removed. A second laser beam was used to provide scattering at a different angle (60°) than the first (25°); it was aligned to intersect the first beam at the measurement location. A liquid aerosol was then sprayed through the measurement location and each beam was focused and realigned separately. When the beam was out of focus, a one millimeter diameter column of scattered light appeared when viewing through the pinhole. Proper focus caused the collection lens to appear completely red, i.e. the laser beam filled the entire collection solid angle. Poor signal to noise results from deviations from best focus because the laser beam transmission solid angle fills only a fraction of the total collection solid angle, the

remainder being filled with flame emission. Final focus was obtained by viewing the scattered light for the desired acetylene-oxygen flame conditions. Through the pinhole, the flame background was barely visible with the laser off. With the laser on, the collecting lens appears filled with laser scattered light, and the phototube aperature is closed to focus on only the central portion of the beam. Focussing proved less crucial in the $A\ell$-O_2 flame since flame emission was negligible and large scattered signals were observed, in most cases.

Steady flame conditions were found to be highly desirable. The acetylene-oxygen flame appeared visually to be steady. The measured flame emission was relatively steady, with ± 10% intensity variations at frequencies of 5-15 Hz. However, the intensity of scattered laser light was not as steady. Regions containing gradients in flame emission oscillated in space over a distance of 1 mm. This oscillation was sufficient to observe 10-100 Hz changes in scattered light emission, which at times dropped to zero when few particulates passed through the focal volume. The intermittent nature of the aerosol occurrence made data reduction more difficult and introduced scatter in the results. Flame oscillations were observed to be due to room air currents, which could not be eliminated. At stoichiometric conditions with no particle formation, stable flame conditions occurred. It was concluded that to operate a rich acetylene-oxygen flame and to limit oscillations of carbon producing regions to less than 1 mm, an enclosed flame apparatus is necessary. A porous plug burner is also necessary to eliminate gradients that occur with our multiple-hole burner. However, flame oscillations that do occur do not in any way affect the measurement technique itself, since all signal fluctuations of frequency less than 1 KHz are filtered out during data reduction. In the enclosed $A\ell$-O_2 flame apparatus, a steady scattered light signal was always observed.

The acetylene flame began to emit intense visible radiation at a fuel-oxygen equivalence ratio (ϕ) of 1.9. The yellow appearance of the flame is generally accepted as an indication of carbon formation[5]. At ϕ=2.5, the bright white flame was an intense radiator of heat. The C/O ratio of the premixed gases is unity at ϕ=2.5, which theoretically indicates the limit of soot formation, since leaner mixtures will result in excess oxygen reacting with carbon produced to form CO. Appearance of a yellow flame at a somewhat leaner equivalence ratio than theoretically predicted is consistent with previous findings[5].

Results obtained for the acetylene-oxygen flame are shown in Figure 4. Typical power spectra of the phototube signal are shown in Figures 5, 6, and 7. Each power spectrum is obtained by Fourier Transforming 2.56×10^5 digital data points. The recorded analog phototube signal was sampled at 16 KHz; data was high pass filtered at 1 KHz. Shot noise is observed to be negligible since the power spectrum asymptotes to zero at high frequencies. Use of an analog spectrum analyzer directly attached to the phototube did not prove feasible since it did not afford the averaging capability of digital processing. Assuming a Lorentz line slope the power spectrum halfwidth (HW) was determined from the relation:

$$HW^2 = MHW^2 - f^2 \qquad (5)$$

Where MHW is the measured halfwidth (i.e. the frequency at which the power spectrum has decreased to one half the maximum measured value), f is the filter frequency (1 KHz), and HW is the actual halfwidth of an unfiltered Lorentzian curve centered at zero frequency.

Mean particle diameters, shown in Figure 4, were determined from the measured HW of the power spectra, using Equation 4. Flame temperature was calculated using the AFRPL ISP computer program, which determines flame temperature and equilibrium concentration of 26 flame species using updated JANNAF thermochemical constants. Calculated flame temperature had a strong dependence on the nitrogen flow rate.

Results obtained in the aluminum-oxygen flame are shown in Figure 8. A scattering angle of 45° and the measurement position 40 cm above the flame were fixed by apparatus window location. The scattered light signal had a constant d.c. component with superimposed 1-5 KHz fluctuations. Measured mean particle diameter varied between 240 and 280 nm for oxygen flowrates between 0.72 cc/sec and 1.1 cc/sec with corresponding argon flowrates of 1.50 cc/sec and 12.7 cc/sec.

Large scatter of $\pm$ 35% in the acetylene-oxygen flame data of Figure 4 is observed. Whether the scatter is due to actual variations in mean particle diameter or due to inaccuracies of the measurement technique cannot be deduced from this study. Further research is necessary to test technique accuracy using a monodisperse aerosol of known particle size and size distribution. It is highly probable that mean particle diameter in the flame does vary as much as the scatter in the data. Regions of carbon formation oscillated in the flame on a submillimeter scale, as described previously. In addition, particle size distributions in similar flames are quite broad at locations 3 cm above the flamefront. Wersborg[6] measured size distribution halfwidth points in a acetylene-oxygen flame to be $\pm$ 50% the mean particle diameter, due to nonuniform agglomeration of particles.

The data of Figure 4 indicates a definite trend of increasing particle size as height above the burner is increased. A theoretical increase of particle size with fuel-oxygen equivalence ratio has been postulated[6], but no definite trend was observed in this study. A typical power spectrum obtained for a location of 0.5 cm above the burner is shown in Figure 6. While initial particle formation and visible radiation occurs at a height of 0.1 cm, sufficient signal to noise was not achieved below a height of 0.5 cm. Scattered light was also not visible through the 1.6 nm bandpass interference filter. Particles at these locations are belived to be too small to detect with the LDS apparatus at temperatures of 2200°K. It is postulated by this author that the technique has a minimum detectable particle size due to particle radiation. As particle size decreases the particle radiation emitted decreases as d^2 while the Rayleigh scattered light decreases as d^6. This limitation will not exist at sufficiently low aerosol temperatures.

An increase in measured spectral halfwidth was observed as scattering angle θ increased from 25° to 60° as seen in Figures 5 and 7. Two incident beams were focused within the focal volume of the detection system which was fixed. When the 25° angle beam was used, the 60° angle beam was blocked, and vice versa. Theory describing laser doppler spectroscopy[1] predicts a $\sin^2 \theta/2$ dependence of spectral halfwidth, for a monodisperse aerosol. Measurements at the two angles were made to compare with theory, which predicts a spectral halfwidth increase of 5.26. For the various flame conditions selected, spectral halfwidth increased by factors between 3.3 and 4.2 as θ increased from 25° to 60°. These large measured changes are felt sufficient to confirm that the spectrum observed was broadened due to particulate Brownian motion. The difference between theoretical and mea-

sured angle variation effects is believed due to deviations from monodispersity. In fact, the differences between dual angle measurements and theory are proposed as a possible technique to determine the particle size distribution.

Electron microscope photographs were taken of carbon particulates sampled or a Nichrome wire at 3 cm above the burner. A typical example is shown in Figure 9. Particulates were observed to be in the 200 nm range, agreeing roughly with LDS results. The scanning electron microscope used was not capable of resolving particles smaller than 50 nm in this sample.

From this research study, several problems inherent to the LDS technique when used in polydisperse aerosols can be postulated. The mean diameter measured will not correspond to any of the commonly used characteristic diameters[3], such as Sauter mean diameter or surface area median diameter. The measured power spectrum will be an average of the broad spectra produced by small, fast moving particles and the narrow spectra of larger particles. The averaging process is further weighted because the latter spectra from large particles will be weighted much more heavily due to a d^6 dependence of Rayleigh scattering intensity. When only small particles are considered, a minimum detectable size also occurs when particle radiation, which varies as d^2, becomes larger than Rayleigh scattered radiation, which varies as d^6. At sufficiently low temperatures this limitation will not occur.

Other factors can contribute to the broadening of the homodyne power spectrum and thereby limit the applicability of the LDS technique. Time of flight broadening has been extensively reviewed in the literature since it gives rise to apparent turbulence in laminar flow systems. Time of flight broadening arises due to the finite duration of the scattered signal from each particle as it traverses the laser beam. The Fourier transform of a finite sine wave is not a delta function but has a Gaussian profile. Superposition of many simultaneous particle signals, each of finite duration and of random phase, results in a homodyne spectral halfwidth of:

$$\underset{TOF}{HW} = \frac{U}{2a} = \frac{U}{2\left(\frac{4\lambda}{\pi}\ \frac{F}{D}\ /\cos\frac{\theta}{2}\right)} \qquad (6)$$

where U is the flow velocity and a is the local beam diameter resulting from focussing laser beam of diameter D with a lens of focal length F. To measure particle size in high velocity flow fields, time-of-flight broadening is minimized by increasing the laser beam diameter, and thus sacrificing spatial resolution.

For the case of rocket exhaust plumes the maximum velocity aerosol measurable with LDS is calculated by insuring that collisional broadening, given by Equation (4) exceeds TOF broadening, Equation (6) by at least a factor of four yielding:

$$U_{MAX}(M/S) = 0.00486\ \frac{a}{d} \qquad (7)$$

For a typical rocket exhaust velocity of 1000 M/S, a laser beam diameter of 2 cm is required to measure particles in the 1.0-100 nm range. This calculation assumes 180° backscatter using an argon laser and 2000° plume temperature.

SUGGESTED FUTURE WORK

1. Particle size distribution measurements may be possible using LDS and a dual angle scattering system. Theoretical work and studies of an aerosol with a known size distribution (i.e. latex spheres) is needed to study biasing effects.

2. Maximum velocities at which LDS spectroscopy is applicable can be studied in jet or rocket exhausts and shock tubes.

3. Simultaneous measurements can be made of mean particle diameter using LDS, meah diameter using Mie theory, flow velocity, and possibly size distribution. Research is presently being conducted at the University of Michigan to study condensation processes with Mie scattering and laser velocimetry techniques. Holography and laser velocimetry is also being used in flame research.

4. The present LDS theory requires modification to apply to low pressure aerosols, as in rocket exhausts. Free molecular flow effects on the drag and diffusion of particulates need to be included in a more consistent manner.

5. Minimum detectable particle size is limited by signal to noise in flames. As particle size decreases, black body radiation decreases as d^2 yet Rayleigh scattered signal decreases as d^6. Improvement can be gained by narrowing the spectral bandpass below 1 nm or use of polarization filters and argon lasers.

CONCLUSIONS

1. A laser Doppler spectroscopy (LDS) system was assembled and used to measure mean particle diameters in the range 40-250 nm (0.04 to .25μm). Measurements were performed in an acetylene-oxygen flame and in a low pressure aluminum-oxygen flame.

2. Mean particle diameter in the acetylene-oxygen flame increased from 40 nm to 250 nm as height above the burner increased from 0.5 cm to 3.0 cm. No effect of varying equivalence ratio from 2.5 to 5.0 was detected. Steady carbon production could not be obtained because of submillimeter oscillations of flame gradients. Scatter in the results was $\pm$ 35%.

3. Electron microscope photographs indicate the presence of 200 nm particles, in approximate a greement with LDS results.

4. Optical allignment was crucial in the acetylene flame to achieve a high signal to flame emission ratio.

5. To check the validity of the technique, the scattering angle was varied from 25° to 60°. Measured spectral halfwidth increased by a factor between 3.3 and 4.2 depending upon flame conditions; a theoretical increase of 5.2 is predicted for monodisperse aerosols. The difference is attributed to deviations from monodispersity of the aerosol.

6. Measurements within 0.5 cm of the flame front were impossible due to low signal to noise. This is believed due to small particle size in this region. Flame emission which varies as d^2 exceeded scattered light, which decreases as d^6 as size decreases. Decreased spectral bandpass and larger laser power is recommended for future work in order to minimize effects of flame background emission.

7. In a polydisperse submicron spray, the measured particle diameter corresponds most closely to the largest particles present, due to a d^6 Rayliegh scattering intensity weighting function.

8. Alumina particulates were produced successfully in an aluminum-oxygen flame operated at 20 to 100 torr. LDS measurements indicate a mean diameter of 280 nm at a location 40 cm above the flame. Electron microscope photographs reveal a polydisperse aerosol with particles as small as 50 nm.

REFERENCES

1. Hinds, W. and Reist, P. C., "Aerosol Measurements by Laser Doppler Spectroscopy," Aerosol Science V. 3, p 501, 1972.

2. Penner, S. S., Bernard, J. M., and Jerskey, T., "Laser Scattering From Moving Polydisperse Particles in Flames, II. Preliminary Experiments," Acta Astronautica, V. 3, p 93, 1976.

3. Fuchs, N. A., and Sutugin, A. G., Highly Dispersed Aerosols, Ann Arbor Science Pub., Ann Arbor, 1970.

4. Benedek, G. B., Polarization, Matter, and Radiation, Presses Universitaires de France, Paris, 1969.

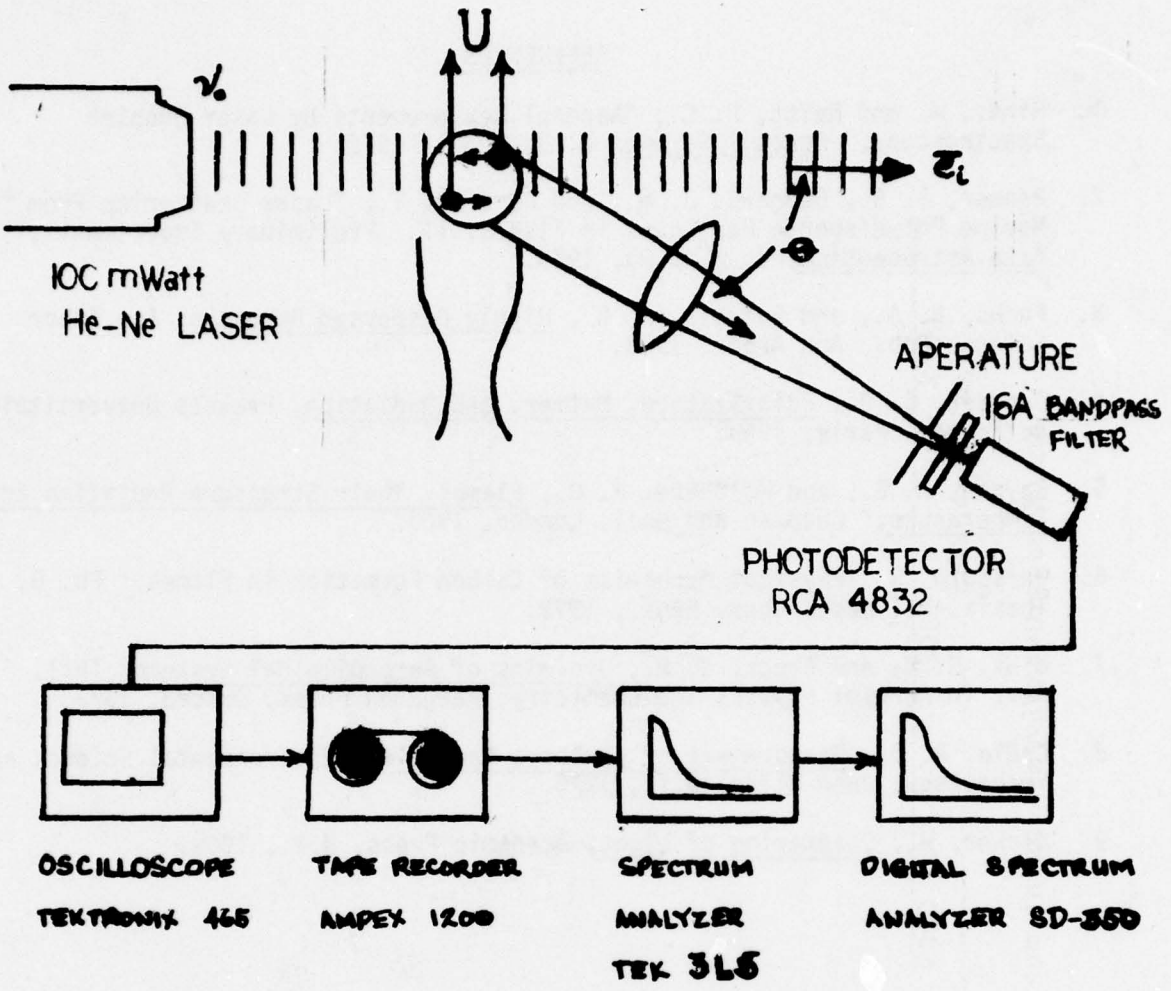
5. Gaydon, A. G., and Wolfhard, H. G., Flames, Their Structure Radiation and Temperature," Chapman and Hall, London, 1960.

6. Wersborg, B. "Physical Mechanism of Carbon Formation in Flames," Ph. D. Thesis, MIT Dept. Chem. Engr., 1972.

7. Hidy, G. M. and Brock, J. R., Dynamics of Aerocolloidal Systems, Intl. Rev. in Aerosol Physics and Chemistry, Pergamon Press, Oxford, 1979.

8. Cadle, R. D., Measurement of Airborne Particles, Environmental Science and Technology, John Wiley, N.Y., 1975.

9. Kerker, M., Scattering of Light, Academic Press, N.Y., 1969.



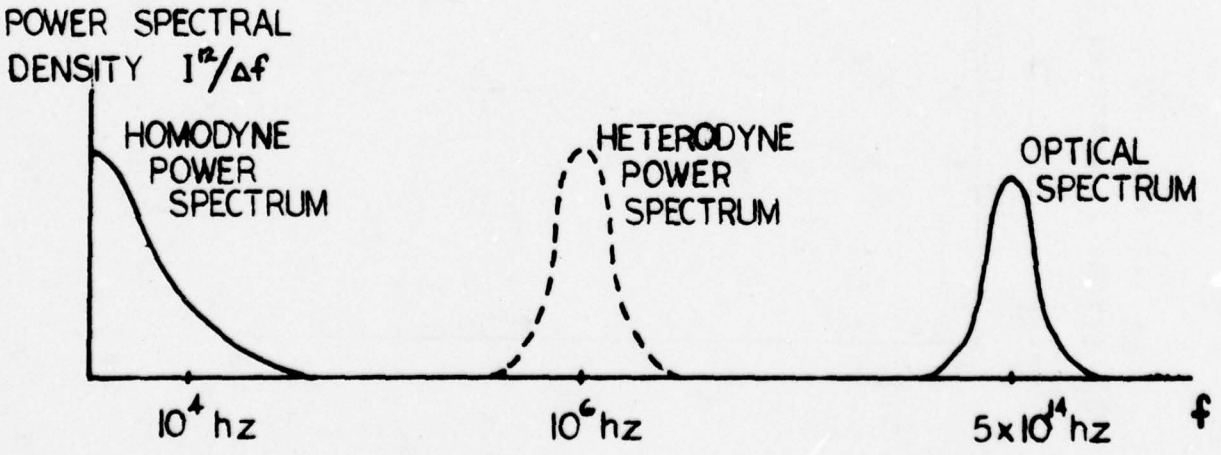


Figure 1, Optical Arrangement and Power Spectra

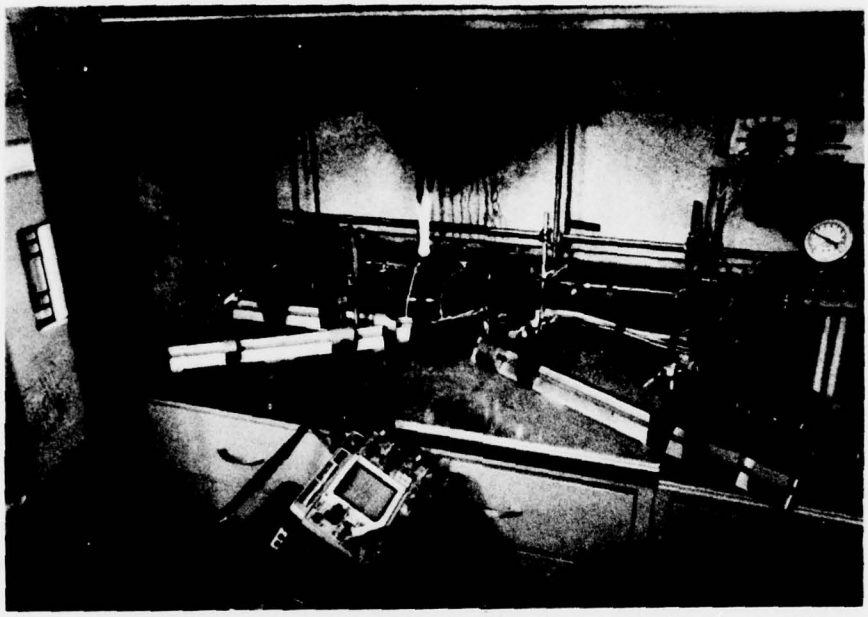


Figure 2. Acetylene-Oxygen Flame Apparatus and Optical System

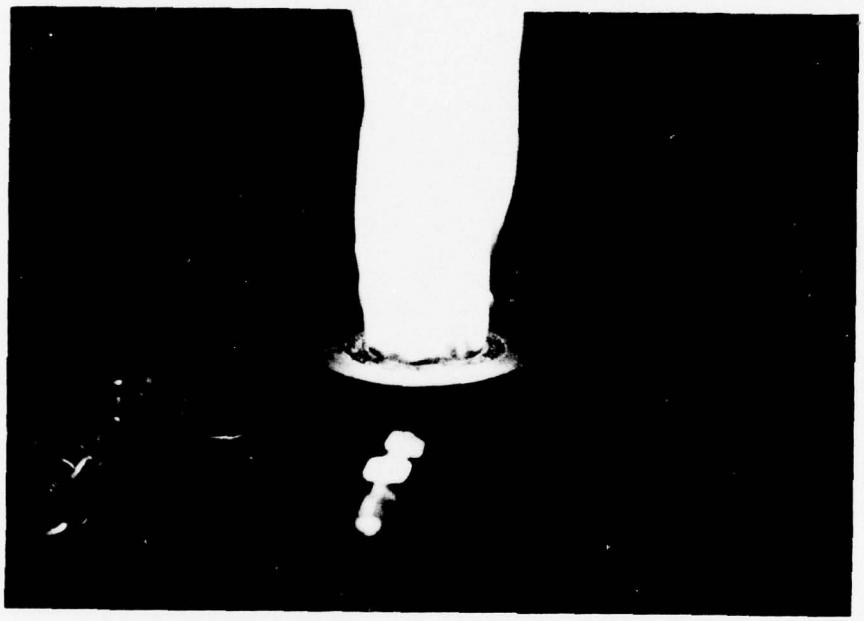


Figure 3. Flat Flame Burner Operated at Equivalence Ratio of 2.5

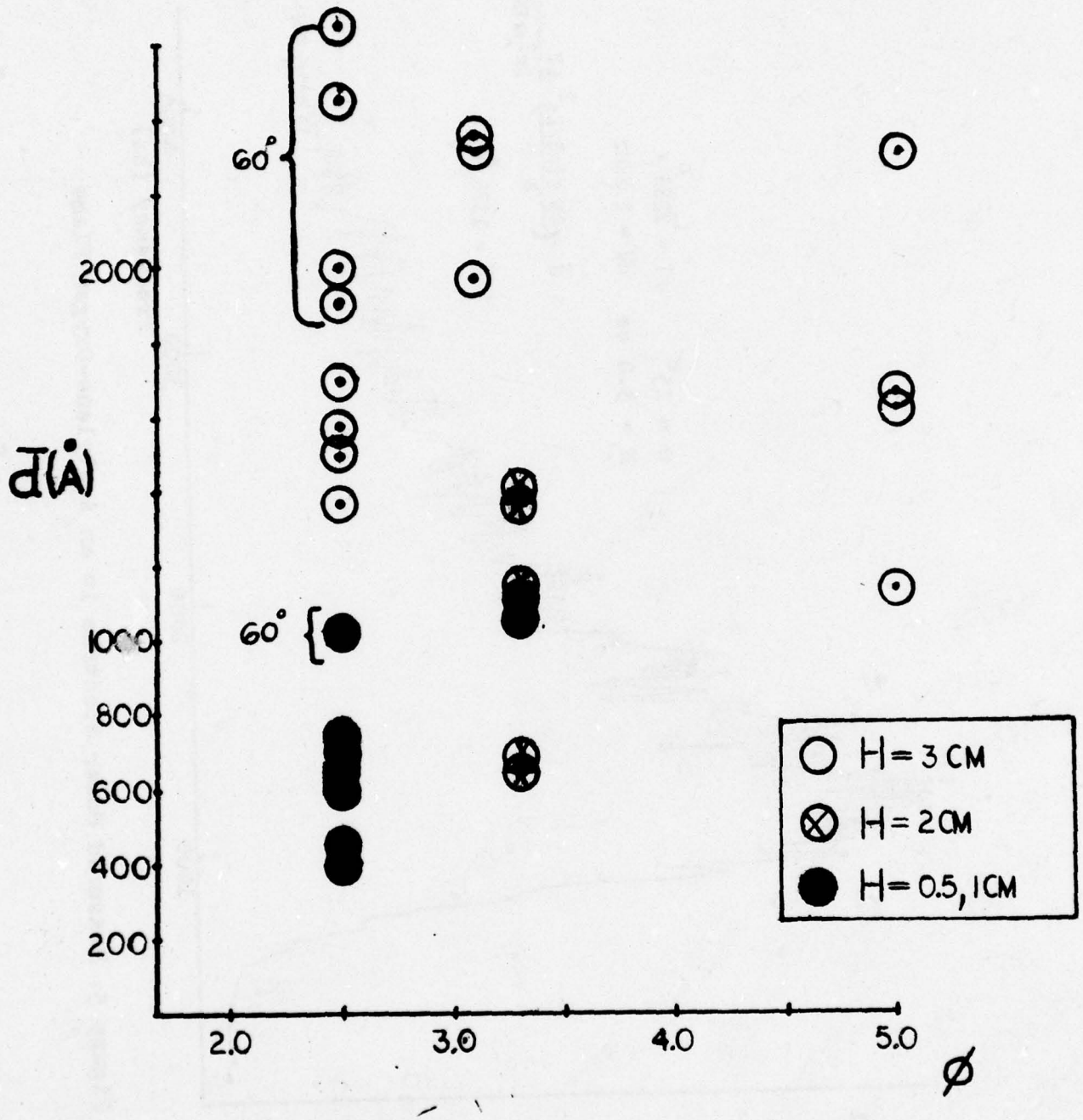


FIGURE 4. MEAN PARTICLE DIAMETER AT VARIOUS EQUIVALENCE RATIOS IN AN ACETYLENE OXYGEN FLAME

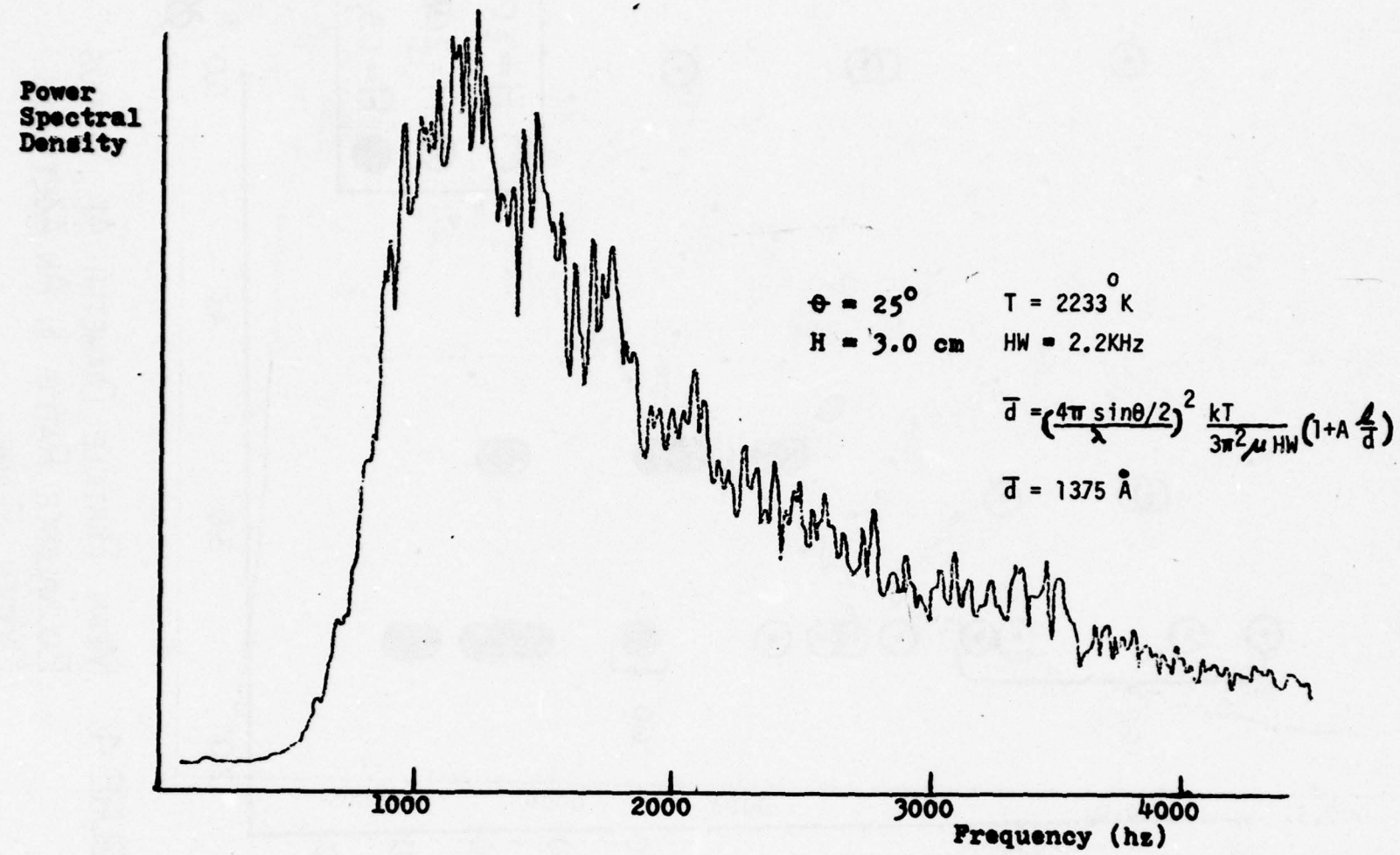


Figure 5. Measured Power Spectrum in an Acetylene-Oxygen Flame

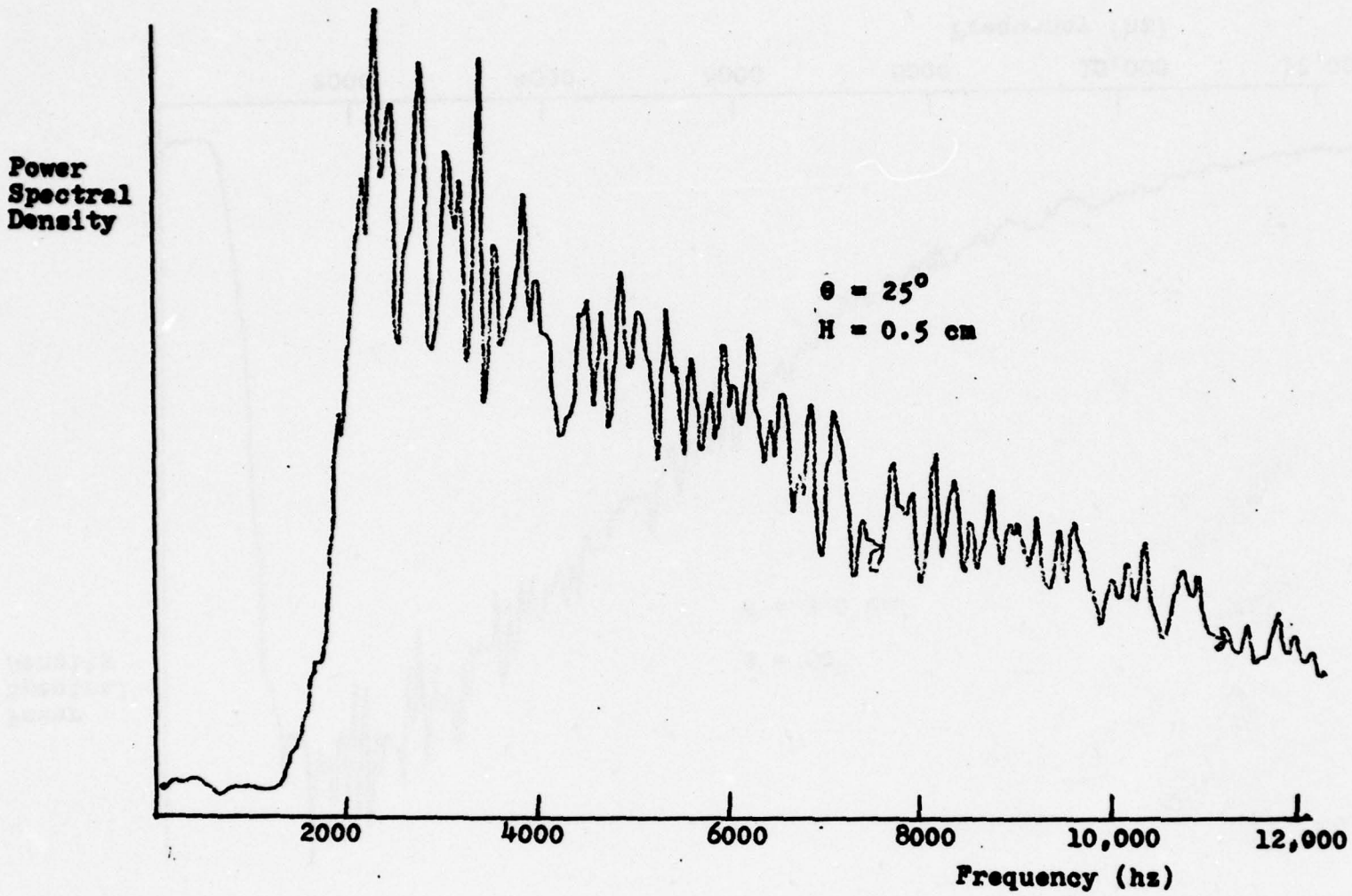


Figure 6.. Measured Power Spectrum in an Acetylene-Oxygen Flame

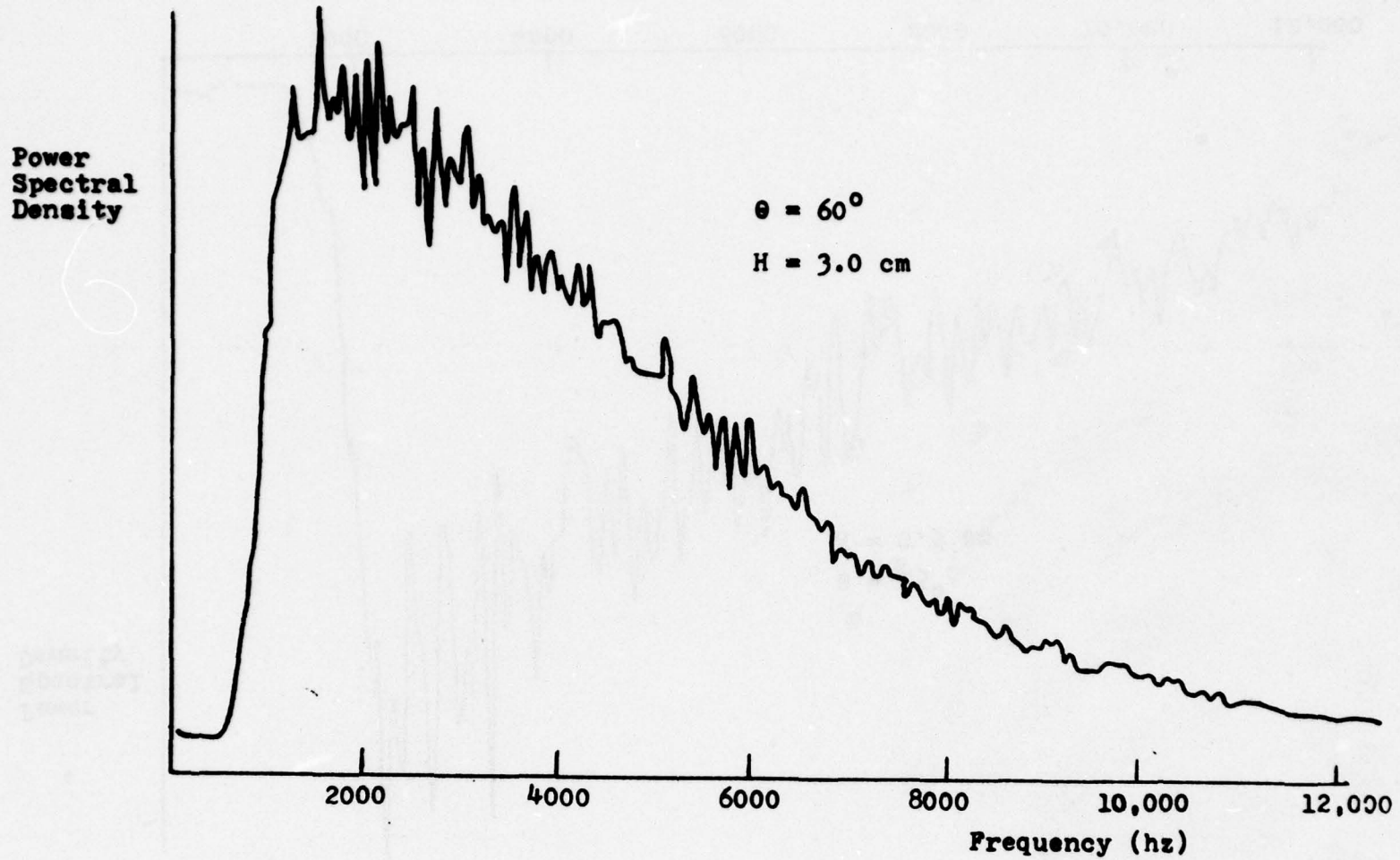


Figure 7. Measured Power Spectrum in an Acetylene-Oxygen Flame

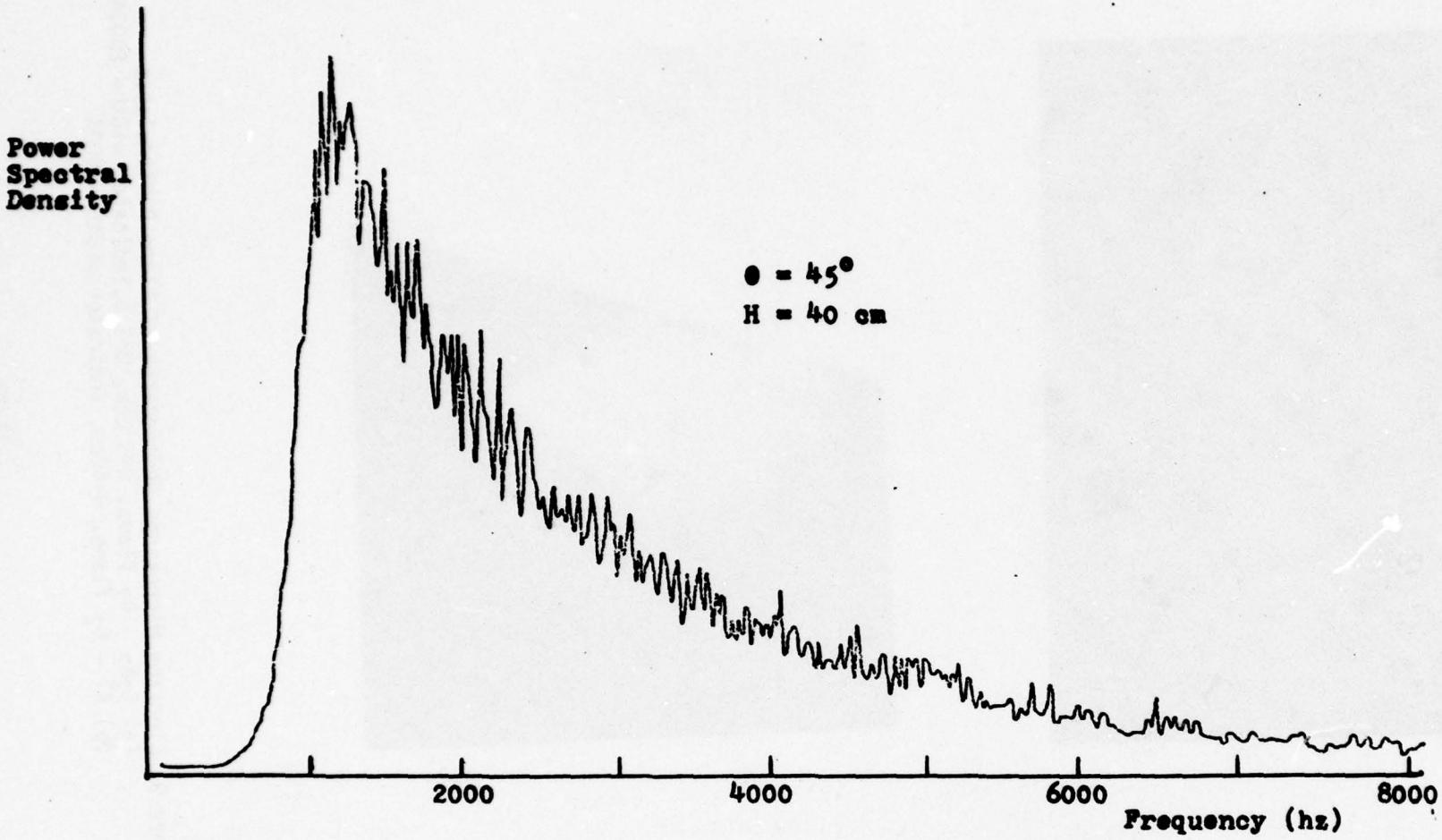
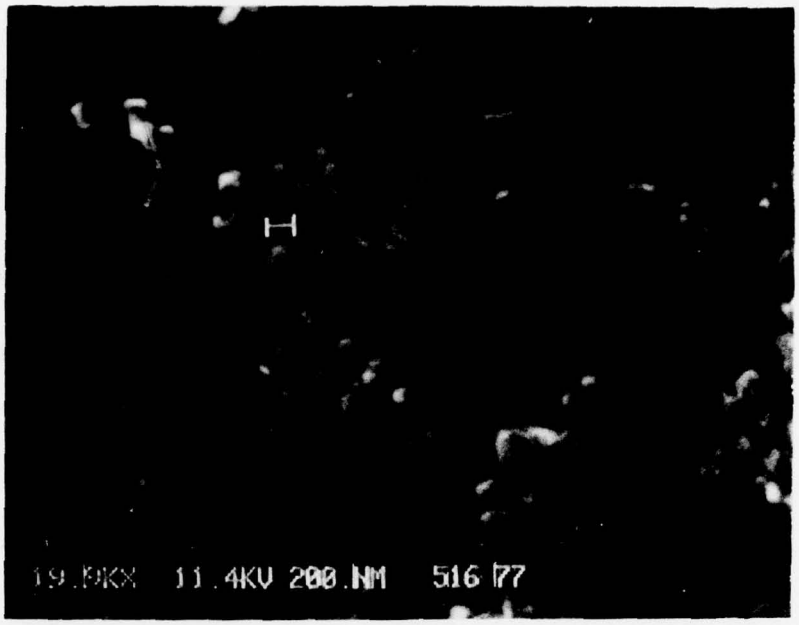


Figure 8. Measured Power Spectrum in an Aluminum-Oxygen Flame



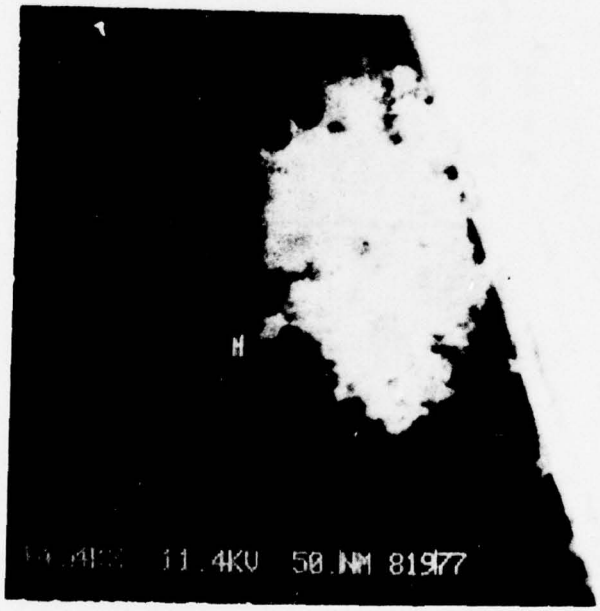


Figure 9. Electron Microscope Photographs of Flame Particulates
(a) C_2H_2 - O_2 flame, H=3.0cm, O=2.5,indicator width= 2000A
(b) Al - O_2 flame, H=40cm, indicator width = 500A

1977 USAF-ASEE SUMMER FACULTY RESEARCH PROGRAM

sponsored by

THE AIR FORCE OFFICE OF SCIENTIFIC RESEARCH

conducted by

AUBURN UNIVERSITY AND OHIO STATE UNIVERSITY

PARTICIPANT'S FINAL REPORT

SOLID TEFLON PROPULSION CONTAMINATION INVESTIGATION

Prepared by:	J. Keith Hartman, Ph.D.
Academic Rank:	Assistant Professor
Department and University:	Physics Department Canisius College
Assignment:	
(Air Force Base) (Laboratory) (Division) (Branch)	Edwards Air Force Base Rocket Propulsion Laboratory Liquid Rocket Division Space Propulsion Branch
USAF Research Colleague:	Lt. Sharon Pruitt
Date:	August 12, 1977
Contract No.:	F44620-75-C-0031

SOLID TEFLON PROPULSION

CONTAMINATION INVESTIGATION

by

J. K. Hartman

ABSTRACT

The design characteristics and operating principles of the solid Teflon pulsed plasma thruster are briefly discussed. An investigation of the present ground based contamination programs and space based contamination programs of the millinewton Teflon thruster is presented. The structure of the exhaust plume and the chemical nature of its constituents are examined in light of current experimental knowledge and the existing data on the effects caused by thruster efflux on spacecraft surfaces is compiled. Facility backscatter interactions are studied and their effect on particle efflux measurements is evaluated. Recommendations are made as to new experimental techniques that will improve the existing ground and space test procedures for measuring particle efflux and spacecraft contamination.

ACKNOWLEDGEMENT

The author is grateful to the Air Force Systems Command for their support of this summer research. A sincere thanks is due to ASEE and Auburn University and, in particular, Mr. Fred O'Brien, Dr. Lawrence Quinn, and Dr. Richard Weiss for their excellent planning and administration of this program. Their work has certainly made this summer more productive and enjoyable.

Lt. Sharon Pruitt, the author's research colleague, was very helpful in quiding the initial phase of the literature search and Dr. Robert Vondra was instrumental in providing physical and historical insight into the Teflon pulsed plasma thruster program. Further, the author would like to thank everyone in the Liquid Rocket Division for their encouragement and friendly demeanor. Also, Dennis Fitzgerald, Eugene Pawlik, Robert Cuffel and Lewis Pless at JPL, Dr. J. M. Sellen, Jr., and Sidney Zafran at TRW, Dr. David Hall at Aerospace Corporation, and Dr. S.J. Kowal of Johns Hopkins Applied Physics Laboratory were very candid with their comments and helpful in our discussions.

INTRODUCTION

As the designed life of satellites reaches the seven to ten year range, weight constraints begin to impose limits as to the amount of propellant that can be carried for stationkeeping, attitude control, and other spacecraft repositioning functions. Hence, propulsion systems with low specific impulse are placed at a severe disadvantage as compared to electric propulsion systems for adoption on missions requiring high total impulse. This has resulted in the development of a number of different types of electric thrusters delivering a high specific impulse. An excellent survey of the state of the art in electric propulsion is given in Reference 1. The solid Teflon pulsed plasma thruster is the only one that will be considered in this article.

The solid Teflon pulsed plasma thruster produces thrust by creating a high voltage, very high current electrical discharge across the face of the Teflon propellant as shown in Figure 1. The ignitor plug provides a small of amount of "seed" plasma to initiate the main discharge and the main discharge capacitor bank supplies the large quantity of electric charge needed. This current ablates the surface of the Teflon, creating a plasma slug, which is accelerated down the channel between the cathode and anode by volumetric magnetic forces[2] as shown in Figure 2. Very high exhaust velocities are attained, on the order of 25 km/sec[3], for the ionized portion of the plume in the millipound thruster. However, there is an appreciable amount of mass that is ejected as neutral particles with relatively low velocities. This significantly reduces the average specific impulse ($\approx$1600 sec)[4] that has been obtained in present thrusters.

The inhomogeneity and complexity of the exhaust plume, as well as the chemical nature of the plume constituents, has caused potential users to be wary of employing this device for control purposes on operational spacecraft. The Russians flew their first Teflon pulsed plasma thruster in 1964 aboard "Zond-2", a flight launched towards Mars[5]. Only three United States satellites (LES-6, TIP-2, TIP-3) have flown with Teflon pulsed plasma thrusters on board and, of these, only the LES-6 thrusters flown[6] in 1968 were able to be adequately tested in space. At the present time, pulsed plasma thrusters have not been accepted for flight on any future spacecraft and it is the purpose of this study to determine what needs to be done to improve user acceptance of these devices.

The general outline followed in assessing the capabilities of existing ground based contamination programs of the millinewton solid Teflon pulsed plasma thruster to meet user needs is as follows. First, a synopsis of the studies on plume characteristics is presented along with several new experimental techniques that may be used in determining plume characteristics and reducing the effect of facility backscatter on particle efflux measurements. The possible effects caused by exhaust particles impinging on various spacecraft surfaces is discussed next. Finally, recommendations and conclusions are made as to new experimental techniques for improving the existing ground and space test procedures so that users' fears of spacecraft contamination from the Teflon thruster efflux may be alleviated.

PLUME CHARACTERISTICS

A fair amount of information has been gathered on plume characteristics using a number of different experimental techniques. The major problem is that there has never been a sufficient number of experiments performed on one solid Teflon pulsed plasma thruster to completely characterize its operation. There has always been a continuing push to advance to higher energy discharges and higher thrust levels before operation at the previous level has been quantified. This fact, coupled with various experimental problems, has led to the existence of a body of knowledge that is only semi-quantitative, especially at the higher thrust level of the millipound thruster. In addition, while a qualitative understanding of the physics involved with the operation of pulsed plasma thrusters exists, theoretical treatments [7-9] to date have only had limited success in dealing with the complex physical behavior of the Teflon plasma. In this section of the report, previous experimental results on the characteristics of the exhaust plume of the solid Teflon thruster will be summarized and several areas for future work will be indicated.

The most complete collection of data exists for the LES-6 solid Teflon pulsed plasma thruster[6] developed by Fairchild Republic Co. for the MIT Lincoln Laboratory and flown in 1968. Most of the plume characterization data was collected after the thrusters were in space during a study that was undertaken with the primary aim of improving the understanding of the basic processes involved in the thruster operation so that a more efficient and higher thrust propulsion unit could be developed. The LES-6 thruster operated at a discharge energy of approximately 2 joules. However, upwards of 30% [10] of this energy was dissipated in the capacitor bank and not delivered to the plasma arc. Approximately 10^{-8} kg of Teflon was emitted per pulse, with 7-8% ionized and the rest oozing off the Teflon in the form of neutral particles. Spectroscopic observation of neutral lines showed that the neutral particles continued to leave the Teflon surface long after the discharge was complete. The average exhaust velocity was 3180 m/s, while the velocity of the plasma was between 32,000 m/s and 40,000 m/s depending on the measurement technique used. An interesting consequence of these velocities and the estimates of the percent of the discharge that is ionized is that the ions can account for all the specific impulse of the thruster. Several different experimental techniques have been employed[10-13] to gather data on the quantities of interest in the plume of the pulsed plasma thruster. Rather than quoting individual references and techniques, all information pertaining to each area of interest will be assembled in single paragraphs to try to present a coherent overview of the present knowledge.

The electron density in the plasma has been determined using a K-band microwave interferometer [10] and a multiple pass Mach-Zehnder interferometer[12] using a He-Ne laser. The microwave interferometer could not measure electron densities above 7×10^{12} cm $^{-3}$ and so it was limited to measuring densities far away from the thruster (about 20 cm) throughout the discharge or near the thruster after a fair amount of time (about 10 μs) had passed since the discharge. Within these limitations, the electron density was measured[10] at different distances from the thruster as a function of time. The Mach-Zehnder

interferometer can detect electron densities above 10^{15} cm^{-3} and was used to determine the average electron density in the arc itself at the fuel surface with hopes of using the information to determine the surface pressure. It was found[12] that the maximum electron density occurs 0.6 μs after initiation of the discharge and is approximately 9.3×10^{16} cm^{-3}. Between 26 mm and 20 cm from the Teflon face, neither of these two interferometers will operate because the electron density falls either above or below the range of detection for that particular instrument.

Employing a Faraday cup[10], it was found from a time-of-flight measurement that the plasma ions have a velocity of 40,000 m/s. This corresponds to the arrival of C_{IV} and F_{IV} ions[11] and indicates that they constitute a sizeable fraction of the total number of plasma ions. The total charge collected was 5.23×10^{-3} C or approximately 3×10^{16} e. This compares well with the optical measurements if the arc volume is on the order of 1 cm^3. The ejected mass would be 10% ionized if all the ions were singly charged. The Faraday cup data is weighted in favor of the more highly ionized species because of their higher velocities. Using the arrival time of the peak ion density at 20 cm, it was found that the ion thermal velocity was 9.3 km/s, which corresponds to an ion temperature of 7.6 eV. That this figure is low is verified by analyzing the Faraday cup data using a theory based on the Boltzmann distribution. The spreading or broadening of the pulse shape yields an ion temperature of 35 eV, but this is probably a bit high since it was assumed that all species were singly ionized. A cone half angle of 18° was measured and the particle distribution was approximately Gaussian.

A spectroscope [10,13] and an image converter camera[11] were also used to obtain velocity information on the plasma. The image converter camera took a picture (10 ns exposure) of the visible plasma every 0.1 μs. The motion of the visible plasma front in these pictures allowed a plasma velocity of 32,000 m/s to be calculated. The spectroscopic measurements demonstrated the complexity of the exhaust plume. As shown in Table 1, there are a number of different ionic species present and each travels with a different range of velocities, as determined from Doppler shift measurements. Note that the higher ionization states, which require 50-60 eV for their formation, travel with the higher velocities. The line broadening due to the thermal motion of the ions yields an ion temperature of 10-15 eV, considerably below that found from the broadening of the pulse shape. This figure is probably more accurate, since no extra assumptions had to be made for this analysis as were made for the pulse broadening analysis.

Table 1* Average velocity ranges for the various species of carbon and fluroine

Species	Velocity (m/sec)	Species	Velocity (m/sec)
C_I	5,000-15,000	F_I	5,000-15,000
C_{II}	20,000-30,000	F_{II}	15,000-25,000
C_{III}	30,000-40,000	F_{III}	25,000-35,000
C_{IV}		F_{IV}	

* From Ref. 13.

The relative intensity of various emission lines of the highly ionized carbon (C_{IV} to C_{III} and C_{III} to C_{II}) gave the electron temperature to be about 3-8 eV, which is much lower than the 20-25eV found from the Langmuir probe[10]. From the lifetimes and location in time of the peak luminosity for the various C and F ion species, it was postulated that the charged species are produced sequentially, rather than at the same time. This is due to changes in the energy available and an increase in the plasma density. At the extreme ends of the scale, the triply ionized species at the start indicate an excess of energy, while the neutrals are formed after there is not enough energy available to ionize them. There was some recombination of ions and electrons observed, e.g., C_{II} to C_I, which helped create the variation in velocity for a given ionized species.

A theoretical model for expansion of the exhaust [12] is coupled with experimental data to find the electron density, total electrical charge, and ion temperature in the exhaust. Also in Ref. 12, using the multipass Mach-Zehnder interferometer, a reversal of phase shift was noted at the surface of the Teflon, indicating a change in dielectric constant from a value less than ϵ_o to a value greater than ϵ_o. Since this was not noted downstream, it was postulated that this effect was due to the formation of neutrals. If one assumes a neutral gas of C and F, but no C_2F_4, a neutral density of 7.6×10^{18} cm^{-3} is calculated. Several other calculations were performed which show that the peak electron and ion gas dynamic pressures are on the order of 4.5×10^5 n/m^2 and the estimated magnetic pressure is 1.6×10^5 n/m^2. Since the gas pressure acts over a smaller area than the magnetic pressure, the gas dynamic force on the Teflon surface is about equal to the total magnetic force.

A series of experiments on a 90 J experimental thruster [14] provide measurements of magnetic flux densities, current distribution, and plasma velocity along the center line of the accelerator. Using a high speed framing camera, pictures of the side and the front of the luminous plasma were taken at 0.5 μs intervals. The total plasma discharge comes off in three separate plasmoids coincident with each quarter cycle of current. The generation of mass at the Teflon surface is continuous and there appears to be a stationary arc at the propellant surface. There is not much lateral spreading of the arc discharge even with the open sides on the accelerator. The velocities of the first two plasmoids as obtained from the photographs are 37,000 m/s and 29,000 m/s respectively. A double electrostatic probe was used as a time-of-arrival probe to determine if there existed any plasma ahead of the luminous front. It was not obvious what the correct time of arrival was, but a reasonable analysis of the data indicated a velocity of 45,000 m/s between 3 and 9.5 cm from the thruster. It was postulated that photoionization in the probe gap caused the initial low level signals, but a more probable alternative might be photoemission from exposed surfaces in the probe area caused by UV radiation from the plasma. The divergence of the time-of-arrival data and the location of the maximum probe signal suggests either that the plasma continues to expand beyond the electrode exit plane or that the leading edge of the plasma consists mostly of electrons which accelerate faster due to their higher mobility. The current distribution measurements correlate well with the luminous front and probe measurements. A two-dimensional measurement capability[15]

was added to the time-of-arrival probe and additional data was collected. It was found that the arc front moves faster at the anode than at the cathode and that most of the acceleration takes place in the first 1.5μs. There was a lack of any apparent boundary layer, indicating that viscosity is not a significant factor in a solid Teflon pulsed plasma thruster. These latter measurements were all within 12 cm of the Teflon surface.

The only relevant information on the millipound pulsed plasma thruster is contained in Ref. 16. However, many of the experiments performed here are suspect because of the problems encountered with backscatter from the walls of the liquid nitrogen cooled vacuum facility. The exhaust consists of 1.5 mg of material ejected per discharge at an average velocity of approximately 17,000 m/s with a flow time of a few tens of μs. It is doubtful that the highly energetic exhaust will be captured even by the Molsink Facility at JPL. The thruster used was equivalent to the millipound pulsed plasma thruster, but was not identical in propellant feed or capacitor energy storage bank. In addition, the mass distribution studies using glass capture cups were made at an energy level of only 200J, and not the 750J operating level of the millipound thruster. The only information of interest to come out of the glass capture cup studies is that the main part of the plume is in a cone angle of $\pm 30^{o}$ to $\pm 40^{o}$ and there is sputter eroding in the center of the plume.

Even though facility backscatter greatly affected results, the mass distribution studies using the quartz crystal microbalances (QCM's) did provide some useful information. Material deposited on a QCM did not boil off as expected when the temperature was raised from -104^{o}C to 48^{o}C. Fairchild postulated that the plume was composed of heavier molecules than monomers of Teflon, but it is just as likely that C, F, and Teflon monomers recombined on the surface of the QCM to form larger molecules with higher boiling points. Sputtering was found to occur within $\pm 40^{o}$ of the thruster centerline. The attachment of collimating tubes to the QCM's seemed to eliminate much of the facility backscatter, but a complete set of measurements was not performed with this arrangement. In addition, the amount of energy stored in the capacitor bank for these firings was not given. Additional measurements with a nude ionization gauge and a QCM located behind the thruster indicated that facility backscatter effects dominated many of the measurements.

Electron temperature and ion density measurements were made using a Langmuir double probe to measure the time varying ionized portion of the plume. The plume would contaminate the probe after only 20 shots, so the probe was periodically cleaned by electron bombardment. The thruster was operated at the 750J energy level. Using Langmuir probe theory, the electron and ion densities as a function of angular position were calculated for 71 cm and 142 cm from the thruster exit plane. The lowest electron density observable was 10^{12} cm^{-3}, so this approach would have filled in the void in the measurements on the LES-6 thruster. One point to note is that all this analysis was based on the plasma being totally comprised of C^{+} and F^{+}, i.e., singly ionized ions only. While this may be true for 71 cm and 142 cm from the thruster, it should definitely be justified in some fashion because the LES-6 thruster had many highly ionized species present in its exhaust plume and here the exhaust plume is from a thruster employing approximately 300 times more energy per pulse than the LES-6 thruster. The ion density and electron temperature on the central axis (71 cm location) of the thruster were 3.8×10^{14} cm^{-3} and 3.8×10^{4}

^{o}K (about 3 eV) respectively at 27.5μs after the thruster fired.

SPACECRAFT INTERACTIONS

Since every extended test of a solid Teflon pulsed plasma thruster has resulted in the formation of an observable deposit on nearby surfaces, spacecraft designers are obviously concerned about the interaction of the exhaust plume of the thruster with the various surfaces on a satellite. No truly definitive studies of these interactions have been performed, but what had been done up to about 1971 is covered in several survey articles[17-19]. Following a review of the known data about the interaction of the solid Teflon exhaust plume and thruster with a satellite, the information required by the design engineer to successfully integrate a Teflon thruster onboard a spacecraft will be discussed.

One major area of concern is, of course, the effect of the particle efflux on the solar arrays that might be on the satellite. There were no problems with this on the LES-6 satellite and it has not appeared to be a problem in any ground tests that have been performed. In one test [16], calibrated flight quality solar cells were exposed to the efflux from a solid Teflon pulsed plasma thruster for 24 hours and then sent back to Spectrolab for recalibration. All results of the recalibration were within the 2% calibration accuracy of the original readings. However, the fact that they were exposed to the atmosphere for at least seven days before recalibration leaves the issue somewhat clouded since it is a known fact that deposits formed by the efflux react with, or at least upon exposure to, the air. Solar cell degradation due to thruster efflux has not appeared to be a problem on the TIP-2 or TIP-3 satellites [20], but then the solar arrays have not deployed correctly and the data is of questionable value, except as a rough indication that a problem doesn't exist. Lastly, it is interesting to note that researchers [21, 22] in the area of solar cell cover technology are using Teflon covers on arrays for protection. Hence, a little more Teflon probably won't harm anything in this case.

Another area of concern is the coating of thermal control surfaces with the efflux from the Teflon thruster. Measurements made at the MIT Lincoln Laboratory [23] on the emissivity and absorptivity of three Kapton samples placed in the exit plane and just to the side of the LES 8/9 thruster demonstrated that the efflux (after 210,000 discharges) did alter the physical properties of the surface (absorptivity fell an average of 11% and emissivity rose an average of 4%). Fairchild [16] used the temperature of small discs placed in the exhaust beam to perform a rough determination of the beam energy distribution. These measurements support the fact that the major portion of the beam lies in a $\pm$ 30^{o} cone angle. Two collimated aluminum samples were placed in the vacuum system and exposed to the thruster efflux. They were then removed from the vacuum and shipped to Battelle Columbus Laboratories to be analyzed by Fourier Transform - Infrared Spectroscopy. There was no complete analysis of the results done, bu the method has some promise. However, here again, the samples should not be exposed to the air as this causes the coating or deposit to be altered. The effects of Teflon coatings on thermal surfaces[24] is already being considered by heat transfer engineers to develop low absorptivity surfaces.

RFI/EMI effects are of very short duration[25] as the RFI is associated with the arc formation[26] and ceases before the first current peak occurs. A flat, broad power spectrum [26,27] is exhibited with individual spikes having random magnitudes and pulse widths being between 100 and 300 ns. These observations were made looking directly into the thruster exhaust cone and involved radiated power levels on the order of 0.015 $mw/m^2/MHz$. The large noise spikes are reduced in magnitude after the thruster has fired in the vacuum for several hundred discharges. This is attributed to the desorption of absorbed gases along with the Teflon when the thruster is first fired. The spacecraft integration studies[28] performed on the LES 8/9 thruster indicate the potential problem areas when one goes to ground or space test a pulsed plasma thruster on a satellite. The use of an ignitron load for air testing does not produce enough RFI. Extreme care must be employed to prevent the formation of ground loops from the plasma. This would not be a problem in space, but did affect telemetry equipment until adequate isolation, shielding, and filtering was employed. The infrared sensor was affected by the EM radiation and also electrostatic pick up from the high voltages present. Again, adequate shielding cured the problem. There was no problem with RFI on the TIP-2 satellite and, now that the thruster has been fired on TIP-3, no problems have occurred except for the apparent loss of several bits of information from the computer memory[20]. Several areas especially need further study. These are in the isolation needed to prevent conducted EMI and the induced voltages generated by the time varying arc voltage and current from reaching the rest of the satellite subsystems[27].

The last area of spacecraft interactions to be discussed is the most sensitive and critical for certain applications. It has been noted by a number of experimenters that the efflux from the solid Teflon pulsed plasma thruster will adhere to glass surfaces (and almost anything else) inside a vacuum facility. This will be an especially serious problem for cryogenically cooled precision optical surfaces. Wolfson[29] has shown that the rate of increase of light scatter from an optical surface is proportional to the fourth power of the particle size. This means that a single particle of 25 micron diameter represents a hazard as serious as approximately one million particles of 0.8 micron diameter. Lynch[30] measured the scatter increase of low-scatter mirrors using a He-Ne laser optical system. It was found that the scatter coefficient changed by a factor of 10 after 1.2×10^6 pulses of a LES 8/9 thruster for a mirror about 15 cm away from the nozzle, but in the exit plane of the exhaust. The addition of a cone to the exhaust reduced the change in the scatter coefficient. Since the particle sizes that develop as the Teflon efflux builds up on a surface are large compared to single atoms, it is clear that extreme care must be taken to insure that the efflux from the solid Teflon pulsed plasma thruster does not impinge on precision optical surfaces.

RECOMMENDATIONS - PLUME CHARACTERISTICS

Many pieces of information are needed to completely describe the efflux from the exhaust of the solid Teflon pulsed plasma thruster. Not only does the plasma itself have to be analyzed, but also a large, ill-defined mass of neutral atoms and molecules that ooze off the face of the Teflon fuel after the plasma leaves. While the plasma portion seems to provide most or all of the thrust, the neutral portion appears to cause most or all of the serious contamination problems. Hence, one obvious way to decrease contamination is to attempt to decrease the neutral portion of the efflux by either forcing the initial formation of plasma away from the Teflon surface faster by an applied magnetic field (probably pulsed) so that the plasma does not heat up the Teflon as much or by sending a secondary discharge into the neutral efflux and hence accelerate it out of the channel at a high velocity. These approaches were not examined in any great detail since the "thrust" of this report was the measurement of efflux and identifying the potential areas of interference with spacecraft operations. However, not only would improvement in this area help lessen contamination, but it would also increase the efficiency of the thruster.

To characterize the plasma portion of the plume one needs to measure the electron and ion densities, temperatures, and velocities as a function of time after the discharge and as a function of distance from the Teflon surface. Several different techniques are available which may be applied to this problem. Some are more effective in certain ranges of the variables than others, but coupling them together should give a comprehensive picture of the development of the plasma. K-band microwave interferometry[10] and a multipass Mach-Zehnder interferometer[12] will measure average electron densities below 10^{12} cm^{-3} and above 10^{15} cm^{-3} respectively. The use of the double Langmuir probe[16] will allow values of ion densities and electron temperatures to be determined over a wide range of values. A simple Langmuir probe[31], while it may perturb the plasma a bit more than the double probe, will allow local ion and electron densities and temperatures to be determined over a wide range of values. There will be some overlap with the other techniques which will permit a checking of experimental values. The velocities[11] and percentages of the various ionized species in the plume may be determined by an optical spectrometer, at least while the plasma is luminous. Electron densities and temperatures can also be obtained from the spectral intensities[32]. The plasma should be examined in the ultraviolet[33], if possible, because a large portion of the radiation emitted is in this region. Lastly, the use of a Faraday cup[10] can tie all this data together and provide a check on the values obtained, since it yields the integrated or total current passing through a plane for a given period of time. Using a simple gridded repeller-type analyzer[34] will allow approximate ion abundances to be determined. These techniques, which have all been tried on pulsed plasma thrusters other than the millipound thruster (except for the Langmuir probe), would allow the plasma portion of the plume to be completely specified as to constitution and location in space and time.

The other portion of the plume, the neutrals, poses a slightly more difficult problem. Again one would like to identify the species that

constitute the neutral efflux, determine the velocity distribution, and learn how the density varies with time and distance. To understand how the neutral efflux progresses is potentially much more important to spacecraft contamination problems than understanding the plasma. If one examines the picture[35] of the exhaust pattern produced on a Teflon sheet by the LES 8/9 thruster after 34 x 10^6 pulses, it is found that the efflux has expanded through about 110° from the centerline of the thruster. While the "nozzles" on this thruster are canted at an angle, this does indicate that scatter into the backward hemisphere must be examined. This is likewise born out by the optical scattering experiments[29] and the absorptivity/emissivity experiments[23] with the LES 8/9 thruster. However, it is unclear in the experiments what effect facility backscatter played in the formation of the contamination that developed. To identify the various neutral species present as to type and quantity a quadrupole mass spectrometer could be used. This will work out in the wings of the distribution, but would most likely get into problems in the highly energetic portion of the plume where sputtering takes place. One still might have to use an electric and/or magnetic field to deflect ionized particles away from the spectrometer or to keep the spectrometer covered until after the plasma has passed by. In addition, the apparatus would probably have to be cleaned rather frequently if it is to work correctly as the neutral beam will be coating the inside with a dielectric layer which will alter its operating effectiveness. The results obtained here should be compared with the published results[36] from vacuum pyrolysis of Teflon. A simpler means[37] of determining the velocity of the neutrals would be to place an ionizing source along the path of the neutral efflux. Then the time of transit of the created ions between two Langmuir probes could be used to calculate the velocity. Quartz crystal microbalances (QCM's) could also be used to determine the mass of material in the wings of the distribution and the result compared with those obtained from the quadrupole mass spectrometer. The percent of the total mass emitted from the thruster that is in the wings of the distribution is the truly critical percentage as far as contamination goes and is the quantity that must be determined accurately. Infrared absorption and/or emission spectroscopy also could be used to find the percentages, identities, and velocities of the molecular species present in the plume as they will be excited in the infrared region of the spectrum.

The above paragraphs are based on the belief that employing collimation techniques will eliminate the more severe effects of facility backscatter for some measurements, at least those occurring in the forward hemisphere. Attempting to make definitive measurements in the backward hemisphere will probably still be a problem since the mass fluxes are so much lower. However, these are the fluxes that cause most of the contamination problems. If it can't be shown by JPL that they can handle the facility backscatter problem satisfactorily, then the only alternative will be to go to time-of-flight experiments. By time-of-flight experiments it is meant that the measurements are made before the plasma portion of the efflux has time to impact the wall and scatter back to where the measurements are taken. This is routinely done for chemical rockets, but the high velocities of the plasma particles will make the measurements much more difficult to obtain for the solid Teflon pulsed plasma thruster. Because of the pulsed nature of the efflux it also will probably be necessary

to have rotating shutters over such devices as QCM's, etc. to prevent backscatter from coating the devices. In this approach, if the data could not be obtained from one pulse, information from a number of separate pulses could be stored digitally and averaged to attain a reasonable accuracy. To gain enough time to shield on experimental device from the facility backscatter, a large vacuum chamber such as the one at the Johnson Space Center may have to be used.

Lastly, several other quantities should be measured in an exploratory fashion to help determine their effects on the distribution of particles in the plume, especially those that may reach the spacecraft. The first quantity is the effect that cone geometry can have on the wings of the distribution. Since it is known that precision optical surfaces can be degraded rather severely by the efflux of the Teflon thruster, it is of paramount importance to be able to demonstrate that it is possible to shield such apparatus from the efflux, or at least control the levels of efflux that will reach the equipment within acceptable limits. One possibility that might be explored is that a Russian paper[38] indicates that a coaxial configuration, rather than rail, focuses the efflux toward the center, which would help alleviate contamination problems. The problems with feeding the Teflon in a coaxial thruster and obtaining even ablation might far outweigh the advantages though. Secondly, while charge exchange ions are not a source of contamination here as they are in mercury ion thrusters since the ions come out before the neutrals, there is still a possibility of particles backscattering out of the exhaust beam due to collisions with the ambient atmosphere at lower altitudes. The particles involved would be the neutrals and, of course, with their low velocities, there would be a considerable chance of backscatter if they underwent a collision. However, if the probability of a collision occurring is low enough, then this source of backward moving Teflon particles would not be significant.

RECOMMENDATIONS - SPACECRAFT INTERACTIONS

From the viewpoint of the spacecraft designer, the effects caused by the parts of the thruster efflux that adhere to various satellite surfaces are much more important than the characteristics of the exhaust plume itself. For example, he does not care about the densities and velocities of the ionized species present in the plume just as long as he can be assured that they will not impinge on his spacecraft. However, he must know what the effect of given mass deposition rates on the satellite surfaces will be.

To obtain the information needed by the designer to successfully integrate solid Teflon pulsed plasma thrusters on a satellite, compatibility (not contamination) tests should be performed for various thermal control surfaces, adhesives, and solar cells. For the thermal control surface, the absorptivity/emissivity of the samples should be determined as a function of the length of the time the sample is exposed to the thruster efflux. Adhesives and solar cells must be checked to see if the efflux causes their properties to be degraded with time. All these measurements should be made in situ for them to have any meaning since the deposits formed change composition upon exposure to air. From the work that has already been done, it appears that solar cell degradation will not be a problem. The proposed work of JPL will probably clear up questions left on the

effect of the efflux on solar cells and on certain thermal control surfaces, but they are wasting their time by saying that "provisions will be made to minimize the sample exposure to air"[39] since the reactions that take place will occur on time scales on the order of milliseconds to seconds maximum. The ex situ measurements are of interest though, in that they will help indicate the significance of any reactions that have taken place. The effect of the thruster efflux on adhesives should be checked, although it is probably not of importance unless the adhesives should happen to be exposed to the energetic part of the exhaust, i.e., that part within the $\pm$ 40° cone angle.

A satellite integration specialist would probably not care what specific material was deposited on the spacecraft surfaces as long as he was certain that he knew what effects this deposit was going to cause. However, he would feel more secure if he knew what materials made up the deposits. Again, for the measurements to have meaning, they should be made in situ rather than ex situ. Since the polymerization of C_2F_4 progresses almost explosively (it takes very little energy to initiate the process), these deposits will for the most part be polymers rather than individual molecules. This would explain the problems Fairchild[3] had in trying to heat up their QCM's to boil off the absorbed molecules. There are a number of techniques that may be used to analyze these deposits. The Fourier Transform Infrared Spectroscopy[40] (FT-IR) employed by Battelle Columbus Laboratories is one good approach. With it one should be able to detect the presence of and distinguish between C_2F_4, CF_4, C_2F_4 polymer, etc. If additional sensitivity is needed, the use of an internal reflection element (IRE) and attenuated total reflection (ATR), an infrared multiple bounce absorption approach, is recommended. The infrared techniques allow one to determine information about molecular bonds, but information about the atoms on the surface before and after exposure to the pulsed plasma plume might be desired. This could be obtained from secondary ion mass spectrometry (SIMS)[41], which could also be used to characterize the composition of the substrate. In this technique, 1-30 keV ions are scattered against the surface and the secondary ions emitted are separated according to the mass-to-charge ratio by a quadrupole mass analyzer as shown in Fig. 3. This allows an identification of the species present to be made. The companion technique of ion scattering spectroscopy (ISS) allows information on polymer bonding and structural properties of contaminants to be obtained. One alternative to actual in situ experiments exists. D. Hall[42] mentioned that there are techniques or equipment available to expose a sample in a vacuum system, package it, remove it, and place it in another vacuum chamber for analysis without ever exposing it to air. If actual in situ experiments cannot be performed, this latter approach should be employed.

The rate at which precision optical equipment, especially cryogenically cooled mirrors, and Channeltron photomultiplier tubes are degraded by exposure to the efflux of the millipound pulsed plasma thruster must be determined. In all probability, what will have to be done here is to determine how to shield these devices from ever having thruster efflux come in contact with them. In addition, EMI must be checked in the IR and UV regions, as well as the optical, since many spacecraft experiments are interested in observing these regions of the electromagnetic spectrum, and the plasma part of the efflux should emit in the UV, while the neutral portion would emit in the IR. The RFI measurements performed by Fairchild[27]

are adequate as far as they go, but the measurements of conductive RFI should definitely be made.

Measurements of the static and dynamic electric and magnetic fields outside the thruster are also needed to assure experimenters that these fields will not interfere with their delicate measurements of the solar wind, the interplanetary plasma, etc. While it is not probable that there is a net charge expelled from the thruster, this should be experimentally verified by electrically isolating the thruster in a test facility (backscatter will be hard to control here) and monitoring the charge build-up that takes place as the thruster fires. The last charging effect that could present severe problems is that Teflon can act as an electret. Even under ground conditions, Teflon tends to build-up a surface charge that does not dissipate of its own accord. In space, where a satellite may have experienced a deposition of Teflon on its surfaces, the flux of charged particles that permeates space may cause a charge accumulation to occur on the satellite. Since designers are already concerned with preventing or controlling spacecraft charging and the occurrence of arcs on board, this is definitely one area that should be explored to determine if it occurs, and if it does, to determine the precautions that need to be taken to prevent it from being a serious problem.

CONCLUSIONS

Given a rather restricted amount of funding, the following program would contain the minimum study needed to be able to successfully integrate the millipound solid Teflon pulsed plasma thruster on a spacecraft. This recommendation pre-supposes that the JPL plume characterization program is successful and is carried through to completion.

A neutral detector should be constructed and the neutral portion in the wings of the beam distribution, including the rear hemisphere, should be studied in detail as to constituents, velocities, and densities. An infrared spectrometer should be used in this study too, as it will not only help answer the above questions, but it will also answer questions about the possibility of infrared EMI from the plume. This work will nicely compliment the work done at JPL. The effects caused by the beam efflux on cryogenically cooled optical surfaces and on Channeltron type photomultiplier tubes should be determined. The possible backscatter of molecules out of the exhaust beam due to collisions with the ambient atmosphere at low altitudes should be checked. The effect of cone geometry on the particle distribution in the exhaust beam should be examined and ways to shield various spacecraft components should be determined. Measurements of conductive RFI should be performed and the UV region of the spectrum should be checked as a possible source of EMI from the plume. An examination of charge accumulation on a Teflon surface as it is exposed to a thin plasma, such as the solar wind, should be undertaken.

The above program is, of course, the barest minimum that might possibly convince someone to fly a solid Teflon pulsed plasma thruster on their spacecraft. It does not come close to meeting the volumes of information and data that have been generated for the 8 cm. mercury ion thruster over the years and utilized in the compilation of a User's Guide[43] for that thruster.

REFERENCES

1. Clark, K. E., "Survey of Electric Propulsion Capability", Journal of Spacecraft and Rockets, Vol. 12, Nov. 1975, pp. 641-654.

2. Jahn, R. G., "Unsteady Electromagnetic Acceleration", Physics of Electric Propulsion, McGraw - Hill, New York, 1968, pp. 257-288.

3. Guman, W. J., and Begun, M., "Pulsed Plasma Plume Studies-Final Report", Fairchild Republic Co., Farmingdale, N.Y., AFRPL-TR-77-2, Nov. 1976.

4. Palumbo, D. J., and Guman, W. J., "Pulsed Plasma Propulsion Technology-Final Report", Fairchild Republic Co., Farmingdale, N.Y., AFRPL-TR-77-May 1977.

5. Zhurin, V. V., "Electric Propulsion in the USSR", AIAA Paper No. 76-1073, AIAA International Electric Propulsion Conference, Key Biscayne, Florida, Nov. 14-17, 1976.

6. Guman, W. J., and Nathanson, D. M., "Pulsed Plasma Microthruster Propulsion System for Synchronous Orbit Satellite", Journal of Spacecraft and Rockets, Vol. 7, Apr. 1970, pp. 409-415.

7. Michels, C. J., Heighway, J. E., and Johansen, A. E., "Analytical and Experimental Performance of Capacitor Powered Coaxial Plasma Guns", AIAA Journal, Vol. 4 , May 1966, pp. 823-830.

8. Kulandin, A. A., Kazarnovskiy, D. M., and Khoroshavin, A. V., "Theory of a Pulsed Plasmoid Accelerator", Magnitnaya Gidrodinamika, No. 2, 1970, pp. 139-141.

9. Palumbo, D. J., and Begun, M., "Plasma Acceleration in Pulsed Ablative Arc Discharges - Interim Report", Fairchild Republic Co., Farmingdale, N.Y., AFOSR-TR-76-0738, Mar. 1976.

10. Vondra, R. J., Thomassen, K., and Solbes, A., "Analysis of Solid Teflon Pulsed Plasma Thruster", Journal of Spacecraft and Rockets, Vol. 7, Dec. 1970, pp. 1402-1406.

11. Vondra, R. J., Thomassen, K., and Solbes, A., "A Pulsed Electric Thruster for Satellite Control", Proceedings of the IEEE, Vol. 59, Feb. 1971, pp. 271-277.

12. Thomassen, K. I., and Tong, D., "Interferometric Density Measurements in the Arc of a Pulsed Plasma Thruster", AIAA Paper No. 72-463, AIAA 9th Electric Propulsion Conference, Bethesda, MD., Apr. 17-19, 1972.

13. Thomassen, K. I., and Vondra, R. J., " Exhaust Velocity Studies of a Solid Teflon Pulsed Plasma Thruster", Journal of Spacecraft and Rockets, Vol. 9, Jan. 1972, pp. 61-64.

14. Palumbo, D. J., and Begun, M., "Plasma Acceleration in Pulsed Ablative Arc Discharges - Interim Report", Fairchild Republic Co., Farmingdale, N.Y., AFOSR-75-0618, 15 Feb. 1974 - 15 Mar. 1975.

15. Palumbo, D. J., and Begun, M., "Plasma Acceleration in Pulsed Ablative Arc Discharges - Interim Report", Fairchild Republic Co., Farmingdale, N.Y., AFOSR-TR-76-0738, 15 Mar. 1975 - 15 Mar. 1976.

16. Guman, W. J., and Begun, M., "Pulsed Plasma Studies - Final Report", Fairchild Republic Co., Farmingdale, N.Y., AFRPL-TR-77-2, Mar. 1977.

17. Lyon, W. C., "Monopropellant Thruster Exhaust Effects Upon Spacecraft", Journal of Spacecraft and Rockets, Vol. 8, July 1971, pp. 689-701.

18. Lyon, W. C., "A Study of the Effects of Teflon Thruster Exhaust Upon a Spacecraft", Hittman Associates, Inc., Columbia, MD, Report No. HIT-443, Contract No. NAS5-9479, Apr. 1970.

19. Hall, D. F., and Lyon, W. C., "Low Thrust Propulsion System Effects on Communication Satellites", Progress in Astronautics and Aeronautics, Vol. 33, The MIT Press, Cambridge, Mass., 1972, pp. 279-306.

20. Kowal, S., personal communication, June 1977, Johns Hopkins Applied Physics Laboratory, Baltimore, MD.

21. Rauschenbach, H. S., and Ratajczak, A. F., " FEP - Teflon Covered Solar Cell Array Advancements", 10th Photovoltaic Specialists Conference, Palo Alto, CA, Nov. 13-15, 1973, Conference Record, N.Y., IEEE, 1974, pp. 264-271.

22. Broden, J. D., and Mazaris, G. A., "The Use of FEP Teflon in Solar Cell Cover Technology", 10th Photovoltaic Specialists Conference, Palo Alto, CA, Nov. 13-15, 1973, Conference Record, N.Y., IEEE, 1974, pp. 272-274.

23. Vondra, R. J., personal communication, MIT Lincoln Laboratory, Lexington, Mass.

24. Congdon, W. M., "Investigation of Reflecting Heat Shield Materials for Outer-Planet Missions", AIAA/ASME, Thermophysics and Heat Transfer Conference, Boston, Mass., July 15-17, 1974, AIAA Paper No. 74-702.

25. Guman, W. J., and Nathanson, D. M., "Pulsed Plasma Microthruster Propulsion System for Synchronous Orbit Satellite", Journal of Spacecraft and Rockets, Vol. 7, Apr. 1970, pp. 409-415.

26. Thomassen, K. I., "Radiation from Pulsed Electric Thrusters", AIAA Paper No. 73-263, AIAA 11th Aerospace Sciences Meeting, Washington, D.C., Jan. 10-12, 1973.

27. Palumbo, D. J., Begun, M., and Guman, W. J., "Pulsed Plasma Propulsion Technology - Interim Report, "Fairchild Republic Co., Farmingdale, N.Y., AFRPL-TR-74-50, July 1974.

28. Vondra, R. J., "The MIT Lincoln Laboratory Pulsed Plasma Thruster", AIAA Paper No. 76-998, AIAA International Electric Propulsion Conference, Key Biscayne, Florida, Nov. 14-17, 1976.

29. Wolfson, R. R., MIT Lincoln Laboratory Memo, Feb. 1973.

30. Lynch, F., MIT Lincoln Laboratory Memo, Mar. 1976.

31. Chen, F. F., " Electric Probes", Plasma Diagnostic Techniques, Huddlestone, R. H., and S. L. Leonard, eds., Academic Press, New York, 1965, Chapter 4.

32. McWhirter, R. W. P., "Spectral Intensities", Plasma Diagnostic Techniques, Huddlestone, R. H., and S. L. Leonard, eds., Academic Press, New York, 1965, Chapter 5.

33. Gubarev, V. Ya., and Kozlov, N.P., "Determining Heat Flux from Plasma to Dielectric in Pulsed Erosion Accelerators", Plazmennyye Uskoriteli, Izd vo Mashinostroyeniye, 1973, pp. 228-230.

34. Ashby, D.E. T. F., Gooding, T. J., Hayworth, B. R., and Larson, A. V., "Exhaust Measurements on the Plasma from a Pulsed Coaxial Gun", AIAA Journal, Vol. 3, June 1965, pp. 1140-1142.

35. Hartman, J. K., personal observation of photograph taken at MIT Lincoln Laboratory, July 1977.

36. Pope, R. B., and Parker, J. A., "Analysis of Ablation Products and Boundary-Layer Chemistry of Ablating Materials with a Mass Spectrometer,"Proceedings of the 1967 High Temperature Technology Conference, Butterworths, London, 1969, pp. 311-321.

37. Vondra, R. J., personal communication, Aug. 1977, AFRPL.

38. Andrianov, A. M., and Alekseyev, Yu. A., "Obtaining Pulsed Plasma Flows in Coaxial Plasma Accelerator with Erosion of Dielectric, "Plazmennyye Uskoriteli, Izd vo Mashinostroyeniye, 1973, pp. 198-200.

39. Pawlik, E. V., and Fitzgerald, D. J., "Plume Characterization of One-Millipound Solid Teflon Pulsed Plasma Thruster", Jet Propulsion Laboratory, Pasadena, CA, Proposal No. 90-753.

40. Griffiths, P. R., "Chemical Infrared Fourier Transform Spectroscopy," Wiley-Interscience, New York, 1975.

41. Fralick, R. D., and Conrad, R. L., "Quantitative Multielement Analysis with SIMS", Research/Development, March 1977, p. 32.

42. Hall, D., personal communication, June 1977, Aerospace Corp., El Segundo,CA.

43. Zafran, S., "User's Application Manual for 8 cm. Mercury Ion Thruster", in final approval stage, TRW Systems, Redondo Beach, CA.

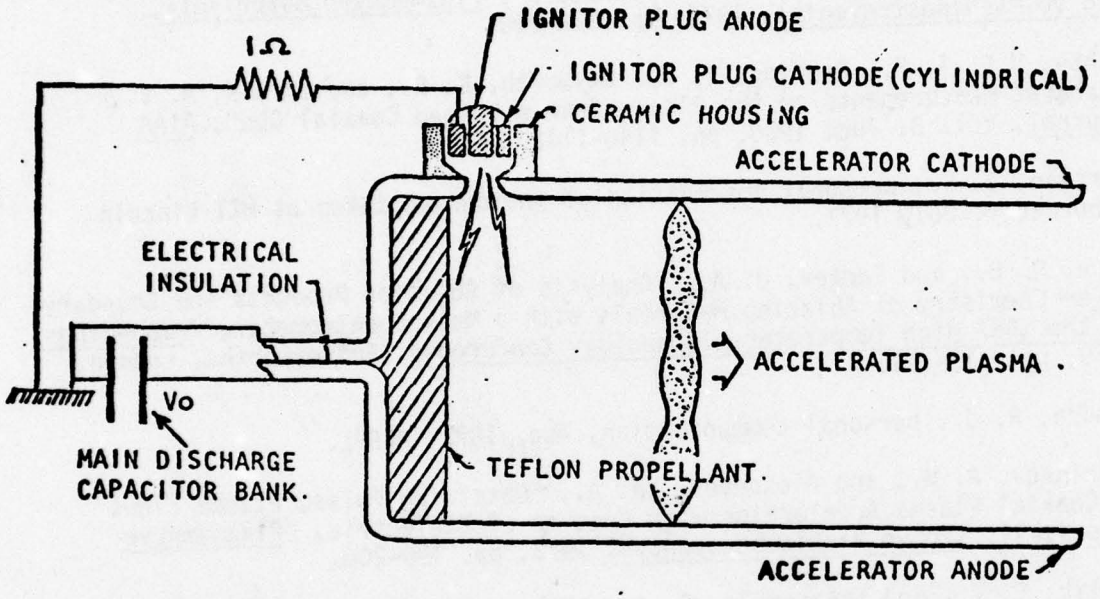


FIGURE 1. Simplified Diagram of Teflon Fueled Thruster

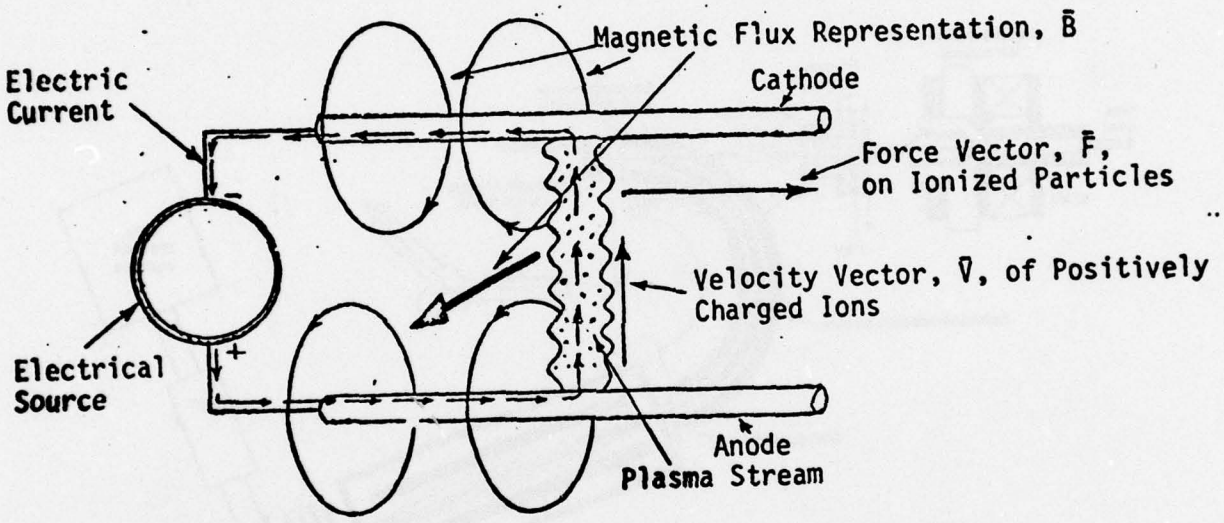


FIGURE 2. Elementary Representation of Electromagnetic Thruster

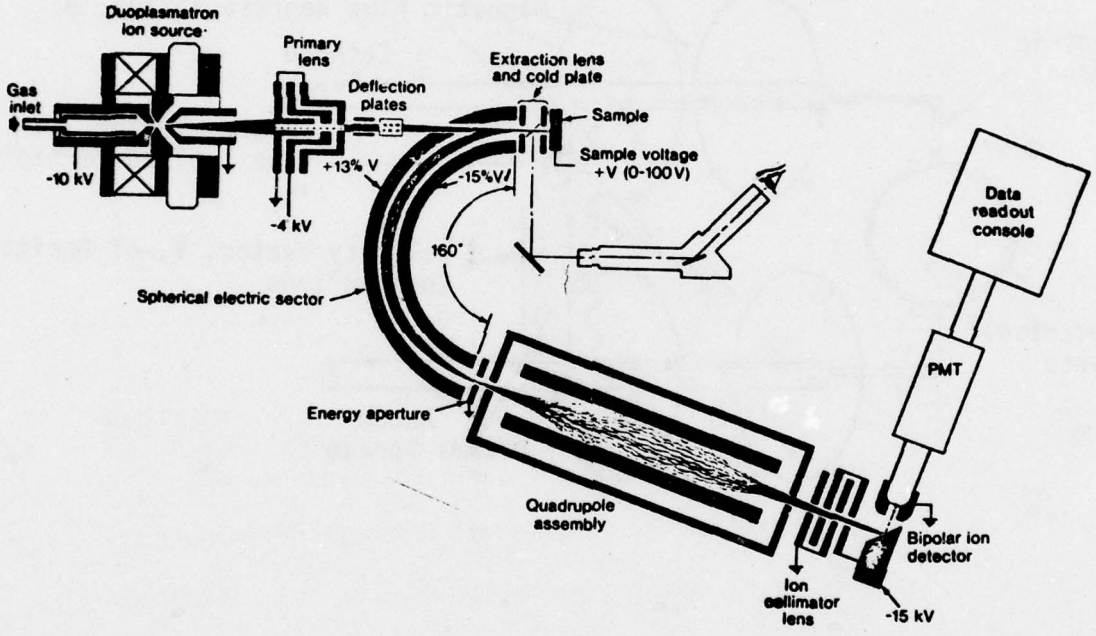


FIGURE 3. Essential elements of ARL quadrupole mass analyzer for solids; bipolar ion detector is in positive ion mode.

1977 USAF-ASEE SUMMER FACULTY RESEARCH PROGRAM

SPONSORED BY:

THE AIR FORCE OFFICE SCIENTIFIC RESEARCH

CONDUCTED BY:

AUBURN UNIVERSITY AND OHIO STATE UNIVERSITY

PARTICIPANTS FINAL REPORT

INFRARED, RAMAN, MASS SPECTROSCOPY AND GAS CHROMATOGRAPHY OF SELECTED FLUORODINITRO PLASTICIZERS

PREPARED BY: Steven Riethmiller Ph.D.

ACADEMIC RANK: Associate Professor

DEPARTMENT AND UNIVERSITY: Chemistry Department, Virginia Military Institute

ASSIGNMENT:

(Air Force Base)	Edwards AFB
(Laboratory)	Air Force Rocket Propulsion Laboratory
(Division)	Technology
(Branch)	Chemical and Materials
USAF Research Colleague:	Louis A. Dee
Date:	August 19, 1977
Contract No:	F 44620-75-C-0031

INFRARED, RAMAN, MASS SPECTROSCOPY AND GAS CHROMATOGRAPHY OF SELECTED FLUORODINITRO PLASTICIZERS

by

Steven Riethmiller

ABSTRACT

The gas chromatograms, infrared, Raman, and mass spectra of samples of fluorodinitroethanol (FDNE) have been recorded. An attempt was made at assigning the vibrational spectrum of FDNE and in identifying the trace impurities in samples of FDNE. Additionally, the infrared spectra of samples of SYEP and FEFO have been recorded.

NOMENCLATURE

AFRPL	Air Force Rocket Propulsion Laboratory, Edwards AFB.
FDNE	2- fluoro-2,2 dinitro ethanol
FEFO	bis(2-fluoro-2,2 dinitroethyl) formal
FTM	fluoro trinitromethane
SYEP	1,3 - bis (2,2 - dinitro - 2 - fluoro ethoxy) - 2,2 - bis (difluoroamino) propane
GC/FTIR	gas chromatography/Fourier transform infrared
GC/mass spec.	gas chromatography/mass spectroscopy

ACKNOWLEDGMENTS

The author is grateful to the United States Air Force and to the Rocket Propulsion Laboratory for being chosen to participate in the summer faculty research program.

Special thanks to Dr's L. P. Quinn and R. R. Weiss for their excellent administration of the program. They both went out of their way to make sure the author and his family had a pleasurable summer.

It has been enjoyable and intellectually stimulating working with Messrs. B. B. Goshgarian, H. Martens, and L. A. Dee. Mr. L. A. Dee has been an invaluable help to the author. His technical abilities and knowledge of the way things work at the Rocket Laboratory have enabled the author to have a very profitable summer.

INTRODUCTION

Certain compounds used as plasticizers have exhibited different casting properties depending upon the manufacturer. It was felt that these differences could be attributed to impurities in the various samples. Vibrational spectroscopy (Infrared and Raman) provides a way of determining what the impurities in the various samples are. By using GC/FTIR and GC/mass spec. instrumental set-ups it should be possible to separate and identify impurities in the 50×10^{-9}g region. If one is able to identify the specific impurities which are causing the casting problem, it may be possible to suggest certain synthetic routes which minimize these impurities.

OBJECTIVES

The objective of our program was to separate and identify the chemical compounds contained in samples of FDNE and SYEP, so that we could hopefully understand the different casting properties of certain plasticizers.

DISCUSSION

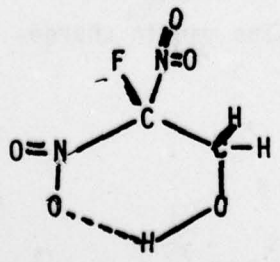
Since the molecules FDNE, SYEP, and FEFO all contain the dinitro fluoro moiety, and since FDNE is a relatively simple molecule (13 atoms), we decided to perform a complete vibrational analysis of the FDNE molecule. Hopefully, if we could completely assign the FDNE molecule and specifically the fluoro dinitro moiety, we could distinguish vibrations which were due to this portion of the more complicated molecules.

There are inherent problems associated with this plan. First, AFRPL has no Raman spectrophotometer but fortunately, one was found at California State University at Los Angeles. The man in charge, Dr. Joseph Bragin,

allowed us to use his instrument so that obtaining Raman data turned out not to be a problem. Second, all the compounds studied have very low vapor pressures (.5mm at 55° for FDNE)[1] at room temperature; this may cause certain experimental difficulties. Thirdly, isotopic species which usually aid in the assignment of the vibrational spectrum are not available. Fourthly, molecules of the type we were interested in have large inter- and intramolecular forces; these forces will lead to broad spectral lines which will be difficult to analyze. Coupling between vibrations will also hinder analysis.

VIBRATIONAL ANALYSES OF FDNE

The infrared spectra and Raman spectra of various liquid samples of FDNE are shown in figures 1 and 2. The infrared spectrum of FDNE with partial interpretation of this spectrum was done by Russian workers;[2] The Raman spectrum has not previously been reported. There are only two possible molecular symmetries for the FDNE molecule. C_s symmetry possesses a plane of symmetry with 33 fundamental modes of vibration that are distributed into 19A' and 14A" modes. The A' modes should be polarized in the Raman spectrum, whereas the A" modes should be depolarized. The other possible configuration of the molecule would be C_1 which possesses no symmetry. In theory all Raman lines of molecules which posses C_1 symmetry should be polarized. Therefore, the presence of depolarized lines should very strongly suggest that the molecule does not possess C_1 symmetry. The geometry of FDNE as proposed by Russian workers is the following:



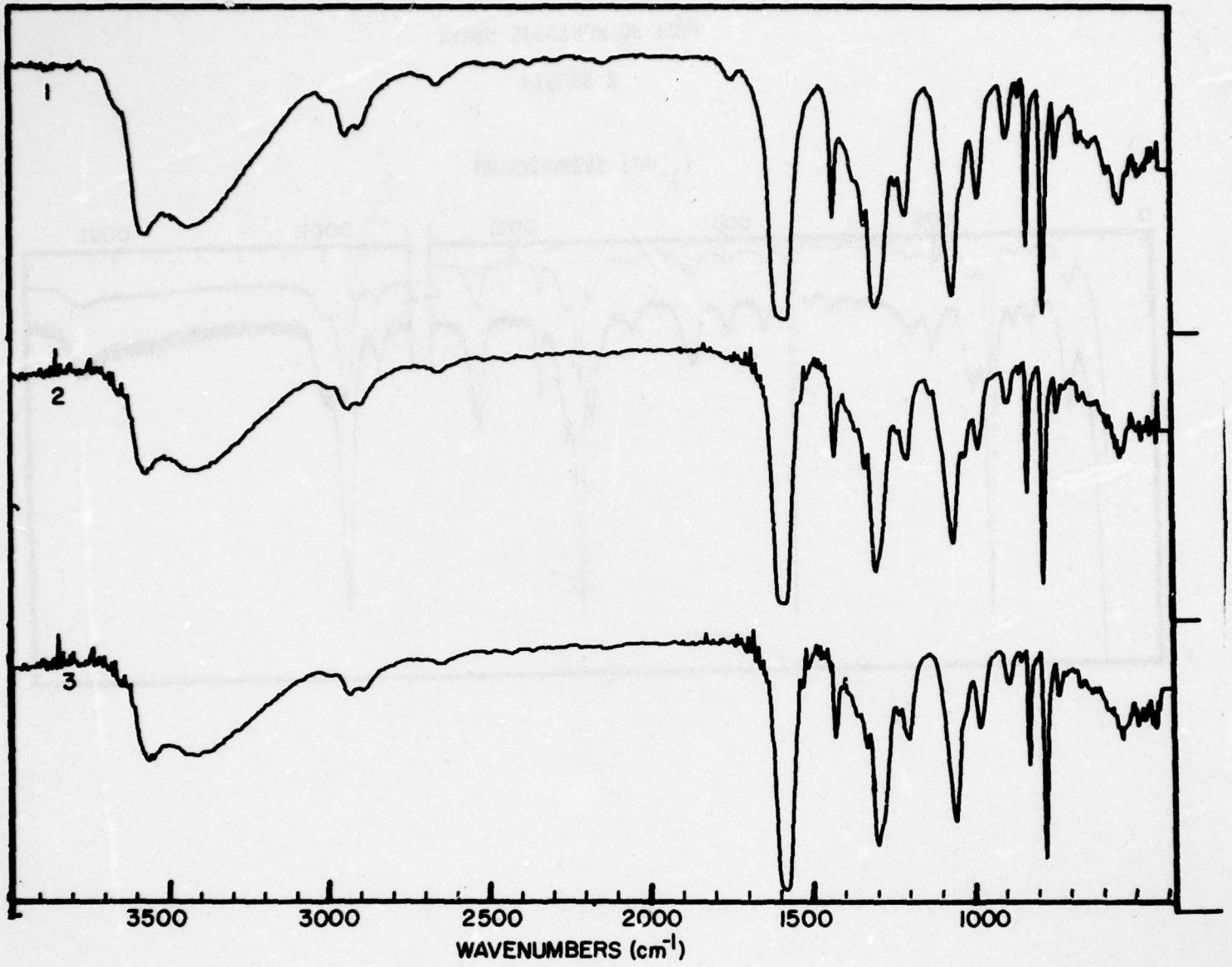


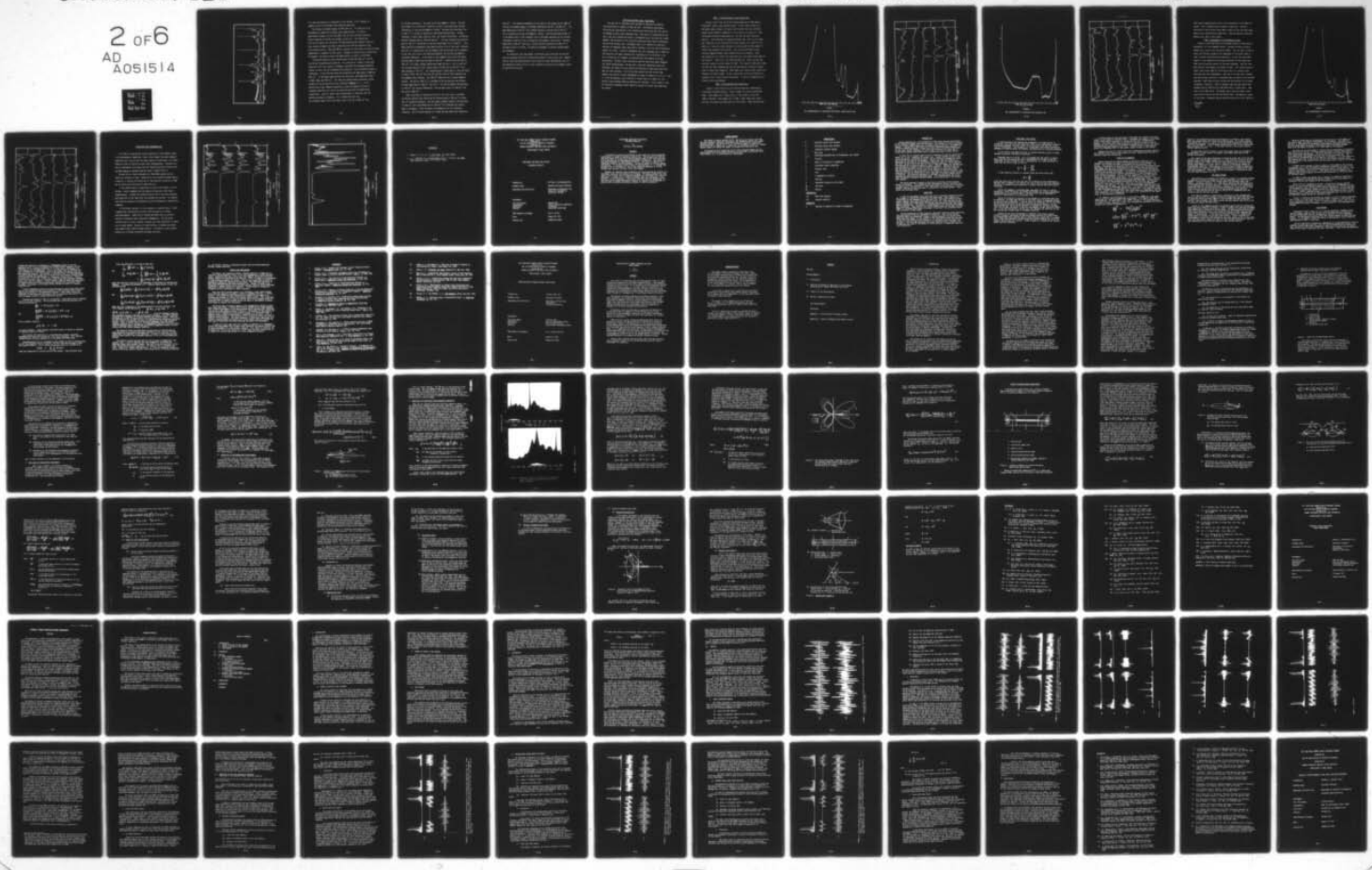
FIGURE 1

I. R. SPECTRA OF FDNE FROM VARIOUS PROCESSES

1. METHYL CYANO ACETATE 2. MALONATE 3. NITROFORM

AD-A051 514 AUBURN UNIV ALA SCHOOL OF ENGINEERING F/G 5/2
1977 USAF-ASEE SUMMER FACULTY RESEARCH PROGRAM. VOLUME II.(U)
SEP 77 J F O'BRIEN F44620-75-C-0031
UNCLASSIFIED AFOSR-TR-78-0349 NL

2 OF 6
AD
A051514



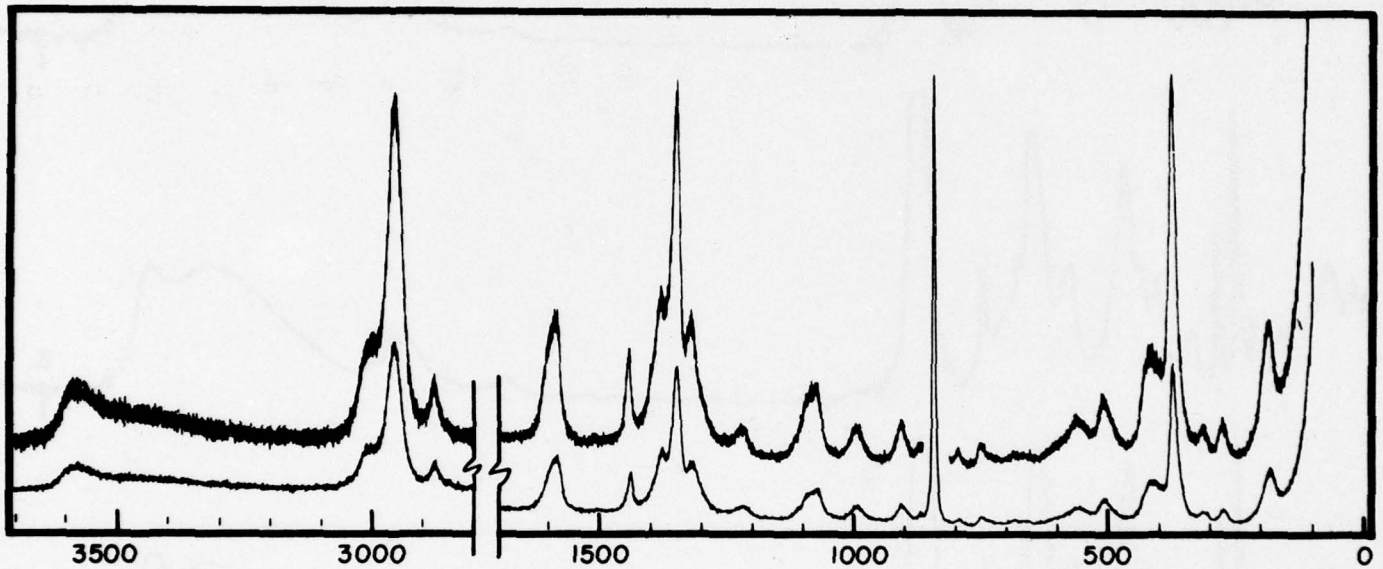


FIGURE 2

RAMAN SPECTRUM OF FDNE

If in fact the molecule is orientated in this fashion, it will possess no symmetry and all of the Raman lines should be polarized.

The infrared and Raman spectra of FDNE were run. It turned out to be experimentally impossible to obtain vapor phase spectra. In various experimental attempts to do so the FDNE, with its very low vapor pressure, simply condensed on the KBr salt windows of the cell. Even heating the cell did not improve the situation; the FDNE preferred the windows of the cell. Also, several attempts were made at obtaining the infrared spectrum of the solid without success. When the FDNE was sprayed on a cold plate at liquid nitrogen temperatures it appeared to form glass. Attempts at annealing were unsuccessful. No attempts were made to obtain the Raman spectra of vapor or solid FDNE.

The medium intensity broad infrared bands at 3570 and 3445 cm^{-1} are the free OH and intramolecularly bound OH. In a solution of 1% FDNE in $CHCl_3$ both bands were still very clearly in evidence, indicating that hydrogen bonded OH stretch is intra- and not intermolecularly bound OH. The CH stretching region is interesting. In the infrared, there are essentially two weak bands at 2956 and 2915 cm^{-1}. In the Raman spectrum there are three very distinguishable bands at 2875, 2955, and 3010 cm^{-1}. All three are unquestionably polarized, giving credence to the structure which has a molecular symmetry of C_1. If the molecule were of C_s symmetry (possessing a plane of symmetry) the two CH stretches should be an A' and A" and should be polarized and depolarized respectively. Since all three lines are polarized, it indicates that the molecule possesses no symmetry. It is interesting that only the strongest Raman line of the three, that is the one at 2955 cm^{-1} has

an infrared counterpart. This must be the CH_2 symmetric stretch. The weak broad Raman line at 3010 cm^{-1}, which has at best a very weak broad infrared counterpart, is the CH_2 antisymmetric stretch. The weak polarized Raman line at 2875 cm^{-1} is either an impurity or combination/overtone band. The NO_2 stretches, of which there should be four, are clearly discernible. The Russian workers[2] reported them at 1320 and 1600 cm^{-1}. The very intense broad infrared band at 1601 cm^{-1} corresponds to the weak broad Raman line at 1595 cm^{-1}. This Raman band has an anomalously high depolarization ratio of .86, which indicates that this is a depolarized line and suggests that the molecule has C_s symmetry. At any rate, this area of the spectrum represents the two NO_2 antisymmetric stretching vibrations. In the region of the symmetric NO_2 stretch the Raman spectrum shows a weak polarized band at 1384 cm^{-1}, a medium polarized band at 1355 cm^{-1} and a weak, perhaps depolarized, band (dp ratio = .67) at 1325 cm^{-1}. The infrared spectrum in this region shows a strong line at 1323 cm^{-1} and a weak shoulder at 1357 cm^{-1}. Our interpretation of these bands is that the bands at 1355 cm^{-1}(R), 1357 cm^{-1}(IR) and 1325 cm^{-1}(R), 1323 cm^{-1}(IR) represent the two symmetric NO_2 stretches. The 1355 cm^{-1} being the out of phase symmetric stretch. The band at 1384 cm^{-1} is assigned as the CH_2 wag plus the OH bend. The weak Raman band at 1448 cm^{-1} (dp ratio = .77) and the medium infrared band at 1450 cm^{-1} are the CH_2 deformation. The CH_2 twist occurs at 1260 cm^{-1} and CH_2 rock at 1006 cm^{-1}.

Other vibrations of interest are the C-F, C-O, C-N, and C-C stretches. The Russian workers[2] have identified the infrared band at 1229 cm^{-1} as being the C-F stretching frequency. Our data shows a medium intensity infrared band at 1230 cm^{-1} and a weak Raman band at 1226 cm^{-1} (C-F stretches are usually weak in the Raman). These two bands are assigned to the C-F stretching vibration. The C-O stretch appears as a broad and weak Raman band centered at

1085 cm^{-1}. The infrared counterpart of this band is the strong line at 1084 cm^{-1}. The two CN stretches appear in the Raman spectrum at 916 cm^{-1}, and 855 cm^{-1}. The weak Raman band at 916 cm^{-1} has a medium intensity infrared bond at 918 cm^{-1} and is assigned as the CN_2 antisymmetric stretch. The polarized band at 855 cm^{-1} in the Raman, which is the strongest line in the Raman spectrum, has an infrared counterpart at 854 cm^{-1} and is assigned at the symmetric CN_2 stretch. The weak Raman band at 802 cm^{-1} which has a strong infrared counterpart at 804 cm^{-1} is assigned as the C-C stretch. No detailed assignment of skeletal bending modes was attempted.

In conclusion, the large number of polarized lines would have one believe that the proposed structure by the Russion workers[2] is the correct one. However, certain lines have depolarization ratios that are within experimental error of the theoretical value of 0.75 so that a molecular structure of C_s symmetry cannot be positively ruled out.

GC/FTIR and GC/Mass Spec. Experiments

The next set of experiments were designed to separate and identify the constituents of samples of FDNE and SYEP. Considerable experimental difficulty was experienced in the interfacing of the GC and the FTIR, but we did manage to obtain some reasonable data. The choice of column material was also a very real problem and finally a diethylene glycol succinate was chosen. However, the resolution of the individual peaks was never really satisfactory and the FTIR and mass spec. instruments were in all probability looking at mixtures of compounds rather than ideally looking at only one type of molecular species at a time. It must be remembered too, that compounds such as FDNE and SYEP have very low vapor pressures and, therefore, will be difficult to GC. As it turned out, all attempts at separating the SYEP samples by GC were unsuccessful. Another viable alternative used for separating these compounds was liquid chromatography. We were able to get good separation using this technique; but sample size was limited and isolation of impurities would have been too time consuming. We did have some success with the various FDNE samples, the results of these experiments are shown in Figures 3, 4, 5, 6, 7, and 8. Since the detector used in GC/FTIR is useful only up to 3300 cm^{-1}, the spectral region between 4000 and 3300 were not recorded. In this region is the O-H stretching fundamental which should be present if alcohol type impurities are present.

FDNE - Fluorochem methyl cyano acetate Run

Figures 3 and 4 show the GC and infrared spectrum of FDNE made by Fluorochem's methyl cyano acetate process. The GC clearly shows five resolvable peaks, however, the base line indicates that the resolution between these different compounds is not as good as it should be. After trying many different column materials, this was the best resolution possible. Time precluded our obtaining GC/mass spec. data on this sample and, therefore, we can only make intelligent guesses as to what the five peaks are. Peak one clearly contains no nitro groups but does appear to contain some carbonyl functionality. This could conceivably be some starting compound (methyl cyano acetate) which was unreacted. Peaks two through five all contain the characteristic nitro peaks around 1600 cm^{-1} and 1320 cm^{-1}. Peak five is all FDNE and peaks two, three, and four may very well contain a certain amount of FDNE. This amount of FDNE which comes out with the other compounds may obscure spectroscopic features of importance on these other compounds. Peak number four contains some interesting features not found in FDNE. It has a peak which could be attributed to a carbonyl, plus it also contains nitro peaks. It may be a compound such as fluoro dinitro acetaldehyde.

FDNE - Fluorochem Malonate Preparation

Figures 5 and 6 show the GC and infrared spectrum of FDNE made by Fluorochem's malonate process. Figure 5 shows five clearly discernible peaks. Peak number one is CH_2Cl_2 which is the solvent in which the FDNE is received. Peak number five is FDNE. Peaks number two, three, and four all possess the characteristic nitro peaks. Peaks two and three

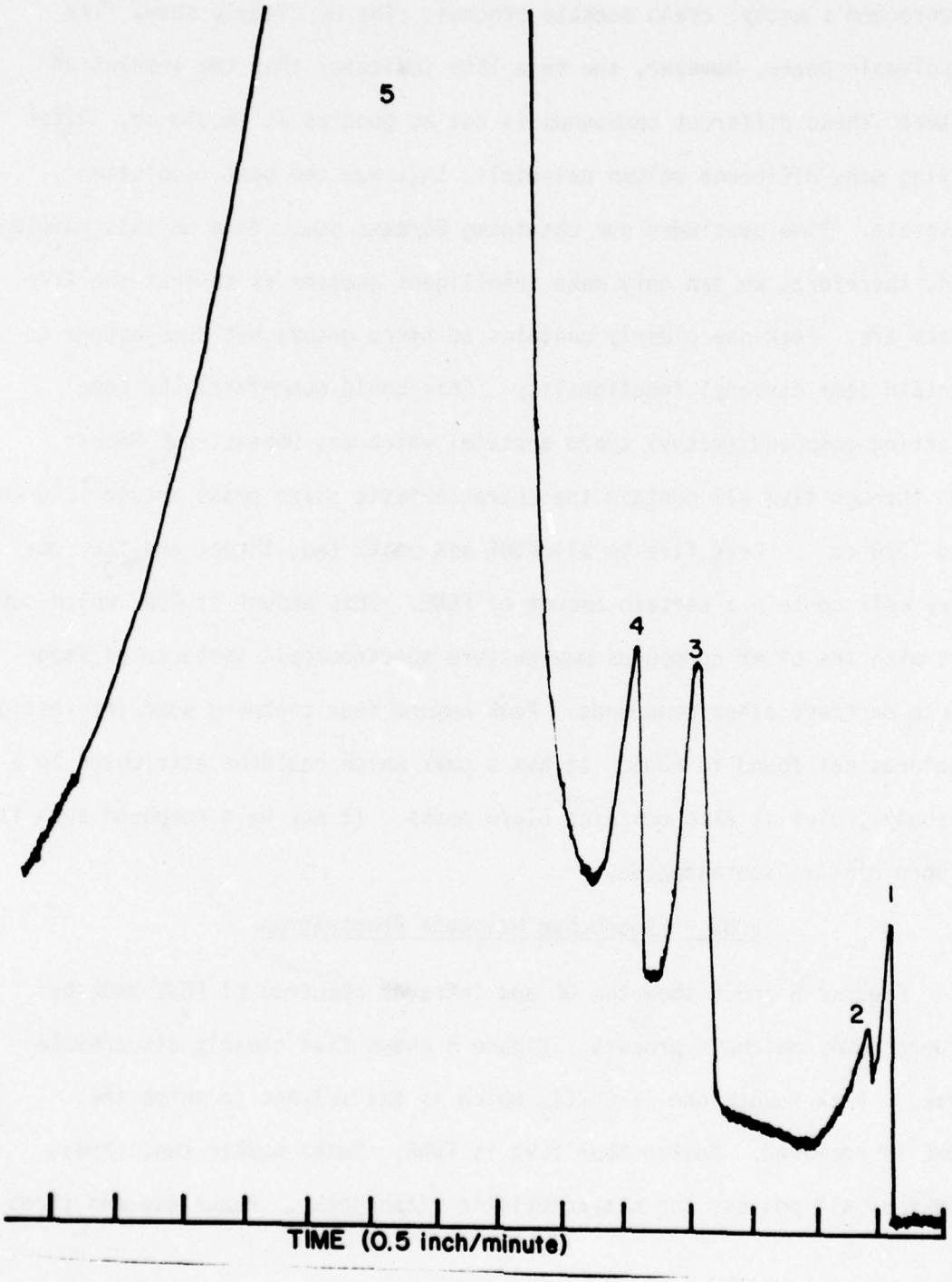


FIGURE 3

GAS CHROMATOGRAM OF FLUOROCHEM FDNE METHYL CYANO ACETATE RUN

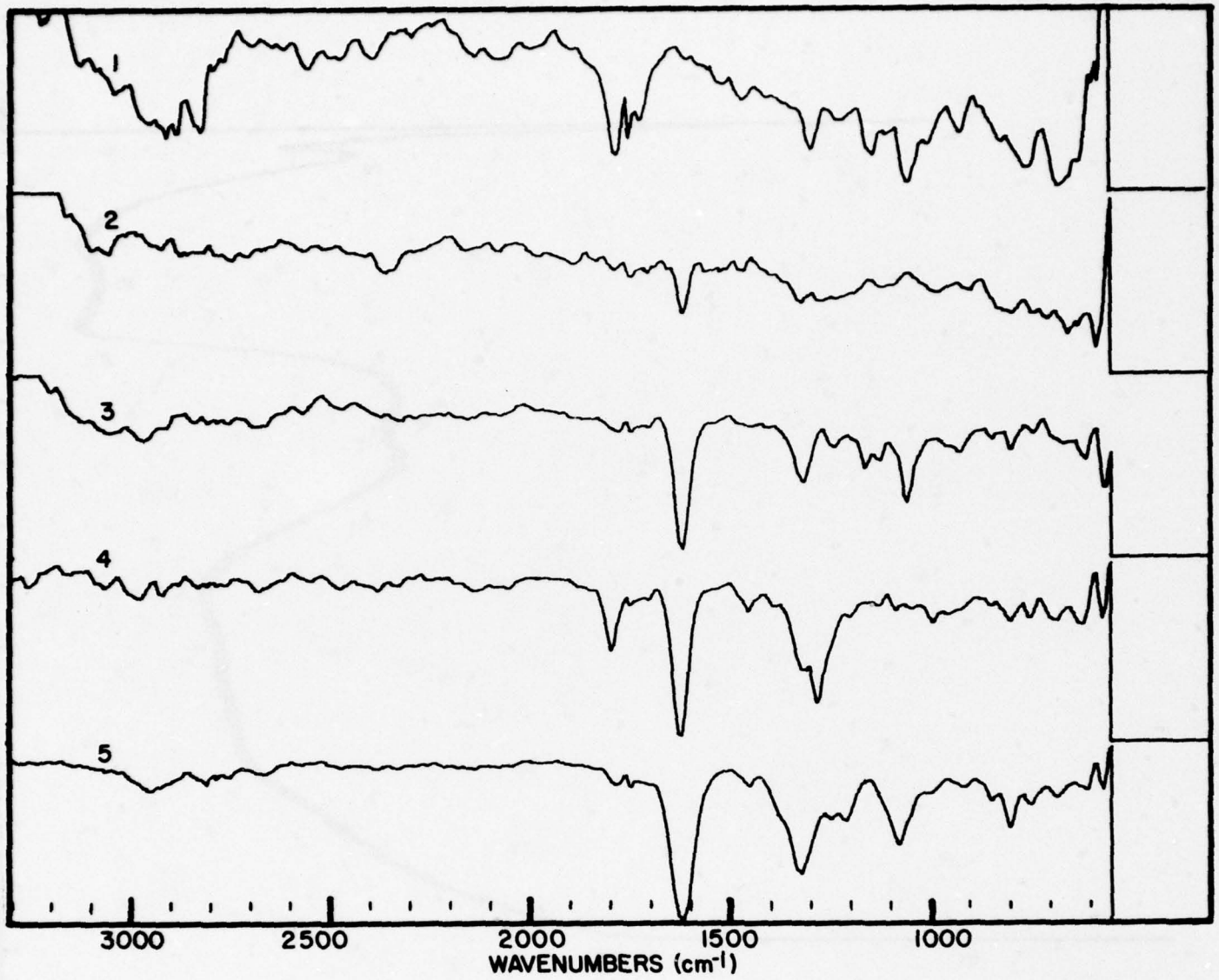


FIGURE 4

I. R. SPECTRA OF COMPONENTS SHOWN IN FIGURE 3

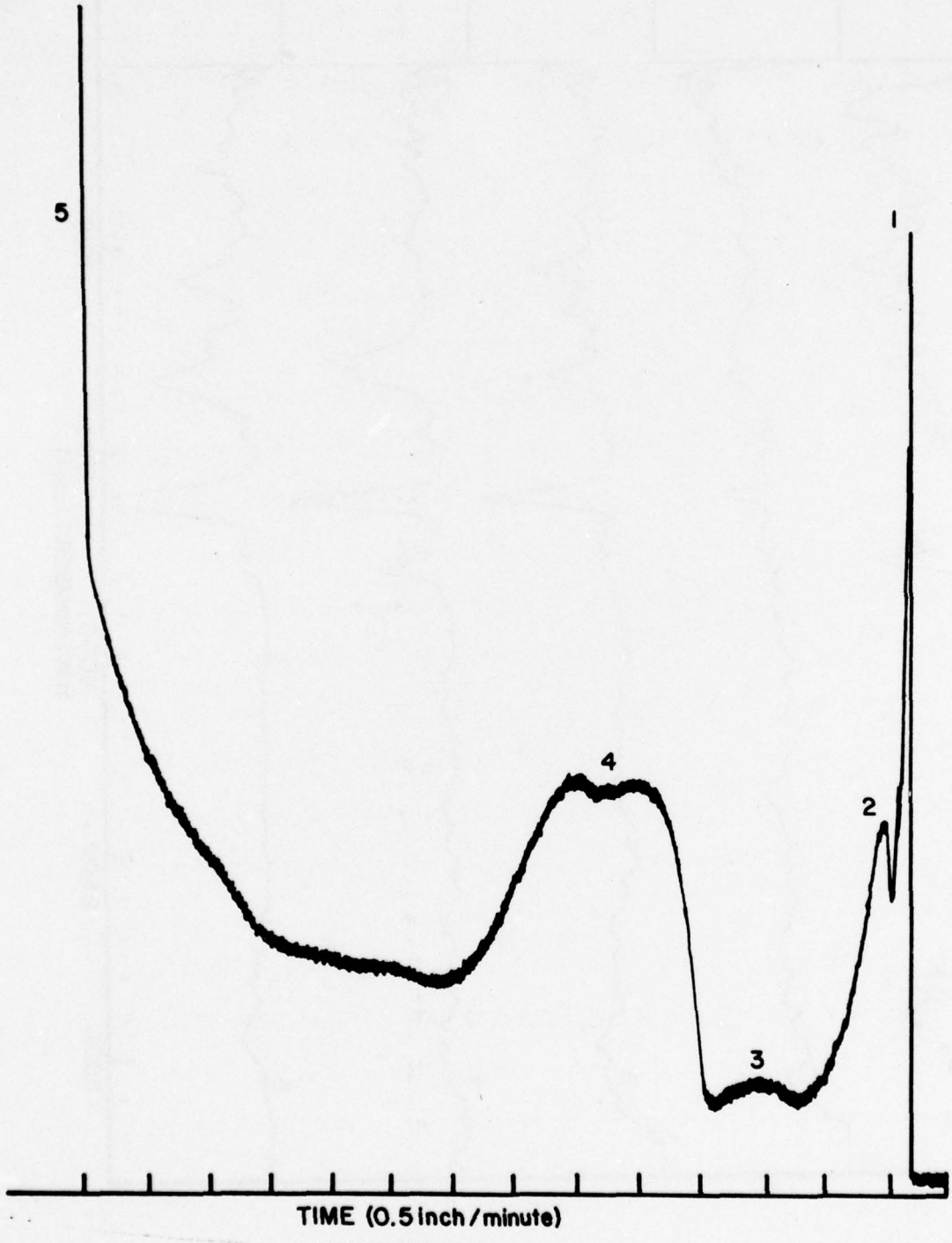


FIGURE 5

GAS CHROMATOGRAM OF FLUOROCHEM FDNE MALONATE RUN

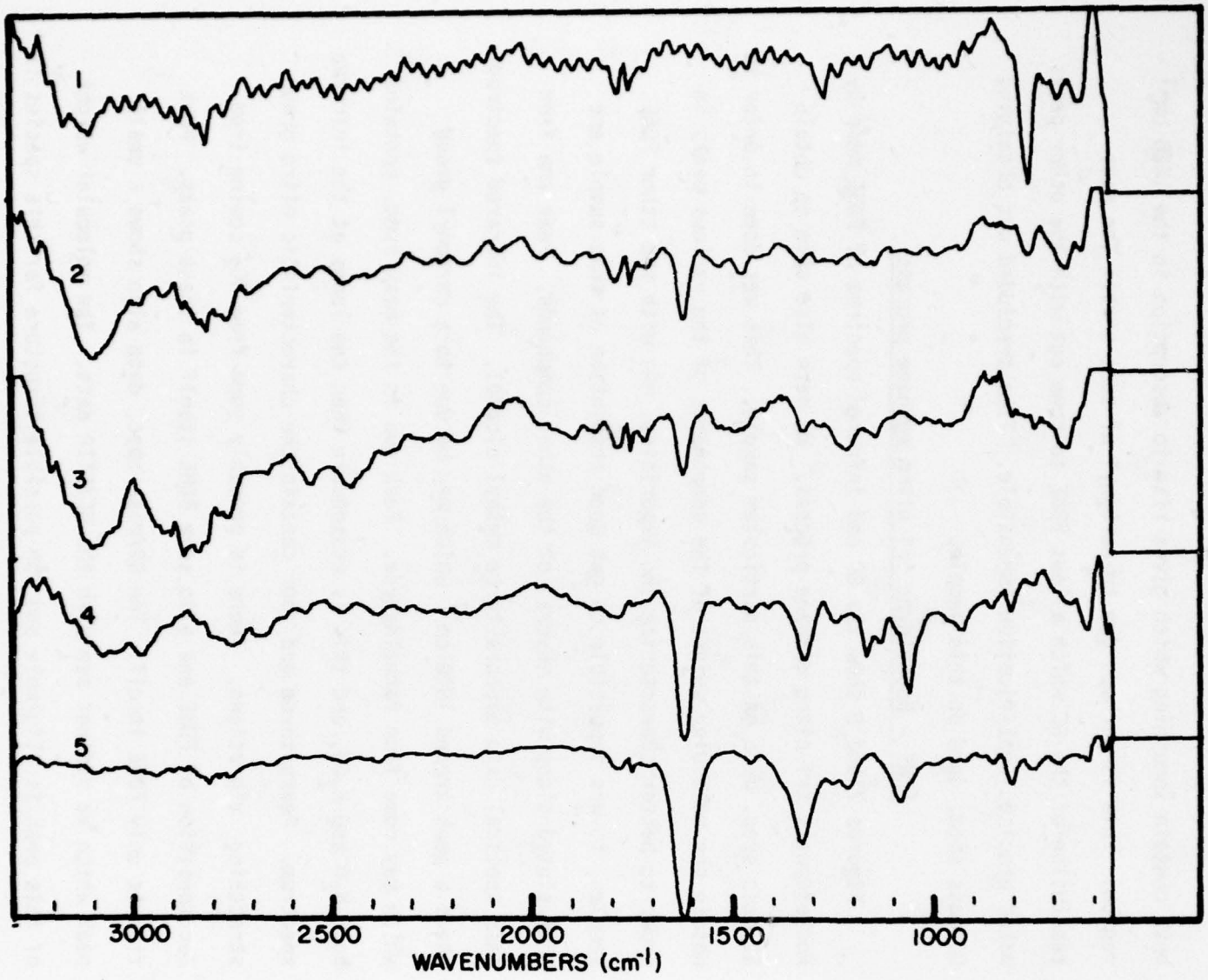


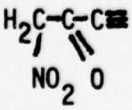
FIGURE 6

I. R. SPECTRA OF COMPONENTS SHOWN IN FIGURE 5

both contain something which gives rise to absorption in the 1880 cm^{-1} region. This is perhaps due to carbonyl of some sort. The poor resolution of the GC which allows FDNE to come out with the other peaks makes precise identification impossible. Time precluded our obtaining GC/mass spec. data on this sample.

FDNE - Rocketdyne tri nitro methane process

Figures 7 and 8 show the GC and infrared spectrum of FDNE made by Rocketdyne's tri nitro methane process. We were also able to obtain GC/mass spec. data on this particular sample. This was done in order to obtain the molecular weight of the components of the various peaks in order to better characterize the impurities. As with the other FDNE samples, it was impossible to get good resolution of this sample and FDNE eluted along with several of the other compounds. Peak one from mass spectral data appears to be methyl alcohol. The infrared spectrum shows a peak around 1800 cm^{-1} which may be due to a carbonyl group which may come from formaldehyde. Peak two in the mass spec. contains both H_2O and H_2CO, and this is reasonable when one looks at the infrared spectrum. Peaks three and four contain the characteristic nitro group stretching vibrations. There is probably some free NO_2 coming from decomposition of FDNE and also some FDNE itself in these peaks. Peak five is only FDNE itself. The GC/mass spec. data also shows a small peak which we did not see with the GC/FTIR data. The molecular weight of this peak is 114g/mole and one possible structure for this species is



.

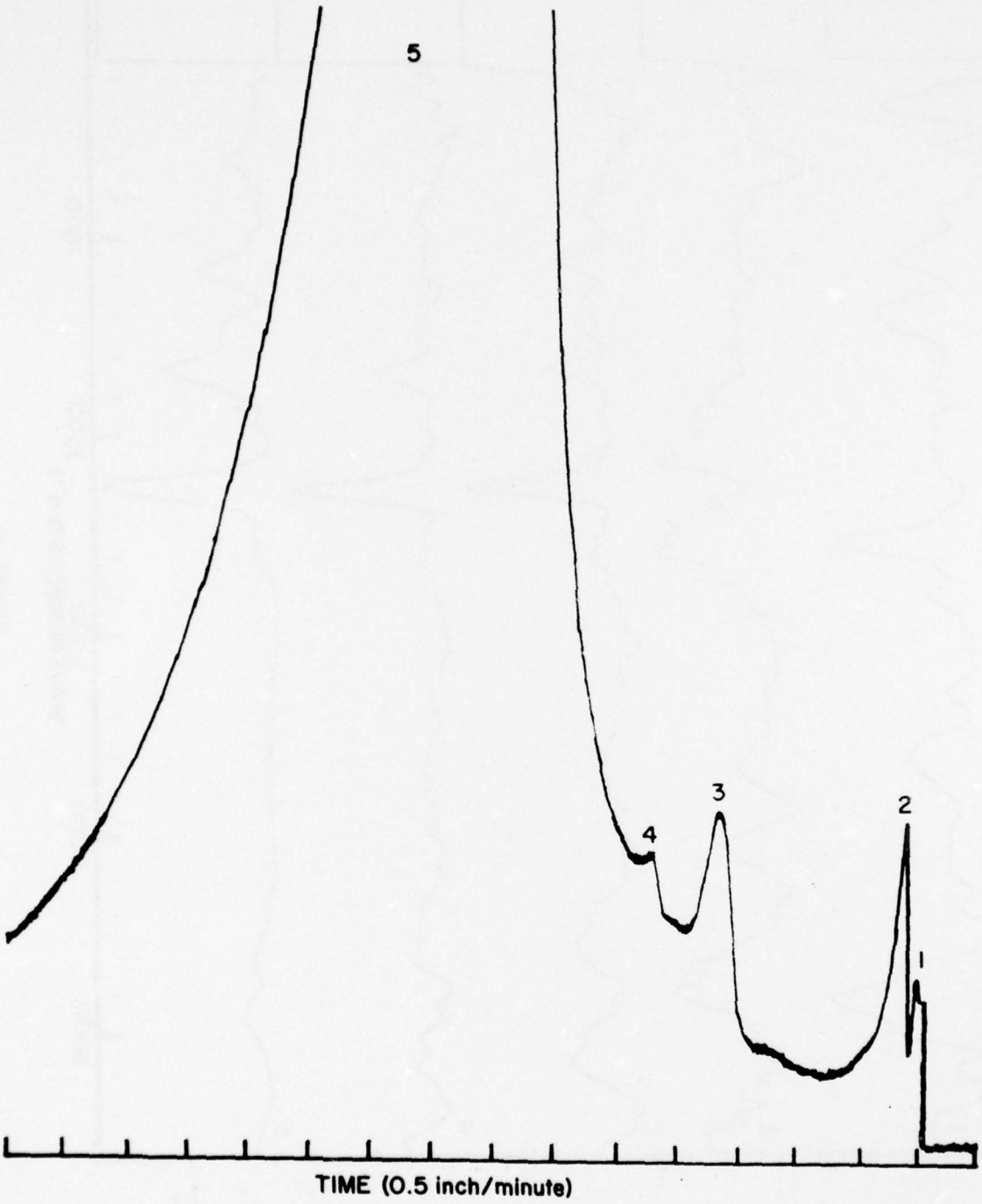


FIGURE 7

GAS CHROMATOGRAM OF ROCKETDYNE FDNE

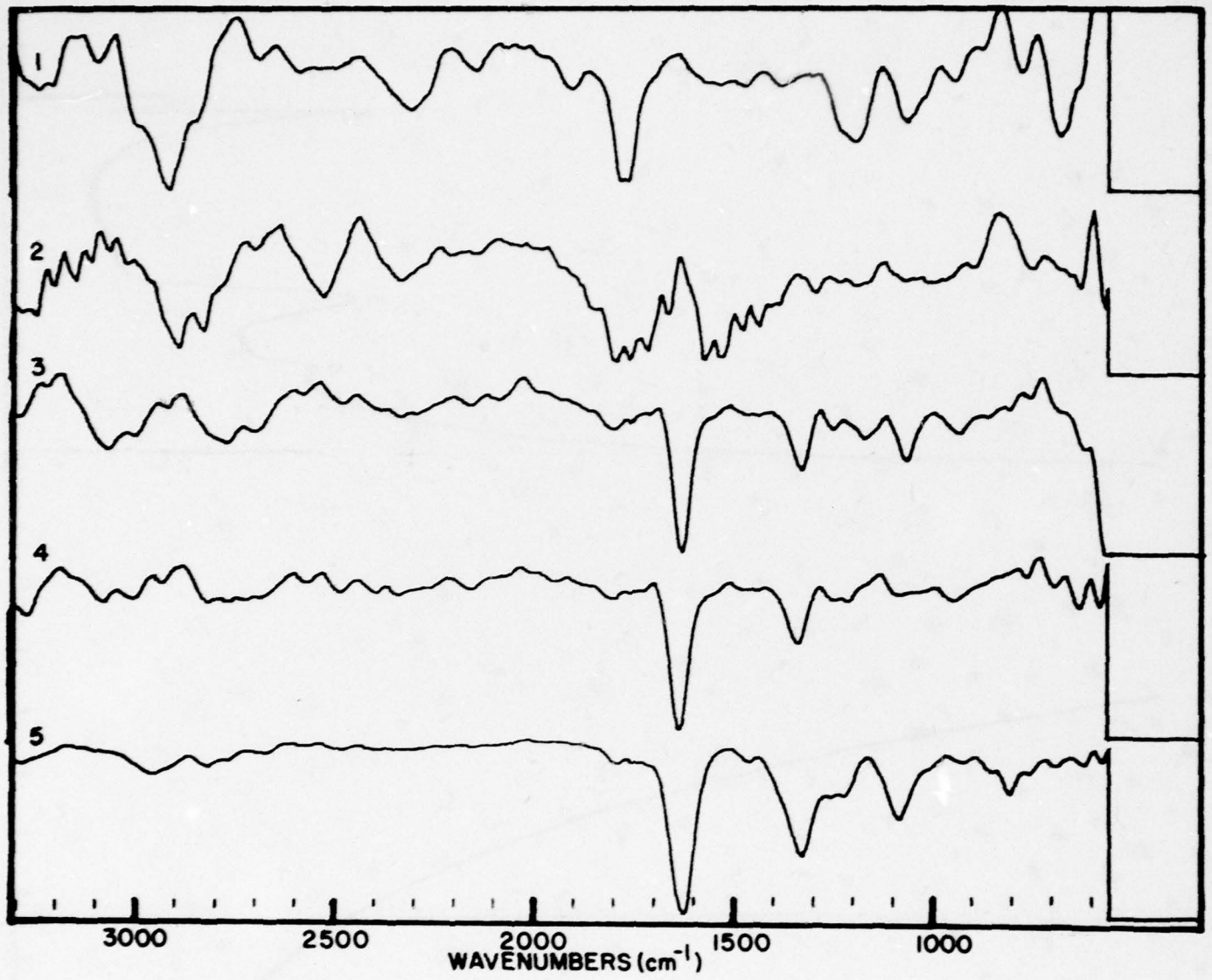


FIGURE 8

I. R. SPECTRA OF COMPONENTS SHOWN IN FIGURE 7

CONCLUSIONS AND RECOMMENDATIONS

Our effort to separate the various impurities in SYEP samples proved to be experimentally impossible. None of the columns tried gave adequate separation and it may be that the vapor pressure of SYEP makes it an almost impossible task to separate by vapor phase chromatography. Therefore, we have no experimental data other than the infrared spectrum of various SYEP and FEFO samples as received from the vendor, Figures 9 and 10.

We were able to obtain information on three FDNE samples and the impurities contained in them. Comparison of the infrared and Raman spectra allowed us to identify and assign most of the important vibrations of FDNE and to identify what the specific impurities are.

If the identification of impurities in various SYEP samples is to be pursued, I would recommend that the samples be separated using liquid chromatography. Although this method would be tedious and time consuming, good separation of the impurities could probably be achieved. The samples could then be examined by conventional GC and IR techniques to identify the compounds.

If vibrational analyses is to be pursued on a research basis, I would recommend that consideration be given to the purchasing of a Raman spectrophotometer. Comparison of infrared and Raman data can provide a wealth of information about vibrational fundamentals. One can obtain excellent data on solids, liquids, and gases and large quantities of sample are no longer needed. Analysis of coated surfaces is another area which very readily lends itself to Raman analysis. It would be a very valuable addition to an already excellently equipped laboratory.

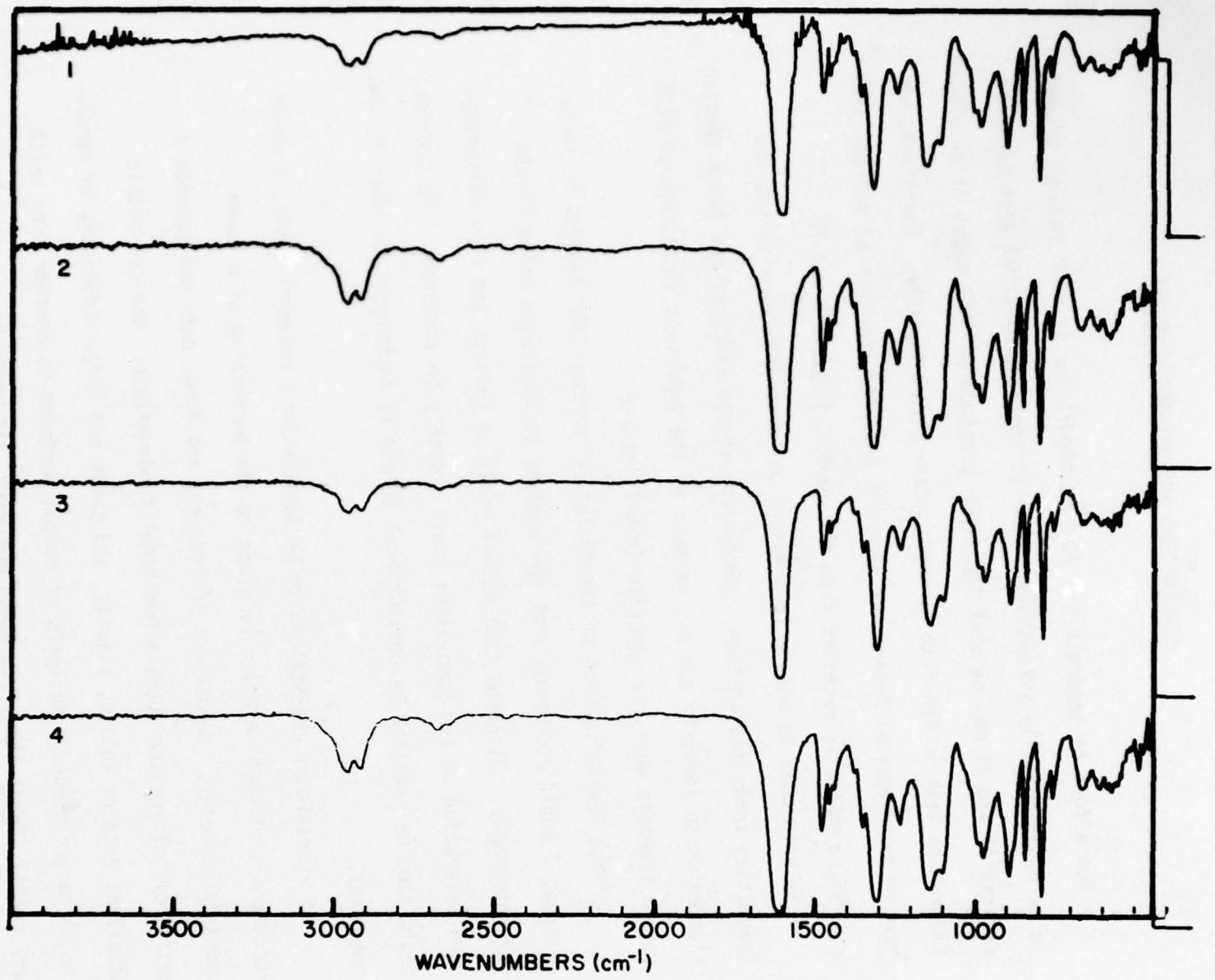


FIGURE 9

I. R. SPECTRA OF VARIOUS SYEP LOTS

1. LOT 4 (COLUMN) 2. LOT 4 (ELUATE) 3. LOT 2 4. FLUOROCHEM PREP

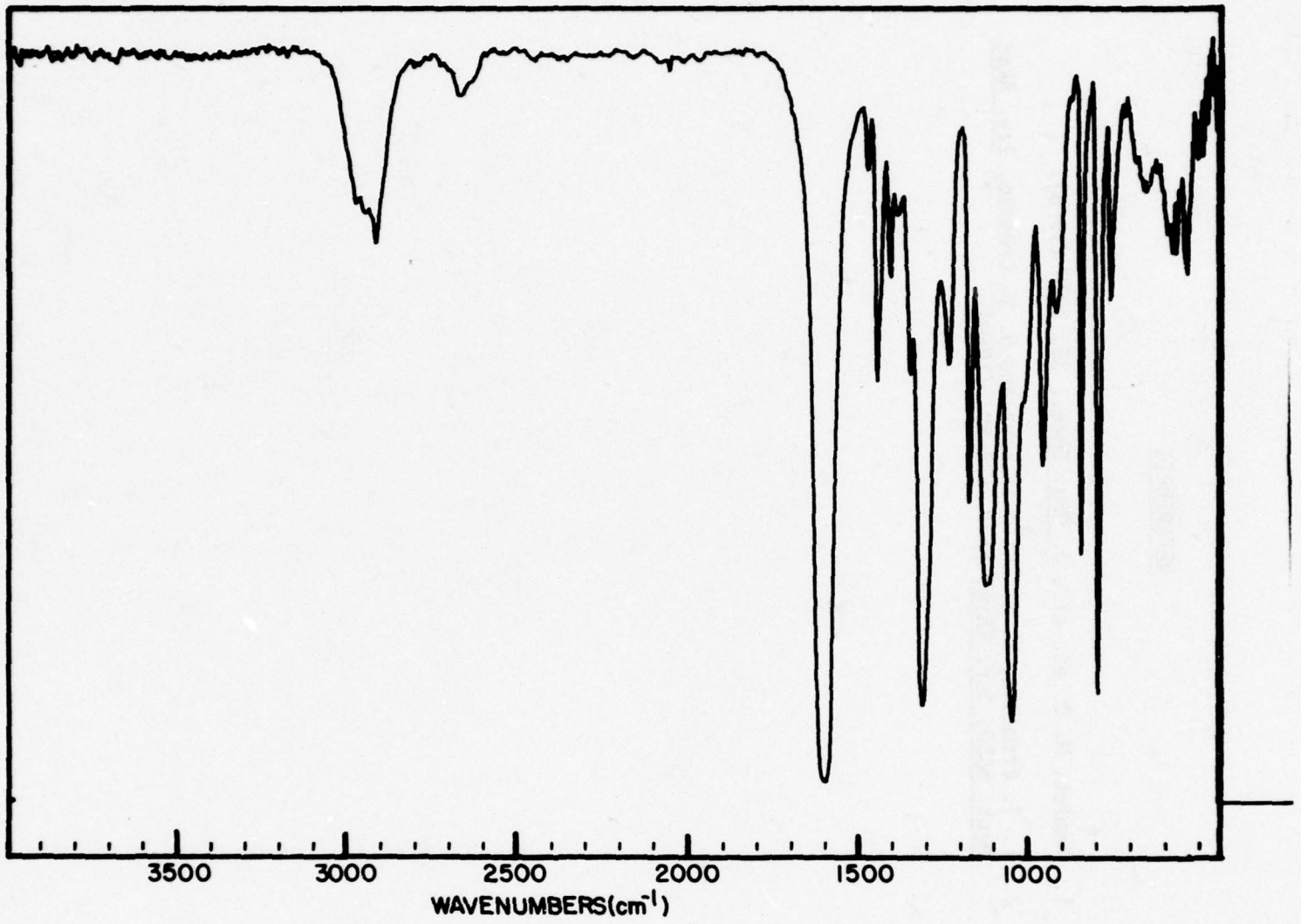


FIGURE 10

I. R. SPECTRUM FEFO, ROCKETDYNE

REFERENCES

1. Kamlet, M. J. et. al., J. Org. Chem., 33, 3070 (1968).

2. L. T. Eremenko, N. G. Zhitomirskaya and G. V. Oreshko, Izv. Akad. Nauk. SSSR, Ser. Khim. (12) 2674-80, (1969).

1977 USAF-ASEE SUMMER FACULTY RESEARCH PROGRAM
sponsored by
THE AIR FORCE OFFICE SCIENTIFIC RESEARCH
conducted by
AUBURN UNIVERSITY AND OHIO STATE UNIVERSITY

PARTICIPANT'S FINAL REPORT

ROTATIONAL AND MEAN FLOW EFFECTS ON MOTOR STABILITY

Prepared by:	William K. Van Moorhem Ph.D.
Academic Rank:	Research Assistant Professor
Department and University:	Department of Mechanical and Industrial Engineering University of Utah
Assignment:	
(Air Force Base)	Edwards AFB
(Laboratory)	Rocket Propulsion Laboratory
(Division)	Technology
(Branch)	Supporting Technology
USAF Research Colleague:	Jay N. Levine
Date:	August 24, 1977
Contract No.:	F44620-75-C-0031

ROTATIONAL AND MEAN FLOW EFFECTS ON MOTOR STABILITY

by
William K. Van Moorhem

ABSTRACT

The growth of pressure oscillations in the cavity of a solid propellant rocket motor is termed a combustion instability. The pressure oscillations have been found to be due to an excited acoustic mode of the cavity and stability analyses can be developed using methods of acoustics. Two approaches have been developed for determining stability. The first is based on an eigenvalue--Green's function approach. The second method is a direct energy calculation. In the basic form of both of these analyses it is assumed that the mean flow is irrotational, and in the eigenvalue approach it is also assumed that the mean flow has a small Mach number.

Methods for removing these assumptions are discussed and the results of a literature survey on this subject are included. The energy approach has been shown to be in error and the source and methods for correcting this error are described. A second area of conflict between these two approaches, "flow turning," is also discussed. Conclusions from this work are suggestions for the direction of needed fundamental research to improve existing methods of analysis and to develop more general methods of stability analysis.

ACKNOWLEDGEMENT

The author is deeply grateful to Mr. Jay Levine and Captain Jack Donn for their guidance, technical assistance, and friendship during this summer research program. The entire staff of the Rocket Propulsion Laboratory, particularly Dr. R. Weiss, Dr. L. Quinn, Mr. W. Andrepont, and Mrs. B. Sumrow, deserve thanks for making the summer an enjoyable and productive one.

The support of this program by the Air Force Systems Command and the superb administration by Auburn University and the ASEE, particularly by Mr. Fred O'Brien, Jr., is also gratefully acknowledged.

NOMENCLATURE

A	Arbitrary scalar flow variable
B	Arbitrary vector flow variable
E	Stagnation internal energy
$\dot{m}$	Mass flow
n, $\hat{n}$	Coordinate perpendicular to streamlines, unit normal
P	Pressure
R	Radius of curvature of streamlines
s	Coordinate along streamlines
S	Entropy, area
t	Time
u	X component of velocity
V	Velocity
X	Coordinate along axis of cylinder
ζ	Vorticity
ρ	Density

SUPERSCRIPTS

(o)	Mean flow quantity
(1)	Acoustic quantity

SUBSCRIPTS

2	Operator or quantity in plane of integration

INTRODUCTION

During operation of a solid propellant rocket motor pressure oscillations in the combustion chamber are often observed. The frequency of the oscillations has led to their identification as an acoustic mode of the gas in the combustion chamber. Although small amplitude oscillations undoubtedly occur regularly in all solid propellant motors, in some cases they grow to significant amplitude. In this case, serious problems can result from variations in thrust and in nozzle heat transfer rates which can,in extreme cases,lead to motor failure.

In order for an acoustic mode to grow in amplitude it must be supplied with energy at a rate exceeding its energy loss. Energy transfer occurs at the cavity boundaries, including the nozzle, and by interaction between the steady mean flow and the acoustic disturbance. Stability,or the lack thereof, is determined by the sign of the difference between the rates of energy addition and loss, values of which are more or less of equal magnitude. An increase in the magnitude of an acoustic mode with time is termed a "Combustion Instability" and two analytical models exist for studying stability. The first model has been developed mainly by Culick (1-5) and is based on an eigenvalue--Green's function approach for the calculation of the pressure in the oscillations. The equations can then be formulated in such a way that the acoustic growth constant is obtained. The resulting expression is dependent on acoustic energy and represents the energy balance described above. This approach makes use of two small parameters, the mean flow Mach number, and the amplitude of the acoustic oscillations.

The second approach is based on the direct calculation of the acoustic energy in the motor. This method has been developed by Cantrell and Hart (6). It requires only the assumption of small amplitude for the acoustic oscillations. However, some errors have been made in interpreting the energy method. These errors are discussed below.

OBJECTIVES

In both of the methods which have been used to determine combustion stability a number of simplifying assumptions have been made. These concern the irrotationality and homogeneity of the mean flow. Rotational effects by themselves, however, have been investigated by Culick (2). Thus the decision was made to broaden the investigation to consider some additional mean flow effects beyond rotationality. The effects of inhomogeneities and high mean Mach number were considered. These effects are closely coupled since as the mean flow Mach number is increased significant variations in the other flow properties occur with variations in Mach number.

As work progressed on these questions additional questions arose concerning the relationship of the two approaches to stability. This in turn raised questions about the eigenvalue --Green's function approach and certain terms which have been added. As the breadth of the investigation grew the aims (due to the time restrictions) were reduced to a literature survey and some brief analyses. This work may therefore raise more questions than it answers, but it does put the state of the method of linear analysis of combustion stability into perspective.

ROTATIONAL FLOW EFFECTS

In most external flow problems the assumption of irrotationality is a good one since vorticity (and rotational flow) is only generated in restricted regions, boundary and shear layers or curved shocks, and the bulk of the flow is irrotational. The assumption of irrotational flow allows considerable mathematical simplification, for example, the definition of a velocity potential.

In an interior flow where the flow is injected uniformly across a curved boundary the entire flow must be rotational.

Consider flow in a cavity. If it is assumed that the cavity is axisymmetric and the flow enters the cavity perpendicular to the walls with the coordinate s along a streamline and n perpendicular to s then Von Mises (7) shows that the vorticity ζ is given by

$$\zeta = \frac{V}{R} - \frac{\partial V}{\partial n}$$

If the injection velocity is constant along the cavity walls then

$$\zeta = \frac{V}{R}$$

along the cavity wall and since the radii of curvature of the streamlines at the wall are, in general, not infinite the flow at the wall must be rotational. Vorticity is constant along streamlines in steady flow and the entire flow is rotational.

Culick (2) suggests a rotational mean flow model for flow in a hollow cylindrical grain and Dunlap, Willoughby and Hermsen (8) provide experimental conformation of this analytic model. Vorticity will also be generated in regions of strong shear as in an external flow.

Culick (2) presents an analysis of the effects of a rotational mean flow on stability. He shows that the form of the final result is unchanged whether or not the flow is rotational. The only effect of rotational flow is to change the velocity distribution at the exit (nozzle) end of the cavity. For the hollow cylindrical grain Culick considers, rotationality increases the mean flow velocity near the center of the exit and reduces it near the cavity boundary. In no case considered by Culick does this decrease the stability of the oscillations and in most cases it increases stability.

Flandro (9) has also investigated a rotational flow effect, however, Flandro's analysis considered not the distributed vorticity of Culick's work but concentrated point vortices such as those shed by a bluff body in a steady flow. Under this assumption Flandro finds that vortex shedding can drive the acoustic oscillations in a cavity. Flandro's model is a crude one but results appear entirely reasonable.

A configuration has been described by Kuentzmann and Lengelle (10) which appears to be related to Flandro's model. Kuentzmann and Lengelle investigated a grain design which consisted of a hollow cylinder with circumferential grooves. This design exhibited an instability, possibly related to vortex shedding and also a shift in the frequencies determined for the no flow cavity and those found experimentally with flow. Although Flandro's work does not explain the frequency shift it does appear highly relevant to this design.

Janardan and Zinn (11) report that nozzle submergence decreases stability. This effect is also likely to be related to vortex shedding and the type of analysis Flandro has carried out.

TYPES OF DISTURBANCES

Before discussing the energy method of predicting stability it is necessary to consider the types of disturbances that can be produced in a cavity. This question has been considered by Chu and Kovasznay (12). By assuming a fluid which is non-moving and uniform before any disturbance occurs, they showed that any small perturbation to the initial fluid can consist of a combination of three basic modes of disturbance. These three are acoustic, vorticity and entropy disturbances. The acoustic disturbance is the only one of the three that involves pressure perturbations (if the disturbances are weak) and that propagates. For an initially homentropic fluid the acoustic waves are isentropic and irrotational. The vorticity mode consists of a rotational velocity field which behaves in an incompressible manner. There is no pressure or entropy fluctuation associated with this mode. Entropy disturbances consist of a region where the entropy of the fluid has been changed, basically a "hot spot" in the flow. There are no pressure disturbances associated with this mode. In the Chu and Kovasznay model both the vorticity and entropy mode of disturbance cannot move. In a moving fluid, however, both of these disturbances are convected with the mean flow. Also under the assumption of a uniform undisturbed state these three modes are independent, each can exist separately, or in combination, but there is no interaction to the lowest order in the perturbation magnitude.

If, however, the undisturbed gas is non-uniform, $\nabla S^{(0)} \neq 0$ say, then modes couple and the situation becomes more complicated. It is easily shown that with $\nabla S^{(0)} \neq 0$ (or $\nabla \rho^{(0)} \neq 0$), since $P^{(0)}$ is constant if $V^{(0)} = 0$ and there are no sources of mass, momentum or heat, that the equations governing the vorticity, pressure and entropy disturbances are

$$\frac{\partial \xi^{(1)}}{\partial t} = \frac{\nabla \rho^{(0)} \times \nabla P^{(1)}}{(\rho^{(0)})^2}$$

$$\frac{1}{(a^{(0)})^2} \frac{\partial^2 P^{(1)}}{\partial t^2} - \nabla^2 P^{(1)} = \frac{\nabla P^{(1)}}{\gamma} \cdot \frac{\nabla S^{(0)}}{C_v}$$

and

$$\frac{\partial S^{(1)}}{\partial t} + \underline{V}^{(1)} \cdot \nabla S^{(0)} = 0$$

Clearly, if the propagating pressure disturbances are limited to the acoustic mode, the acoustic waves will excite the vorticity mode. At a point, entropy fluctuations also occur as a result of the velocities produced by acoustic and vorticity disturbances. Thus the modes become coupled even in this simple case where the mean flow is at rest. If the mean flow has a non-uniform velocity further coupling results.

An additional form of coupling results when source terms are included in the equations. A heat source, for example, can produce both acoustic and entropy disturbances.

As a result of the above discussion it should be clear that in all but the simplest cases (uniform mean properties) it is not possible to excite only the acoustic mode of the chamber without exciting either or both vorticity and/or entropy disturbances. Since all three of these disturbances are energy containing these ideas have a great deal of relevance to any energy method for investigating stability. These concepts are by no means limited to combustion stability but are important in development of theories for generation of sound and sound propagation. Some recent work on this subject is described by Howe (13) and Yates and Sandri (14, 15).

THE ENERGY METHOD

The stability of an acoustic oscillation in a cavity is a classical problem in acoustics and stability conditions have been developed, see Morse (16) for example. Classical acoustics has almost always not included a mean flow velocity, and energy relations are obtained by combining the perturbed forms of the momentum and continuity equations. Cantrell and Hart's (6) approach to combustion stability followed the classical approach for a cavity but included a mean flow and was derived directly from the perturbed energy equation. Zinn (17) later obtained similar results without first integrating over the volume as Cantrell and Hart had done.

This type of approach is particularly attractive in that although both Cantrell and Hart, and Zinn assumed irrotational homentropic mean flow they made no assumption about mean Mach number or that the mean flow had uniform properties. Thus it appears that their results are more general than Culick's and is certainly simpler and more direct.

Culick (4, 18) compared the Hart and Cantrell result with his results and found them to be identical provided: 1) terms of higher order than he considered were dropped and 2) there are no source terms. The need to drop terms of higher order than carried by Culick is to be expected but the problem with including source terms (particles in the flow can act as sources of mass, momentum and energy) is more serious. If the Hart and Cantrell analysis is repeated with source terms the results do not agree with Culick's. Culick explains this disagreement as resulting from considering the total energy in the cavity rather than just the acoustic energy but does not offer further explanation. This is best understood by recalling the results of the previous section.

There are three types of disturbances that can occur in the chamber but only one of them, the acoustic disturbance, is of interest. The stability analysis is concerned with the growth of the pressure perturbations and these are only associated with acoustic disturbances while the energy argument deals with the energy contained in all three types of disturbances.

The effect of the three modes is clearly seen by considering a fluctuating heat source in the cavity. As noted above, this source produces both acoustic waves and entropy disturbances. The actual mechanism is a heating of the gas in a region which then expands and does work on the surrounding gas. The motion of the surrounding gas is the acoustic disturbance. It is the energy of the acoustic wave that is desired but the Hart and Cantrell approach treats both the energy in the acoustic wave and the energy stored in gas in the entropy disturbance.

If there are no sources so that no energy is being added to the existing disturbances and if only the acoustic perturbation quantities are used in calculating the energy of the disturbances, then the acoustic energy results. This result is equivalent with Culick's. When there are sources, however, this approach does not distinguish into which mode the energy is flowing and gives an incorrect result.

In order to apply the energy type of approach to combustion stability it will be necessary to eliminate the energy in both vorticity and entropy disturbances from the total energy of the disturbances.

Morfey (21) has attempted to do this. He derives an energy equation similar to the Hart and Cantrell equation but using only the momentum and continuity equation, thus eliminating the entropy disturbances. He also separates out vorticity disturbances, however he does not completely eliminate them from his result. Morfey's approach appears to be the type needed to allow a direct energy analysis of stability but the energy associated with vorticity needs to be completely removed except for interactive terms.

Culick, in addition, has offered one further criticism of energy approaches. This is that it is not clear how an effect which is known as "flow turning" is to be incorporated into them. Culick is forced to simply "patch" this into his three-dimensional analysis although it arises naturally in the one-dimensional problem.

FLOW TURNING

Beginning in 1972, Culick (3, 4, 5, 18) has developed a somewhat controversial concept, known as flow turning, which he argues must be included in the three dimensional analysis of combustion stability of solid propellant motors. The controversy associated with this concept appears to arise from two sources: 1) the manner in which the effect is derived and 2) lack of physical understanding of what is occurring.

Culick's derivation is based on a comparison of the one-dimensional stability problem, including mass addition, with the same three-dimensional problem, with mass injection on the lateral boundaries, after the flow velocities and derivatives in the lateral directions have been eliminated. Since in the one-dimensional

problem mass addition is introduced as inhomogeneous terms in the flow equations, while in the three-dimensional problem (before reduction to one-dimension) it is a boundary condition, it is clear that a difference will occur between the two approaches. Culick then argues that by including the mass injections as a distributed source he can maintain an analogy with the one-dimensional problem. This analogy is desirable since in a one-dimensional injection problem the injected gas is "mixed" with the original stream without any discussion of how this "mixing" or "averaging" process occurs. Clearly, viscosity will play a role in the steady state mixing and an entropy increase occurs (see (20) for example). Culick, however, needs to model the acquisition of acoustic motion by a non-oscillating gas injected into an acoustic field. His model is analogous to the steady mixing problem and results in entropy production (5).

A brief fundamental analysis has been developed in which terms which would lead to flow turning effects arise naturally in the transition from a three-dimensional problem to a one-dimensional problem. These results while not answering all the questions which have arisen in connection with Culick's results do appear to help in understanding his results.

Consider the problem of flow in a cylindrical cavity where flow is injected across the lateral boundary. The three-dimensional equations governing this flow can be written as

$$\frac{\partial \rho}{\partial t} + \nabla \cdot (\rho \underline{V}) = 0$$

$$\frac{\partial (\rho \underline{V})}{\partial t} + \nabla \cdot (\rho \underline{V}\underline{V}) + \nabla P = 0$$

and

$$\frac{\partial (\rho E)}{\partial t} + \nabla \cdot (\rho \underline{V} E) + \nabla (P \underline{V}) = 0$$

with a boundary condition

$$\rho \underline{V} \cdot \hat{n} = -\dot{m}$$

on lateral boundary. Other boundary conditions would, of course, be required to completely pose the problem.

Now consider the reduction to a one-dimensional problem, retaining dependance only along the cylindrical axis, the X direction. This could be accomplished by the usual approach or by the method described below.

One-dimensional flow is considered by most authors to give an average value of the flow properties across a channel, but this idea does not seem to have been applied formally. Let us define the average value of a variable A as

$$\langle A \rangle = \frac{1}{S} \int_S A \, d\sigma$$

where the integration is carried out over the channel cross sectional area.

Using the definition it is easily shown that

$$\int_S \frac{\partial A}{\partial t}\, d\sigma = \frac{\partial}{\partial t}(\langle A \rangle S)$$

and

$$\int_S \nabla \cdot \underline{B}\, d\sigma = \int_S \frac{\partial B_x}{\partial x}\, d\sigma + \int_S \nabla_2 \cdot \underline{B}_2\, d\sigma$$

$$= \frac{\partial}{\partial x}(\langle B_x \rangle S) + \oint \hat{n}_2 \cdot \underline{B}_2\, dl$$

where the subscript 2 applies to the components in the plane of S and the line integral is around the perimeter of S. Applying these results to the flow equations yields

$$\frac{\partial}{\partial t}(\langle \rho \rangle S) + \frac{\partial}{\partial x}(\langle \rho u \rangle S) = -\oint \hat{n}_2 \cdot \rho \underline{V}_2\, dl$$

and

$$\frac{\partial}{\partial t}(\langle \rho u \rangle S) + \frac{\partial}{\partial x}(\langle \rho u u \rangle S) = -\oint \hat{n}_2 \cdot \rho u \underline{V}_2\, dl$$

$$\frac{\partial}{\partial t}(\langle \rho E \rangle S) + \frac{\partial}{\partial x}(\langle \rho u E \rangle S) = -\oint \hat{n}_2 \cdot \rho \underline{V}_2 E\, dl$$

where only the X component of the momentum equation has been retained. The first integral can be rewritten as $\oint \hat{n}_2 \cdot \rho \underline{V}_2\, dl =$

$\oint \hat{n} \cdot \rho \underline{V}\, dl = -\oint \dot{m}\, dl$ using the boundary condition and represents the mass injection on the lateral boundary. The other integrals represent the X component of injected momentum and injected energy. These are the equations Culick (3) begins with in his one-dimensional analysis, if particles and heat sources are ignored, yet they are obtained from the three-dimensional problem. Thus, it appears that the averaging technique allows the lateral boundary condition to be retained as an inhomogeneous term while the usual technique of dropping lateral derivatives and velocity components results in difficulties with this lateral boundary condition.

This analysis shows how terms which are the source of flow turning can arise naturally by an applying averaging condition in the reduction of three-dimensional flow equations to one-dimension. It makes it clear that the flow turning effect results from a boundary condition in the full three-dimensional problem.

The analysis carried out here does not tell us what is happening in the acoustic case. A similar approach has been attempted by perturbing the equations before they averaged, however, the results are not equivalent to the usual one-dimension acoustic equations. The cause of this is presently not clear. There still remains some questions: 1) Does the mechanism by which a non-oscillating gas acquires acoustic oscillations result in entropy production?

2) Can Culick's results be explained directly from the three-dimensional problem, without patching?

RESULTS AND CONCLUSIONS

At present, the eigenvalue--Green's function analysis of combustion instability, as developed by Culick, is the only fundamentally correct approach extant. Questions have been raised about this method, particularly the flow turning effects and these need to be resolved. First, it needs to be determined if flow turning as modeled is correct. This can be accomplished by detailed mathematical modelling coupled with experiment. The techniques necessary to make these measurements have been developed (19). Second, it needs to be determined if these effects can be obtained directly from the three-dimensional equations or whether patching is necessary. If the effect is viscous, as claimed by Culick, patching will remain necessary.

Grain and nozzle designs appear to be following a trend toward designs which would be expected to produce a system of unsteady vorticies, a "vortex street." This effect has been considered by Flandro (9) and needs to be reviewed and extended in light of the present design trends. This is particularly important as Flandro's results indicate that finite strength vortex disturbances tend to produce unstable motors and there is experimental evidence which tends to support this conclusion.

The Culick type of analysis appears to be fundamentally limited to small Mach number mean flows, a restriction entirely avoided by the energy approach. Thus, correct development of the energy method would eliminate this limitation and provide a more general method of analysis. Development of this method will require correct formulation of the acoustic energy in a non-uniform flow, a question which is being investigated in connection with jet noise. Also, a complete understanding of "flow turning" will be necessary before this type of analysis can be accepted. The energy approach, if used with a mean flow, will require a separate mode calculation, but finite element numerical methods for this type of calculation are being developed and need to be encouraged.

It should be clear that there are a number of questions of a fundamental nature that need answers both to more firmly establish the present analysis and to begin development of a more general approach. This report is certainly not an exhaustive list of such topics but it does treat the major question and, it is hoped, will provide some guides for future fundamental analysis.

REFERENCES

1. Culick, F.E.C., "Acoustic Oscillations in Solid Propellant Rocket Chambers," Astronautics Acta, 12, 113, 1966.

2. Culick, F.E.C., "Rotational Axisymmetric Mean Flow and Damping of Acoustic Waves in a Solid Propellant Rocket," AIAA J., 4, 1462, 1966.

3. Culick, F.E.C., "The Stability of One-Dimensional Motions in a Rocket Motor," Combustion Science and Technology, 7, 165, 1973.

4. Culick, F.E.C., "Stability of Three-Dimensional Motions in a Combustion Chamber," Combustion Science and Technology, 10, 109, 1975.

5. Culick, F.E.C., "Remarks on Entropy Production in the One-Dimensional Approximation to Unsteady Flow in Combustion Chambers," Combustion Science and Technology, 15, 93, 1977.

6. Cantrell, R.H. and Hart, R.W., "Interaction between Sound and Flow in Acoustic Cavities: Mass, Momentum and Energy Considerations," J. Acoustical Society of America, 36, 697, 1964.

7. Von Mises, R., Mathematical Theory of Compressible Fluid Flow, Academic Press, New York, 1958.

8. Dunlap, R., Willoughby, P.G., and Hermsen, R.W., "Flowfield in the Combustion Chamber of a Solid Propellant Rocket Motor," AIAA J, 12, 1440, 1974.

9. Flandro, G.A., "The Influence of Mean Flow on Rocket Motor Stability," Vol. III, AFRPL TR 72103, Air Force Rocket Propulsion Lab, Edwards Air Force Base, CA, 1972.

10. Kuentzmann, P. and Lengelle, G., "Recent Research Activity at ONERA on Combustion Instability and Erosive Burning," 1977 Joint AFOSR/AFRPL Rocket Propulsion Meeting, 1977.

11. Janardan, B.A. and Zinn, B. T., "Effect of Nozzle Submergence upon Stability of Solid Rockets," AIAA J., 14, 109, 1976.

12. Chu B., and Kovasznay, L.S.G., "Non-Linear Interactions in a Viscous Heat-conducting Compressible Gas," J. Fluid Mechanics, 3, 494, 1957.

13. Howe, M.S., "Contributions to the Theory of Aerodynamic Sound, with Applications to Excess Jet Noise and the Theory of the Flute," J. Fluid Mechanics, 71, 625, 1975.

14. Yates, J.E. and Sandri, G., "Bernoulli Enthalpy: A Fundamental Concept in the Theory of Sound," Progress in Astronautics and Aeronautics, Vol. 43, I. R. Schwartz, Ed., American Institute of Aeronautics and Astronautics, New York, 1976.

15. Yates, J. E. and Sandri, G., "The role of Bernoulli Enthalpy in the Scattering of Sound," AIAA Paper 76-5, 1976.

16. Morse, P. M., Vibration and Sound, McGraw-Hill, New York, 1948.

17. Zinn, B. T., "Longitudinal Mode Acoustic Losses in Short Nozzles," NWC TP 5206 Revision 1, Naval Weapons Center, China Lake, CA, 1972.

18. Culick, F. E. C., "Interaction between the Flow Field, Combustion and Wave Motions in Rocket Motors," NWC TP 5349, Naval Weapons Center, China Lake, CA, 1972.

19. Culick, F.E.C., "Measurements of Energy Losses Associated with Interactions between Acoustic Waves and a Steady Flow Field," Final Report Contract No. F04611-75-C-0010, California Institute of Technology, Pasadena, 1976.

20. Zucrow, M. J. and Hoffman, J. D., Gas Dynamics, Wiley, New York, 1976.

21. Morfey, C. L., "Acoustic Energy in Non-Uniform Flows," J. Sound and Vibration, 14, 159, 1971.

1977 USAF-ASEE SUMMER FACULTY RESEARCH PROGRAM
sponsored by
THE AIR FORCE OFFICE SCIENTIFIC RESEARCH
conducted by
AUBURN UNIVERSITY AND OHIO STATE UNIVERSITY

PARTICIPANT'S FINAL REPORT

INVESTIGATION OF RAMAN EMISSION FROM PLASMA

Prepared by:	Tse-Wen, HSU, Ph D
Academic Rank:	Assistant Professor
Department and University:	Department of Electrical Engineering Villanova University
Assignment:	
(Air Force Base)	Griffiss AFB
(Laboratory)	Rome Air Development Center
(Division)	Surveillance Division
(Branch)	Surveillance Technology Branch
USAF Research Colleague:	Mr. R. Hunter Chilton
Date:	August 19, 1977
Contract No:	F44620-75-C-0031

INVESTIGATION OF RAMAN MICROWAVE EMISSION FROM PLASMAS

by
T. W. HSU

ABSTRACT

This report is concerned with the investigation study of a beam-plasma device patented by two AFCRL research workers. The proposed interaction mechanism and the device model have been examined from the engineering point of view. It is found that by an appropriate choice of beam and plasma parameters, and their operating conditions, coherent (but not monochromatic) radiation at about twice the plasma frequency can be achieved by resonant Raman scattering from the plasma waves through the inhomogeneites in the plasma charge distribution.

The absence of delicate mechanical microwave resonant or slow-wave structures, very high power relativistic electron beam, and very large DC magnetic fields is the main feature of the proposal. Simplicity, relatively very high source efficiency of the microwave power, and long reliable life are other features which may be important considerations when development costs and competitive economics of the device products are considered.

Preliminary study was performed to ascertain the feasibility of the device and its capability of delivering the very large quantities of electromagnetic radiation at millimeter wavelengths, and for the lacking of supporting data from experiment, our investigation is inconclusive.

Theoretically, counter-streaming beam-plasma model should be employed to realize the potentialities of the device in terms of output power, however, the complexities in the engineering design of the beam-plasma interaction chamber and microwave system associated with such model may pose a serious obstacle in early stage of development. It is suggested that during the initial stage of development, single-beam model should be used simply to demonstrate its potentialities. To this aim, microwave circuitry for collecting and redirecting the electromagnetic radiation out of the plasma volume is provided. Several engineering models are proposed and design information given.

Several other problem areas have been identified and discussed. Future research program is outlined and possible ways for future development are suggested.

ACKNOWLEDGEMENTS

The author wishes to express his gratitude to the Air Force Office of Scientific Research for their support of this summer research project, without their support this work could not have been carried out. He would like also to thank Mr. Frank E. Welker for the amenities enjoyed in OCTP during the period of this work. A deep appreciation is due to the ASEE and Auburn University, in particular, Mr. J. Fred O'Brien, Jr., and Mr. John P. Huss of RADC/XP for their excellent administration of the program.

It has been a pleasure and a professionally gratifying experience to work with my very capable research colleague, Mr. R. Hunter Chilton of RADC/OCTP. To him the author wishes to express a deep gratitude.

The author is most indebted to Dr. B. Prasad and Mr. C. C. Leiby, Jr., of AFCRL, Hanscom AFB, for many stimulated discussions, and their numerous data concerning their work.

To Mr. S. Kredel and his staff at the RADC Technical Library, the author wishes to thank them for their assistance in literature matters. Finally, the author wishes to offer his sincere thanks to Mrs. Myrta Wilcox for her patience in getting this report typed beautifully.

CONTENTS

Abstract

Acknowledgements

I. Introduction

II. Physical Principles of Operation of the Proposed Beam-plasma Millimeter Wave Power Oscillator

III. Result of the Investigation

IV. Design of Demonstration Model

Concluding Remakrs

References

Appendix A. Brief Review of Prasad's Theory

Appendix B. Design of Demonstration Models B and C.

I. INTRODUCTION

One of the more pressing problems in present day microwave technology is that of producing a tunable source of coherent radiation in the millimeter and submillimeter wave lengths (from 1-0.1 mm). The physicists have been interested in such a millimeter wave source for their molecular and atomic spectoscopy study. The potential uses of millimeter waves in engineering applications are almost too numerous to mention. For example, in radar system design, it could give us high resolution radar for guided missiles, precision gun and rocket fire control, accurate station-keeping in fleet formations,...., to name just a few. For communication engineers, we like to think of the progress in millimeter wave field as extending the frontiers of communication electronics beyond the crowded microwave spectrum, and into a new frequency region where the spectrum density is low and signal channels less crowded. The very high frequencies and the quasi-optical properties which characterize millimeter and submillimeter waves would enhance many secret communication systems both within the atmosphere and above it. Very long-range pencil-beam communications may be easily realized and yet require only a small antenna. These and many other possible applications to engineering system design and military systems particularly communications and navigations have long been recognized. Thus, from the technological point of view, the availability of a coherent tunable millimeter wave power source would make possible a significant advance in all these and many other special purpose communication systems.

The biggest road block in the full realization of these advantages is the engineering one of constructing an efficient coherent source of millimeter wave tubes which are capable of providing adequate power at millimeter wavelengths and below. The various problems associated with fragile RF structures and high density electron beams have, up to the present time, blocked the extension of conventional microwave-tube techniques down to one-millimeter or shorter wavelengths. At these very short wavelengths, conventional microwave tubes would be so tiny that watch making techniques are required. Furthermore, in conventional microwave and millimeter wave devices, beam interaction and RF dissipation on delicate interaction structures limit power handling capacity.

The limitations of conventional microwave tube devices have stimulated the exploitation of more unconventional approaches to the problem of producing a tunable source of electromagnetic radiation in millimeter and submillimeter wavelength regions, and in this respect, the RADC/OCTP section has long been actively involved in the development of high power millimeter wave tubes. The recent development of the gyrotron is a typical example of our endeavor.

Recently, two AFCRL research workers, at Hanscom AFB, Massachusetts, proposed a somewhat unconventional microwave device which, according to their patents,[1] is capable of generating very large amounts of microwave power at millimeter and submillimeter wavelengths that are coherent and tunable. The concept behind this scheme is based on the electron beam interaction in a warm plasma.

The idea of utilizing plasma oscillation frequency as a parameter in determining the radiation frequency of the device system is an attractive one. Since the frequency of electron oscillation in a plasma is the "natural" frequency associated with the electron, no external radio frequency structure is required for the determination of the radiation frequency of the device. Indeed, this frequency of electron oscillation is related, in a good approximation, solely to the number density of the electrons in the plasma which is controllable by gas discharge. The beam-plasma interaction offers other attractions too. In a beam-plasma device, high power can be handled at high frequencies (i.e., at millimeter and submillimeter wavelengths), since delicate mechanical structures are replaced by the gaseous plasma which can be relatively huge physically. Besides, large size electron beams which has been one of the bottlenecks in extending the conventional microwave tubes into millimeter wave region, can be employed prolifically to enhance the device output power.

Gas discharge phenomena have been used in many microwave applications, such as gaseous microwave noise sources and gases TR and ATR radar switch tubes. Moreover, because gas discharge can be varied and controlled electronically, their potential utilization in a variety of other microwave devices such as electronically variable reactances, attenuators, phase shifters, electronic switches and couplers, electronically tunable resonant cavities and microwave slow-wave circuits, have also long been recognized. This latter property has been studied extensively[2], a complete review of the literature is impractical, but it needs only to point out that in microwave slow-wave circuit applications the plasma column serves purely as a non-active circuit element which is capable of supporting a slow electromagnetic wave propagating through it. Utilization of gas discharge phenomena to generate very large power at millimeter and submillimeter wavelengths is relatively new.

The application of plasma oscillations to the solution of the problem of generation of millimeter wave power from plasma in gaseous discharge and from the thermally generated plasma in impurity semi-conductors has been discussed by Lamperts.[3] Pasad-Lieby device is to operate on the second harmonic generation principle by means of an interaction mechanism known as stimulated

Raman Resonant Scattering Process in a warm plasma. A single incident wave scattered from plasma density fluctuation at plasma oscillation frequency, ωpe[4] is shifted in frequency by ωpe. The scattered wave can then interact with the incident wave to enhance both the plasma fluctuations and the scattered wave. The incident wave, thus, generates a plasma wave from which it is itself scattered. In Prasad-Lieby device the incident wave (or the so-called induced background waves by them) is excited by means of another scattering process known as the "Rayleigh Scattering." This is a process due to the scattering of the Langmuir electron wave (or the longitudinal electrostatic wave) from the inhomogeneities in plasma ion distribution. The Langmuir electron wave is, in turn, excited by the injection of an unmodulated electron beam into the plasma.

It is very important to point out that although the output power of Prasad-Lieby device depends critically upon the injected beam current and beam power, however, only non-relativistic beam may be needed for its satisfactory working. When this is compared with the very large relativistic beam used in NRL megawatt millimeter wave tube[5], the Prasad-Lieby device shows greater potentiality as a high power millimeter wave tube.

Another important feature of Prasad-Lieby device is the absence of large DC magnetic fields. Although a small externally applied DC magnetic field may be required for the confinement of the electron beam in this device, however, this is to be contrasted with the super-conducting magnet needed for their operation in a new class of millimeter wave tubes employing cyclotron fast wave interaction.[6]

The proposed gain mechanism of this second harmonic generation process is somewhat similar to that commonly used to explain the phenomena of Type III solar radio bursts. The phenomena of solar radiation have been investigated by astro-physicists and engineers for the past several decades. The details of the solar radio waves generation are not too clear[7]. It has been observed that the region of Type III solar bursts emission shifts in the solar corona with a velocity from 0.2C to 0.8C (C is the velocity of light) which shows up in an observed decrease in the frequency of the emission (i.e., a frequency drift). No case has been observed with velocities less than 0.2C. The maximum probability for the appearance of a radio-burst is from about 0.35 to 0.5C[8]. At each instantaneous level corresponding to the distance from the photosphere radiation is generated at frequencies close to the Langmuir and twice the Langmuir (second harmonic) frequency corresponding to the electron density at that height. The second harmonic usually has a frequency somewhat less than twice the frequency of the fundamental ($\omega^2/\omega pe \simeq 1.8$ to 2.0). Both fundamental and second harmonics are found in most Type III radio bursts and the intensity of the emission at both frequencies is about the same. However it is commonly

accepted that a two-step process in the stream particles-plasma interaction must have been involved, i.e.:

(a) The stream particles excites longitudinal plasma waves by a Čerenkov radiation mechanism and

(b) The plasma waves generated are converted into a radiative transverse electromagnetic wave by scattering on the inhomogeneities in plasma electron distribution.

The second process is believed to be responsible for the second harmonic radiation in Type III solar bursts. The density in-homogeneities responsible for this frequency doubling must themselves be plasma waves[9].

The objective of this investigation was most importantly, to ascertain, from an engineering point of view, whether Prasad-Lieby device is capable of accomplishing the functions as proposed, that is:

(1) The potentiality in the generation of millimeter and submillimeter waves.

(2) The coherency and the monochromaticity in the radiated electromagnetic waves.

(3) The capability of delivering the very large output power at relatively high efficiency.

The other objectives are:

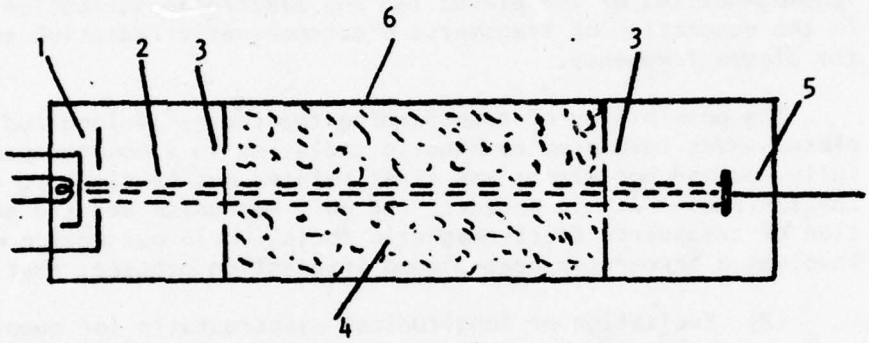
(5) To draw up a prototype model for laboratory demonstration of the device potentialities, and

(6) To define a research and development program in order to further demonstrate the feasibility of the device as an engineering proposition.

In Section II, the device model and its physical principles of operation are presented. A review of Prasad-Leiby theory will appear in Appendix A. Results of our investigation study as well as recommendations for future research and development are given in Section III. As an initial step in the exploitation of the device potentialities, several engineering models are presented in Section IV, and design considerations as well as design procedures are outlined there.

II. Physical Principles of Operation of the Proposed Beam-Plasma Millimeter Wave Power Oscillator

The physical principle and gain mechanisms of the beam-plasma device to be described in the following are based on Prasad-Leiby's two theoretical papers(10,11), a brief review of which will appear in Appendix A. Basically, Prasad-Leibys' model is a power oscillator consisting of, in its most elementary form, a beam-plasma interaction chamber and a source of directed un-modulated high velocity but non-relativistic electron beam as sketched in Figure 1.



1 - Electron gun
2 - Electron beam
3 - Metallic foil
4- Plasma chamber (method of plasma generation not shown)
5 - Collector
6 - Cylindrical glass tube

Figure 1. Sketch of the Beam-Plasma Device

The plasma, which may be either discharge generated or electron beam generated, is unmagnetized, warm, uniform and collisionless. The electron beam which may be produced by any one of the electron gun systems employed in klystrons and traveling wave tubes, is of the low density type, having an electron density (n_b) about 2 to 5% of the plasma electron density (n_e).

An electron beam traversing through a warm plasma excites electron oscillations in the plasma. The waves associated with such oscillations are the Langmuir electron waves which are non-radiative longitudinal electrostatic waves. They cannot escape from the plasma volume. The plasma electrons are accelerated by the waves propagating through it. The accelerated electrons in turn emit radiation (both transverse and longitudinal), if the plasma were completely uniform the radiation emitted would simply reproduce the waves themselves. However, in a warm plasma, the presence of both ion and electron density fluctuations result in scattering and coupling of various types of waves.

Since electrons tend to follow the ions so as to maintain charge neutrality, and so there will be electron density fluctuations associated with ion density fluctuations. There are also density fluctuations associated with Langmuir electron oscillations as well as density fluctuations due to the random motion of the electrons. The scattering of these waves on the inhomogeneities of the plasma ion and electron distribution results in the generation of transverse electromagnetic radiation at twice the plasma frequency.

The possibility of transforming the energy of longitudinal plasma waves into electromagnetic radiation in a homogeneous and fully ionized hot plasma was first pointed out by Ginzburg and Zhelezniakov[12]. In essence, the gain mechanism and the generation of transverse electromagnetic radiation in our device model involves a three-step beam-plasma interaction process; that is

(A) Excitation of longitudinal electrostatic (or pump) waves in the plasma by the injection of fast electron beam.

(B) Production of the background induced plasma waves - also longitudinal electrostatic waves via the "Rayleigh scattering" of the pump waves on the inhomogeneities of the plasma ion distribution.

(C) Generation of the transverse electromagnetic radiation via the "Raman scattering" of the induced background plasma waves on the inhomogeneities in the plasma electron distribution.

Each of these processes will be elaborated in the following:

A. Excitation of Longitudinal Pump Waves

When a warm, uniform, collisionless plasma is traversed by a beam of fast, but non-relativistic charged particles, spatially growing waves will result from the excitation of oscillation of plasma electron by the beam through a non-linear interaction mechansim, and the interaction of oscillating plasma electron back to the beam (ion-acoustive wave will be excited too). The wave amplitude increases

exponentially with distance along the beam and the rate of growth for a constant exciation frequency rises sharply near the plasma frequency, ωpe. In the meantime, the ion-acoustic waves act as a trigger for the instability and lock the initial phase of the unstable waves. Moreover, if the instability is driven by a cold, weak electron beam in a plasma, it will be stabilized by the trapping of plasma particles mechanism. Since the spectrum of these unstable waves is so narrow that only a single frequency grows, and in the vicinity of the point where the wave is excited in the plasma, the particles are trapped in the wave potential wells. The trapping of the plasma particles limits the instability, and the trapped particles cause oscillation in the amplitude of the excited wave and the growth of new waves the so-called sidebands. Sidebands are found symmetrically placed around the main peak in the frequency spectrum, displaced by an amount given by[13]

$$\Delta\omega_0 = \sqrt{(e/m)\, E_0 k_0} = (1/2)\, k_0 \Delta v \qquad (1)$$

where e and m are the charge and mass of electron

E_0 is the wave electric field

k_0 is the wave number

$\Delta v = v_p - v_{ph}$, v_p is the particle velocity and v_{ph} the phase velocity of the wave.

This trapping effect has been analyzed (14) and experimentally observed (15).

The non-linear interaction between an electron beam and a plasma has been studied extensively since the first observation of Langmuir [16]. We make no attempt to review the literature. What remains is for us to point out that this beam excited non-radiative longitudinal electrostatic waves will constitute the pump waves or incident waves in our beam-plasma model, which in accordance with Prasad-Leibys' symbolism (11) is represented by

$$\underline{E}_0(\underline{r}, t) = \hat{\underline{k}}_0\, U \exp\left[\, i(\underline{k}_0 \cdot \underline{r}) - \omega_0 t \,\right] \qquad (2)$$

where $\underline{E}_0(\underline{r}, t)$ is the electric field vector of the pump waves

$\hat{\underline{k}}_0 = \underline{k}_0 / k_0$ is the unit vector in the direction of the wave vector $\underline{k}_0$ with k_0 its wave number

ω_0 is the angular frequency of the pump-wave

$\underline{r}$ is the position vector of the observation point.

The wave number K_o and frequency ω_o satisfy the dispersion relation[17]

$$\omega_o^2 = \omega_{pe}^2 + 3K_o^2 v_{Te}^2 \qquad (3)$$

where

$$\omega_{pe} = [4\pi n_e e^2/m_e]^{1/2}$$

is the electron plasma frequency, with n_e the average electron density in cm^{-3}, e charge density and m_e the mass of electron

$$v_{Te} = [KT_e/m_e]^{1/2}$$

is the thermal velocity of the electron, with T_e the electron temperature, K Boltzmann Constant.

Such waves can propagate in the plasma with practically no (Landau) dumping if ω_o is close to ω_{pe} (i.e., when K_o is very small compared with the inverse Debye Length ($K_o \ll \lambda_D^{-1} = \omega_{pe}/v_{Te}$). Furthermore, the condition for propagation is that the phase velocity of the waves (v_{ph}) must be greater than the thermal velocity of the plasma electron (v_{Te}); i.e., $v_{ph} (\simeq v_b) > v_{Te}$, where v_b is the beam electron drift velocity, and for un-damped wave propagation, the following condition must satisfy also:

$$v_{ph} (\approx v_b) > \sqrt{3}\, v_{Te} \qquad (4)$$

In summary, the electrostatic pump waves are produced by the interaction of a non-relativistic electron beam with a warm plasma when the drift velocity (v_b) of the beam electrons exceed the average thermal velocity (v_{Te}) of the plasma electrons. Such waves are narrow pockets of quasi-stable Langmuir waves which propagate in the direction of the beam. The wave number and frequency distributions are peaked[18] at (K_o, ω_o) with $\omega_o \gtrsim \omega_{pe}$, and $K_o \approx \omega_o/v_b$.

B. Production of the Background Induced Waves

In the next step, as the incident, or pump waves propagate through the plasma medium, they are scattered by the ion density fluctuations in the plasma. The scattered wave consists of two component waves: (1) The strong, but non-radiative longitudinal electrostatic wave, and (2) The much weaker transvers electromagnetic wave which radiates out of the plasma volume. The frequency of the

scattered wave remains nearly the same as that of the incident pump wave. This is in accordance with the dispersion relation (17)

$$\omega_1^2 = \omega_{pe}^2 + 3 k_1^2 v_{Te}^2$$

or $$\omega_1 \approx \omega_{pe} + (3/2) k_1^2 v_{Te}^2 / \omega_{pe}^2 \qquad (5)$$

where ω_{pe} and v_{Te} have been defined in (3)

ω_1 is the Rayleigh scattered longitudinal wave and k_1 its wave number.

This is known as the "Rayleigh Scattering" process in plasma. Now, since the Rayleigh scattered longitudinal component wave is incapable of escaping from the plasma volume, it will raise the amplitude of space charge density fluctuation well above the thermal level in the bulk of the plasma, and hence contributes to a growing coherent background induced wavefield, $E_L(\omega_1, \kappa_1)$ with $\omega_1 \approx \omega_0$ and $k_1 \approx k_0$ in the pumped but stable plasma. The angular distribution of the scattered wave is that of an electric dipole given by (See Appendix A).

$$\underline{E}_1(\underline{r},\omega_1,\sigma) = -\hat{\underline{n}}_1(\hat{\underline{n}}_1\cdot\hat{\underline{k}}_0)\left[\frac{U\omega_{pe}^2}{12\pi n_e v_{Te}^2}\right]\left[(2\pi)^3\delta(\omega_1-\omega_0)\langle\Delta N^M(\underline{\kappa}_1-\underline{k}_0)\rangle\right] \times\left[\exp(ik_0-\sigma)r/r\right] \qquad (6)$$

The spatial distribution of the Rayleigh Scattered wave power is shown in Figure 2.

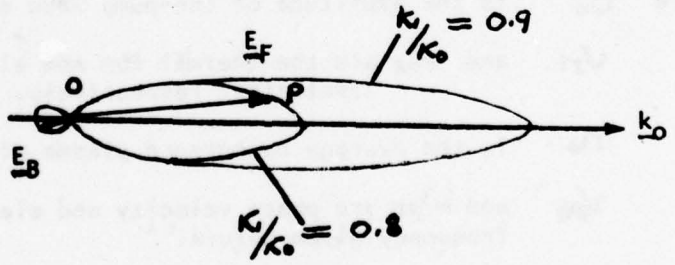


Figure 2. Asymmetrical Dipole Spatial Distribution of the Rayleigh Scattered Wave Power.
$\underline{E}_F$ -The Forward-Lobe Electric Field
$\underline{E}_B$ -The Backward-Lobe Electric Field.

This is a polar diagram. The $\underline{k}_0$ axis is the direction of the electron beam. The line segment drawn from the reference "0" to P a point on the $k_i / k_0 = 0.8$ curve represents the direction and intensity of the electric field at P. We notice that the very strong forward-lobe electric field varies greatly as the ratio k_i / k_0 is varied, whereas, the much weaker backward-lobe fields remain practically unaltered for a similar change.

C. Generation of Transverse Electromagnetic Radiation

When the non-radiative Rayleigh Scattered component waves, i.e., the longitudinal induced background waves, (ω_i, k_i), propagate through the plasma volume, a small percentage of these waves are backscattered on the inhomogeneities in the charge distribution of the plasma resulting in a Raman Scattered transverse electromagnetic waves which radiate out of the plasma volume at twice the electron plasma frequency ($\sim 2\omega_{pe}$). Since the inhomogeneities, or the fluctuations of plasma electron density are associated with the Langmuir electron wave, which is, in turn, producing the pump-waves, it appears as though this scattering and generation of second harmonic waves result when the induced background plasma waves scatter off their cousins, the waves which have been generated a moment before by some preceeding particles, much like the wakes of a long line of speed boats. There will be a continual overtaking and scattering of one wave by another because the spectrum of the induced waves is distributed both in angle and in frequency, and each component has its own group velocity.

Under certain conditions, when the energy of the incident of pump wave exceeds a certain threshold condition, the waves become phase locked with each other, enhanced Raman emission occurs, and the resulting radiation becomes coherent. This threshold condition is given by (Appendix A).

$$U_0^2 > 6 \times 10^3 \left[\frac{m n_0 v_{Ti}^2}{F(a)} \right] \left(\frac{v_{Te}}{v_{ph}} \right)^6 \left(\frac{\omega_{pe}}{\nu} \right) \qquad (7)$$

where U_0 is the amplitude of the pump wave electric field

v_{Ti} and v_{Te} are the thermal ion and electron velocities respectively.

n_0 is the average background plasma electron density

v_{ph} and ω_{pe} are phase velocity and electron plasma frequency given before.

This coherence of the electromagnetic radiation at discrete frequency bands by an electron beam interacting with a warm plasma have been experimentally observed[18].

Leiby's data (Figure 3) was obtained from flow stabilized DC discharges in argon gas at very low (2-2.5 μm) pressures. The

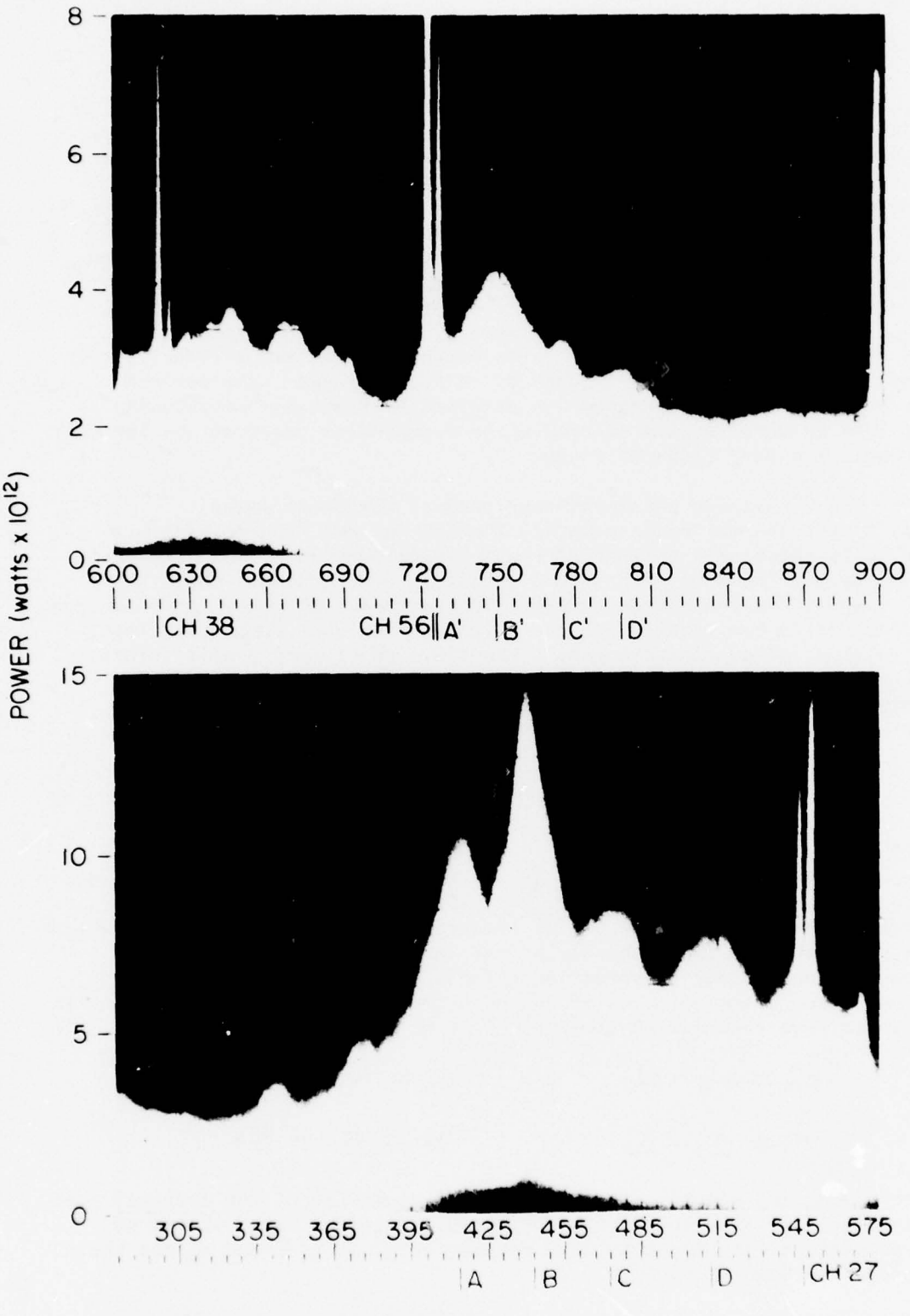


Figure 3. Radiation Signal of a DC discharge (argon gas) Beam-plasma device, monitored by an external dipole antenna.

discharge tube is of length $\sim$ 80 cm and inner radius $\sim$ 2.3 cm. The electron beam ($\sim$10 eV/electron) employed is narrow and was injected into an otherwise thermal plasma ($\sim$2 eV/electron) along the tube axis. Four bands of electromagnetic radiation have been observed, and far-field signals were detected by 4 different (λ = 136, 70, 50, 40 cm) dipole antennas and the near-field ones by a 6.8 cm monopole probe, a 3.5 cm diameter loop and a 2-turn coil around the discharge tube. The signals displayed on a spectrum analyzer were qualitatively the same for all detectors and were identified as $\omega_{pe}/\sqrt{2}$ (dipole), ω_{pe}, $\sqrt{2}\,\omega_{pe}$ (weak and sometimes missing), and $\sim 2\,\omega_{pe}$ (Raman) bands. As in Type III radio bursts[8], the Raman band was actually $\sim 1.7\,\omega_{pe}$ and 20% as strong as the ω_{pe}-band. A much narrower, sharper and stronger Raman band spectrum was obtained by Professor Horshkowitz at Iowa University, and the radiation frequencies observed (by Langmuir probe) were very close to $2\,\omega_{pe}$.

Since Rayleigh scattered longitudinal component waves, [has a suprathermal phase velocity which follows from eq. (5)] which is comparable to that of the incident pump wave, and like the pump waves, the wave is undamped (Landau), and by Gauss' Law, they will appear as the charge density fluctuations, $\nabla\cdot\underline{E}_L(\underline{r},\omega_1)$ in the plasma which can readily interact with the incident pump wave field, $\underline{E}_0(\underline{r},\omega_0)$; also, interchangably, the field, $\underline{E}_L(\underline{r},\omega_1)$, will interact with the charge fluctuations associated with the pump wave field through the divergence relation, $\nabla\cdot\underline{E}_0(\underline{r},\omega_0)$. These interaction relations appear in the form:

$$\underline{S}(\underline{r},t) = \left(\frac{e}{m}\right)\left\{\underline{E}_L\,\nabla\cdot\underline{E}_0 + \underline{E}_0\,\nabla\cdot\underline{E}_L\right\} \qquad (8)$$

which is the source functions, $\underline{S}$, Prasad used to evaluate the Raman scattered electric field, $\underline{E}_T(\underline{r},\omega)$. (See Appendix A). Furthermore, electron density flucuates at the electron plasma frequency, ω_{pe}, which is comparable to the frequency of the incident pump wave, and by momentum and energy conservation principle, the scattering process gives rise to the emission of enhanced transverse Raman radiation[19] in a three-wave interaction process[20], that is

$$\begin{aligned} \omega_1 &= \omega_2 - \omega_0 \quad \text{or} \quad \omega_2 = \omega_1 + \omega_0 \\ \underline{k}_1 &= \underline{k}_2 - \underline{k}_0 \quad \text{or} \quad \underline{k}_2 = \underline{k}_1 + \underline{k}_0 \end{aligned} \qquad (9)$$

where ω_0, ω_1 and ω_2 are the angular frequencies of the incident pump, Rayleigh scattered longitudinal electrostatic, and Raman scattered transverse electromagnetic wave respectively, k_0, k_1 and k_2 are their respective wave vectors.

Futhermore, Since $\underline{k}_0$ and $\underline{k}_2$ are much greater in magnitude than $\underline{k}_1$ (except for relativistic energy beam), transverse waves can only be produced by a "head-on" scattering collisions of the longitudinal electrostatic waves. This is in accordance with the three-wave, or coherent interaction process. These are radiative transverse electromagnetic waves which are capable of escaping from the plasma volume. Furthermore, since $\omega_1 \approx \omega_0$ ($\approx \omega_{pe}$)as discussed in (II$_b$), it follows from eq (9) that $\omega_2 \approx 2\omega_{pe}$. The radiation frequency is, therefore, twice the electron plasma frequency. This process of non-linear coupling between two electrostatic waves and one electromagnetic wave is in accordance with the mechanism of second harmonic generation proposed by the sturrock et al.[21]

The angular distribution pattern of the Raman scattered waves is that of an electric quadrupole, characteristic of a spontaneous Raman scattering process in the plasma [12] [22]. It is illustrated in Figure 4, and in the far field approximation the electric component of the Raman scattered transverse electromagnetic wave is given by:

$$\underline{E}_T(\underline{r},\omega_2) = \left(\frac{ieu}{m}\right)\left[\frac{\exp(ik_2 r)}{4\pi c^2 r}\right]\left\{\frac{(\hat{\underline{n}}\times\underline{k}_0)}{k_0}\,\frac{(k_2^2 - 2\underline{k}_2\cdot\underline{k}_0)}{|\underline{k}_2-\underline{k}_0|}\right.$$

$$\left.\times(2\pi)^3\left|\underline{E}_L(\underline{k}_2-\underline{k}_0,\sigma,\omega_2-\omega_0)\right|\right\} \qquad (10)$$

where $\kappa_2 = (\omega_2^2 - \omega_{pe}^2)^{1/2}/c$.

$\underline{\kappa}_2 = \hat{\underline{n}}\,\kappa_2$

and $\hat{\underline{n}} = \underline{r}/r$ is the unit vector specifying the arbitrary direction of observation of the transverse Raman radiation field.

c is the velocity of light.

σ is a small positive real number signifying an outgoing wave decreasing (slowly) in amplitude after scattering at source situated anywhere inside the scattering Volume

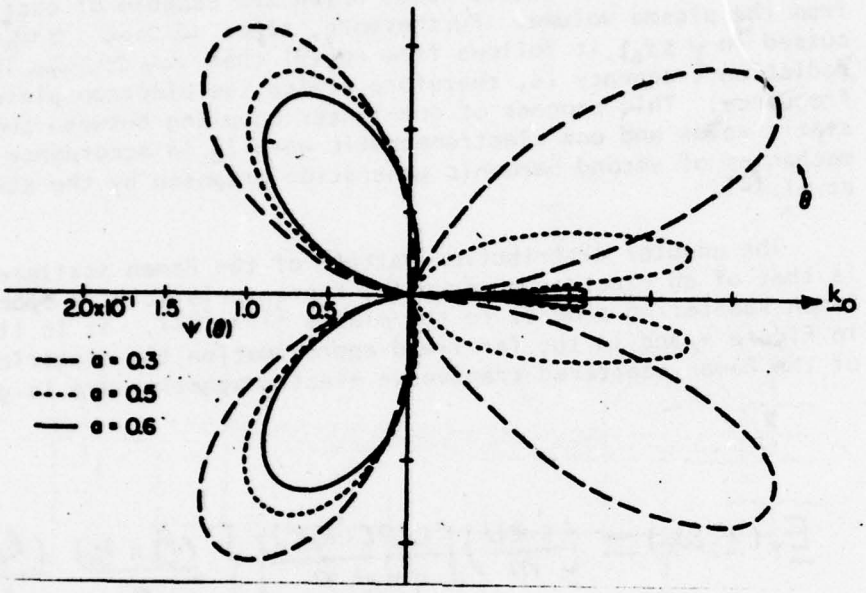


Figure 4. The directional pattern $\Psi(a,\theta)$ for the emission of the enhanced second-harmonic radiation in the warm uniform plasma, for a=0.3, a-015, and a=0.6, (By Courtesy of B. Prasad).

Since, the Raman scattered wave is transverse electromagnetic waves, the magnetic field can be computed readily to yield

$$\underline{B}_T(\underline{r},\omega_s) = (\hat{\underline{n}} \times \underline{E}_T)\left[1-(\omega_{pe}/\omega_s)^2\right]^{1/2} \quad (11)$$

The time-average energy flux of Raman scattered transverse electromagnetic radiation can be computed, and the volume emissivity, that is, the total intensity per unit volume determined, the result (Appendix A) is given by

$$Q^c_{em}(2\omega_{pe}) \simeq \frac{\sqrt{3}\,F(a)}{45(2\pi)^{3/2}}\left(\frac{W_0^2\omega_{pe}^a v_{Te}}{m n_0^2 c^5 v_{Te}}\right)\left(\frac{v_{ph}}{v_{Te}}\right)^5 \quad (12)$$

where the factor F (a) depends upon the fluctuation density function which characterized the plasma, and
For non-thermal conditions F can be as large as 10 to 100.

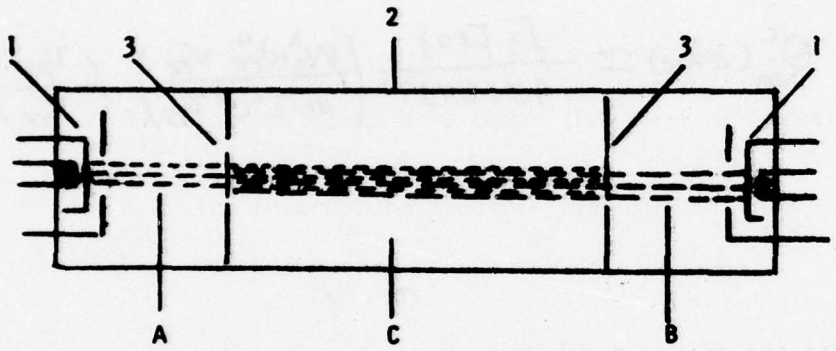
The maximum interaction power density for the Raman scattered radiation at $2\omega_{pe}$ has been calculated (1) in terms of physical size and the beam-plasma interaction length L, and the injection beam current density, J_b, as well as the beam power P_b. The formula obtained is

$$P_{max}(2\omega_{pe}) = 3.6819\times10^{-20} L P_b F \alpha^8 \quad (13)$$

where α is the ratio of electrostatic wave phase velocity, v_{ph}, to the mean thermal velocity of the plasma electrons, v_{Te}, L is in cms, J_b in amperes/cm^2, and P_b in watts/cc.

Counter-Streaming Beam-Plasma Model

In Prasad-Leiby second patent (1_b), counter-streaming beam plasma model instead of a single beam system is employed. This is illustrated schematically in Figure 5.



1 - Electron gun

2 - Cylindrical glass tube

3 - Metallic foil

A - Right-directed electron beam

B - Left-directed electron beam

C - Beam-plasma interaction chamber (method of plasma production not shown.

Figure 5. Schematic Diagram of a Counter-Streaming Beam-Plasma Device Model.

Based on Prasad-Leiby Computation[11], it is found that resonant Raman scattering of longitudinal (Rayleigh-scattered)

induced waves on inhomogeneities of the plasma electron distribution in a counter-streaming electron-beam plasma system is capable of generating 10 to 100 times as much coherent electromagnetic radiation (at $\sim 2\omega_{pe}$) as would be produced by a single beam-plasma system. In a single beam-plasma device, generation of Raman scattered transverse electromagnetic radiation is due to the "head-on" collisional interaction of the Rayleigh-scattered induced background waves on the fluctuations of plasma charge density, hence, only a small portion of the relatively weak Rayleigh-backscattered lobe, E_{LB}, contribute to the Raman process, the much stronger forward scattered lobe, E_{LF}, makes little or no contribution to this process. It is clear that greatly enhanced coherent Raman transverse radiation output should result if oppositely directed pump-waves (such as would be excited by counter-streaming electron beam) were present in the plasma so that both lobes of both sets of longitudinal (Rayleigh-scattered) induced plasma waves would participate in the Raman scattering process. Thus, if the source function $\underline{S}$ of a single beam-plasma device(as given by eq (8)) is rewritten in a slightly different form, then we will have the following expression;

$$\underline{S}_{BR}^{aa} = \left(\frac{e}{m}\right)\left\{ \underline{E}_{LB}^{a} \nabla\cdot\underline{E}_{OR}^{a} + \underline{\underline{E}}_{OR}^{a} \nabla\cdot\underline{E}_{LB}^{a} \right\} \qquad (14)$$

Where the superscript "a" refers to the field quantities associated with beam A, (that is, the right-directed electron beam). The first subscript in the two electric field expressions, (that is, E_L and E_O) refers to the longitudinal (Rayleigh-scattered) induced wave field and the pump-wave field respectively; where the second subscripts "B" and "R" represent the Backward-Lobe of the longitudinal plasma wave field and Right-directed pump-wave field respectively. The double sub- and super-scripts which appear in the source function $\underline{S}$, are adopted to identify a source function arisen from the "head-on" collisional interaction between the Backward-lobe of the longitudinal plasma wave field (generated by beam A) and the pump-wave field (excited by the Right-directed electron beam, i.e., beam A).

Using the new symbolism, we can write down a second set of source function arisen from the "head-on" collisional interaction between the wave fields and the fluctuations of electron density associated with the Left-directed electron beam,(i.e., beam B). This is expressed in the form:

$$\underline{S}_{BL}^{bb} = \left(\frac{e}{m}\right)\left\{ \underline{E}_{LB}^{b} \nabla\cdot\underline{E}_{OL}^{b} + \underline{\underline{E}}_{OL}^{b} \nabla\cdot\underline{E}_{LB}^{b} \right\} \qquad (15)$$

Accordingly, the angular distribution of the Rayleigh-scattered induced background wave will have an asymmetric dipole distribution just like that of Figure 2, except that, in the present case, both the forward-and backward-lobes are reversed. This is illustrated in Figure 6.

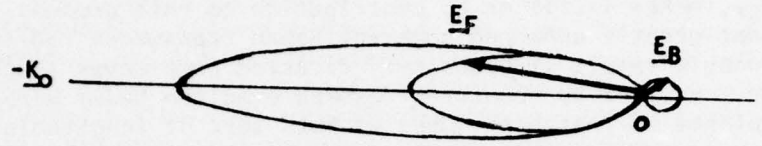


Figure 6. Asymmetrical Dipole Spatial Distribution of the Rayleigh Scattered Wave Power (For Left-directed) Electron Beam.

$\underline{E}_F$ - The Foward-Lobe Electric Field

$\underline{E}_B$ - The Backward-Lobe Electric Field

Furthermore, in a counter-streaming beam-plasma model, two additional sets of source functions are produced because of the mutual "head-on" collisional interaction that exists between two sets of the longitudinal (Rayleigh-scattered) plasma wave fields and two sets of charge density flucuations. These are:

(1) Interaction arisen from the "head-on" collision between the right-directed electron beam excited pump-wave field, $\underline{E}^a_{oR}(W_o, \underline{K}_o)$ and the forward longitudinal (Rayleigh-scattered) induced background wave field, $\underline{E}^b_F(W_1, K_1)$ produced by the Left-directed electron beam, (i.e., beam B), that is

$$\underline{S}^{ba}_{FR} = \left(\frac{e}{m}\right)\left\{\underline{E}^a_{LF}\,\nabla\cdot\underline{E}^b_{oL} + \underline{E}^b_{oL}\,\nabla\cdot\underline{E}^a_{LF}\right\} \quad (16)$$

(2) Interaction as a result of the "head-on" collision between the Left-directed electron beam excited pump-wave field, $\underline{E}^b_{oL}(W_o, -\underline{K}_o)$, and the forward-lobe longitudinal (Rayleigh scattered) induced background wave field, $\underline{E}^a_{LF}(W_1, K_1)$,

Produced by the right-directed electron beam, that is

$$\underline{S}_{FL}^{ab} = \left(\frac{e}{m}\right)\left\{ \underline{E}_{LF}^{a} \nabla\cdot\underline{E}_{oL}^{b} + \underline{E}_{oL}^{b} \nabla\cdot\underline{E}_{LF}^{a} \right\} \qquad (17)$$

Eqs (14, (15), (16), and (17) constitute a set of four souce functions in a counter-streaming beam-plasma model, and their relationships are best illustrated in Figure 7. As a consequence,

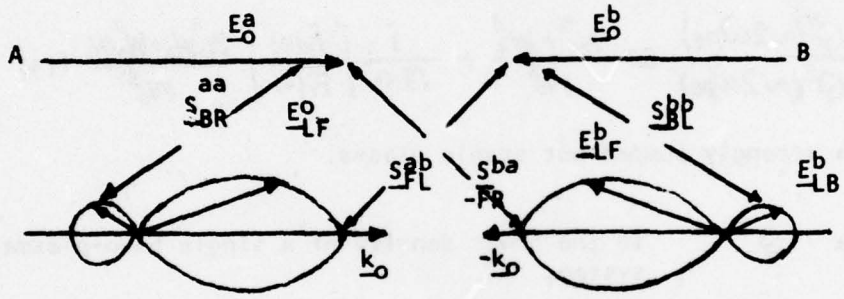


Figure 7. Four sets of possible enhance Raman Scattering Interactions in a Counter-Streaming Beam-plasma Device.

A---Right-directed pump-wave field.

B---Left-directed pump-wave field.

There will be four sets of possible enhanced Raman scattering interactions in a counter-streaming beam-plasma device. In as much as these four source functions are linearly independent, their individual contributions to the Raman scattered tranverse electromagnetic radiation power output from the device are also independent and may be calculated separately and the volume emissivities for the enhanced coherent Raman power densities $Q(\sim 2\omega_{pe})$ calculated accordingly. For non-isothermal plasma, Prasad and Leiby have obtained the following formula:

$$\frac{Q^T(\sim 2\omega_{pe})}{Q^S(\sim 2\omega_{pe})} = \frac{W_1^2 + W_2^2}{W_0^2} + \frac{2}{\sqrt{3}\,a}\left(\frac{F_3(a)}{F_1(a)}\right)\frac{W_1 W_2}{W_0^2} \qquad (18)$$

for a weakly pumpled plasma, and

$$\frac{Q^T(\sim 2\omega_{pe})}{Q^S(\sim 2\omega_{pe})} = \frac{W_1^3 + W_2^3}{W_0^3} + \frac{1}{\sqrt{3}\,a}\left[\frac{F_3(a)}{F_1(a)}\right]\frac{W_1^2 W_2 + W_2^2 W_1}{W_0^3} \qquad (19)$$

for a strongly pumped but stable plasma.

where Q^S is the power density of a single beam-plasma system,

Q^C is the total power density of a counter-streaming beam-plasma device,

$U_{1,2}$ are the amplitudes of the counter-streaming beam generated pump waves,

W_0 is the energy density of the pump-wave in the single-beam system,

$W_{1,2}$ is the electrostatic field energy density for the two anti-parallel pump waves.

$F_i(a)$ are the normalized spatial integrals, with $F_3(a)/F_1(a)$ between 2 and 3 for physically meaningful value of a.

$a = v_{ph}/c$

The maximum interaction power density for a physically realizable

counter-streaming of beam-plasma device has been obtained by Leiby[11], and it is given by

$$\Phi^{c}_{max}(\sim 2\omega_{pe}) = 0.229\left[\sqrt{3}+\frac{\bar{\nu}}{\omega}\right]\left[\frac{m_i}{T_e}\right]^{1/2}\alpha^{10}(L J_b P_b)^{3/2} \qquad (20)$$

for the case of $T_e/T_i = 20$, $\bar{\nu}/\omega = 0.1$,

where Te and Ti are the electron and ion temperatures respectively.

$\bar{\nu}$ is the electron collision frequency

m_i is the mass of the ions.

$\alpha = v_{ph}/v_{Te}$, L, J_b and P_b have been defined before.

III Result of the Investigation

In this section we shall discuss the result from our exploratory investigation study, and to examine to what extent that our objectives have been reached. To this aim, we shall itemize our observation as follows:

(A). The very short microwave frequency generating capability of the device.

Since the frequency determining mechanism employed in the device is based on the second harmonic generation from electron beam-plasma interaction mechanism, this doubling plasma frequency property has been subjected to numerous theoretical investigation as discussed in Sections I and II, its theoretical foundation is beyond any doubt. Experimentally this property has also been observed in Laboratory plasma at low frequencies (18),as well as in far-infrared region (22).

The coherence of the generated wave is controlled by the pump-wave field, if the pump-wave field is coherently excited the emitted radiation is coherent also. The coherence of the pump-wave can be insured by an appropriately choosing electron beam power. However, it is to be noted that the radiation frequency is not monochromatic, but has a finite bandwidth which is intrinsic in the gain mechanism employed by the device; and this is one of the problem areas.

(B). The very large power generating capability and the very high efficiency working potentiality of the device.

Although the intensity of second harmonic radiation has been observed to be as strong as the fundamental in the solar radio bursts; in one of recent Iowa University Laboratory observations (18)amplitude of second harmonic has shown to exceed

the fundamental amplitude; and despite its theoretical claims, our conclusion must remain, at most, inclusive because of the lacking in any experimental evidence. However, we do recognize the device potentialities and many other attractive features, but, the major problem area concerning the development of this type of millimeter wave tube must be the amount of its realizable output power.

Although the counter-streaming beam-plasma model is capable of generating 10 to 100 times as much coherent microwave power (at $\sim 2\omega_{pe}$) as would be produced by a single beam-plasma system, the complexity in the design of beam plasma interaction chamber and microwave collector system must be important factors to be considered and, it is, therefore, not recommended for the initial stage in the development of this type of new millimeter wave tube.

It should also be pointed out that the emitted radiation as calculated from eq (12) depends critically on the value of the pump-wave energy density W_0. Thus, an appropriate and efficient mechanism for producing high pump field energy is required such that the pumped plasma remains stable.

As far as the electronic conversion efficiency is concerned, the proposed device model has a theoretical maximum efficiency of 33.3%. This is based on Shapiro (23) estimation. Shapiro has shown that, in reaching the quasilinear steady state in a plasma, an electron beam will lose approximately 75% of its initial energy of directed motion. One-third will be deposited in the electrostatic electron wave fields, one-third goes into increasing the thermal energy of the plasma electron (in accordance with equipartition) and the balance (1/12th) goes into increasing the thermal energy of the beam current. Therefore, the theoretical possible maximum conversion efficiency is about 33.3%.

Since equal amount of beam power go into the electrostatic electron wave fields, and into heating of the electron gas, and since the conversion efficiency of the beam-plasma interaction is inversely proportional to 4th power of the plasma electron temperature (T_e^{-4}). It is clear that heating of the electron gas imposes a serious limitation for the device. Therefore, the device will have to operate in a pulse mode. The choice of pulse parameters, such as pulse length and duty ratio, must be investigated.

(C). Other Limitations and problem areas.

Apart from the limitations discussed in (B), there are several limitations and conditions which are considered to be of vital importance for a satisfactory working of the device.

They are:

(1) Microwave Collector System - Since the Raman scattered transverse electromagnetic wave from the beam-plasma interaction is readily radiated out of the plasma volume, and the radiation field has a quadrapule distribution pattern (Fig. 4), irrevitably, there will be problems associated with such radiation. Therefore, microwave collector system design might be complicated and this problem must be resolved before any model can be devised.

(2) Threshold -There is a threshold level below which no enhanced Raman emission is possible. This is defined by eq (7).

(3) Electron beam-Energetic but non-relativistic electron beam is required. The beam may be produced by any electron gun used in conventional microwave tubes. Since the beam diameter is not a limiting factor larger beam diameters may be prolifically employed. However the beam density, n_b, must be small compared with the plasma electron density, n_e ($n_b < 0.02 \sim 0.05\, n_e$).

(4) Method of Plasma Production - Plasma may be produced from cesiam or argon, at low pressure ($\sim 10^{-4}$ Torr) and it may be electron beam generated or DC discharge generated. Each of these methods of plasma production should be investigated so as to determine which is a better engineering prospect. A warm plasma is required for the gain mechanism to operate. However, plasma electron (and ion) temperature must be chosen to satisfy several conflicting factors, such as power output, efficiency, etc.

(D) Recommendation

Despite all these limitations and problems, the proposed device model does possess several attractive features which are important in any power microwave tube design. For example, the turnability of the radiated frequency, the simplicity in the engineering design, the absence of delicate mechanical microwave resonance or slow wave structures, the very high power relativistic beam, and the very large DC magnetic field. These are good features when development costs and competitive economics of the device products are considered. Therefore, we consider that the proposed device model is a good engineering proposition if the device can work as it is intended. Based on our visit to the AFCRL and subsequent numerous conversations over the phone with the two inventors at Hanscom AFB. We all realize that a great deal of work should be done both theoretical as well as experimental before any feasible engineering model can be built. We, therefore, recommend:

(1) <u>Experimental Work</u>:

(a) To find ways and means to get the emitted electromagnetic radiation out of the plasma interaction chamber, so that the theoretical foundation of the device model

can be verified. To this aim, experiment can be carried out at lower frequency, for at these frequencies, many university plasma laboratories are equipped to perform such work.

(b) The exercise of (a) should be extended in steps from lower microwave (say, 500 MHz), to higher microwave (in the 5-GHz to 10 GHz region), and finally to millimeter and submillimeter wavelengths.

(c) Simultaneously, experiments should be performed to optimize the device operating conditions in terms of the relative electron beam and plasma volume, and others.

(2) Theoretical Work:

(a) Stability problem - Since the amount of power emitted from the proposed gain mechanism depends critically on the pump wave energy density, thus, an appropriate and efficient mechanism for producing high pump field energy is required such that the pumped plasma remains stable.

(b) Monochromaticity of the emitted radiation - Since the broadening of the radiation spectrum is intrinsic due to Doppler effect and collision, investigation should be done to see whether Laser techniques could be used to produce a Monochromatic electromagnetic radiation.

(c) Beam-plasma interaction volume - Since the total output that the device radiates out of the plasma volume depends on the size of the interaction volume where the major part of the electrostatic field energy is stored. Mathematically, how this interaction volume can be determined may be a matter of importance in future engineering design.

(d) Noise problem - Based on early experimental work on two-beam space charge amplifier (24), such tubes were very noisy and give rather low output and effiiciencies. Presumably for these reasons, little further development work has been carried out in spite of the structural simplicity of those tubes. The proposed beam-plasma device will encounter a similar problem, especially the noise problem, since it is intrinsic for any tube device operating on a similar principle. Therefore, the noise problem must be resolved theoretically as well as experimentally.

(e) Amplification possibility - Although the proposed device is a power oscillator, hence, its usefulness is rather limited. The possibility of adopting a similar interaction mechanism to convert the oscillator into an amplifier should also be investigated.

(3) Design of Demonstration Model

In order to demonstrate the potentiality and feasibility of the device model, several engineering models have been proposed and their design procedures will be given in the next section.

IV. Design of Demonstration Model

(a) Design Considerations:

In all models considered in the following only the single electron beam-plasma model will be considered for reasons discussed in Section III. Even in this simpler model, its complicated radiation pattern does not make the design task any easier. However, it is to be noted (Figure 4) that the radiation becomes more and more backward with respect to the pump-wave vector, $\underline{k}_o$ as the phase velocity of the pump-wave increases to six-tenths of the velocity of light, C; and based on this characteristic some optimum microwave system may be found. This predeteremines the parameter of the electron beam. Thus, by choosing $a = 0.6$, the beam voltage required to satisfy this condition is determined by the relation

$$v_b = \sqrt{2\,(e/m)\,V_b}\,, \quad \text{hence} \quad V_b = (0.6\,c)^2/2e/m = 92\text{-KV}.$$

Under such operating conditions, the beam-plasma interaction mechanism will radiate a directional pattern as shown in Figure 8, and

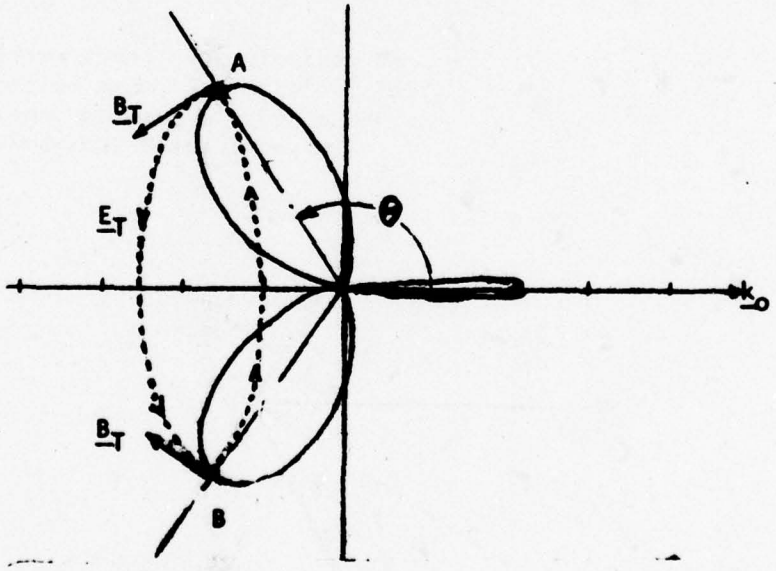


Figure 8. Transverse Electric-and Magnetic-Field Distribution of the Backward-Loabe Radiation Pattern for Case a = 0.6.

by eqs(10) and (11), the electric field has circular symmetry property as shown and the magnetic field vector, $\underline{B}$,

(not completely shown in Figure 8) is in the direction specified by the vector, $\hat{n} \propto \underline{E}_T$, where $\hat{n} = \underline{r}/r$, is the unit vector specifying the direction by which the Raman radiation is observed, At, and only at, Points A and B, the magnetic vector $\underline{B}$ lies on the plane of the paper since the electric vector $\underline{E}_T$ is perpendicular to the plane of the paper at these points.

This field distribution characteristic provides us valuable information in choosing a particular microwave system. Moreover, since our main purpose of this exercise is to get the radiation power out of the plasma volume, no consideration has been given to the choice of a particular plasma production system or technique. However, a cylindrical plasma chamber will be used for reasons of convenience in the fabrication of a complete system.

Three models will be presented in this report. However, in order to meet the official guide-lines on the length of the report, only the simplest and the preferred model is given in this section. The more complicated two models will appear as Appendix B. One of these, the model B, employs a circular electric TE^{o}_{01p} mode dielectric-filled cylindrical cavity. The other, model C, also a cylindrical cavity, is operating in a dual cavity TE^{o}_{01p} (at $\sim 2\omega_{pe}$) and TM^{o}_{01q} (at ω_{pe}) modes.

(b) Demonstration Model A

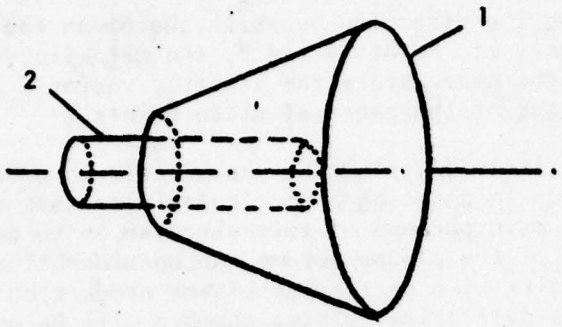
This is the simplest model that can be fabricated without involving a major engineering undertaking; and since, the microwave collector system is separated and external to the beam-plasma interaction system, each system can be optimized in its operating condition, hence, this is a preferred model. As can be seen from Figure 9 the beam-plasma interaction chamber is of the cylindrical varieties. The microwave collector system consists of a conical metal horn with its neck-end open to allow for the installation of the beam-plasma chamber along the axis of the horn. The flared angle, ϕ , of the horn is chosen to generate a parallel beam (array) pattern which can be radiated out of the mouth of the horn.

With reference to Figure 9c, and from a simple geometrical consideration (ray-theory), it can be shown that for a parallel ray pattern output from the horn, the following condition must be satisfied**

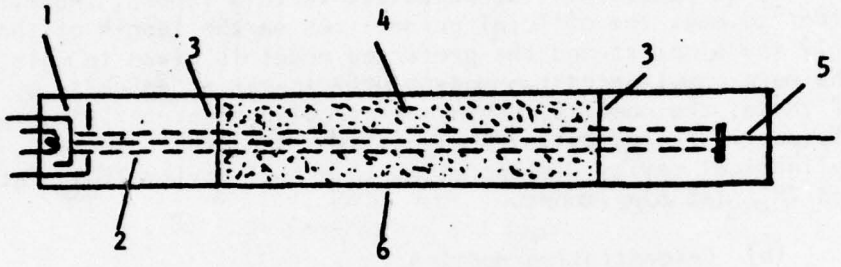
$$\phi = \theta/2$$

where θ is the angle the backward radiation ray makes with the positive $\underline{k}_o$ axis. For further information on horn design, the book, "Electromagnetic Horn Antenna" (25) should be consulted.

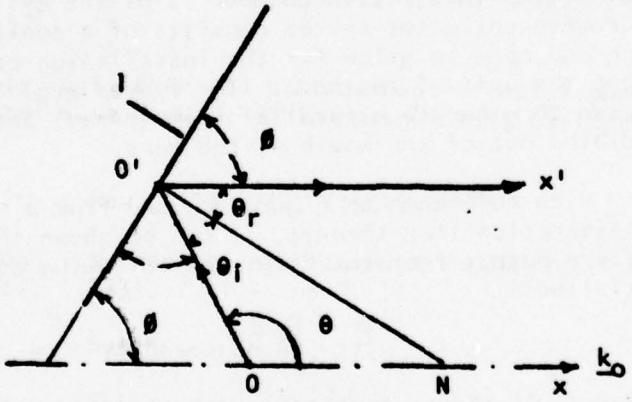
** With reference to Figure 9c, if OO' is the emitted ray from the plasma at Point O, then, by the Law of reflection, $\theta_i = \theta_r$, where $O'N$ is the normal drawn at O' and normal to the horn



(a) Schematic Diagram: 1 - Conical Horn,
2 - Beam-plasma Tube.



(b) Beam-plasma tube: 1 - Electron Gun,
2 - Electron beam, 3 - Metallic foil,
4 - Plasma Chamber, 5 - Collector,
6 - Cylindrical Glass Tube.



(c) Determination of the flared angle ϕ of the Conical horn: 1 - Horn surface, $\underline{k}_0$ - Direction of the electron beam, OO' - Direction of the emitted ray, O'x' - Direction of the parallel ray.

Figure 9. Demonstration Model A.

surface at that point. If $o'x'$ is the direction of the generated parallel ray, then $o'x' /\!/ ox$. Hence

$$\phi + \theta_r = 90^0$$

and

$$\phi = 90^0 - \theta_r = 90^0 - \theta_i$$

but $$\alpha + \theta_i = 90^0$$

hence $$\phi = \alpha$$

also $$\phi + \alpha = \theta$$

$$\therefore \quad \phi = \theta/2$$

Concluding Remarks

In order to meet the official guide-lines on the length of the report, the contents of both appendices A and B are not included in this report. However, in a separate report to the RADC/OCTP Section, both appendices are included.

REFERENCES

(1) (a) B. Prasad and C.C. Leiby, Jr., U.S. Patents, 3,944,946, March 16, (1976).

(b) B. Prasad and C. C. Leiby, Jr., U.S. Patent (being accepted) 1977.

(2) For example, see "Engineering Proceedings-Wave Interaction and Dynamic Nonlinear Phenomena in Plasma." The Pennsylvania State University, College of Engineering, University Park, Pennsylvania, September (1963).

(3) M. A. Lamport, J. Appl. Phys. 27, 5 (1956).

(4) M. Bornatiei, A. Cavaliere, and F. Englemann, Phys. Fluids, 12, 2362 (1969).

(5) Microwaves (Laser Technology), Pg. 12, December (1976).

(6) (a) J. Borr, Phys. Lett. 14, 293 (1955).

(b) J. P. Beasley, PROC. 6th, Int'l Conference on Microwave and Optical Generation and Amplification, Cambridge, 132, (1966).

(c) B. Kulke and R. IN. Wilmarth, Proc. IEEE 57, 219 (1969).

(d) V. A. Zhurakovskiy, Radiotekhnika; Electronika, 9,8-1527 (1964).

(e) A.A. Kurayeu et al, Radiotekhnika; Electronika, 19,5, 1046 (1974).

(f) H.R. Jory, E.L. Lien and R,S. Symons, "Final Report Millimeter Wave Study", Varian Associates, California, (1975).

(7) M.H. Cohen, Phys. Rev., 123, 711, (1961).

(8) S.A. Kaplan and V.N. Tsytovich, "Plasma Astrophysics ", Porgamon Press, (1973), P. 104 and P. 140.

(9) M.H. Cohen, J.Geophys.Research,67, 2729, (1962).

(10) B. Prasad, Phys. Fluids, Volume 19, 464, (1976).

(11) B. Prasad and C. C. Leiby (Private Communications).

(12) V.L. Ginzburg and V.V. Zheleznyakov, Astron Zh.35, 694 (1958) (Soviet Astron.-A.J. 2, 653, (1958)).

(13) T.M. O'Neil, Phys, Fluids, 8, 570, 2255, (1965).

(14) (a) W.E. Drummon, J.H. Malmberg, T.M. O'Neil, and J.R. Thompson, Phys. Fluids, 13, 2422, (1970).

(b) J.R. Thompson, Phys. Fluids, 14, 1532, (1971).

(c) T.M. O'Neil, J.H. Winfrey, and J.H. Malmberg, Phys. Fluids, 14, 1204, (1971).

(15) (a) J.H.A. VanWakeren and H.J. Hapman, Phys,Rev.Lett., 34, 1499, (1975).

(b) K.W. Gentle and J. Lohr, Phys. Fluids, 16, 1464, (1973).

(c) H. Ikezi, R.P.H. Chang, and R.A. Stern, Phys. Rev. Lett., 36, 1047, (1976).

(16) I. Langmuir, Phys. Rev. Lett., 26, 585, (1975).

(17) L. Spitzer, Physics of Fully Ionized Gases, New York, (1956).

(18) (a) C.C. Leiby, Jr., (Private Communication).

(b) Prof. N. Hershokowitz, Dept of Physics and Astronomy, University of Iowa, (Private Communication).

(19) G. Bekefi, Radiation Processes in Plasmas (Wiley, New York, 1966), Pg. 145.

(20) (a) V.N. Tsytovich, "Nonlinear Effect in Plasma" (Plenum, New York, 1970), P. 103.

(b) N.M. Kroll, A. Ron, and N. Rostoker, Phys. Rev. Lett., 13, 83, (1964).

(c) T.R. Hartz and R.E. Barrington, Proc. IEEE, 57, 1108, (1969).

(d) B.L. Sansfield, R. Nodwell, and I. Meyer, Phys. Rev. Lett., 26, 1219, (1971).

(e) N.M. Rosenbluth and G.S. Liu, Phs. REv. Lett., 29, 701, (1972).

(f) B.I. Cohen, A.N. Kahfmann, and K.M. Watson, Phys. Rev. Lett.

(g) I. Meyer, Phys. Rev. A., 6, 2229, (1972).

(h) Yu. M. Aliev, et al, Sov. Phys. - JETP, 34, 564 (1972).

(i) G. Schmidt, Phys. Fluids, 16, 1676 (1973).

(j) A. Kh. Nazaryan, Sov. Phys. Tech. Tech. Phys., 20, 603 (1976).

(21) P. A. Sturrock, in Proceedings of the AAS-NASA Symposium on the Physics of Solar Flares, National Aeronautics and Space Adminstration, Washington, (1964), p. 357.

(22) C. Chin-Fatt and Hans R. Griem, Phys. Rev. Lett., 25, 1644 (1970).

(23) V.D. Shapiro, Sov. Phys. JETP, 17, 416 (1963).

(24) (a) A. V. Haeft, PROC. I.R.E. 1849, 37.4.

(b) J. R. Pierce and W. B. Hebenstreit, Bell Syst. Tech. J., 1849, 28, 33.

(25) A. W. Love, Electromagnetic Horn Antenna, IEEE Press (1976).

(26) Y. Terashima and N. Yajma, Progr. Theor. Phys. 443 (1963).

(27) V. V. Zheleznyakov and V. V. Zaitsev, Sov. Astron. -AJ. 14, 250 (1970).

(28) E. Merzbacker, "Quantum Mechanics", (Wiley, New York, 1961), P 224.

(29) P.M. Morse and H. Feshback, "Methods of Theoretical Physics" (McGraw-Hill, New York, 1353), PP. 856 and 1497.

APPENDIX A, "Brief Review of Prasad's Theory" and

APPENDIX B, "Design of Demonstration Models B and C" to be published.

1977 USAF-ASEE SUMMER FACULTY RESEARCH PROGRAM
sponsored by
THE AIR FORCE OFFICE SCIENTIFIC RESEARCH
conducted by
AUBURN UNIVERSITY AND OHIO STATE UNIVERSITY

PARTICIPANT'S FINAL REPORT

AUTOMATIC SPEECH PROCESSING-SPEECH ENHANCEMENT

Prepared by:	Russell J. Niederjohn, Ph.D
Academic Rank:	Associate Professor
Department and University:	Department of Electrical Engineering Marquette University
Assignment:	
(Air Force Base)	Griffiss AFB
(Laboratory)	Rome Air Development Center
(Division)	Intelligence and Reconnaissance
(Branch)	Intelligence Applications
USAF Research Colleague:	Captain Robert A. Curtis, Ph.D
Date:	26 August 1977
Contract No.:	F44620-75-C-0031

AUTOMATIC SPEECH PROCESSING-SPEECH ENHANCEMENT

ABSTRACT

The enhancement of speech intelligibility in the presence of high noise levels is an important consideration in many practical communication situations. The work documented in this report describes the results of an examination of several methods for processing speech so as to result in an enhancement of its intelligibility in the presence of wideband random noise. Four particular processing methods are considered in this work: (a) INTEL, a method which involves processing in both the first and second order spectral domains; (b) spectral subtraction, a method which involves a simple subtraction of the average noise spectrum from the first-order spectrum; (c) minimum mean square error filtering, a method which involves filtering speech in such a way as to minimize the mean square error between a signal and its expected value in noise; and (d) methods based upon suppressing the frequency content of a speech plus noise signal between pitch harmonics of the speech signal.

In order to carry out a study of methods for the enhancement of speech intelligibility in noise, two general-purpose computer processing systems were implemented. The first is a terminal interactive system for the generation, analysis, and graphic display of synthetic voiced speech sounds. Through the use of this system a considerable insight into the effect of various processing algorithms upon speech and upon speech in noise has been effected.

The second computer processing system has been developed for the processing of real speech. This system involves the use of a DDP-116 data converter and a Honeywell 6000 Computer. Communication between these two computers is by means of seven track magnetic tape. In use, this system facilitates the input, process, and playback of real speech utterances. Through this system the effect of numerous processing algorithms upon normal speech in noise has been studied.

While both of these processing systems have been developed for, and applied to, a study of processing techniques for enhancing the intelligibility of speech in noise, the computer programs generated have purposely been made general purpose so as to facilitate their future use at RADC for other speech processing and signal processing tasks.

The effect of several processing algorithms (based upon the four methods mentioned) has been studied for numerous synthetic voiced speech sounds and for two, twelve second, real speech utterances. These two speech utterances were generated by a male talker; one utterance in a signal-to-noise ratio of +6 dB, the other utterance in a signal-to-noise ratio of -6 dB. Overall results indicate that; while the greatest speech enhancement success has been achieved with the INTEL and the minimum mean square error filtering methods, the four methods studied each offer a significant potential for speech intelligibility enhancement in noise.

ACKNOWLEDGEMENTS

The author of this report is grateful to many persons who contributed to make this summer at the Rome Air Development Center a very valuable experience.

The author is very appreciative of the interest and help of Captain Robert A. Curtis. Captain Curtis served as "research colleague" and contributed both his time and his ideas to the work described in this report. The help of Dr. Bruno Beek, Mr. Richard Vonusa and Mr. Michael Heffron of the Speech Processing Group at the Rome Air Development Center is sincerely appreciated. Also, the assistance of Mr. Albert Proctor, Mr. David Clark and Mr. Robert Doane who helped with the preparation of the computer programs and the other work associated with the Honeywell 6000 Computer is appreciated.

To not acknowledge the administrative assistance of Mr. J. Fred O'Brien, Director of the "USAF/ASEE Summer Faculty Research Participation Program" would be a major oversight. The work of Mr. O'Brien resulted in the smooth operation of the program and, in a major way, contributed to the technical success achieved by the project. The author of this report is very thankful for the help of Mr. O'Brien.

The author of this report would also like to express his appreciation for the interest and help of several other persons at the RADC who contributed to this project. Three of these persons include Mr. John Huss, who coordinated the program at the local level; Mrs. Emma Kimpton who typed this report and Mr. Kirk Starczewski who prepared the figures contained in this report.

Finally, the author wishes to thank the United States Air Force and the American Society for Engineering Education who sponsored and coordinated the activities of the program.

TABLE OF CONTENTS

PAGE

I. INTRODUCTION
- A. SPEECH IN NOISE AT THE LISTENER
- B. SPEECH IN NOISE AT THE SPEAKER
- C. THIS REPORT

II. DISCUSSION

III. RESULTS
- A. INTEL PROCESSING METHOD
  - 1. Discussion
  - 2. Tests With Real Speech
  - 3. An INTEL Extension
- B. SPECTRAL SUBTRACTION METHOD
  - 1. Discussion
  - 2. Tests With Real Speech
- C. MINIMUM MEAN-SQUARE-FILTERING METHOD
  - 1. Discussion
  - 2. Tests With Real Speech
- D. METHODS BASED UPON PITCH TRACKING
  - 1. Discussion
  - 2. Tests With Real Speech

IV. CONCLUSIONS

REFERENCES

APPENDIX

I. INTRODUCTION

The understanding of speech contaminated by the presence of noise is an important consideration in many practical communication situations. Consider the airplane or helicopter pilot in a noisy cockpit attempting to communicate with ground based personnel; or consider the worker in the environment of noisy machinery attempting to communicate via telephone or other means with personnel outside the noise environment.

There are two cases for the speech in noise situation. First, there is the case where the noise is present at the speaker (1-6); second, there is the case where the noise is present at the listener (7-19). Each case presents a somewhat different situation. In the case of noise at the speaker, there is an opportunity to suppress the noise (relative to the speech) prior to its reception by the listener. thus resulting in an enhanced signal-to-noise ratio and hopefully more intelligible speech. In the case of noise at the listener, while there is no opportunity to suppress the noise; there is an opportunity to process the speech prior to its encounter with the noise. Conversely, in the first case, since the noise is already present with the speech there is no opportunity to process the uncorrupted speech signal. In the second case, since the noise is in the environment of the listener, there is no opportunity to suppress the noise level.

There are several types of noise which may contaminate a speech signal. These include: impulse noise, large amplitude sine-wave or sum of sine-wave noise, a conflicting speaker, and wideband random noise. The enhancement of speech intelligibility in the presence of each of these noise types is under study by the Rome Air Development Center (1-3, 20). It is the purpose of the present study to consider the enhancement of speech intelligibility in the presence of wideband random noise.

A. SPEECH IN NOISE AT THE LISTENER

One obvious method for improving the intelligibility of speech in noise at the listener is to simply decrease the level of the noise. Although there exist methods for decreasing the noise levels produced by noisy equipment; these methods often do not reduce the noise levels sufficiently or are too expensive or too inconvenient to be practical.

Another obvious method for improving the intelligibility of speech in noise at the listener is to simply increase the power of the speech signal, thus resulting in a more favorable signal-to-noise ratio. Although such a technique may work in certain low-level noise situations; in high noise levels, the need to conform within a pre-established maximum sound level may prohibit the use of this simple technique. As a result, a method for enhancing the intelligibility of speech in high noise levels, without increasing the signal power, is desirable.

Several studies related to the intelligibility of speech in noise (at the listener) have been reported (7-19). In these studies, various techniques for processing speech (prior to reception by the listener) have been evaluated. Three particular techniques (8, 10, 11) have been recently reported and have been shown to offer intelligibility

enhancement for speech in white noise at various signal-to-noise ratios and in one case in the environment of recorded power generating noise (9). These three techniques involve processing speech by: (a) high-pass filtering followed by infinite-amplitude clipping (8), (b) high-pass filtering (11), and (c) high-pass filtering followed by rapid amplitude compression (8-9). At a signal-to-noise ratio of 0dB (noise at 90 dB (re. .0002 dy/cm^2)) an intelligibility of greater than twice normal speech is obtained by processing speech by any of these three methods. At other signal-to-noise ratios a similar intelligibility enhancement is also achieved.

B. SPEECH IN NOISE AT THE SPEAKER

One technique which may sometimes be successfully applied for enhancing the intelligibility of speech in the environment of noise at the speaker makes use of a noise-canceling or close-speaking microphone. In some cases such a microphone may not be sufficient because the noise is at too high a level. In other cases it may not be possible to use such a microphone because it's too inconvenient for the speaker, because the speaker is unable to wear such a microphone, or because the speech is already added to the noise when it is available for listening. As a result, a processing technique for enhancing the intelligibility of speech contaminated with noise is desired. Several techniques have been investigated for the case of noise at the speaker. These techniques include high-pass filtering followed by infinite amplitude clipping (4), a technique known as "INTEL" which involves gating the second-order spectrum and the subsequent retransformation back into the time-domain (1-2), and methods based upon the use of linear prediction (5-6). While the techniques investigated for this case have displayed encouraging results, a significant enhancement in the intelligibility of speech in noise at the speaker has not been achieved.

C. THIS REPORT

While both cases for speech processing in noise have many practical applications and while both cases are of considerable interest, greater application and interest exists within the Air Force for the later case (i.e., speech in noise at the speaker). As a result, the remainder of this report and the work performed in its preparation are directed specifically toward this later case.

The research work documented in the following sections of this report has included an analysis and study of methods for processing speech so as to result in an enhancement of its intelligibility in the presence of noise at the speaker. In this direction two specific approaches have been pursued. The first approach involves the development of interactive software for the analysis and study of processing techniques applied to synthetically generated voiced speech. For this study, interactive programs have been developed for the Honeywell 6000 accessed via a Tektronix 4002A CRT for the generation, processing, and graphic display of synthetically generated voiced speech sounds. This interactive system is described in detail in a recent report (29). The results obtained with this system are described in Section III of this report.

The second approach involves the development of a general purpose, batch-oriented, speech processing system for real speech and its use in the study of speech in noise processing techniques. This system involves magnetic-tape communication between the DDP-116 data converter and the Honeywell 6000 computer. Programs for analog to magnetic-tape conversion, previously developed by Captain Robert Curtis, are utilized. Programs for the input and output of this magnetic-tape to/from the Honeywell 6000 computer and general purpose programs for processing the data contained on these magnetic-tapes are described in a recent report (29). In Section III of this report the results obtained using this system for processing speech contaminated with noise are described.

II. DISCUSSION

The most successful present technique for enhancing the intelligibility of speech in noise at the listener is the technique known as "INTEL" (an acronym for INTelligibility Enhancement by Liftering). This technique has been developed under the direction of the RADC (1-2). While only a small speech intelligibility gain has been achieved by this method, a significant enhancement of the listenability of speech in noise has been demonstrated.

It is one purpose of this work to investigate the operation of the INTEL technique through both an examination of the results of processing synthetic voiced sounds and through the processing of real speech. The results of this examination are presented in Section III-A.

One problem with the INTEL technique is that it requires four Fourier Transformations, two forward and two reverse. Since calculating a Fourier Transform is computationally time consuming, it is of interest to explore methods which require fewer transforms. As a result, three additional approaches to speech intelligibility enhancement are explored in this work with preliminary results documented in the next section of this report. These three approaches are: (a) spectral subtraction, (b) minimum mean square error (MSE) filtering (21), and (c) methods based upon pitch tracking.

Spectral subtraction is of interest since it is computationally and conceptually relatively simple. It involves the subtraction of the estimated noise spectrum from the transform of the speech plus noise signal. After subtraction, the resulting spectrum is retransformed into the time-domain. Support for this technique can be gained from an intuitive analysis of speech plus noise and from its seeming similarity to "gating" which is performed on the second-order spectrum in the INTEL technique. One problem with subtraction is that it requires some determination of both the magnitude and the spectrum of the noise. In the INTEL technique, the magnitude of the noise is automatically accounted for (when gating to zero is used) and the spectrum of the noise is assumed flat. In the results presented in Section III-B for spectral subtraction it is assumed (as a first approximation) that the noise has a flat frequency spectrum (i.e., white) with a magnitude equal to the average first-order spectrum magnitude above 2.5 KHz.

A method for determining a filter which minimizes the mean square error between a signal embedded in noise and its estimated value, assuming

the signal and noise are uncorrelated, can be shown to be given by (21):

$$H(jw) = \frac{Sss(w)}{Sss(w)+Snn(w)} \qquad \text{(eq. 1)}$$

where:

Sss(w) = the estimated spectrum of the signal, and

Snn(w) = the estimated spectrum of the noise.

Using the longtime average speech spectrum for Sss(w) and the measured spectrum of the noise for Snn(w), the transfer function H(jw) can be calculated. Then, multiplying H(jw) by the spectrum of the input speech signal and performing an inverse transformation results in the processed speech output.

This method is attractive for two reasons. First, it is an optimum method (in the least mean square sense) for separating a signal from noise. Second, it is computationally simple to implement since it is a simple filtering process which can be performed in the frequency domain after transformation, or perhaps on the time-domain signal using digital filtering techniques. A complication of the method is that it requires an estimate of the noise spectrum. It is unclear at this point how the results of this method vary as a function of the error in estimating the noise spectrum. In the experiments described in Section III-C it is assumed that the noise spectrum is flat with an average magnitude equal to the magnitude above 2.5 KHz.

Speech in noise enhancement through methods based upon pitch extraction seem intuitively attractive. This is a result of the fact that the energy of a speech signal exists at harmonics of the pitch frequency while the energy of noise is distributed throughout the spectrum. From a knowledge of the pitch frequency, those lines in the spectrum not at harmonics of the pitch frequency can be suppressed leaving, hopefully, speech enhanced in the presence of noise. Several problems influence this method. There is the problem of accurately tracking the pitch frequency, even in a non-noise environment. There is, on the one hand, a desire to analyze speech over a long time segment to gain as much information about the signal as possible. There is, on the other hand, a desire to analyze a short interval so that changes in the pitch frequency during the analysis interval will not be significant. A recent report by Parsons and Weiss (3) suggests that the optimum segment size should be 40.8 msec. A segment of 51.2 msec is used in this work.

Previous results obtained with methods based upon pitch tracking have not been particularly encouraging (1-2, 20). It has been suggested that even when the pitch frequency is accurately determined, for example from the original uncorrupted speech signal, such methods have not been shown capable of significant speech enhancement in noise. The use of comb filtering, for example, has not been found effective for improving the intelligibility of speech in noise. A discussion of the use of comb filtering for speech in noise enhancement is contained in a recent report by Weiss, Aschkenasy, and Parsons (1). Another report, by Weiss and Aschkenasy (2), discusses an experiment with pitch tracking in which

good results were reported when the pitch frequency was found adequate. Details of this method are somewhat sketchy. However, pointed out in this report are the difficulties in determining pitch, particularly at low signal-to-noise ratios, and the distortion produced by inaccurate pitch tracking and by analyzing unvoiced speech by a harmonic analysis.

An interesting method for pitch tracking and some interesting results obtained, from a relatively crude processing method based upon pitch tracking, are described in Section III-D.

III. RESULTS

An analysis of several speech in noise enhancement methods has been carried out: (1) using synthetically generated speech and (2) using real speech. This analysis has provided a basic insight into several speech in noise analysis methods and into the speech in noise situation in general. The four subsections of this section describe each of the four analysis methods introduced in the last section and contain representative output from the synthetic speech generation and synthetic speech analysis programs (29). In addition, the results obtained with real speech are discussed.

For the synthetic speech illustrations, results for the vowel /a/ have been selected for all four methods. Formant data is from Peterson and Barney (22)*. A pitch period of 9 ms was selected and signal-to-noise ratios of ∞ (no noise) and 0dB were used. Figure 1 illustrates the synthetic speech output for these two conditions.

For the intelligibility tests with real speech two utterances are used. Both were spoken by Captain Robert A. Curtis and each is about 12 sec in duration. The first utterance contains speech as follows: "Testing...one...two...three...four...five...six...seven... eight...nine... ten... we were away a year ago." The second utterance contains, "We were away a year ago...testing...one...two...three...four...five...six... seven...eight...nine...ten... may we all learn a yellow lion roar...Hawaii." The first utterance is in a signal-to-noise ratio of approximately +6 dB; the second is in a signal-to-noise ratio of approximately -6 dB. While this corpus of speech data is hardly sufficient to quantitatively evaluate speech intelligibility, it is sufficient to make a preliminary study of the processing methods and to make several qualitative observations.

A. INTEL PROCESSING METHOD

The INTEL algorithm is described in two recent reports (1-2). This author's interpretation of the algorithm from these reports indicates that the analysis of a single time-frame of 512 points (51.2 ms) consists of the following sequence of steps:

(a) Input 512 time samples;

(b) Apply a triangular window to the time samples;

(c) Perform a 512 point FFT;

*F1: ampl. = 1, freq. = 730 Hz, alpha = 27 Hz; F2: ampl. = .5, freq. = 1090 Hz alpha = 28.5 Hz; F3: ampl. = .04, freq. = 2240 Hz, alpha = 46.5 Hz

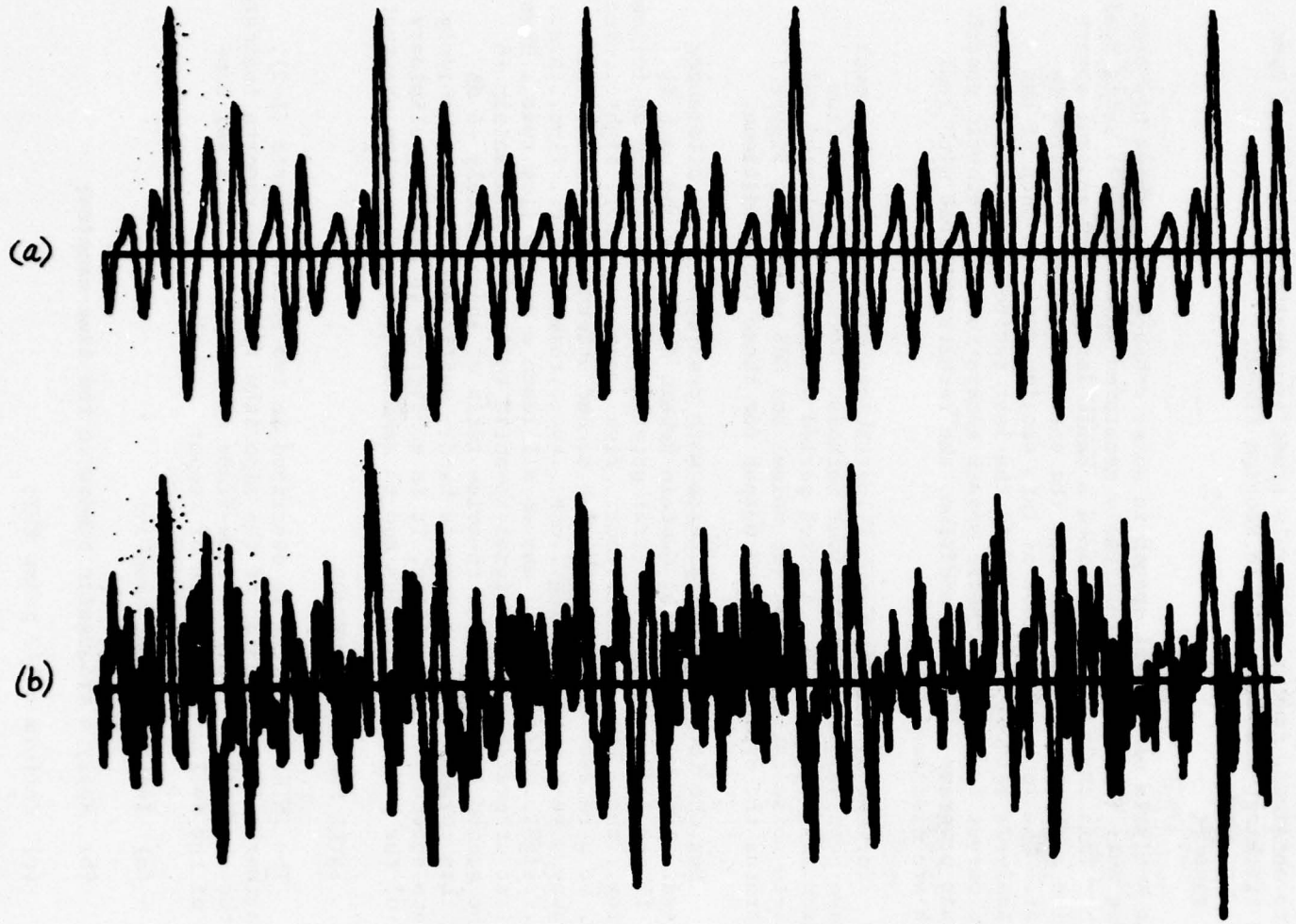


FIGURE 1. Time waveform of the synthetic vowel /a/ as generated by "SPEECH"; (a) no noise, (b) signal-to-noise ratio of 0dB.

(d) Set to zero the magnitude spectrum above 2.5 KHz;

(e) Square root the magnitude spectrum;

(f) Reverse the signs of all odd numbered magnitude harmonics;

(g) Perform a 512 point FFT on the magnitude spectrum as a real signal with zero imaginary part;

(h) Set the magnitude of the five low frequency harmonics to zero (gating);

(i) Perform a 512 point IFFT;

(j) Reverse the signs of the real part of all odd numbered harmonics;

(k) Square the real part of the spectrum, make it a magnitude and restore the phase from the original time waveform; and

(l) Perform a 512 point IFFT to result in the output time signal.

The input time waveform and the result after each processing step listed in the previous paragraph are illustrated in Figure 2 for: (1) no noise (left) and (2) a signal-to-noise ratio of 0dB (right).

1. Discussion

A discussion of the overall INTEL speech processing method can be found in two recent reports (1-2). The discussion here assumes general familiarity with the INTEL method.

From Figures 2a - 2c the effect of noise on both the time waveform as well as on the magnitude and phase of the frequency spectrum can be observed. From Figure 2c, it is noticed that the effect of noise on the frequency spectrum is to add a randomized baseline shift to the magnitude of the spectrum and a seeming randomization of the phase characteristic. The phase of the spectrum of the speech plus noise signal is apparently not without information, however, since greater intelligibility has been achieved with INTEL by restoring the input phase rather than discarding it in producing the processed output (20).

In step e of the INTEL process a square root of the magnitude spectrum is taken. In a recent report (2), Weiss and Aschkenesy go to great lengths to demonstrate that a justification for this square root operation centers around the fact that such an operation causes an increased fraction of the noise energy (relative to the speech energy) to be concentrated in the region near the origin in the second order spectrum (Figure 2g) than would otherwise be present. It is therefore argued (2) that such a square root operation makes it possible to more completely remove the noise. What is unclear to the present author is whether the "extra noise" energy found near the origin in the second order spectrum is due to the original noise being moved or, more simply, the first order spectrum flattening which is caused by the square root operation. Following this latter argument, it is then not a desirable

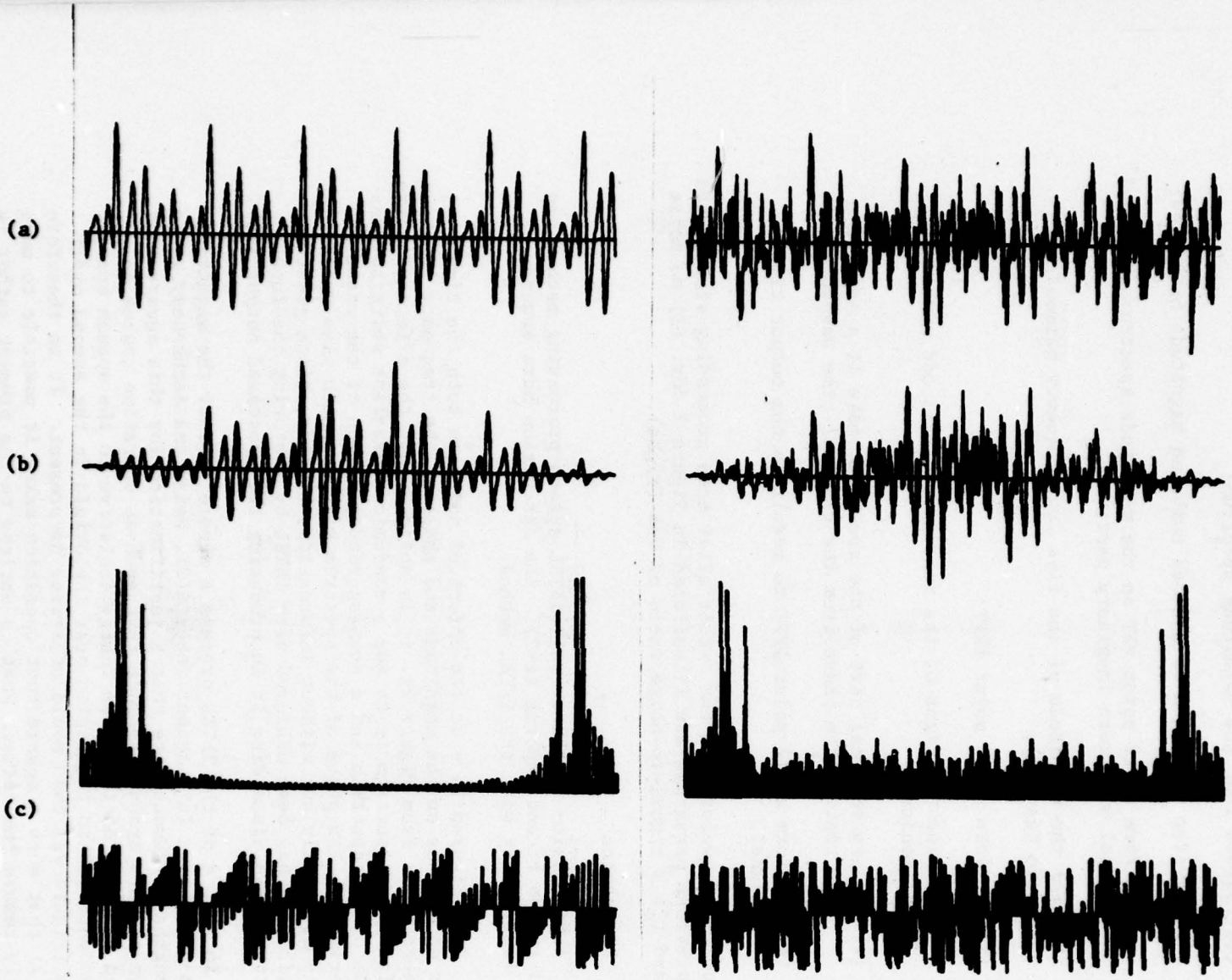


FIGURE 2. The Intel process applied to the synthetically generated vowel /a/. Each waveform shown is after the corresponding step listed in the first paragraph of Section III-A; left is for a S/N = ∞, right is for a S/N = 0dB.

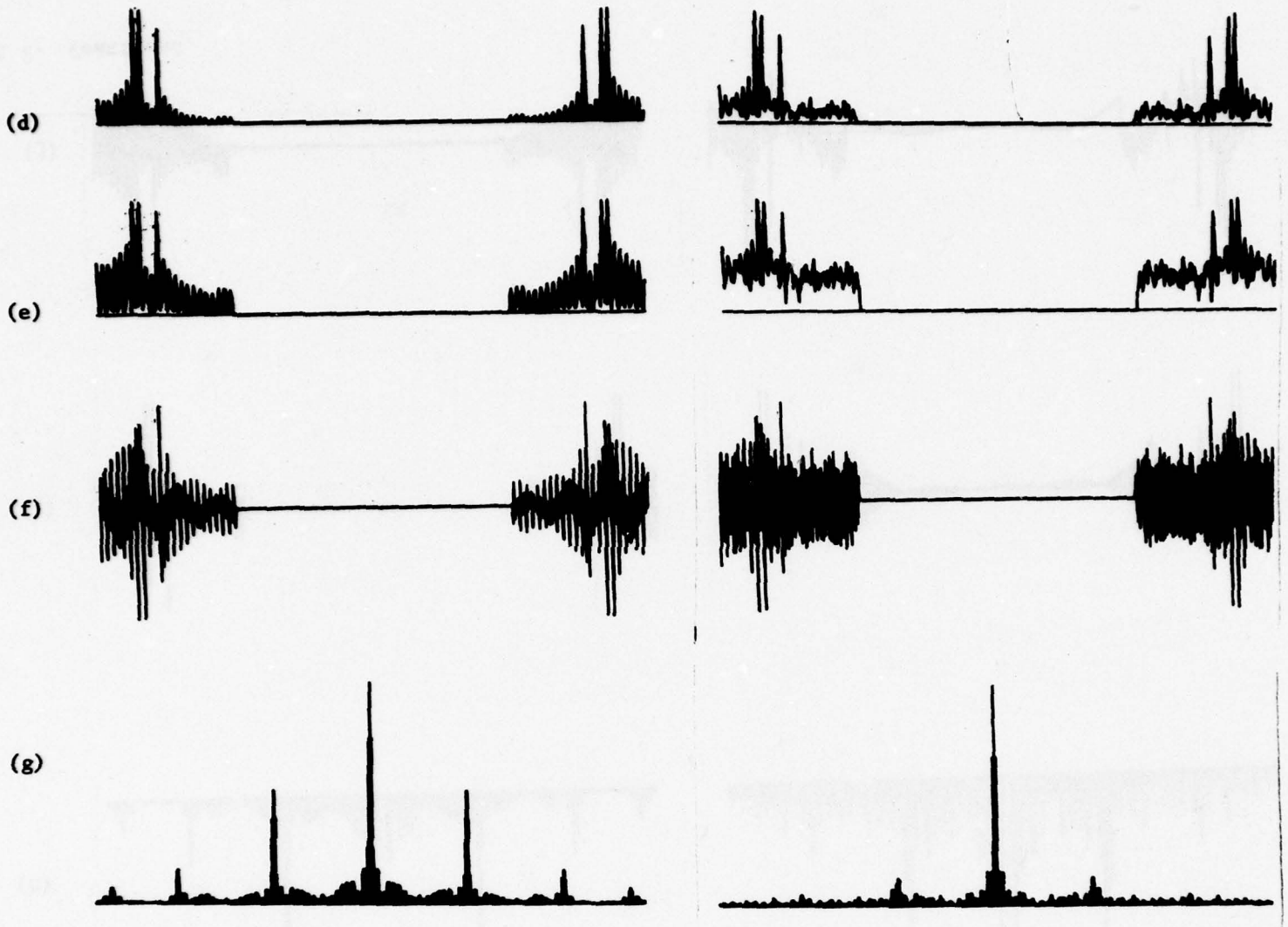


FIGURE 2. Continued

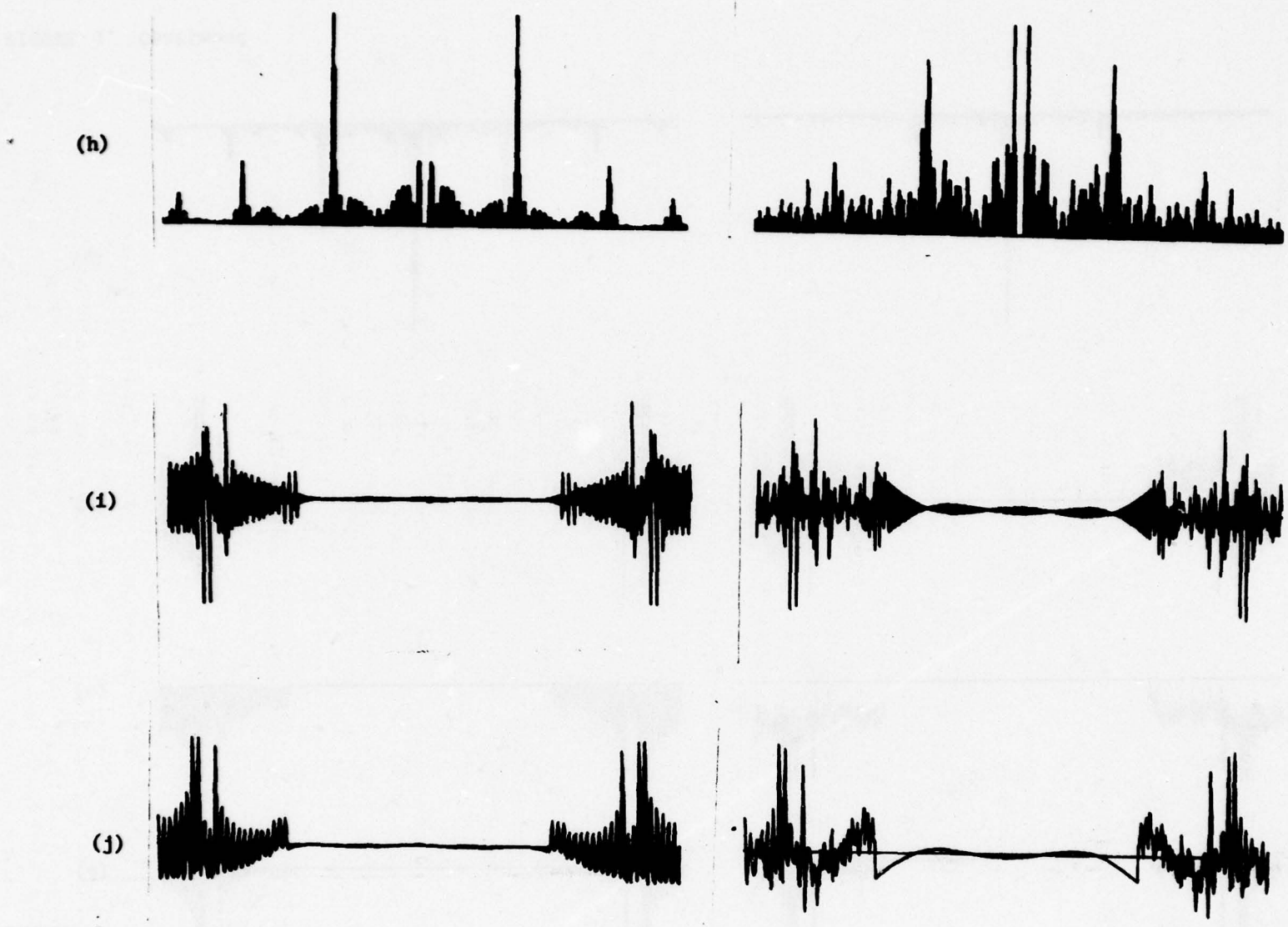


FIGURE 2. Continued

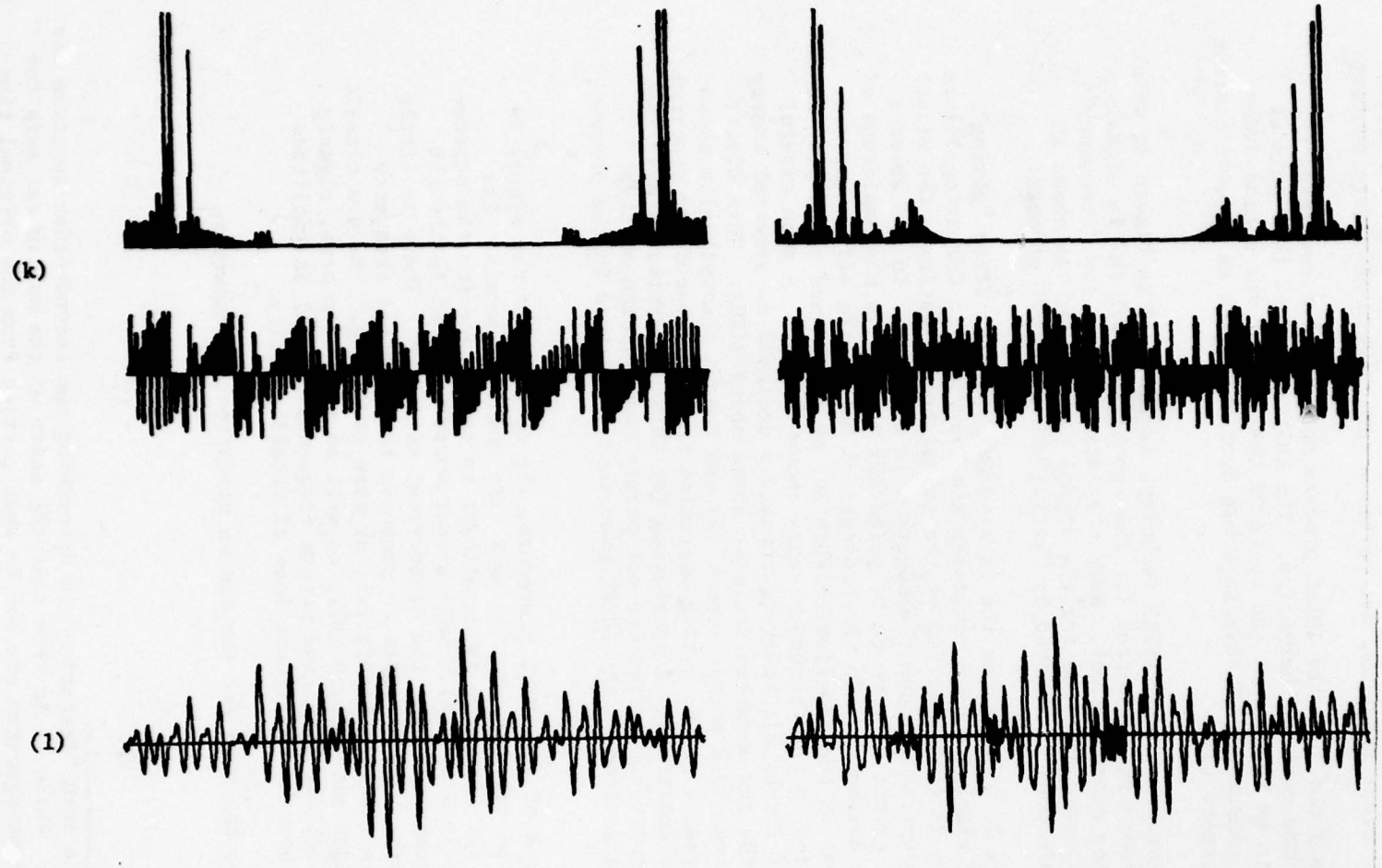


FIGURE 2. Continued

feature of square rooting which causes increased energy near the origin of the second order spectrum, but rather a consequence of square rooting.

Steps f and j of the INTEL process both involve reversing the signs of all odd numbered harmonics. The only effect of this pair of sign reversals is to reverse the scale of the axis of the second-order spectrum. A computational advantage has been suggested as a justification in a recent report (2).

The essence of the INTEL technique is observed in Figure 2g which shows the second-order spectrum for the synthetic vowel /a/ in signal-to-noise ratios of ∞ and 0dB. Note the large peak at low "frequency"* in the second order spectrum for the signal plus noise. As shown in Figure 2h, this peak is removed by "gating" in the INTEL process.

Figure 2i illustrates the first-order spectrum after "gating" and Figure 2j after the sign reversals are "reversed". Comparing Figure 2j with Figure 2e (the spectrum of the signal before gating), the effect of the gating operation upon the spectrum is observed. In the absence of noise, the effect appears to be primarily a shift in the amplitude of all magnitude harmonics. In the presence of noise, the effect appears to be a removal of the baseline (Figure 2e) by a downward shift plus an added distortion in the frequency range above 2.5 KHz. A more careful observation of Figure 2j, however, reveals a decrease in spectral energy at about 1.5 KHz and a marked increase above about 2 KHz. This distortion was observed in a recent report (2) and can be theoretically shown to be a consequence of the gating operation in the second order spectrum. A method for automatically compensating for this distortion is described in a recent report (2). Time did not permit the addition of this compensation algorithm to the INTEL procedure programmed in the present work.

In step k of the INTEL procedure, the spectrum of the signal is squared prior to retransformation back into the time-domain. The justification for this step is an attempt to compensate for the square-root operation in step e(2). This author wonders why it is thought necessary to compensate for the square-root operation. There is little reason to suspect that attempts to preserve the original frequency spectrum are necessarily beneficial, or even desirable. The now classic work of Licklider and Pollack (27), as well as work of others, clearly shows that speech can withstand severe frequency as well as amplitude distortion without a significant loss of intelligibility.

To test the need for the square operation, a comparison of

*The use of the term "frequency" in describing the second-order spectrum may be confusing. While it is true that the units of the horizontal axis for the second-order spectrum are not Hz when carried from the original time waveform; the units are Hz if we consider the first-order spectral signal like a time waveform as seems to be a convenient way for viewing the INTEL Technique. In any case, a clear distinction of which spectrum is being discussed when using the term "frequency" will be made.

speech processed by the INTEL procedure, both with and without the square operation were examined by listening. Speech processed without squaring sounded very much like the unprocessed original. This indicates that apparently the square operation is essential to the INTEL process. This surprising result (surprising to this author anyway) leaves open several unanswered questions regarding the use of the square root and square operations in the INTEL process.

One question remaining is why square rooting (and subsequent squaring) has been observed to improve the intelligibility of speech in noise relative to not square rooting. One argument is because the result of these two operations is to modify the output frequency spectrum in such a way as to emphasize lower frequency components relative to higher frequency components. Since lower frequency components tend to best survive the noise, speech square rooted (followed by squaring) would be expected to sound better (enhanced listenability) in noise. Whether this process results in enhanced intelligibility remains to be demonstrated.

The argument of the previous paragraph would suggest that the root used in the rooting operation (step e) should be dependent upon the signal-to-noise ratio. This is, in fact, what has been observed with the INTEL Process (2, 20), root factors of one-third and one-half being found best dependent upon the signal-to-noise ratio.

One final observation about the INTEL technique can be made from Figure 2e. From this figure it is observed that the INTEL process does not preserve the triangular time weighting applied in step b. This may or may not result in any significant distortion depending upon how successive triangularly weighted windows sum. This particular problem has been previously observed and some work at compensating for this distortion has been pursued (20).

2. Tests with Real Speech

From listening to the two utterances (described at the beginning of this section) processed by INTEL, the advantages of processing speech in noise (by INTEL) are apparent. Clearly, speech processed by the INTEL technique "sounds better." This has been described as enhanced "listenability." While there is some question as to whether there is an enhanced intelligibility through the use of the INTEL technique, there seems no question as to a perceived improvement in the signal-to-noise ratio.

A recent communication (28) in evaluating the INTEL technique in signal-to-noise ratios of -5 dB, 0 dB, +5 dB, and no-noise, found little intelligibility gain for INTEL processed versus unprocessed speech.

3. An INTEL Extension

Figure 2g, the second-order spectrum for speech in no noise and at a signal-to-noise ratio of 0 dB, clearly reveals an increased amplitude near the origin which results from the additive noise. In the INTEL technique described with Figure 2 and Section III-A-1, a suppression of this second-order spectral peak to zero was implemented as described in two recent reports (1,2). Looking at Figure 2g (no noise), however,

reveals that even for normal speech this peak is non-zero. In fact, from an observation of several synthetically generated speech sounds without noise, it appears that the peak in the second-order spectrum near the origin is usually approximately twice the amplitude of the peak due to the formant frequency envelope.

Pursuing this observation, an experiment was carried out in which the INTEL technique (step h) was changed to suppress this low frequency peak (and other low frequency harmonics) by a factor which causes the zero frequency peak to be twice the amplitude of the formant peak in the processed output. This is accomplished by calculating a factor in the second-order spectrum given by:

$$X = \frac{\text{amplitude of the zero frequency component}}{\text{amplitude of the maximum formant envelope component}}$$

and dividing each of the ten low frequency, second-order harmonics by half this factor.

Upon listening to the result in comparison with INTEL a small improvement in intelligibility, listenability, and naturalness seemed apparent.

The use of this modification to the INTEL technique has advantages other than (perhaps) enhanced intelligibility. First, it should result in less distortion of the type shown in Figure 2j (and described earlier) since the "gate" is less severe. (This fact was not verified with synthetic speech.) Second, it results in an overall system automatically compensated for a changing signal-to-noise ratio.

A method of suppressing the zero frequency peak in the second-order spectrum by fixed factors has been previously investigated with INTEL (20). Results have indicated that a suppression of the peak by about one-third worked best at a signal-to-noise ratio of 0 dB. From Figure 2g, it can be noted that this is in very close agreement with causing the zero-frequency peak to be twice the formant peak as described in the previous paragraph.

B. SPECTRAL SUBTRACTION METHOD

As previously discussed, one problem with the INTEL technique is that it requires four Fourier Transformations. A process which is intuitively appealing, appears similar in function to "gating" in the INTEL technique, and requires only two Fourier Transformations is simple spectral subtraction.

The basic method implemented for spectral subtraction consists of the following sequence of five steps:

(a) Input 512 time samples;

(b) Apply a triangular window to the time samples;

(c) Perform a 512 point FFT;

(d) Estimate the average noise level from the magnitude of the spectrum above 2.5 KHz, subtract this level from the magnitude spectrum

and zero all frequency components above 3 KHz; and

(e) Perform a 512 point IFFT to result in the output time signal.

The input time waveform and the result from steps b and c above are the same as for the INTEL technique and are illustrated in Figure 2. The results for steps d and e are illustrated in Figure 3 for: (1) no noise (left) and (2) a signal-to-noise ratio of 0dB (right).

1. Discussion

One problem which results when subtracting from the magnitude spectrum involves the action to be taken when a difference results in a magnitude of less than zero. The method employed in this work for the subtraction of a level from the magnitude of the spectrum (step d previous paragraph) is slightly more complex than simple subtraction. If the value of the magnitude of a component is greater than the noise level, the noise level is subtracted from the magnitude value. If the value of the magnitude of a component is less than or equal to the noise level, that magnitude is divided by two.

From Figure 3d, it appears that the simple method employed to estimate and subtract the noise is not totally effective. Comparing Figure 3d with Figure 2k, the output spectrum from INTEL, reveals that INTEL appears to do a significantly better job at reducing noise than the subtractive method. Examining the time waveforms for the output from the spectral subtraction method (Figure 3e) and INTEL (Figure 2e) reveals that the spectral subtraction technique does not modify the time waveform as severely in the absence of noise. Probably a greater amount of subtraction (greater noise suppression) would be beneficial.

2. Tests With Real Speech

The results obtained for the processing of the real speech utterances described in the first paragraph of Section III confirm the expectations of the previous paragraph. The signal-to-noise ratio does not sound particularly enhanced over that obtained by simply zeroing the frequency range above 3 KHz and the intelligibility does not appear improved.

As a second experiment with subtractive noise cancellation, an additional processing step was added between steps d and e of the subtractive method. This additional process involves the use of a filter to emphasize the second formant frequency range. The characteristic of this filter was chosen to have a rising slope of 18 dB/octave below 1 KHz, a passband from 1 KHz to 2 KHz, and a falling slope of 12 dB/octave above 2 KHz. At a signal-to-noise ratio of -6 dB, the speech with high frequency emphasis sounds less intelligible than that with subtraction alone. This is probably due to the fact that enhancing the second formant frequency range is detrimental since (at this low signal-to-noise ratio) the second formant range is so heavily obscured by noise. At a signal-to-noise ratio of +6 dB it is not clear whether the high frequency emphasis is helpful or not. Certainly, such an emphasis causes the speech to be less natural sounding in both cases.

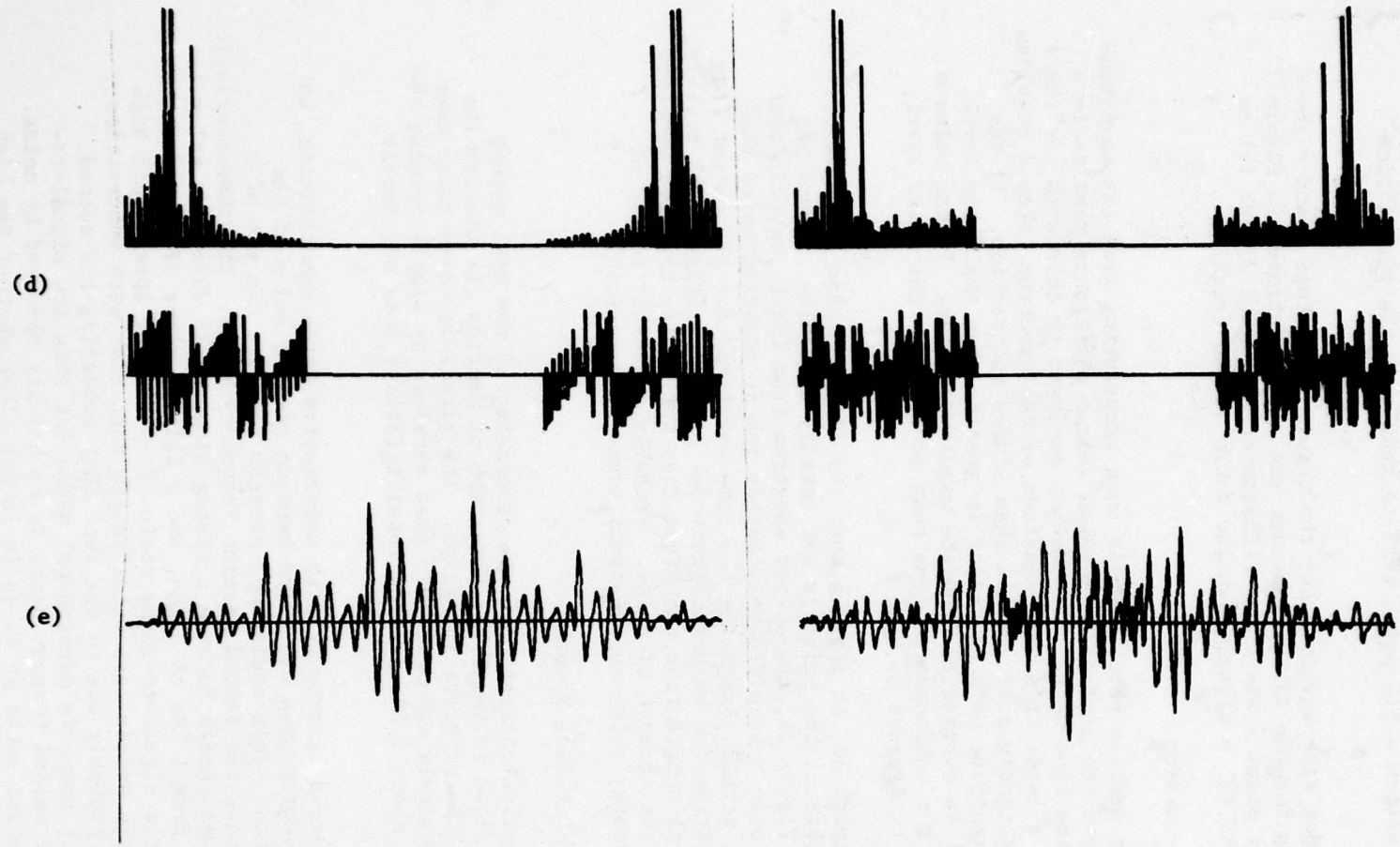


FIGURE 3. The spectral subtraction process applied to the synthetically generated vowel /a/. Steps a - c are the same as Figure 2. Steps d and e are illustrated after the corresponding step listed in the second paragraph of SectionIII-B;left is for a S/N = ∞ , right is for a S/N = 0 dB.

C. MINIMUM MEAN-SQUARE-ERROR FILTERING

As indicated in Section II of this report, the method of minimum mean square error filtering is an attractive technique for processing speech in noise for two main reasons. First, it is an optimum method (in the least mean square error sense) for filtering a signal in noise; and second, it can be implemented in a computationally efficient manner (relative to other techniques).

The implementation used for this method is based upon an analysis from Papoulis (21) as described in Section II of this report. The implementation consists of the following sequence of five steps:

(a). Input 512 time samples;

(b). Apply a triangular window to the samples;

(c). Perform a 512 point FFT;

(d). Estimate the expected noise level from the magnitude of the spectrum above 2.5 KHz, estimate the expected signal from the long-time average for normal speech, and modify the magnitude spectrum using the filter H(jw) as given by Eq. 1 (Section II); and

(e). Perform a 512 point IFFT to result in the output time signal.

The input time waveform and the results from steps b and c above are the same as those illustrated in Figure 2. The results for steps d and e are illustrated in Figure 4 for: (a) no noise (left) and (2) a signal-to-noise ratio of 0 dB (right).

1. Discussion

A discussion of the minimum mean square error filtering process is contained in Section II of this report. A theoretical justification of Eq. 1 can be found in Papoulis (21).

From Figure 4 it can be observed that the magnitude of the frequency spectrum of the ouput (Figure 4d) with and without noise are surprisingly similar. The output spectrum after noise removal (right) appears very free from noise. The output time waveform after noise removal (Figure 4e) also appears very noise free.

One additional advantage of the minimum mean square error filtering method of processing speech for an enhancement in noise is that the method is directly extendible for processing speech in nonwhite noise environments. The only change required is a modification of Snn(w) in Eq. 1. In addition, if a technique were developed for detecting the presence of speech in noise, the absence of speech could be used to continually update a running noise estimate. This running noise estimate could then be readily incorporated into Eq. 1.

2. Tests With Real Speech

Like Figure 4 displays, the results achieved for processing

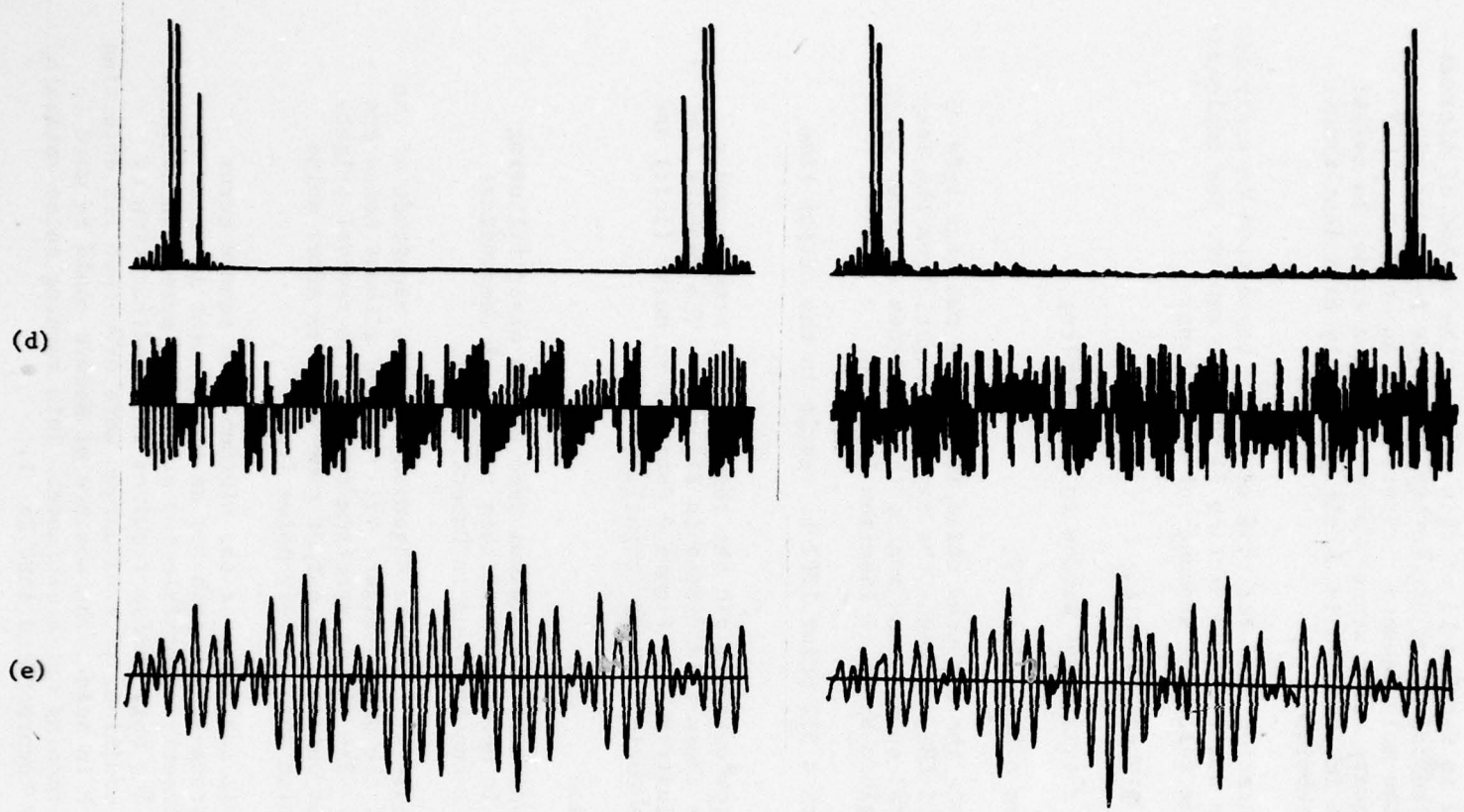


FIGURE 4. The minimum mean square error filtering process applied to the synthetically generated vowel /a/. Steps a - c are the same as Figure 2. Steps d and e are illustrated after the corresponding step listed in the second paragraph of Section III-C; left is for a S/N = ∞, right is for a S/N = 0 dB.

real speech in noise (signal-to-noise ratios of +6 dB and -6 dB) by the method of minimum mean square error filtering are very encouraging. The signal-to-noise ratio is significantly enhanced, the naturalness unchanged, and the intelligibility sounds improved.

Two experiments were carried out with real speech, one using the procedure outlined in the second paragraph of this subsection (and illustrated in Figure 4), the other with the addition of a zeroing of all magnitude components above 2.5 KHz between steps d and e. In both cases the results were very good with little observable difference between them. An examination of Figure 4d indicates that there is very little energy above 2.5 KHz such that little change would be expected.

For many reasons, the method of minimum mean square error filtering appears to offer a great potential for speech in noise intelligibility enhancement.

D. METHODS BASED UPON PITCH TRACKING

As described in Section II of this report, methods of enhancing the intelligibility of speech in noise based upon pitch analysis are intuitively attractive. However, as also indicated in Section II, such methods have, in general, produced discouraging results (20).

In order to experiment with methods based upon pitch tracking, a technique was implemented which consists of the following sequence of steps:

(a) Input 512 time samples;

(b) Apply a triangular window to the samples;

(c) Perform a 512 point FFT;

(d) Determine the pitch frequency using a method to be described and zero all magnitude components between pitch harmonics; and

(e) Perform a 512 point IFFT to result in the output time signal.

The input time waveform and the results from steps b and c above are the same as for the INTEL technique and are illustrated in Figure 2. The results after steps d and e are illustrated in Figure 5 for: (1) no noise (left) and (2) a signal-to-noise ratio of 0 dB (right).

1. Discussion

A discussion of the use of pitch extraction methods for speech intelligibility enhancement in noise is contained in Section II of this report.

The method used for estimating the pitch frequency from the spectrum of speech plus noise consists of determining that integer frequency (F_0) between 80 Hz and 250 Hz which maximizes the following

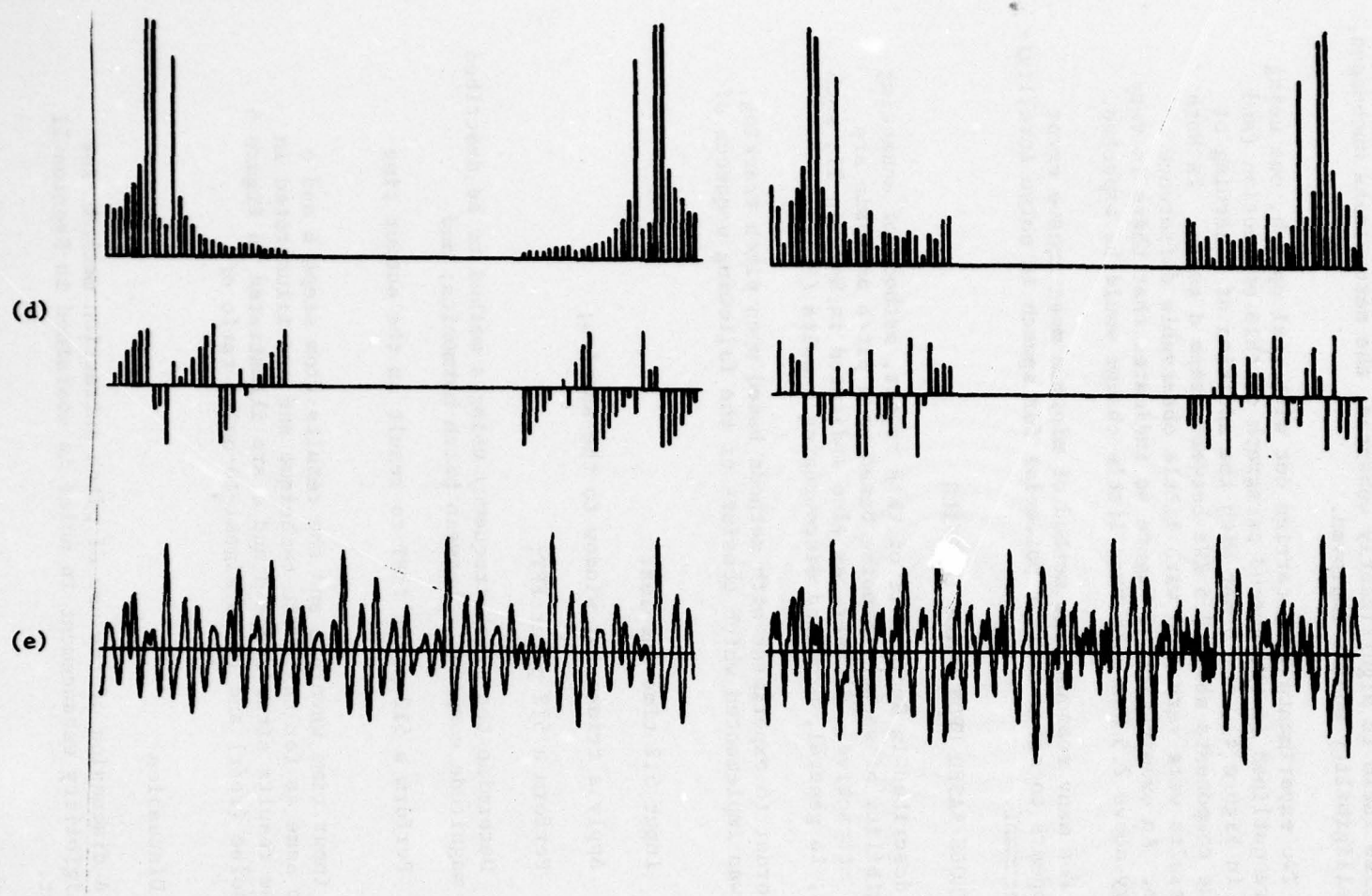


FIGURE 5. The process based upon pitch extraction applied to the synthetically generated vowel /a/. Steps a - c are the same as Figure 2. Steps d and e are illustrated after the corresponding step listed in the second paragraph of Section III-D; left is for a S/N = ∞, right is for a S/N = 0 dB.

function:

$$\frac{1}{N} \sum_{i=1}^{N} F(i \cdot F_0)$$

(Eq. 2)

where:

N = the greatest integer such that $N \cdot F_0 \leq 3000$ Hz

F(i.Fo) is that line of the magnitude spectrum closest to the frequency $i \cdot F_0$.

The results of Figure 5d display the expected spectrum of the output. With several tests on synthetic voiced sounds, at several signal-to-noise ratios from +6 dB to -6 dB, the pitch frequency was determined quite accurately (to within a few percent) using the method.

The output time waveform (Figure 5e) indicates the appearance of considerable improvement for the enhancement of speech in noise by using this method based upon pitch tracking..

2. Tests With Real Speech

Three experiments based upon pitch extraction and the method outlined earlier in this subsection were performed with real speech. These involve three degrees of suppression of non-pitch magnitude components in step d. These three degrees of suppression are: (1) suppression to zero, (2) suppression by a factor of two, and (3) suppression by a factor of four.

When the non-pitch components are suppressed to zero, a strong, low frequency distortion, probably a result of the time analysis window, is apparent. As the degree of suppression is lessoned the strong window distortion diminishes, however, at the expense of increased noise. At a high suppression of non-pitch harmonics (suppression to zero), there is a noticable loss of intelligibility, particularly at a signal-to-noise ratio of -6 dB. This is probably due to the inaccuracy in pitch tracking which is greater at lower signal-to-noise ratios. With a suppression of non-pitch harmonics to other than zero, the method is able to tolerate greater pitch tracking errors without as serious a degradation of speech intelligibility.

To determine some measure of the accuracy of the pitch tracking algorithm applied to real speech, two simple experiments were performed. First, a listing was created of the pitch values determined for the utterance at a signal-to-noise ratio of +6 dB. While no standard of comparison for the determined pitch values was available, the printed values seemed reasonable for a male speaker. The printed values were generally fairly continuous with fundamental frequency values between 110 Hz and 120 Hz during voiced speech intervals

As a second experiment, a constant frequency of 10 Hz was subtracted from each pitch measurement and the result was used to generate the output waveform in the usual manner. Upon listening to the result it was found unintelligible.

Overall, the intelligibility results using this pitch tracking method sound of lesser intelligibility than either the INTEL or the minimum mean square error filtering methods. There are, however, a number of improvements which could be added to the basic method and which might substantially improve this first attempt. It is this author's feeling that methods based upon pitch tracking offer the potential to result in an enhancement of speech intelligibility in noise and that such methods should not be overlooked because of past discouraging results.

IV. CONCLUSIONS

This study has explored several methods for the enhancement of speech intelligibility in the presence of wideband random noise at the speaker. This exploration has involved a study of the effect of the methods upon synthetically generated voiced sounds in noise as well as on real speech in white noise at two signal-to-noise ratios.

Four basic methods have been investigated: (a) INTEL, (b) spectral subtraction, (c) minimum mean square error filtering, and (d) methods based upon pitch tracking. Several variations in each basic method have been tested and numerous experiments with speech in noise have been performed. The experiments with synthetic speech have provided a substantial insight into not only the four methods, but also the speech in noise situation in general. Through the experiments with real speech, some qualitative results for the speech processing methods have been presented.

It appears from the experiments with synthetic and real speech that all four methods have the potential to result in an enhancement of the intelligibility of speech in noise. While the qualitative intelligibility results obtained during this work have indicated that, of the methods tested, the INTEL method and the method based upon minimum mean square error filtering seem to result in the greatest enhancement of speech in noise, the other methods should not be discarded. There are several reasons to suspect that substantial improvement in the intelligibility of speech in noise can be obtained through the use of each of the four basic techniques.

REFERENCES

1. M.R. Weiss, E. Aschkenasy, and T. W. Parsons, "Study and development of the INTEL Technique for Improving Speech Intelligibility," Technical Report No. RADC-TR-75-108, Rome Air Development Center, Griffiss Air Force Base, New York, April 1975.

2. M. R. Weiss and E. Aschkenasy, "Automatic Detection and Enhancement of Speech Signals," Technical Report No. RADC-TR-75-77, Rome Air Development Center, Griffiss Air Force Base, New York, March 1975.

3. T.W. Parsons and M.R. Weiss, "Enhancing/Intelligibility of Speech in Noisy or Multi-talker Environments," Technical Report No. RADC-TR-75-155, Rome Air Development Center, Griffiss Air Force Base, New York, June 1975.

4. I.B. Thomas and A. Ravindran, "Intelligibility Enhancement of Already Noisey Speech Signals," J. Aud. Eng. Soc., 22, 234-236, 1974.

5. M.R. Sambur and N.S. Jayant, "LPC Analysis/Synthesis from Speech Inputs Containing Quantizing Noise or Additive White Noise," IEEE Trans. Acoustics, Speech, and Signal Processing, ASSP-24, 488-494, 1976.

6. S.F. Boll, "Improving Linear Prediction Analysis of Noisy Speech by Predictive Noise Cancellation," 1977 IEEE International Conf. on Acoustics, Speech, and Signal Procesisng, 10-12, 1977.

7. R.J. Niederjohn, "A Comparison of Three Recently Reported Methods of Processing Speech for the Enhancement of Speech Intelligibility in High Noise Levels," Proceedings of the Midwest Symposium on Circuits and System, 325-331, 1976.

8. R.J. Niederjohn and J. H. Grotelueschen, "The Ehancement of Speech Intelligibility in High Noise Levels by High-pass Filtering Followed by Rapid Amplitude Compression," IEEE Trans. Acoust., Speech, and Sig. Proc., ASSP-24, 277-282, 1976.

9. R.J. Niederjohn and J. H. Grotelueschen, "Speech Intelligibility Enhancement in a Power Generating Noise Environment," IEEE Trans. Acoustics, Speech, and Signal Processing, accepted for publication.

10. I.B. Thomas and R.J. Niederjohn, "The Intelligibility of Filtered Clipped Speech in Noise," J. Aud. Eng. Soc., 18, 299-303, 1970.

11. I.B. Thomas and W.J. Ohley, "Intelligibility Enhancement Through Spectral Weighting," 1972 Conference on Speech Communication and Processing, 360-363, 1972.

12. J.P. Egan and F.M. Wiener, "On the Intelligibility of Bands of Speech in Noise," J. Acoust. Soc. Am., 18, 435-441, 1946.

13. I. Pollack and J.M. Pickett, "Masking of Speech by Noise at High Sound Levels," J. Acoust. Soc. Am., 30, 127-130, 1958.

14. I. Pollack and J.M. Pickett, "Intelligibility of Peak-Clipped Speech at High Noise Levels," J. Acoust. Soc., Am., 31, 14-16, 1959.

15. J.C.R. Licklider, "Effects of Amplitude Distortion on the Intelligibility of Speech," J. Acoust. Soc., Am., 18, 429-434, 1946.

16. G.A. Miller and S. Mitchell, "Effects of Distortion on the Intelligibility of Speech at High Altitudes," J. Acoust. Soc. Am., 19, 120-125, 1950.

17. W. Wathen-Dunn and D.W. Lipke, "On the Power Gained by Clipping Speech in the Audio Band," J. Acoust. Soc. Am., 30, 36-40, 1958

18. E.A. Kretsinger and N.B. Young, "The Use of Fast Limiting to Improve the Intelligibility of Speech in Noise," Speech Monogr., 27, 63-69, 1960.

19. H. Drucker, "Speech Processing in a High Ambient Noise Environment," IEEE Trans. Audio and Electroacoust., AU-16, 165-168, 1968.

20. Personal communication with Dr. Bruno Beek and Captain Robert Curtis, Rome Air Development Center, Griffiss Air Force Base, New York.

21. A.Papoulis, "Probability, Random Variables, and Stochastic Processes," McGraw-Hill Book Company, New York, 1965, pp 403-406.

22. G.E. Peterson and H.L. Barney, "Control Methods Used in a Study of Vowels," J. Acoust. Soc. Am. 24, 175-184. 1952.

23. N.R. French and J.C. Steinberg, "Factors Governing the Intelligibility of Speech Sounds," J. Acoust. Soc. Am., 19, 90-119, 1947.

24. H.K. Dunn and S.D. White, "Statistical Measurements on Conversational Speech," J. Acoust. Soc. Am., 11, 278-288, 1940.

25. I.B. Thomas, "The Second Formant and Speech Intelligibility," Proc. Nat. Elect. Conf., 23, 544-548, 1967.

26. I.B. Thomas, "The Influence of the First and Second Formants on the Intelligibility of Clipped Speech,: J. Audio Eng. Soc., 16, 182-185, 1968.

27. J.C.R. Licklider and I. Pollack, "Effects of Differentiation, Integration, and Infinite Peak Clipping Upon the Intelligibility of Speech," J. Acoust. Soc. Am., 20, 42-51, 1948.

28. Personal Communication from J.S. LIM, A.V. Oppenheim and L.D. Braida.

29. R. J. Niederjohn, "The Development of a Computer Speech Processing System and its Use for the Study and Development of Processing Methods for Enhancing the Intelligibility of Speech in Noise," Technical Report, Rome Air Development Center, Griffiss Air Force Base, New York, Submitted for publication.

1977 USAF-ASEE SUMMER FACULTY RESEARCH PROGRAM

sponsored by

THE AIR FORCE OFFICE OF SCIENTIFIC RESEARCH

conducted by

AUBURN UNIVERSITY AND OHIO STATE UNIVERSITY

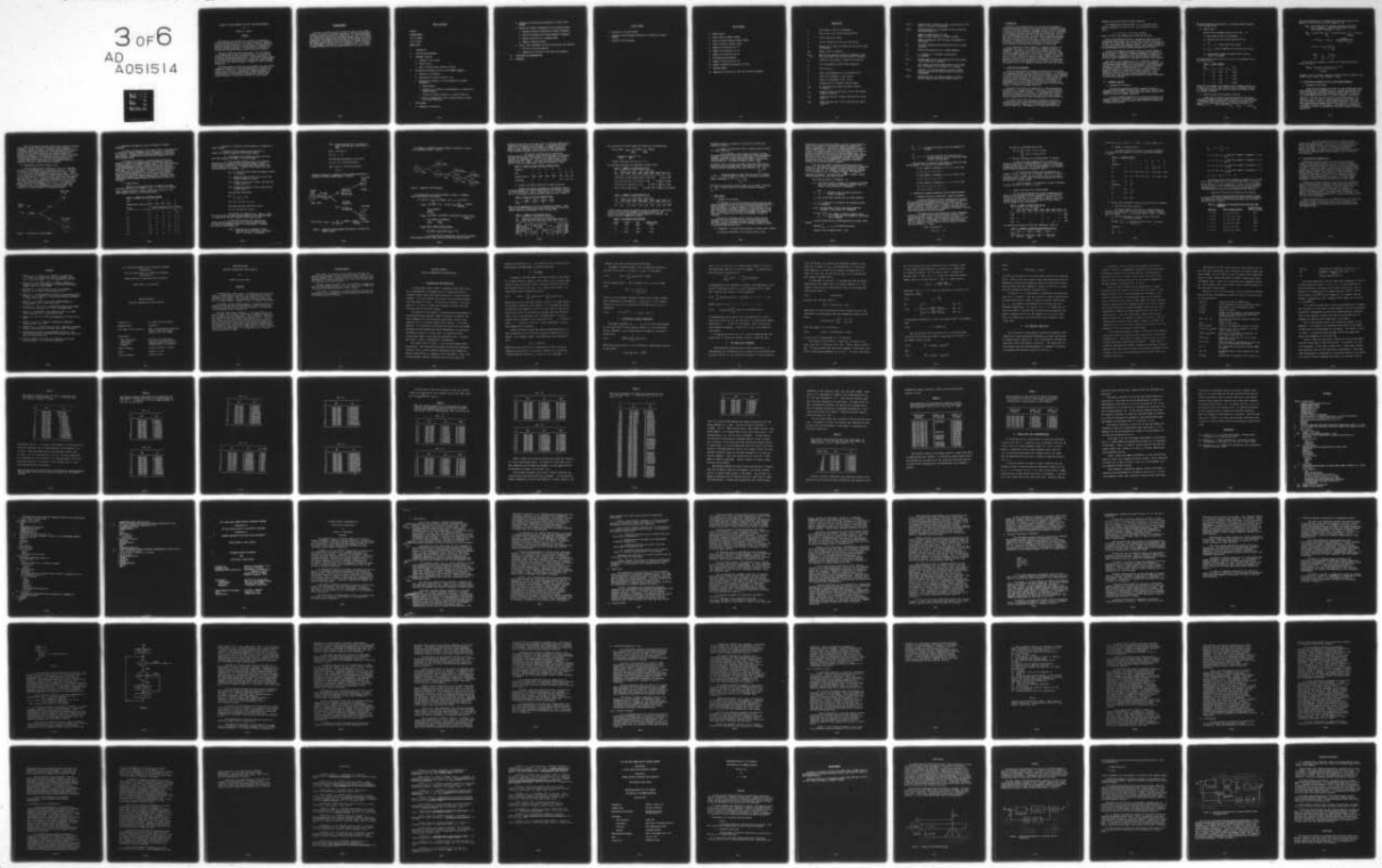
PARTICIPANT'S FINAL REPORT

DESIGN OF SYSTEM DIAGNOSTIC AND FAULT ISOLATION PROCEDURES

Prepared By:	Theodore J. Sheskin, Ph.D.
Academic Rank:	Assistant Professor
Department and University:	Department of Industrial Engineering Cleveland State University
Assignment:	
(Air Force Base)	Griffiss AFB NY
(Laboratory)	Rome Air Development Center (RADC)
(Division)	Reliability and Compatibility
(Branch)	Reliability
USAF Research Colleague:	Jerome Klion
Date:	August 19, 1977
Contract No.:	F44620-75-C-0031

AD-A051 514 AUBURN UNIV ALA SCHOOL OF ENGINEERING F/G 5/2
1977 USAF-ASEE SUMMER FACULTY RESEARCH PROGRAM. VOLUME II.(U)
SEP 77 J F O'BRIEN F44620-75-C-0031
UNCLASSIFIED AFOSR-TR-78-0349 NL

3 OF 6
AD A051514



DESIGN OF SYSTEM DIAGNOSTIC AND FAULT ISOLATION PROCEDURES

by

Theodore J. Sheskin

ABSTRACT

The purpose of this research is to initiate the development of promising new approaches to the cost effective design of diagnostic and fault isolation procedures. This effort is oriented specifically toward the design of built-in-test (BIT) diagnostic subsystems for military electronics equipment. The objective is to minimize the average costs associated with the repair of electronic systems.

Two basic problems have been investigated. The first problem is to determine the sequence of diagnostic tests to be executed to isolate the failed unit from the group of modules identified by the BIT whenever the equipment malfunctions. An original solution proposed for this problem is the application of probabilistic dynamic programming, which is guaranteed to generate a sequence of tests of minimum average cost.

The second problem is to partition the equipment into near optimum subgroups of modules, such that the average cost of isolating the faulty unit is minimized. A new heuristic approach applied to this problem involves the use of deterministic dynamic programming to derive weights for the subgroups of modules, and a binary linear program to produce a low cost partition based on these weights.

ACKNOWLEDGEMENT

The author is grateful to the Air Force for support of this summer research. He found it a rewarding experience in his professional growth. He is particularly grateful to Mr. Jerome Klion, his research colleague, for providing him with a highly stimulating research topic, and offering him guidance, encouragement, and the benefit of many helpful discussions. Appreciation is expressed to the other personnel of the RBRT Section and Mr. Anthony Coppola, Section Chief, for providing a cordial and helpful work environment. Appreciation is also expressed to Mr. J. Fred O'Brien of Auburn University for his fine administration of the summer program.

TABLE OF CONTENTS

ABSTRACT

ACKNOWLEDGEMENT

LIST OF FIGURES

LIST OF TABLES

NOMENCLATURE

I. INTRODUCTION

II. OBJECTIVES AND BACKGROUND

III. SECONDARY ISOLATION

- A. Statement of the problem.
- B. Sample problem.
- C. Search procedure during secondary isolation.

IV. OPTIMIZING THE SEQUENCE OF TESTS IN THE PRIMARY DIAGNOSTIC

- A. Statement of the problem.
- B. Determination of states following a test.
- C. Optimizing the sequence of tests by probabilistic dynamic programming.
  1. Sample problem.
  2. Structure of a sequential testing diagram as a probabilistic dynamic program.
  3. Solution for primary isolation to a single failed unit.
  4. Bounds on computational effort, assuming primary isolation to a single failed unit.

V. PARTITIONING

- A. Statement of the problem.

B. Formulation of the partitioning problem as a binary linear program.

C. Deterministic dynamic programming to derive subgroup weights.

1. Subgroup isolation by deterministic dynamic programming.

2. Outline of procedure for assigning weights to subgroups.

3. Sample calculations for a subgroup weight.

4. Summary of subgroup weights.

D. Binary linear programming solutions for partitions into subgroups.

1. Partition into three subgroups.

2. Comparison of solutions for partitions into subgroups.

VI. CONCLUSIONS AND RECOMMENDATIONS

VII. REFERENCES

LIST OF FIGURES

1. Structure of a Testing Diagram.

2. Sequential Testing Diagram Formulated as a Probabilistic Dynamic Program.

3. Sequential Testing Diagram.

LIST OF TABLES

1. Sample Problem.
2. Primary Tests for Sample Problem.
3. Values of Several Possible Terminal States.
4. Values of the Four Terminal States.
5. Summary of Calculations for n=2.
6. Summary of Calculations for n=3.
7. Summary of Calculations for n=4.
8. An Optimum Testing Sequence.
9. Summary of Calculations for n=2.
10. Summary of Remaining Calculations for $h^*(s)$.
11. Subgroup Weights.
12. Comparison of Solutions for Partitions into Three Subgroups.

NOMENCLATURE

N	Total number of LRUs in the equipment.
λ_i	Failure rate of the ith LRU (failures/10^6 hr).
λ_T	Failure rate of the system.
p_i	A priori probability of failure of the ith LRU.
t_i	Average time to remove and replace the ith LRU and retest the equipment.
$n(j)$	Number of LRUs in subgroup j.
$MH_{[j]}$	Mean cost for secondary isolation of subgroup j, given that an equipment fault has been isolated to subgroup j.
P_j	Probability that subgroup j contains the failed LRU.
T_k	A test performed by the BIT primary diagnostic.
C_k	Cost of test T_k
S	State of the equipment prior to performing test T.
Y	State of the equipment if test T passes.
Z	State of the equipment if test T fails.
$\overline{C}$	Expected cost of a sequential testing diagram.
δ_{iW}	$\begin{cases} 0, & \text{if the ith LRU is known to be good in state W.} \\ 1, & \text{otherwise.} \end{cases}$
P_W	Probability that the failed LRU is one of the untested elements in state W.
$P(Y)$	Probability that test T passes, given that the current state is S.
$P(Z)$	Probability that test T fails, given that the current state is S.

$f(s,T)$	Expected cost of a sequence of tests, given that the current state is S and test T is performed.
$f^*(S)$	Minimum expected cost of a sequence of tests, given that the current state is S.
n	Number of untested LRUs in a state. Number of stages remaining in a dynamic program.
K	Number of subgroups of LRUs into which the equipment is partitioned.
R_j	The weight representing the minimum total cost to isolate subgroup j.
r_j	Minimum total expected cost to isolate subgroup j.
x_j	$\begin{cases} 1, & \text{if subgroup j is included in the partition.} \\ 0, & \text{otherwise.} \end{cases}$
N-K+1	Maximum number of LRUs in any subgroup when the equipment is partitioned into K subgroups.
M	Total number of different subgroups which can be formed when the equipment is partitioned into K subgroups.
$h(S,T)$	Total cost of a testing sequence to isolate a desired subgroup, given that the current state is S and test T is performed.
$h^*(S)$	Minimum total cost of a testing sequence to isolate a desired subgroup, given that the current state is S.

I. INTRODUCTION

The goal of this research effort is to initiate the development of promising new techniques which can be applied to the cost-effective design of built-in-test (BIT) diagnostic subsystems and fault isolation procedures. In airborne and ground electronics equipment, increasing use is being made of BIT diagnostics because they make it possible to have fewer and less qualified maintenance personnel, and fewer pieces of external test equipment, which are generally quite expensive. Two promising new approaches conceived during the project study period are described in this report. The report is intended to be of assistance to the Air Force in the identification of various logical approaches to designing diagnostics and for determining the most promising avenues for future study.

Let us assume that a primary equipment is composed of modular line replaceable units (LRUs), all of which can be assumed to operate independently. The LRUs have sufficiently low probabilities of failure so that the probabilities of multiple failures can be neglected. Whenever the equipment malfunctions, a single LRU is assumed to have failed, and the BIT will automatically execute a primary sequence of diagnostic tests to identify the group of LRUs which contains the faulty unit. Secondary isolation will be performed by semi-automatic or manual means, which incur time and other equipment costs, to isolate the failed LRU. The defective unit will be removed and replaced, and the system retested.

II. OBJECTIVES AND BACKGROUND

A brief survey was made of procedures for dealing with the following three important problems in fault diagnosis and isolation: (1) Determination of a troubleshooting sequence which minimizes the expected cost of secondary isolation to locate the single failed unit within a group of LRUs identified by the BIT primary diagnostic; (2) Generation of a least expected cost testing sequence to be executed by the automatic BIT diagnostic; (3) Development of an efficient method of partitioning the equipment into mutually exclusive groups of LRUs which can be called out by the primary diagnostic following an equipment malfunction.

The result of the survey for problem one is a search procedure by Butterworth (3), Firstman and Gluss (6), and Gluss (7) which minimizes the mean cost of secondary isolation. This troubleshooting sequence is described in Section III of this report. Both Johnson et al (10) and Chang (4) have proposed methods for dealing with the second problem. The only reference found for treating problem three is MIL-STD-1591(12).

Two figures of merit which have been proposed for constructing a sequence of tests that can be executed by an automatic diagnostic are the information gain (Johnson et al (10))and the distinguishability criterion (Chang (4)). Both methods fail to guarantee minimal cost

sequences, but usually produce efficient procedures.

The information gain figure of merit, F_k, is the ratio of the ambiguity removed by a test to the cost, C_k, of performing the test. That is,

$$F_k = (-P \log_2 P - (1-P) \log_2 (1-P))/C_k$$

where P is the a priori probability that the test will pass.

The distinguishability criterion is designed to select a test which distinguishes each untested LRU in the current state from every other untested LRU in that state. The test that comes closest to distinguishing all pairs of untested LRUs should be selected. This criterion appears to be less appealing than the information gain criterion because it does not distinguish between LRUs with different probabilities of failure.

A promising new approach conceived during this research program is the application of probabilistic dynamic programming to the design of a testing sequence. In contrast to the other approaches surveyed to date, which require less computational effort but may produce a suboptimal solution, dynamic programming will guarantee an optimum testing sequence.

Most authors, such as Benowitz et al (1), assume that functional elements were packaged together during the design of the equipment. The only reference surveyed which treats the problem of partitioning modular equipment into groups of modules to be called out by the BIT following an equipment malfunction is MIL-STD-1591 (12). In that document a heuristic procedure is outlined which can yield different partitions depending on the choice of the initial subset of modules. A new, potentially efficient heuristic procedure proposed in this report utilizes binary linear programming and deterministic dynamic programming to partition the equipment.

III. SECONDARY ISOLATION

A. Statement of the Problem.

Following an equipment malfunction, secondary isolation is performed by semi-automatic or manual means, which incur time and other equipment costs, to locate the single failed unit within a group of LRUs called out by the BIT automatic diagnostic.

A search procedure adapted from the literature (Butterworth (3), Firstman and Gluss (6), and Gluss (7)) is presented which specifies the sequence in which to remove and replace LRUs to minimize the mean time to locate the failed unit.

The search procedure can be applied to the sample problem introduced in the following section.

B. Sample Problem.

Suppose that an equipment consists of four LRUs. Let

N = total number of LRUs in the equipment.

λ_i = failure rate of the ith LRU (failures/10^6 hr).

$\lambda_T = \sum_{i=1}^{N} \lambda_i$ = failure rate of the system.

$p_i = \lambda_{i/\lambda_T}$ = a priori probability of failure of the ith LRU.

t_i = average time to remove and replace the ith LRU and retest the equipment.

Using hypothetical values for the λ_i's and t_i's, the equipment can be specified by Table 1.

TABLE 1 - SAMPLE PROBLEM

LRU_i	λ_i	p_i	t_i	p_{i/t_i}
1	90	0.45	6	0.075
2	60	0.30	3	0.100
3	40	0.20	5	0.040
4	10	0.05	1	0.050

Assume that the manpower and equipment cost of secondary isolation is $1.00 per unit of time. Hence, the mean time for secondary isolation is identical to the mean cost, which is chosen as the figure of merit for secondary isolation.

C. Search Procedure During Secondary Isolation.

Assume that a malfunction has been localized by the primary diagnostic to subgroup j which contains n(j) LRUs. For a series system of independent LRUs, Butterworth (3) indicates that the mean time to repair will be minimized by removing and replacing the LRUs in the sequence 1, 2, ..., n(j), such that $p_{1/t_1} > p_{2/t_2} > \ldots > p_{n(j)/t_{n(j)}}$

This testing sequence will be followed during secondary isolation of any subgroup of LRUs called out by the BIT diagnostic. Let

$MH_{[j]}$ be the mean cost for secondary isolation of the failed unit in subgroup j, given that an equipment fault has been isolated to subgroup j. Then,

$$MH_{[j]} = (p_1 t_1 + (1-p_1)\left(\frac{p_2}{1-p_1}\right)(t_1+t_2) + (1-p_1-p_2)\left(\frac{p_3}{1-p_1-p_2}\right)(t_1+t_2+t_3)$$

$$+\ldots+(1-p_1-p_2-\cdots-p_{n(j)-1})\left(\frac{p_{n(j)}}{1-p_1-p_2-\cdots-p_{n(j)-1}}\right)$$

$$(t_1+t_2+\ldots+t_{n(j)})) \Big/ \sum_{i=1}^{n(j)} p_i$$

$$= \sum_{i=1}^{n(j)} p_i \sum_{k=1}^{i} t_k \Big/ \sum_{i=1}^{n(j)} p_i$$

The mean cost for secondary isolation of the subgroup consisting of LRUs 1, 3, and 4 is

$$MH_{[134]} = \frac{p_1 t_1 + p_4(t_1+t_4) + p_3(t_1+t_4+t_3)}{p_1+p_3+p_4} = 9.57$$

The mean costs for secondary isolation of several different subgroups, each identified by an index j, are presented in Table 3.

IV. OPTIMIZING THE SEQUENCE OF TESTS IN THE PRIMARY DIAGNOSTIC

A. Statement of the Problem.

Assume that the equipment consisting of N LRUs has been partitioned into K mutually exclusive subgroups of LRUs. Whenever the equipment fails, the BIT automatically executes a sequence of primary diagnostic tests to isolate the subgroup which contains the single faulty LRU. A known cost, C_k, is associated with each test, T_k, which is included in the primary diagnostic. The total cost of locating a particular bad element is the sum of the costs of the built-in tests along the path which leads from the initial state, in which no LRUs are known to be good, to the final state representing the subgroup containing the faulty unit, plus the cost of secondary isolation of that subgroup. The objective is to determine the sequence of tests to be executed by the BIT which produces the minimum average cost.

Most of the authors surveyed to date use the criterion of minimum average cost for the selection of the best of several diagnostic procedures. However, the number of different testing sequences possible for equipment with more than ten LRUs is far too large for a direct evaluation of the minimum average cost by exhaustive enumeration. Therefore, alternative criteria which may indirectly reflect the average cost have been proposed. Two alternative figures of merit are the information gain (Johnson et al (10)) and the distinguishability criterion (Chang (4)). Both methods fail to guarantee minimal cost sequences, but usually produce efficient procedures.

B. Determination of States Following a Test.

Using the nomenclature of Johnson et al (10), let S represent the state of the equipment prior to performing the test T. This state is given by an N-bit number containing only the bits 0 and 1. There is a 1 in each position corresponding to LRUs not yet tested. There is a 0 in each position corresponding to elements known to be good. In the initial state there are 1's in all positions since none of the elements have been tested. State Y represents the equipment if test T passes. This state is computed by multiplying S and T bit by bit with no carry. State Z represents the equipment if test T fails. It is computed by multiplying S and $\bar{T}$, the complement of T, bit by bit without carry. A sequence of tests can be represented by a testing diagram. The structure of a testing diagram is illustrated in Figure 1.

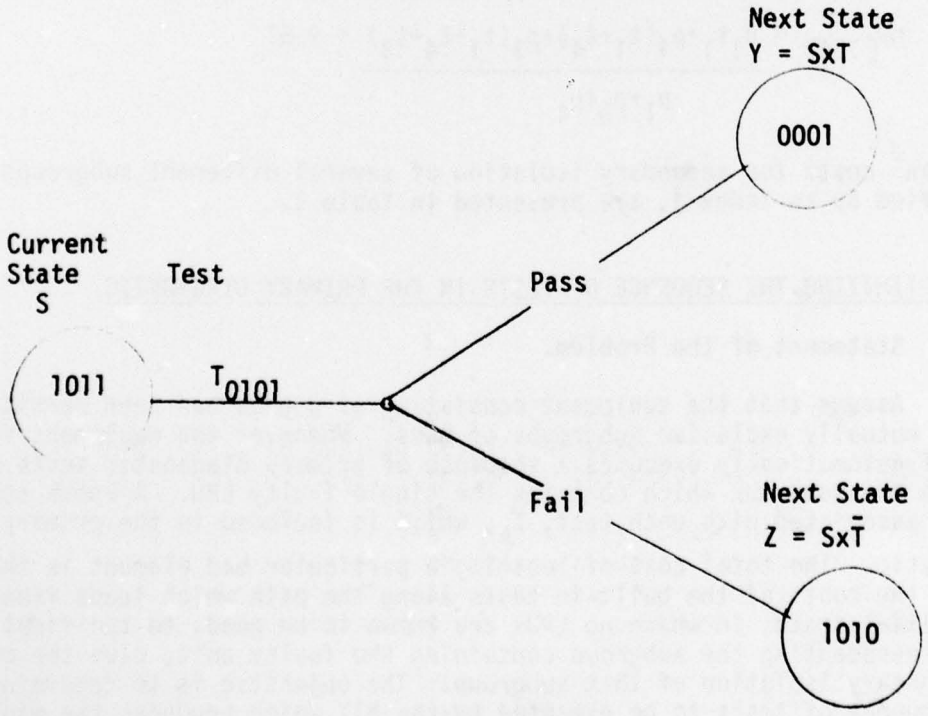


Figure 1. Structure of a Testing Diagram

C. Optimizing the Sequence of Tests by Probabilisitc Dynamic Programming.

An original contribution of this research effort is the application of probabilistic dynamic programming (9) to the design of a sequential test procedure. The application of dynamic programming to this problem shows promise of developing into a more effective approach than any of those surveyed to date.

To formulate the search for a minimum expected cost testing diagram as a probabilistic dynamic program, the equipment states are treated as stages in a sequential decision process. The solution procedure is implemented backwards, using a recursive relationship, from final states corresponding to the groups of LRUs into which the equipment is partitioned. At each state a set of possible decisions consists of all of the tests which can be performed. In contrast to the information gain (10) and distinguishability (4) criteria, which may generate a suboptimal solution because each decision is based on testing only a single state, probabilistic dynamic programming will guarantee a least expected cost testing sequence because the optimization is over all of the states.

1. Sample Problem.

Johnson et al (10) indicate that the number of different tests which can exist for N elements is $2^{N-1} - 1$. For the four element sample problem introduced in Table 1, seven built-in tests, T_k, and their respective costs, C_k, are defined in Table 2.

TABLE 2 - PRIMARY TESTS FOR SAMPLE PROBLEM

LRU i	1	2	3	4	
Probability of Failure p_i	0.45	0.30	0.20	0.05	
Test T_k	Binary Designation of Test				Cost C_k
T_1	1	1	0	0	\$3
T_2	1	0	1	0	5
T_3	1	0	0	1	4
T_4	1	0	0	0	1
T_5	0	1	0	0	6
T_6	0	0	1	0	2
T_7	0	0	0	1	7

2. Structure of a sequential testing diagram as a probabilistic dynamic program.

A sequential testing diagram can be formulated as a probabilistic dynamic program for the following reasons.

a. The problem can be divided into stages, such that each stage represents the number of untested elements.

b. The next state following a test is not completely determined by the current state and the test performed. Rather, the next state is dependent on the probabilities that the test on the current state will pass or fail. To compute these probabilities, the following notation is introduced. Let

δ_{iw} = $\begin{cases} 0, & \text{if the ith LRU is known to be good in state W.} \\ 1, & \text{otherwise} \end{cases}$

P_W = probability that the failed LRU is one of the untested elements in state W.

P(Y) = probability that test T passes, given that the current state is S.

P(Z) = probability that test T fails, given that the current state is S.

Using the above definitions,

$$P_W = \sum_{i=1}^{N} \delta_{iW} p_i, \text{ and}$$

$$P(Y) = P_Y / P_S, \; P(Z) = P_Z / P_S$$

Since each test must either pass or fail,

$$P_S = P_Y + P_Z, \text{ and } P(Y) + P(Z) = 1$$

c. The principle of optimality holds. That is, given the current state, an optimal testing sequence for the remaining states is independent of the tests executed in the previous states.

d. A recursive relationship that identifies the optimum testing sequence at each state, given the optimum testing policies for the subsequent states, can be formulated. To develop the recursive relationship, let

f(S,T) = expected cost of a sequence of tests, given that the current state of the equipment is S and test T is performed.

$f^*(S)$ = minimum expected cost of a sequence of tests, given that the current state is S. Thus,

$$f^*(S) = \min \{f(S,T)\}$$

$$T=T_1, T_2, \ldots, T_7$$

The recursive relationship is of the form

$$f(S, T_k) = C_k + P(Y)f^*(Y)+P(Z)f^*(Z)$$

$$f^*(S) = \min \{C_k + P(Y)\, f^*(Y)+P(Z)f^*(Z)\}$$

$$\text{all } T_k$$

The basic structure of a sequential testing diagram formulated as a probabilistic dynamic program appears in Figure 2.

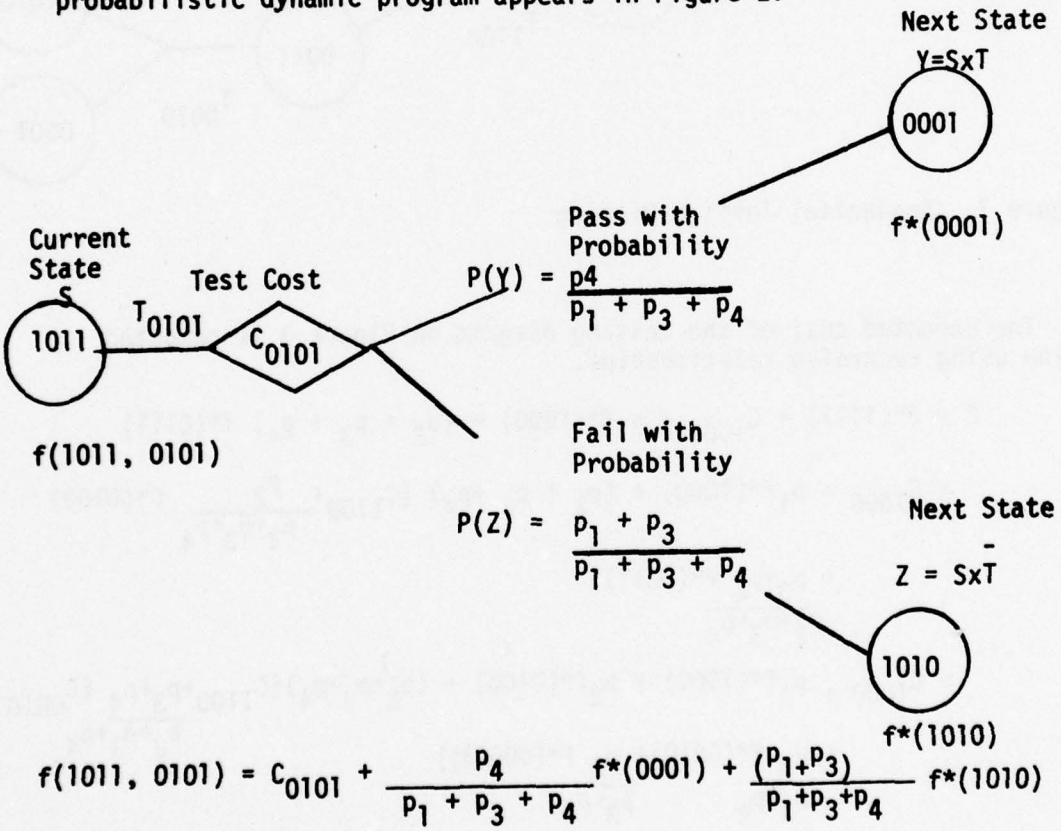


Figure 2. Sequential Testing Diagram Formulated as a Probabilistic Dynamic Program

An example of a sequential testing diagram is presented in Figure 3 for the equipment defined in Table 2.

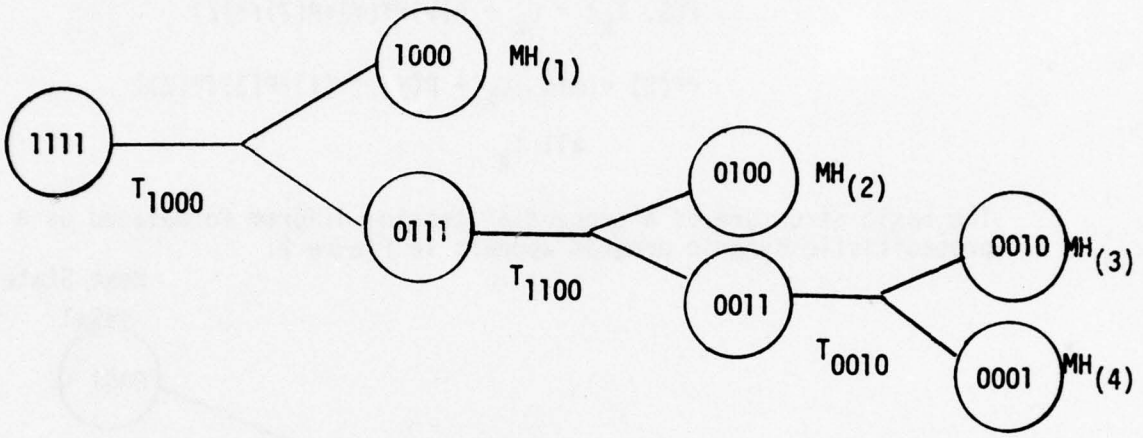


Figure 3. Sequential Testing Diagram

The expected cost of the testing diagram in Figure 3 is computed below using recursive relationships.

$$\bar{C} = f^*(1111) = C_{1000} + p_1 f^*(1000) + (p_2 + p_3 + p_4)\, f^*(0111)$$

$$= C_{1000} + p_1 f^*(1000) + (p_2 + p_3 + p_4)\left(C_{1100} + \frac{p_2}{p_2+p_3+p_4} f^*(0100) + \frac{p_3+p_4}{p_2+p_3+p_4} f^*(0011)\right)$$

$$= C_{1000} + p_1 f^*(1000) + p_2 f^*(0100) + (p_2+p_3+p_4)\left(C_{1100} + \frac{p_3+p_4}{p_2+p_3+p_4}\left(C_{0010} + \frac{p_3}{p_3+p_4} f^*(0010) + \frac{p_4}{p_3+p_4} f^*(0001)\right)\right)$$

$$= C_{1000} + p_1 MH(1) + p_2 MH(2) + p_3 MH(3) + p_4 MH(4) + (p_2+p_3+p_4)\, C_{1100} + (p_3+p_4)\, C_{0010} = \$7.8$$

e. Using the recursive relationship, the solution procedure moves backwards stage by stage, each time finding the optimal testing

sequence for each state of that stage, until it finds the optimal testing diagram when starting at the initial state. To implement the backward recursion, let n represent both the number of untested LRUs and the number of stages remaining. Since each state is unique, designation of the stage will be omitted from the notation for the expected cost.

f. The solution procedure begins by equating the expected values of the terminal states, which correspond to the subgroups into which the equipment is partitioned, to the mean costs of secondary isolation for these subgroups. Thus, for each terminal state S, the terminal value $f^*(S) = MH_{(j)}$. The values of several possible terminal states for the four element sample problem are displayed in Table 3.

TABLE 3 - VALUES OF SEVERAL POSSIBLE TERMINAL STATES

Subgroup j	1	2	3	4	6	9	13
LRUs	1	2	3	4	13	24	134
Terminal State S	1000	0100	0010	0001	1010	0101	1011
$f^*(S)=MH_{(j)}$	6	3	5	1	7.54	3.14	9.57

3. Solution for primary isolation to a single failed unit.

Probabilistic dynamic programming will be applied to derive a minimum expected cost testing diagram which provides primary isolation to a single failed unit. That is, the partition (1, 2, 3, 4) is assumed. For n = 1, the values of the four terminal states are given in Table 4.

TABLE 4 - VALUES OF THE FOUR TERMINAL STATES

S	1000	0100	0010	0001
f*(S)	6	3	5	1

When n=2, the computations for f*(S) are summarized in Table 5. Empty cells in the table represent tests that will not produce the specified terminal states, and are assumed to incur infinite costs.

TABLE 5 - SUMMARY OF CALCULATIONS FOR n=2.

S \ T_k	$f(S,T_k) = C_k + P(Y)\, f^*(Y) + P(Z)\, f^*(Z)$								
	1100	1010	1001	1000	0100	0010	0001	f*(S)	T^*_k
1100		9.8	8.8	5.8	10.8			5.8	1000
1010	8.69		9.69	6.69		7.69		6.69	1000
1001	8.5	10.5		6.5			12.5	6.5	1000
0110	6.8	8.8			9.8	5.8		5.8	0010
0101	5.71		6.71		8.71		9.71	5.71	1100
0011		9.2	8.2			6.2	11.2	6.2	0010

The calculations for f(0110, 0100) and f*(0110) are illustrated below.

$$f(0110, 0100) = C_{0100} + \frac{p_2}{p_2+p_3} f^*(0100) + \frac{p_3}{p_2+p_3} f^*(0010)$$

$$= 6 + \frac{0.30}{0.50}(3) + \frac{0.20}{0.50}(5) = 9.8$$

$$f^*(0110) = \min(6.8, 8.8, 9.8, 5.8) = 5.8$$

The remaining calculations are summarized in Tables 6 and 7.

TABLE 6 - SUMMARY OF CALCULATIONS FOR n=3

S \ T_k	$f(S,T_k) = C_k + P(Y) f^*(Y) + P(Z) f^*(Z)$								
	1100	1010	1001	1000	0100	0010	0001	$f^*(S)$	T^*_k
1110	8.63	10.52	9.89	6.89	11.52	7.63		6.89	1000
1101	8.50	10.87	9.19	6.87	11.19		12.50	6.87	1000
1011	9.07	11.28	10.07	7.07		8.07	13.28	7.07	1000
0111	7.45	10.45	9.36		10.45	7.45	12.36	7.45	1100,0010

TABLE 7 - SUMMARY OF CALCULATIONS FOR n=4

S \ T_k	$f(S,T_k) = C_k + P(Y) f^*(Y) + P(Z) f^*(Z)$								
	1100	1010	1001	1000	0100	0010	0001	$f^*(S)$	T^*_k
1111	8.9	11.35	10.15	7.80	11.85	8.50	13.60	7.80	1000

By moving forward through the tabulated solutions, beginning in the initial state, S=1111, at n=4, and ending in a terminal state at n=1, two alternative minimum expected cost testing sequences are produced. One optimal solution is summarized in Table 8.

TABLE 8 - AN OPTIMUM TESTING SEQUENCE

STAGE	STATE	TEST	EXPECTED COST
4	1111	1000	$7.80
3	0111	1100	7.45
2	0011	0010	6.20

The testing diagram corresponding to the solution in Table 8 was presented in Figure 3.

4. Bounds on computational effort, assuming primary isolation to a single failed unit.

As the equipment is partitioned into smaller subgroups, the computational effort required by probabilistic dynamic programming increases. To obtain an upper bound on the number of calculations required, suppose that dynamic programming is used to isolate to the single failed unit. The number of states at stage n is $\binom{N}{n}$. In terminal states no dynamic programming computations are necessary because no BIT tests are performed. Hence, the total number of states requiring dynamic programming recursive calculations is $\sum_{n=2}^{N} \binom{N}{n}$.

The maximum number of tests that can exist for N elements is $2^{N-1}-1$. An upper bound on the number of calculations required by dynamic programming is $(2^{N-1}-1) \sum_{n=2}^{N} \binom{N}{n}$.

The value of f*(S) must be stored in memory for all states. Therefore, $\sum_{n=1}^{N} \binom{N}{n}$ different values of f*(S) must be retained in memory.

V. PARTITIONING

A. Statement of the Problem.

The equipment is to be partitioned into mutually exclusive and exhaustive subgroups of LRUs such that following an equipment malfunction the BIT diagnostic tests will be executed to isolate the fault to a particular subgroup. Secondary isolation will be performed on the subgroup called out by the primary diagnostic to locate the single failed unit. The problem is how to partition the equipment into subgroups so that the total expected cost of primary and secondary isolation is minimized.

Most of the literature on fault isolation assumes that the equipment under test was partitioned into functional groups during its design. The only systematic procedure surveyed for partitioning LRUs into subgroups to be called out by an automatic diagnostic routine is contained in MIL-STD-1591 (12).

B. Formulation of the partitioning problem as a Binary Linear Program.

An original contribution of this research effort is the

formulation of the partitioning problem as a binary linear program (9) which utilizes weights derived for each subgroup by deterministic dynamic programming (9). Deterministic dynamic programming is used to assign subgroup weights so that they are independent of any testing diagram. The proposed approach is a heuristic procedure which will not guarantee an optimum partition with the minimum expected cost. The heuristic procedure has been applied to the four element sample problem described in this report, and has generated a minimum cost partition. On the basis of this limited computational experience, the proposed approach shows promise of developing into a potentially effective technique for partitioning modular equipment.

Since the total number of different partitions grows quite rapidly, it is not feasible to determine the best partition by enumerating all possible partitions and computing the least expected cost testing sequence for each one. It is,however, feasible to enumerate subgroups. If g is the number of LRUs in a subgroup, then $\binom{N}{g}$ is the number of subgroups of g elements each which can be formed. In Table 3 several different subgroups have been formed for N=4.

The following notation is introduced. Let

R_j = the weight assigned to subgroup j to represent the minimum total cost of primary and secondary diagnostic tests to isolate a single failed unit in subgroup j.

$P_j = \sum_{i=1}^{n(j)} p_i$ = probability that the single failed LRU is located in subgroup j.

$r_j = PR_{j\,j}$ = minimum total expected cost to isolate subgroup j.

$x_j = \begin{cases} 1, & \text{if subgroup j is included in the selected partition} \\ 0, & \text{otherwise} \end{cases}$

N-K+1 = maximum number of LRUs in any subgroup when the equipment is partitioned into K subgroups.

$M = \sum_{j=1}^{N-K+1} \binom{N}{j}$ = total number of different subgroups which can be formed when the equipment is partitioned into K subgroups.

The partitioning problem is formulated below as a binary linear program.

Minimize $\sum_{i=1}^{M} r_i\ x_i$ is the objective function

subject to the following N+2 constraints:

$\sum_{i=1}^{M} x_i = K$, to ensure that exactly K out of M subgroups are selected.

$\sum_{i=1}^{M} n_i x_i = N$, to ensure that the sum of the LRUs in the selected subgroups is equal to the total number of LRUs in the equipment.

One constraint is required for each element to ensure that each LRU must appear in one and only one selected subgroup.

If LRU 1 appears in subgroups i, j, k, l, s, and d, then

$$x_i + x_j + x_k + x_l + x_s + x_d = 1$$

If LRU 2 appears in subgroups i, j, p, q, m, and n, then

$$x_i + x_j + x_p + x_q + x_m + x_n = 1$$

If LRU N appears in subgroups m, n, r, w, s, and d, then

$$x_m + x_n + x_r + x_w + x_s + x_d = 1$$

$x_i = 0$ or 1, for $i = 1, 2, \ldots, M$

C. Deterministic Dynamic Programming to Derive Subgroup Weights.

1. Subgroup isolation by deterministic dynamic programming.

A separate deterministic dynamic program must be solved to derive a weight for each subgroup which can be included in a partition. The dynamic program is deterministic because only one of the two successor states determined by a test is retained. The other successor state is discarded. The state which is retained following a test is the one which, after further testing if necessary, will produce a terminal state corresponding to the desired subgroup.

The nomenclature for the deterministic dynamic programming formulation is similar to the notation introduced in Section IV.C.2. for the probabilistic version. Let h(S,T) be the total cost of a sequence of tests to isolate a desired subgroup, given that the current state is S and test T is performed. Let h*(S) be the minimum total cost of a sequence of tests to isolate a desired subgroup, given that the current state is S. Hence,

$$h^*(S) = \min_{T=T_1, T_2, \ldots, T_7} \{h(S,T)\}$$

The recursive relationship has the form

$$h(S, T_k) = \begin{cases} C_k + h^*(Y), & \text{if test } T_k \text{ passes} \\ C_k + h^*(Z), & \text{if test } T_k \text{ fails} \end{cases}$$

2. Outline of procedure for assigning weights to subgroups.

a. Form all possible subgroups which can satisfy the constraints specified for a desired partition. Such constraints might include a minimum size or a maximum size for subgroups, or a prohibition on subgroups of certain sizes. For the sample problem of four elements, several different subgroups are displayed in Table 3.

b. The value of each terminal state corresponding to a subgroup j is $MH_{(j)}$, the mean cost of secondary isolation for subgroup j. The values, h*(S), of several possible terminal states for the sample problem are given in Table 3, where f*(S) must be replaced by h*(S) for the deterministic dynamic program.

c. For each subgroup j use deterministic dynamic programming to compute the weight, R_j. Then, $r_j = P_j R_j$.

3. Sample calculations for a subgroup weight.

To illustrate how deterministic dynamic programming can be applied to calculate subgroup weights, the weight, R_2, for subgroup 2 = (LRU 2), will be computed. For n=1, h*(0100) = 3 from Table 3. The calculations for h*(S) with n=2 are summarized in Table 9. Empty cells represent tests that will not produce the specified terminal state, and are assumed to incur infinite costs.

TABLE 9 - SUMMARY OF CALCULATIONS FOR n=2

	T_k	$h(S, T_k) = C_k + h^*(0100)$								
S		1100	1010	1001	1000	0100	0010	0001	h*(S)	T_k*
1100			8	7	4	9			4	1000
0110		6	8			9	5		5	0010
0101		6		7		9		10	6	1100

The remaining calculations for h*(S) are summarized in Table 10.

TABLE 10 - SUMMARY OF REMAINING CALCULATIONS FOR h*(S)

S	1110	1101	0111	1111
h*(S)	6	7	6	7
T_k*	1000,0010	1100,1001, 1000	1100	1100,1000

The solution is $R_2 = h^*(1111) = 7$. Hence, $r_2 = P_2 R_2 = 0.30(7) = 2.1$

4. Summary of subgroup weights.

The weights obtained by deterministic dynamic programming for several different subgroups of the sample problem are displayed in Table 11.

TABLE 11 - SUBGROUP WEIGHTS

LRUs	1	2	3	4	12	13	14	23
Subgroup j	1	2	3	4	5	6	7	8
R_j	7	7	7	6	9.6	12.54	10.1	9
P_j	0.45	0.30	0.20	0.05	0.75	0.65	0.50	0.50
r_j	3.15	2.10	1.40	0.30	7.20	8.15	5.05	4.50

LRUs	24	34
Subgroup j	9	10
R_j	6.14	8
P_j	0.35	0.25
r_j	2.15	2.00

D. Binary Linear Programming Solutions for Partitions into Subgroups.

1. Partition into three subgroups.

The sample problem is partitioned into three subgroups by a binary linear program which utilizes the subgroup weights. Setting N=4, K=3 subgroups, N-K+1 = 2, the maximum number of LRUs in a subgroup, and $M = \sum_{i=1}^{2} \binom{4}{i} = 10$, the number of binary variables, yields the following formulation.

Minimize $\sum_{i=1}^{10} r_i x_j$, where the values of the r_i's are given in Table 11,

subject to

$$\sum_{i=1}^{10} x_i = 3$$

$$\sum_{i=1}^{4} x_i + 2 \sum_{i=5}^{10} x_i = 4$$

$x_1 + x_5 + x_6 + x_7 = 1$, since LRU 1 appears in subgroups 1, 5, 6, and 7.

$x_2 + x_5 + x_8 + x_9 = 1$, since LRU 2 appears in subgroups 2, 5, 8, and 9.

$x_3 + x_6 + x_8 + x_{10} = 1$, since LRU 3 appears in subgroups 3, 6, 8, and 10.

$x_4 + x_7 + x_9 + x_{10} = 1$, since LRU 4 appears in subgroups 4, 7, 9, and 10.

$x_i = 0$ or 1, for $i = 1, 2, \ldots, 10$

The solution, which is easily obtained by enumeration of the sums of the subgroup weights for all six possible partitions, is $x_1=x_3=x_9=1$, and all other $x_i = 0$. Thus, partition (1, 3, 24) is correctly selected as the one with the lowest expected cost. The sum of the corresponding subgroup weights, $r_1 + r_3 + r_9 = 6.7$, which is a lower bound for 6.9, the minimum expected cost of a testing diagram for this partition.

2. Comparison of Solutions for Partitions into Subgroups.

Solutions obtained by adding the subgroup weights produced by deterministic dynamic programming for partitions into three subgroups are compared with solutions for the minimum expected costs of testing these partitions in Table 12.

TABLE 12 - COMPARISON OF SOLUTIONS FOR PARTITIONS INTO THREE SUBGROUPS

PARTITION	SUM OF SUBGROUP WEIGHTS	MINIMUM EXPECTED COSTS OF TESTING
1 3 24	$r_1 + r_3 + r_9 = 6.7$	6.9
1 2 34	$r_1 + r_2 + r_{10} = 7.25$	7.5
1 4 23	$r_1 + r_4 + r_8 = 7.95$	8.45
2 3 14	$r_2 + r_3 + r_7 = 8.55$	9.95
3 4 12	$r_3 + r_4 + r_5 = 8.9$	9.5
2 4 13	$r_2 + r_4 + r_6 = 10.55$	11.9

The results summarized in Table 12 demonstrate that the sum of the subgroup weights for a partition derived by deterministic dynamic programming provides a lower bound on the minimum expected cost of a testing sequence for that partition generated by probabilistic dynamic programming. This result is to be expected because the deterministic dynamic programs minimize the sum of the costs of isolating the individual subgroups rather than the expected cost of testing the entire partition.

VI. CONCLUSIONS AND RECOMMENDATIONS

Methodologies have been proposed for treating three important problems in the design of diagnostic and fault isolation procedures. A search procedure has been adapted from the literature for determining the sequence in which to locate the single failed unit during secondary isolation. Probabilistic dynamic programming has been proposed as a new approach which is guaranteed to generate a minimum cost sequence of BIT primary diagnostic tests. A new, potentially effective heuristic procedure for partitioning the equipment into subgroups of LRUs to be called out by the primary diagnostic utilizes deterministic dynamic programming to derive weights for the subgroups, and binary linear programming to produce a low cost partition based on these weights.

The heuristic procedure proposed for partitioning the equipment has been applied successfully to the small sample problem described in this report. Future research is recommended to determine the computational feasibility of this approach for larger, practical problems. Of particular interest is the question of whether the deterministic dynamic programming procedure for deriving subgroup weights will still produce a low cost partition as the number of LRUs is increased. If it does not, then alternative procedures for solving the partitioning problem will have to be investigated.

Another important future task is the determination, from program data, of actual life cycle costs for the tests of the BIT diagnostic. It would also be useful to investigate whether the probabilistic dynamic programming approach can be utilized in the presence of errors in the BIT diagnostic tests.

REFERENCES

1. Benowitz, N., D.F. Calhoun, G.E. Alderson, J.E. Bauer, and C.T. Joeckel, "An Advanced Fault Isolation System for Digital Logic", IEEE Trans. Comput., Vol C-24, pages 489-497, May 1975.

2. Brule, J.D., R. A. Johnson, and E. J. Kletsky, "Diagnosis of Equipment Failures", IRE Transactions on Reliability and Quality Control", RQC-9, 23-24 April 1960.

3. Butterworth, R., "Some Reliability Fault - Testing Models", Ops. Res., Vol 20, pages 335-343, March/April 1972.

4. Chang, H. Y., "A Distinguishability Criterion for Selecting Efficient Diagnostic Tests", AFIPS Proc. of Spring Joint Computer Conference, 32, pages 529-534, 1968.

5. Chang, H.Y., E.G. Manning, and G. Metze, Fault Diagnosis in Digital Systems, Wiley - Interscience, 1970.

6. Firstman, S.I., and B. Gluss, "Optimum Search Routines for Automatic Fault Location", Ops. Res., Vol. 8, No.4, July/August 1960.

7. Gluss, B., "An Optimum Policy for Detecting a Fault in a Complex System", Ops. Res., Vol. 7, pages 467-477, 1959.

8. Goldman, A.S. and T.B. Slattery, Maintainability, John Wiley & Sons, 1967.

9. Hillier, F.S. and G.J. Lieberman, Introduction to Operations Research, Holden - Day, 1974.

10. Johnson, R.A., E.J. Kletsky, and J. D. Brule, "Diagnosis of Equipment Failures", SURI, Rept. No. EE577-594T1, April 1959. AD-213876.

11. Maintainability Engineering Design Notebook, Revision II, and Cost of Maintainability. Martin Marietta Aerospace Corp. RADC-TR-74-308, Vol I-III, January 1975.

12. Military Standard. On-Aircraft, Fault Diagnosis, Sub-Systems, Analysis/Synthesis Of. MIL-STD-1591, January 1977.

1977 USAF/ASEE SUMMER FACULTY RESEARCH PROGRAM

sponsored by

THE AIR FORCE OFFICE OF SCIENTIFIC RESEARCH

conducted by

AUBURN UNIVERSITY AND OHIO STATE UNIVERSITY

PARTICIPANT'S FINAL REPORT

MAXIMUM ENTROPY SPECTRAL DEMODULATOR INVESTIGATION

Prepared by:	Dr. Robert Guy Van Meter
Academic Rank:	Professor
Department and University:	Dept. of Mathematical Sciences State University College Oneonta, New York 13820
Assignment:	
(Air Force Base)	Griffiss Air Force Base
(Laboratory)	Rome Air Development Center
(Division)	Communications and Control
(Branch)	Communications Transmission
USAF Colleague:	Captain Kenneth E. Wilson
Date:	August 19, 1977
Contract Number:	F44620-75-0031

MAXIMUM ENTROPY

SPECTRAL DEMODULATOR INVESTIGATION

by

Robert Guy Van Meter

ABSTRACT

A transmitted signal, which is masked by noise and, possibly, interference, is assumed to be sinusoidal with Hertz-frequency which varies with time over some finite set F of positive real numbers. The received continuous-time signal s(t) is sampled every T seconds to get a discrete-time signal.

The object of this investigation is to evaluate the performance of the maximum entropy method (= MEM; also called "linear prediction by the covariance method") in estimating the transmitted signal frequencies.

For the simple case in which $F = \{f_1\}$ and there is no interference, the problem of obtaining confidence intervals for f_1 appears to be intractable. Thus, computer simulation was used to assess the sampling variability of f_1. The initial effort in this direction involved the case of no noise other than quantization noise resulting from the analog-to-digital conversion of the signal and computer roundoff noise. The results of this simulation showed excellent performance of the MEM for sampling of the signal with a 12-16 bit analog-to-digital converter when $F = (0, 6000)$ and f_1 is not too close to either 0 or 6000.

ACKNOWLEDGMENT

The author is grateful to the AFOSR and the ASEE for sponsoring the Summer Faculty Research Program, which in his opinion appears to be valuable to the Air Force and has great potential for enhancing the quality of both the research and the teaching of the participant.

Special thanks are due to Mr. Fred O'Brien of Auburn University, the Program Director, and Mr. John Huss of RADC for their excellent administration of the Program.

The author is indebted to Captain Kenneth E. Wilson for proposing a very interesting and challenging problem and for his patience and helpfulness.

MAXIMUM ENTROPY
SPECTRAL DEMODULATOR INVESTIGATION

1. INTRODUCTION AND OBJECTIVES

A transmitted signal, which is masked by noise and, possibly, interference, is assumed to be a sinusoid with Hertz-frequency which varies over some finite set F of positive real numbers. Let "s(t)" denote the value of the resulting continuous-time signal at time t. Of particular interest is the case where #F = 2; that is, where the frequency switches back and forth between two distinct values.

The object of this study is to evaluate the performance of the maximum entropy method (= MEM) of spectral estimation for short segments of a discrete-time signal which results from sampling s(t) at uniformly spaced time instants. To be more specific, it is desired to estimate the uncertainty of the MEM estimates of the transmitted signal frequencies, by obtaining confidence intervals, for the cases (a) received signal = transmitted signal + noise and (b) received signal = transmitted signal + noise + (purposeful) interference.

The simple case (a) with $F = \{f_1\}$ was considered almost exclusively. The (analytical) problem of obtaining confidence intervals for f_1, which requires determining the probability density function for f_1, appears to be intractable. Thus, late in the program, computer simulation was used to study the

sampling variability of f_1. The results of this simulation are encouraging; the MEM seems to perform quite well.

2. THE MODEL

In general, the MEM models functional values as the output oa a linear discrete system (= LDS); that is, as a linear combination of past functional values (outputs of the LDS) and past and present inputs to the LDS. This leads to the linear, constant coefficient, difference equation

$$(2.1) \qquad f(kT) = -\sum_{j=1}^{p} a_j f((k-j)T) + G\sum_{i=0}^{q} b_i u((k-i)T),$$

where the a_j and b_i are real numbers, $b_0 \underline{\underline{df}}\ 1$, G is the system gain factor (a positive real number), T is the sampling period (a positive real number), $u((k-i)T)$ is the input to the LDS at time $(k-i)T$, and k is any positive integer such that the functions f and u are defined at the indicated times. As (2.1) enables one to "predict" $f(mT)$ from $f((m-1)T)$, ... , $f((m-p)T)$, $u(mT)$, ... , $u((m-q)T)$, the name "linear prediction" is also associated with this method.

There are several other equivalent representations of a LDS in addition to the difference equation formulation [1; pp. 85-86]. For frequency-domain considerations, the representation

$$S(z) = H(z)U(z),$$

where $S(z)$ and $U(z)$ are the z-transforms of $s(kT)$ and $u(kT)$ respectively and $H(z)$ is a rational function of z called the "system transfer function," is useful [1; pp. 220-282]. In

general, H(z) will have both zeros and poles.

We model a received signal s by a difference equation of the form (2.1) with q = 0 and G = 1; that is, we assume

$$s(kT) = -\sum_{j=1}^{p} a_j s((k-j)T) + u(kT) \tag{2.2}$$

for all appropriate k. For the model (2.2), it can be shown that

$$H(z) = \frac{1}{1 + \sum_{j=1}^{p} a_j z^{-j}}.$$

Thus H is an "all-pole" transfer function with p poles, namely, the p solutions of the equation $1 + \sum_{j=1}^{p} a_j z^{-j} = 0$ or, equivalently (if $z \neq 0$, as is required by the definition of the z-transform),

$$z^p + a_1 z^{p-1} + \ldots + a_{p-1} z + a_p = 0. \tag{2.3}$$

3. ESTIMATION OF MODEL PARAMETERS

The model parameters $a_1, \ldots, a_p$ in (2.2) are approximated by the usual type of least-squares analysis in the time-domain [2; pp. 563-567]. For a given positive integer m, we predict s(mT) to be

$$\widetilde{s(mT)} \underline{\underline{df}} -\sum_{j=1}^{p} \tilde{a}_j s((m-j)T), \tag{3.1}$$

where the $\tilde{a}_j$ are chosen so as to minimize an appropriate function of the errors

$$e(kT) \underline{\underline{df}} s(kT) - \widetilde{s(kT)}$$

for $k < m$. In the case of a deterministic signal, $\sum e^2(kT)$ is minimized over some set of previous samples. In case we minimize the sum of squared errors

$$\sum_{k=m-N}^{m-1} e^2(kT) \quad \left(= \sum_{k=0}^{N-1} e^2((m-N+k)T)\right.$$

corresponding to the preceding N samples, the technique is called the "covariance method" of linear prediction [2; p. 564]. This leads to the system of linear equations

$$(3.2) \quad \sum_{j=1}^{p} \tilde{a}_j(m,N)\phi_{ij}(m,N) = -\phi_{0i}(m,N) \quad (i = 1, 2, \ldots, p),$$

where, for all $(i,j) \in \{1, \ldots, p\} \times \{1, \ldots, p\}$,

$$(3.3) \quad \phi_{ij}(m,N) \underline{\underline{df}} \sum_{k=0}^{N-1} s((m-N+k-i)T)s((m-N+k-j)T),$$

for determining the $\tilde{a}_j$ which yield the prediction of $s(mT)$. From (3.2) and (3.3), we see that the $N + p$ consecutive samples $s((m-N-p)T), \ldots, s((m-1)T)$ are needed. Thus if we do not allow negative arguments, $s((N+p+1)T)$ is the first sample we can predict.

In making the prediction (3.1), we are assuming that the input $u(mT)$ is completely unknown, which is often the case.

4. THE ANALYTICAL APPROACH

The analytical determination of the frequencies $f_i \in F$ exhibited by the transmitted signal involves (a) calculating the $\phi_{ij}(m,N)$ from (3.3), (b) solving the system of linear equations

(3.2) for the $\tilde{a}_j$, (c) solving the polynomial equation (2.3) with "$\tilde{a}_j$" in place of "a_j", (d) determining θ_i in the polar form $r_i \exp(\pm J\theta_i)$ of each of the complex conjugate pairs of roots of (2.3), and (e) multiplying the θ_i by an appropriate real number to obtain the f_i.

As indicated in Section 1, an attempt was made to handle analytically the simple case of a single frequency ($F = \{f_1\}$) signal in noise with no interference; that is, we assume the transmitted signal is

$$A\sin(2\pi f_1 t) \tag{4.1}$$

and that the received signal is

$$s(t) = A\sin(2\pi f_1 t) + n(t),$$

where n(t) is a zero-mean Gaussian noise process [3; pp. 219-222] which is uncorrelated with the transmitted signal and for which

$$E[n(t)n(t+k)] = \begin{cases} \sigma^2 & (k = 0), \\ 0 & (k \neq 0). \end{cases}$$

Thus the samples of s are given by

$$s(kT) = A\sin(2\pi f_1 kT) + n(kT). \tag{4.2}$$

In this case, a 2-pole model ($p = 2$) suffices.

The roots of (2.3) with $p = 2$ and "$\tilde{a}_j$" in place of "a_j" are z_1 $\underline{\text{df}}$ $(-\tilde{a}_1 + \sqrt{d})/2$ and z_1 df $(-\tilde{a}_1 - \sqrt{d})/2$, where d $\underline{\text{df}}$ $\tilde{a}_1^2 - 4\tilde{a}_2$. It can be shown that the radian argument in the polar form of z_1 is the radian-frequency f_1 in (4.2). (In fact, this poten-

tial for ferreting out the frequencies of a sinusoidal signal is the reason linear prediction is useful to us, rather than its predictive powers. We can always "wait" T seconds and measure s(mT).) Thus, as f > 0, z_1 must be a non-real complex number; that is, we must have $\tilde{a}_1^2 - 4\tilde{a}_2 < 0$. Hence we have

$$z = -(\tilde{a}_1/2) + J(\sqrt{4\tilde{a}_2 - \tilde{a}_1^2})/2,$$

where $4\tilde{a}_2 - \tilde{a}_1^2 > 0$. It is easy to show that z_1 has polar form $r_1\exp(J\theta_1)$, where

(4.3) $$r_1 = \sqrt{\tilde{a}_2}$$

and

(4.4) $$\theta_1 = \begin{cases} \pi/2 & (\tilde{a}_1 = 0), \\ \tan^{-1}(-\sqrt{4\tilde{a}_2 - \tilde{a}_1^2}/\tilde{a}_1) + \pi & (\tilde{a}_1 > 0), \\ \tan^{-1}(-\sqrt{4\tilde{a}_2 - \tilde{a}_1^2}/\tilde{a}_1) & (\tilde{a}_1 < 0). \end{cases}$$

If we measure frequencies in Hertz and require that $F \subset (0,6000)$, then

(4.5) $$f_1 = (6000/\pi)\theta_1.$$

Now, $\tilde{a}_1$ and $\tilde{a}_2$ in the expression for f_1 can be obtained explicitly by solving the system of equations (3.2) with p = 2. By Cramer's Rule, we have

(4.6) $$\tilde{a}_1 = (\phi_{12}\phi_{02} - \phi_{22}\phi_{01})/\Delta$$

and

(4.7) $$\tilde{a}_2 = (\phi_{21}\phi_{01} - \phi_{02}\phi_{11})/\Delta,$$

where

$$\Delta \stackrel{df}{=} \phi_{11}\phi_{22} - \phi_{12}\phi_{21} \tag{4.8}$$

and the ϕ_{ij} are given by (3.3) and involve the s(kT) as given by (4.2). Even in this very special case, the complicated chain of operations linking the assumptions about the transmitted signal and the noise with the frequency f_1 makes it difficult to determine the probability density function for f_1.

In case #F = 2, a 4-pole model is appropriate and the equation (2.3) is quartic. The four roots of a quartic equation can be given explicitly in terms of radicals and the coefficients $a_1, \ldots, a_4$; however, the expressions for these roots are extremely complicated. Of course, if #F > 2, a model with at least six poles is required and no analog of the quadratic and quartic formulas exists for the equation (2.3) in such cases. Thus, for these cases, we can not mimic the treatment of the 2-pole case.

5. THE COMPUTER SIMULATION

The first part of the program involved an extensive investigation of linear prediction techniques and their application to communications theory [1]. This investigation included the analytical effort described in Section 4. The second part of the program involved the development of a computer simulation to determine the sampling variability of the f_1.

In Sections 1 and 4, we did not elaborate on the term "noise." Noise is a fundamental limitation on the performance of physical systems such as radar devices. Some possible sources of noise are clutter, cosmic radiation, and thermal motion of the electrons and ions in the receiver components and the antenna rurroundings [3; pp. 3-5].

There are other limitations on performance in signal-processing that are based on the fact that the values of variables in models of real-world systems are, typically, real numbers with decimal representations which are non-terminating or terminate only after a large number of digits, whereas, digital signal-processing equipment (which for various reasons has largely supplanted analog equipment) seldom allows representations of numbers (or other symbols) with more than 64 precision bits. One such limitation, "quantization noise," results from use of an analog-to-digital converter (= ADC) in sampling the continuous-time signal. Another, "roundoff (or chopping) noise," results from rounding (or chopping) sums and products to fit the computer's word length.

In the simulating done to date, an effort has been made to assess the sampling variability due to quantization noise and roundoff noise. Such noise is always present as we can not do infinite-precision sampling and arithmetic. Further work is needed to determine the effect of purposeful man-made interference and the type of noise cited in the second paragraph of this section. Also, we have considered only the 2-pole model discussed in Section 4.

Some features of the simulation which look peculair owe to the fact that, previously, some processing of actual signals was done at RADC. An 8-bit ADC was used to produce 8-bit approximations of signal values and blocks of 2048 of these were stored on magnetic tape. Later, this information was computer-processed. The programs used in the present study include portions of the previously-used program.

Below is a list of key variables in the simulation programs along with the corresponding variable (if any) in Section 4 and its interpretation:

TSA (T)	sampling period (1/12000 sec.);
F1 (f_1)	Hertz-frequency of the transmitted signal;
A (A)	amplitude of the transmitted signal
NP (p)	number of poles;
N (N)	number of error terms in the minimization process for determining the prediction coefficients $\tilde{a}_j$ in (3.1);
NN (= N + p)	the number of previous samples needed to predict s(mT)
NB ( )	number of ADC bits;
S(J) (s(jT))	value of the received signal at time jT;
P(I,J) ($\phi_{ij}(m,N)$)	coefficient of $\tilde{a}_j$ in equation i of the linear system (3.3);
PO(I) ($\phi_{0i}(m,N)$)	constant on the right in equation i of the linear system (3.3);
R(K) (r_1)	magnitude of the root of (2.3) in the upper half-plane;
F(K) (f_1)	Hertz-frequency corresponding to the root of (2.3) in the upper half-plane;
FC ( )	the radian-Hertz conversion factor $6000/\pi$ in (4.5);
DEL (Δ)	the determinant of the system (3.3) (see (4.8));
A1 ($\tilde{a}_1$)	coefficient in equation (2.3) with p = 2;

A2 (a_2)	coefficient in equation (2.3) with p = 2;
AM	arithmetic mean of S $\underline{df}$ {s(mT): m ε {6, 7, ... , 2048}};
SD	standard deviation of S.

We assume henceforth that the amplitude A (measured in volts) of the transmitted signal is in [-5, 5]. In the simulation of the ADCs behavior, the signal S(J) in the interval [-5, 5], of length 10, is mapped into the integer interval $[-2^{NB-1}, 2^{NB-1}]$ by following $x \longmapsto (2^{NB}/10)x$ by chopping to an integer, and the integer is mapped back into a computer real number in [-5, 5] by $x \longmapsto (10/2^{NB})x$.

In a certain average sense, binary representations of numbers have $\log_2(10)$ (= 3.32) times as many symbols as do the corresponding decimal representations when both representations terminate. Thus it was apparent to the writer that the 8-bit ADC was not adequate for dealing with frequencies in (0, 6000).

One of the programs used in the simulation appears in the Appendix. Its purpose is to determine the effect of the number of ADC bits on the performance of the model. The results, given in Table 1, of executing this program confirm the conclusion. about the inadequacy of the 8-bit ADC.

Table 2 shows the variation of AM and SD with N, the number of error terms used in the minimization. In case NB = 14, central processor (= CPU) time is given also. These times include the execution time for the statistical calculations. Thus absolute differences are meaningful to the determination of the effect on execution time of changing the value of N, whereas relative

TABLE 1

Mean AM and standard deviation SD of predictions for the number of ADC bits NB = 2, 3, ... , 16, 27* with A = 1.5, N = 3, and F1 = 3250.

NB	AM	SD
2	6000.0000	2749.9994
3	3497.7974	1677.3801
4	3252.4888	226.23133
5	3248.9677	78.865247
6	3249.5983	33.414235
7	3249.6557	21.808373
8	3249.9485	11.663445
9	3249.9887	4.8569507
10	3249.9991	2.4628091
11	3250.0001	0.77203118
12	3250.0004	0.22295413
13	3249.9985	0.18255417
14	3249.9960	0.15308648
15	3250.0002	0.075419844
16	3250.0008	0.034125918
27	3250.0001	0.0066758151

differences are not. It appears that adding 1 to the value of N increases execution time by approximately (1/3)(0.0001) hr. or 0.12 sec. Note that execution of the program involves 2043 (= 2048 - (3 + 2)) calculations of an f_1. Thus the added time for calculation of each value of f_1 is approximately $5 \cdot 10^{-5}$ sec. Execution times are of interest as the ultimate goal is real-time implementation of the model.

*Here we have used 27 precision-bit floating-point representations and arithmetic with the ADC simulation portion of the program deleted.

TABLE 2

Mean AM and standard deviation SD of predictions for the number of error terms used in the minimization N = 2, 3, ... , 12 with A = 1.5, F1 = 3250, and NB = 8, 10, 12, 14, 16, and 27.

NB = 8

N	AM	SD
2	3250.0737	15.632812
3	3249.9485	11.663445
4	3249.9371	9.3071191
5	3249.8821	7.1128755
6	3249.8813	6.0597079
7	3249.8710	5.2067635
8	3249.8677	4.4239790
9	3249.8625	3.3021908
10	3249.8594	2.8550067
11	3249.8582	2.2166742
12	3249.8565	2.0223015

NB = 10

N	AM	SD
2	3250.0018	2.9927573
3	3249.9991	2.4628091
4	3249.9970	2.0885355
5	3249.9975	1.7026238
6	3249.9979	1.6084557
7	3249.9978	1.2938950
8	3249.9922	1.0680774
9	3249.9925	0.73630817
10	3249.9945	0.56215978
11	3249.9921	0.39859506
12	3249.9906	0.35790581

NB = 12

N	AM	SD
2	3249.9978	0.28106676
3	3250.0004	0.22295413
4	3250.0015	0.14402156
5	3250.0015	0.13972569
6	3250.0001	0.081098709
7	3250.0009	0.067171544
8	3249.9994	0.059041822
9	3250.0011	0.044649824
10	3250.0009	0.047537731
11	3249.9999	0.052555363
12	3250.0009	0.046175324

NB = 14

N	AM	SD	CPU TIME
2	3249.9988	0.21686259	0.0009
3	3249.9960	0.15309648	0.0009
4	3249.9997	0.11826708	0.0010
5	3249.9983	0.10109097	0.0010
6	3249.9958	0.066045111	0.0010
7	3249.9998	0.059400090	0.0011
8	3249.9980	0.052958412	0.0011
9	3249.9972	0.032415771	0.0011
10	3250.0021	0.037008012	0.0012
11	3249.9973	0.038732876	0.0012
12	3250.0007	0.033104122	0.0012

NB = 16

N	AM	SD
2	3249.9999	0.045065880
3	3250.0008	0.034125918
4	3249.9995	0.024391433
5	3249.9991	0.021149200
6	3250.0010	0.019371934
7	3249.9993	0.015833400
8	3249.9985	0.013296252
9	3249.9994	0.011714947
10	3249.9999	0.010651756
11	3249.9995	0.0083492643
12	3250.0000	0.0071696392

NB = 27

N	AM	SD
2	3250.0003	0.0087628514
3	3250.0001	0.0066758151
4	3250.0000	0.0042304078
5	3250.0000	0.0027758344
6	3250.0000	0.0017828080
7	3250.0000	0.0020461476
8	3250.0000	0.0021599298
9	3250.0000	0.0019517387
10	3250.0000	0.0015333511
11	3250.0000	0.00091071260
12	3250.0000	0.0010223139

The next table shows the variation of AM, SD, and the signal-to-(quantization and roundoff) noise ratio SNR, given by $20 \cdot \log_{10}(2^{NB}A/10)$, with A.

TABLE 3

Mean AM, standard deviation SD, and signal-to-(quantization and roundoff) noise ratio SNR for the amplitude of the transmitted signal A = 0.5, 1.0, 1.5, ... 5.0 with N = 3, F1 = 3250, and NB = 10, 12, 14, and 16.

NB = 10

A	AM	SD	SNR
0.5	3249.9668	6.9402777	34.185400
1.0	3249.9982	2.0219451	40.205999
1.5	3249.9991	2.4628091	43.727824
2.0	3249.9991	1.5623139	46.226599
2.5	3249.9962	1.5531899	48.164799
3.0	3250.0001	0.77203118	49.748425
3.5	3250.0002	1.3622908	51.087360
4.0	3250.0012	0.72204416	52.247199
4.5	3250.0019	0.42808743	53.270249
5.0	3249.9961	0.98476960	54.185400

NB = 12

A	AM	SD	SNR
0.5	3249.9991	1.5623139	46.226599
1.0	3250.0012	0.72204416	52.247199
1.5	3250.0004	0.22295413	55.769024
2.0	3249.9994	0.53745331	58.267799
2.5	3249.9979	0.44305741	60.205999
3.0	3249.9985	0.18255417	61.789624
3.5	3250.0007	0.20943003	63.128560
4.0	3249.9981	0.27760254	64.288399
4.5	3250.0016	0.16504455	65.311449
5.0	3250.0001	0.16447618	66.226500

NB = 14

A	AM	SD	SNR
0.5	3249.9994	0.53745331	58.267799
1.0	3249.9981	0.27760254	64.288399
1.5	3249.9960	0.15309648	67.810224
2.0	3250.0001	0.12638791	70.308999
2.5	3250.0036	0.086964880	72.247199
3.0	3250.0002	0.075419844	73.830824
3.5	3249.9987	0.056363066	75.169760
4.0	3250.0002	0.056470926	76.329598
4.5	3250.0023	0.025813821	77.352649
5.0	3249.9998	0.049159881	78.267799

NB = 16

A	AM	SD	SNR
0.5	3250.0001	0.12638791	70.308999
1.0	3250.0002	0.056470926	76.329598
1.5	3250.0008	0.034125918	79.851424
2.0	3249.9998	0.033097830	82.350199
2.5	3250.0016	0.024226625	84.288399
3.0	3250.0005	0.017549278	85.872024
3.5	3249.9992	0.021185211	87.210959
4.0	3249.9992	0.018053080	88.370798
4.5	3250.0004	0.015683560	89.393849
5.0	3249.9998	0.015091892	90.308999

Table 4 shows the variation of AM and SD with the frequency F1 of the transmitted signal. As there are 14-bit ADCs available commercially and model performance is quite good with NB = 14 according to Table 1, we let NB = 14.

The strange variation of SD with F1 results from the sampling process and finite precision arithmetic. As the possible signal frequencies are less than 6000 Hz., we must sample at the

TABLE 4

Mean AM and standard deviation SD of predictions for F1 = 125, 250, 375, ... , 5875 with NB = 14, N = 3, and A = 1.5.

F1	AM	SD
125	119.24084	36.594588
250	249.51668	13.343529
375	374.99050	2.1931926
500	499.99242	2.2354304
625	624.99677	1.6018316
750	750.00167	0.41421278
875	874.99947	0.93162946
1000	999.99837	0.73667024
1125	1124.9997	0.35508527
1250	1250.0013	0.36510814
1375	1374.9998	0.33071683
1500	1499.9985	0.24333926
1625	1624.9985	0.24277011
1750	1750.0004	0.10973179
1875	1875.0006	0.10363140
2000	2000.0000	0.
2125	2124.9995	0.18358279
2250	2250.0019	0.073796298
2375	2375.0001	0.21530845
2500	2499.9964	0.090456136
2625	2625.0006	0.12147366
2750	2750.0028	0.15310039
2875	2875.0002	0.18313020
3000	3000.0000	0.
3125	3124.9978	0.18266767
3250	3249.9960	0.15309648
3375	3374.9995	0.12147751
3500	3500.0056	0.090457460
3625	3625.0008	0.21415340
3750	3749.9958	0.073787051
3875	3874.9984	0.18436528
4000	4000.0000	0.
4125	4124.9997	0.10363143
4250	4249.9976	0.10972426
4375	4374.9999	0.24238029
4500	4499.9988	0.24332672
4625	4624.9993	0.33069280
4750	4750.0037	0.36511440
4875	4875.0005	0.35509441

F1	AM	SD
5000	4999.9958	0.73666593
5125	5124.9982	0.90562031
5250	5250.0022	0.41419801
5375	5375.0008	1.5328385
5500	5500.0052	2.2354247
5625	5625.0086	2.1931942
5750	5750.4873	13.343526
5875	5880.7836	36.559757

rate of at least 12000 samples per second according to the Sampling Theorem [1; p. 291]. Thus we are led to letting T = 1/12000. For F1 = 2000 (respectively, 3000, 4000), we have α df $2k\pi F1/12000 = k\pi/3$ (respectively, $k\pi/2$, $2k\pi/3$) and $\sin(\alpha) = .50$ (respectively, 1.0, .50) in exact arithmetic. As the library SIN function is accurate to 8 decimal digits, $\sin(\alpha)$ is exact and $1.5\sin(\alpha)$ is also exact with two significant decimal digits. In these cases, it can be shown that the first step in the simulation of the ADCs behavior leads to an integer if NB = 14; thus the ADC simulation leads to the exact frequency F1 as the predicted frequency. Thus, the value 0 for SD in case F1 = 2000, 3000, or 4000 is explained. Similar reasons for other irregularities can be given.

The program leading to Table 4 was executed with F1 ranging from 125 to 5875 by steps of 25; however, for obvious reasons not all of these values appear in the table. The original attempt at execution for F1 ranging from 25 to 5975 lead to execution-time errors. Further work showed that the trouble begins

somewhere in the intervals [100, 125) and (5875, 6000). Obviously, as F1 approaches 0^+ (6000^-), the radian measure of θ_1 in (4.4) must approach 0^+ (π^-). Thus the discriminant d $\underline{\text{df}}$ $4\tilde{a}_2 - \tilde{a}_1^2$ must approach 0 in both cases. Printing values of some intermediate variables for the bad cases showed that d took on negative values with increasing frequency as F1 got closer and closer to 0^+ (6000^-). Quantization and roundoff noise had taken its toll.

The next table shows the variation of AM and SD with block size. Ultimately, a block size smaller than 2048 may be used. We note that the performance of the model is reasonably uniform over block size.

TABLE 5

Mean AM and standard deviation SD of predictions for block size = 8, 16, 32, 64, 128, 256, 512, 1024, and 2048 with NB = 14, F1 = 3250, and A = 1.5.

BLOCK SIZE	AM	SD
8	3249.9163	0.10430552
16	3249.9741	0.19046609
32	3249.9907	0.14852447
64	3249.9952	0.16077075
128	3249.9980	0.15215203
256	3249.9989	0.15498016
512	3250.0002	0.15291365
1024	3249.9998	0.15360796
2048	3249.9960	0.15309648

Finally, relative frequencies and cumulative relative frequencies of the predictions were obtained in the absence of the

probability density function (= PDF) and the distribution function (= DF).

TABLE 6

Approximations of the probability density function PDF and the distribution function DF of the predictions with NB = 14, N = 3, A = 1.5, and F1 = 3250.

PREDICTION INTERVAL	APPROX. PDF ON INTERVAL	APPROX. DF AT RIGHT
3249.45-3249.50	0.041605482	0.041605482
3249.50-3249.55	0.	0.041605482
3249.55-3249.60	0.	0.041605482
3249.60-3249.65	0.	0.041605482
3249.65-3249.70	0.	0.041605482
3249.70-3249.75	0.	0.041605482
3249.75-3249.80	0.16691140	0.20851689
3249.80-3249.85	0.	0.20851689
3249.85-3249.90	0.083700441	0.29221733
3249.90-3249.95	0.16691140	0.45912873
3249.95-3250.00	0.20802741	0.66715614
3250.00-3250.05	0.	0.66715614
3250.05-3250.10	0.16642193	0.83357808
3250.10-3250.15	0.083210965	0.91078904
3250.15-3250.20	0.083210965	1.00000000

The "grainy" nature of the above results is again the effect of quantization and roundoff. To partially negate these effects the program was run again with the quantization portion missing so that 27-bit floating-point representations and arithmetic prevail.

TABLE 7

Approximations of the probability density function PDF and the distribution function DF of the predictions with N = 3, A = 1.5, F1 = 3250, and 27-bit floating-point representations and arithmetic.

PREDICTION INTERVAL	APPROX. PDF ON INTERVAL	APPROX. DF AT RIGHT
3249.985-3249.990	0.12922173	0.12922173
3249.990-3249.995	0.081742535	0.21096427
3249.995-3250.000	0.28095937	0.49192364
3250.000-3250.005	0.36514929	0.85707294
3250.005-3250.010	0.064121390	0.92119432
3250.010-3250.015	0.042094959	0.95790504
3250.015-3250.020	0.042094959	1.00000000

6. CONCLUSIONS AND RECOMMENDATIONS

As indicated earlier, the problem of obtaining confidence intervals for the $f_i \in F$ appears to be intractable, even for the simple case of a single-frequency signal ($F = \{f_1\}$) in noise. However, simulation of the single-frequency case, with the only noise being quantization and roundoff noise, has shown that the MEM performs quite well in terms of sampling variability of f_1.

If results similar to those in Table 1 hold for the two-frequency signal simulation and the frequencies differ by, say, 50 Hz., it is obvious (as SD = 11.7) that an 8-bit ADC is inadequate and that an ADC giving 12-16 bits is desirable. A catalog search has shown that 12-bit ADCs with 2μsec. sampling time and

and 14-bit ADCs with 50 μsec. sampling time are available commercially.

From Table 2 with NB = 14, we see that model behavior is good with N = 3 but that SD can be decreased by a factor of approximately 4/5 (that is, to 1/5 of its value for N = 3) by increasing N to 12 at the cost of increasing CPU time by a factor of approximately 1/3. If the single-frequency case were of practical interest, it would not seem desirable to increase N in view of the desire to operate in real-time and the good performance of the model with N = 3 (and NB = 12-14).

From Table 3 with NB = 12 (or 14), we see that model performance is good with transmitted signal amplitude A = 1.5. However, SD can be decreased by a factor of approximately 3/4 (or 5/6) by increasing A to 4.5.

From Table 4, we see that model performance is quite good for $f_1 \in (1000, 5000)$ but deteriorates rapidly as f_1 approaches 0^+ and 6000^-. Again, if similar results hold for the two-frequency signal case, values of f_1 and f_2 in [1500, 4500] would give excellent results.

Table 5 shows that model performance is quite uniform and good for block sizes ranging from 128 to 2048. Thus a reduction of block size to the vicinity of 128, as is anticipated, will not adversely effect results.

There remains a substantial amount of work to be done in assessing the performance of the MEM in case $\#F \geq 2$. In the two-frequency signal case, operation counting shows that Gauss

elimination is decidedly superior to use of Cramer's Rule. Also, it is likely that use of some iterative algorithm for finding polynomial roots is better than use of the quartic formula (which generally requires use of the cubic formula) for solving (2.3) with p = 4. Of course, for #F $\geq$ 3 (p $\geq$ 6) no formula exists for solving (2.3). A substantial portion of the computing time is required by the COV subroutine, which is probably as efficient as is possible. With the real-time goal in mind, it is vital that the most efficient algorithms for solving linear systems and polynomial equations be found.

REFERENCES

[1] Cadzow, J. A., Discrete-time Systems, Prentice-Hall, Englewood Cliffs, New Jersey,1973.

[2] Makhoul, J., "Linear Prediction: A Tutorial Review," Proceedings of the IEEE, Vol. 63, No. 4, April 1975.

[3] Robinson, E. A., Statistical Communication and Detection, Hafner, New York, 1967.

APPENDIX

```
CMETA  PROGRAM META
       DOUBLE PRECISION TSA,TPI,TC,W1
       COMMON/SAMP/S(2048)
       COMMON/FREQ/F(2048)
       COMMON/RMAG/R(2048)
       COMMON/PHI/P(2,2)
       COMMON/PHO/PO(2)
       COMMON/TFRQ/F1
C      ASSIGN VALUES TO VARIABLES
       DATA TSA,TPI/83.3333333333333333D-6,6.28318530717958647/
       DATA PI,FC,F1/3.14159265,1909.85931,3250./
       DATA KU,A,NP,N,AM,SD/2048,1.5,2,3,0.,0./
       NN=NP+N
       KL=NN+1
C      LOOP TO CALCULATE AND PRINT PREDICTED FREQUENCIES FROM (4.4) AND
C      (4.5)AND MEAN AND STANDARD DEVIATION THEREOF FOR NUMBER OF BITS =
C      2,3,...,16
       DO 5 NB=2,16
         WRITE (6,200) NB
  200    FORMAT (18H NUMBER OF BITS = ,I3//)
C        CALCULATE EXACT TRANSMITTED SIGNAL VALUE FROM (4.1)
         W1=F1*TPI
         DO 10 J=1,2048
           FJ=J-1
           TC=FJ*TSA
           TS=W1*TC
   10    S(J)=A*SIN(TS)
C        SIMULATION OF ADC QUANTIZATION OF THE SIGNAL
         NBP=2**NB
         PNB=NBP
         DV=10./PNB
         DVI=PNB/10.
         DO 15 J=1,2048
           X=S(J)
           X=X*DVI
           KP=X
           X=KP
   15    S(J)=X*DV
C        CALCULATE COEFFICIENTS FOR AND SOLVE LINEAR SYSTEM (3.2) USING
C        (4.6)-(4.8)
         DO 20 K=KL,KU
           KK=K
           CALL COV(NP,NN,KK)
           DEL=P(1,1)*P(2,2)-P(1,2)*P(2,1)
           A1=(P(1,2)*PO(2)-PO(1)*P(2,2))/DEL
           A2=(P(2,1)*PO(1)-PO(2)*P(1,1))/DEL
C          CALCULATE AND PRINT PREDICTED FREQUENCY
           F(K)=FC*ARCTA(-A1,SQRT(4*A2-A1*A1))
           R(K)=SQRT(A2)
   20    WRITE (6,300) K,R(K),F(K)
  300    FORMAT (1X,I8,2G20.8)
```

```
C       CALCULATE AND PRINT MEAN AND STANDARD DEVIATION OF PREDICTIONS
        CALL STATS (AM,SD,KL,KU)
    5 WRITE (6,400) AM,SD
  400 FORMAT (1X,2G20.8///)
      STOP
      END
      SUBROUTINE COV(NP,NN,LP)
      COMMON/SAMP/S(2048)
      COMMON/PHI/P(2,2)
      COMMON/PHO/PO(2)
C     CALCULATE THE PHI(I,J) OF (3.3)
C     CALCULATE DIAGONAL ELEMENTS, PHI(J,J), OF COVARIANCE MATRIX -
C     ASSIGN TO P(J,J)
      L=LP-1
      NI=NN-NP
      NL=LP-NI
      B=0.
      DO 5 J=NL,L
    5 B=B+S(J)*S(J)
      DO 10 J=1,NP
        K=LP-J
        I=NL-J
        B=B+S(I)*S(I)-S(K)*S(K)
   10 P(J,J)=B
C     CALCULATE REMAINDING PHI(I,J)
      DO 15 KK=1,NP
        B=0.
C       CALCULATE PHI(0,KK) - ASSIGN TO PO(KK)
        DO 20 J=1,NI
          N=LP-J
          M=N-KK
   20   B=B+S(N)*S(M)
        PO(KK)=B
C       CALCULATE PHI(I,J),J-I=KK,1<I<NP-1,2<J<NP - ASSIGN TO P(I,J)
        IF (KK.EQ.NP) GO TO 15
        DO 25 K=1,NP-KK
          I=K
          J=KK+K
          N=LP-K
          M=N-KK
          N1=NL-K
          M1=N1-KK
          B=B+S(N1)*S(M1)-S(N)*S(M)
          P(I,J)=B
   25   P(J,I)=B
C       THE PREVIOUS STATEMENT TAKES ADVANTAGE OF SYMMETRY OF
C       COVARIANCE MATRIX
   15 CONTINUE
      RETURN
      END
```

```
      SUBROUTINE STATS (AM,SD,KL,KU)
C     STATS CALCULATES THE MEAN AND STANDARD DEVIATION OF THE
C     KU-(NP+N) PREDICTED FREQUENCIES F(J)
      COMMON/FREQ/F(2048)
      COMMON/TFRQ/F1
      S1=0.
      S2=0.
      XN=KU-KL+1
      DO 5 J=KL,KU
        S1=S1+F(J)
    5 S2=S2+(F(J)-F1)**2
      AM=S1/XN
      SD=SQRT(S2/XN)
      RETURN
      END
      FUNCTION ARCTA(X,Y)
C     ARCTA CALCULATES RADIAN FREQUENCY DETERMINED BY ROOT X+JY OF
C     (2.3) BY USE OF (4.4)
      DATA PI,HPI/3.14159265,1.57079632/
      IF (X) 1,2,3
    1 ARCTA=ATAN(Y/X)+PI
      RETURN
    2 ARCTA=HPI
      RETURN
    3 ARCTA=ATAN(Y/X)
      RETURN
      END
```

1977 USAF-ASEE SUMMER FACULTY RESEARCH PROGRAM

sponsored by

THE AIR FORCE OFFICE OF SCIENTIFIC RESEARCH

conducted by

AUBURN UNIVERSITY AND OHIO STATE UNIVERSITY

PARTICIPANT'S FINAL REPORT

SOFTWARE DESIGN VALIDATION

AND

ARTIFICIAL INTELLIGENCE

Prepared by:	Ralph M. Weischedel, Ph.D.
Academic Rank:	Assistant Professor
Department and University:	Department of Statistics & Computer Science University of Delaware Newark, Delaware 19711
Assignment: (Laboratory) (Division) (Branch)	Griffiss Air Force Base Rome Air Development Center Information Sciences Information Processing
USAF Research Colleague:	William E. Rzepka
Date:	August 12, 1977
Contract No.:	F44620-75-C-0031

SOFTWARE DESIGN VALIDATION AND ARTIFICIAL INTELLIGENCE

by

Ralph M. Weischedel

ABSTRACT

An emerging trend in software design is the use of formal languages to specify a design precisely. Because it is a formal language, automated aids for use in design validation may be possible. This paper examines specific areas of artificial intelligence research that potentially offer automated aids to design validation.

Automatic proof of program correctness is examined for the possibility of proving that a design satisfies its functional requirements. A spinoff of correctness proof research has been symbolic execution of programs, a technique for systematically examining the various program paths on classes of inputs, rather than specific numerical input. If the formal language in which the design is specified is procedural, this research might be adapted to these languages so that a validation team could systematically examine the design by symbolic execution.

An alternative approach to design validation would be to provide a breadboard system corresponding to the design at design review. The end user of the system under development could then experiment with the system, constituting a design validation. Such a breadboard would have to be created within a very brief period of time, so that software development is not significantly slowed. Automatic programming research is examined for this goal.

Each area of research is briefly surveyed, providing an example of the approach, the potential payoff in design validation, the state of the art, significant technological gaps faced in the research, and a prognosis for its future in design validation.

Our conclusions include specific areas of research that are needed for artificial intelligence to be applied in software design validation.

1. INTRODUCTION

Of the four phases of software development: requirements specification, design, implementation and testing, design plays a central, crucial role. Large software projects, typical of Air Force needs, may be characterized as having greater than 100,000 source statements and 50 or more programmers. To effectively carry out a project of such size, good engineering and mathematical principles are necessary for detailed, precise description of the design, to insure that each member of the programming team provides a component that exactly fits with all of the other components. The need is compounded not only by the magnitude of such projects, but also by unavoidable personnel turnover on projects of such duration.

Unfortunately, the development of such engineering and mathematical principles for large software projects is still in its infancy. Consequently, assumptions by various members of the programming staff about the design frequently occur. Unlike programming errors, which the individual programmer may find rather quickly by testing his or her component independent of others, errors stemming from mismatched assumptions about the design specification are highly likely to go undetected until the integration test.

For instance, Boehm, et. al. (1975) reports on a case study sponsored by Rome Air Development Center, about a well-managed software project which was delivered on time and within budget. Sixty-four percent of the detected error types were traced to the design phase; only 36% of the error types were programming errors. Refining this analysis showed that 45% of all error types were design errors not found until integration test or later. Only 9% of all error types were programming errors that went undetected until integration test.

Not only are design errors difficult to detect, but also they are costly to fix. Boehm, et. al. (1975) report on other data indicating that design errors take about twice the time to diagnose and correct, compared to coding errors.

Therefore, software design validation is of great importance. At present, thorough, effective, software design reviews are very difficult to conduct, in large part because designs are specified using flowcharts with English descriptions in the boxes. The disadvantage of English as a design language is ambiguity in the description and lack of precision. This may lead to unrecognized misunderstanding between designer and ultimate user, as well as numerous possibilities for inconsistent assumptions among implementors, giving rise to errors mentioned above. The

problems of flowcharts as a software specification have been frequently discussed in the literature on programming methodology and software engineering. One further, serious disadvantage of English descriptions and flowcharts for specifying design is that at design review, they may give the illusion of understanding the design, even though important design issues may have been overlooked. Oftentimes, the only basis for evaluating a design is projected cost and a checklist that the contractor promises to fulfill all of the requirements.

In contrast to such design descriptions, a new trend in design specification is to use a formal language, based on insights from programming languages and mathematical notation. Some examples include WELLMADE of Honeywell Information Systems (Boyd, 1977) and SPECIAL of Stanford Research Institute (Robinson, et. al. 1977). Formal languages, of course, are unambiguous and precise. Furthermore, their precision demands that both designer and design validator address specific issues that might be overlooked otherwise.

There are disadvantages to formal design languages, however. Long specifications in any formal language seem difficult to understand, and some training is naturally important to use them. This probably makes an independent validation team necessary at design review. (That may be an advantage though, for their detailed scrutiny of a design should have multiplied savings in total software development cost.) Creating a design using a formal language is extremely difficult, as is convincing oneself that it does what one wants conceptually. Also, there are technical limitations to formal design languages which may be removed in the near future. Specifically, such languages need to be more natural, richer in their descriptive ability, and better able to represent concurrent processes.

However, the disadvantages seem to be outweighed by the following aspects, in addition to precision and lack of ambiguity. First, the formal languages may be used to specify exactly the functions a module will carry out and its interface to other modules without specifying how the module carries out its function. Parnas (1972a, 1972b, 1977) has shown how such module specifications offer modifiability and fault tolerance to software systems. Modifiability is possible since any group of programs satisfying the module's functional and interface specification may be used in the software system; therefore, software changes, as demand changes during the software life cycle, may be isolated to one module. Fault tolerance may be enhanced, by stating in the formalism for the module,

what response the module should make to exceptional conditions.

Second, formal design languages, by their precision and lack of ambiguity, offer less chance for mismatched assumptions among programmers and designers.

Third, formal design languages offer the possibility of stronger design validation and review. In particular, the potential exists for

1) verifying rigorously that a design meets the functional requirements,

2) assessing how modifiable and maintainable competing designs are,

3) estimating whether the system will meet performance requirements, and

4) providing the user quickly with a concrete system to examine (corresponding to the design).

Achieving the potential in (1) and (4) above will be a recurrent theme in this paper.

Since a design would then be a formal specification, automated aids might be developed for assisting in design validation. This brings us to the objectives of this project.

2. OBJECTIVES

One objective of this project has been to isolate areas of artificial intelligence research which could lead to automated aids for software design validation. For each area of research, potential payoffs, the state of the art, and obstacles have been identified. A second objective has been a prognosis for each area of research and recommendations of research areas which seem most promising for application to software design validation.

Section 3 presents brief preliminary material necessary for understanding the obstacles encountered in the research described later. A section for each area of research follows. In section 7, we briefly describe possible alternative approaches to automated aids in design review, alternative in the sense that they do not use artificial intelligence research as heavily, and are potential short term solutions with less ambitious goals.

3. PRELIMINARIES

For our purposes, let us take the goal of artificial intelligence (AI) to be to enable computers to perform tasks that are normally associated with intelligence and understanding, such as reasoning, programming, communicating in a human language, vision, problem solving, and learning. Before discussing AI research relevant to software design validation, we discuss two topics that are used in several research approaches, theorem provers and subgoal analysis.

Theorem provers or deduction systems have their origin in mathematical logic or symbolic logic. Around the turn of the century, several paradoxes motivated mathematicians to study the nature of proofs. To do this, artificial languages were defined, along with a means of evaluating whether an assertion in the language is true. Furthermore, inference rules are independently defined for deducing an assertion from premises. The sequence of premises and inference rules used to deduce an assertion are intended as a model of a mathematical proof of a theorem. The artificial language plus its set of inference rules is called a formal system.

An important fact is that applying the inference rules is a pure pattern-matching process, totally mechanical and syntactic in nature. It was therefore natural for computer scientists to implement formal systems as computer programs, called theorem provers or deduction systems.

For any formal system, two questions arise, related to the original motivation of paradoxes. Is every statement that can be deduced in the formal system true (according to the independently defined truth evaluation rules)? Is every true statement of the artificial language deducible using the inference rules?

For any artificial language, there are, in general, many sets of inference rules which yield the same set of deducible facts. First order predicate calculus is the class of equivalent systems most often used in mathematics and computer science. The reason is threefold: 1) it does model a significant portion of the form of mathematical statements, 2) the deducible statements are the true statements and only the true statements, and 3) formal systems of higher order, which are significantly richer, sacrifice property (2). (A rigorous treatment of this may be found in Mendelson (1964)).

An example statement in first-order predicate calculus is

$$(\forall w)(\exists z)\ (P(x,y,z) \supset Q(f(x),f(y),w)).$$

This might represent the property of function f being continuous at point x: "for every w, there is a z, such that

$|x-y| \leq z$ implies $|f(x)-f(y)| \leq w$," though it represents innumerable other interpretations as well. An example inference rule is that, if we have statements of the form $A \supset B$ and A, both of which are axioms, premises, or previously deduced statements, then we may deduce B. Resolution and natural deduction systems are both examples of first-order formal systems. (Manna (1974) presents examples of both.)

The means of implementing first-order formal systems on a computer are well-known. However, there are at least four difficulties with all first-order systems. First, as the number of assumptions grows or the length of the statement to be proved grows, the number of possibilities that must be examined to find a proof grows very rapidly. So much so, that the term "combinatorial explosion" is used to convey the rapid growth of possibilities.

Second it is a well-known, mathematically proved fact that any algorithm that can deduce all deducible statements of a first-order system must get into an infinite loop when given some statements not deducible in the first-order system. That is, the problem of ascertaining whether a statement in a first-order system is deducible, is undecidable, and is equivalent to the halting problem. Therefore, any algorithm must be artificially halted, leaving the user uncertain as to whether the statement is not deducible or simply needed more time.

A third difficulty is related to using theorem provers for a given application. Recall that the inference rules work in a pure pattern-matching way; the symbols or names for variables, constants, predicates, or functions have no significance. Hence, to use any facts in an application area, a user or programmer must translate the facts into the artificial language himself. This is not an easy task for people; overlooking any fact may render the desired statement undeducible, simply because the system was not supplied enough assumptions.

A fourth difficulty is that deductions in first-order systems are very hard for people to create or to understand. For instance, mathematicians themselves do not use first-order systems to prove their theorems. Rather, they freely mix mathematical notation and reasoning expressed in human languages in both the statement of a theorem and its proof. One might try to overcome the difficulty of combinatorial explosion by having a human interactively guide the theorem prover, so that only the most meaningful strategies are followed in a particular deduction. However, this fourth problem renders such human interaction difficult.

Many artificial intelligence (AI) researchers have turned to alternative models of reasoning, other than theorem provers. Such research is a core area of AI known as knowledge representation and inference. Several of the potential applications (discussed in later sections) of AI to software design validation use theorem proving. Consequently, research into alternatives to theorem proving, such as models of reasoning and knowledge representation and organization would be of great value in making these applications practical, provided of course, that such research was general enough to embrace the problems and needs in reasoning about software.

Subgoal analysis as a model of problem-solving, like theorem proving, is an aspect of several research areas to be discussed. Suppose one can model a problem as some goal to be achieved and a set of legitimate actions that may be performed to achieve any goal. Then, one can model problem-solving as searching for a sequence of actions that will achieve the goal. A well-known approach is to use some heuristics or rules of thumb for breaking goals into subgoals, such that if one finds a solution (sequence of actions) for each subgoal, then one can form a solution to the original goal from those solutions. This is the divide and conquer approach to solving a problem, and is a natural strategy to people. This method is general enough that theorem provers may be implemented this way.

The state of the art in subgoal analysis is that programming languages, such as QLISP (Wilber, 1976) and MICRO-PLANNER (Sussman, et. al., 1971), exist for people to conveniently and compactly express the goals, legitimate actions, and heuristics for any particular problem-solving application. As with theorem provers, facts of the application domain must be encoded, but this time as procedures representing legitimate actions, heuristics, and goals that are immediately solvable. What facts are included affects not only whether there is a solution but also the form of the solution. Combinatorial explosion can easily occur in such problem-solving systems. However, unlike first order predicate calculus, the programmer may use features of the programming language to group facts of knowledge and to suggest what strategies to try first, when to give up, etc., in an attempt to avoid combinatorial explosion. User interaction to guide a system is also possible. Such programming languages are one aspect of AI research in knowledge representation and models of reasoning.

We will use the terms "deduction system" and "theorem provers" to cover both traditional deduction in logic and subgoal analysis used to derive proofs of theorems.

We next consider the areas of AI research which offer payoff in software design validation: symbolic execution, automatic program verifiers, and automatic programming. For each area, we define it, give an example, indicate its potential in software design validation, present the state of the art, list obstacles to current technology, and attempt a prognosis for its development in software design validation, specifically suggesting research that could significantly aid in applying the technique to design.

4. SYMBOLIC EXECUTION OF PROGRAMS

The difference between symbolic execution of programs and standard program execution is analogous to the difference between algebraic manipulation and arithmetic. Rather than the programmer giving specific values as input, such as 1 or 3.14, symbols are given as input, such as b or c. The purpose is to compute the outputs as an algebraic expression of the input values, when possible. Consider the following trivial program segment, written in pidgin-Algol.

```
begin
read  x,y;
z:= x/2 +y
x:= x**2;
print  x, z
end
```

If the user signifies the symbolic input to x as b and y as c, symbolic execution indicates that the output for x is b , z is b/2 +c, and y would be c, if it were printed.

Of course, it is not possible to compute the symbolic outputs for general programs; otherwise, the halting problem would be solvable. If in a conditional statement if...then...else, the test depends upon the input values, then the symbolic executor cannot determine whether the then clause or else clause should be executed. Hence, there are two different program "paths" to investigate. Similarly, if the loop exit test depends on the symbolic inputs, a separate possibility or path must be investigated for each number of executions of the loop, 1,2,3, etc.

Assignment to arrays also creates different possible paths. In the program segment, A[I]:=0; A[J]:=1, reference to A[I] afterwards creates two different paths or

possibilities, because the value of A[I] is 1 if I=J and 0 otherwise.

Consequently, symbolic execution systems typically compute a set of possible paths; for each program path, the symbolic values of all program variables is computed, along with the conditions on the input which must be true for the path to be taken. Some systems also try to generate sample input values satisfying those path conditions. King (1975) and Boyer, et. al. (1975) provide several examples of symbolic execution systems. The user may interactively direct the system to examine particular paths. Alternatively, the user may place a bound on the number of loop iterations, and request that all paths be examined within those bounds.

The motivation for such systems is an automated aid to program testing, which enables one to systematically test a program on a class of inputs rather than individual cases. Symbolic execution aids one to explore the possible program paths in an orderly way, while demonstrating the computation in general rather than on a specific case.

Suppose one had a breadboard system corresponding to a design at design review. Then, a validation team could systematically explore the breadboard system, seeking points where the design does not conform to requirements.

The state of the art is such that symbolic execution systems exist for restricted subsets of programming languages, such as a small subset of PL/I, and a subset of FORTRAN. A typical restriction of such systems is that conditions in if...then...else be linear inequalities, e.g. $3x+2y \leq z$ but not $x^2 \leq z$ nor $xy \leq z$.

Several obstacles exist to this approach to program testing. First, the number of paths to be examined mounts very rapidly with nesting of loops and/or conditional statements. Assignment to arrays also increases the number of paths to be examined.

A major stumbling block is the use of procedures; systems currently must expand the procedure into paths for each procedure call, rather than once for all time. This results from using program execution as the paradigm, as opposed to mathematically proving properties of a program. Consequently, subroutines, in conjunction with the problem of nested loops and conditionals may potentially lead to a combinational explosion of paths.

Deduction systems are a component of symbolic execution systems, in general. They are used to rule out

impossible paths through the program. For instance, suppose x is an input variable never changed by the program. Then, in examining a partially developed path, if one has assumed $x<0$, any continuation of that path that would assume $x>0$ is impossible. Of course, all problems with deduction systems discussed previously are therefore inherited by symbolic execution. By restricting the language to tests which are linear inequalities, current systems avoid the problems of deduction systems, since linear programming and integer programming offer special purpose deduction systems without such problems.

Restrictions to cases solvable by linear programming and integer programming also enable test case generation for a given path. Test case generation in general has been proved unsolvable by any algorithm.

One other serious obstacle is dealing with data structures. The large body of knowledge about algebraic simplification gives much of the power of symbolic execution. There is no similar body of knowledge for simplification of expressions involving data structures for nonnumeric algorithms.

In summary, symbolic execution is a very natural and useful approach to program debugging. It is analogous to program testing. However, it cannot guarantee that a program is error-free. In fact, Howden (1976) proves that there can be no algorithm, that, given any program, will find a finite set of test cases guaranteeing absence of errors.

In order for symbolic execution to be useful in design validation, solutions to the obstacles of subroutine evaluation and algebraic manipulation of data structures seem essential.

5. AUTOMATIC PROGRAM VERIFICATION BY CORRECTNESS PROOFS

The goal of an automatic program verification system is to provide a proof that a program is correct. Such a system has three inputs: the program to be proved, its formal specification called the input and output assertions, and some intermediate assertions about the internal states of the program's computation. The output is either a complete, rigorous proof that the program is correct, or a message indicating that no proof was found. Let us abbreviate such a system and research pertaining to these systems as PP.

The input assertion, output assertion, and intermediate assertions are expressed in a formal language, most often first order predicate calculus. Proof of correctness is usually divided into two parts, called partial correctness and termination. Partial correctness proves that if input satisfies the input assertion, and if the program terminates, then the corresponding output satisfies the output assertion. Termination proves that, if the input satisfies the input assertion, then the program terminates.

PP offers to software design validation the possibility of rigorously proving that a design meets its functional requirements. If the formal specification of the design is procedural, then one could try to prove its correctness by PP. If the design specification is nonprocedural, then one might adapt PP to prove certain properties of the design, corresponding to its functional requirements.

In Figure 1, we have a program for findng the maximum of an array of N elements. (Assignment is indicated by ":=" throughout this paper.) For expository purposes in analyzing partial correctness, we exhibit an equivalent flowchart in figure 2.

```
begin
MAX:= A[1];
I:=2;
while I≤N do
   begin
   if A[I] > MAX then MAX:=A[I];
   I:=I+1
   end
end
```

Figure 1

In the flowchart, we have named certain points. B is the entry; D is the exit; and C is a point on the only loop in the flowchart. For every loop in a flowchart, the programmer must select any particular point, called a cutpoint. (For our convenience, we will call the entry and all exits cutpoints also.) For each cutpoint, the programmer must supply an assertion of the relations which hold between the program variables at that point. These are the intermediate assertions. In programming languages such as JOVIAL, FORTRAN, and PL/I, an intermediate assertion is necessary for every FOR, WHILE, or DO loop, and every labeled statement for which there is a corresponding GOTO.

For our example flowchart, the input assertion at B could be just $N \geq 1$. The output assertion at D is

$$(\forall j)\ (1 \leq j \leq N \supset A[j] \leq MAX).$$

Let us choose the intermediate assertion at C to be

$$(\forall j)\ (1 \leq j < I \supset A[j] \leq MAX).$$

This completes the input to a PP system.

PP systems generally have three components: a parser to check that syntax rules are satisfied, a verification condition generator, and a deduction system. The verification condition generator algorithmically splits the program into a finite number of paths and constructs lemmas called verification conditions, one for each path. If PP can prove each of the verification conditions, then the program has been proved partially correct.

The paths are defined to be all program execution paths from one cutpoint to another (including entry and exit points) such that the path contains no intervening cutpoints. For our example program, there are only four

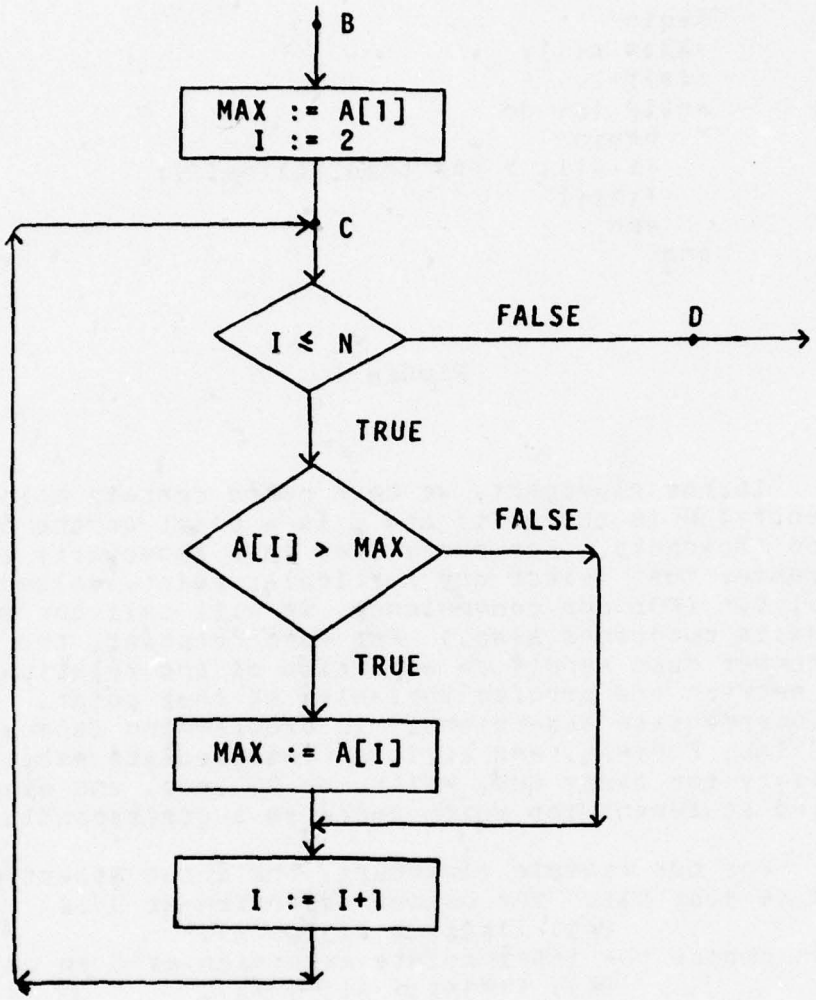


Figure 2

such paths: B to C, C to C when A[I] > MAX, C to C when A[I] ≤ MAX, and C to D. Each such path is just a simple sequence of program statements, which transform the state of the program. The lemma corresponding to each path is to prove that if the intermediate assertion Q holds at the beginning of the path, and if the path is taken, then the intermediate assertion R holds at the end of the path. Proving each such lemma proves partial correctness since any execution of the program going from entry to exit is guaranteed to satisfy the input-output formal specification.

However, one cannot simply try to prove Q⊃R for a given path, because the values of program variables do not correspond at the two different cutpoints. Consequently, PP must go forward along the path, symbolically executing the program path, and substituting the new variable values in Q, yielding Q'. If P is the condition that the path is taken, then the lemma or verification condition is given by Q'&P⊃R. The deduction system would be called to prove this formula in first order predicate calculus. (Some PP systems move backward along the path and substitute into R; however the purpose is the same conceptually. One simply substitutes the computed variable values in R, giving R', and proves Q&P⊃ R'.)

For our sample program, the verification conditions are as follows, using the backward substitution method:
for path B to C, N≥1⊃(∀j) (1≤j<2⊃A[j]≤A[1]);
for path C to C with A[I]>MAX, (∀j) (1≤j<I⊃A[j]≤MAX) & A[I]>MAX & I≤N⊃(∀j) (1≤j<I+1⊃A[j]≤A[I]);
path C to C with A[I]≤MAX, (∀j) (1≤j<I⊃A[j]≤MAX) & A[I]≤MAX & I≤N⊃(∀j) (1≤j<I+1⊃A[j]≤MAX); and
for path C to D, (∀j) (1≤j<I⊃A[j]≤MAX) & I>N ⊃ (∀j) (1≤j≤N⊃A[j]≤MAX).

Of course, as a PP system does substitution in either the forward or backward direction, the assertion will become quite complex as the new values corresponding to the right hand side of an assignment are substituted for the simple variable or array element on the left hand side. Consequently, algebraic simplification systems are embedded in PP.

Each verification condition must be proved by a deductive system which is part of PP.

Termination of programs is very difficult to deal with in mechanical verification systems, and is therefore omitted frequently. One scheme to prove termination of

programs is to use (usually different) intermediate assertions, generate verification conditions, and prove each of these in turn. Intermediate assertions for termination can be intuitively considered as asserting that each loop is executed only a finite number of times because each loop traversal significantly shortens the computation.

A very good introduction to partial correctness, verification conditions, and termination is presented in Manna (1974). A briefer presentation, along with a discussion of obstacles in PP research, appears in Manna and Waldinger (1976).

The state of the art in PP is represented by Good, et. al. (1975) and Elspas, et. al. (1977). Let us consider the Elspas system, which is sponsored by Rome Air Development Center. It proves programs of up to about 50 lines of JOVIAL code, depending heavily on interaction with the user. User interaction is necessary for the deduction system both to guide it (to avoid combinatorial explosion) and also to supply necessary assumptions. The assumptions correspond to facts about the application area and the input-output assertions of any subroutines used by the program. In this way, programs organized in a top-down structured programming manner may be proved top-down such that the structure of the proof corresponds to the hierarchical program structure.

Consequently, it is practical now using PP to prove the correctness of small, crucial algorithms. However, there are several obstacles to PP, which present serious difficulties, particularly for very large systems as commonly occur in practice.

First, correctness proofs do not guarantee complete reliability of a system, though they do rigorously demonstrate the logical and conceptual flawlessness of a system. This is simply an aspect of making a mathematical model and mathematical proof. Parnas (1977) has pointed out how such important reliability issues as software response to failure of a memory unit are ignored by correctness proofs. The finite precision of computer arithmetic and overflow conditions are frequently ignored because of the great complexity involved. Parallelism and nondeterminism have not been modelled well yet, nor have general side-effects.

Of course, all of the difficulties of deduction systems and theorem provers are also obstacles to PP

systems, since they are the crucial component in the proof process. Furthermore, undecidability and combinatorial explosion are characteristics of first order predicate calculus deduction systems. This has caused some computer scientists such as Dijkstra (1975) to wonder whether such automatic systems can ever prove large, practical programs.

User direction of the deduction system is used to alleviate combinatorial explosion in many systems. However, this places a very heavy burden on the person, for the reasoning is very low-level and machine-like, rather than the level at which he or she would reason mathematically about a program.

Another heavy demand on the person is supplying the intermediate assertions of the program. Expressing these in the formal language can be very difficult. Forgetting to include a seemingly insignificant fact in an assertion can cause the proof to fail. Because of this, some pioneering research has begun in automating the process of suggesting facts to be included as intermediate assertions. Dershowitz and Manna (1977), German and Wegbreit (1975), and Tamir (1976) report on such research.

Another serious difficulty to PP is what to do when the PP system fails to prove a program correct. There are several possible causes, and one is not sure which one or ones are responsible. The program may have one or more bugs which must be found. If the program is correct, the input assertion, output assertion, or intermediate assertions may be incorrect. Even if the assertions are correct, they may be incomplete, thereby causing the proof to fail. Assuming the PP system itself has been proved correct, undecidability of first-order predicate calculus guarantees that no PP system based on it can be halted without the possibility that a proof would eventually be found.

With all of these obstacles, what kind of prognosis can be made? Much progress has been made in the ten years since proving programs was first suggested. It is practical now to prove small programs, whose correctness is crucial or which are used as subroutines in numerous applications.

Some fundamental research, however, is needed. We quote from Elspas, et. al. (1977), page 5, "The bottleneck in developing an automatic verification technology is the development of more potent deductive mechanisms than are currently available." Particularly, models of reasoning that would closer approximate the level at which a person

reasons would be an important breakthrough. Such research is usually called inference techniques, models of thought, or knowledge representation and organization in artificial intelligence. This would lighten the burden on a user who must now interactively guide deduction systems.

Another way to radically change the task of the deduction system and of user interaction has been suggested by Wegbreit (1977). In this approach, the programmer gives additional information related to the intermediate assertions. This additional information, regarding the quantifiers "for all" and "there exists" enables a significantly simpler deduction mechanism to prove theorems. In fact, the simpler deduction system is decidable; that is, the deduction system will always halt and prove the theorem or show that it is not true. The additional information required of the programmer does not seem more difficult than the intermediate assertions, which he or she must supply already. Consequently, this appears to be a major breakthrough in correctness proofs, though further research is needed.

As a design validation tool, PP seems to be a long-term, distant goal. If automatic correctness proofs of designs were practical, the life cycle cost of software would be reduced, for vast numbers of design errors could be eliminated.

However, even now proofs by humans of certain key properties of a design are practical. For instance, Feiertag, et. al. (1977) discusses proving security of a software system design. A project in which several properties of a design were proved by people could offer a valuable experiment of whether design errors are significantly reduced, as one would expect.

An alternative to proving that a design meets its functional requirements is to provide a breadboard system for a particular design at design review for the user to validate that functional requirements are met. This leads us to consider automatic programming as a way of providing such a breadboard.

6. AUTOMATIC PROGRAMMING (AP)

We might define automatic programming as using the computer itself to perform significant stages of the creation of a computer program. Biermann (1976) presents a broad survey of the spectrum of research in this area. We will discuss two artificial intelligence approaches: the use of subgoal analysis and restricted domain AP systems.

The input to an AP system in both of these approaches is a nonprocedural description of the input-output behavior of a desired program; the AP system would output a program satisfying the requirements. By "nonprocedural description" we mean that the input-output behavior is defined, but no procedure for achieving that behavior has been given. First-order predicate calculus, SPECIAL (Roubine and Robinson, 1976), and WELLMADE (Boyd, 1977) are examples of nonprocedural languages for specifying input-output behavior of a program or set of programs.

Program generation does not occur in a vacuum; some knowledge about the application area is needed. Some approaches to AP presume the AP system builder included this knowledge a priori. Others presume the user supplies such knowledge interactively, perhaps as intermediate assertions the AP system might use.

The payoff in design validation would be the ability to quickly provide a breadboard system corresponding to a design. An Air Force user would be able to test the breadboard and experiment with it to determine both whether the design meets the functional requirements and whether the original requirements provide a satisfying system.

6.1. SUBGOAL ANALYSIS

Let us consider the use of subgoal analysis in automatic programming first. One way to view this is as an attempt to mechanize the reasoning involved in structured programming and top-down design. The WELLMADE design methodology of Honeywell (Boyd, 1977) has the same goal, but a person creates the design or program rather than an artificial intelligence system doing so.

Frequently, results from automatic correctness proof research are used in this approach to AP; a program segment can be derived by the system only if it can be proved to achieve intermediate assertions before and after it. Consequently, any derived program has a correctness proof with it.

The target language of a program being developed usually is a mini-language having simple, well-defined semantics, such as the structured programming constructs or pure LISP. The original goal of the system is the output assertion. It divides this into subgoals, using the heuristics of subgoal analysis. Each subgoal corresponds to deriving a segment of code or proving a theorem (which would prove that generation of a particular program construct is correct). When all subgoals have been reduced to goals which the system knows how to achieve, solutions of each subgoal can be combined to form the program. Of course, the input assertion may be used as an assumption. Creation of the intermediate assertions may be attempted by the system or given interactively by a person.

For example, suppose a subgoal of the system is Q, and suppose that an intermediate assertion is P (perhaps supplied by the user). A loop of the form while B do S can be used to change the state of the computation from P to Q if the AP system can prove that $P \& \neg B \supset Q$ and that P is an invariant under statement S.

Manna and Waldinger (1975, 1977) are examples of the state of the art in this research. (Waldinger and Levitt (1974) presents a program verification system based on subgoal analysis for deduction, and therefore represents the program correctness ideas that such AP systems are related to.) Only very small programs have been generated by such systems.

Just as with deduction systems, combinatorial explosion of the number of possibilities to be examined is a serious obstacle. Supplying knowledge of the application area is a major problem, and affects not only whether a solution will be found but also what type of solution will be found.

Since this research is still in its infancy, prognosis and analysis of major obstacles is somewhat

premature. This is fundamental research in general-purpose AP systems. Human interaction with such a system will probably always be a necessity. In fact, one of the benefits we expect from such research is to expose precisely what parts of the program creation process can be done by machine and what parts are the responsibility of a person. Manna and Waldinger (1975) state on page 205, "we hope we have managed to convey in this paper the promise of program synthesis, without giving the false impression that automatic synthesis is likely to be immediately practical."

6.2. RESTRICTED DOMAIN

An alternate approach to automatic programming is to select a particular application area and then to construct a special purpose AP system for generating programs in that area. This avoids most of the obstacles of the subgoal analysis approach and of program proof systems because deduction is replaced by special-purpose models of reasoning and knowledge in the application area. Let us call this approach "restricted domain" since it provides a special-purpose system for a given application area.

For a given application area, vast amounts of detailed, real-world knowledge may be encoded as data or procedures in the AP system. This knowledge can comprise heuristics about probable program structures useful for particular types of problems in the application. Rules for encoding efficient programs may also be included. Though the principles of building such AP systems, many of the rules used in them, and the structure of such AP systems would be the same from one application area to another, the vast amounts of detailed knowledge would be specific to each application area.

A major advantage of restricted domain systems is that the restricted domain and vast amounts of knowledge for it permit English as the language with which the user may describe the desired program. Therefore, nonprogrammers may easily use such a system to describe their problem and obtain a program for it.

Heidorn (1976) surveys research in this area. One completed prototype (Heidorn, 1972) wrote GPSS

programs for simulations involving simple queueing models. The nonprocedural description of the needed program is given in English. A dialog in English proceeds between man and machine to fill in information missing from the informal specification. A portion of a sample dialog is presented in Table 1; the complete dialog is roughly twice as long and appears in three tables, pages 303-305 of Heidorn (1976). A GPSS program was generated for the need identified in the dialog. Heidorn (1972, 1976) are good introductions to the state of the art.

1. when a vehicle arrives at a station, it leaves there immediately if the length of the line at a pump in the station is not less than 2.
2. 75 percent of the vehicles are cars and a fourth are trucks.
3. there is just 1 pump.
4. a simulation run time of 8 hours is desired.
5. ask questions for further info.
6. HOW OFTEN DO THE VEHICLES ARRIVE AT THE STATION?
7. the arrivals of vehicles are normally distributed with a mean of 8 minutes.
8. WHAT IS THE STANDARD DEVIATION OF THE NORMAL DISTRIBUTION?
9. 1 minute.
10. OTHERWISE, WHAT DO THE VEHICLES DO?
11. what?
12. AFTER ARRIVING AT THE STATION, IF THE LENGTH OF THE LINE AT THE PUMP IN THE STATION IS NOT LESS THAN 2, THE VEHICLE WILL LEAVE THE STATION. OTHERWISE, WHAT DO THE VEHICLES DO?
13. they are serviced.
14. WHERE ARE THE VEHICLES SERVICED?
15. at the pump.
16. HOW LONG ARE THE VEHICLES SERVICED AT THE PUMP IN THE STATION?
17. vehicle service times are exponential.

Table 1

(Lower case indicates user input. Upper case is computer response. This portion of dialog is from Heidor (1976), page 303.)

For this type of system to become practical, basic research on two major obstacles must succeed. The first is that domains for such systems are simply too restricted; the scope of these systems needs to be much broader. Research in knowledge representation and organization applied to AP is therefore essential.

Second, the English dialog capabilities of such systems should be much richer. Natural language processing research is needed particularly in richer models of dialog context and in providing meaningful responses to English that exceeds the system's understanding ability.

Our prognosis for domain restricted systems is very positive. We expect that such systems will become practical for certain application areas, probably within ten years. (General-purpose AP systems appear to be much farther away.) Application areas for which restricted domain AP systems will be practical are likely to have the following properties. 1) Relatively similar programs are frequently needed in the application area. 2) Formal input-output specification of the desired program is difficult or inconvenient. (The dialog facility is particularly appropriate for refining nebulous concepts of the user). 3) Nonprogrammers need the results of the program. (The English dialog facility is ideal for enabling nonprogrammers to get the needed program without the problems of using a programmer as an intermediary.) One further possibility of English input is to enable nonprogrammers to suggest strategies for writing the program. Nonprogrammers probably have a general idea of how the problem might be solved; such ideas provide a strategy which could greatly aid such AP systems.

Let us take a brief aside to clarify an apparent contradiction. In section 1, we argued strongly against design specifications expressed in English and for formal specification of designs. On the other hand, we have just extolled the possibility of English descriptions as input to restricted domain AP systems. These are not contradictory, for the user and needs in each case are vastly disparate. A design of a large system which will be implemented by 50 or more programmers demands the rigor,

completeness, and lack of ambiguity of a formal language, because varying interpretations of the design by the implementors bring serious, costly software errors. The designer using the formal language is an experienced, technical, software engineer, from whom such precise reasoning is expected. The user of a restricted domain system is not a technician used to expressing ideas in formal languages, and may use the AP system infrequently. Furthermore, he is an individual working alone; so, informal specification does not offer misunderstandings among a large staff. These differing needs naturally require differing solutions.

What is our prognosis for AP in software design validation? No research has begun on generating a software system corresponding to a formal design specification. However, some aspects of this problem make it more tractable than the general problem of AP. The breadboard system generated to conform to a design would be used by the ultimate end-user of the software system to experimentally validate that the functional requirements are met by the design. Since it is only a breadboard, its efficiency may largely be ignored. Furthermore, many aspects of the design, such as components for providing data structures, seem conceptually simpler to synthesize than many programs, such as numerical analysis routines. Therefore, the AP system should be considerably simpler than might otherwise be expected. Nevertheless, the state of the art in AP is probably not able to support this task yet. However, a sophisticated programming environment, mixing procedures generated by a limited AP system with procedures supplied by the designer, does seem possible. Its payoff in design validation and software life-cycle cost is potentially very great. We therefore recommend research and development in such a sophisticated programming environment using AP technology.

7. ALTERNATIVES

In this section we consider two alternatives to the previously described aids to design validation. They are alternatives in that they are

shorter term solutions and do not necessarily depend on artificial intelligence research.

For the goal of providing a breadboard quickly, one alternative to automatic programming is to implement the design in a very high level language. Those languages provide sophisticated data structures, such as sets, queues, stacks, and relational data bases, as primitives. Using these languages it is possible to build complex systems rapidly, though execution of the programs is very inefficient compared to execution in more standard languages. QLISP (Wilber, 1976) is an example of such a language. It is an open question whether one or two people working for a month or two could provide a breadboard for a design of a large software system. Actually trying this for a design of a large software system is needed. If it is possible, using a very high level language, validating a design would correspond to the Air Force user experimenting with the breadboard to determine whether the design meets its functional requirements.

A second alternative addresses the difficulty of creating complete, precise designs. A major problem is the vast detail which must be dealt with. Also, forming a complete, correct, formal specification in a formal language is a demanding task, (as is forming any complete, correct design, regardless of the language). For example, Gerhart and Yelowitz (1976) analyze several examples of published algorithms whose formal specification is incomplete or incorrect. One way to aid a designer to create complete, correct formal specifications is to provide a library or data base of formal specifications of components or modules common to many applications. Formal specifications of data structure modules are an example. Such a data base would enable the designer to use the work of others for low-level modules without having to re-create their formal specifications. This would aid a validation team as well, for properties previously proved about the module specification can be stored with it, and need not be proved again by the validation team. This idea was apparently first suggested by Engelman, et. al. (1975).

For such a data base or library of formal specifications to become a practical aid in design,

appropriate ways to characterize and summarize the properties of a module are needed. Otherwise, the amount of information and detail in the data base would overwhelm the designer and validation team.

Ways to describe and summarize a module's formal specification is particularly crucial if the data base is to be automated. Standard data base management systems and information retrieval systems are not appropriate since formal specifications are much richer semantically than simple facts or bibliographic references. We therefore recommend research into means of summarizing and characterizing formal specifications of modules, particularly so that eventual automation of data base searches for appropriate formal design specifications is possible.

In the final sections, our research recommendations are reviewed plus further conclusions.

8. CONCLUSIONS AND RECOMMENDATIONS

Formal specification of a design offers several significant advantages in design validation. It forces both designer and validation team to address detailed design issues which might be ignored otherwise, and which, if ignored, are likely to lead to software errors. Formal specification is a mathematical tool for precisely defining the function of a module and its interface to other modules. Since the design is in a formal language, automated aids are possible for design validation. In this paper, we have examined two possibilities: 1) proving that a design meets its functional requirements or 2) quickly providing a breadboard system with the design so that the design may be validated by testing.

In artificial intelligence, research in automatic program proving systems (PP) offers the potential of achieving (1). Proofs of certain properties of designs by people is already possible. We recommend that a large software system be developed, using human proofs that crucial properties are satisfied by the formally specified design; the purpose is to qualitatively check the impact of such proofs on design review and on software development. Rather than investigating automating such proofs,

some basic research in PP systems for programs (rather than designs) is still needed. In particular, alternatives to present deduction systems should be investigated, such as Weabreit's (1977) approach; also, research in models of thought closer to human levels of reasoning is needed.

Providing a breadboard system for Air Force users to employ in design validation should have very high payoff. One way to provide a breadboard rapidly enough to be used in design validation is offered in automatic programming. We recommend exploratory development of a programming environment which mixes present automatic programming technology and designer-supplied procedures for specifications beyond current automatic programming technology. No one has attempted such a programming environment thus far. A further possibility which should be investigated is creating a breadboard within a month or two by one or two programmers using a very high-level language such as QLISP.

Though not immediately applicable to design validation, we highly recommend research in "restricted domain" automatic programming systems, since that is the approach to automatic programming which should become practical first. Although it is very promising, basic research in two areas is still needed for it to become practical. Research in knowledge representation and organization is needed if the application area for which such a special purpose system is constructed is to be broad enough to be of practical value. Research enabling richer English dialog, effective response to incompletely understood English input, and user suggestions for program structure is needed as well.

One final area of research recommended would be preparatory to providing a data base of formal design specifications of commonly used modules. Such a library would be a great aid to designers so that the formal specifications need not be re-created for each system. The preparatory research would study what properties are important to distinguish and characterize one formal design from another for modules with similar purposes.

All of the research suggested has several characteristics in common. Each possesses very high

payoff potential for design and/or software development. All are long term goals where significant technological gaps exist. Hence, they are very exploratory in nature.

Therefore, the best course is to pursue many approaches simultaneously at a modest level of funding, recognizing that these are long term goals. Some will prove to be more fruitful than others, at which time more concentrated efforts will be needed

REFERENCES

Biermann, Alan W., "Approaches to Automatic Programming" in Advances in Computers, vol. 15, Academic Press, 1976.

Boehm, B.W., R.K. McClean, and D.B. Urfrig, "Some Experience with Automated Aids to the Design of Large-Scale Reliable Software," IEEE Transactions on Software Engineering, vol. SE-1, number 1, March, 1975.

Boyd, Donald L., "WELLMADE Design Methodology," Honeywell Productivity Symposium, April, 1977.

Boyer, Robert S., Bernard Elspas, and Karl N. Levitt, "SELECT -- A Formal System for Testing and Debugging Programs by Symbolic Execution," in International Conference on Reliable Software, SIGPLAN Notices, vol. 10, #6, June, 1975.

Dershowitz, Nachum and Zohar Manna "Automatic Program Annotation," unpublished, March, 1977.

Dijkstra, Edsger W., "Correctness Concerns and, Among Other Things, why They are Resented," International Conference on Reliable Software, SIGPLAN Notices, vol. 10, #6, June, 1975.

Elspas, B., K.E. Shostak, and J.M. Spitzen, "A Verification System for JOCIT/J3 Programs (Rugged Programming Environment-RPE/2) SRI Technical Report 5042-1 Computer Science Laboratory, Stanford Research Institute, Menlo Park, CA, April, 1977.

Engelman, C, E. A. Lamagna, and R.P. Witt, "Iterative Software Synthesis (ISS)," unpublished working paper, #20427 The Mitre Corporation, Bedford, Mass., November, 1975.

Feiertag, R.J., K.N. Levitt, and L. Robinson, "Proving Multilevel Security of a System Design," Technical Report CSL-48, Stanford Research Institute, Menlo Park, CA, April, 1977.

Gerhart, S.L. and L. Yelowitz, "Observations of Fallibility in Application of Modern Programming Methodologies," IEEE Transactions on Software Engineering, vol. SE-2, #3, September, 1976.

German, S.M. and B. Wegbreit., "A synthesizer of Inductive Assertions" IEEE Transactions on Software Engineering, vol. SE-1, #1, March, 1975.

Good, Donald I, Ralph L. London, and W. W. Bledsoe, "An Interactive Program Verification System," IEEE Transactions on Software Engineering, vol. SE-1, #1, March, 1975.

Heidorn, G. E., "Natural Language Inputs to a Simulation Programming System," Technical Report NPS-55HD72101A, Naval Postgraduate School, Monterey, CA, October, 1972.

Heidorn, G. E., "Automatic Programming Through Natural Language Dialogue: A Survey," IBM Journal of Research and Development, vol. 20, #4, July, 1976.

Howden, William E., "Reliability of the Path Analysis Testing Strategy," IEEE Transactions on Software Engineering, Vol. SE-2, #3, September, 1976.

King, James C., "A New Approach to Program Testing," Proceedings of the International Conference on Reliable Software, SIGPLAN Notices, vol. 10, #6, June, 1975.

Manna, Zohar, Mathematical Theory of Computation. New York: McGraw-Hill Book Company, 1974.

Manna, Zohar and Richard Waldinger, "Knowledge and Reasoning in Program Synthesis," Artificial Intelligence, vol. 6, 1975.

Manna, Zohar and Richard Waldinger, "The Logic of Computer Programming," unpublished draft Oct., 1976.

Manna, Zohar, and Richard Waldinger, "The Automatic Synthesis of Recursive Programs," to appear in Proceedings of The Fifth International Joint Conference on Artificial Intelligence, August, 1977.

Mendelson, E. Introduction to Mathematical Logic: Van Nostrand-Reinhold, Princeton, New Jersey, 1964.

Parnas, D. L., "A Technique for the Specification of Software Modules with Examples," CACM, vol. 15, #5, May, 1972 (a).

Parnas, D. L., "On the Criteria to be Used in Decomposing Systems into Modules," CACM, vol. 15, #12, December, 1972 (b).

Parnas, D. L. "The Influence of Software Structure on Reliability," In Raymond T. Yeh, (ed.). Current Trends in Programming Methodology, vol. 1, Software Specification and Design, Englewood Cliffs, NJ: Prentice-Hall, Inc., 1977.

Robinson, Lawrence, Karl N. Levitt, Peter G. Neumann, and Ashok R. Saxena, "A Formal Methodology for the Design of Operating System Software," In Raymond T. Yeh, (ed.) Current Trends in Programming Methodology, vol. 1, Software Specification and Design, Englewood Cliffs, NJ: Prentice-Hall, Inc., 1977.

Roubine, Olivier and Lawrence Robinson, SPECIAL Reference Manual, Technical Report CSG-45, Stanford Research Institute, Menlo Park, CA 94025, Aug., 1976.

Sussman, G.J., T. Winograd, and E. Charniak, "Micro Planner Reference Manual," Artificial Intelligence Memo No. 203A, Artificial Intelligence Laboratory, Massachusetts Institute of Technology, Cambridge, Mass. 1971.

Tamir, Moshe, "ADI: Automatic Derivation of Invariants," unpublished Master's Thesis, The Weizmann Institute of Science, Rehovot, Israel, August, 1976.

Waldinger, R. J. and K. N. Levitt, "Reasoning about Programs," Artificial Intelligence, vol. 5, #3, Fall, 1974.

Wegbreit, B., "Constructive Methods in Program Verification," IEEE Transactions on Software Engineering, vol. SE-3, #3, May, 1977.

Wilber, B. M., "A QLISP reference manual," Technical note, Stanford Research Institute, Menlo Park, CA, March, 1976.

1977 USAF-ASEE SUMMER FACULTY RESEARCH PROGRAM

Sponsored by

THE AIR FORCE OFFICE SCIENTIFIC RESEARCH

Conducted by

AUBURN UNIVERSITY AND OHIO STATE UNIVERSITY

PARTICIPANT'S FINAL REPORT

ENGINEERING ANALYSIS OF THE DYNAMICS AND CONTROL OF THE HUMAN CENTRIFUGE

TYPE A/F 37V-1

Prepared by:	Thomas J. Jones, Sc.D.
Academic Rank:	Associate Professor
Department and University:	Engineering Science Trinity University
Assignment:	
(Air Force Base)	Brooks AFB
(Laboratory)	USAF School of Aerospace Medicine
(Division)	Crew Technology Division
(Branch)	Biodynamics Branch
USAF Research Colleague:	Kent K. Gillingham, M.D., Ph.D.
Date:	July 15, 1977
Contract No.:	F44620-75-C-0031

ENGINEERING ANALYSIS OF THE DYNAMICS AND CONTROL OF THE HUMAN CENTRIFUGE

Type A/F 37V-1

by

T. J. Jones

Abstract

The type A/F 37V-1 Human Centrifuge at the USAF School of Aerospace Medicine at Brooks AFB is capable of G-onset rates of approximately two G per second. Control of the centrifuge is effected by an operator in an adjacent control room who monitors the G force on the centrifuge's gondola and makes appropriate adjustments to control the rpm of the centrifuge.

For certain purposes this centrifuge is lacking in two important aspects. First, lack of control of the G forces by the gondola's passenger himself distracts from the centrifuge's usefulness. This is true because for certain training programs it is desirable for the subject to have this control. Second, G onset rates not greatly exceeding two G per second are inadequate for simulation of G stress situations of interest to medical researchers.

The purpose of this study was therefore twofold.

1. Control

Investigate methods for achieving closed-loop control of the Human Centrifuge via commands from the pilot riding in the gondola.

2. Increased G-onset rates

Provide analysis of possible techniques for increasing the G-onset rate of the Human Centrifuge.

It is shown that a electronic control system can be implemented. Increasing G-onset rates is a more formidable task with a much greater cost.

Acknowledgment

The author is grateful to the Air Force AFOSR, ASEE, the USAF School of Aerospace Medicine, and Auburn University and Mr. Fred O'Brien for support of this summer research.

My special thanks to all the people at VNB at Brooks AFB and in particular to Dr. Kent Gillingham, my research colleague.

Introduction

The USAFSAM Human Centrifuge was designed to impose acceleratory G stress on a passive subject seated in a gondola at the end of a revolving arm. Control of the amount of G stress imposed is effected by an operator in a control room overlooking the centrifuge. Because of the high level of sustained and repetitive G forces which can be generated by current Air Force fighter aircraft, it is anticipated that a continuing requirement exists to train pilots to withstand these high G forces by proper use of anti-G straining maneuvers in conjunction with anti-G protective equipment. For the Human Centrifuge to provide an adequately realistic simulation of the environment of flight, the pilot to be trained must have control of the G force imposed, as he would through the control stick in an aircraft. In addition, for optimum simulation, the centrifuge should be capable of producing G onset rates on the order of from one G to six or eight G per second.

The principle of operation of the centrifuge is as follows: the normal acceleration felt by the subject riding in the gondola simulates G stresses due to aircraft maneuvers. From basic mechanics $a_n = r\omega^2$. Therefore, for a fixed radius r the G force is proportional to the square of the angular velocity, ω. Figure 1 shows the principal parts of the centrifuge.

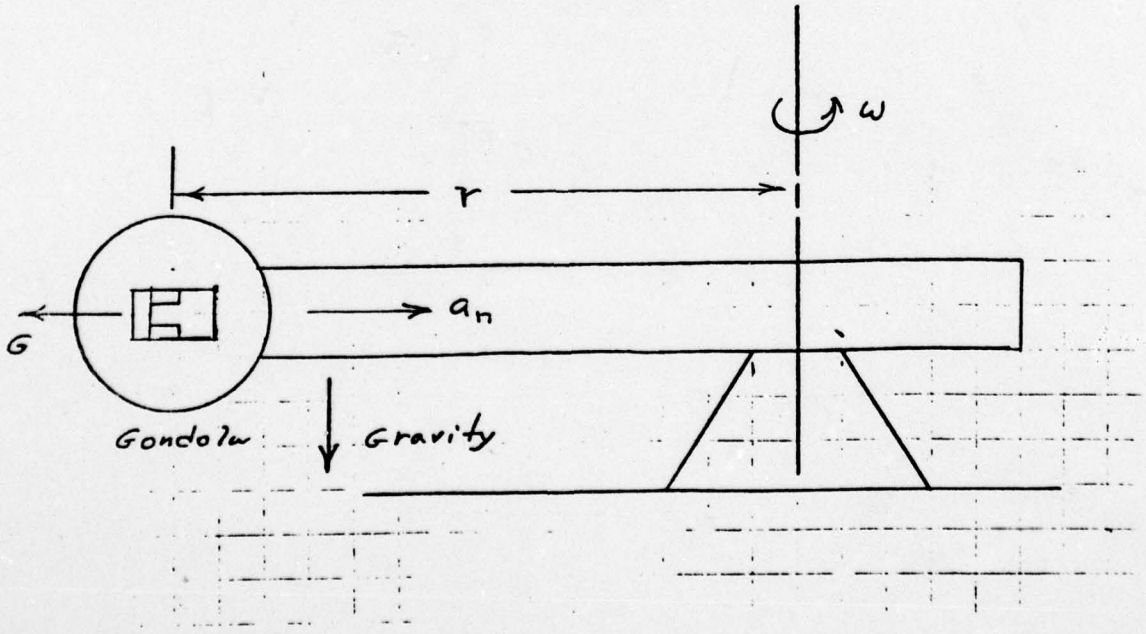


Figure 1. Diagram of the Human Centrifuge.

Control

The objective of this portion of the study was to consider methods for the pilot to control his own G forces. It turned out that this could not in any way be achieved simply by moving a duplicate of the existing control room controls into the gondola. As will be seen, the control room controls are too cumbersome for this purpose. Furthermore, they could not readily be adapted to an action similar to the control stick inputs of an airplane.

For pilot control, a closed-loop system is necessary such that a control stick position commands a certain G force. Analysis revealed that a Type 0 system employing either tachometer on accelerometer feedback relating normal acceleration (G force) to input voltage commands would be satisfactory. Normally this could be a simple velocity loop as shown in Figure 2.

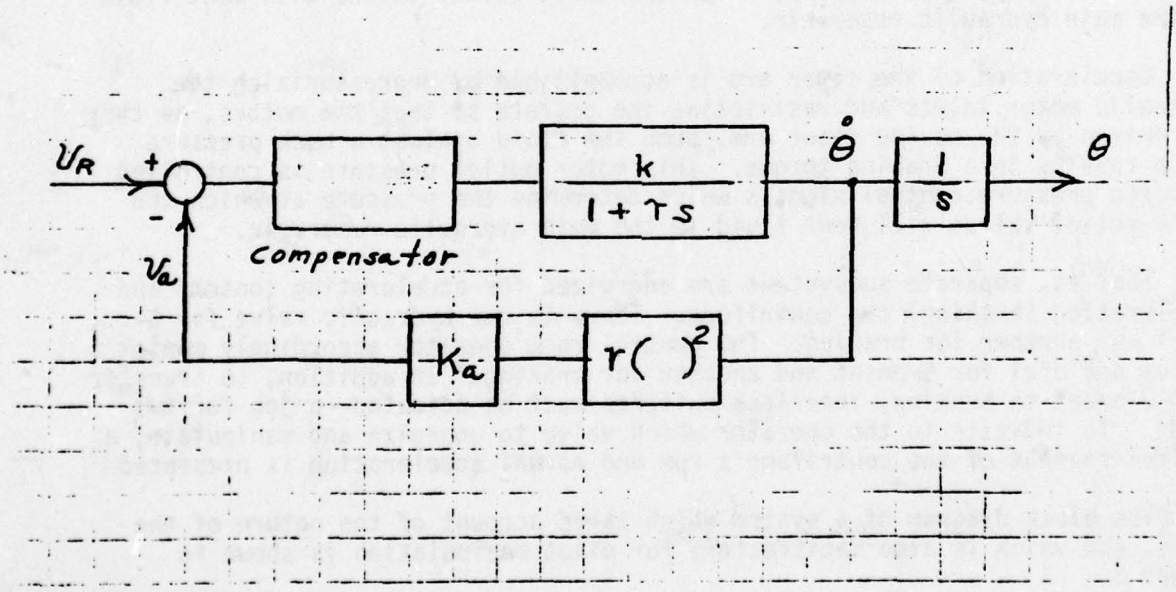


Figure 2. Possible configuration of a velocity loop for controlling .

From experimental data and calculations the approximate values for κ and τ were determined as:

κ = 0.0635 rad/sec/volt

τ = 0.6 sec.

Either a tachometer or an accelerometer is available for the feedback element.

A complicating element in the analysis however, was the nature of the existing design of the plant. Details of the plant's operation can be stated briefly as follows:

Five variable-volume pumps are driven by the four electric pump drive motors to supply pressurized fluid which turns the fluid motors. The fluid motors drive the rotor arm through gear trains. Motor speed, which is proportional to fluid flow through the motor, is adjusted by means of a servo control which varies the output volume of the pumps. When pump output exceeds motor flow, motor inlet pressure increases, producing higher motor torque. This motor inlet pressure is controlled by onset pressure control signals which determine the pressure at which the onset relief valves will vent fluid to the main hydraulic reservoir.

Deceleration of the rotor arm is accomplished by depressurizing the hydraulic motor inlets and restricting the outlets so that the motors, as they are driven by the moving rotor arm, pump the fluid against a back pressure which results in a braking torque. This motor outlet pressure is controlled by brake pressure control signals which determine the pressure at which the brake relief valves will vent fluid to the main hydraulic reservoir.

That is, separate subsystems are energized for accelerating (onset) and decelerating (braking) the centrifuge. There is one hydraulic valve for G-onset and another for braking. The control room operator accordingly manipulates one dial for G-onset and another for braking. In addition, to transfer from G onset to braking, interlock switches must be actuated--a job for two hands. To indicate to the operator which valve to energize and manipulate, a digital readout of the centrifuge's rpm and normal acceleration is presented.

The block diagram of a system which takes account of the nature of the plant, and which is also satisfactory for pilot manipulation is shown in Figure 3.

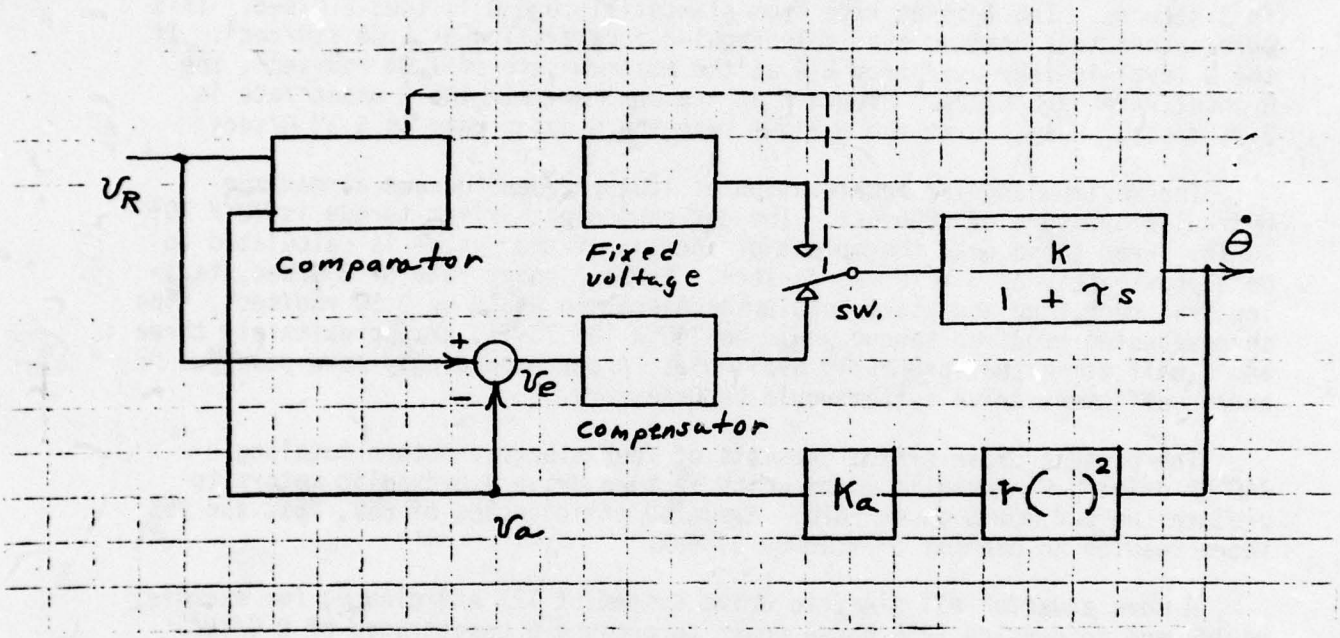


Figure 3. Possible configuration for a suitable control system for gondola pilot.

This is one of the simplest possible workable configurations. It was devised under the constraint of being maximally compatible with the existing equipment. Accelerometer feedback is employed only during G-onset, and a fixed braking is supplied for decelerating. In operation a control stick command produces a voltage, V_R, which in equilibrium is almost cancelled by from the feedback accelerometer. A small V_e is maintained in order for this Type 0 system to hold a constant angular velocity. When control stick pressure is relaxed, or partially relaxed, the comparator senses that $V_R < V_a$ and the switch is actuated to apply a fixed braking voltage. The schematic of an electronic system to accomplish the control functions, while interfacing with existing equipment, is shown in Appendix A.

Increased G Onset Rate

It is apparent that a significant G-onset rate increase would be costly. This is true because G-onset rates are limited by the available power from the system's output members.

Specifications on the present system indicate a capability of 0 G to 6 G in 3 seconds. The G-onset rate from standstill to 6 G is thus 2 G/sec. This corresponds to a maximum available angular acceleration of 1.04 rad/sec^2. If the G level is increased from 2 G at the maximum rate of 1.04 rad/sec^2, the G onset rate is 3 G/sec. From 4 G at the maximum rate the G onset rate is 3.96 G/sec. From 8 G at the maximum rate the G onset rate is 5.3] G/sec.

The maximum angular acceleration of 1.04 rad/sec^2 occurs at maximum hydraulic pressure of 5000 psi. The corresponding maximum torgue is 70 X 10^3 76-ft. From these data the moment of inertia of the system is calculated to be approximately 67.3 X 10^3 76-ft-sec^2. For a G onset rate of 8 G/sec starting from rest, the necessary angular acceleration would be 3.59 rad/sec^2. The corresponding required torque would be 242 X 10^3 76-ft, or approximately three and a half times that presently available. A correspondingly more powerful and/or efficient drive system would be necessary.

The present drive system consists of four electric motors totaling 740 HP driving 5 hydraulic pumps which in turn drive 4 hydraulic motors to produce the maximum G onset rate. Assuming efficiencies of 85%, 75%, and 75% there results an overall efficiency of 48%.

A more powerful all electric drive system of 72% efficiency, for example, would have to develop 1250 horse power to produce G onset rates of 8 G/sec.

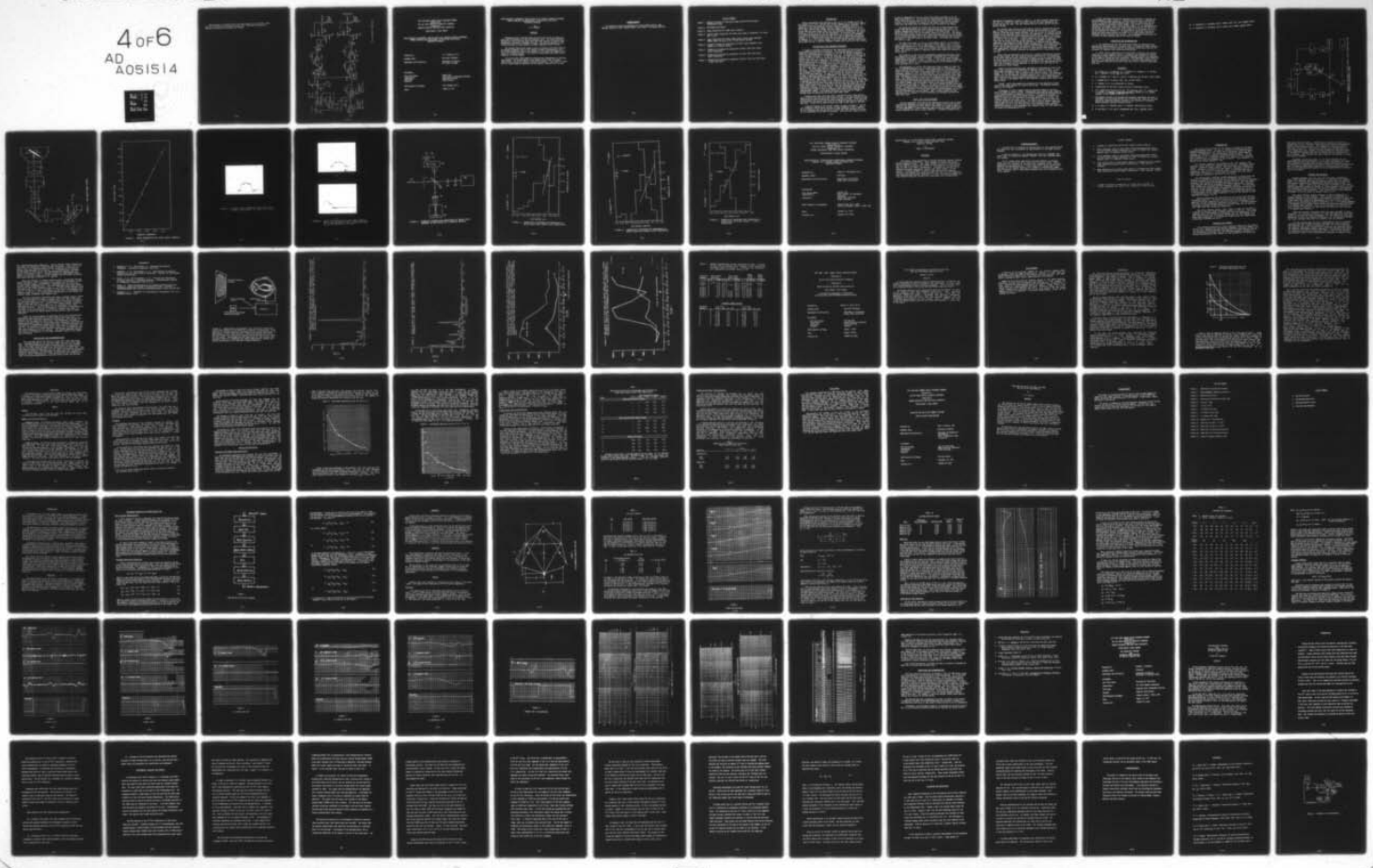
A preliminary study indicates that this could be achieved in a number of ways. Five gauged 250 horse power variable-speed SCR-controlled drive motors developing the required power would cost approximately $165,000. A single 1250 horse power motor would probably cost about $70,000. Modifications at an additional cost, possibly as high as $200,000, would have to be made to the centrifuge and building if the change to all-electric drive were to be accomplished. A possibly less expensive alternative would be the acquisition of unused motors from other government facilities.

Conclusions

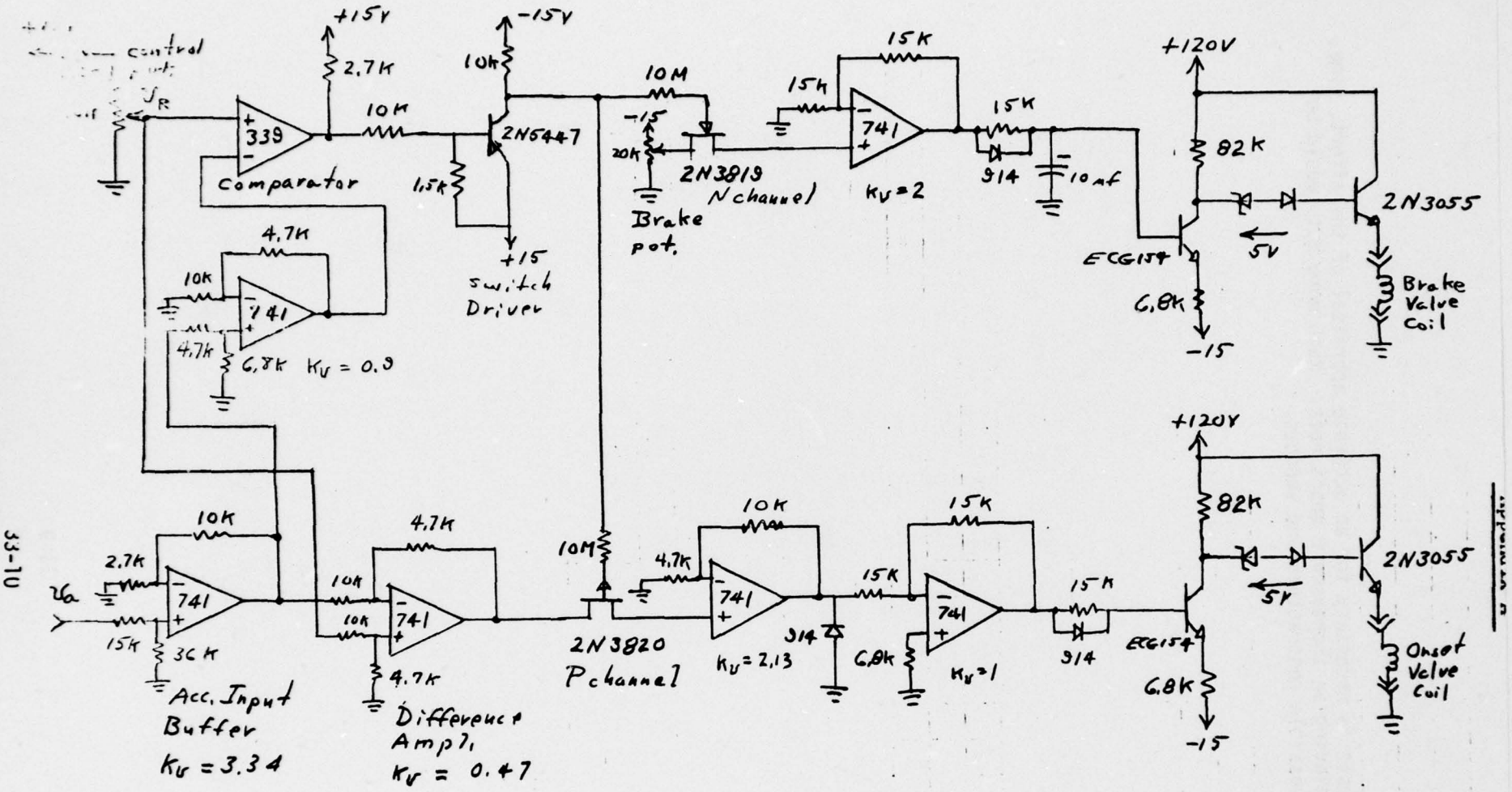
Fabrication and testing of the electronics for the control system (error detector, comparator, electronic switch, and interfacing circuits) have been started. Results to date indicate that this portion of the project should be continued through test runs on the centrifuge. It is anticipated that a suitable control system is practical and attainable.

AD-A051 514 AUBURN UNIV ALA SCHOOL OF ENGINEERING F/G 5/2
1977 USAF-ASEE SUMMER FACULTY RESEARCH PROGRAM. VOLUME II.(U)
SEP 77 J F O'BRIEN F44620-75-C-0031
UNCLASSIFIED AFOSR-TR-78-0349 NL

4 OF 6
AD
A051514



More analysis is necessary for an accurate appraisal of the effort, time, and cost of achieving an increased G onset rate. Much more data would be required from possible contractors and vendors.



ELECTRONIC CONTROL

1977 USAF-ASEE SUMMER FACULTY RESEARCH PROGRAM
sponsored by
THE AIR FORCE OFFICE OF SCIENTIFIC RESEARCH
conducted by
AUBURN UNIVERSITY AND OHIO STATE UNIVERSITY

PARTICIPANT'S FINAL REPORT

INVESTIGATION OF ULTRASHORT 1060 NM LASER PULSE INDUCED INTENSITY DEPENDENT DAMAGE PROCESSES AND DEVELOPMENT OF AN ON-LINE PULSE WIDTH MEASURING TECHNIQUE

Prepared by:	D. D. Venable, Ph.D.
Academic Rank:	Assistant Professor
Department and University:	Department of Physics St. Paul's College
Assignment:	
(Air Force Base)	Brooks AFB
(Laboratory)	USAF School of Aerospace Medicine
(Division)	Radiation Sciences
(Branch)	Laser Effects
USAF Research Colleague:	John Taboada, Ph.D.
Date:	August 5, 1977

INVESTIGATION OF ULTRASHORT 1060 NM LASER PULSE INDUCED INTENSITY DEPENDENT DAMAGE PROCESSES AND DEVELOPMENT OF AN ON-LINE PULSE WIDTH MEASURING TECHNIQUE

BY
D. D. VENABLE

ABSTRACT

Broadband visible light has been observed at the retina of Rhesus primates when irradiated with 1060 nm picosecond light. The energy threshold observed for this effect was much lower than that required to produce superbroadening or dielectric breakdown in water. The required energies at the retina were equal to those needed to produce immediate retinal lesions.

The retinal effects were found to occur at energies near those required to generate broadband light at the fiberous surface of photographic film. This latter effect was shown to be dependent on the number and temporal separation of irradiating pulses. This result is consistent with recent investigations of retinal damage.

An on-line pulse width measuring technique was implemented on a Nd:glass laser system. The system employs a 256 element diode array, two image intensifiers, and the two photon fluorescence technique. The system is linear over its entire range of operation and has temporal resolution of 0.4 psec.

ACKNOWLEDGEMENT

The research project was conducted as a joint effort with Dr. John Taboada, Physicist, Laser Effects Branch, USAF School of Aerospace Medicine.

LIST OF FIGURES

Figure 1. Schematic diagram of diode array image intensified two photon fluorescence setup.

Figure 2. TPF-diode array optics

Figure 3. Image intensified TPF diode array linearity

Figure 4. Typical image intensified TPF diode array signal, Pulsewidth = 4.5 psec. P/B = 2.5:1

Figure 5. Image intensified TPF diode arramy scans of main pulse separated from a satellite pulse by (a) 12 psec and (b) 30 psec

Figure 6. Schematic diagram for observation of white light produced in the region of a fiberous surface

Figure 7. Probability histogram for generation of white light with single pulse irradiation.

Figure 8. Probability histogram for generation of white light with single pulse irradiation.

Figure 9. Probability histogram for generation of white light with two pulses-12 psec separation.

INTRODUCTION

Recent experimental data obtained by Ham, et al (1), Goldman, et al (2), and Taboada, et al (3,4) indicate that retinal damages due to ultrashort 1060 nm radiation is possibly caused by nonlinear intensity dependent processes. A comparison of the retinal damage threshold (ED_{50}) observed by Ham, et al (1) for 35 psec 1060 nm single pulses and that obtained by Taboada, et al (4) for 6 psec 1060 nm single pulses shows that the integrated irradiance at the retina differ by a factor of 8 for the two experiments. On the other hand, the power flux densities observed for the two experiments are in much closer agreement. A value of 57 GW/cm^2 was observed by Ham, et al and 37 GW/cm^2 was observed by Taboada, et al. These results along with the multiple pulse effects observed by Taboada, et al (3) strongly suggest a nonlinear optical process scaling with pulse power and not a transient (thermal) process which scales with total energy.

ON-LINE PULSE WIDTH MEASURING TECHNIQUE

In order to accurately characterize the laser pulses (5) an on-line pulse width measuring technique was developed. The technique employed a Reticon RL256EC/17 photodiode array in conjunction with the two photon fluorescence (TPF) technique developed by Giordmaine, et al (6). A schematic diagram of the system is shown in Figure 1. In the TPF technique, the laser pulse is made to overlap with itself in a cell containing a dye solution with an absorption band at twice the laser frequency. The probability for two photon absorption in the overlap region is enhanced by 6 to 2 with respect to the background, for mode-locked pulses. A 5 μW argon laser beam (AL) was made to coincide with the Nd:glass radiation for alignment purposes. The argon beam's frequency 477 nm is such that a continuously fluorescence trace can be maintained in the dye cell. The diode array (DA) was located so that this trace was imaged onto the array. Since alignment must be precise, a system providing vernier motion was included on the array holder. Lateral motion of 0.05 mm and rotational motion of 1^o were required. In order to optimize the signal to noise ratio, a signal integration scheme was implemented. The signal from a photodiode (FM) monitoring the flashlamp fluorescence was used to send a read signal to the diode array control electronics (DAC). When this signal is received the array is scanned and the signal levels at all diodes are set to zero. The signal from a fast photomultiplier tube (PMT) used to monitor the laser output was used to send a second read pulse to a time delay (TD) and after the delay time to the diode array control. The delay time of 5 msec was determined by measuring the fluorescence lifetime of the TPF signal. The two read signals were obtained from the gated outputs of the oscilloscopes (OS1 and OS2) that displayed the photodetector signals. The delayed read pulse was also used to trigger a storage scope for monitoring the diode array signal (OS3).

A quarter wave plate ($\lambda/4$) was used in conjunction with a beam splitter (BS2) to obtain the two light paths in the TPF cell. The beam splitter was 50% transmitting and 50% reflecting for 1060 nm unpolarized light. Since the laser was polarized, the quarter wave plate was oriented to equalize the intensity in each path. A lens (L1) is used to focus the light at the center of the cell.

A detailed drawing of the system's optics is shown in Figure 2. The TPF cell contained 1.3×10^{-4} molar solution of Kodak Rhodamine 6G dye in ethanol. An f/1.3 Tektronix 125 lens was used to collect the light from the TPF trace. M is an adjustable mirror used for alignment. An 80 mm focal length lens (L2)

is used to compensate for the pin cushion distortion introduced by the two image intensifiers (II). The intensifiers are RCA 8605/V1 with resolution of 70 line pairs per mm and provide a gain of 3,000 optically coupled in tandem. Finally, a f/1.9 Tektronix C27 camera (C) was used to image the intensified signal onto the diode array (DA) mounted at the film plane of the camera.

The system was focused by rotating the array to an angle perpendicular to the trace and maximizing the signal received from the argon trace. The system's response was measured for a uniformly illuminated source. The response was found to be flat for the entire length of a 17 mm cell. The system TPF cell-to-oscilloscope readout scale factor was determined to be 2.02 psec/mm for an oscilloscope sweep rate of 50 μsec/division, by measuring the CRT imaged spacings of a 1 mm grid placed at the object plane. The diodes were scanned at a rate of 1 MHz.

The laser pulse width is given by $\Delta T(sec)=NMX/c$, where c is the speed of light in mm/sec, N is the index of refraction of the medium (1.35), M is the system magnification and X is the FWHM reading of the peak at the oscilloscope. The system's resolution was found to be limited by the diode width, 0.39 psec/diode. The system is capable of measuring laser pulse widths with energies as low as 300 μJ.

The linearity of the system was determined by measuring the array's output voltage for a diffuse surface uniformly illuminated with a light source attenuated by known neutral density filters. A plot of the output voltage versus relative intensity is shown in Figure 3. The square of the correlation coefficient is .989 for a linear regression analysis of the ordered pairs. The array saturates at 2.1 volts.

The photograph of a typical TPF diode array trace is shown in Figure 4. The oscilloscope parameters are 50 μsec/division and 0.5 volts/division. The camera used has unit magnification. The signal shown has a calculated pulse width of 4.5 psec and a peak to background ratio 2.5:1. There are several advantageous features in this improved technique. The array system gives immediate information concerning the laser pulse width and quality for every laser shot. The inherent signal to noise ratio is enhanced over photographic techniques, thus increasing the sensitivity of the detection signal. Because of this, more detailed information concerning pulse structure can be obtained. As a typical example, two photographs showing a main pulse accompanied by a satellite pulse are shown in Figure 5. The spacing between the main pulse and the satellite pulse shown in Figures 5A and 5B are 12 psec and 30 psec, respectively. It should be noted that these pulses cannot be resolved with the fastest oscilloscopes available. The three peaks shown in the photographs are due to multiple overlapping of the two pulses. Thus a valuable system has been developed that is capable of giving information on picosecond structure for every laser shot.

WHITE LIGHT YIELD EXPERIMENT

Several experiments investigating the generation of white light at rough surfaces were conducted and these results were compared with similar experiments for the generation of white light at the retina of a rhesus primate (7). In these experiments a fundus camera was used to view the target region while being irradiated with 1060 nm 6 psec radiation. A schematic diagram of the

experimental arrangement is shown in Figure 6. For the biological experiments, the lens (L1), water cell (WC), and target surface (TS) were replaced by the primate eye and the laser light was focused onto the retinal macular and paramacular regions.

The incident laser energy was calibrated by placing a Hadron Cone Calorimeter of known sensitivity at the target area and cross-calibrating a United Detector Technology Laser Energy Evaluator (LEE) (8) for use as a monitor. Energy calibration was performed before and after each experiment. An infrared 1060 nm bandpass filter (IBF) was placed immediately before the LEE detector to prevent interference from stray light. A neutral density filter (ND) was used to extend the range of the LEE detector. A beam splitter (BS) allowed for passage of light into the target area and the LEE detector. In addition, white light generated at the target was imaged through the beam splitter onto the viewing port of the fundus camera (FC) and visually observed (OB). An infrared blocking filter (IF) was used to protect the observer from reflected laser radiation. These experimental techniques are similar to those used by other groups (9). For all experiments the incident radiation was apertured with a 5 mm circular aperture (S).

White light was observed at the retina of a properly anesthetized and maintained rhesus monkey for laser energies greater than 25-35 μJ. The occurrence of the white light was highly statistical in nature but was not generated unless the laser energy was sufficient to produce immediate retinal lesions. No white light was observed at threshold energies for producing 1-24 hours delayed lesions. There was no evidence for the generation of the white light continuum at the ED_{50} value for retinal damage.

Several in-vitro experiments were conducted to investigate the role of the white light continuum in the production of immediate retinal lesions. In the experimental arrangement shown in Figure 6, the lens (L1) had a 35 mm focal length. A 1-cm long cell (WC) contained triple distilled water. The interactive surface (FS) was the backside of exposed polaroid film. The interaction of the laser light with the surface produced broadband white light at laser energies about a factor of two greater than of that required to produce white light at the rhesus retina.

Figures 7 and 8 show probability histograms for the production of white light at the target surface for single 6 psec pulses. The observed threshold was 68 μJ or 61 GW/cm^2.

Differences in retinal damage threshold apparently depend on the pulse width and number of pulses (2,3,4). Experimental investigations were conducted in our research effort to determine if similar effects could be observed for the generation of white light at the target surface. A probability histogram is shown in Figure 9 for irradiation by two pulses separated by 11.6 psec. The threshold value for this case, 16.5 μJ, is found to be a factor of four less than the threshold for single pulses. This result clearly indicates that the process does not scale with total energy in the picosecond regime. Additional experiments using 2, 4, and 13 pulses with 7 nsec separation were conducted. Within the accuracy of our experiments the threshold values for these cases were all found to be approximately 45 μJ.

A final experiment involved the observation of dielectric breakdown and superbroadening in water (9,10,11). Recently published data in references 10 and 11 indicate that superbroadening takes place at intensities near the values observed for threshold retinal damage. The results in reference 9 indicate that the power levels should be much higher. In our experimental observations, the target surface was removed from the water cell and the irradiated area was observed for white light production in the manner similar to the one discussed in reference 9. No production of continuum light was observed for laser pulse energies up to 800 μJ. For higher energy dielectric breakdown and self-focusing were observed. The corresponding intensities for the onset of these processes were on the order of $1TW/cm^2$.

CONCLUSIONS AND RECOMMENDATIONS

1. An inexpensive on-line TPF diode array system for picosecond pulse analysis has been provided for a Nd:glass laser. A theoretical study to determine multiple pulse structure from the corresponding diode array scan will be paramount for complete laser system characterization.

2. White light is generated at the retina when irradiated with energies sufficient to cause immediate lesions. Broadband light generated by surface interaction has been shown to be an intensity dependent process with dependence on the number of pulses and pulse separation. More meaningful results would be obtained if the experiments were repeated with a surface target material that more accurately emulates the retinal tissue and allows for precise theoretical modeling.

REFERENCES

1. W. T. Ham, Jr, H. A. Mueller, A. I. Goldman, B. E. Newman, L. M. Holland, and T. Kuwabara, Science 185, 362 (1974).

2. A. I. Goldman, W. T. Ham, Jr., and H. A. Mueller, Exp. Eye Res. 21:457 (1975).

3. J. Taboada and R. W. Ebbers, Appl. Opt. 14:1759 (1975).

4. J. Taboada, et al, to be submitted to Science.

5. A description of the laser system in given in references 3 and 4.

6. For a theoretical discussion on the TPF technique, see R. G. Greenhow and J. Schmidt, in Advances in Quantum Electronics, edited by D. W. Goodwin (Academic Press, London, 1974), Vol. 2.

7. The animals involved in this study were procured, maintained, and used in accordance with the Animal Welfare Act of 1970 and the 'Guide for the Care and Use of Laboratory Animals' prepared by the Institute of Laboratory Animal Resources, National Research Council.

8. J. A. Labo, D. R. Marston, and P. C. Laudieri, SAM-TR-74-50, (1974).

9. W. Lee Smith, P. Liu, and N. Bloembergen Phys. Rev, A 15:2396 (1977).

10. A. Penzkofer, A. Laubereau, and W. Kaiser, Phys. Rev. Lett. 31L863 (1973).

11. A. Penzkofer, A. Seilmeier, and W. Kaiser, Opt. Commun. 14:363 (1975).

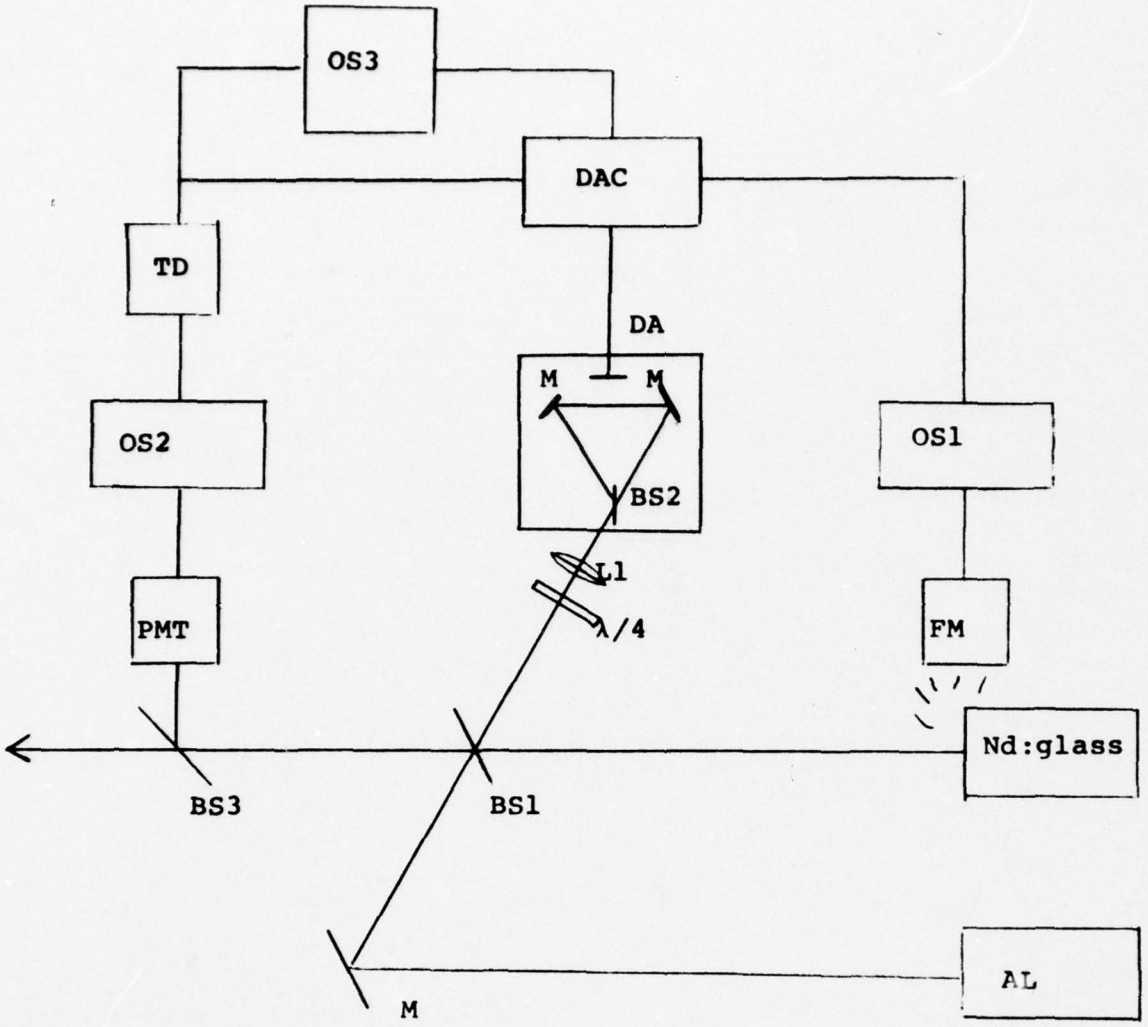


FIGURE 1: SCHEMATIC DIAGRAM OF DIODE ARRAY IMAGE INTENSIFIED TWO PHOTON FLUORESCENCE SETUP

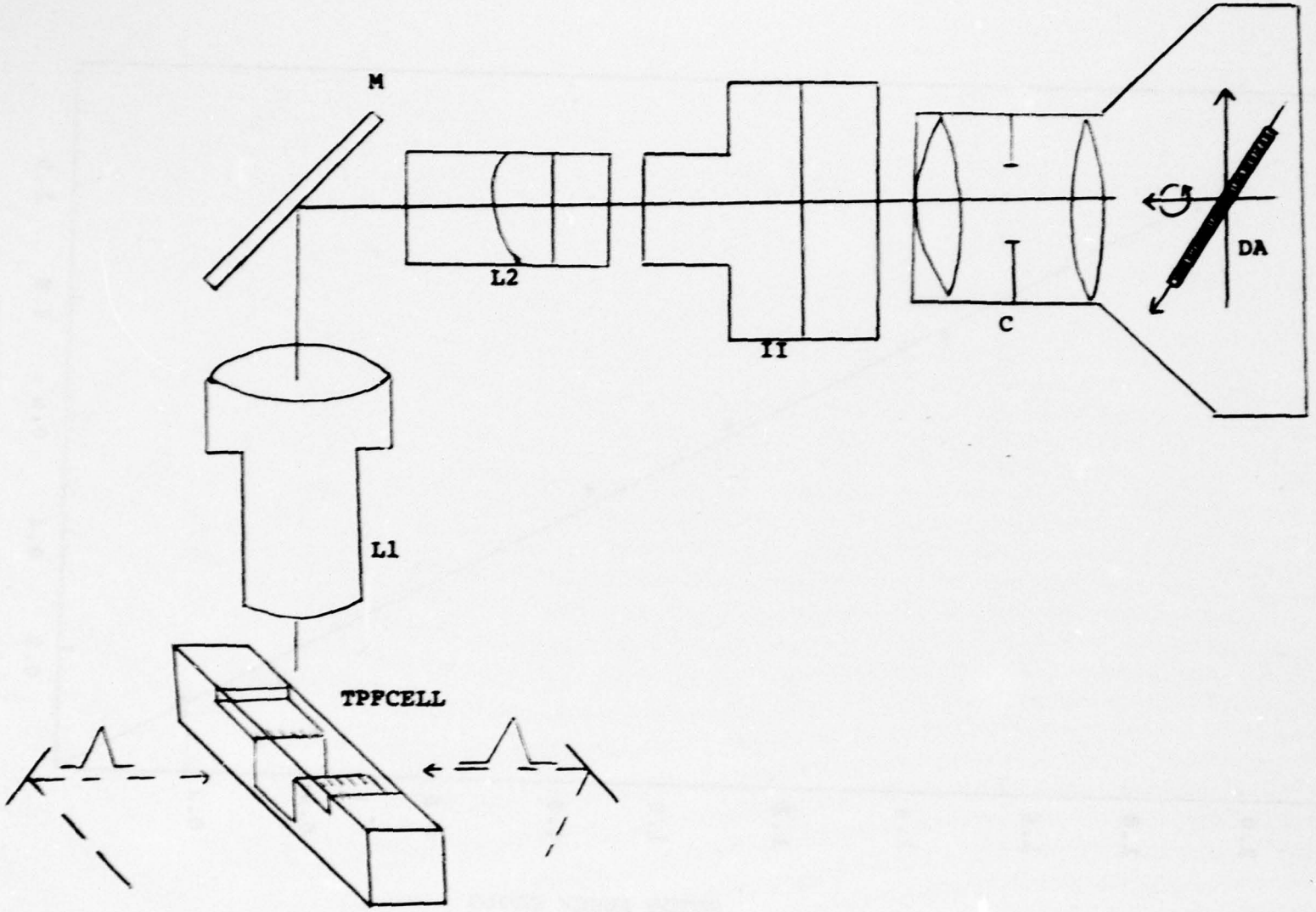


FIGURE 2: TPP- DIODE ARRAY OPTICS

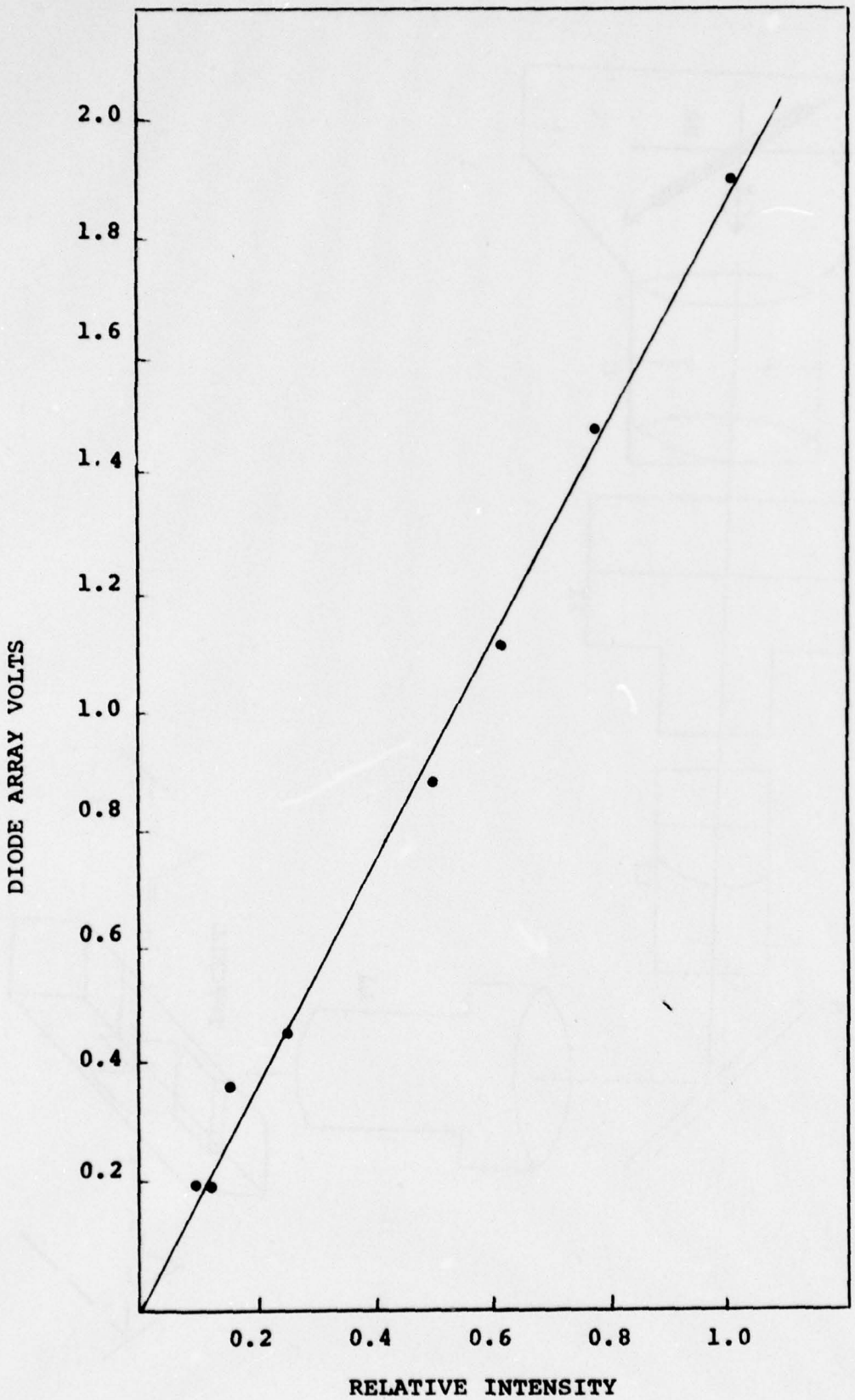


FIGURE 3: IMAGE INTENSIFIED TPF DIODE ARRAY LINEARITY

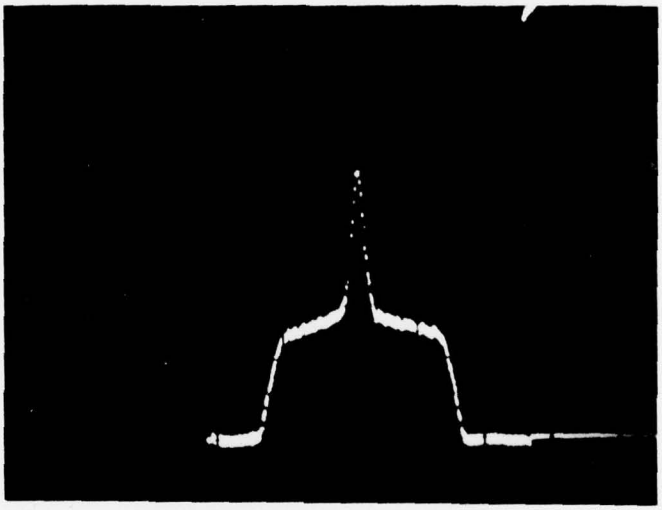
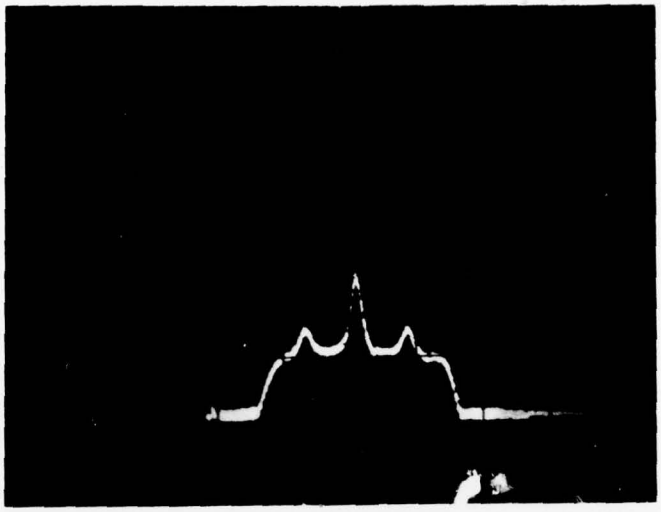
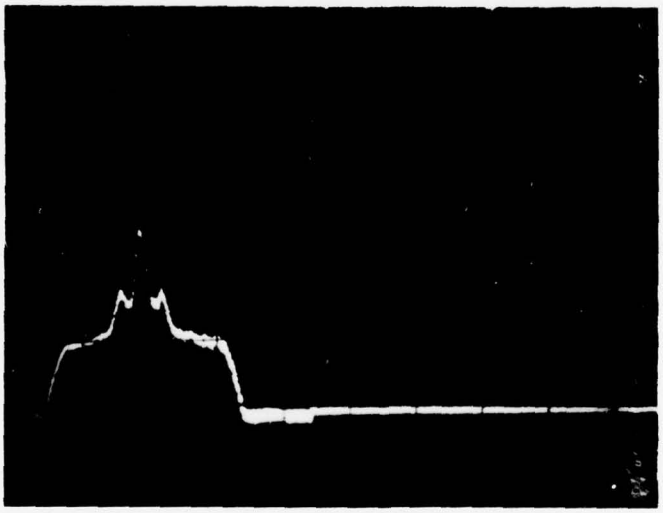


FIGURE 4. TYPICAL IMAGE INTENSIFIED TPF DIODE ARRAY SIGNAL, PULSE WIDTH = 4.5 PSEC. P/B = 2.5:1



B



A

FIGURE 5: IMAGE INTENSIFIED TPF DIODE ARRAY SCANS OF MAIN PULSE SEPARATED FROM A SATELLITE PULSE BY (A) 12 PSEC AND (B) 30 PSEC

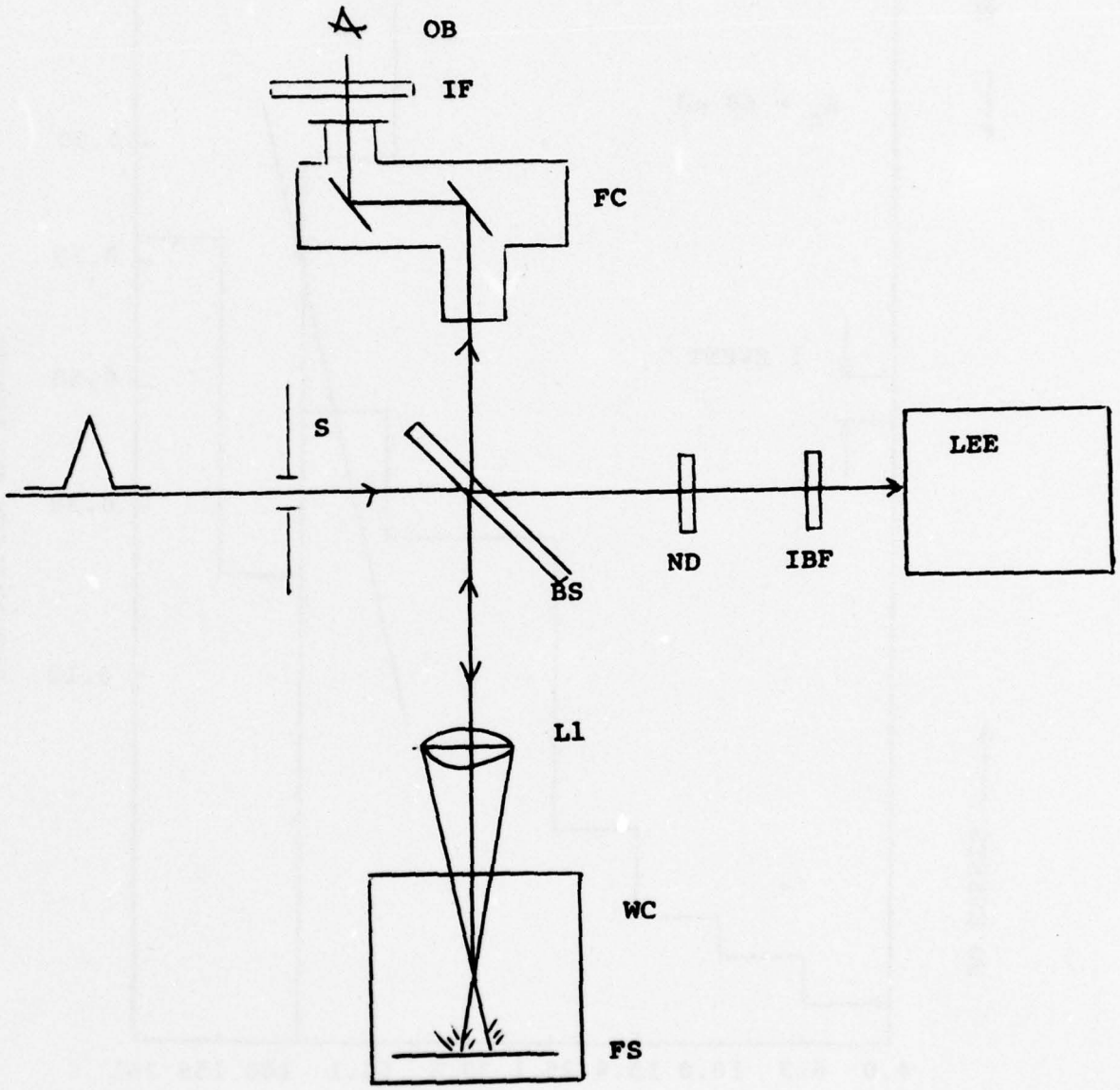


FIGURE 6: SCHEMATIC DIAGRAM FOR OBSERVATION OF WHITE LIGHT PRODUCED IN THE REGION OF A FIBEROUS SURFACE

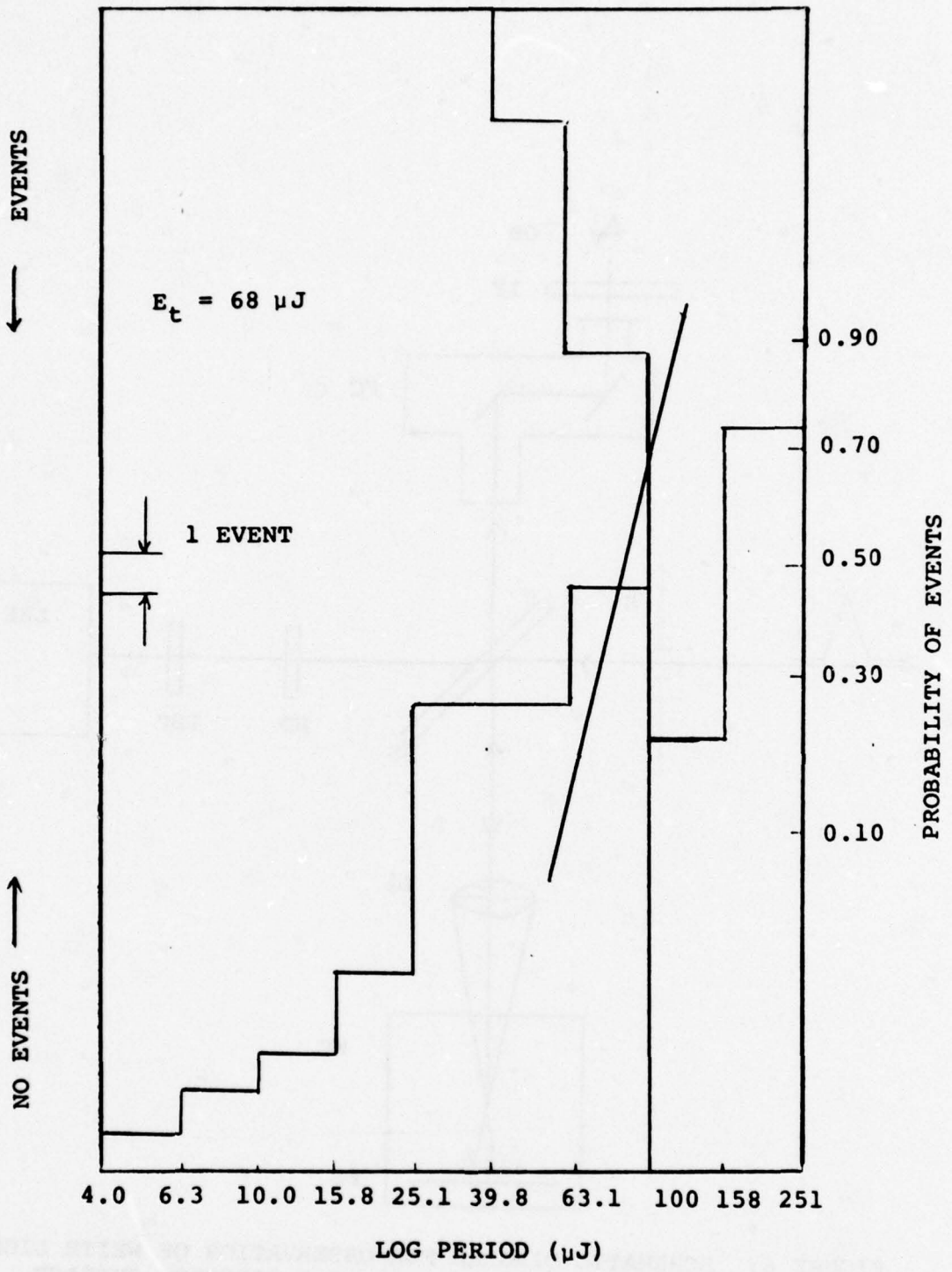


FIGURE 7. PROBABILITY HISTOGRAM FOR GENERATION OF WHITE LIGHT WITH SINGLE PULSE IRRADIATION.

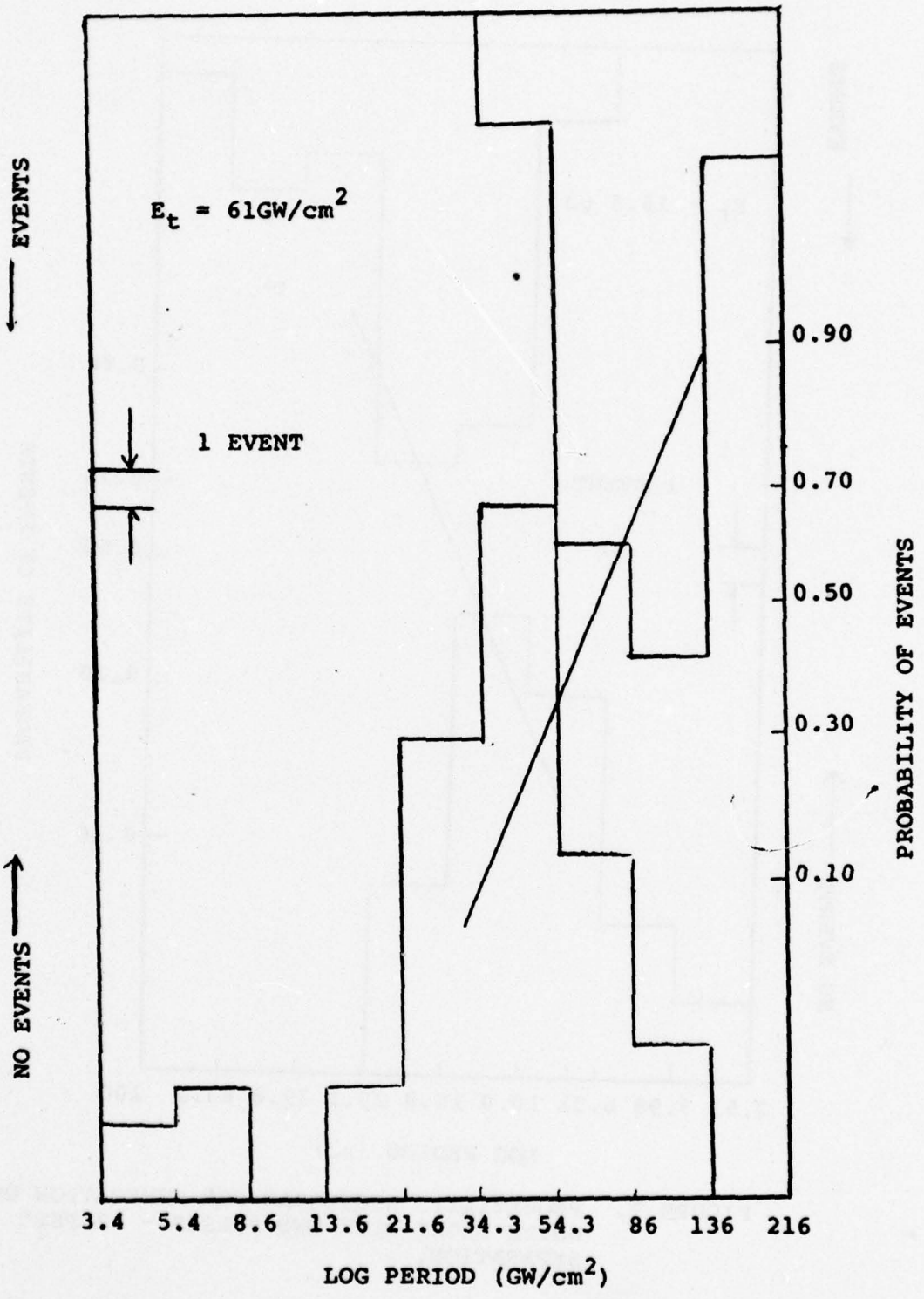


FIGURE 8. PROBABILITY HISTOGRAM FOR GENERATION OF WHITE LIGHT WITH SINGLE PULSE IRRADIATION.

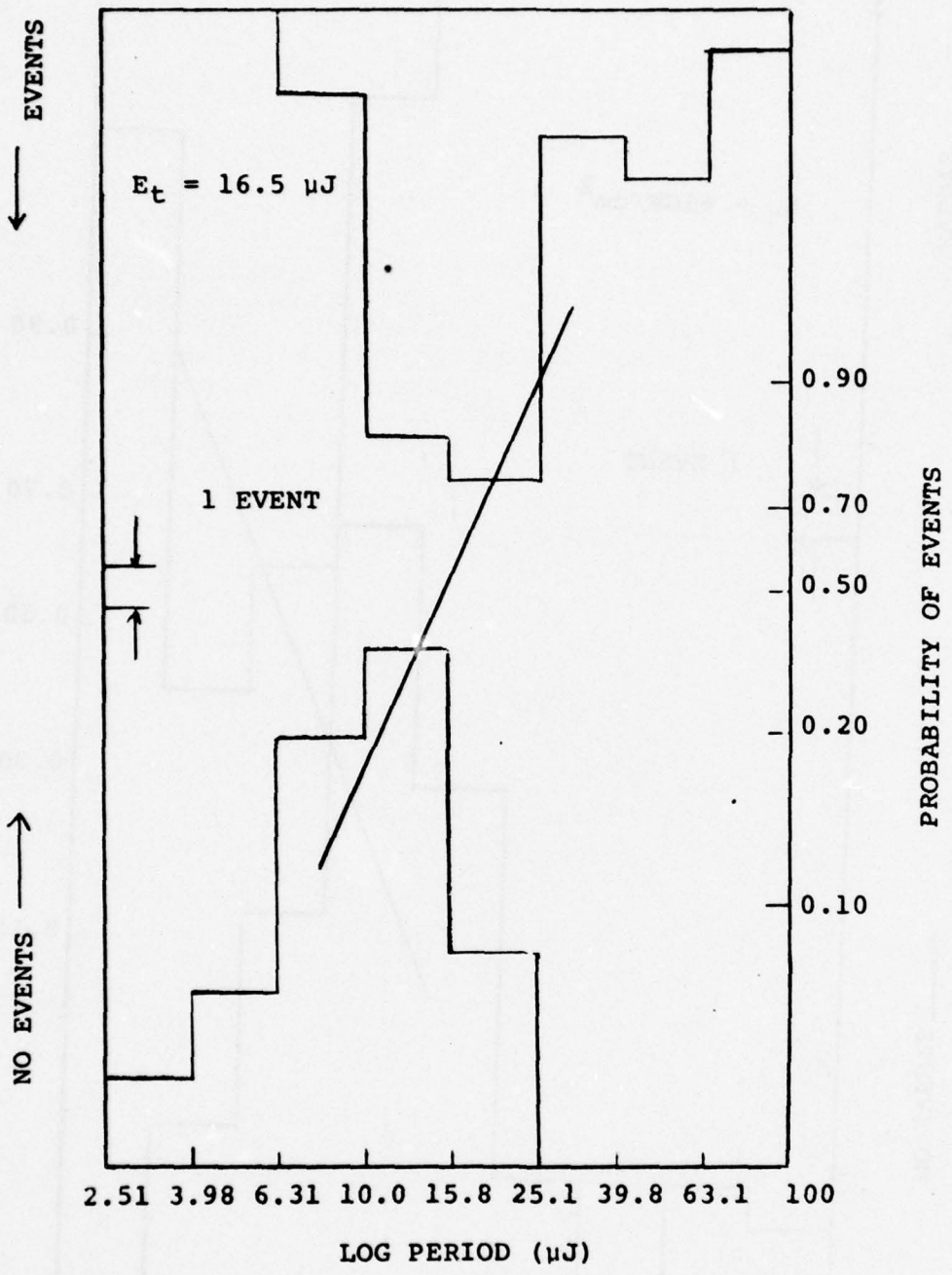


FIGURE 9. PROBABILITY HISTOGRAM FOR GENERATION OF WHITE LIGHT WITH TWO PULSES - 12 PSEC SEPARATION.

1977 USAF-ASEE SUMMER FACULTY RESEARCH PROGRAM
sponsored by
THE AIR FORCE OFFICE SCIENTIFIC RESEARCH
conducted by
AUBURN UNIVERSITY AND OHIO STATE UNIVERSITY

PARTICIPANT'S FINAL REPORT

APPLICATION OF A SPECIALIZED STATISTICAL COMPUTER PROGRAM, ALPHAF, TO A VISUAL EVOKED RESPONSE DATA ANALYSIS SYSTEM

Prepared by:	James M. Verlander Ph.D.
Academic Rank:	Lecturer
Department and University:	Department of Biology Texas A&M University
Assignment:	
(Air Force Base) (Laboratory)	Brooks AFB USAF School of Aerospace Medicine
(Division)	Radiation Sciences Laser Effects
USAF Research Colleagues:	Ralph Allen Ph.D. and William Gibbons, Major, USAF, BSC
Date:	August 12, 1977
Contract No.:	F44620-75-C-0031

APPLICATION OF A SPECIALIZED STATISTICAL COMPUTER PROGRAM, ALPHAF, TO A VISUAL EVOKED RESPONSE DATA ANALYSIS SYSTEM

by
JAMES M. VERLANDER

ABSTRACT

The brain, upon perceiving a visual stimulus, shows a change in its electrical activity. This change is called the Visual Evoked Response (VER). The Laser Effects Branch is planning to use the VER to observe any change in the function of the retina due to insult by laser irradiation. A method of statistically comparing evoked responses, before and after insult, is required. Program ALPHAF, a specialized statistical computer program, was tested and found suitable for the task of comparing two uncorrelated evoked responses. A task of placing ALPHAF into the USAFSAM computer library was undertaken and accomplished.

ACKNOWLEDGEMENTS

I would like to express my appreciation to the United States Air Force for its invitation to participate in the ASEE Faculty Program.

A word of thanks to the Biometrics Division, USAFSAM, for their help in inserting program "ALPHAF" into the USAFSAM computer system.

To Dr. Ralph Allen and Major William Gibbons, a special thank you for inviting me to join their research team. Their response to my working on the team was rewarding to me both personally and professionally. They taught me a great deal about the use of the evoked response as a means of monitoring human brain function, and I feel these lessons will be of benefit later in my career.

FIGURE LEGENDS

1. Diagram of recording set-up for visual evoked studies.

2. Power spectral plot of the human electroencephalogram showing the visual evoked response at 6 and 12 cycles per second. Target size, 30 degrees visual angle.

3. Power spectral plot of the human electroencephalogram showing the visual evoked response at 6 and 12 cycles per second. Target size, 3.5 degrees visual angle.

4. Time series plot of peak power found in consecutive five second time intervals during visual stimulation. Test subject: Gibbons

5. Time series plot of peak power found in consecutive five second time intervals during visual stimulation. Test subject: Norris

LIST OF TABLES

1. ALPHAF statistical comparison of third time interval of figure 4 against all other time intervals of that figure.

INTRODUCTION

The electrical activity of the brain is known as the electroencephalogram (EEG). It can be assumed to represent physiological functioning of the brain as it processes incoming data (sensory information), as it generates outgoing motor control information, or as it performs psychological activity. If the brain responds to a stimulus, there is a change in the outgoing EEG activity that is related to the stimulus. This response is called "the Evoked Response" (ER).

Any sensory modality can produce an ER, for example, the auditory sense (Hearing), visual sense (Vision), olfactory sense (Smell), chemical sense (Taste), and touch and pain (Somatosensory). Usually a stimulus is very short in duration and low in intensity, and its ER is likewise short in duration and low in amplitude; therefore it is not easy to discern the high amplitude ongoing background activity of the brain.

An investigator studying evoked responses is faced with the problem of extracting the ER out of the ongoing EEG activity. If the stimulus is held constant the resulting ER will be constant; however, the ongoing background activity is not. One can therefore extract the ER by a process of signal averaging, a method that yields the Averaged Evoked Response (AER)(5). If the stimulus is of the visual sense, the averaged response is called the Average Visual Evoked Response (AVER). This technique is utilized in most evoked response laboratories around the world; but a disadvantage of the AVER technique is one of EEG record length required to obtain the ER.

Another technique for analyzing the ER is the Fast Fourier Transform (FFT)(2). By use of the FFT, one may derive the power spectral density function of the ER; that is, the power of the EEG wave in any frequency spectrum of interest. The FFT analysis technique requires an EEG record of shorter time for ER extraction than does the averaging technique.

The Laser Effects Branch (RZL) began a study of the VER as a method to qualify laser-induced insults to the eye. The investigators were interested in evaluating the two techniques of ER data acquisition, the averaging method and the FFT method, and they were interested in a method of quantifying any significant differences between two ER's.

OBJECTIVE OF EFFORT

The primary objective of this research effort was the application of a specialized statistical computer program, ALPHAF, (3), to the data analysis system utilized by the Laser Effects Branch. The insertion of ALPHAF into the USAFSAM computer system required considerable team effort by the Biometrics Division and

the Laser Effects Branch. ALPHAF was originally written as a subroutine for the National Aeronautics and Space Administration VIBAN3 statistical program. The computers used for ALPHAF at NASA were the UNIVAC 1108 and the CYBER. The USAFSAM system utilizes an IBM 360. Along with the problem of different computer languages there arose a problem concerned with definition of "degree of freedom" derived by VIBAN3 and the USAFSAM computer system. The problem has been resolved and ALPHAF is ready for use at USAFSAM.

Secondary objectives were (1) to help evaluate the two techniques of ER investigation, (2) to help calibrate the Laser Lab's methods and techniques against other laboratories, i.e., participate in reproducing the results found by other laboratories, and (3) acquire additional training in electrophysiology that would be of professional benefit to this investigator's research area of interest.

METHODS AND RESULTS

ALPHAF provides the user with the following information about any frequency band of interest: (1) computes and reports power, (2) computes and reports average power, and (3) computes and reports statistical standardized normal distributions, a D statistic. Table 1 shows the application of ALPHAF to the power density spectral curves of Figure 4. Time interval three, at both the stimulus frequency and at the double frequency, was compared with the other time intervals. Time intervals are significantly different if the D value is greater than $\pm$ 1.96.

The Laser Effects Branch produces a VER by presenting a visual stimulus to the subject. This involves producing on a Hewlett-Packard display scope a grid pattern of vertical dark and light bars; the light bar becomes dark and the dark bar becomes light in an alternating fashion (Figure 1) (1). The visual pattern is produced with a square wave spatial distribution and alternated in a square wave fashion. This is to say that the intensity of light across a vertical bar and actual switching of bars occurs in a square wave fashion.

There are several variables that one must consider in this research: (1) the rate at which the light and dark bars alternate, known as the counter phase frequency, (2) the number of bars per degree of vision, the spatial frequency, (3) the contrast between the light and dark bars and (4) overall size of pattern.

In the initial part of this investigation both an averaged response and the ongoing EEG were recorded for later analysis. The protocol for a typical experiment was (1) to hold constant the spatial frequency, target size, contrast and intensity while (2) varying the counter phase frequency. The subject was asked to close his eyes for two minutes, then to look at the target. The subject's EEG's were continuously recorded on magnetic tape

for computerized data reduction. Thirty seconds after opening of the eyes, the averaging technique was initiated. Using this protocol, over 150 separate power density spectral plots were obtained from analysis of the data. It is impossible to present all of these in this text, but representative samples are presented in Figures 2 and 3. Another series of experiments were made in which the target size was changed and the other variables were held constant (Figures 2, 3, and 4).

When one observes a visual pattern with a particular counter phase frequency (CPF), the brain will respond by producing a VER at the counter phase (fundamental) frequency and at twice the counter phase frequency (1). Our investigations have also found this to be the case (Figures 2 and 3). We have also observed that the amplitude of the ER is related to the size of the target (Figures 2, 3, and 4). Thus, the Laser Lab was able to reproduce the results found by prior investigators pertaining to the effects of counter phase frequency and target size.

The VER literature indicates that when a person views a stimulus, the VER does not reach a steady state for some time; that is, the amplitude of the VER increases with time until reaching a steady state potential (4). We confirmed the increase in amplitude of the VER with time; however, the "steady state" potential was observed not to be constant, but to fluctuate with time (Figures 3 and 4). Such an observation indicates a requirement on the part of an investigator to carefully choose that point in time during which he should apply his particular type of data analysis.

There is a requirement to calibrate daily the physiological monitoring and data analysis system used by the Laser Lab. A Hewlett-Packard Gaussian random noise generator was studied and found to be suitable for this task. The generator provides a Pseudo-Gaussian signal of known amplitude, frequency and duration. The signal is reproduced identically every time the generator is cycled. By inputing the known signal into the ER monitoring system, the output of the data analysis system can be compared with the known parameters of the signal. The pesudo-gaussian generator was set to function in the same frequency band of the human EEG (0-30 cps).

CONCLUSIONS AND RECOMMENDATIONS

The original goals set forth in this work task have been met. Program ALPHAF is on-line and ready for use by the Laser Lab. The pseudo-gaussian signal has been used to test ALPHAF, and it has been found suitable for calibrating the monitoring and data analysis system that will be used by the Laser Lab. Our preliminary efforts indicate that the Laser Lab had the equipment, methods, techniques, and personnel to duplicate the investigations of other laboratories. This observation was essential before initiating experiments involving laser insult to the eye.

REFERENCES

1. Campbell, F. W., and Maffei, L. Contrast and Spatial Frequency. Scientific American, May 1974.

2. Campbell, F. W., and Robson, J. G. Application of Fourier Analysis to the Visibility of Gratings. Journal of Physiology, (1968) 197:551-566.

3. Fails, A. M., and Verlander, J. M. Statistical comparison of power spectra: A computer program. International Journal of Biomedical Computing (1977)8:1-10.

4. Regan, D. Some characteristics of average steady-state and transient responses evoked by modulated light. Electro-encephalography and Clinical Neurophysiology (1966) 20:238-248.

5. Thompson, R. F. Methods in Physiological Psychology: Vol 1-B. Academic Press, 1974.

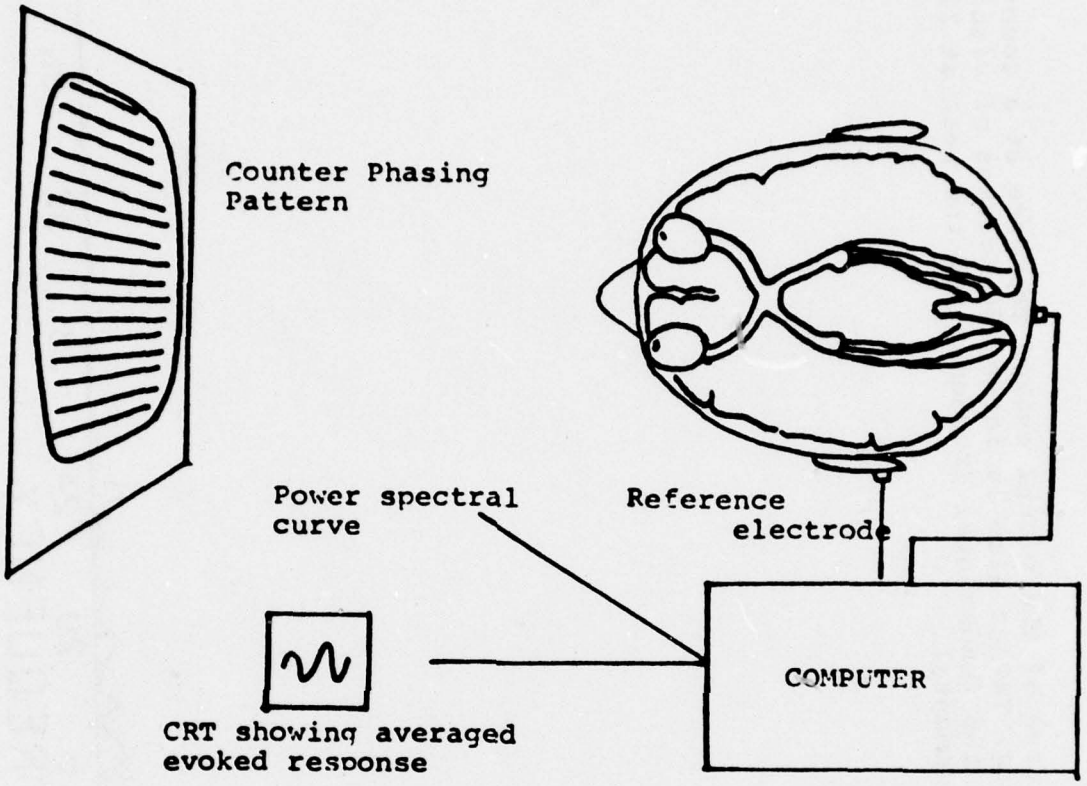


Figure 1. Experimental arrangement for recording electrical potentials evoked in the brain by a grating is depicted. When grating is counter phased a characteristic evoked potential is generated in the visual cortex. These potentials are small and are masked by electrical signals arriving from other parts of the brain. Electrodes on the head pick up the signals and transmit them to a computer for data reduction by either the signal averaging or FFT method of data analysis.

Figure 2. Power spectral curve of the visual evoked response at a counter phase frequency of 6 cps. Target size is large, 30 degrees of visual angle. Peak at 6 cps is the fundamental frequency and the peak at 12 cycles is at twice the fundamental.

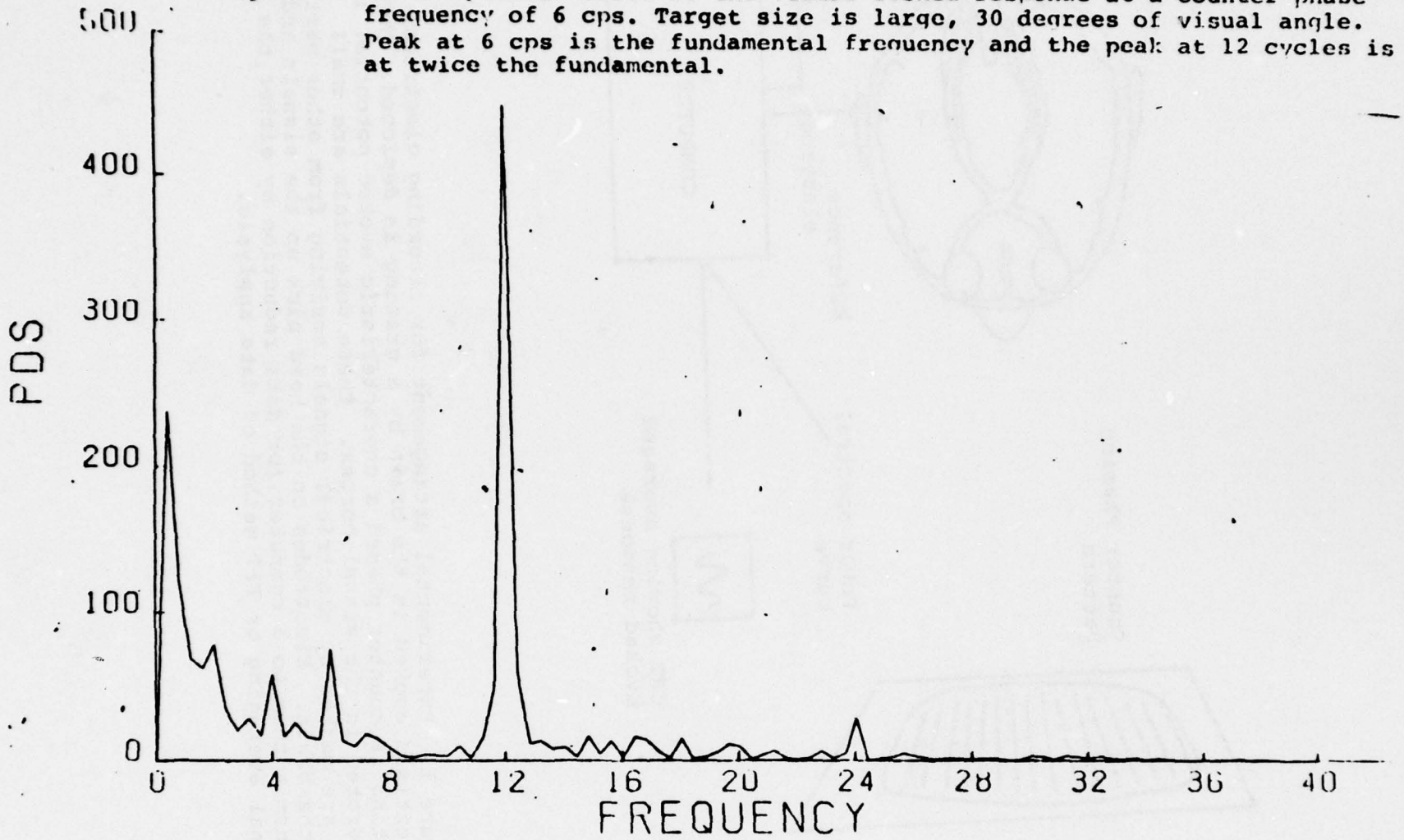


Figure 3. Power spectral curve of the visual evoked response at a counter phase frequency of 6 cps. Target size is small, 3.5 degrees of visual angle.

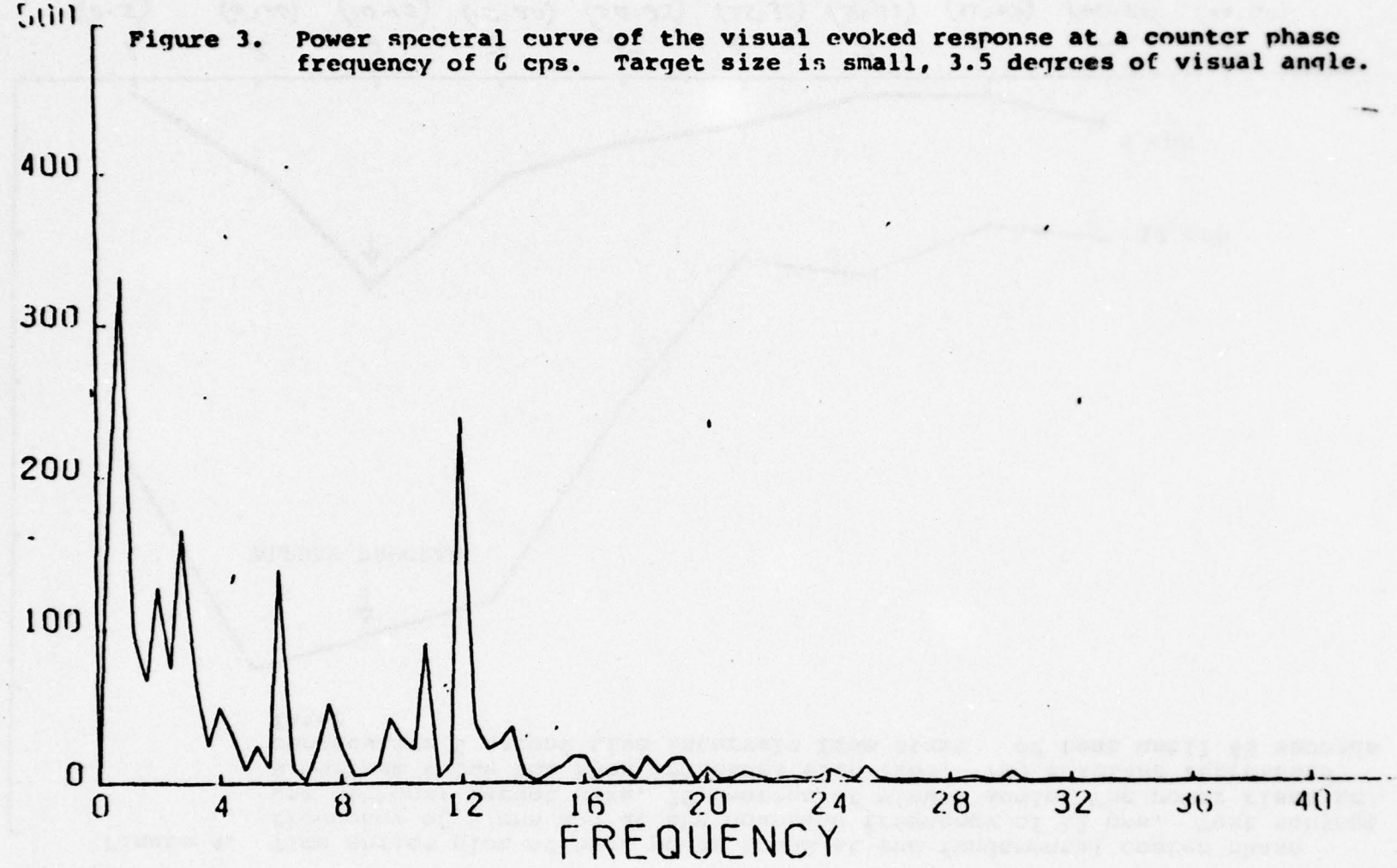


Figure 4. Time series plot of peak power found at the fundamental couter phase frequency of 6 cps and at the doubling frequency of 12 cps. Test subject was Gibbons; target size, 30 degrees of visual angle. The power rises to a maximum value but then decreases with time. The abscissa represents consecutive 5 second time intervals from start of test until 45 seconds later

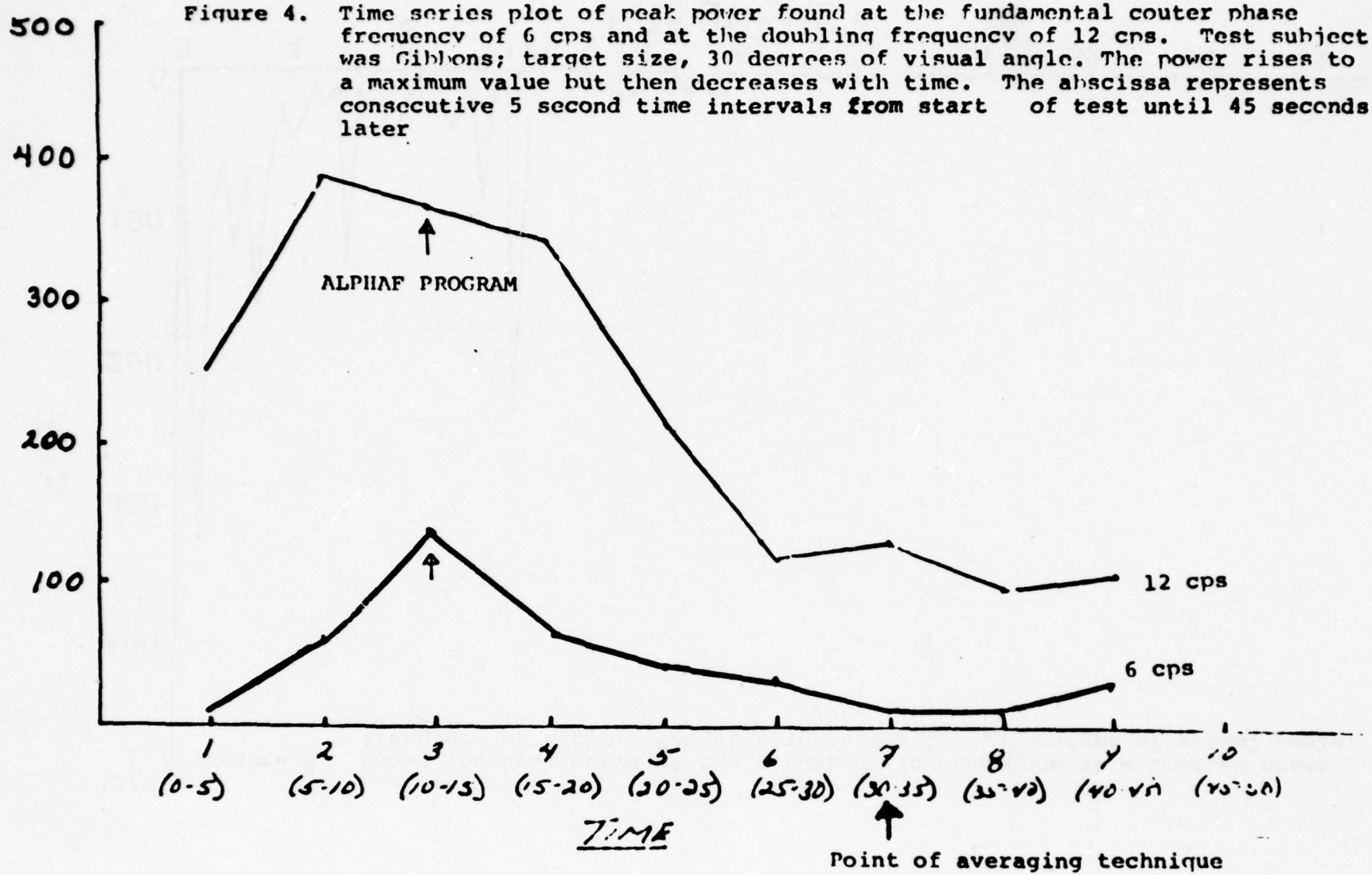


Figure 5. Time series plot of peak power for counter phase rate of 6 cps. Subject was Norris; target size, 30 degrees of visual angle. Subject shows a fluctuating power at both the fundamental and the doubling frequencies.

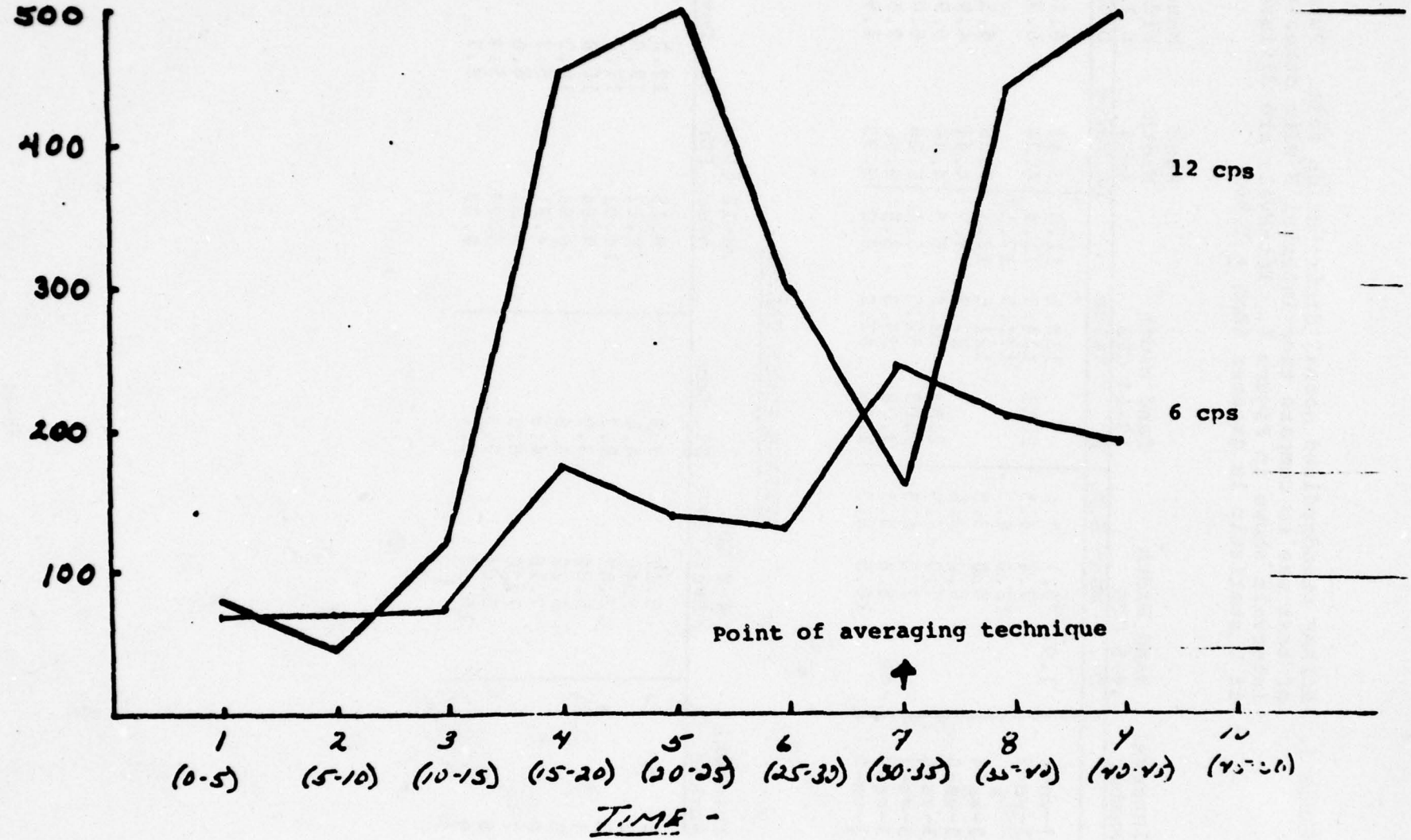


TABLE 1. ALPHAF standardized normal distribution test. Purpose of test was to compare time interval 3 with other time intervals shown in Figure 4. Intervals are different if D statistic is greater than ± 1.96.

Interval Number	Band Width 4-8 CPS			Band Width 10-14 CPS			Band Width 4-14	Band Width 0-14
	D	Mean	S.D.	D	Value		D Value	D Value
3-vs-1	1.97	5.1	3.5		119.1	11.9	3.43	6.26
3-vs-2		7.4	4.5	2.13	114.2	11.4	4.28	6.35
3		12.0	8.3		171.5	17.15		
3-vs-4		5.8	3.9		121.6	12.1	3.69	6.51
3-vs-5		6.2	3.6		87.7	8.7	4.44	4.94
3-vs-6		7.8	4.9	2.53	53.0	5.3	4.96	6.95
3-vs-7		7.3	6.5	3.03	51.5	5.1	6.26	6.08
3-vs-8		5.6	3.3	3.78	39.3	3.9	6.58	9.50
3-vs-9		10.5	8.9	2.99	62.2	6.2	2.93	4.99

AVERAGE POWER VALUES

Interval Number	4-8 CPS Aver. PWR	4-8 CPS St. Dev	8-12 CPS Aver. PWR	8-12 CPS St. Dev
1	5.17	3.5	9.15	12.2
2	7.40	4.5	9.12	19.0
3	12.07	8.3	14.01	17.4
4	5.80	3.9	9.68	16.8
5	6.22	3.6	6.98	10.5
6	7.18	4.9	4.91	5.7
7	7.30	6.5	4.91	6.6
8	5.64	3.3	3.94	5.4
9	10.53	8.9	8.23	8.7

1977 USAF - ASEE Summer Faculty Research Program

sponsored by

The Air Force Office Scientific Research

conducted by

Auburn University and Ohio State University

Participant's Final Report

Fixed Capacity Measurement of Attentional Load Using Dual-Task Performance Operating Curves

Prepared by:	Herbert A. Colle, Ph.D.
Academic Rank:	Associate Professor
Department and University:	Department of Psychology Wright State University
Assignment:	
(Air Force Base)	Williams AFB
(Laboratory)	Human Resources Laboratory
(Division)	Flying Training
(Branch)	Research
USAF Research Colleage	James F. Smith
Date:	August 19,1977
Contract No.	F44620-75-C-0031

Fixed Capacity Measurement of Attentional Load Using Dual-Task Performance Operating Curves

Herbert A. Colle

Abstract

A fixed attentional capacity theory of human attentional limitations was tested to determine its ability to predict the combination of tasks pilots could perform together without noticeable decrements. Three cognitive tasks and a simulated formation flying task were performed singly and in pairs.

Performance operating curves generated by dual-task performance on pairs of the cognitive tasks were estimated successfully. Their equivalent attentional demands were found. The flying task had a very small but measurable attentional demand as determined from dual-task performance. Performance on the cognitive tasks that were performed together with the flying task were consistant with the capacity theory. However, the small attentional demand needed to perform the flying task prevented a strong test of the theory.

Acknowledgment

I thank the Air Force Systems Command for its financial support which allowed me to spend the summer conducting this research. I thank ASEE and Auburn University, especially Mr. Fred O'Brian, Mr. Paul Thurstone, and Major David E. England for their careful administration of the project.

Members of the Flying Training Research Branch of the Human Resources Laboratory, Williams Air Force Base were most generous in their support and help. They made the summer enjoyable as well as productive. In particular, I thank Colonel J. D. Boren Commander HRL/FT, Mr. James F. Smith, Branch Chief and Mr. Gary Reid, Basic Research Task Leader. My special thanks go to Dr. Joseph C. DeMaio who collaborated with me on this project and who helped immeasurably with its execution. I also thank Airman Randy G. Cline for his repeated assistance.

Introduction

The limitations imposed on human performance by attentional capabilities have engendered several attempts to describe the nature of this attentional system (Broadbent, 1958: Deutsch & Deutsch, 1963; Kahneman, 1973; Mornay, Norman, 1968). In complex human activities, such as piloting an aircraft, these limitations may become severe, leading to substantial performance decrements. It would be useful to be able to measure the attentional demand made by a task or set of tasks so that the compatibility of combinations of them could be predicted and used to aid in the design of instrument systems and flight procedures that optimize performance while minimizing the likelihood of producing a critical overload. It would also be desirable to have a good measure of attentional demand in order to determine when student pilots had sufficient attentional resources to advance to a more demanding part of the syllabus.

Recently, Norman & Bobrow (1975, 1976) described a fixed capacity theory of attentional limitation which, if proven reasonably accurate, could be used to provide measures of attentional demand. The theory predicts that every person has a maximum attentional capacity, r_m, and that each task an individual is required to perform draws on this attentional reservoir. Provided that there is no structural interference between them, two tasks will be compatible with one another if the sum of the attentional resources required by each one is less than or equal to r_m, i.e. $r_1 + r_2 \leq r_m$. Two tasks satisfying this condition will be called capacity-compatible. Thus a task has a single number r_i that characterizes its demand, regardless of the component subprocesses utilized to perform the task.

At present, there is no direct measure of the demand, r_i required by a task at a given level of performances. For each task, there is assumed to be a weakly monotone relationship between r and the level of task performance. If r and task performance increase together, task performances is said to be resource-limited in that range. The existence of resource-limited performance provides a usable method for testing the assumptions of the fixed capacity theory and, if the test is successful, a method for constructing a metric to measure attentional demand.

If two tasks are resource-limited, then increasing the attentional resources devoted to task 1, r_1, should increase its performance without affecting task 2 until $r_1 + r_2 = rm$. Thereafter, task 2 performance should decrease as task 1 increases. This performance trade off is called a performance operating curve POC. Figure 1 shows two hypothetical performance operating curves. In the range where $r_2 = r_m - r_1$ a POC can be represented by the parametric equation $P_1 = f(r)$, $P_2 = g(r_m - r)$, where P_1, P_2 denote task 1 and 2 performances and f, g are performance resource functions.

Figure 1. Performance Operating Curves and Performance Equivalence Points

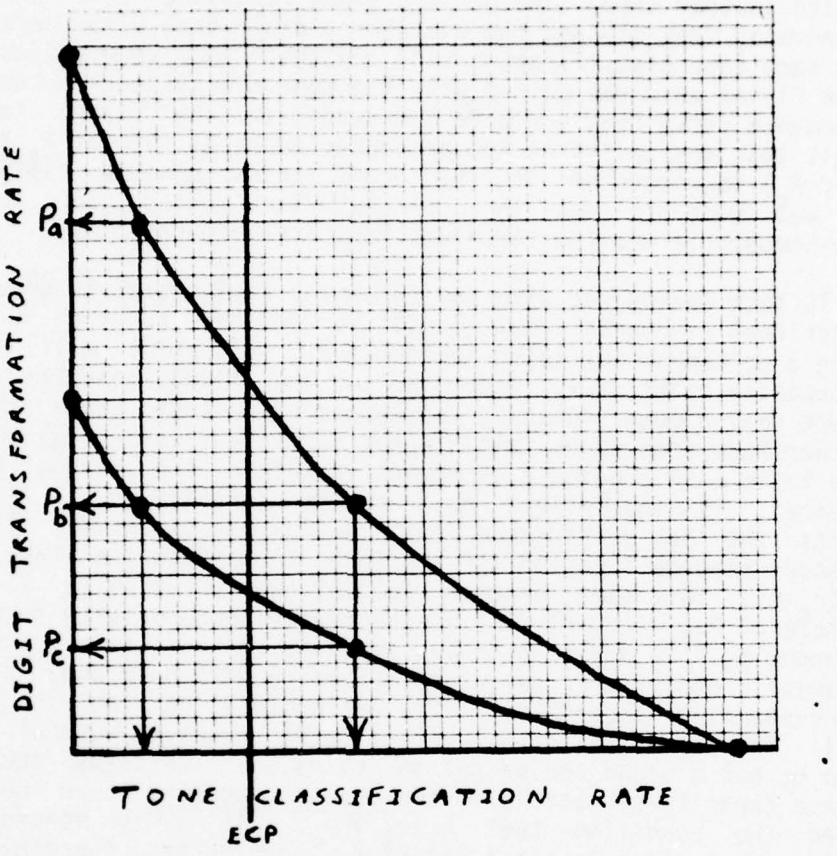


Figure 1 shows an important property of the fixed capacity theory. Assume that the top curve was generated by pairing a digit shadowing task, DTO, with a tone classification task, TC, and that the bottom curve was generated by pairing a "plus-three" digit transformation task with the TC task. Figure 1 indicates that a rate of performance P_a on the DTO task should require the same attentional resources as the rate of performance P_b does for the DT+3 task because both of them allow the same rate of performance on the TC task. Likewise, P_b of DTO should be equal in resource demand to P_c of DT+3. A performance-equivalency curve between DTO and DT+3 performance can be generated in this way.

The fixed capacity theory predicts that performance equivalency points are equal in resource demand and, therefore, should act similarly when they are paired with another task. The present study (examines) this prediction. The digit shadowing task DTO and the plus-three digit task DT+3 were each paired with the same tone classification task and their POCs were estimated. Next, a formation flying task was paired with the tone classification task to find the TC performance ratio that could be combined with the flying task. Finally, each digit task was tested at two presentation rates (DTO at P_a & P_b, DT+3 at P_b and P_c) to determine if the digit tasks behaved similarly. An attempt was made to set the presentation rates so that one was capacity-compatible and the other was capacity-incompatible.

The TC task was paired with the formation flying task in order to estimate the attentional resources that could be devoted to the TC task without producing a decrement in flying performance. This point will be called the excess capacity point, ECP. According to the fixed capacity theory, since pilots are called upon routinely to perform other tasks while they fly, they must either have some excess attentional capacity (i.e. r rm) or the addition of these tasks will produce a decrement in either the flying or other task performance. If the pilots have excess capacity $r_m - r$ this value constrains the TC performance that would be expected. If g is the performance-resource function for the tone classification task, P_{TC} would equal $g(r_m-r)$. This same excess capacity would allow a digit-shadowing performance of $P_{DTO}=f(r_m-r)$ if f is the performance-resource formation for digit shadowing. If digit shadowing is resource-limited in this range, then the parametric equation $P_{DTO}=f(r_m-r)$, $P_{TC}=g(r)$ will hold and, therefore, the corresponding excess capacity performance on the TC task would be $P_{TC}=g(r)$. The value $g(r)$ cannot be evaluated exactly without knowing the function g, but a bound can be put on its value. Two tasks such as DTO and flying are capacity-compatible if the excess capacity used on TC for each satisfies the condition that $r_1+r_2 \geq r_m$. If g is monotone, then $g(r_1+r_2) \geq g(r_m)$. If g is not a positively accelerated function in the estimation range then $g(r_1) + g(r_2) \geq g(r_1+r_2)$. Therefore, $g(r_1) + g(r_2) \geq g(r_m)$. Letting $r_2=r_m - r_1$ yields $g(r_1) + g(r_m-r_1) \geq g(r_m)$ and $g(r_1) \geq g(r_m) - g(r_m-r_1)$. That is, the excess capacity point of the digit-shadowing task in terms of its corresponding TC task performance, $g(r_1)$, is greater than or equal to the maximun rate of performance on the TC task performed simply minus the rate of performance possible on TC while flying. The excess capacity point ECP = g(rm) - g(rm-r) is marked with a vertical line in Fig. 1. According to the fixed capacity theory, performance levels of DTO and DT + 3 to the right of this line will be compatible with the flying task; whereas, levels substantially to the left of it probably will be incompatible.

Objectives

The present project is a preliminary attempt to evaluate the feasiblility of using a fixed capacity attentional theory to measure attentional demand. A valid measure of attentional demand with properties such as those decsribed herein would be useful as a cognitive parameter that could be used to help design human performance systems. It also could be used to monitor the course of training. A prediction of the fixed capacity theory was to be experimentally evaluated.

Method

Subjects

Four intructor pilots from the 87th FTW, Williams Air Force Base, volunteered to participate in the experiment.

Appartus and Task Descriptions

Formation Flying. The simulator decribed by Wood, Hagin, O'Connor, and Myers (1972) was used to test the pilot's formation flying performance in the various experimental conditions. The simulator presents a visual display of a lead aircraft which can be made to perform various standard maneuvers. The pilot controls his relative motion to it from a fixed cockpit, The simulator allows a range of flying activities, but during the test phases of the present experiment, the lead aircraft performed sinusoideald altitude variations with a peak to peak amplitude of 1000 feet (305m) while flying with a fixed heading at 320 knots. The flight dynamics simulated the characteristics of a T-38 aircraft. The pilot was to maintain fingertip position on the lead aircrafts right wing.

Cognitive Tasks. Two different types of cognitive information processing tasks were used. Both tasks used stimuli which were presented auditorily via tape recordings. In the tone classification task, the ouput from each recorder was presented monaurally to the earphones in a headset. For the tone classification task, blocks of two-tone sequences were recorded at a fixed rate. Blocks at the rates of 0.3, 0.5, 0.7, 0.9, 1.1, 1.3, 1.5 and 1.75 tones per second were recorded. Each of the two tones had an equal propability of being the tone presented. The tones had frequencies of 2135 and 321 Hz and a common duration of 100 msec. They were presented at an easily audible intensity. The ouput from the recording was sent to the left earphone.

In the tone classification task, the pilot's task was to classify the tones as either high or low in pitch by pressing the trigger switch on the control stick for high tones and the intercom switch on the throttles for low tones. Each of the switches activated a small light. Scoring was performed manually by an experimenter who compared the lighted display with the correct response which was listed on a prepared data sheet.

For the digit transformation tasks blocks of digit sequences were recorded at a fixed rate. Blocks at the rates of 0.25, 0.50, 0.75, 1.00, 1.50 and 2.00 digits per second were recorded. Only the digits 1-6 were used and each had an equal probability of occurring. The digits were recorded by using a pulse code modulation technique to digitize a speech sample, equate the six digits in intensity and shorten them until each one had a duration of 250 msec. Each digit was clearly intelligable and was presented at an easily audible intensity to the right carphone.

Two different digit transformation tasks were used. The DTO task was a shadowing task in which the pilot had to say aloud the name of the digit presented. The DT+3 task was an addition task in which the pilot had to add three to the digit presented and say the name aloud. An experimenter monitored the pilot's speech and compared it for correctness with the answers on a prepared data sheet.

Procedure

The experiment consisted of five different sessions of testing. Each pilot received all five sessions. During session 1 the pilots practiced each task individually. They received seven 2-min trials on the tone classification task with rates that ranged from 0.7 to 1.75 tones/sec. They received three 2-min trials on the DTO task (1.0, 1.5, and 2.0 digits/sec) and three 2-min trials of the DT+3 tasks (0.5, 1.0, and 1.5 digits/sec). They were allowed to fly in the simulator for at least 15 min, executing a variety of maneuvers.

During sessions 2 and 3 the two digit tasks were paired with the tone classification task to estimate their performance operating curves. Only one of the digit tasks was performed together with the tone task during each session. The order of testing was counterbalanced across pilots.

At the beginning of each session the pilot received two blocks of three trials. On one block of trials the pilot performed the tone task and on the other he performed the digit task that he would be tested on later in the session. Following this, he received three blocks of three trials of digit task-tone task combinations. During each block the presentation rate of the digit task was held constant while the tone task rate was varied. The presentation rates were 0.25, 0.75 and 1.0 digits/sec for the shadowing task and were 0.25, 0.50 and 0.75 digits/sec for the plus-three task. The order of testing was randomly determined for each pilot. On the first trial of a block all of the pilots received the same tone task rate. On the next two trials the tone task rates wre increased or decreased by one step in an attempt to bracket the 10% error point.

[1] The first two pilots tested used another switch on the stick instead of the interform switch on Day 1.

The sequence of events on each trial was as follows. The first ten tones classified were not scored. After five of them were presented the digit task began. The digit performance during the second five tones was not scored. A two-min test session followed. The pilots were told to give priority to the tone task.

During session 4 the pilots performed the tone task together with the formation flying task. The session again began with three 2-min trials in which the pilot performed each task singly. Following this each pilot received two blocks of five flying-tone task combinations. On each of the five trials within a block the pilot received a different rate of the tone task. The rates used for both blocks were 1.1, 1.3, 1.5, and 1.75 tones/sec and 0.0 tones/sec (i.e., no tones were presented). The order of testing the presentation rates was randomly determined within each block for each pilot.

The sequence of events on each trial was as follows. the pilot was allowed to achieve a stable fingertip position first with the lead aircraft flying straight and level and then while it performed altitude variations. Following his signal the tone task was started. Scoring started after 10 tones were presented and continued for two min. An instructor pilot assigned to HRL rated the pilot's performance during the two-min trial. He used the 12-point scale described in Reid & Cyrus (1974).

During session 5 both digit tasks were paired with formation flying in two separate blocks of trials. For practice each pilot had three trials of formation flying singly and two trials with each digit task singly immediately before the trial block on which it was used. The test trials consisted of two blocks of four trials. On two of them the pilot performed formation flying together with the digit task. On the other two they performed the digit task alone. The presentation rates that were used were selected individiually for each pilot as described in the introduction. The same rates were used on the dual-task and single-task trials. Testing order was counterbalanced. The sequence of trial events was similar to that used during session 4.

Results and Discussion

Tone-Digit Performance Operating Curves

The performance operating curves relating DTO and DT+3 performance to tone classification performance were estimated by finding the maximum rate at which each task could be performed singly and the maximum rate at which the tones could be classified for each of the three digit transformation rates that were used. The rate at which a pilot made errors on 10 percnet of his responses was taken to be the maximum rate. The 10 percent error rate was estimated separately for each pilot. Figures 2 and 3 show these individual estimates as well as the means of the individual estimates. The numbers arbitrarily identify the pilots. Missing pilot numbers occurred because the three-rate interpolation procedure did not always yield a clear-cut estimate of the 10 percent error rate. Because the pilots usually made errors on both

tasks in the dual-task conditions and because the function relating their error tradeoffs is unknown, the 10 percent error criterion was taken as the sum of the percentage of errors made on each task. Weighting each percentage by the number of stimuli presented during a 2-minute trial did not appear to change the estimates appreciably and, therefore, was not used.

Figure 2. Performance Operating Curves for DTO vs. TC

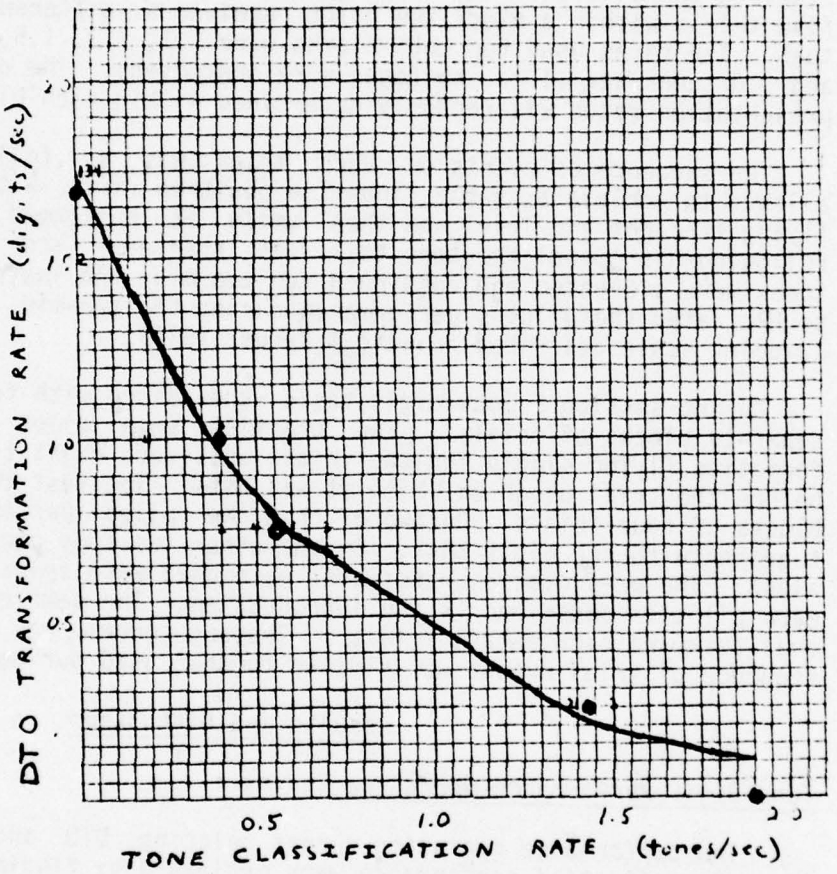


Figure 2 shows how performance on the shadowing task DTO covaried with performance on the tone classification task. The rate at which shadowing could be successfully performed decreased substantially as the rate at which tone classification could be successfully performed increased. The curve drawn through the points is the exponential function, $P_{DTO}=1.74 \exp(-1.45$

P_{TC}) that provided the best fit to the mean performances. A linear regression on the transformed scores was used to find the best-fitting function. The fit appears to be reasonably good ($r = -0.997$) and was somewhat better than the best-fitting linear function. The mismatch between the rightmost point and the curve is due to the estimation procedure. The zero rate of DTO performance (i.e. tone classification alone) was set at 0.1 to allow it to be logrithmically transformed. Setting the value of zero DTO performance closer to zero appared to have little influence on how well the estimated curve fit the data. More sensitive estimation procedures were not attempted because the maximum rate that tone classification could be performed single was inadequately estimated; the value shown may be an underestimate.

The maximum rate of classifying tones singly was inadequately estimated because the testing procedure did not permit the testing of rates greater than 1.75/sec and the pilots made errors on fewer then 10 percent of the tones at this rate. The mean percentage of errors for Days 1-4 on the 1.3, 1.5, and 1.75 tone/sec rates were 2.5, 4.6 and 6.6 percent respectively. The corresponding means for Days 3 and 4 only were 2.4, 3.5 and 4.1 percent. The 1.9 tones/sec value shown in Fig. 2 is a rough extropolation.

Figure 3. Performance Operating Curves for DT + 3 vs. TC

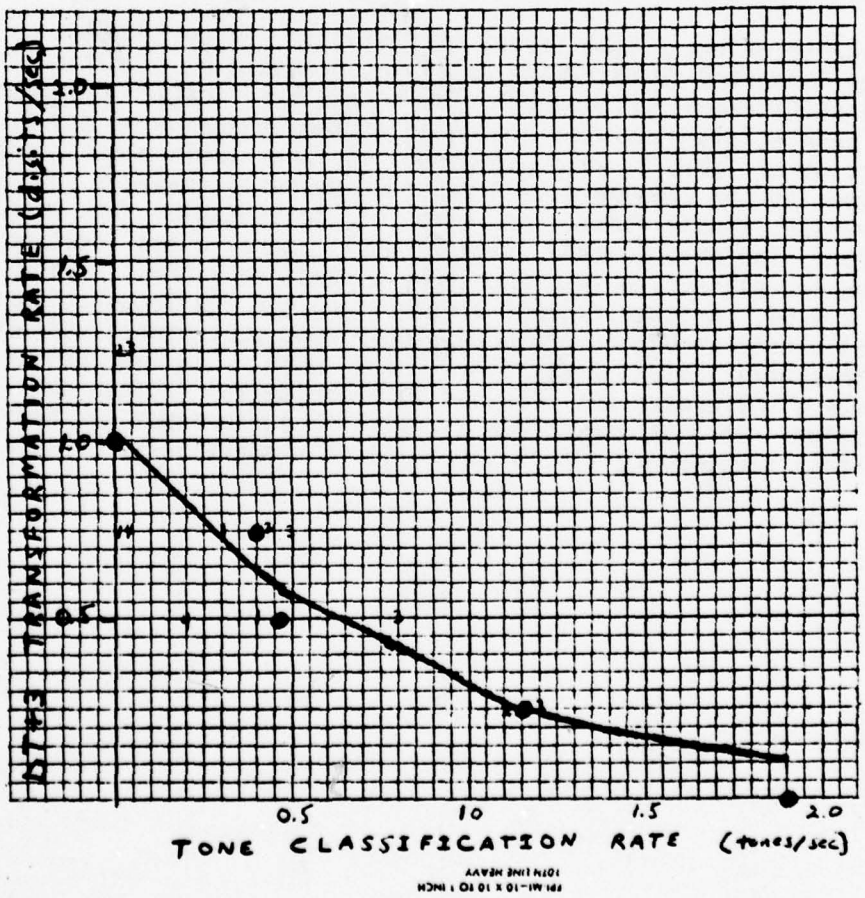


Figure 3 shows the performance operating curve for the plus-three versus tone classification tasks. They were treated in the same way as the data in Figure 2. The best-fitting exponential function ($r = -0.992$) had the equation $P_{DT+3} = 1.03\exp(-1.23\ P_{TC})$. The rate at which the plus-three transformation had a demand equal to that produced by a given rate of shadowing can be found by treating the two best-fitting exponentials as parametric equations and solving. The resulting power function, $P_{DT+3} = 0.644\ P_{DTO}^{0.848}$, describes this equivalency and it will be called their performance-equivalence function. The rate of DT+3 performance is denoted as P_{DT+3} and the rate of DTO performance is denoted as P_{DTO}.

Flying Versus Tone Classification

To estimate the attentional demand made by the formation flying task, an attempt was to be made to determifne the rate of tone classification at which each pilot made errors on 10 percent of the tones presented. The mean percentages from the two blocks are presented separately for each pilot in the middle section of Table 1. Using the estimation procedures as before, only pilots 2 and 3 had estimable maximum demand rates (1.5 and 1.0 tones/sec, respectively). Pilots 1 and 4 had successful classification rates while flying that exceeded the scoring capabilities of the present experiment.

Because of the slight effect of flying on classification performance, a test was conducted to determine if flying produced a significant decrease in tone classification performance. The tone classification performance from the single task trials that were presented at the beginning of day 4, shown in the top section of Table 1, were compared to the performance under dual task conditions at the same rates. A reported-measures analysis of variance with dual versus single task and rate of presentation as main effects was conducted. The pilots made significantly more classification errors when theyflew and classified than when they classified without flying, $F\ (1.15) = 17.48$, $p < .01$. Neither rate of presentation nor the interaction of rate with the dual-single condition produced significant performance differences for the rates that were tested, $F\ (2.15) < 1.0$ for both. It is unlikely that this performance difference was produced by experimental fatigue over the course of the session. If anything, Block 2 dual-task performance was better than Block 1 dual-task performance (10.9% versus 11.9% respectively).

Table 1

Tone Classification Error Percentages and IP Ratings of Flying from Single and Dual Task Combinations

Pilot	Tone Presentation Rates 0	1.0	1.3	1.5	1.75
Tone Classification Singly					
1	--	--	0.0	0.0	5.2
2	--	--	7.1	3.3	5.7
3	--	--	3.2	3.9	5.2
4	--	--	0.0	0.0	0.0
Tone Classification While Flying					
1	--	3.8	3.5	9.7	7.8
2	--	5.6	7.1	9.7	12.6
3	--	12.1	28.8	17.5	22.6
4	--	3.4	4.5	4.2	3.6
Rating of Flying					
1	10.0	9.5	9.5	9.5	10.0
2	8.0	8.0	8.5	8.0	7.5
3	8.5	7.0	7.5	7.5	7.0
4	9.0	8.5	8.5	8.5	8.5

Ratings of the pilots' flying performance did not appear to be affected by the classification rates used. The mean ratings for the two blocks are presented in the bottom section of Table 1. The five treatment conditions were not significantly different from each other, $F(4, 12) = 2.26$.

Flying versus Digit Transformations

The inability to estimate the maximum rate at which the tone classification could be performed singly, together with the problem created by the small attentional demand produced by the flying task made it impossible to confidently use the procedure described in the introduction to select compatible and incompatible presentation rates for each task. It was impossible to find rates that definitely exceeded the compatibility point but that did not exceed the maximum single task rate whose use would have made the prediction trivial.

Despite the inability to predict the compatibility point reliably, Day 5 testing was conducted to check the prediction that the performance equivalency rates for the two different digit tasks should act similarly regardless of how they affect flying. There should be no type of task by rate interaction for equivalent rates. This test rests on weaker assumptions, but it only becomes convincing if there are some rate-dependent performance decrements. The rates were estimated separately for each pilot, and are presented in Table 2.

A repeated measures analysis of variance was performed on the difference scores obtained by subtracting the percentage of errors made under the single task conditions from the percentage of errors made under the corresponding dual-task conditions. The analysis was inappropriate because of severe violations of its homogeneity of variance and normality assumptions. It was used because of its power. Nevertheless, neither the main effects of task type and of compatible versus incompatible presentation rate nor their interaction were statistically significant; $F(1,9) = 1.57,\ 0.79,\ 1.41$ respectively. A similar analysis of the dual-task ratings of flying performance also revealed no significant differences, $F(1,9)$ all < 1.

Table 2
Compatible and Incompatible Presentation
Rates Used with each Task

Condition	Pilot 1	2	3	4
Incompatible				
DTO	1.50	1.50	1.50	1.50
DT+3	0.75	1.00	1.00	0.75
Compatible				
DTO	0.75	1.00	1.00	0.75
DT+3	0.50	0.75	0.50	0.50

Conclusions

The successful determination of POC curves for the cognitive tasks shows that even different kinds of cognitive processing appear to have trading relationships. Kalsbeek and Sykes (1967) did determine a POC but both tasks used were classification tasks. By generating two different POCs for the transformation tasks against a common classification task, it was easy to rule out single response competition due to response execution as the major contribution producing the POCs. The rates of performing DT+3 was much slower than the rate of performing DTO for a common TC rate. Also, this allowed the two transformation tasks to be equated. Kalsbeck (1968) made a similar equation, but he used a physiological measure, sinus arythmia, to equate them. In both cases some test for the validity of the equation is needed.

Unfortunately, the attempt to test the validity of the performance equivalence function was not successful. The flying task required too little attentional demand. The test did show the advantage of this approach. Typically, dual-task studies, whether with cognitive tasks (Kerr, 1973) or with tracking tasks which are similar to the flying tasks used in the present study (Poulton, 1974), have constructed thin task difficulty so that at least one experimental condition produced performance differences. These measures provide ordinal information of difficulty over this narrow range but they do not allow a comparative evaluation of demand needed in terms of the total resources available. In the present experiment, flying was shown to demand resources but by being able to compare it to other tasks using the same metric (i.e. the two cognitive tasks) the demand was seen to be rather small.

1977 USAF-ASEE SUMMER FACULTY RESEARCH PROGRAM

sponsored by

THE AIR FORCE OFFICE SCIENTIFIC RESEARCH

conducted by

AUBURN UNIVERSITY AND OHIO STATE UNIVERSITY

PARTICIPANT'S FINAL REPORT

SIMULATOR FOR AIR-TO-AIR COMBAT PLATFORM MOTION SYSTEM INVESTIGATION

Prepared by:	John A. Seevers, PhD
Academic Rank:	Associate Professor
Department and University:	Department of Mechanical Engineering Calif. Polytechnic State University
Assignment:	
(Air Force Base) (Laboratory) (Division) (Branch)	Luke Air Force Base Human Resources Laboratory Flight Training
USAF Research Colleague:	William Hopkins
Date:	September 16, 1977
Contract No.:	F44620-75-C-0031

SIMULATOR FOR AIR-TO-AIR COMBAT PLATFORM MOTION SYSTEM INVESTIGATION

by

J. A. Seevers

ABSTRACT

The Simulator for Air-to-Air Combat (SAAC) motion platform presently has limited value for student training in the air-to-air combat environment. Because of peculiarities in the motion system, pilots "feel" like they are in a simulator instead of the real aircraft. There are several factors that contribute to the status of the motion platform being less than representative of the aircraft. First, the motion platform lags the input command by a noticeable amount. The platform's motion is about a multiple set of axes rather than a single axis as the command would direct. Also, because of physical constraints on the size of the system, the magnitude and duration of the motion are limited. A fourth major problem with the motion is that when the excursion is near the maximum allowable, the motion is stopped too abruptly and this stopping is readily perceived by the pilot (the washout problem).

Instrumentation has been provided to monitor the SAAC's motion platform behavior and a series of experiments performed to document this behavior. One of the most significant results obtained was that the motion platform has a natural frequency of only about 1/2 Hz. Additional quantities that describe the motion system's performance are also discussed.

ACKNOWLEDGMENT

The author is sincerely grateful to the Air Force Systems Command for support of this summer research. A deep appreciation is due to ASEE and Auburn University for administration of the project. In particular, thanks are due Mr. Fred O'Brien.

The author is indebted to the Human Resources Laboratory Flight Training Division for profiding a cordial work environment. In particular, the author would like to thank Mr. Bob Bunker, Mr. San Dock, Mr. Bill Hopkins and Mr. Ralph Foster for their help and support.

LIST OF FIGURES

Figure 1. SAAC Motion System Block Diagram

Figure 2. Acceleramometer Mounting Locations

Figure 3. Heave Leg Positions

Figure 4. Position and Acceleration Dead Time

Figure 5. 10 Inch Y Step

Figure 6. 5 Inch Z Step

Figure 7. 0.2 Radian Yaw Step

Figure 8. 0.2 Radian Pitch Step

Figure 9. 0.2 Radian Roll Step

Figure 10. Washout for Y Accelerations

Figure 11. Bode Plot of Legs 1, 2 and 3

Figure 12. Bode Plot of Legs 4, 5 and 6

Figure 13. Bode Plot for Heave Accelerations

Figure 14. Bode Plot for Pitch Accelerations

Figure 15. Typical Frequency Response Data

LIST OF TABLES

1. Leg Scale Factors
2. Leg Maximum Velocities
3. Platform Rotation Points
4. Platform Step Responses

INTRODUCTION

The Simulator for Air-to-Air Combat (SAAC) was designed to provide pilots with a realistic experience in training for air combat engagements. In addition to the visual images displayed, the system has motion capabilities that allow onset motion cues to be presented. These cues are short duration velocities and accelerations of the motion platform which should present the illusion of the initial phases of entry into a maneuver. The intent of motion is to provide a more realistic, and hence, a better training environment for pilots.

The SAAC consists of two F-4E cockpits mounted one each on 60 inch-stroke, synergistic six-degree-of-freedom motion systems. Cockpit movement is based upon the computed six degrees of aircraft motion freedom and is correlated with the motion of the simulated aircraft. All aircraft stability derivatives are accounted for in such a manner that aircraft movement in any degree of freedom will influence movement along or about the axes of the motion system. The sensations of motion are intended to be representative of sensations experienced in the operational aircraft.

In addition to being used as a research tool, the SAAC is being used as a training device for F-4E pilots as part of their normal training sequence. Presently, training officers find the motion of the system to be significantly different from sensations experienced in the actual aircraft. In fact, it is actually felt by instructor pilots that better training is accomplished with the platform motion system turned off. Hence, the motion system is not presently used in pilot training.

As a first step in an effort to try to improve the existing system to the point where it can be used as a viable training tool, it was necessary to develop a program to accurately describe the dynamics of the existing system. This characterization assumes added importance in light of tests conducted for the Scientific Advisory Board that seem to indicate exceptionally long system lags between the time an imput is made and the time of the resulting motion. These tests conducted on the SAAC also suggest somewhat irregular behavior of the motion platform [1]. Verification of degraded motion might very well explain pilot's reluctance to train with the motion system on.

OBJECTIVES

The primary objective of the present investigation is to document the motion of the existing system in a state of adjustment that is consistent with that normally seen by student pilots and to compare this performance with established criteria. Additional objectives are to establish important parameters that adequately describe the system, establish the equipment necessary to monitor the system, recommend a test procedure to check the motion platform for faithfulness, and identify weak areas where the system needs to be improved.

BACKGROUND AND MOTION PLATFORM DESCRIPTION

Block Diagram Representation

A block diagram of the basic components that comprise the motion system are shown in Figure 1. Cockpit control movements are transformed into electrical analog signals and then digitized by an ADC/DI converter at a frequency of 20 iterations per second. The digitized control inputs are fed into the flight equations which are updated at 20 times per second. The output of this block is a series of digital signals that represent aircraft position, velocity and acceleration, both linear and angular. These signals are then fed into a program that computed platform leg lengths (at 10 times per second), and converted to analog signals by the DAC at 20 times per second. These analog signals for the legs then are processed as analog signals by the motion electronics cabinet which produces a reference signal that is nulled out when the platform achieves the desired attitude. The result is the platform accelerates and a position change can be noted.

In light of the block diagram in Figure 1, the primary intent of the present investigation can be restated as to describe the system dynamics of the pertinent blocks individually and of the overall system. All blocks taken together would be the through-system dynamics from the stick input to the platform motion as the output. In the limited investigation undertaken here, it was felt that greatest emphasis should be placed upon instrumenting and documenting the right-hand half of the block diagram, i.e., from the motion platform driving software package through the resulting platform motion.

Platform Acceleration Equations

Before instrumenting the platform, the acceleration equations for any point on the platform need to be established. Also, the angular acceleration of the platform needs to be expressed in terms of linear accelerations of points on the platform. From Meriam [2], the absolute acceleration of any point P on a translating and rotating body expressed as a vector

$$\underline{a}_p = \underline{a}_o + \dot{\underline{\omega}} \times \underline{r}_{p/0} + \underline{\omega} \times (\underline{\omega} \times \underline{r}_{p/0}) \tag{1}$$

where 0 is any other point on the same rigid body, $\underline{\omega}$ and $\dot{\underline{\omega}}$ are the absolute angular velocity and acceleration of the rotating body and $\underline{r}_{p/0}$ is the vector representing the distance from the point 0 to point P. Using aircraft axes with X out the nose, Y out the right wing and Z down, equation 1 can be expanded into

$$a_{p_x} = a_{o_x} + Z(\dot{q} + pr) + Y(pq - \dot{r}) - X(q^2 + r^2) \tag{2}$$

$$a_{p_y} = a_{o_y} + Z(qr - \dot{p}) - Y(p^2 + r^2) + X(\dot{r} + pq) \tag{3}$$

$$a_{p_z} = a_{o_z} - Z(p^2 + q^2) + Y(\dot{p} + qr) + X(pr - \dot{q}) \tag{4}$$

where p, q and r are the aircraft angular velocities while X, Y, and Z are the coordinate distances from point 0 to point p. Physically let point 0 be the geometric centroid of the platform and point p_1 be the location of the first linear acceleramometer and p_2 be the location of the second linear

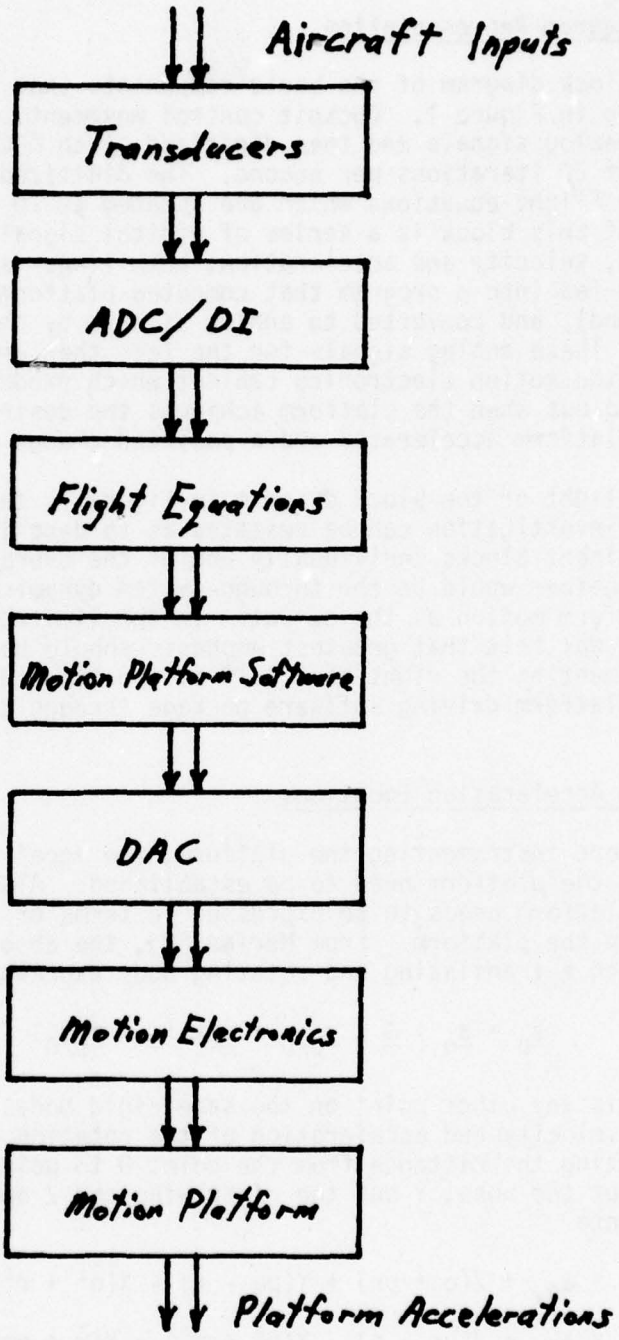


FIGURE 1

SAAC MOTION SYSTEM BLOCK DIAGRAM

acceleramometer. Assume that all points p and O are in the same X-Y plane. Find the angular acceleration $\dot{p}$ using linear acceleramometers. Apply equation 4 twice with $X_1 = 0 = X_2$ (acceleramometers mounted on the y-axis), subtract and rearrange. The result is:

$$\dot{p} = \frac{1}{y_1 - y_2} (a_{pz_1} - a_{pz_2}) - qr \tag{5}$$

In a similar manner

$$\dot{q} = \frac{1}{x_1 - x_2} (a_{pz_2} - a_{pz_1}) + pr \tag{6}$$

$$\dot{r} = \frac{1}{y_1 - y_2} (a_{px_2} - a_{px_1}) + pq \tag{7}$$

or

$$\dot{r} = \frac{1}{x_1 - x_2} (a_{py_1} - a_{py_2}) - pq \tag{8}$$

In the above equations, the quantity $(x_1 - x_2)$ or $(y_1 - y_2)$ is the distance between the mountings for acceleramometers 1 and 2. According to Singer's specifications on the SAAC [3], the maximum angular velocities are 15 degrees/second. Consequently, the product of angular velocities is less than 0.068 rad/sec^2. Furthermore, if motion is driven about one axis at a time, only extraneous angular velocity terms would appear at all. The result is that the product of angular velocity terms can be dropped from the angular acceleration equations leaving

$$\dot{p} = \frac{1}{(y_1 - y_2)} (a_{pz_1} - a_{pz_2}) \tag{9}$$

$$\dot{q} = \frac{1}{(x_1 - x_2)} (a_{pz_2} - a_{pz_1}) \tag{10}$$

$$\dot{r} = \frac{1}{(y_1 - y_2)} (a_{px_2} - a_{px_1}) \tag{11}$$

or

$$\dot{r} = \frac{1}{(x_1 - x_2)} (a_{py_1} - a_{py_2}) \tag{12}$$

A difference in linear accelerations can easily be found using an analog "summing" circuit similar to the one in the appendix.

APPARATUS

A plan view of the motion platform showing the locations of the accelera-mometer mounting points is shown in Figure 2. All acceleramometers are mounted within one inch of the plane defined by the pivot points. A complete detailed listing of the test equipment used to monitor the motion of the platform is in the appendix.

In the electronics or signal processing sense, we are dealing with a very, very low frequency phenomena and as a result do not expect any deterioration of the signals due to our monitoring equipment. Linear acceleramometers have a natural frequency around 110 Hz which is 10 times greater than the 10 Hz maximum of excitation of the platform for our experiments. The angular acceleramometers list a natural frequency of 29 Hz which indicates deterioration can be expected to start above 6 or 7 Hz. In actuality, platform response deteriorates so badly before 5 Hz that this restriction is rather academic. The gain-better circuits have a one-half power fog of 30 Hz which is also well above meaningful data. In addition to the equipment shown in the appendix, a "mixing box" was utilized to facilitate gathering data and switching circuits.

PROCEDURE

The procedure was essentially the same for gathering all data: 1) Use the signal generator to establish the input, either a sine wave or an extremely low frequency square wave to be used as a step; 2) to monitor the reference signal on an oscilloscope and/or the brush recorder; 3) record the system or subsystem's responses (displacements or accelerations) on the brush recorder or the FM recorder.

During testing, it was found that if accelerations were to be recorded, the air conditioner for the platform's vestical system had to be turned off. It generated vibrations that were transmitted to the platform structure. These vibrations created extreme noise interference in all acceleramometer measurements.

RESULTS

Numerous tests were conducted to investigate various aspects of the total system. Each phase of the investigation will be discussed separately.

Positions

Five separate articles of information were gathered in this series of tests. First, a common analog step input signal was applied at the motion electronics cabinet by-passing all digital computer hardware. Since all legs were driven with the same signal, it was expected that the responses would be identical. The results for a step input of -5 volt to +5 volt are in Table I. The accuracy of the length measurement is $\pm$ 1/32 inch for all legs.

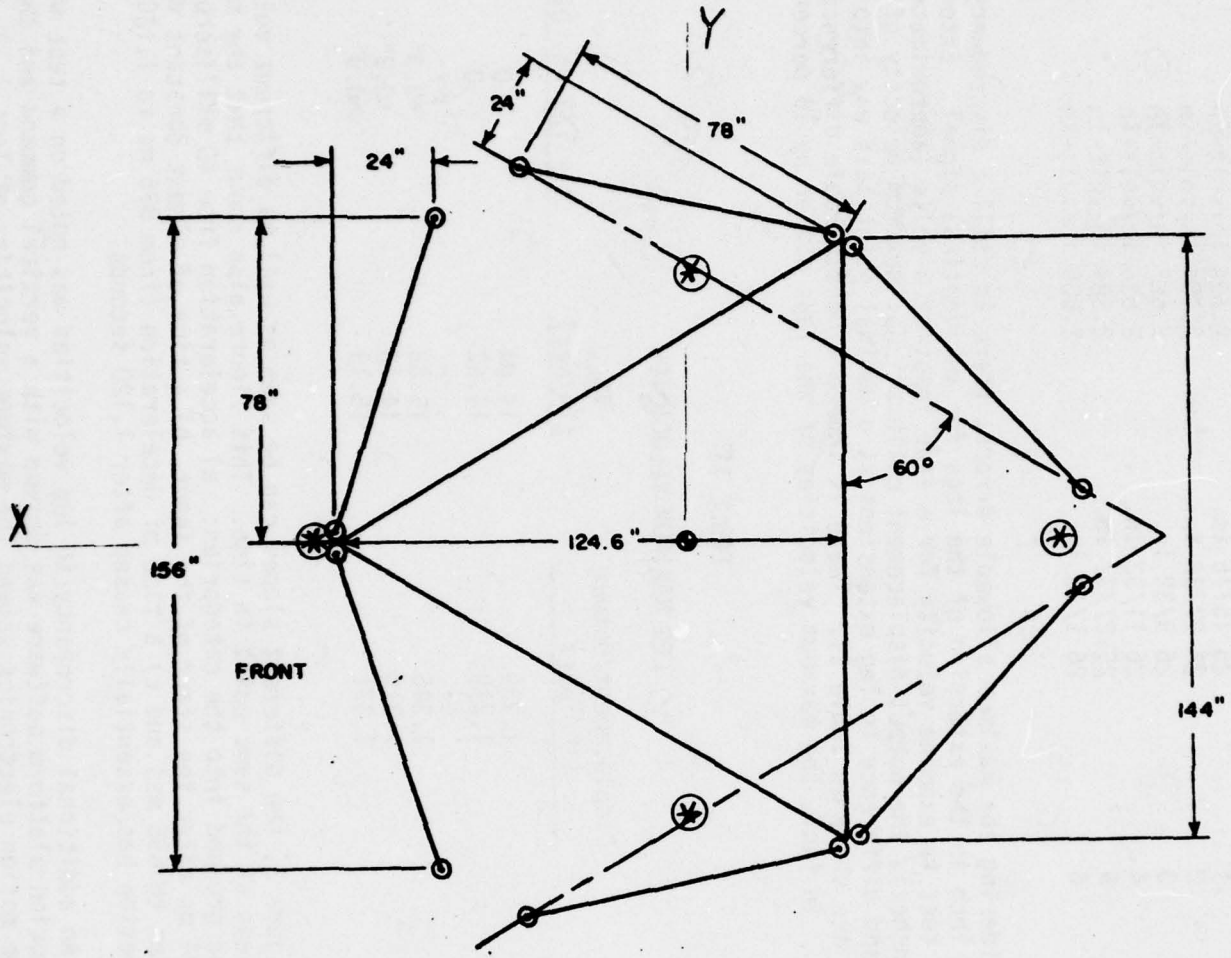


FIGURE 2

ACCELERAMOMETER MOUNTING LOCATIONS

TABLE I

LEG SCALE FACTORS

Leg	Leg Travel	Leg Scale Factor
1	25 15/16 in.	2.594 in/volt-in
2	25 27/32 in.	2.584 in/volt-in
3	26 9/32 in.	2.628 in/volt-in
4	26 11/32 in.	2.634 in/volt-in
5	25 27/32 in.	2.584 in/volt-in
6	26 1/16 in.	2.606 in/volt-in

Considering the maximum allowable errors, there is still a discrepancy of 7/16 inch in the extension of the legs for an identical signal. Extending this test to examine velocity for a step input of 6 volts (approximately 16 inches), the output displacement calibrations, maximum velocity of each leg and difference in leg extensions at a nominal point half way into the step are shown in Table II. There is indeed a considerable difference in legs. In fact, the maximum velocities of the legs differ by 13 percent.

TABLE II

LEG MAXIMUM VELOCITIES

Leg	Displacement/Output (in/V_{out})	V_{max} (in/sec)	t = 1/2 Ht. Diff.
1	1.339	14.04	0
2	1.319	14.52	0
3	--	--	--
4	1.345	15.83	+0.3"
5	1.319	14.10	+0.2"
6	1.331	15.19	+0.9"

In figure 3, the different slopes can be seen as well as different values of the legs at the same point in time. This figure also shows that the motion can be grouped into the categories: a) acceleration from 40 milliseconds (ms) to 104 ms after the start of the input, b) a time of almost constant velocity (104 ms to 696 ms) and c) a time of deceleration (from 696 ms to 1.120 sec). The motion has essentially ceased after 1.120 seconds.

An additional discrepancy in leg velocities was noted on a test when the motion platform software was driven with a vertical command and the inputs to the motion electronics showed the maximum velocities of legs 1, 2, 4, 5, 6 to be about 140 in/sec while leg 3 was about 110 in/sec. This is disturbing and indicates a definite problem in the software or the DAC. In other modes of motion this could produce extraneous accelerations of the platform.

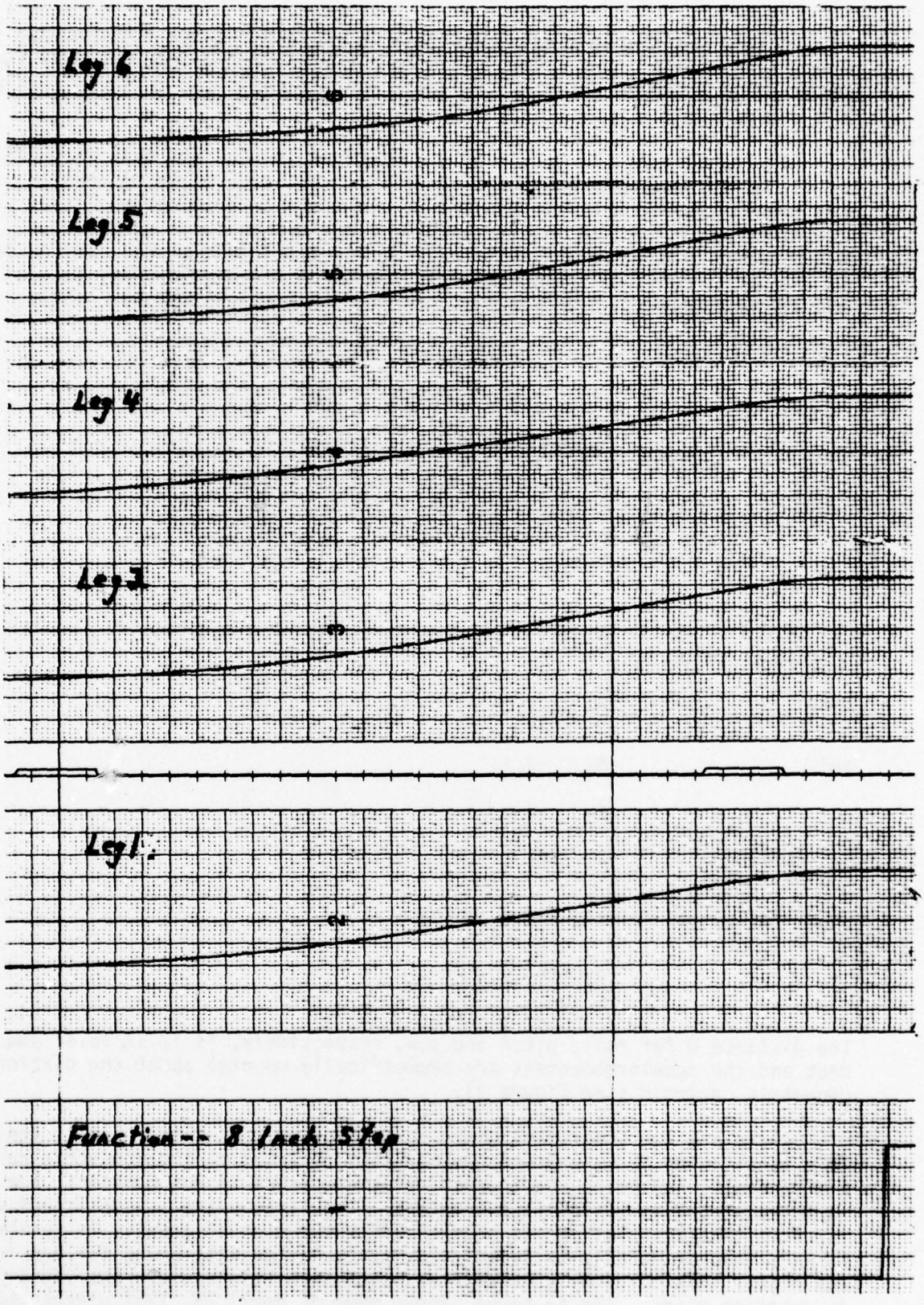
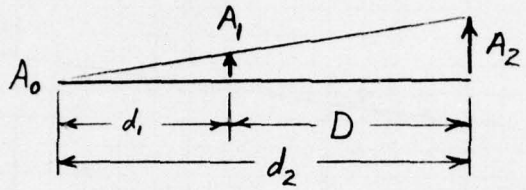


FIGURE 3

HEAVE LEG POSITIONS

Another positional finding was that in Yaw the angular displacement is almost linear with input. The following yaw scale factor was observed for inputs of -0.1, -0.2, -0.3 and -0.4 volt respectively: 55.4, 55.3, 56.4 and 56.8 degrees/volt.

After observing the motion of the platform it was felt that it would be beneficial to determine the location of the axis about which an angular acceleration was occurring. Consider a profile view showing two linear acceleramometers with an angular acceleration such as to produce linear accelerations along the sensitive axis of the acceleramometers. Let d_1 be the distance from acceleramometer 1 to the point of rotation (may be positive or negative) and D be the distance between acceleramometers. Note: $d_2 = D + d_1$.



Let A_1 and A_2 be the linear acceleration of the acceleramometers in addition to that of point 0.

Then $$A_{1\ total} = A_0 + A_1$$

and $$A_1 = -d_1\alpha$$

$$A_2 = -d_2\alpha$$

subtracting $$A_2 - A_1 = -(d_2 - d_1)\alpha = -D\alpha$$

substituting and solving for d_1 we have

$$d_1 = \frac{-A_1}{\alpha} = \frac{A_1 D}{A_2 - A_1}$$

The distance D for roll, pitch and yaw, respectively, is 12.17, 16.47 and 16.04 feet and the acceleramometers are symmetrically mounted about the platform geometric centroid (see Figure 2).

There are two important points to be made by this data. First, the platform is pitching about a point considerably in front of the geometric centroid and secondly, the point about which rotation occurs is not constant, i.e., it moves around to a significant extent. The first point is consistent with the fact that the platform is heavier and the center of gravity is farther forward than originally believed. The center of gravity being further forward and higher than originally calculated might also help explain the variation in rotation point. (An in-house Singer memo of April 25, 1977 places the center of gravity 6.22 feet aft of the forward pivot and 4.43 feet above the plane of pivots.)

TABLE III

PLATFORM ROTATION POINTS

Axis	Reference Acceleramometer	Positive Jerk	d_1 (feet) A_{max}	Negative Jerk
Positive Roll	+Y	-6.69	-6.66	-6.59
Negative Roll	+Y	-7.66	-5.66	-3.65
Positive Pitch	+X	-8.24	-5.49	-4.94
Negative Pitch	+X	-5.44	-6.54	-7.53
Positive Yaw	+X	-8.02	-7.11	-8.60
Negative Yaw	+X	-8.5	-7.57	-8.02

Dead Time

Dead time refers to the time between which an event should occur without any system delays and the time the event actually does occur. In the present context, it refers to the time between an applied step input and the time when resulting motion occurs. First it should be mentioned that on one test an 8 millisecond difference in dead time was observed between the six legs when a step was applied to the motion software program and the leg command signals were monitored. This large of a discrepancy was only observed on one out of about 15 tests but even at this seldom of an occurrence rate could prove troublesome.

Figure 4 clearly shows the difference in observed dead time of position and acceleration for the same step input. This step input to heave was applied at the motion electronics cabinet. The differences between the 40 ms position dead time and 16 ms acceleration dead time is very logical considering position is a double integration of acceleration and that acceleration would have to occur over some period of time before position displacement could be seen. Expressed another way, if the time rate of change of acceleration (jerk) is about 5g/sec, then if we assume that we can see 0.005 inch or more platform movement, it would take about 25 ms of platform acceleration before we could see any platform motion at all. This would be an additional 25 ms dead time in the position observation over acceleration. Consequently, using position outputs for any type of absolute dead time investigation is extremely dangerous at best.

Over a series of 25 step inputs to the Y, Z, roll, pitch and yaw axes, the observed acceleration dead times range from 0.080 seconds to 0.168 seconds with an uncertainty for each reading of about 0.008 seconds. Even taking into account this uncertainty, there is about an 80 millisecond difference in dead times for observed acceleration. This is not surprising as this input was processed by the software program at the rate of 10 times per second, or 0.100 seconds between samples.

Acceleration Step Responses

At this point, some mention should be made of what values are appropriate to acceleration levels in order to present a proper cue to a pilot. Gundry [5] established the fact that subliminal levels change depending on the

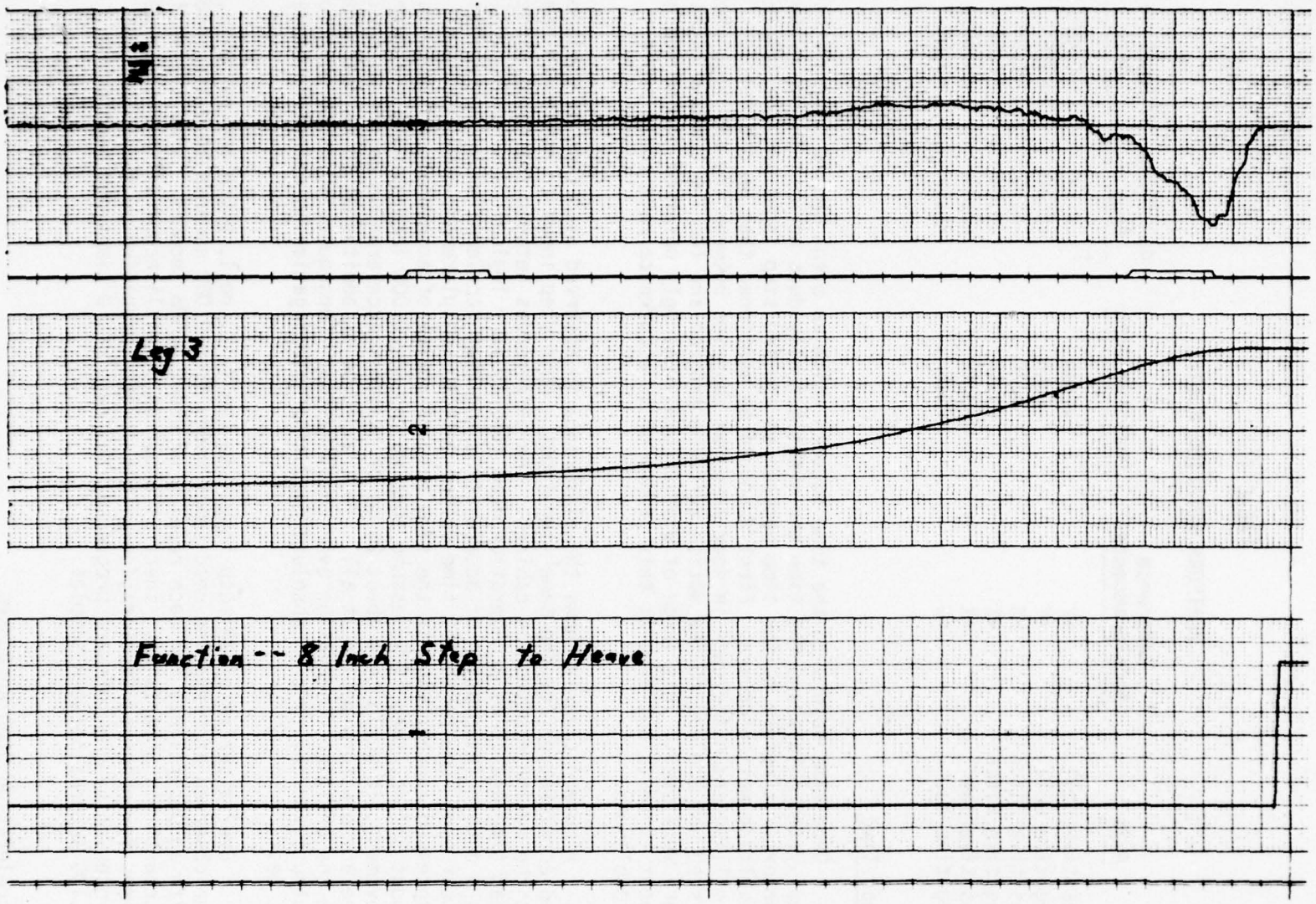


FIGURE 4

POSITION AND ACCELERATION DEAD TIME

difficulty of the tasks being performed by the pilot. As air-to-air combat is very demanding, accepted literary values may not be applicable. However, lacking any better data, we will use generally accepted perception values of 0.08g for translational and 0.01 rad/sec^2 for angular accelerations. A typical value for subliminal translational jerk value is 0.08 g/sec.

A series of acceleration tests were conducted where the motion electronics cabinet was driven with a step input to determine the absolute capability of the physical platform. During this test, two linear acceleramometers were mounted on the platform, one 8 feet forward and one 8 feet aft of the geometric centroid. For a commanded platform step of 7.2 inches up the front acceleramometer showed a maximum acceleration of 0.38g and a maximum jerk of 6.8 g/sec while the back acceleramometer showed 0.48g and 11.2 g/sec. For a platform down command, the front showed 0.32g and 7.1 g/sec while the back indicated 0.40g and 12.5 g/sec, respectively. The duration of positive acceleration was about 0.470 sec. The difference between the front and rear acceleramometer indicates a pitch acceleration coupling of 0.235 rad/sec^2. This is 23 times larger than threshold values. The excessive weight and forward center of gravity would contribute to this problem. Apparently, MIL-STD-1558 establishes the requirement that longitudinal and lateral accelerations should be at least ± 0.6g with vertical being at least ± 0.8g. Clearly the SAAC does not have the capability to even come close to this level.

Next, the motion software program was driven with a long period square wave to generate step responses about a neutral platform position. The results are summarized in Table IV. It should be pointed out that platform up is +Z motion (as opposed to down for aircraft axes).

In Table IV, jerk was determined by graphically taking the slope of the acceleration curve at its steepest point. This rapid change in acceleration would manifest itself as a change in seat pressure on the pilot and should be quite noticeable. Washout values may be found in the table for a positive motion by looking at the maximum negative value for that variable's acceleration.

The linear motions of Y and Z are not too bad as far as inducing extraneous linear accelerations. However, by almost any comparison that can be drawn, the angular accelerations are not consistent with desired values. Washout values are excessive and cross couplings between desired platform motions and other axes are alarming. Cross coupling should be restricted to that induced by the software package logic where desired representations for platform position of the SAAC are [4].

$$X_P = 4(2.25A_{X_A} - \sin\theta)$$

$$Y_P = 2(2\ r_A - A_{Y_A}) - 36\ \phi_P$$

$$Z_P = -2(1 + A_{Z_A})$$

$$\theta_P = 0.625 \sin\theta + 0.3125q_A$$

$$\phi_P = 0.125\ p_A$$

$$\psi_P = (1/16)\ (r_A + (1/16)\ \beta)$$

TABLE IV

PLATFORM STEP RESPONSES

NOTES: 1. Maximum values are indicated
2. Units: rad/sec^2, rad/sec^3, g, g/sec

Motion	- $\dot{p}$ +		- $\dot{q}$ +		- $\dot{r}$ +		- $\ddot{y}$ +		- $\ddot{z}$ +		- jerk +	
+5"Y	.20	.20	.08	.08	.50	.68	.04	.12	.01	.01	-.8	1.9
-5"Y	.25	.20	.06	.06	.20	.15	.12	.05	.01	.01	2.0	.5
+10"Y	.30	.33	.12	.12	.15	.45	.10	.19	.02	.02	.9	2.4
-10"Y	.35	.33	.06	.06	.15	.20	.19	.11	.01	.01	2.8	.9
"Noise Level"	.08		.03		.04		.006		.006			
+5"Z	.19	.19	.08	.12	.18	.18	.01	.02	.04	.14	.8	4.4
-5"Z	.15	.10	.16	.08	.20	.35	.02	.02	.16	.04	2.7	1.1
+10"Z	.35	.25	.16	.12	.30	.28	.01	.03	.05	.26	1.5	8.5
-10"Z	.38	.25	.16	.12	.35	.63	.04	.03	.27	.07	5.4	1.6
+.2ϕ	.70	1.30	.12	.16	1.10	.55	.10	.22	.04	.02	6.0	27.2
-.2ϕ	1.55	.65	.16	.12	.80	.55	.17	.10	.04	.04	23.6	6.3
+.2θ	.25	.30	.47	1.33	.9	.95	.06	.05	.12	.05	5.6	24.1
-.2θ	.20	.10	1.41	.55	1.15	.70	.04	.06	.02	.08	32.6	7.0
+.4θ	.30	.20	.86	2.11	1.00	1.00	.10	.07	.17	.14	15.2	39.1
-.4θ	.20	.20	2.35	.78	1.25	.75	.09	.11	.07	.14	34.3	11.9
+.2ψ	.10	.10	0.0	.12	.45	2.25	.02	.02	.05	.02	52.1	104.2
-.2ψ	.30	.25	.16	.16	1.65	.55	.03	.02	.04	.06	28.4	11.8
+.4ψ	.25	.37	.25	.43	1.30	2.81	.12	.14	.05	.07	41.1	130.2
-.4ψ	.30	.18	.24	.59	2.75	1.75	.05	.07	.07	.11	50.4	22.0

where p_A, q_A and r_A are in rad/sec.

A_{X_A}, A_{Y_A} and A_{Z_A} are in units of g.

β is in degrees.

X_p, Y_p and Z_p are in inches. (NOTE: For the platform equations, Z_p is positive upwards.)

θ_p, ϕ_p and ψ_p are in radians.

Clearly, the lateral and longitudinal modes of motion should not be coupled. Table IV shows coupling, especially pitch inducing yaw which indicates the motion system is not behaving properly. Much of this coupling was visually evident during the acquisition of the data. Figures 5 through 10 are strip chart recordings of the platform's accelerations for various step inputs.

Figures 5 and 10 clearly demonstrate the washout problem. The washout phase of the motion which is supposed to be below a subliminal level is almost 50 percent of the cue signal. This washout is governed by a linear washout scheme and the problem could be greatly reduced if a nonlinear washout scheme similar to Parrish's was employed [6]. Figure 6 illustrates the effect vertical motion has on yaw and roll. This is undesirable and no yaw or roll acceleration should be observed for vertical motions. Figure 7 demonstrates a bad quirk in the system for yaw motions. The slope of the acceleration curve changes abruptly several times during the course of the cues. It is not known what causes this behavior, but whatever is doing it should be removed.

Frequency Response

Linear systems theory states that for a sinusoidal input to stable linear dynamic system the steady state output will be a sine wave of the same frequency. As a result, linear dynamic systems may be completely characterized by the amplitude ratio and the phase angle of the output as a function of the frequency of the input signal. One graphical representation of this data is the Bode plot [7,8] where the amplitude is expressed as log-magnitude, Lm which is defined as:

$$Lm(G) = 20 \log_{10}|G(i\omega)|$$

where $G(i\omega)$ is the transfer function of the process relating the output to the input.

Sinusoidal position responses were recorded for each of the six legs. In addition, frequency responses were recorded for the platform's acceleration in both heave and pitch for small amplitude motion. Bode plots of the results are presented in Figures 11 through 14.

The data used to generate these Bode plots showed several interesting features that cannot be included on the plots themselves. First, at frequencies above 2 Hz there was a noticeable lack of symmetry in the platform's motion, i.e., the amplitude and velocity of the up motion was less than the down motion. Also, above 2 Hz, large variations developed in the peak amplitudes at a constant frequency and higher harmonies appeared in the output.

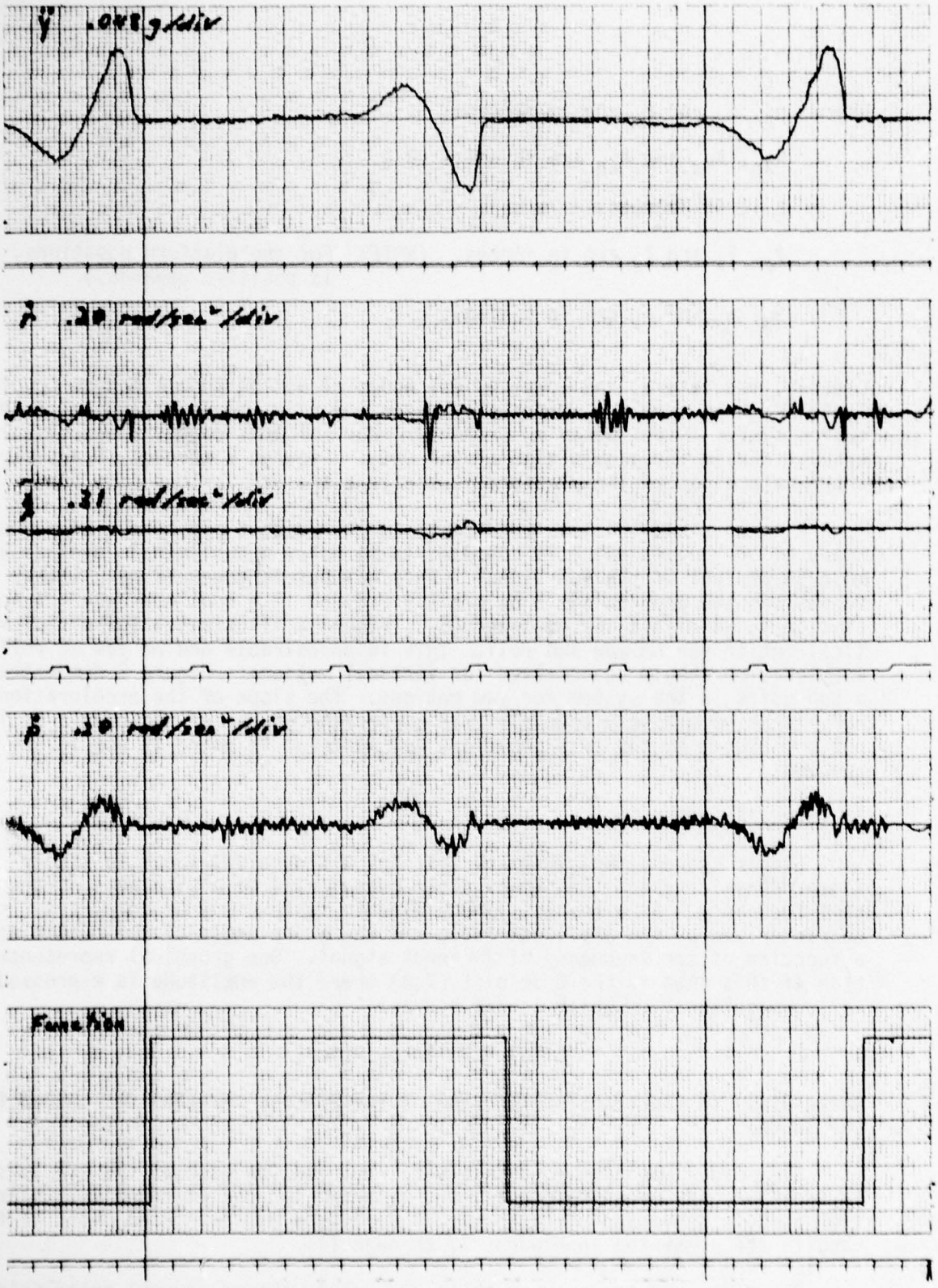


FIGURE 5

10 INCH Y STEP

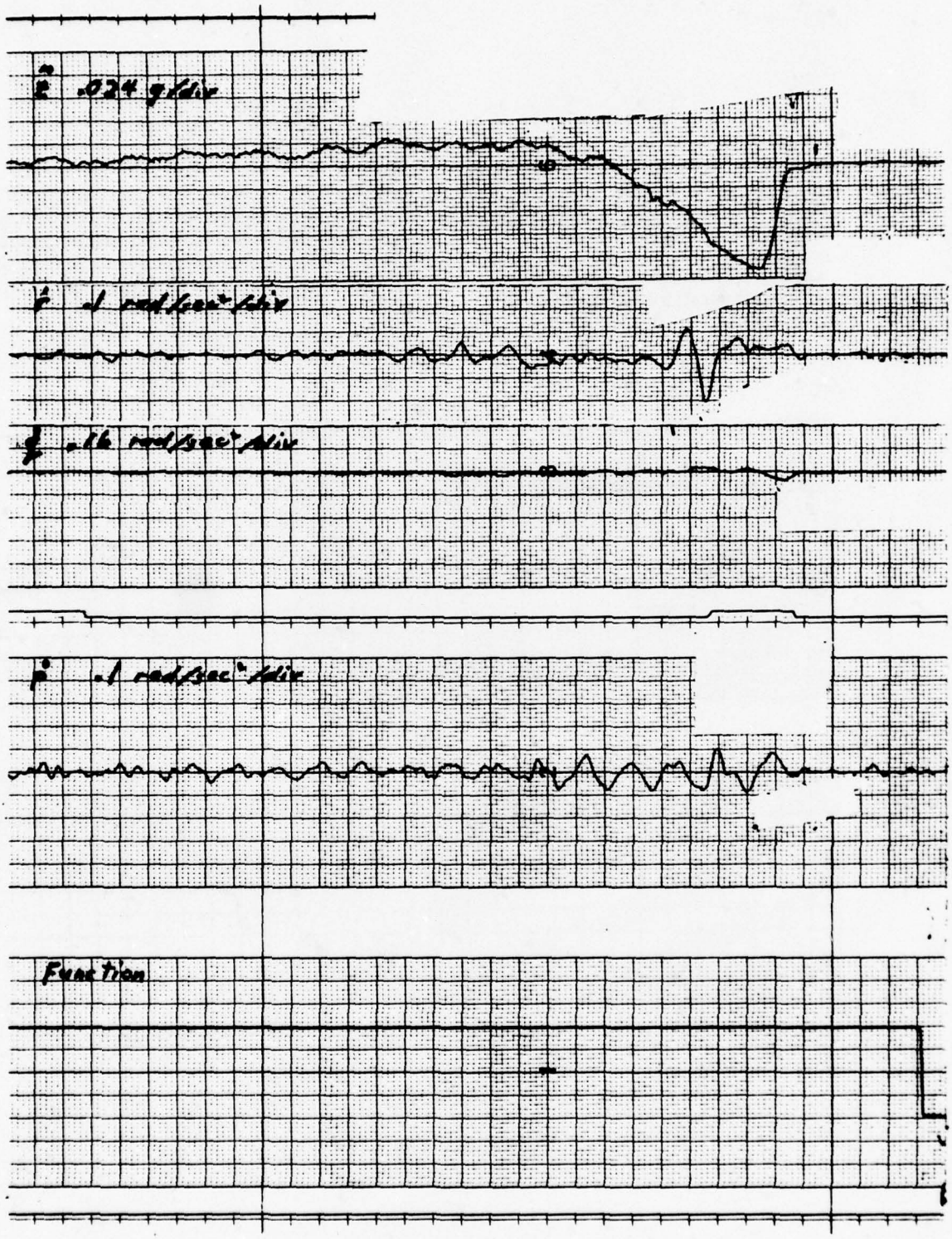


FIGURE 6

5 INCH Z STEP

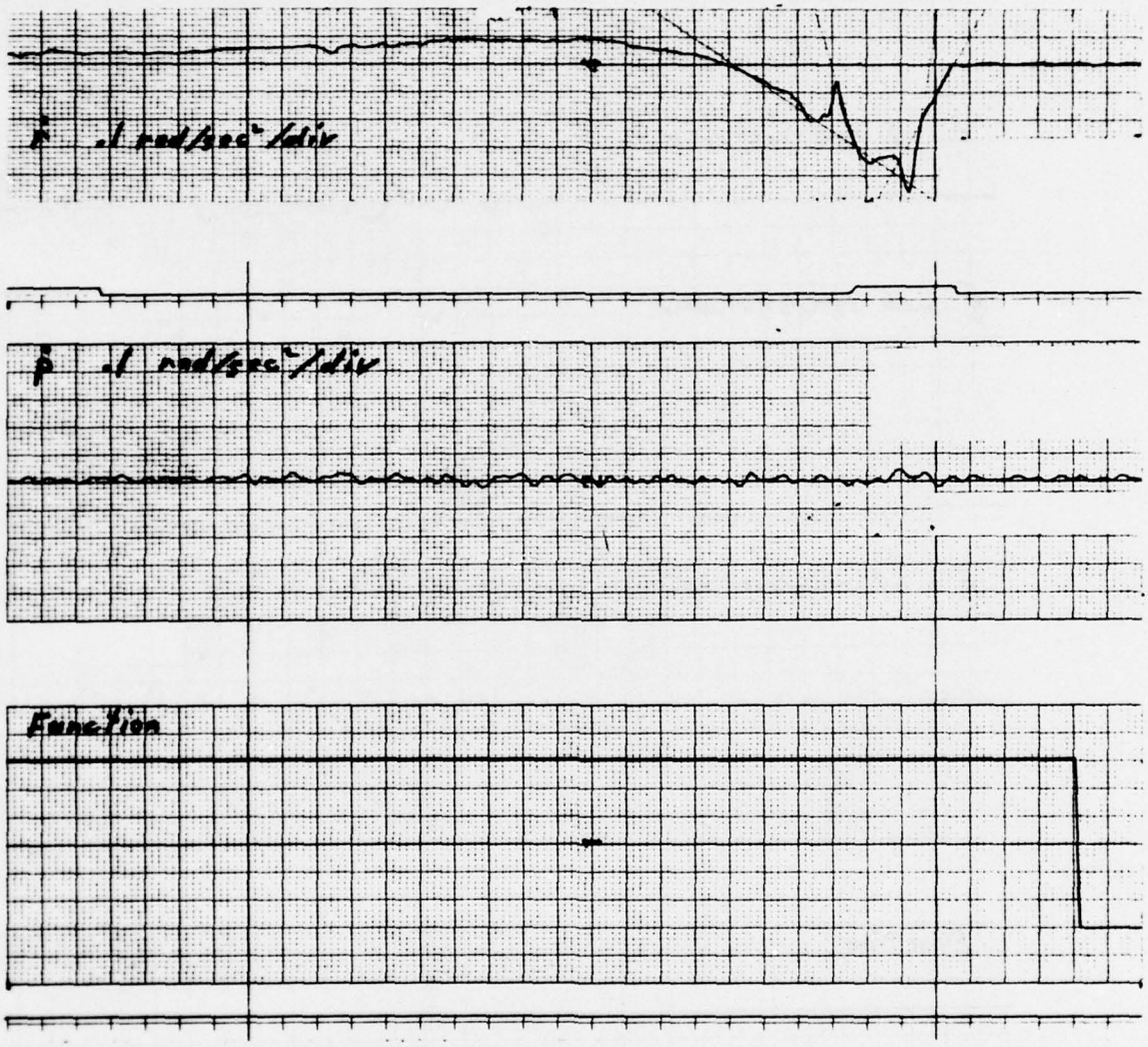


FIGURE 7

0.2 RADIAN YAW STEP

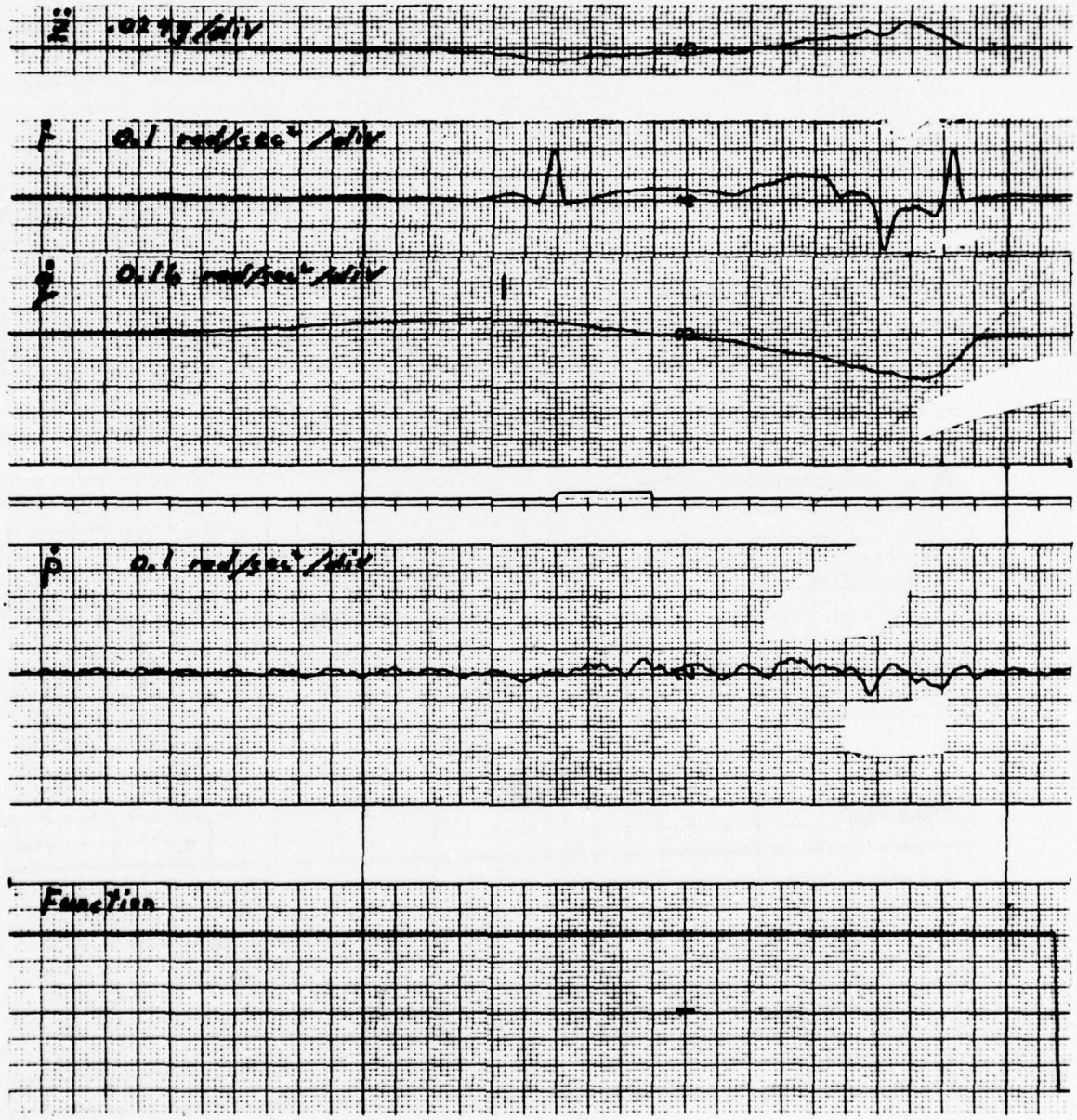


FIGURE 8

0.2 RADIAN PITCH STEP

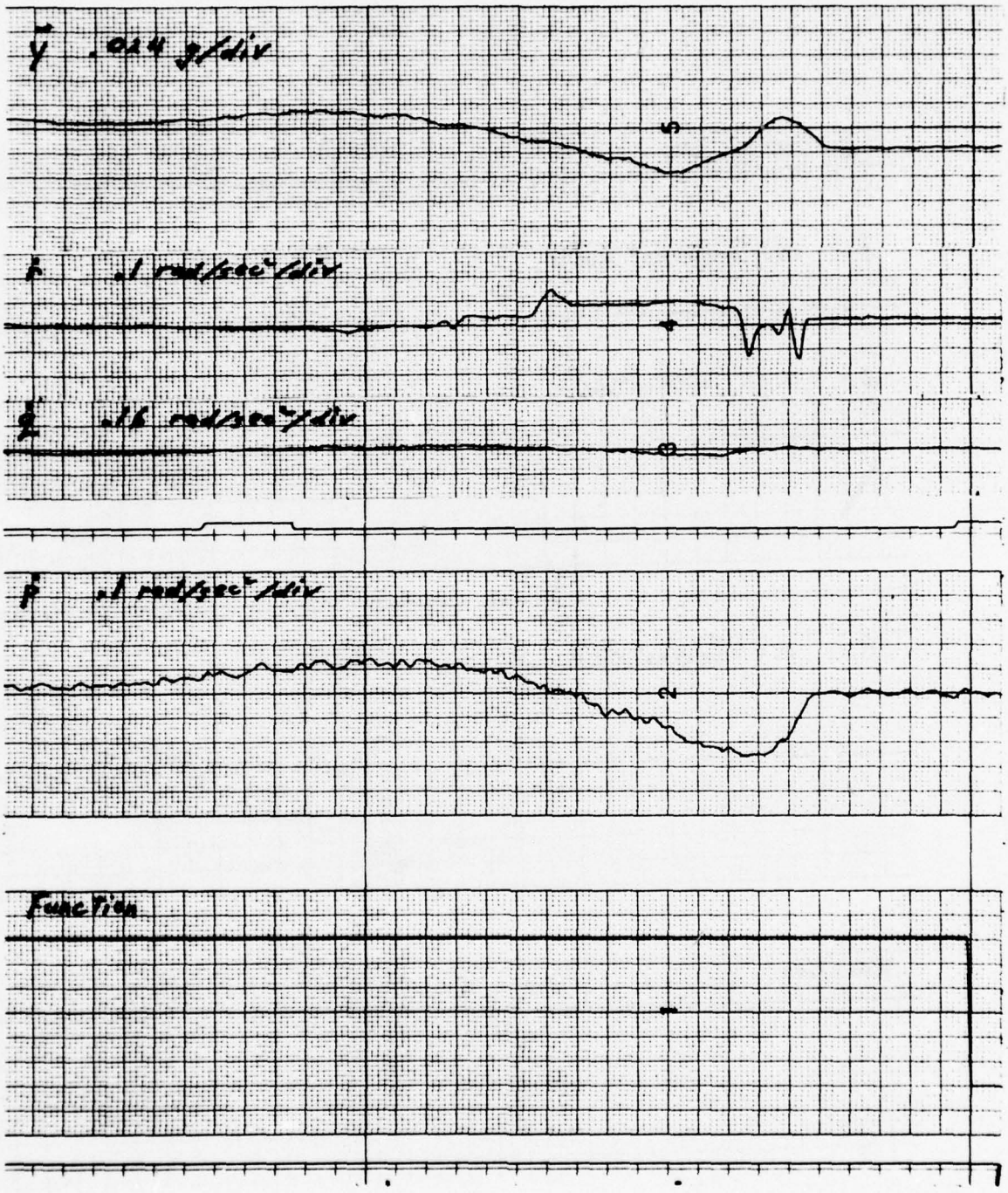


FIGURE 9

0.2 RADIAN ROLL STEP

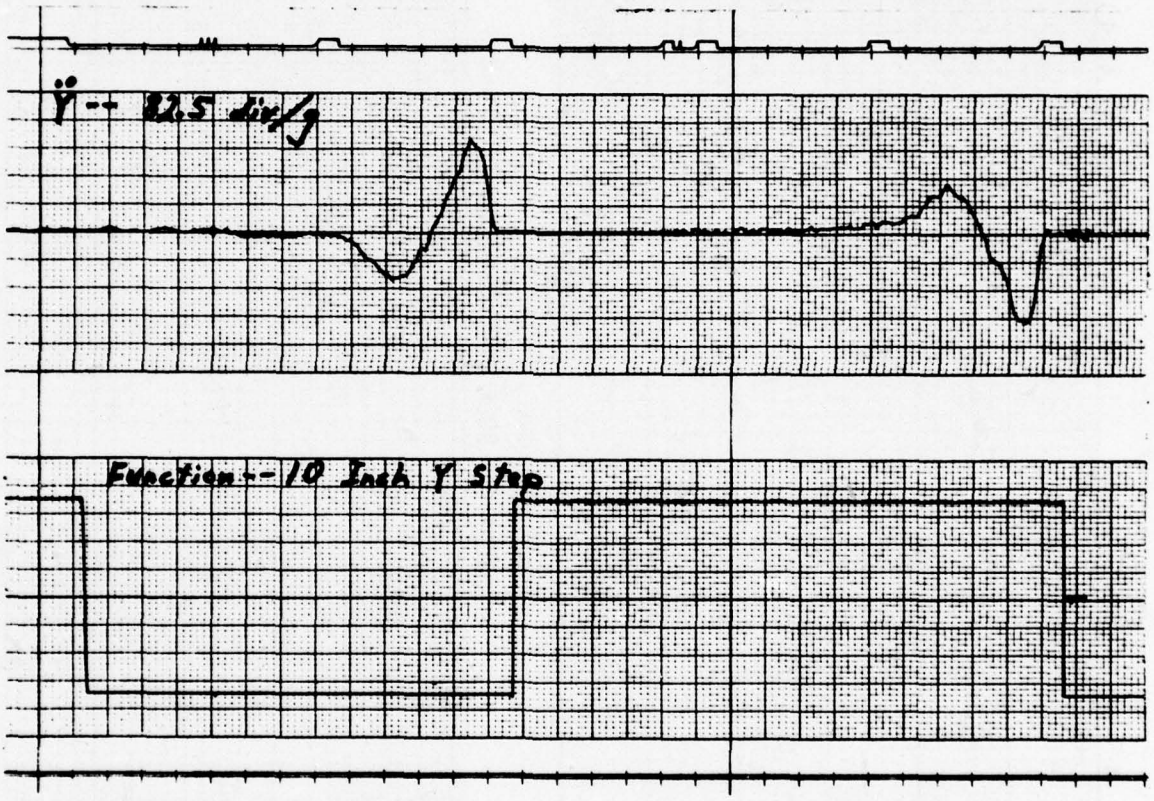


FIGURE 10

WASHOUT FOR Y ACCELERATIONS

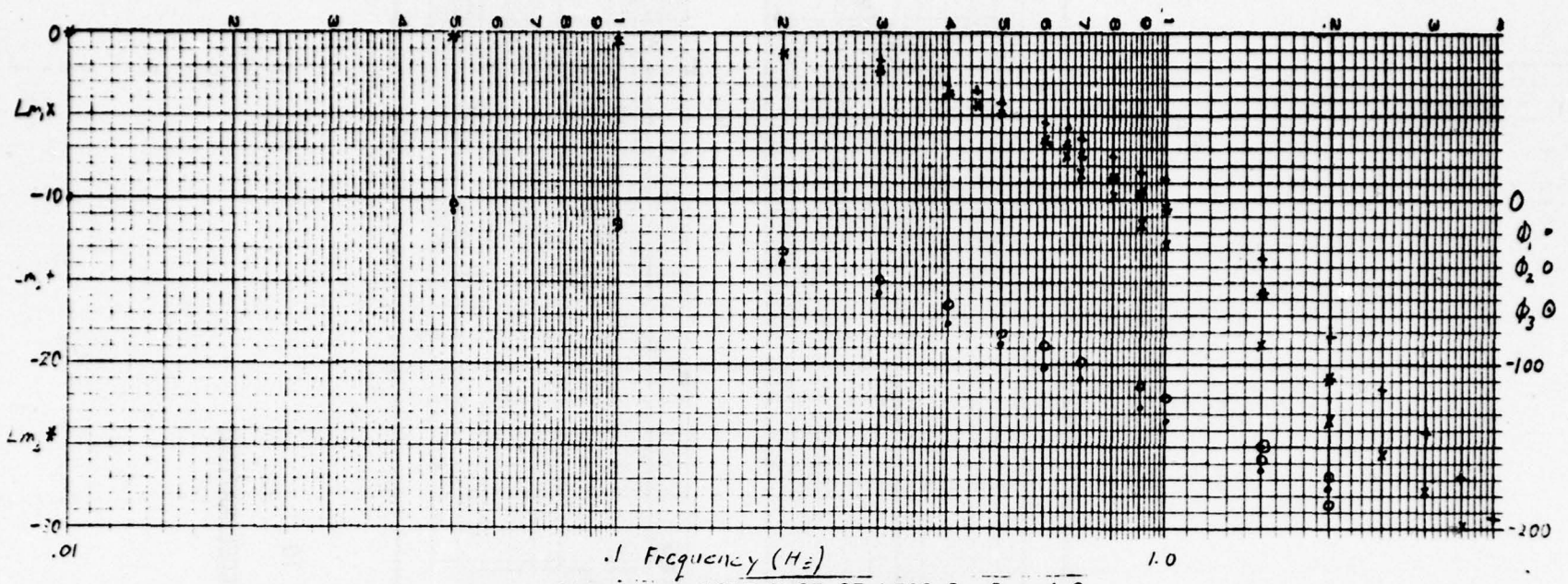


FIGURE 11 BODE PLOT OF LEGS 1, 2 and 3

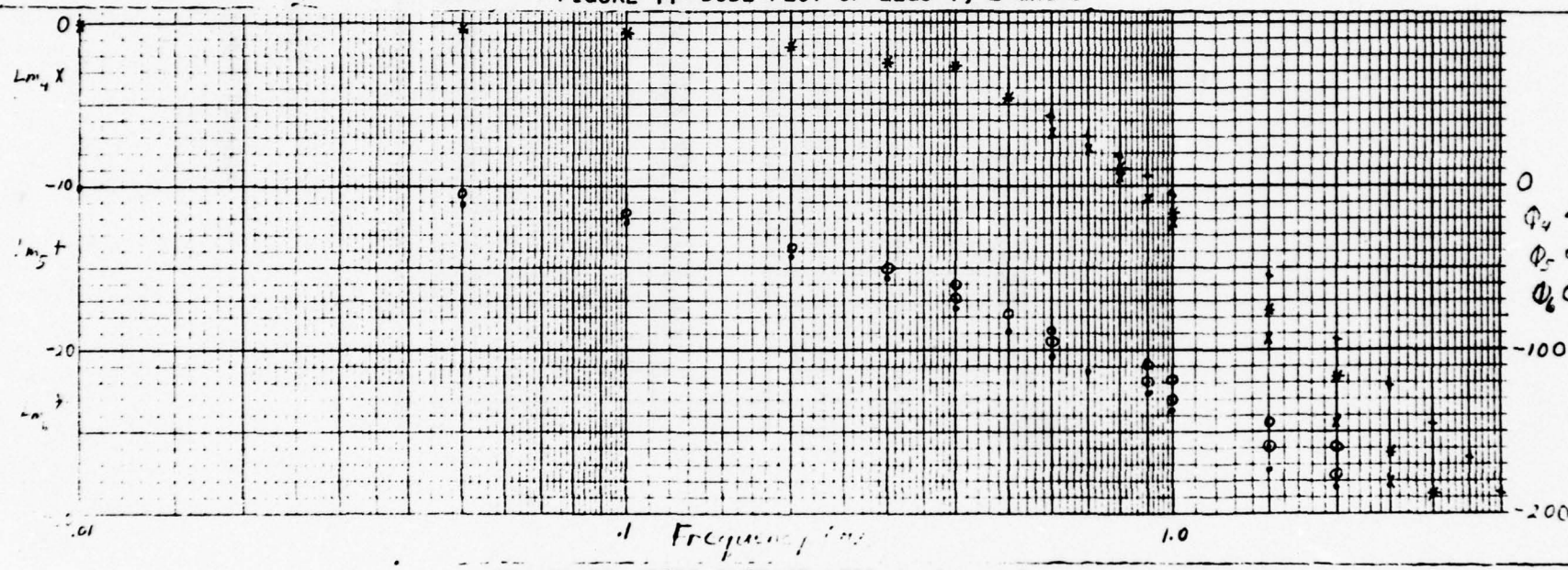


FIGURE 12 BODE PLOT OF LEGS 4, 5 and 6

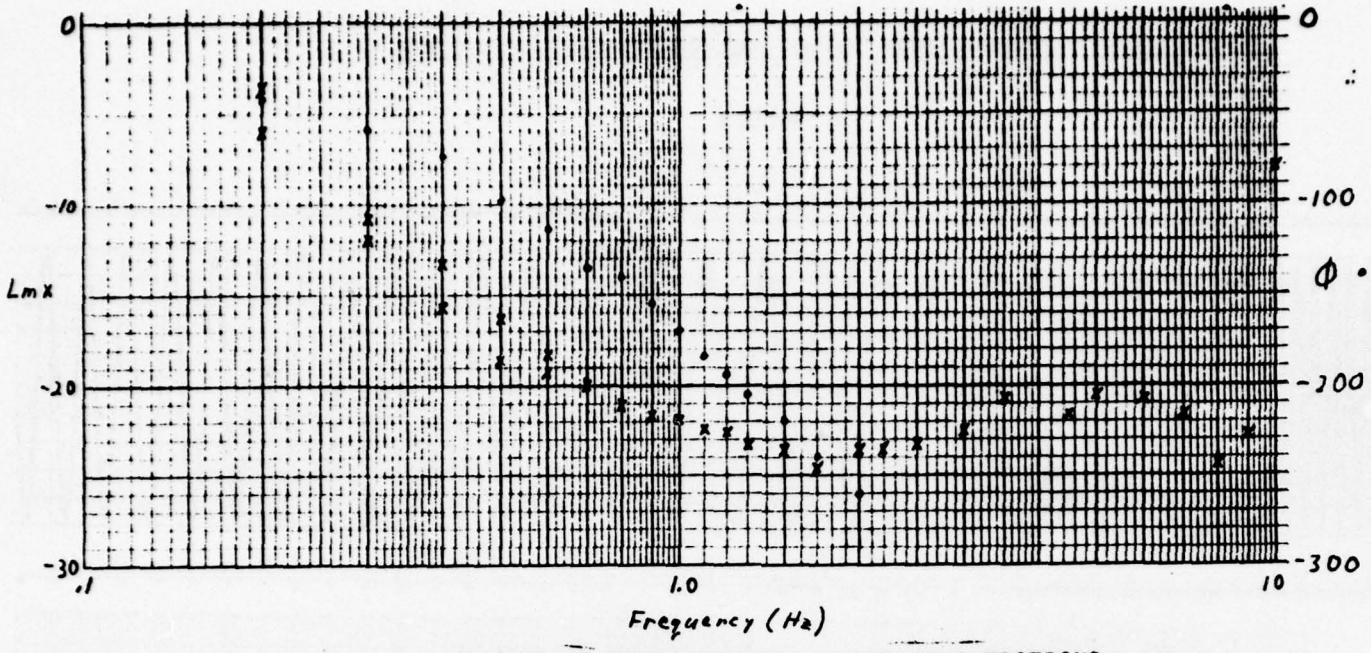


FIGURE 13 BODE PLOT FOR HEAVE ACCELERATIONS

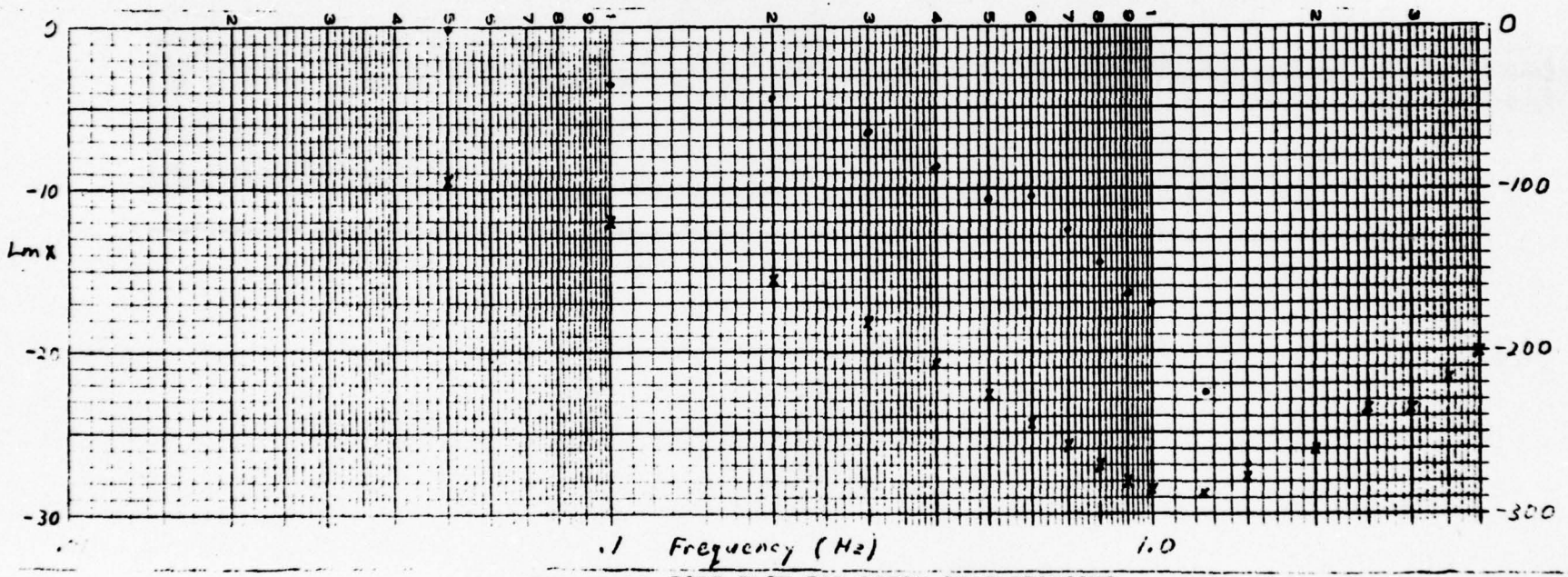


FIGURE 14 BODE PLOT FOR PITCH ACCELERATIONS

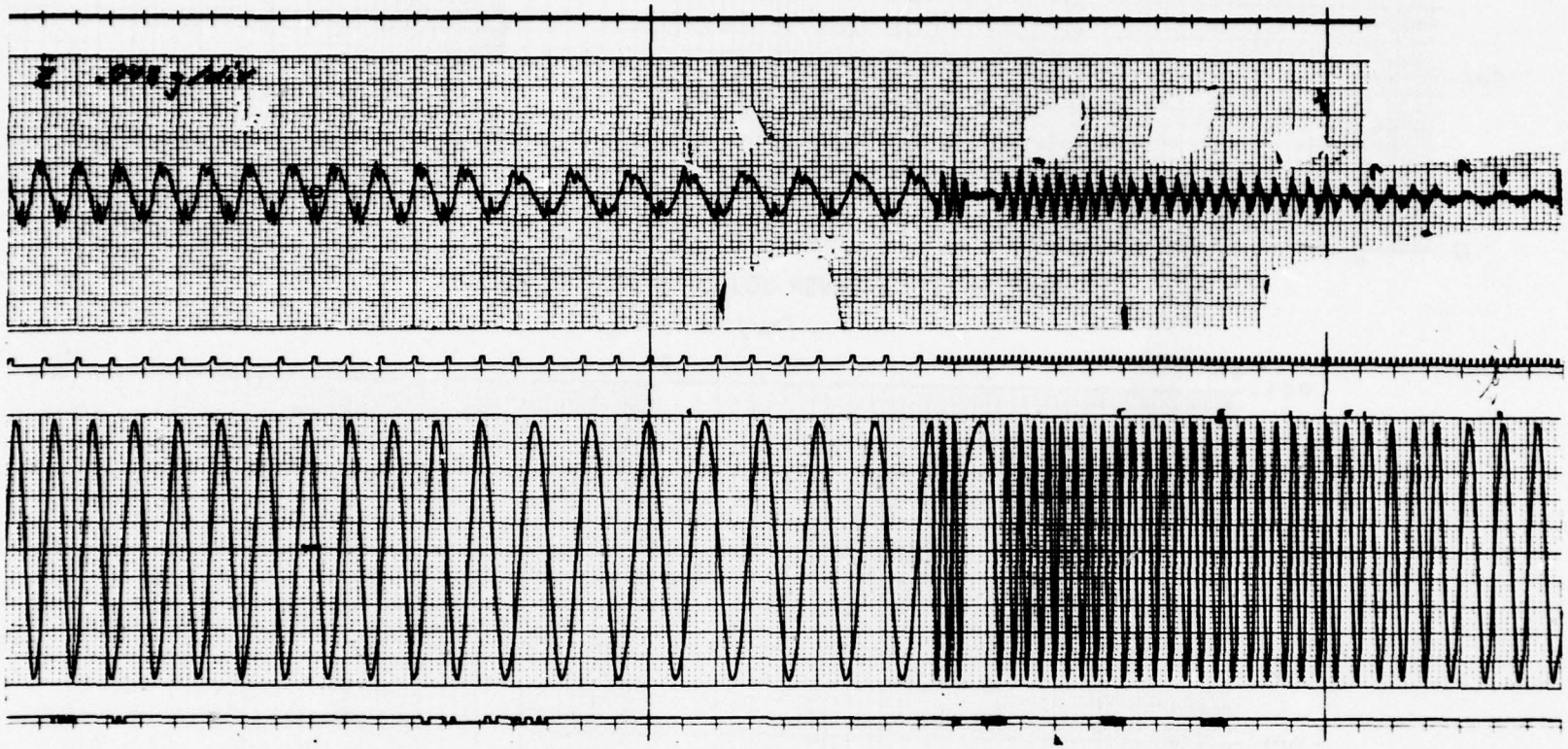


FIGURE 15

TYPICAL FREQUENCY RESPONSE DATA, HEAVE 5 INCH STROKE

Some degradation of the motion occurred at input frequencies under 1 Hz (Figure 15).

Based on the Bode plots and the time histories for sinusoidal inputs, it is the author's opinion that platform motion has deteriorated to the point where it must be considered non-linear for input signals above 3 Hz. In some cases the non-linear aspect of the motion may significantly affect results at frequencies as low as 0.5 Hz.

From the Bode plots, for low frequencies the platform's response pretty well behaves like an overdamped second order linear dynamic system with a slight difference in each individual leg. If the natural frequency is taken as the frequency when the phase angle is 90^{o}, then the natural frequencies of the six legs are 0.52, 0.62, 0.56, 0.51, 0.61 and 0.56, respectively. The Bode plots for accelerations also suggest an overdamped second order system with a natural frequency of about 1/2 Hz.

Due to time limitations, no attempt was made to formulate a mathematical model for the system from the Bode plots.

CONCLUSIONS AND RECOMMENDATIONS

The first conclusion that must be reached is that the SAAC motion system is not performing at a level desired for training purposes. It is felt that there are four areas where deficiencies exist. First, the present motion hardware is not functioning properly and should be repaired and "tuned up" to specifications. Specific problems that should be remedied are the cross couplings of motions and the abruptness of certain modes of motion. Secondly, there is a question of whether the hardware has the basic capability of meeting MIL-STD-1558 governing motion platform systems. The third area of lacking is in the software package associated with the SAAC. As an example, the present logic calls for the acceleration of the platform's centroid, rather than a point corresponding to the pilot. The fourth area that needs improvement is in the basic simulator logic of the best method to present cues to the pilot. For example, a non-linear washout scheme should greatly improve the illusion of aircraft motion.

The platform has been instrumented such that its motion can be studied. A comparison now needs to be made between what the platform is capable of and conditions that exist in the actual aircraft during air-to-air engagements.

Furthermore, an investigation needs to be performed on the most realistic way to use the platform's motion capability to simulate the actual aircraft.

REFERENCES

1. Unpublished data gathered for the Scientific Advisory Board's June meeting at Williams Air Force Base, Chandler, Arizona, June 1977.

2. Meriam, J. L., Dynamics, 2nd Edition, John Wiley and Sons, New York.

3. "Technical Specification for a 60-Inch Stroke Six-Degree-of-Freedom Motion System," Singer Products Division, The Singer Company, Binghamton, New York, May 6, 1972.

4. Singer Department Phase IV

5. Gundry, A. J., "Thresholds to Roll Motion in Flight Simulator," Visual and Motion Simulation Conference, Dayton, Ohio, April 26-28, 1976.

6. Parrish, R. V. and D. J. Martin, Jr., "Empirical Comparison of a Linear and a Nonlinear Washout for Motion Simulations," AIAA 13th Aerospace Sciences Meeting paper 75-106, January 1975.

7. Brewer, J. W., Control Systems: Analysis, Design and Simulation, Prentice-Hall, 1974.

8. Harrison, H. L. and J. G. Bollinger, Introduction to Automatic Controls, 2nd edition, International Textbook Company.

1977 USAF-ASEE SUMMER FACULTY RESEARCH PROGRAM
sponsored by
THE AIR FORCE OFFICE OF SCIENTIFIC RESEARCH
conducted by
AUBURN UNIVERSITY AND OHIO STATE UNIVERSITY

PARTICIPANT'S FINAL REPORT

THE RADIATIVE LIFETIME and QUENCHING CROSS SECTIONS OF THE $A^2\Sigma^+$ STATE OF GeF

Prepared by:	Richard A. Anderson
Academic Rank:	Professor
Department and University:	Department of Physics University of Missouri-Rolla
Assignment:	
(Air Force Base)	Kirtland Air Force Base
(Laboratory)	Air Force Weapons Laboratory
(Division)	Advanced Laser Technology Division
(Branch)	Chemical Laser Branch
USAF Research Colleague:	Captain Steven J. Davis, PhD
Date:	August 12, 1977
Contract No.:	F44620-75-C-0031

THE RADIATIVE LIFETIMES and QUENCHING CROSS SECTIONS OF THE $A^2\Sigma$ STATE OF GeF

by
Richard A. Anderson

ABSTRACT

Certain diatomic intermediate species such as SiF, GeF, etc., are primary candidates for chemically pumped electronic transition lasers. In the case of SiF and GeF, the $a^4\Sigma^-$ state is probably long lived and it may be possible to obtain lasing between the $a^4\Sigma^-$ and $A^2\Sigma^+$ level. Several parameters must be examined to produce lasing between these states. In this paper the lifetime of the $A^2\Sigma^+$ state, the laser induced fluorescence spectrum from the $A^2\Sigma^+$ state, and quenching rates of this state by the He, N_2, and SF_6 were measured.

In this experiment laser induced fluorescence was produced in a SiH_4 and F_2 or GeH_4 and F_2 flame directly. Initially, a SiH_4 and F_2 flame was excited with a pulsed nitrogen laser pumped dye laser. Both the lifetime and laser induced fluorescence spectrum of the $A^2\Sigma^+$ state were observed. Our lifetime was 247ns and agreed well with the 230±20ns measured by Davis and Hadley[1].

In the GeH_4 and F_2 flame the (0,2), (0,1) and (0,0) transitions were most intense in the laser induced spectrum. Zero pressure lifetimes were measured for the $v'=2$ and 1 levels of the $A^2\Sigma^+$ state and were 847±48 and 1035±193ns respectively. On the basis of our limited data, the zero pressure lifetime of the $v'=0$ level approximately the same as the other levels.

No quenching was observed for He. Only lower limit values can be given for the quenching rates of the $v'=1$ and 2 levels for N_2 and SF_6. No quenching rates could be measured for the $v'=0$ level. The quenching rates of N_2 on the $v'=1$ and 2 states are $0.919\pm.077\times10^6$ and $1.287\pm.151\times10^6$ $(\text{sec Torr})^{-1}$, respectively. For SF_6 the quenching rates were $0.252\pm.047\times10^6$ and $0.234\pm.038\times10^6$ $(\text{sec Torr})^{-1}$, respectively.

INTRODUCTION

During the past thirty years the spectra, spectroscopic constants, dissociation energies, and ionization potentials of GeF have been reported[2-7]. Many of these results have been summarized in a report by Suchard[8]. Eleven different band systems have been identified and eight excited doublet states and the lowest quartet state have been assigned. Spectroscopic constants are well known for the ground states, $X^2\pi_{1/2}$ and $X^2\pi_{3/2}$, and the $A^2\Sigma^+$, $B^2\Sigma^+$, and $a^4\Sigma^-$ states. Lifetimes have not been measured for any of the excited states.

Studies on the GeF molecule have been more limited than on SiF since in each case the molecules are produced in an electric discharge in GeF_4 or SiF_4. GeF_4 is not commercially available and must be specially prepared and this has limited the number of investigations on GeF.

Until this study it has been impossible to measure the lifetime of the $A^2\Sigma^+$ state of GeF in an electric discharge where GeF is re-excited by some pulsed means. In this study the GeF molecule was formed in a GeH_4 and F_2 flame and a pulsed dye laser tuned to a resonance wavelength of the first spin component of each absorption band re-excited the molecule. The laser induced fluorescence spectrum was recorded by wavelength scanning the laser over the region of the GeF absorption band. The lifetime was measured by recording the decay of this fluorescent light.

The lifetime of the $A^2\Sigma^+$ state of GeF is needed to calculate transition probabilities of the $A^2\Sigma^+ \rightarrow X^2\pi$ transition. Reliable transition probabilities are needed to determine abundances of GeF in stellar atomospheres, to determine the reliability of theoretical wavefunctions which are used to calculate Franck-Condon factors and transition moments, and to determine potential optical gains in laser applications. The GeF molecule is a candidate for a potential chemical laser via the $a^4\Sigma^- \rightarrow A^2\Sigma^+$ transition.

Quenching rate coefficients for three added foreign gases were determined for the GeF molecule. These data are of interest if a chemical laser is developed using the GeF molecule. The amount of quenching of both the $a^4\Sigma^-$ and $A^2\Sigma^+$ states must be known for a large number of gases which might be produced or used in a chemical laser system.

Three objectives of this research were accomplished.

(a) A flame of GeH_4 and F_2 was used to produce the GeF molecules and the best pressure parameter was determined to produce a laser induced fluorescence spectrum of the $A^2\Sigma^+ \rightarrow X^2\pi$ transition of GeF over the region from 4100-4500 A.

(b) Lifetimes of the $v'=0$, 1, 2 levels of the $A^2\Sigma$ state were determined at several total flame pressures so the zero pressure lifetime can be determined for each level.

(c) Lifetimes of the GeF molecule were determined for several pressures of added foreign gases, He, N_2 and SF_6, and from the Stern Volmer curves the quenching rate coefficients were evaluated.

EXPERIMENTAL APPARATUS AND RESULTS

A fluorescence cell used by Captain R. A. Armstrong in previous research was modified to include side arms with Brewster angle windows which were opposite each other and laser light was incident through them. The laser light from a Molectron Spectroscan 10 dye laser was focussed to a tight beam in the center of the fluorescence cell. Two elongated windows at right angles to the side arms and the laser beam allowed us to view the laser induced fluorescence. The flame nozzle position could be varied in vertical position so different positions of the flame could be irradiated by the laser. A two inch diameter ring with ten holes was placed on the bottom of the cell. Foreign gases could be introduced into the flame region with minimum disruption of the flame. The ring was four inches below the nozzle.

The GeF spectrum of the $A^2\Sigma^+ \rightarrow X^2\pi$ transition in a GeH_4 and F_2 flame was recorded. A McPherson Model 218 0.3 m monochromator, RCA 1P28 photomultiplier, Keithley Model 155 microvoltmeter and null detector, Hewlett Packard Model 7100BM strip chart recorder with a 17500A plug-in amplifier and a Power Designs Model 2K-10 photomultiplier power supply

were used to record the flame spectrum. This spectrum was compared with those of Andrews and Barrow[2], Martin and Merer[7], and Suchard's[8] tables. The spectrum was in agreement with those in the literature after the monochromator was calibrated with a Hg lamp. Figure 1 is a schematic of the apparatus.

In order to determine if a lifetime could be measured directly in a flame, a SiH_4 and F_2 flame was examined. Optimum pressures of He, SiH_4, and F_2 were determined by maximizing the SiF $A^2\Sigma^+ \rightarrow X^2\pi$ laser induced fluorescence emission. The laser beam was carefully focused into the cell to obtain maximum signal and the filtered photomultiplier was carefully adjusted. The SiF was pumped by the first spin component of the (0,0) band of the $A^2\Sigma^+ \rightarrow X^2\pi$ transition and the second spin components of the fluorescence was detected with the photomultiplier. A lifetime of 247 ns was measured. Capt Davis and Dr. Hadley[1] had measured a zero pressure lifetime of 230±20 ns for the $v'=0$ level of the $A^2\Sigma^+$ state of SiF. Davis and Hadley did not observe self quenching in the SiF signal. They produced SiF in a microwave discharge in SiF_4. The agreement was excellent indicating the technique would work. A laser induced fluorescence spectrum of the SiH_4 and F_2 flame was recorded and the (1,2) transition was most intense while theoretically (0,0) transition should be most intense.

The line width of the Molectron Spectroscan 10 dye laser was recorded at 4243Å. Molectron 70354-2 Bis-MSB dye was used in the laser.

A McPherson Model 2051 1m monochromator, 931A photomultiplier, Keithley Model 155 microvoltmeter and null detector, Hewlett Packard Model 7100BM strip chart recorder with a 17500A plug-in amplifier, and Power Designs Model 2K-10 power supply were used to record the laser line width. In Figure 2 is the recorded laser line and its width is about 6 Å.

A Products for Research, Inc. Model TE-104-TS-RF refrigerated housing with a RCA31034 photomultiplier tube, filtered with a Ealing 26-4275 broad band cut-off filter, was our detector for the GeF emission. The detector was powered by the Power Designs Model 2K-10 power supply operated at 1000V. The signal from the photomultiplier was amplified with a Hewlett Packard Model 461A wide band amplifier. A PAR Model 162 boxcar integrator with a 164 plug-in integrated the signal from the amplifier. The output from the boxcar was recorded on the Hewlett Packard Model 7100BM strip chart recorder. The time base of the boxcar recorder system was calibrated by recording a sine wave from a Hewlett Packard Model 3310A function generator whose frequency was measured on a Hewlett Packard Model 5327A counter.

The detection system had to be continuously checked for overload from scattered laser light before data were recorded. The output from the Hewlett Packard Model 461A amplifier was monitored on a Tektronix Model 454 oscilloscope. Overloading of the photomultiplier led to ringing and undershoot of the signal at the end of the laser pulse. The

voltage applied to the photomultiplier was varied to ascertain if overloading occurred. Each data run was monitored for photomultiplier overload before it was recorded. We also ran tests to check for imprisonment of radiation by taking data of the laser induced fluorescence emission at several different laser beam positions in the cell. No imprisonment was noted.

Theory shows that the Franck-Condon factor is largest for the (0,1) transition and decreased in the order (0,2) and 0,0). These transitions of the $A^2\Sigma^+$ system were pumped at the wavelengths of the first spin component which are 4163, 4236 and 4310Å for the (0,2), (0,1) and (0,0) transitions, respectively. Using both the Molectron 70354-2 Bis-MSB and 70335-2C120 dyes the laser induced fluorescence spectrum of GeF was recorded from 4100-4500Å. The laser was set at the peak intensity of the (0,2) band at about 4163Å and the boxcar integrator was scanned in time well past the peak (~150ns) and held at this time position in the decaying fluorescence signal. With the optics, photomultiplier position, and the gas pressure adjusted for maximum signal, the laser was scanned from 4100-4500Å using the two dyes and the laser induced fluorescence emitted by the cell was recorded. Figure 3 is this spectrum. The three major transitions, (0,0), (0,1), and (0,2) are seen along with some other laser induced emission bands.

Using the Bis-MSB dye and the Ealing 26-4275 filter the laser induced fluorescence could easily be observed for the $v'=1$ and 2 levels

of the $A^2\Sigma^+$ state. The filter had a transmittance of approximately 0.001 for the first spin component of the (0,2) band and approximately 0.01 for the (0,1) band. For the second spin components of the (0,2) and (0,1) transitions the transmittances are approximately 0.30 and 0.70, respectively. For the (0,2) and (0,1) transitions the second spin component was nearly exclusively observed. The scattered laser light tuned to the wavelenths of the first spin components viewed through the filter was negligible.

In order to pump the (0,0) transition C120 dye was used and again the GeF in the fluorescence cell was pumped on the first spin component of the $A^2\Sigma^+ \rightarrow X^2\pi$ transition. Using the Ealing 26-4275 filter the transmittance of this component at 4310Å was approximately 0.25 and the second spin component at 4492Å was 0.85. Since large amounts of the laser pumping light at 4310Å were transmitted by the filter, there were serious problems with scattered laser light. In both the foreign gas quenching and self quenching experiments, the fluorescence signal was reduced and it became very difficult to detect the fluorescence signal from the scattered laser light. It should be mentioned that in the case of SiH_4 and F_2 flame, there was no problem with scattered light. The SiF was pumped at 4368Å and the fluorescence signal of the second spin component occurs at 4400Å. The Ealing 26-4275 filter has a high transmittance of both of these lines, approximately 0.4 to 0.5, so scattering should have been strong in this system, but it was not a problem.

We were able to take two self quenching lifetime measurements without scattering problems for the (0,0) transition. These measurements were at 6.2 and 7.2 Torr and the lifetime values were 667 and 639 ns. In order to make either of these two measurements the incident light had to be baffled so there was an actual loss of pump light. For the (0,1) and (0,2) transitions the focussed laser beam could be transmitted into the cell without baffling of the main laser beam. Two apertures were used to remove some fringing light which did not correspond to the main laser beam. It was impossible to make foreign gas measurements for N_2 and SF_6 on the (0,0) transition.

Figures 4 and 5 show typical decay curves for the (0,2) transition at a given He, GeH_4 and F_2 total pressure (background pressure 0.8 Torr, helium pressure 6 Torr, fluorine pressure .12 Torr, and germane pressure .15 Torr). Figure 4 is the raw decay curve for the $v'=2$ level of the $A^2\Sigma^+$ state of GeF and Figure 5 is the semilog curve of this data. These figures show typical signal to noise of the data.

In Figures 6 and 7 are shown the self quenching data for the $v'=1$ and 2 levels of the $A^2\Sigma^+$ state. In this case the smallest total pressure was 6.2 Torr and this corresponded to the He, GeH_4 and F_2 mixture which gave the best laser induced fluorescence signal. The pressure in the system was changed by varying the pumping speed through the fluorescence chamber which led to a proportional change in the He, GeH_4, and F_2

pressures. The settings on the needle valves for GeH_4 and F_2 and the flow meter settings on helium dilutants were not changed. The total pressure was varied by an amount of 5 Torr by varying the pumping speed on the chamber. The variation in the lifetime over these pressure changes are shown in the figures. The points were fit by the least squares method and from the zero pressure intercepts the lifetimes were calculated. For the $v'=1$ and 2 levels of the $A^2\Sigma^+$ state of GeF the zero pressure lifetimes are 1035±193 and 847±48 ns, respectively.

Quenching measurements were made for three foreign gases, He, N_2, and SF_6. Helium did not show quenching over a pressure range of 6 Torr. Helium is the carrier gas for the GeH_4 and F_2 flame and could be used in any chemically pumped laser which might be developed.

Nitrogen might also be a possible carrier gas for a chemical laser and it is definitely an atmospheric pollutant to an evacuated chemical laser. The quenching of both the $v'=1$ and 2 levels by N_2 was examined. Nitrogen strongly quenched both levels, so when 1.5 Torr of N_2 was added, meaningful signals were difficult to resolve from the scattered light and noise. Since gases were not mixed directly with the He dilutants but were introduced by the ring at the bottom of the chamber, we are not certain of complete mixing with the flame at all pressures. If the amount of mixing was not complete and varied with the added gas

pressure, one would not expect the quenching to be linear. As a result, the Stern Volmer curves would be curved lines not straight lines as expected from theory.

$$\frac{1}{\tau} = \frac{1}{\tau_o} + kp \qquad (1)$$

where τ is the measured lifetime, τ_o the lifetime without foreign gases added, k the quenching rate coefficient, and p the foreign gas pressure. Figures 8 and 9 are the Stern Volmer curves for both N_2 and SF_6 for the $v'=1$ and 2 levels. For both gases and levels the data can best be fit by a straight line. Also the curves for both gases and for both levels intercept the reciprocal lifetime axis at the same point. This intercept should correspond to the reciprocal of the lifetime for these levels at a total gas pressure of 6.2 Torr (fluorine pressure 0.12 Torr and germane pressure 0.15 Torr).

Sulfur hexafluoride is an extremely stable molecule and should have a small quenching effect on the flame. The data indicates for both levels that the quenching is small, but not entirely negligible.

Since we can not be entirely certain of complete mixing under all foreign gas pressures, the quenching rate coefficients evaluated from the Stern Volmer plots in Figures 8 and 9 will be considered to be lower limits on their value. The data were fit by the least squares method.

For the $v'=1$ and 2 levels for N_2, the quenching rate coefficients are $0.919\pm.077\times10^6$ and $1.287\pm.151\times10^6$ (sec Torr)$^{-1}$ and for SF_6 they are $0.252\pm.047\times10^6$ and $0.234\pm.038\times10^6$ (sec Torr)$^{-1}$ respectively. From the intercepts the lifetimes of the $v'=1$ and 2 levels at a total gas pressure of 6.2 Torr can be evaluated and are 606±20 and 655±53 and 660±17 and 633±12 ns for N_2 and SF_6, respectively. These values correspond closely with the measured lifetimes for this gas pressure of 658 ns for the $v'=1$ level and 641 ns for the $v'=2$ level.

DISCUSSION AND CONCLUSIONS

Laser induced fluorescence of the GeF molecule can be easily observed in a GeH_4 and F_2 flame. From the laser induced fluorescence spectrum it is seen that the (0,1) and (0,2) fluorescence are adequate so reliable self quenching lifetimes could be evaluated over several total pressures in the fluorescence cell. Figures 4 and 5 are typical decay curves for the $v'=2$ level. Figures 6 and 7 are the self quenching curves for the $v'=1$ and 2 levels. From zero pressure intercept the lifetimes of these states are 1035±193ns for $v'=1$ and 847±ns for $v'=2$. The difference in lifetime between these states is greater than the error expected in the experiment. From our data the $v'=2$ level has a slightly shorter lifetime than the $v'=1$ level.

It was impossible to make as extensive measurements of self quenching on the $v'=0$ level as on the $v'=1$ and 2 levels. Large amounts of

scattered laser light were observed in the (0,0) emission because the filter had a large transmittance at the laser wavelength. The self quenching signal would become buried in the noise when the total pressure increased because of quenching and shortening of the flame. From our limited data, the zero pressure lifetime of the $v'=0$ level should be close to the zero pressure lifetimes of the $v'=1$ and 2 levels.

The lifetime of GeF is four to five times longer than the lifetime measured for SiF. This increase might be expected as one progresses to heavier members of the monofluorides of the carbon subgroup. Even though, they are not good candidates for chemical laser the lifetimes of various vibrational states of SnF and PbF should be measured.

From our quenching data we can conclude that He does not quench the GeH_4 and F_2 flame, so it is a desirable carrier gas. Relatively stable SF_6 gas has a measurable quenching effect on the flame and would be a less desirable carrier gas. N_2 quenches the flame strongly and can not be used as a carrier gas and must be excluded from the system. The measured quenching rate coefficients are lower limits since we are uncertain of complete mixing in the flame. The lifetime evaluated from Stern Volmer plots are in excellent agreement with lifetimes measured at a total gas pressure of 6.2 Torr.

In future experiments our quenching rate coefficients for foreign gases must be re-measured. The foreign gases should be used as the

carrier gases or mixed with the helium carrier gas. In this way, the foreign gas pressure can be accurately known in the flame region.

ACKNOWLEDGEMENTS

The author is indebted to the entire staff of the Space Laser Technology Section of the Chemical Laser Branch of the Advanced Laser Technology Division of the Air Force Weapons Laboratory for providing a pleasant and helpful work environment. I am especially grateful to Captain Steven Davis and Major David Olson for providing the equipment, facilities, and technical assistance. The project would not have been completed without the valuable assistance of Leonard Hanko, Virginia Hanratty and James Francis.

REFERENCES

[1]S. J. Davis and S. G. Hadley, "Measurement of the radiative lifetime of the $A^2\Sigma^+(v'=0)$ state of SiF," Phys. Rev. A14 114650 (1976).

[2]E. B. Andrews and R. F. Barrows, "A,B-X Systems," Proc. Phys. Soc. A63 185-91 (1950).

[3]J. W. C. Johns and R. F. Barrows, "Ionization Potential," Proc. Phys. Soc. 71, 476-84 (1958).

[4]R. F. Barrows, D. Butler, J. W. C. Johns, and J. L. Powell, "Ultraviolet and Infrared Systems," Proc. Phys. Soc. 73, 317-20 (1959).

[5]T. C. Ehlert and J. L. Margrave, "Dissociation Energy," J. Chem. Phys. 41, 1066-72 (1964).

[6]Y. Y. Kuzyakov, "Determination of Energy of Dissociation of Certain Monoholides of Carbon Subgroup," Vesta. Mosk. Univ. Kim. 3, 21-4 (1968).

[7]R. W. Martin and A. J. Merer, "Rotational Structure in the $A^2\Sigma^+$, $B^2\Sigma^+$, and $a^4\Sigma^- - X^2\pi$ Transitions of GeF," Can. J. Phys. 51, 125-43 (1973).

[8]S. N. Suchard, "Spectroscopic Constants for Selected Heteronuclear Diatomic Molecules," Vol II, pp G38-43, Aerospace Corporation Report No. TR-0074(4641)-6, Air Force Report No. SAMSO-TR-74-82 (29 March 1974).

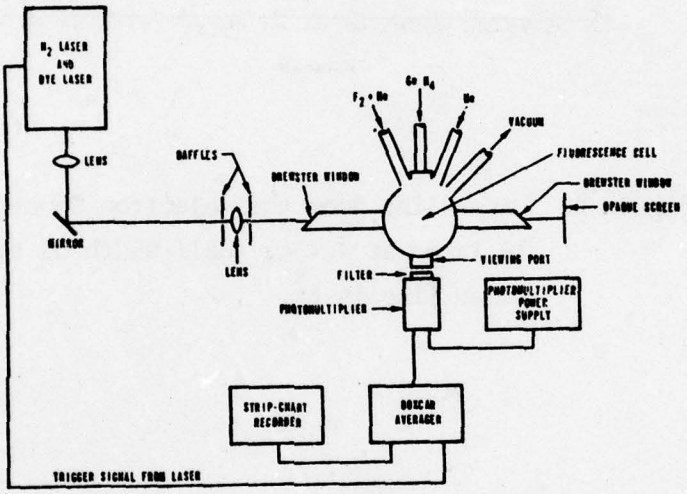


Figure 1. Schematic of the apparatus.

AD-A051 514 AUBURN UNIV ALA SCHOOL OF ENGINEERING F/G 5/2
1977 USAF-ASEE SUMMER FACULTY RESEARCH PROGRAM. VOLUME II.(U)
SEP 77 J F O'BRIEN F44620-75-C-0031
UNCLASSIFIED AFOSR-TR-78-0349 NL

5 OF 6
AD A051514



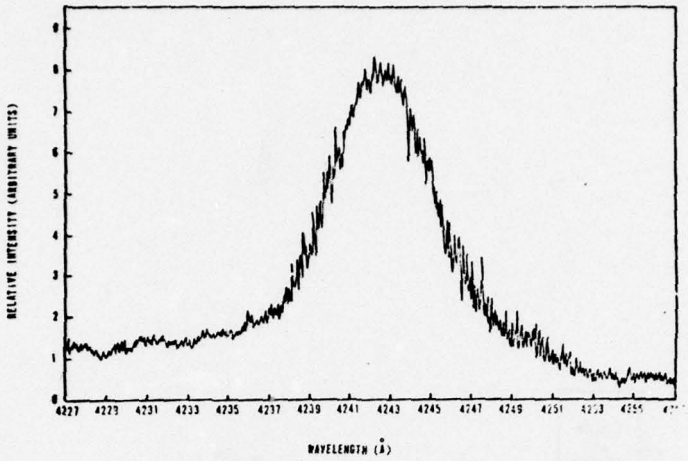


Figure 2. Laser line from the Molectron Spectroscan 10 laser at 4243Å. Half width of the laser line is 6Å.

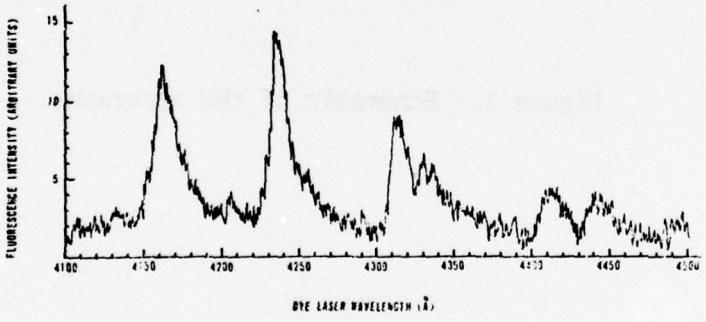


Figure 3. Laser induced fluorescence spectrum of GeF over the region from 4100-4500Å.

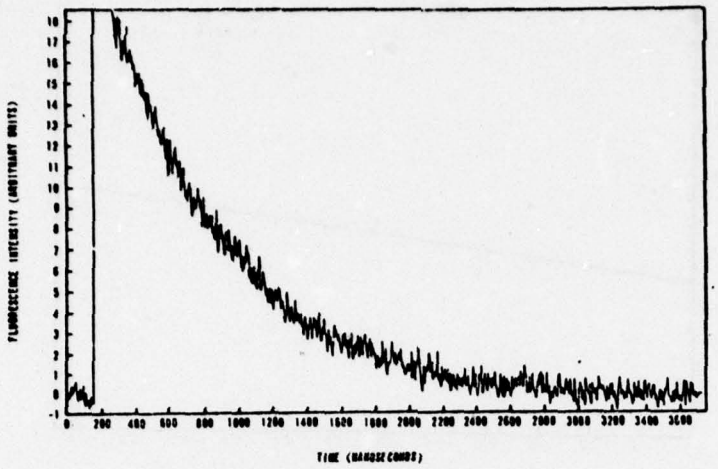


Figure 4. Typical decay curve of the $v'=2$ level of the $A^2\Sigma^+$ state pumped at 4163Å corresponding to the first spin component of the (0,2) transition.

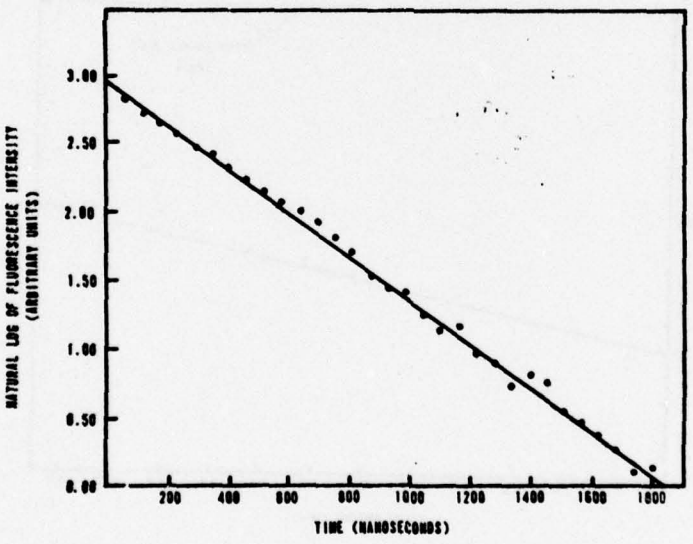


Figure 5. Semilog plot of the data. The decay time for this curve is 629ns.

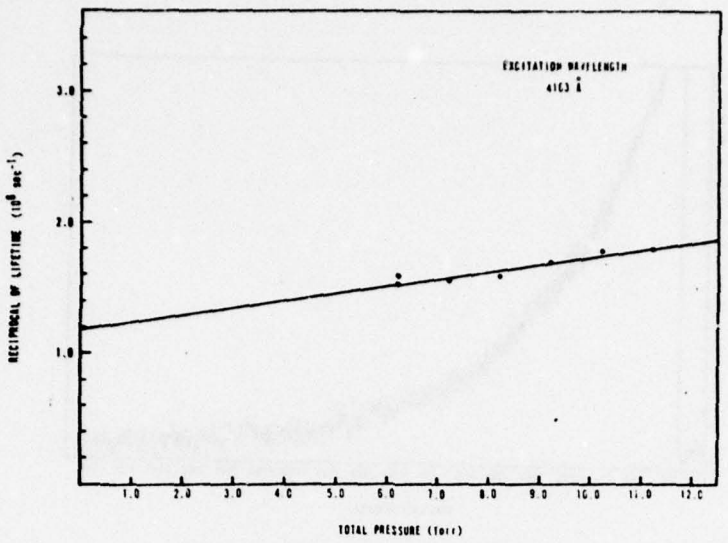


Figure 6. Self quenching curve of the reciprocal of the lifetime of the $v'=2$ level of the $A^2\Sigma^+$ state versus the total pressure in the fluorescence cell.

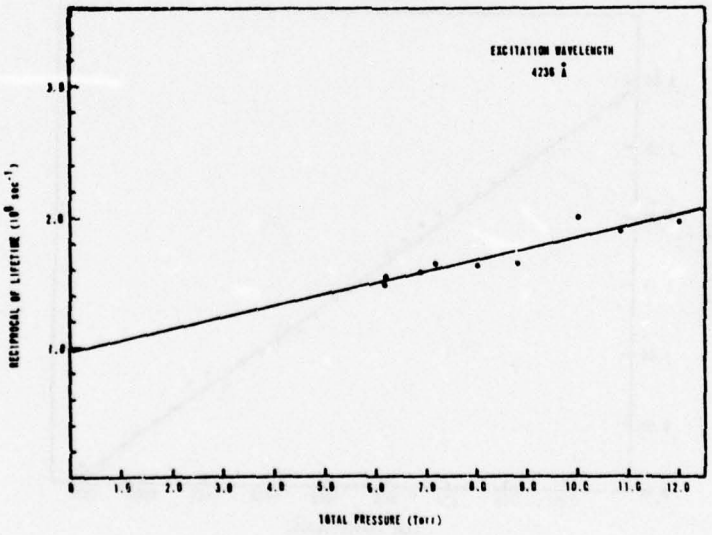


Figure 7. Self quenching curve of the reciprocal of the lifetime of the $v'=1$ level of the $A^2\Sigma^+$ state versus the total pressure in the fluorescence cell.

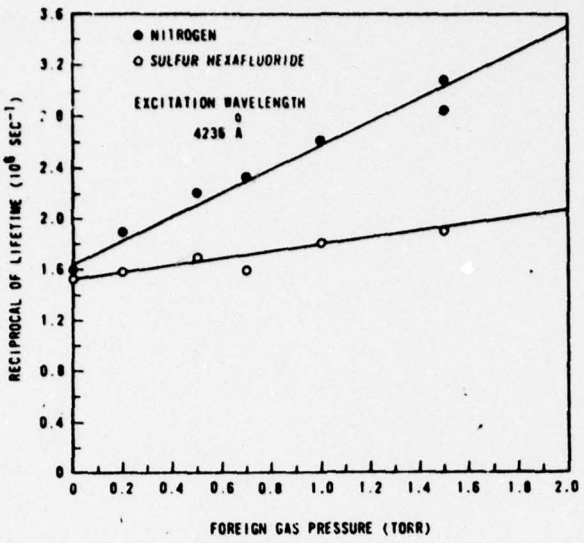


Figure 8. Stern Volmer curve for the $v'=2$ level of the $A^2\Sigma^+$ state of GeF for SF_6 and N_2.

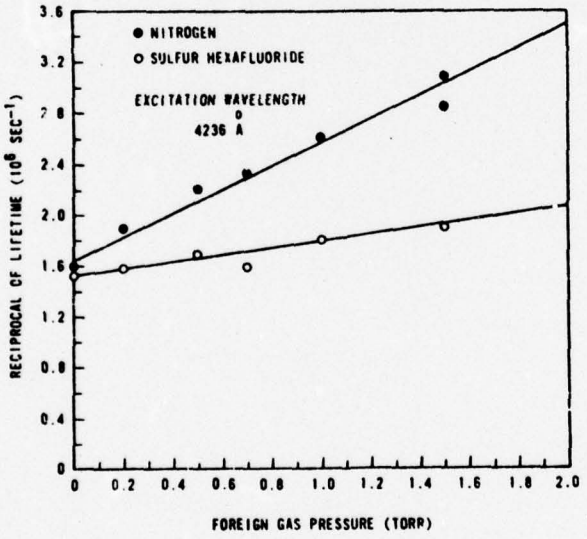


Figure 9. Stern Volmer curve for the $v'=1$ level of the $A^2\Sigma^+$ state of GeF for SF_6 and N_2.

1977 USAF-ASEE SUMMER FACULTY RESEARCH PROGRAM
sponsored by
THE AIR FORCE OFFICE SCIENTIFIC RESEARCH
conducted by
AUBURN UNIVERSITY AND OHIO STATE UNIVERSITY

PARTICIPANT'S FINAL REPORT

TRANSIENT FIELDS FROM A VERTICALLY POLARIZED DIPOLE RADIATOR WITH A RAMP-FUNCTION INPUT VOLTAGE

Prepared by:	Dr. Martin D. Bradshaw
Academic Rank:	Professor
Department and University:	Electrical Engineering and Computer Science Department University of New Mexico
Assignment:	Kirtland Air Force Base Air Force Weapons Laboratory Electronics Aircraft and Missile
USAF Research Colleague:	Dr. J. Philip Castillo
Date:	August 5, 1977
Contract No.:	F44260-76-C-0031

TRANSIENT FIELDS FROM A VERTICALLY POLARIZED DIPOLE RADIATOR WITH A RAMP-FUNCTION INPUT VOLTAGE

by

M. D. Bradshaw

ABSTRACT

The objective for this effort was to study the correlation between theory and experiment for the transient radiated fields for one of the various EMP simulators now in existence. The specific antenna studied was the vertically polarized dipole radiator.

The latest previous analytical work was compared with existing experimental data on the VPD-1 facility at the Air Force Weapons Laboratory. The theoretical values were found to be larger than the measured values. The model which was used in this analysis had a unit-step type of input voltage to the antenna.

An analysis was performed in which the input voltage was changed from the unit-step function to a ramp-function which becomes a constant value at some time T_1, which is a variable. For small values of this parameter, the fields compare closely to those of the previous model. However, they do match the experimental values more closely.

The final part of the study examined the effect of the finitely conducting ground screen and earth over which the antenna is erected. The previous studies have all assumed ground planes which were perfect conductors, of infinite extent. A method of handling the ground plane and earth conduction effects is presented.

ACKNOWLEDGMENTS

The author appreciates the initiative of the Air Force Office of Scientific Research for supporting a summer research program of this type. The work of ASEE and Auburn University, in particular, Mr. Fred O'Brien and of Dr. Guenther's Office, in administering the program in an excellent manner is certainly appreciated by this participant.

The author especially wishes to thank the fine crew at the ELA branch of the Air Force Weapons Laboratory for providing an exciting and interesting working environment. The services and facilities provided by the entire group were excellent. For fear of overlooking someone, I won't list individual names, but I appreciate the help which each has provided in their own way.

Finally, I wish to thank my colleague, Dr. J. Philip Castillo, for providing encouragement, insight and advice in completing the project.

All in all, it has been a most interesting and enjoyable summer and I again want to thank each person or organization which made it possible for me to be a participant.

LIST OF FIGURES

Figure 1 Comparison of Measured and Calculated E_θ field at r = 55 meters for VPD-1 Facility

Figure 2 Comparison of Measured and Calculated $\tilde{E}_\theta$ field at r = 55 meters for VPD-1 Facility

Figure 3 Comparison of Peak Measured and Calculated E_θ fields as a function of γ

Figure 4 Ramp-Input Used for Analysis

Figure 5 $\gamma_1'(0)$ as a function of T_1/t_h for $\theta = 90°$ and $\alpha = 1$

Figure 6 Dependence of $\gamma_1'(0)$ on θ for $\alpha = 1$ and $T_1/t_h = 0.10$

Figure 7 Comparison of Step and Ramp Solution for E_θ for r = 55 meters, $T_1/t_h = 0.10$

Figure 8 Comparison of Step and Ramp Solution for E_θ for r = 300 meters, $T_1/t_h = 0.10$

Figure 9 Peak values of E_θ versus γ, Step and Ramp Inputs

Figure 10 Peak values of rE_θ versus γ, Step and Ramp Inputs

Figure 11 Ground Attenuation Factor, $|\tilde{G}_e(\omega_h)|$ as a Function or ω_h, for Typical Earth Parameters

Figure 12 Ground Plane Gain Factor, $|\tilde{G}_p(\omega_h)|$, as a Function of ω_h, for good ground plane

Figure 13 Product of Ground Attenuation Factor and Ground Plane Gain Factor as a function of ω_h.

Figure 14 $\tilde{E}_\theta$ at r = 55 meters, Including Earth and Ground Plane Effects

LIST OF TABLES

Table 1 Computed Values of $\tilde{G}$ as a function of ka

Table 2 Ground Plane Gain as a Function of ω_h

INTRODUCTION

In connection with the analysis of EMP effects, there has been a great deal of interest in the calculation of the transient fields radiated by various types of antennas. Because most of these antennas have very complicated geometrics, it is very difficult to model them exactly in order to derive an analytical expression which can accurately represent these transient radiated fields. Furthermore, most of the analyses have used simplified models of the pulser and include ground effects by assuming that the antenna is on a perfectly conducting ground plane which is infinite in extent. In addition, the current distribution on the antenna is generally assumed to be of a type which lends itself to analytical techniques.

A good example of the above procedure is in the papers which have analyzed the fields of the vertically polarized dipole EMP facilities, either in use or planned at the Air Force Weapons Laboratory. Baum has used a transmission line model to determine the far-fields of this antenna when it is resistively loaded.[2,3] The effects of the near field components is included by the process described by Singaraju and Baum.[4] They show that the additional field terms present can be derived from a knowledge of the far-field value of the theta component of the electric field.

There are more involved approaches which model the antenna as a collection of wires and use a moment technique to model the current distribution and calculate the fields of the antennas. Blackburn and Taylor[5] used this technique to compute the fields radiated by an antenna similar to a Hybrid Simulator located at the Air Force Weapons Laboratory.

The major difference between these two approaches is the amount of computer time needed to calculate the radiated fields. The "fine-grain" structure of the field is obtained by the moment method, but there is a corresponding increase in the time and size of the computer analyses.

The initial objective of the study was to compare the theoretical values of the fields radiated by the vertically polarized dipole with the experimental results which had previous been obtained.[6-7] In the process of this investigation, it became apparent that the model used had some problems which would not allow good agreement between experimental and calculated values. Therefore, a different form of the generator model input voltage was studied, which produced somewhat closer agreement. However, there was still a divergence between the analytical and experimental values and it was felt that this might be due to the assumption regarding the ground plane. There has been considerable work done for steady-state situation with respect to ground conditions[8,9,10,11] and, more recently the problem of transient radiation with the presence of a finitely conducting ground has been studied.[12,13,14] The effects of the ground plane and finitely conducting ground are very difficult to work into a completely theoretical analysis. However, it was possible to include these effects in a simplified manner in the frequency domain. By making use of the FFT, then, the effects in the time-domain could be studied.

The report is broken into three major sections: The comparison of the radiated fields with experimental data using the model of [4] ; the analyses of these fields when the input is changed from a step to a ramp-input; and, the effects on both of these models when a finitely conducting ground screen of limited extent is assumed to lie on top of a finitely conducting homogeneous plane ground.

COMPARISON OF THEORETICAL AND EXPERIMENTAL FIELDS FOR THE VPD-1 FACILITY

The VPD-1 facility is described in detail elsewhere.[6] The fields were mapped at several locations under two different efforts.[6,7] In this section, these experimental results will be compared with the analytical results derived by Singaraju and Baum.

In making the computations, it was found simpler to use the E_θ field in the form given by Baum in [1] and then perform the indicated operations in order to get the final results. In addition, it was found that a relatively simple form for the fields in the frequency domain could be obtained by straightforward complex number manipulations.

A brief review of the method used in [4] will be given here.

Define the following quantities.

$\widetilde{E}_{f_\theta}(\bar{r})$ = far-field theta component, in frequency domain

$E_{f_\theta}(\bar{r})$ = far-field theta component, in time domain

The field in the frequency domain is expressed in terms of a normalized far-field, $\tilde{f}_1'(\theta)$ as

$$\widetilde{E}_{f_\theta}(\bar{r}) = \frac{V_0}{2\pi f_g} \frac{e^{-\gamma_0 r}}{r} \tilde{f}_1'(\theta) \qquad (1)$$

where:

f_g = geometric factor $\approx \frac{1}{\pi} \ln\left(\frac{2h}{a}\right)$ (2a)

h = half-height of antenna (2b)

a = mean radius of antenna (2c)

γ_0 = complex propagation constant, in free space, = s/c (2d)

V_0 = voltage applied to antenna by pulser, volts (2c)

Now define the quantities $\tilde{f}_2'(\theta)$ and $\tilde{f}_3'(\theta)$ as

$$\tilde{f}_2'(\theta) = \frac{1}{S_h}\tilde{f}_1'(\theta) \tag{3}$$

$$\tilde{f}_3'(\theta) = \frac{1}{S_h^2}\tilde{f}_1'(\theta) \tag{4}$$

where: S_h = normalized radian frequency = $S\left(\frac{h}{c}\right)$ (5)

The total field is now expressed as a combination of $\tilde{f}_1'(\theta)$, $\tilde{f}_2'(\theta)$ and $\tilde{f}_3'(\theta)$ of the form

$$\tilde{E}_\theta = \left[\frac{V_0 k_h}{2\pi f_g}\right]\frac{e^{-\gamma_0 r}}{r}\left[\tilde{f}_1'(\theta) + \frac{h}{r}\tilde{f}_2'(\theta) + \left(\frac{h}{r}\right)^2\tilde{f}_3'(\theta)\right] \tag{6}$$

where: r = radial distance from center of antenna to point of observation

(7)

In a similar fashion, the $\tilde{E}_r$ and $\tilde{H}_\phi$ fields can be expressed as:

$$\tilde{E}_r = 2\cot\theta\left[\frac{V_0 k_h}{2\pi f_g}\right]\frac{e^{-\gamma_0 r}}{r}\left[\frac{h}{r}\tilde{f}_2'(\theta) + \left(\frac{h}{r}\right)^2\tilde{f}_3'(\theta)\right] \tag{8}$$

$$\tilde{H}_\phi = \frac{1}{Z_0}\left[\frac{V_0 k_h}{2\pi f_g}\right]\frac{e^{-\gamma_0 r}}{r}\left[\tilde{f}_1'(\theta) + \frac{h}{r}\tilde{f}_2'(\theta)\right] \tag{9}$$

In the time domain, the far-field theta component is expressed as:

$$E_{f_\theta}(r,t) = \left[\frac{V_0}{2\pi f_g}\right]\frac{1}{r}f_1'(\theta) \tag{10}$$

where: $f_1'(\theta)$ is the inverse Laplace transform of $\tilde{f}_1'(\theta)$

Define the two corresponding quantities $f_2'(\theta)$ and $f_3'(\theta)$ now as

$$\mathcal{F}_2'(\theta) = \int_0^{\gamma_h} \mathcal{F}_1'(\theta)\, d\gamma_h \tag{11}$$

$$\mathcal{F}_3'(\theta) = \int_0^{\gamma_h} \mathcal{F}_2'(\theta)\, d\gamma_h \tag{12}$$

where γ_h is the normalized retarded time defined as

$$\gamma_h = \left(\frac{ct - r}{h}\right) \tag{12}$$

The time-domain fields corresponding to the frequency domain fields given by (6), (8), and (9), are respectively

$$E_\theta(\bar{r},t) = \left[\frac{V_0}{2\pi f_g}\right]\frac{1}{r}\left[\mathcal{F}_1'(\theta) + \frac{h}{r}\mathcal{F}_2'(\theta) + \left(\frac{h}{r}\right)^2\mathcal{F}_3'(\theta)\right] \tag{13}$$

$$E_r(\bar{r},t) = 2\cot\theta\left[\frac{V_0}{2\pi f_g}\right]\frac{1}{r}\left[\frac{h}{r}\mathcal{F}_2'(\theta) + \left(\frac{h}{r}\right)^2\mathcal{F}_3'(\theta)\right] \tag{14}$$

$$H_\phi(\bar{r},t) = \frac{1}{Z_0}\left[\frac{V_0}{2\pi f_g}\right]\frac{1}{r}\left[\mathcal{F}_1'(\theta) + \frac{h}{r}\mathcal{F}_2'(\theta)\right] \tag{15}$$

Now using the form of $\mathcal{F}_1'(\theta)$ as derived initially in [1], we have

$$\mathcal{F}_1'(\theta) = \frac{\sin\theta}{2(S_h+\alpha)}\left\{\frac{1}{(1-\cos\theta)}\left[\frac{e^{-S_h(1-\cos\theta)}-1}{S_h(1-\cos\theta)} + 1\right]\right. \tag{16}$$

$$\left. + \frac{1}{(1+\cos\theta)}\left[\frac{e^{-S_h(1+\cos\theta)}-1}{S_h(1+\cos\theta)} + 1\right]\right\}$$

where: (17)

$$\alpha = 1 + C_a/C_g$$

and c_a = antenna capacitance (18a)

c_g = generator capacitance (18b)

Following Baum, we can write the time-domain form of this function as

$$\gamma_1'(\theta) = \frac{\sin\theta}{2}\left\{\left[\left(\frac{1}{(1-\cos\theta)} + \frac{1}{(1+\cos\theta)}\right)e^{-\alpha\gamma_h}\right.\right.$$

$$\left. - \frac{1}{\alpha}\left(\frac{1}{(1-\cos\theta)^2} + \frac{1}{(1+\cos\theta)^2}\right)(1-e^{-\alpha\gamma_h})\right] u(\gamma_h) \qquad (19)$$

$$\left. + \left[\frac{1-e^{-\alpha\gamma_1}}{\alpha(1-\cos\theta)^2}\right] u(\gamma_1) + \left[\frac{1-e^{-\alpha\gamma_2}}{\alpha(1+\cos\theta)^2}\right] u(\gamma_2)\right\}$$

where:

$$\gamma_1 = \gamma_h - (1-\cos\theta) \qquad (20a)$$

$$\gamma_2 = \gamma_h - (1+\cos\theta) \qquad (20b)$$

Performing the integrations indicated by equations (11) and (12) result in

$$\gamma_2'(\theta) = \frac{\sin\theta}{2}\left\{\left[c_2\gamma_h + \frac{c_1-c_3}{\alpha}(1-e^{-\alpha\gamma_h})\right] u(\gamma_h)\right.$$

$$+ c_3\left[\gamma_1 - \frac{1}{\alpha}(1-e^{-\alpha\gamma_1})\right] u(\gamma_1) \qquad (21)$$

$$\left. + c_4\left[\gamma_2 - \frac{1}{\alpha}(1-e^{-\alpha\gamma_2})\right] u(\gamma_2)\right\}$$

$$\gamma_3'(\theta) = \frac{\sin\theta}{2}\left\{\left[\frac{c_3}{2}\gamma_h^2 + \frac{(c_1-c_3)}{\alpha}\gamma_h + \frac{c_3-c_1}{\alpha^2}(1-e^{-\alpha\gamma_h})\right] u(\gamma_h)\right.$$

$$+ c_3\left[\frac{\gamma_1^2}{2} - \frac{1}{\alpha}\left(\gamma_1 - \frac{1}{\alpha}(1-e^{-\alpha\gamma_1})\right]\right] u(\gamma_1) \qquad (22)$$

$$\left. + c_4\left[\frac{\gamma_2^2}{2} - \frac{1}{\alpha}\left(\gamma_2 - \frac{1}{\alpha}(1-e^{-\alpha\gamma_2})\right]\right] u(\gamma_2)\right\}$$

Where, for compactness, C_1, C_2, C_3 and C_4 are defined as:

$$C_1 = \frac{1}{1-\cos\theta} + \frac{1}{1+\cos\theta} \qquad (23a)$$

$$C_2 = -\frac{1}{\alpha}\left[\frac{1}{(1-\cos\theta)^2} + \frac{1}{(1+\cos\theta)^2}\right] \qquad (23b)$$

$$C_3 = \frac{1}{\alpha(1-\cos\theta)^2} \quad (23c) \qquad C_4 = \frac{1}{\alpha(1+\cos\theta)^2} \quad (23d)$$

The form of these answers appear to be different than those given in [4], but the use of trigonometric substitutions shows that the results are identical. Note that for this form of the answers, the important case of $\theta = 90°$ is easily handled since $C_1 = 2$, $C_2 = 2/\alpha$, $C_3 = C_4 = 1/\alpha$ and $\gamma_1 = \gamma_2 = \gamma_h$. Thus the solutions are greatly simplified for this particular case.

Using the same idea in the frequency domain, we can write the expression given in equation (16) in the form

$$\tilde{\gamma}_1'(\theta) = \frac{\sin\theta}{2(\alpha + s\omega_h)} \left\{ \frac{1}{1-\cos\theta}\left[\frac{e^{-s\omega_1}-1}{s\omega_1} + 1\right] + \frac{1}{1+\cos\theta}\left[\frac{e^{-s\omega_2}-1}{s\omega_2} + 1\right]\right\} \quad (24)$$

where: $s\omega_h$ = normalized frequency = S_h (25a)

$$\omega_1 = \omega_h(1-\cos\theta) \quad (25b) \qquad \omega_2 = \omega_h(1+\cos\theta) \quad (25c)$$

Now, note that the bracketed quantity in equation (6) may be put in the form.

$$[\ \ ] = \left|\tilde{\gamma}_1'(\theta)\right| \left[\sqrt{G_1^2 + G_2^2}\ \angle \tan^{-1}\frac{G_2}{G_1}\right] \quad (26)$$

Where:

$$G_1 = \left[1 - \left(\frac{h}{r\omega_h}\right)^2\right]\cos\beta_1 + \frac{h}{r\omega_h}\sin\beta_1 \quad (27)$$

$$G_2 = \left[1 - \left(\frac{h}{r\omega_h}\right)^2\right]\sin\beta_1 - \frac{h}{r\omega_h}\cos\beta_1 \quad (28)$$

and β_1 is the phase angle of $\tilde{\gamma}_1'(\theta)$. In this form only the magnitude and angle of the $\tilde{\gamma}_1'(\theta)$ term needs to be computed to get the total $\tilde{E}_\theta(r)$ field, for any particular $\left(\frac{r}{h}\right)$ value.

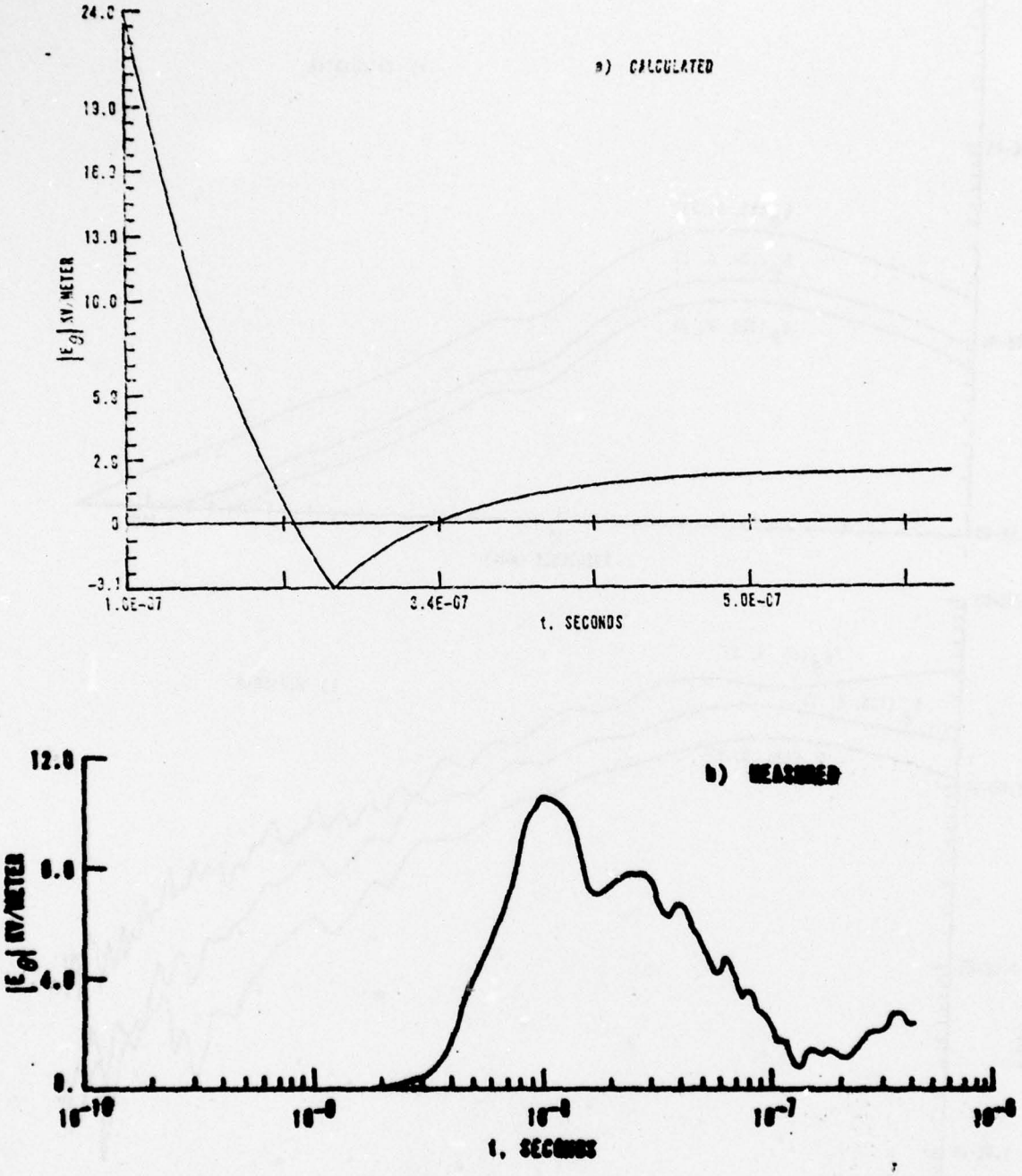


Figure 1 Comparison of Measured and Calculated E_θ field at r=55 meters for VPD-1 Facility

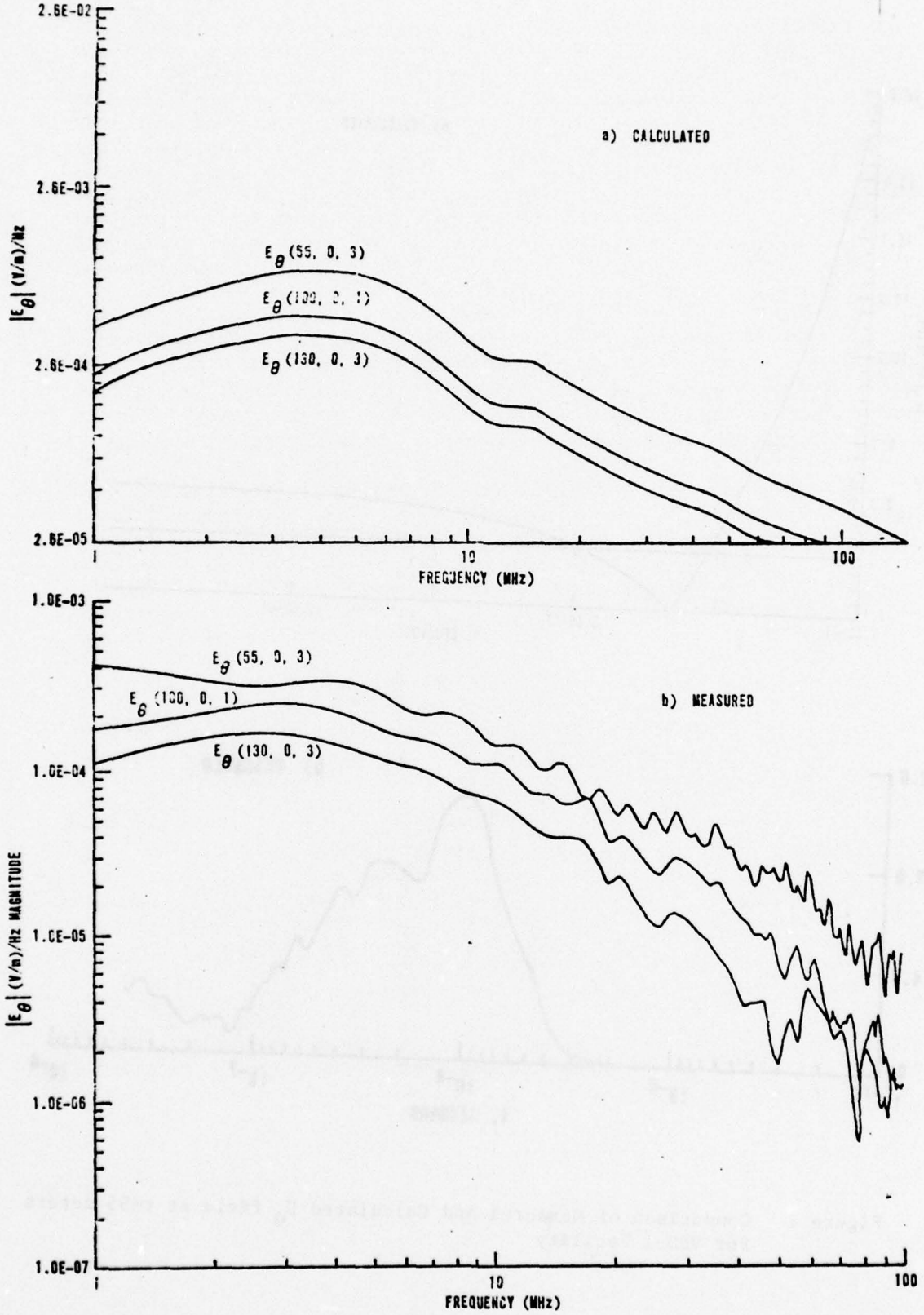


Figure 2 Comparison of Measured and Calculated $\tilde{E}_\theta$ field at r=55 meters for VPD-1 Facility

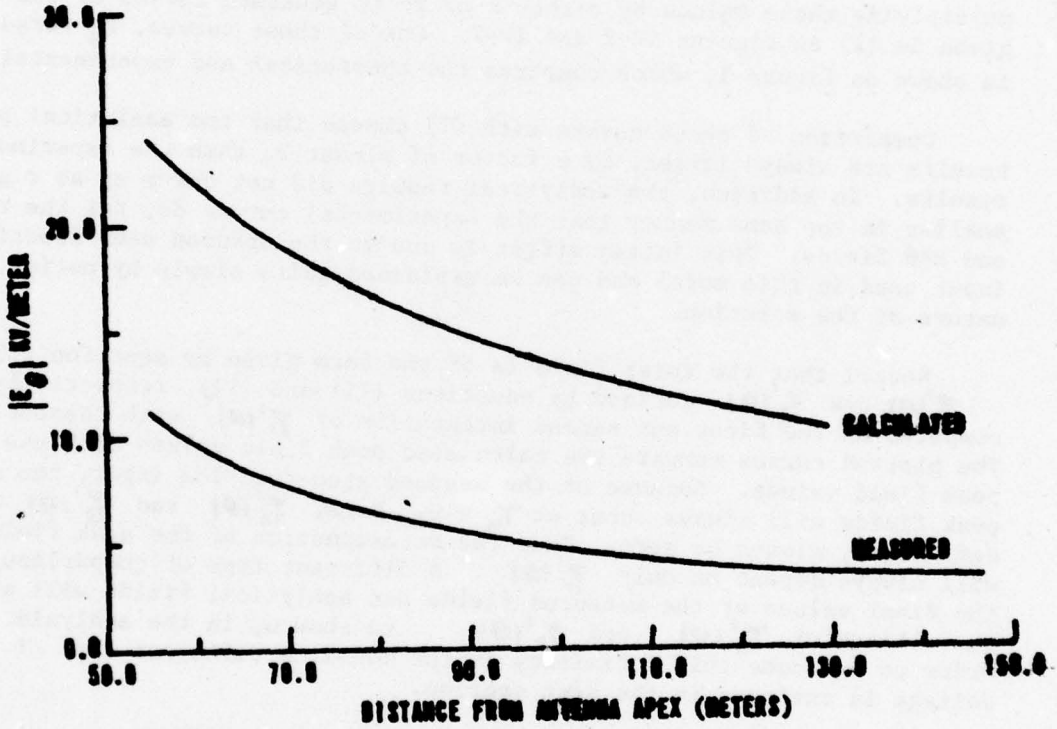


Figure 3 Comparison of Peak Measured and Calculated E_θ fields as a function of ϑ

These expressions were put on a small computer and plots made to check the agreement with the plots given in (4). The $\gamma_1'(0)$, $\gamma_2'(0)$, $\gamma_3'(0)$, and $|\gamma_1'(0)|$ terms all were in good agreement. However, when the total field quantities were computed, i.e. H_ϕ, E_r and E_θ, there appeared to be some difference in the plots. In addition, note that the time scale on the time-domain plots from (4) do not appear to be correct. The calculated field is compared with a measured field from (6) on Figure 1. Note the difference between the curves, especially the peak amplitude of the pulse. The frequency domain results are compared on Figure 2. Again, note the differences between the theoretical and experimental values.

Next, these equations were manipulated into a form where curves could be generated which could be compared with the experimental data obtained in (7). This involved computing the peak value of E_θ and B_ϕ and then multiplying these values by either r or r^2 to generate curves of the form given in (7) as Figures IV-2 and IV-7. One of these curves, E_θ versus γ is shown on Figure 3, which compares the theoretical and experimental values.

Comparison of these curves with (7) showed that the analytical peak results are always larger, by a factor of almost 2, than the experimental results. In addition, the analytical results did not curve up as r gets smaller in the same manner that the experimental curves do, for the rEθ and rBØ fields. This latter effect is due to the assumed step function input used in this model and can be explained quite simply by noting the nature of the solution.

Recall that the total field is of the form given by equation (13), where $\gamma_2'(0)$ and $\gamma_3'(0)$ defined by equations (11) and (12), respectively, are computed as the first and second integration of $\gamma_1'(0)$ with respect to γ_4. The plotted curves compare the calculated peak field values with the measured peak field values. Because of the assumed step-function input, the calculated peak fields will always occur at $\gamma_4 = 0$. Here, $\gamma_2'(0)$ and $\gamma_3'(0)$ will, by definition, always be zero. Thus the determination of the peak field values will always depend on only $\gamma_1'(0)$. A different type of comparison, i. e., the final values of the measured fields and analytical fields will allow the effects of $\gamma_2'(0)$ and $\gamma_3'(0)$ to show up in the analysis. In order to overcome this deficiency in the model, a different type of input voltage is analyzed in the next section.

ANALYSIS OF THE FIELDS FOR A RAMP-TYPE INPUT

The same basic model as used in (1) will be used here. However, instead of a step input, a ramp which becomes a constant value, will be used. This waveform is shown below in Figure 4.

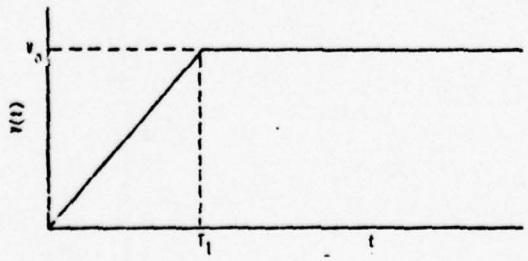


Figure 4 - Ramp-Input Used for Analysis

By using the "gate function" defined by Cheng,[15] we can write this as

$$V(t) = \frac{V_0 t}{T_1}\left[u(t) - u(t-T_1)\right] + V_0\, u(t-T_1) \qquad (29)$$

In the frequency domain

$$V(s) = \frac{V_0}{T_1 s^2}\left[1 - (T_1 s + 1)\, e^{-T_1 s}\right] + \frac{V_0}{s} e^{-T_1 s} \qquad (30)$$

Simplifying

$$V(s) = \frac{V_0}{T_1 s^2}\left(1 - e^{-T_1 s}\right) \qquad (31)$$

Note that this expression has the correct limiting value as $T_1 \rightarrow 0$. By the use of the method of L'Hospital, one can easily show that V(s) goes to V_0/s as $T_1 \rightarrow 0$. Note that by adjusting T_1, the "rise-time" of the pulser voltage can be analytically controlled. However, this is still a very simplified model of the pulser.

We now follow, exactly, the procedure used by Baum in (1) and replace $\frac{V_0}{s}$ by $\frac{V_0}{T_1 s^2}\left(1 - e^{-T_1 s}\right)$

Solving for $\tilde{I}(0)$, we find

$$\tilde{I}(0) = \frac{V_0 t_h \left[1 - e^{-\frac{T_1}{t_h} S_h}\right]}{(T_1/t_h) Z_{oo} S_h (S_h + \alpha)} \qquad (32)$$

where t_h and Z_{oo} are as defined by Baum. Note that the evaluation of the field, using the integral of equation (21) in (1), is not affected by this change in the input voltage and the normalized waveform given by equation (16) is therefore modified to become

$$\tilde{V}_1'(\theta) = \frac{\sin\theta}{2}\left[\frac{1 - e^{-\frac{T_1}{t_h} S_h}}{(T_1/t_h)}\right]\frac{1}{(S_h + \alpha)}\left\{\frac{1}{S_h(1-\cos\theta)}\right.$$

$$- \frac{1}{S_h^2(1-\cos\theta)^2}\left(1 - e^{-S_h(1-\cos\theta)}\right) \qquad (33)$$

$$\left. + \frac{1}{S_h(1+\cos\theta)} - \frac{1}{S_h^2(1+\cos\theta)^2}\left(1 - e^{-S_h(1+\cos\theta)}\right)\right\}$$

A check of the algebra and normalization factors introduced to this point can be made by again letting $(T_1/k_4) \to 0$ with the result that equation (33) will reduce to that given by (16).

(Note: the terms $\tilde{y}_1'(\theta)$, $\tilde{y}_2'(\theta)$, etc. will be used in the same sense in which they were used in the previous sections. It is to be understood that these <u>are</u> <u>not</u> the same values as obtained previously, but a new set of variables corresponding to the ramp-input voltage. When comparisons are made they will be labeled "step" and "ramp" as appropriate.)
Multiplying the $\left(1 - e^{-\frac{T_1}{k_4} s_4}\right)$ term in, we obtain the following result:

$$\tilde{y}_1'(\theta) = \frac{\sin\theta}{2(T_1/k_4)} \left\{ \frac{C}{s_4(s_4+\alpha)} - \frac{D}{s_4^2(s_4+\alpha)} + \frac{e^{-s_4 A}}{A^2 s_4^2 (s_4+\alpha)} \right.$$

$$+ \frac{e^{-s_4 B}}{B^2 s_4^2 (s_4+\alpha)} - \frac{C e^{-s_4 T_1/k_4}}{s_4(s_4+\alpha)} + \frac{D e^{-s_4 T_1/k_4}}{s_4^2(s_4+\alpha)}$$

$$\left. - \frac{e^{-s_4 (A + T_1/k_4)}}{A^2 s_4^2 (s_4+\alpha)} - \frac{e^{-s_4 (B + T_1/k_4)}}{B^2 s_4^2 (s_4+\alpha)} \right\} \quad (34)$$

where:

$$A = 1 - \cos\theta \quad (35a) \qquad B = 1 + \cos\theta \quad (35b)$$

$$C = \frac{1}{A} + \frac{1}{B} \quad (35c) \qquad D = \frac{1}{A^2} + \frac{1}{B^2} \quad (35d)$$

Invert (34) now to obtain $y_1'(\theta)$.

$$y_1'(\theta) = \frac{\sin\theta}{2(T_1/k_4)} \left\{ \left[\frac{C}{\alpha}(1 - e^{-\alpha\gamma_4}) + \frac{D}{\alpha}\left(\frac{1 - e^{-\alpha\gamma_4}}{\alpha} - \gamma_4\right) \right] u(\gamma_4) \right.$$

$$- \left[\frac{C}{\alpha}(1 - e^{-\alpha\gamma_3}) + \frac{D}{\alpha}\left(\frac{1 - e^{-\alpha\gamma_3}}{\alpha} - \gamma_3\right) \right] u(\gamma_3)$$

$$- \frac{1}{A^2\alpha}\left[\frac{1 - e^{-\alpha\gamma_1}}{\alpha} - \gamma_1 \right] u(\gamma_1) + \frac{1}{A^2\alpha}\left[\frac{1 - e^{-\alpha\gamma_4}}{\alpha} - \gamma_4 \right] u(\gamma_4) \quad (36)$$

$$\left. - \frac{1}{B^2\alpha}\left[\frac{1 - e^{-\alpha\gamma_2}}{\alpha} - \gamma_2 \right] u(\gamma_2) + \frac{1}{B^2\alpha}\left[\frac{1 - e^{-\alpha\gamma_5}}{\alpha} - \gamma_5 \right] u(\gamma_5) \right\}$$

In this expression

$$\gamma_1 = \gamma_h - (1-\cos\theta) \quad (36a) \qquad \gamma_2 = \gamma_h - (1+\cos\theta) \quad (36b)$$

$$\gamma_3 = \gamma_h - \tau_1/v_h \quad (36c) \qquad \gamma_4 = \gamma_h - (1-\cos\theta) - \tau_1/v_h \quad (36d)$$

$$\gamma_5 = \gamma_h - (1+\cos\theta) - \tau_1/v_h \quad (36e)$$

Note that the original step input resulted in three "switch-on" times, γ_h, γ_1, and γ_2. The ramp input includes terms with these switch-on times and introduces three new times, γ_3, γ_4 and γ_5. Each one of the three new times corresponds to one of the original times with an additional delay of τ_1/v_h. The functional form is the same, with a negative sign and this amount of delay. Thus, the original positive going ramp is followed by a negative going ramp, of the same slope, with this delay of τ_1/v_h. Note also that the functional form of the terms with unit step multipliers of γ_h, γ_1 and γ_2 are different because of the ramp input.

In order to get $\gamma_2'(\theta)$ and $\gamma_3'(\theta)$, equations (11) and (12) must be used again. The result of these integrations produces functions of the form shown below:

$$\begin{aligned}\gamma_2'(\theta) = \frac{\sin\theta}{2(\tau_1/v_h)} \Bigg\{ & \left[(c+\tfrac{D}{\alpha})\left(\frac{\gamma_h}{\alpha} - \frac{1}{\alpha^2}(1-e^{-\alpha\gamma_h})\right) - \frac{D}{2\alpha}\gamma_h^2\right] u(\gamma_h) \\ & - \left[(c+\tfrac{D}{\alpha})\left(\frac{\gamma_3}{\alpha} - \frac{1}{\alpha^2}(1-e^{-\alpha\gamma_3})\right) - \frac{D}{2\alpha}\gamma_3^2\right] u(\gamma_3) \\ & + \frac{1}{A^2\alpha}\left[-\frac{\gamma_1}{\alpha} + \frac{1}{\alpha^2}(1-e^{-\alpha\gamma_1}) + \frac{\gamma_1^2}{2}\right] u(\gamma_1) \\ & - \frac{1}{A^2\alpha}\left[-\frac{\gamma_4}{\alpha} + \frac{1}{\alpha^2}(1-e^{-\alpha\gamma_4}) + \frac{\gamma_4^2}{2}\right] u(\gamma_4) \\ & + \frac{1}{B^2\alpha}\left[-\frac{\gamma_2}{\alpha} + \frac{1}{\alpha^2}(1-e^{-\alpha\gamma_2}) + \frac{\gamma_2^2}{2}\right] u(\gamma_2) \\ & - \frac{1}{B^2\alpha}\left[-\frac{\gamma_5}{\alpha} + \frac{1}{\alpha^2}(1-e^{-\alpha\gamma_5}) + \frac{\gamma_5^2}{2}\right] u(\gamma_5)\end{aligned} \quad (37)$$

$$\gamma_3'(\theta) = \frac{\sin\theta}{2(\tau_1/t_{h_1})}\left\{\left[(c+\frac{D}{\alpha})\left(\frac{\gamma_4^2}{2\alpha}-\frac{1}{\alpha^2}\left(\gamma_4-\frac{1}{\alpha}(1-e^{-\alpha\gamma_4})\right)\right)-\frac{D}{6\alpha}\gamma_4^3\right]u(\gamma_4)\right.$$

$$-\left[(c+\frac{D}{\alpha})\left(\frac{\gamma_3^2}{2\alpha}-\frac{1}{\alpha^2}\left(\gamma_3-\frac{1}{\alpha}(1-e^{-\alpha\gamma_3})\right)\right)-\frac{D}{6\alpha}\gamma_3^3\right]u(\gamma_3)$$

$$+\frac{1}{A^2\alpha}\left[-\frac{\gamma_1^2}{2\alpha}+\frac{1}{\alpha^2}\left(\gamma_1-\frac{1}{\alpha}(1-e^{-\alpha\gamma_1})\right)+\frac{\gamma_1^3}{6}\right]u(\gamma_1)$$

$$-\frac{1}{A^2\alpha}\left[-\frac{\gamma_4^2}{2\alpha}+\frac{1}{\alpha^2}\left(\gamma_4-\frac{1}{\alpha}(1-e^{-\alpha\gamma_4})\right)+\frac{\gamma_4^3}{6}\right]u(\gamma_4) \qquad (38)$$

$$+\frac{1}{B^2\alpha}\left[-\frac{\gamma_2^2}{2\alpha}+\frac{1}{\alpha^2}\left(\gamma_2-\frac{1}{\alpha}(1-e^{-\alpha\gamma_2})\right)+\frac{\gamma_2^3}{6}\right]u(\gamma_2)$$

$$-\frac{1}{B^2\alpha}\left[-\frac{\gamma_5^2}{2\alpha}+\frac{1}{\alpha^2}\left(\gamma_5-\frac{1}{\alpha}(1-e^{-\alpha\gamma_5})\right)+\frac{\gamma_5^3}{6}\right]u(\gamma_5)$$

Note that, to be really descriptive, we should define these functions as $\gamma_1'(\theta,\alpha,\tau_1/t_{h_1})$ since changing any of these parameters will change the shape of the function. The values for $\gamma_1'(\theta)$, $\gamma_2'(\theta)$ and $\gamma_3'(\theta)$ plotted in (4) are the values of these functions for $\tau_1/t_{h_1} = 0$.

The manner in which the $\gamma_1'(\theta)$ function varies with τ_1/t_{h_1}, for fixed values of θ and α, is shown in Figure 5. The curve is plotted for $\theta = 90°$ and $\alpha = 1$, which is an important case. The parameter τ_1/t_{h_1} which came in naturally by the normalization process is identical with the parameter γ_R, the normalized risetime, defined in (6). Similar curves have been calculated for $\gamma_2'(\theta)$ and $\gamma_3'(\theta)$, but will not be shown here because of space limitations. They are plotted in an AFWL report.[16] The variation of $\gamma_1'(\theta)$ with θ, for $\alpha = 1$ and τ_1/t_{h_1} equal to 0.10 is shown in Figure 6. The curves given here should be compared with those in (4).

There is not a large difference between these functions for the step and ramp inputs when τ_1/t_{h_1} has the value of 0.10. The effect would be more pronounced if τ_1/t_{h_1} were larger. The major effect introduced into the field calculation is that, at least for small values of τ_1/t_{h_1}, the peak electric

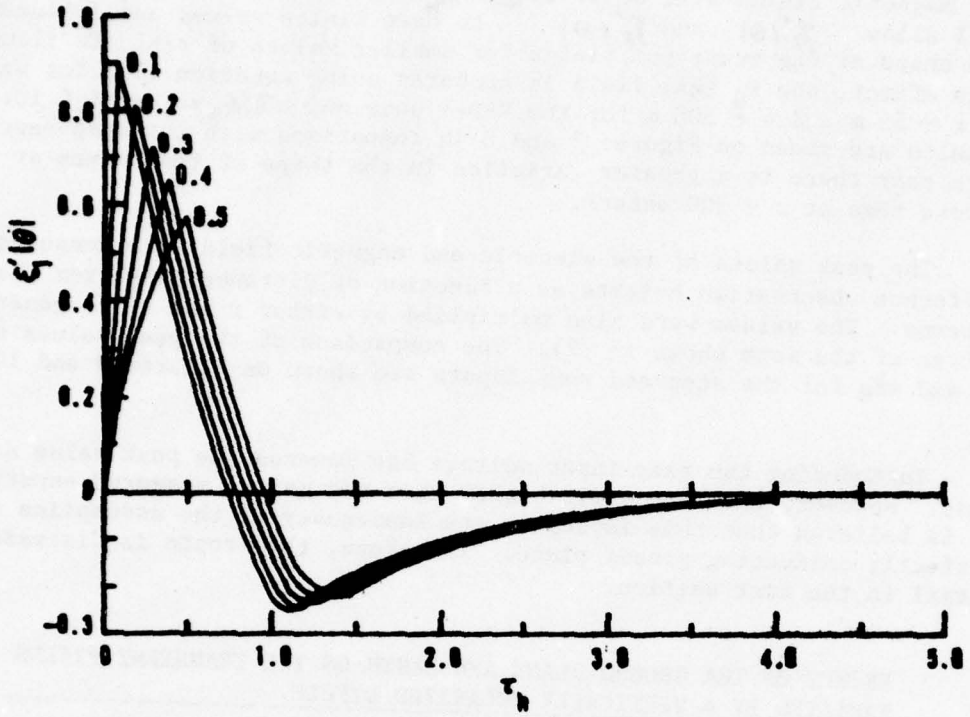


Figure 5 $\gamma_1'(\theta)$ as a function of T_1/t_h for $\theta = 90°$ and $\alpha = 1$

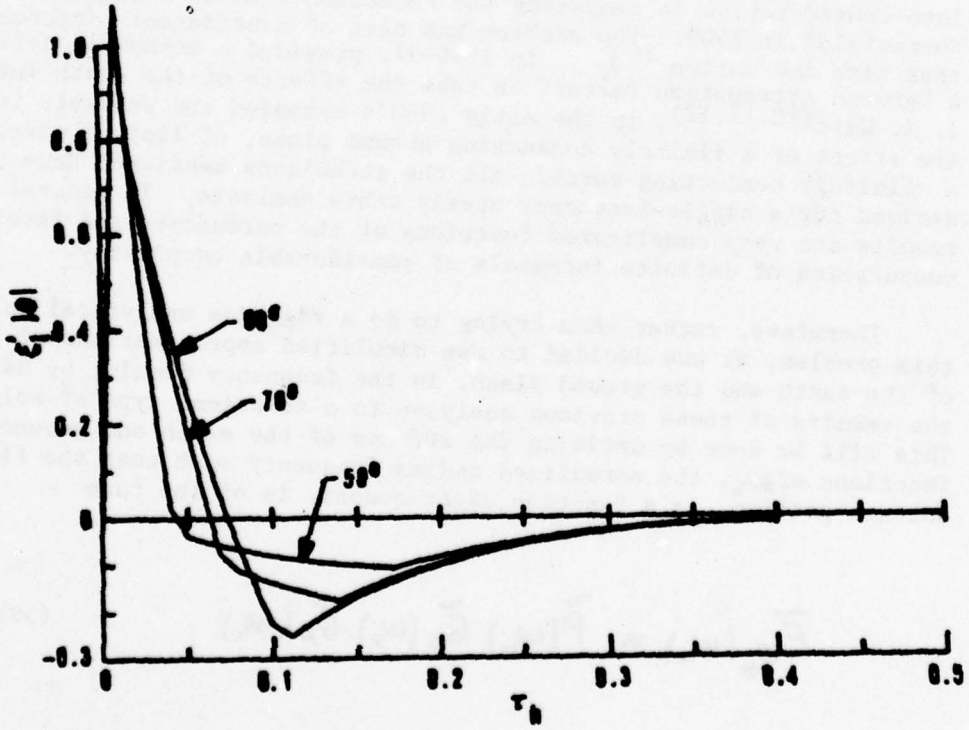


Figure 6 Dependence of $\gamma_1'(\theta)$ on θ for $\alpha = 1$ and $T_1/t_h = 0.10$

and magnetic fields will occur at $\tau_h = \tau_1/\kappa_h$ now, instead of $\tau_h = o$. This will allow $f_2'(0)$ and $f_3'(0)$ to have finite values and influence the shape of the transient fields for smaller values of r/h. To illustrate this effect, the E_θ $(\tilde{r},s)$ field is computed using equation (13) for values of r = 55 m and 4 = 300 m for the VPD-1 data and a τ_1/κ_h value of 0.10. The results are shown on Figures 7 and 8 in comparison with the step-input case. Note that there is a greater variation in the shape of the curves at r = 55 meters than at r = 300 meters.

The peak values of the electric and magnetic field were computed for different observation heights as a function of distance away from the antenna. The values were also multiplied by either r and r^2 to generate curves of the form shown in (7). The comparison of the peak values of E_θ and rE_θ for the step and ramp inputs are shown on Figures 9 and 10.

Introducing the ramp input voltage has lowered the peak value somewhat. However, they are still higher than the values measured experimentally. It is believed that this is due to the inadequacy of the assumption of a perfectly conducting ground plane. Therefore, this topic is discussed in detail in the next section.

EFFECT OF THE GROUND PLANE AND EARTH ON THE TRANSIENT FIELDS RADIATED BY A VERTICALLY POLARIZED DIPOLE.

The earliest attempt to take the effect of a finitely conducting earth into consideration in computing the radiation from an antenna was done by Sommerfeld[8] in 1909. The problem has been of considerable interest since that time and Norton [9], in 1936-37, provided a method of defining a "ground attenuation factor" to take the effects of the earth into account. J. R. Wait[10,11,12], in the early 1960's extended the analysis to include the effect of a finitely conducting ground plane, of limited size, lying on a finitely conducting earth. All the techniques mentioned here have been derived for a single-frequency steady state analysis. In general, the results are very complicated functions of the parameters and involve the computation of definite integrals of considerable complexity.

Therefore, rather than trying to do a rigorous analytical solution of this problem, it was decided to use simplified approximations of the effects of the earth and the ground plane, in the frequency domain, by adapting the results of these previous analyses to a transient type of solution. This will be done by defining the effects of the earth and ground plane as functions of ω_h, the normalized radian frequency such that the final antenna pattern, as a function of frequency, is of the form

$$\tilde{E}_{f_\theta}(\omega_h) = \tilde{P}(\omega_h)\,\tilde{G}_e(\omega_h)\,\tilde{G}_p(\omega_h) \qquad (39)$$

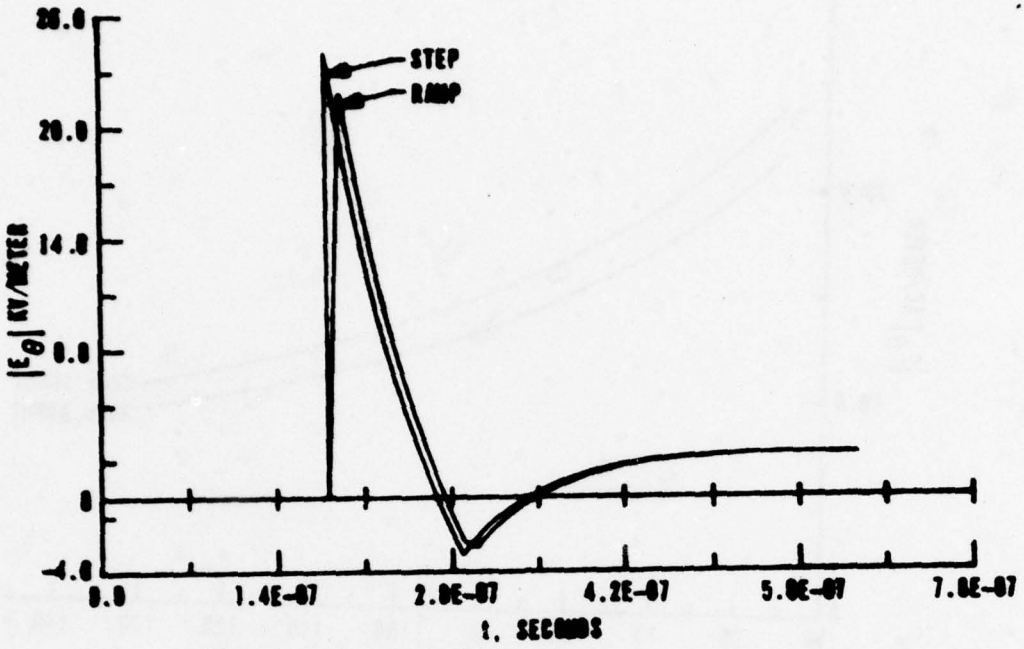


Figure 7 Comparison of Step and Ramp Solution for E_θ for r = 55 meters, $T_1/t_h = 0.10$

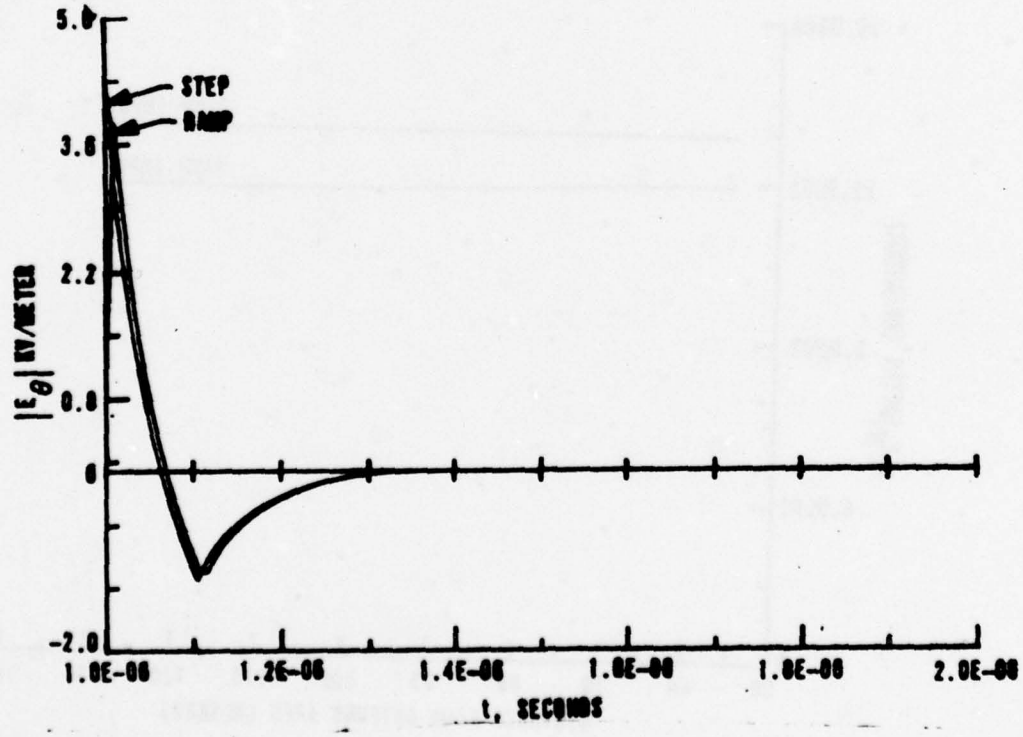


Figure 8 Comparison of Step and Ramp Solution for E_θ for r = 300 meters, $T_1/t_h = 0.10$

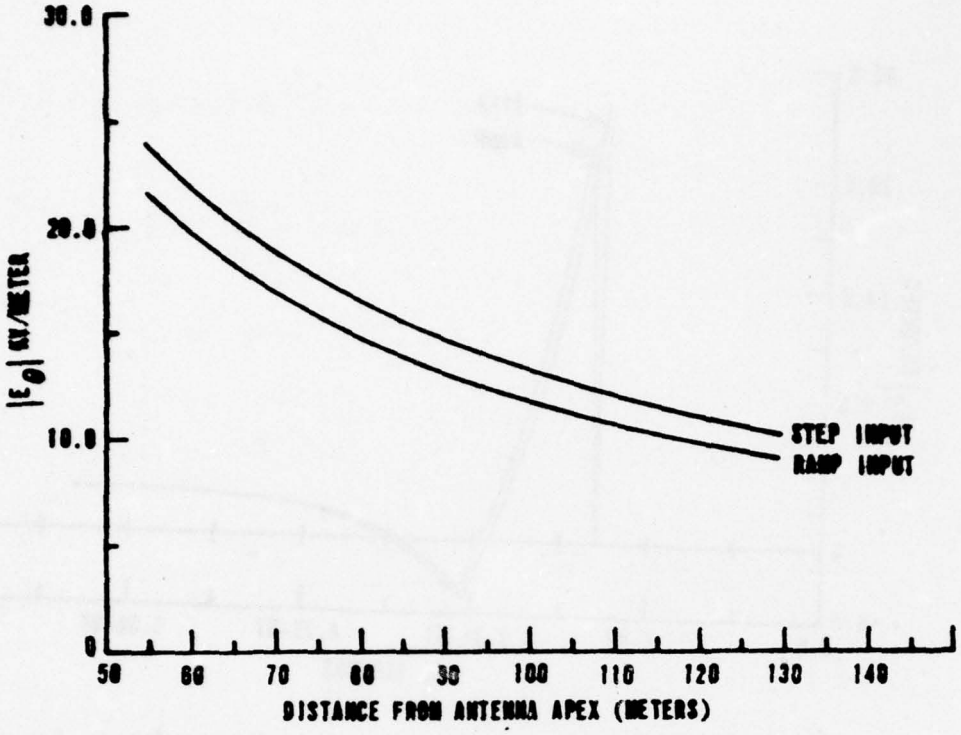


Figure 9 Peak values of E_θ versus ϑ, Step and Ramp Inputs

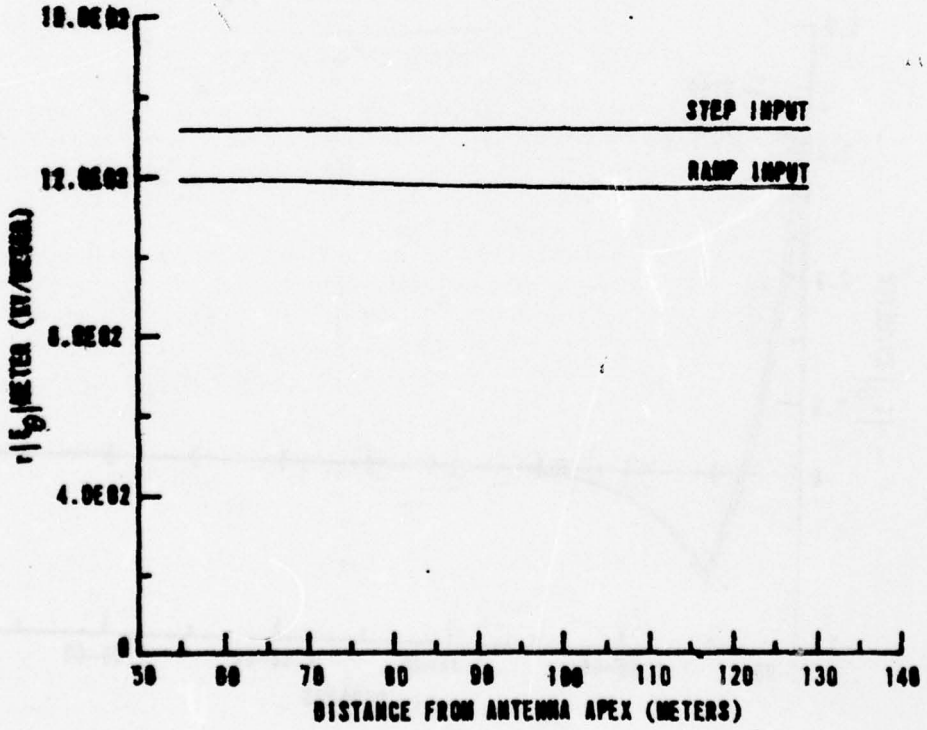


Figure 10 Peak values of rE_θ versus ϑ, Step and Ramp Inputs

where:

$\tilde{P}(\omega_h)$ = free space pattern (40a)

$\tilde{G}_e(\omega_h)$ = Earth attenuation factor (40b)

$\tilde{G}_p(\omega_h)$ = Ground Gain factor (40c)

The earth attenuation factor and ground plane gain factors will be defined in such a manner that their product will become a constant equal to 2, for all frequencies for a perfectly conducting ground plane of infinite extent. In the other limit, as the size of the ground plane shrinks to zero, $\tilde{G}_p(\omega_h)$ will approach a value of 1.0 and only the earth attenuation factor will be present.

We will consider the earth attenuation factor first. Following Norton(9) we can define the attenuation factor o the form

$$\tilde{F} = \left[1 + j\sqrt{\pi w} e^{-w}\, \mathrm{erfc}(-j\sqrt{w})\right] \tag{41}$$

where: $$w = \frac{j\beta r U^2}{2}(1 - U^2\cos\psi)\left[1 + \frac{\sin\psi}{U\sqrt{1 - U^2\cos^2\psi}}\right] \tag{42}$$

and: $$U^2 = \frac{1}{\varepsilon_r + jX} \tag{43}$$

$$X = \frac{18 \times 10^3 \sigma}{f_{mhz}} \tag{44}$$

$$\mathrm{erfc}(-j\sqrt{w}) = \frac{2}{\sqrt{\pi}} \int_{-j\sqrt{w}}^{\infty} e^{-\gamma^2} d\gamma \tag{45}$$

$$\psi = 90 - \theta \tag{46}$$

At the surface of the earth, where $\psi = 0$, the absolute value of this function has been evaluated and is of the form:

$$A = |\tilde{F}| = \left|1 + j\sqrt{\pi p_1}\, e^{-p_1}(\mathrm{erfc}(-j\sqrt{p_1}))\right| \tag{47}$$

where:

$$P_1 = P e^{jb} \tag{48}$$

$$P \approx \frac{\pi r}{\lambda x} \cos b \tag{49}$$

$$b \approx \tan^{-1}\left(\frac{1+\varepsilon_r}{x}\right) \tag{50}$$

Norton has provided an empirical function which approximates this curve, of the form

$$A = \frac{2+0.3P}{0.6P^2+P+2} - \sqrt{\frac{P}{2}}\, e^{-\frac{5}{8}P} \sin b \tag{51}$$

It is this latter function which we shall use to define $|\tilde{G}_e(\omega_h)|$. We need to have A as a function of ω_h. By using the substitution, $\omega_h = 2\pi f\left(\frac{h}{c}\right)$, (49) can be put into this form

$$P = \frac{\omega_h^2\left(\frac{r}{h}\right)\cos b}{72\pi \times 10^9 \sigma (h/c)} \tag{52}$$

Using typical values of σ and ε_r from (6) of $\varepsilon_r = 15$, $\sigma = 12\times10^{-3}$ mhos/meter and the h value of the VPD-1, curves of $|\tilde{G}_e(\omega_h)|$ as a function of ω_h were computed for r values of 55 and 300 meters. These curves are shown on Figure 11.

The ground plane gain factor is not obtained so simply. Wait [10] shows that the effect of the ground plane can be approximated by a factor $(1+\Omega)$ which is multiplied by the ground attenuation factor of Norton. For a circular screen of radius a which is large compared to the wavelength of interest, he shows that this factor is of the form

$$1+\Omega_a \approx 1 + \frac{z-z_a}{z_0} e^{-j\pi/4}\, \tilde{G} \tag{53}$$

where $\tilde{G}$ is an integral over the ground screen of the form

$$\tilde{G} = \frac{j}{(2\cos\psi)^{1/2}}\left[\frac{1}{\sin(\psi/2)}\int_0^{\left(\frac{4ka}{\pi}\right)^{1/2}\sin\psi/2} e^{-j\left(\frac{\pi}{2}\right)x^2}\,dx - \frac{j}{\cos(\psi/2)}\int_0^{\left(\frac{4ka}{\pi}\right)^{1/2}} e^{-j\left(\frac{\pi}{2}\right)x^2}\,dx\right] \tag{54}$$

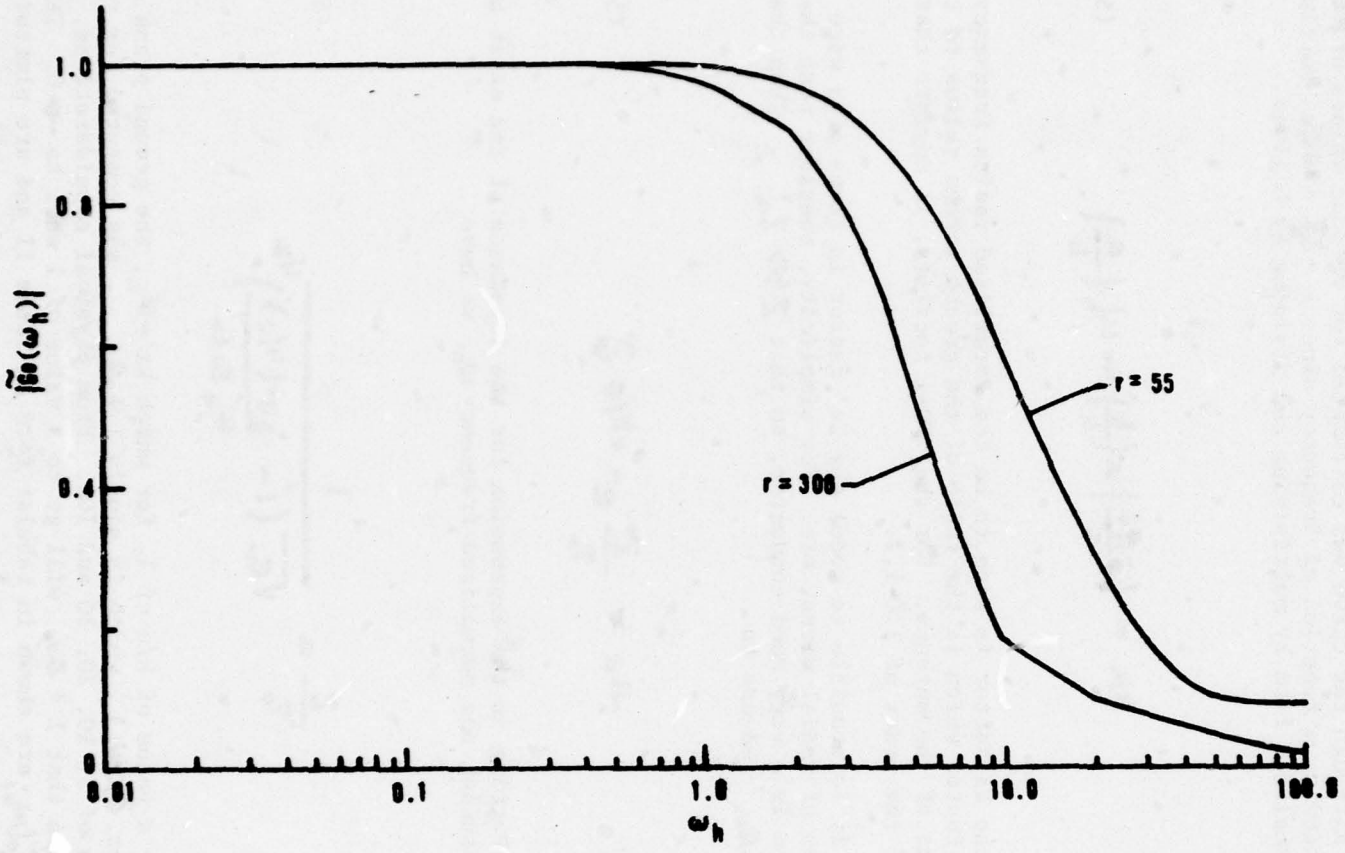


Figure 11 Ground Attenuation Factor, $|\tilde{G}_e(\omega_h)|$ as a Function of ω_h, for Typical Earth Parameters

and Z is the impedance of the earth, Z_a is the impedance of the screen and η_0 is the impedance of free space. He gives values of the $\tilde{G}$ function for ka values of 5, 10, 20, 30 and 100, in a set of tables. Values of $\tilde{G}$, both magnitude and phase, for a ψ value of 0° are shown, in tabular form in Table 1.

Although the curve was calculated for various values of ka, it can be regarded as a function of frequency since $k = \frac{2\pi}{\lambda} = 2\pi f/c$. Putting this into a normalized form by multiplying and dividing by h gives

$$ka = \left(\frac{2\pi f}{c}\right) a\left(\frac{h}{h}\right) = \omega_h \left(\frac{a}{h}\right) \qquad (55)$$

and the ka factor is seen to be the normalized radian frequency ω_h, multiplied by a factor which is the ratio of the ground screen radius to the half height of the antenna. For the VPD-1 facility, it appears that this ratio is of the order of 1.0-1.2.

It is possible to model the Za' factor in terms of a wire grid, or a series of radial wires, etc. For simplicity, consider that the ground screen is a very good conductor, so that $Z \gg Z_a'$. Then the expression for Ω_a reduces to

$$\Omega_a \approx \frac{Z}{\eta_0} e^{-j3\pi/4} \tilde{G} \qquad (56)$$

Putting in the expression for the impedance of the earth and introducing the normalized frequency ω_h, we have

$$\frac{Z}{\eta_0} = \frac{1}{\sqrt{\varepsilon_r}\left(1 - \frac{j\sigma(h/c)}{\omega_h \varepsilon_0 \varepsilon_r}\right)^{1/2}} \qquad (57)$$

Using a value of h/a of 1, for which $ka = \omega_h$, the ground plane gain factor, $\tilde{G}_p(\omega_h)$, which is simply $1 + \Omega_a$, was computed for values of ka of 5, 10, 20, 30 and 100. From physical considerations, it can be seen that $1 + \Omega_a$ will go to a value of 1 when $ka \rightarrow 0$. The values of $\tilde{G}_p(\omega_h)$ are shown in tabular form in Table II and are plotted in Figure 12.

ka	$\lvert\tilde{G}\rvert$	$\angle\tilde{G}$
5	1.3667	77.14°
10	2.2347	79.42°
20	3.2088	83.07°
30	3.9966	85.08°
100	7.6424	87.48°

TABLE 1 COMPUTED VALUES OF $\tilde{G}$ AS A FUNCTION OF ka

ω_h	$\lvert\tilde{G}_p(\omega_h)\rvert$	$\angle\tilde{G}_p(\omega_h)$
0	1	0°
5	1.1308	11.12°
10	1.3363	17.78°
20	1.6108	22.26°
30	1.827	24.55°
100	2.7658	30.34°

TABLE II GROUND PLANE GAIN AS A FUNCTION OF ω_h

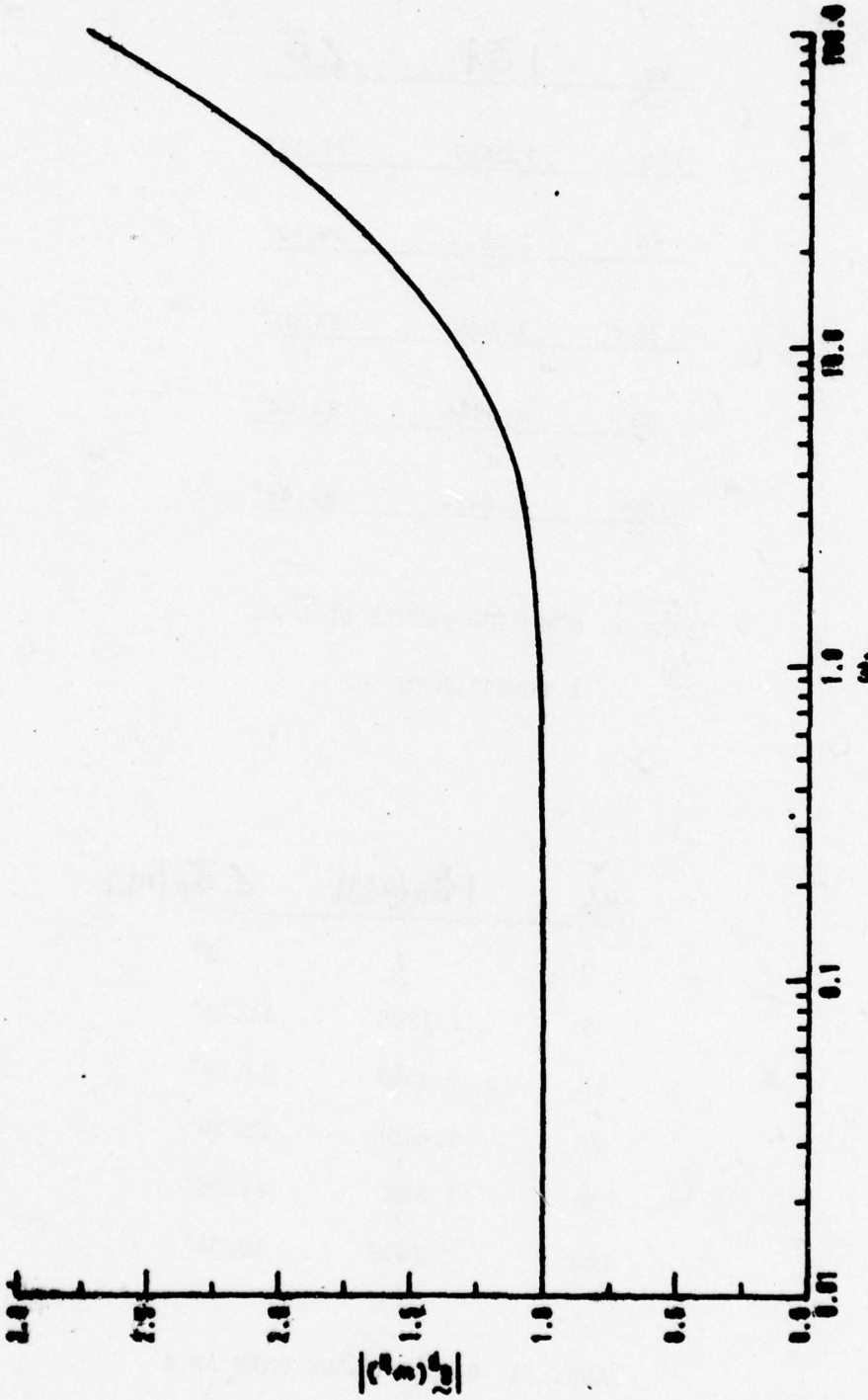


Figure 12 Ground Plane Gain Factor, $|\tilde{G}_p(\omega_h)|$ as a Function of ω_h, for good ground plane

Recall that this factor must be multiplied by the earth attenuation factor, which is shown on Figure 11. When the two curves are multiplied together, the resulting curve is as shown on Figure 13.

From equation (39), it can be seen that the $\tilde{E}_{\phi\theta}(\omega_h)$ antenna pattern, in the frequency domain, is obtained by multiplying this curve by the free space antenna pattern curve, given by equation (6), using the appropriate γ functions. Note that before, with the assumed ground plane of infinite extent, the pulser voltage Vo was doubled. With the effects of $\tilde{G}_e(\omega_h)$ and $\tilde{\Gamma}_a(\omega_h)$ in the analysis, the pulser voltage to be used is the actual value.

Performing the multiplication of the free pattern given by equation (6) with the curve of Figure 13 results in the curve shown on Figure 14. Also shown is the curve obtained by solving equation (6) directly. The bottom curves shown on Figure 14 were obtained by using the approximate analysis of equation (51) and a more lengthy series expansion of (47). The two curves agree well over most of the ω_h values.

Note that the lower curve is approximately one-half of the value of the upper curve up to about ω_h equals 10.0 and then the effect of the losses become quite noticeable as the lower curve drops more rapidly as the frequency is increased.

An attempt was made to perform an inverse Fourier Transform on this curve in order to obtain the corresponding time-function. However, it was not possible to get the inversion routine working completely correctly and this result was not available when this report was completed. See reference(16) for more complete details.

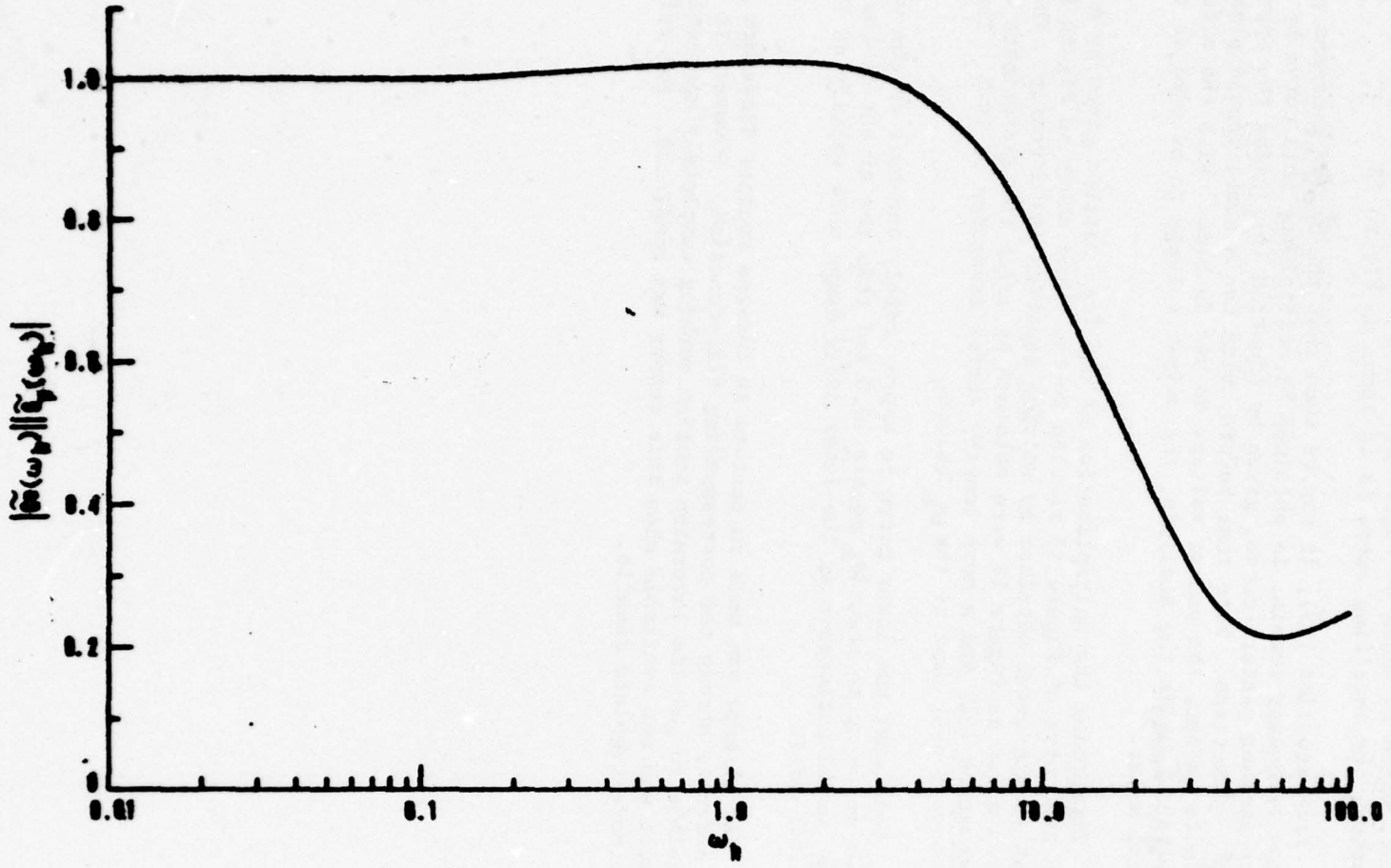


Figure 13 Product of Ground Attenuation Factor and Ground Plane Gain Factor as a function of ω_h.

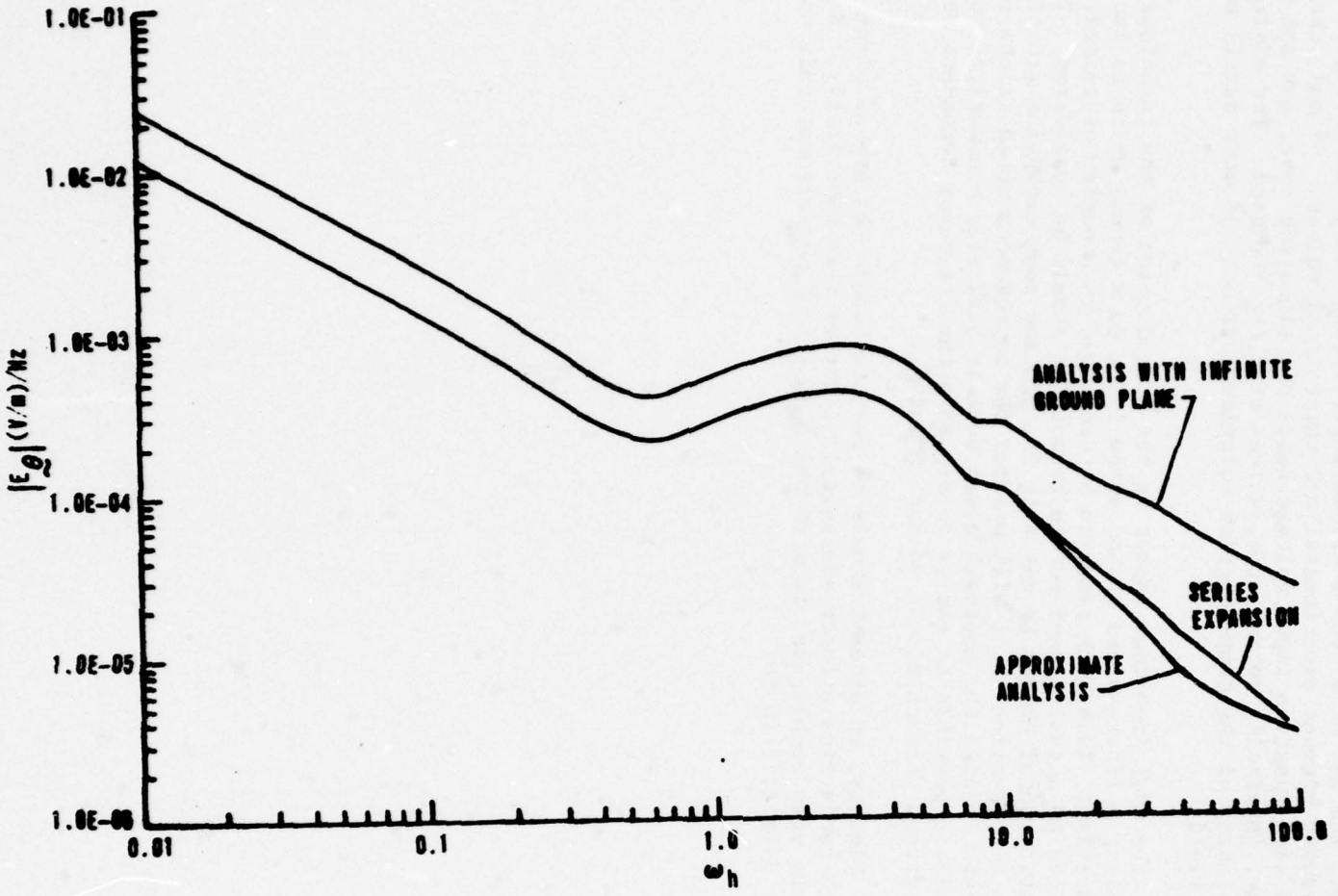


Figure 14 $\tilde{E}_\theta$ at r = 55 meters, Including Earth and Ground Plane Effects

CONCLUSIONS AND RECOMMENDATIONS

There are several conclusions which can be drawn from this study. First, the use of a step-function input voltage does not give good agreement between experimental and theoretical values. Second, changing to a ramp-function input voltage helps the situation some, but not unless large, physically unrealistic, values of T_1/t_h are used. The additional complexity of the ramp-function solution does not add more detail about the fields.

The most important aspect is the introduction of the technique for handling a finite sized ground plane lying on a ground which is imperfectly conducting. This work needs to be continued in a number of points. The effects of actual ground screen geometrics should be considered. The existing model should be run with the pre and post expansion ground plane data to determine if it will predict the improvement noted in the measured values. Because the approach given here is basically a numerical one, it should be possible to easily incorporate the frequency dependent nature of the ground characteristic values, σ and ε_r.

Finally, an attempt should be made to handle the ground plane and earth conduction effects analytically, rather than numerically. Because of the very complicated form of the $\tilde{\sigma}_c(\omega_n)$ and $\tilde{\sigma}_p(\omega_n)$ factors, this may be very difficult to do.

References

1. C. E. Baum, "Resistively Loaded Dipole Antenna Based on a Transmission Line Model for the Antenna," Sensor and Simulation Notes, Note 81, April 1969.
2. T. T. Wu, R. W. P. King, "The Cylindrical Antenna with Nonflecting Resistive Loading," IEEE Trans G-AP, AP-13, May 1965, P. 369-373.
3. L. C. Shen, R. W. P. King, "The Cylindrical Antenna with Nonflecting Resistive Loading," IEEE Trans G-AP, AP-13, Nov 1965, P. 998.
4. B. K. Singaraju, C. E. Baum, "A Simple Technique for Obtaining the Near Fields of Electric Dipole Antenna from Their Far Fields." Sensor and Simulation Notes, Note 213, March 1976.
5. R. F. Blackburn and C. D. Taylor, "On the Electromagnetic Fields from a Hybrid Type of EMP Simulator," Sensor and Simulation Notes, Note 211, Nov 1975.
6. "Vertically Polarized Dipole Evaluation," Final Report, Contract F29601-71-C-0018, EG&G, Inc., March 1972.
7. Vertically Polarized Dipole Field Mapping, Final Report, Contract F29601-71-C-0028, The Boeing Company, July 1972.
8. A. N. Sommerfeld, "Uber die Ausbreitung der Wellen in der Drahtlosen Telegraphie," Ann Physics (4), Vol 28, P. 665, 1909.
9. K. A. Norton, "The Propagation of Radio Waves Over the Surface of the Earth and in the Upper Atmosphere," PROC IRE, Vol 24, Pt 1, P. 1367-1387, 1936 and Vol 25, Pt II, P. 1203-1236, 1937.
10. J. R. Wait, "Effect of the Ground Screen on the Field Radiated by a Monopole," IRE Trans, G-AP, AP-4, April 1956, P. 179-181.
11. J. R. Wait, L. C. Walters, "Influence of a Sector Ground Screen on the Field of a Vertical Antenna." Natl Bur. Std. (U. S.) Monograph 60, April 1963, P. 1-23.
12. J. R. Wait, "Transient Response of A Dipole Over a Circular Ground Screen," IEEE Trans, G-AP, AP-17, Nov 1969, P. 806-809.
13. D. A. Hill, "The Transient Fields of a Hertzian Dipole in the Presence of a Dielectric Half-Space," Radio Science, Vol 6 Aug-Sep 1976, P. 1129-1138.
14. D. C. Chang and R. J. Fisher, "A Unified Theory on Radiation of a Vertical Electric Dipole Above a Dissipative Earth," Radio Science, Vol 9, Dec 1974, P. 1129-1138.
15. D. K. Cheng, Analysis of Linear Systems. Addison-Wesley Publishing Company, Inc., Reading, Massachusetts, 1959, P. 171.
16. M. D. Bradshaw, "Transient Fields From a Vertically Polarized Dipole Radiator," (To be published as AFWL Technical Report).

1977 USAF-ASEE SUMMER FACULTY RESEARCH PROGRAM

Sponsored by

THE AIR FORCE OFFICE OF SCIENTIFIC RESEARCH

Conducted by

AUBURN UNIVERSITY AND OHIO STATE UNIVERSITY

FINAL REPORT

LIQUEFACTION POTENTIAL OF SOILS UNDER BLAST LOADS

Prepared by: Wayne A. Charlie, Ph.D., P.E.
Assistant Professor
Department of Civil Engineering
Colorado State University

Assignment: Kirtland AFB, New Mexico
AFWL/DES-G
Civil Engineering

USAF Research Colleague: Steve Melzer
AFWL/DES-G
Kirtland AFB, New Mexico

Date: August 15, 1977

Contract Number: F44620-75-C-0031

LIQUEFACTION POTENTIAL OF SOILS

UNDER BLAST LOADS

by

Wayne A. Charlie, Ph.D., P.E.

ABSTRACT

Air Force Office of Scientific Research (AFOSR) sponsored research recently led to the identification of an anomalous ground motion wave. This motion was produced by an explosion and, apparently, originated from a saturated sand layer at the Pre DICE THROW test site, located on the White Sands Missile Range, New Mexico. In addition, sand boils were also observed to occur on the test. At the Watching Hill test events (PRAIRIE FLAT, DIAL PACK and SNOW BALL) at the Defense Research Establishment at Suffield, Alberta, Canada, similar motions were observed. Water spouts and sand boils were observed soon after these explosions. At the KOA nuclear explosion, located at Eniwetok Atoll, sand boils and large vertical settlements of the ground surface were observed.

Predicting liquefaction potential from earthquake loadings by analyzing field and laboratory data is reviewed in this paper. Possible extension of liquefaction theory to include ground shock induced liquefaction produced by high-explosive test events is discussed. This information will assist in improving the crater and ground shock prediction techniques as well as identifying soil properties which may prove critical to the eventual design and assessment of Air Force strategic missile systems.

ACKNOWLEDGMENT

The author wishes to thank the ASEE/USAF for research support, Dr. Arthur Guenther, Steve Melzer, Lt Col Frank Leech, Lt Col James Neal, Capt Al Schenker and Capt Lou Karably of the Air Force Weapons Laboratory, Kirtland AFB, New Mexico, for their help and cooperation.

INDEX

I. Introduction

II. Description of Liquefaction

III. Review of Liquefaction Caused by Earthquakes

A. Present Knowledge of Soil Liquefaction

B. Evaluating Soil Liquefaction Potential

C. Laboratory Tests

D. Analysis of Laboratory Data

E. Analysis of Liquefaction Potential

IV. Extension of Liquefaction Prediction to Include Blast-Induced Ground Shock

A. Laboratory Investigations of Liquefaction

B. Field Investigations of Liquefaction

C. Ground Motion and Liquefaction

V. Methods to Reduce Liquefaction Potential

VI. Conclusions and Recommendations

Appendices

A. Results of Tests on Niigata, Japan, Sand

B. Determining Field Relative Densities

I. INTRODUCTION

Investigations of the soils at a site of an Air Force strategic missile system may be divided into two categories: those for determining the static soil properties, and those for determining the effects of ground shock (produced by high explosives) which include the dynamic soil properties. These dynamic soil properties are used to predict cratering and ground shock environments and the dynamic behavior of the structure. Knowledge of dynamic soil properties includes the possible changes in soil properties which may occur after initial loading. This topic has received little attention or funding, principally because it has only recently started to be perceived as a problem, especially as related to the liquefaction of sands under blast loadings.

The Air Force Office of Scientific Research (AFOSR) sponsored research recently led to the identification of an anomalously low frequency (2-hertz) ground wave. The waveforms were observed at the closest ranges (80 ft) as well as in the seismic regime. This motion was produced by an explosion, and apparently originated from a saturated sand layer at the Pre DICE THROW test site located on the White Sands Missile Range, New Mexico (Melzer, 1977). Subsequent research has identified the far-field low frequency motion to be the theoretically predicted fundamental Rayleigh mode (Reinke, 1977). The close-in low frequency motion (dubbed the "X-wave") has an origin less certain, but is now attributed to the failure and liquefaction of the sands beneath ground zero. An unusual flat-bottomed crater and sand boils were also observed. At the Watching Hill test events (PRAIRIE FLAT, DIAL PACK and SNOW BALL) at the Defense Research Establishment at Suffield, Alberta, Canada, similar motions were observed. Also, water spouts and sand boils were observed soon after the explosion. At the KOA nuclear explosion, located at Eniwetok Atoll, water spouts, sand boils and large vertical settlements were observed (Ristvet and Tremba, 1977).

The possibility and extent of liquefaction of saturated sands from blast loading and the resultant effect on Air Force strategic missile systems are important. Depending on conditions such as soil type, density of the soil, groundwater level, stratification, slope of the ground surface and nature of superimposed structures, liquefaction may lead to formation of cracks and fissures, sand boils, subsidence, tilting, landslides, uplift of bouyant submerged structures, foundation failures, etc.

II. DESCRIPTION OF LIQUEFACTION

The almost universal nature of all materials, including soil, to lose strength with increasing number of repeated loadings is termed "fatigue." Experimental repeated load research on many materials has shown that the number of cycles required to reach failure increases with decreasing cyclic stress intensity. For sands, one large stress in loose, dry sand would lead to rearrangement of grains and volumetric compaction. When a saturated loose sand is subjected to strains sufficient to cause intergranular slip, compaction is retarded because the water cannot drain instantaneously to accommodate the volume change. Therefore, the relaximg sand skeleton transfers some of its intergranular or effective stress to the pore-water, and the pore-water pressure

rises. The increase of pore-water pressure reduces the effective stress in the soil, thereby, reducing the shearing strength of the soil. The larger the increase in pore-water pressure, the greater the loss in strength of a cohesionless soil (Terzaghi and Peck, 1967). The term liquefaction, as used herein, describes a process in which a saturated cohesionless soil loses strength when subjected to vibrations, earthquakes or blast loadings sufficient to cause compaction resulting in an increase in pore-water pressure. Catastrophic failure in recent earthquakes shows that liquefaction poses a high damage potential to civil engineering structures. Although structures may survive the earthquake motions, the loss of strength of the soil deposit (due to liquefaction) upon which the structures are founded has caused severe damage. Lateral movements, settling, raising and tilting of structures have been observed. Major damage to structures from landslides triggered by liquefaction has also been observed (Idriss and Seed, 1967; Seed, 1968).

Blasting and ground motion generated by the impact of excavating machinery have caused liquefaction in very loose sands and cohesionless silts where only one or a few cycles of repeated stress were sufficient to build up large pore pressures (Sowers and Sowers, 1970; Terzaghi and Peck, 1968; Florin, 1961; Puchkov, 1962). The possibility of soil liquefaction, as a result of very large blast loadings, is evident.

III. REVIEW OF LIQUEFACTION CAUSED BY EARTHQUAKES

Earthquakes create alternating stresses, as do shock loadings. Because of the concern with the safety of nuclear power plant structures founded on soil deposits that may be susceptible to liquefaction, considerable research efforts have been directed to methods of evaluating the liquefaction potential of soil deposits subjected to earthquakes. Liquefaction prediction from earthquake loadings by analyzing field and laboratory data is reviewed. Possible extension to include ground shock produced by high explosive test events is discussed in Section IV.

During or shortly after some earthquakes, extensive damage to engineering structures, along with extensive failures of natural slopes, has occurred as a result of liquefaction of saturated sandy soils. Some structures have settled more than three feet and have often been accompanied by severe tilting. Some buried empty tanks have floated above the ground surface. Extensive damage to structures on and below natural slopes that have failed has also been observed.

In addition to foundation and slope failures, there is usually other physical evidence of liquefaction. Water, in the form of springs and sand boils, has been observed coming from the ground soon after an earthquake (Idriss and Seed, 1967; Seed and Idriss, 1967). Changes in ground motion, as a result of liquefaction, have also been observed. During the Niigata earthquake on June 17, 1964 (maximum ground acceleration of the order of 0.16 g), the soil below an apartment building liquefied during the earthquake. Strong motion seismographs were located in the basement and on the fourth floor of the apartment building. The record shows a marked change in the form of the record from a predominantly short period motion to a long period motion, presumably at the time of the onset of soil liquefaction below the building, after about 8 seconds of ground motion (Japan National Committee, 1965).

A. PRESENT KNOWLEDGE OF SOIL LIQUEFACTION

Geotechnical engineers have known for some time the general conditions necessary for liquefaction. Terzaghi first described the mechanics of flow failure due to liquefaction. Casagrande (1936) described the significance of liquefaction of loose saturated sands subjected to unidirectional loading. After the liquefaction failure of the Fort Peck Dam in 1938 (Middlebrooks, 1942; Corps of Engineers, 1939), various papers amplified these considerations and introduced the concept that liquefaction can also occur as the result of several types of vibration, including earthquakes and explosions (Koppejan, Van Wamelem and Weinberg, 1948; Peck and Kaun, 1948). Published case histories and research conducted on liquefaction of sands during earthquakes have been collected and reviewed. Table 1 summarizes the site conditions, ground motions and field behavior of a number of cases in which sand deposits have or have not liquefied during earthquakes (Seed and Idriss, 1971). Note that liquefaction occurred in all earthquakes reported where the relative density was less than 50 percent; although, in some cases, liquefaction occurred at relative densities up to 72 percent where the duration of shocking was long and/or the maximum ground acceleration was quite strong. Table 2 summarizes liquefaction-induced landslides due to earthquakes (Seed, 1967). Table 3 summarizes site conditions of earthquake induced settlements to saturated sands (Lee and Albaisee, 1974).

Theoretical and analytical methods to predict the undrained response of saturated sands leading to liquefaction are discussed below:

During an earthquake, a soil element is subjected to a series of alternating shear stresses. If a sample of saturated sand is subjected to cyclic loading, it may remain stable for some number of cycles and then suddenly become unstable. As shown in Figure 1, the pore-water pressure (p.w.p.) progressively builds up as compaction takes place. As the p.w.p. builds up, the effective stresses are reduced, and the shear strength of the soil is reduced. When the p.w.p. equals the confining stress, the effective stresses equal zero, and a cohesionless material has no shear strength. This loss of strength under cyclic loading due to p.w.p. increase is known as liquefaction.

Both observations of field performance and laboratory investigations have shown that the liquefaction potential of a soil deposit from ground motions depends on many relationships. Although the specific relationships are very much site specific and require careful laboratory and field studies, a review of case histories of earthquake-induced soil liquefaction shows the following significant factors:

1. Soil Type.

   Liquefaction initiates in saturated cohesionless (sandy) soils. Uniformly graded soils appear to be more prone to liquefaction than well graded soils (Ross, et al. (1969); Lee and Fitton (1969) and that for uniformly graded soils, fine sands tend to have a higher liquefaction potential than coarse sands, gravelly soils, silts or clays. Limited data appears to indicate that an increase in the clay fraction reduces the liquefaction potential (Seed, 1967).

2. Initial Relative Density.

TABLE 1.—SITE CONDITIONS AND EARTHQUAKE DATA FOR KNOWN CASES OF LIQUEFACTION AND NONLIQUEFACTION

(After Seed and Idriss, 1971)

Earthquake (1)	Date (2)	Magnitude (3)	Site (4)	Approximate distance from source of energy release, in miles (5)	Soil type (6)	Depth of water table, in feet (7)	Critical depth, in feet (8)	Average penetration resistance at critical depth $\bar{N}$ (9)	Relative density, as a percentage (10)	Maximum ground surface acceleration, in units of g (11)	Duration of shaking, in seconds (12)	Field behavior (13)	References (14)
Niigata	1802	6.6	Niigata	24	Sand	3	20	6	53	0.12	≈20	No liquefaction	Kawasumi (10)
Niigata	1802	6.6	Niigata	24	Sand	3	20	12	64	0.12	≈20	No liquefaction	Seed and Idriss (26)
Niigata	1887	6.1	Niigata	29	Sand	3	20	6	53	0.08	≈12	No liquefaction	Kawasumi (10)
Niigata	1887	6.1	Niigata	29	Sand	3	20	12	64	0.08	≈12	No liquefaction	Seed and Idriss (26)
Mino Owari	1891	8.4	Ogaki	20	Sand	3	45	17	65	≈0.35	≈75	Liquefaction	Kishida (12)
Mino Owari	1891	8.4	Ginan West	20	Sand	6	30	10	55	≈0.35	≈75	Liquefaction	Kishida (12)
Mino Owari	1891	8.4	Unuma	20	Sand and gravel	6	25	19	75	≈0.35	≈75	No liquefaction	Kishida (12)
Mino Owari	1891	8.4	Ogase Pond	20	Sand	8	20	16	72	≈0.35	≈75	Liquefaction	Kishida (12)
Santa Barbara	1925	6.3	Sheffield Dam	7	Sand	≈15	25	—	40	≈0.2	15	Liquefaction	Seed et al. (28)
El Centro	1940	7.0	Brawley	5	Sand	≈15	≈15	—	58	≈0.25	30	Liquefaction	Ross (23)
El Centro	1940	7.0	All-Am. Canal	5	Sand	≈20	≈25	—	43	≈0.25	30	Liquefaction	Ross (23)
El Centro	1940	7.0	Solfatara Canal	5	Sand	5	≈20	—	32	≈0.25	30	Liquefaction	Ross (23)
Tohnankai	1944	8.3	Komei	100	Sand	5	13	4	40	≈0.08	≈70	Liquefaction	Kishida (12)
Tohnankai	1944	8.3	Meiko St.	100	Silt and sand	2	8	1	30	≈0.08	≈70	Liquefaction	Kishida (12)
Fukui	1948	7.2	Takaya	4	Sand	11	23	18	72	≈0.30	≈30	Liquefaction	Kishida (12)
Fukui	1948	7.2	Takaya	4	Sand	3	23	28	90	≈0.30	≈30	No liquefaction	Kishida (12)
Fukui	1948	7.2	Shonenji Temple	4	Sand	4	10	3	40	≈0.30	≈30	Liquefaction	Kishida (12)
Fukui	1948	7.2	Agr. Union	4	Sand and silt	3	20	5	50	≈0.30	≈30	Liquefaction	Kishida (12)
San Francisco	1957	5.5	Lake Merced	4	Sand	8	10	7	55	≈0.18	18	Liquefaction	Ross (23)
Chile	1960	8.4	Puerto Montt	≈70	Sand	12	15	6	50	≈0.15	≈75	Liquefaction	Lee (15)
Chile	1960	8.4	Puerto Montt	≈70	Sand	12	15	8	55	≈0.15	≈75	Liquefaction	Lee (15)
Chile	1960	8.4	Puerto Montt	≈70	Sand	12	20	18	75	≈0.15	≈75	No liquefaction	Lee (15)
Niigata	1964	7.5	Niigata	32	Sand	3	20	6	53	0.16	40	Liquefaction	Seed and Idriss (26)
Niigata	1964	7.5	Niigata	32	Sand	3	25	15	70	0.16	40	Liquefaction	Kishida (11)
Niigata	1964	7.5	Niigata	32	Sand	3	20	12	64	0.16	40	No liquefaction	Seed and Idriss (26)
Niigata	1964	7.5	Niigata	32	Sand	12	25	6	53	0.16	40	No liquefaction	Seed and Idriss (26)
Alaska	1964	8.3	Snow River	60	Sand	0	20	5	50	≈0.15	180	Liquefaction	Ross et al. (24)
Alaska	1964	8.3	Snow River	60	Sand	8	20	5	44	≈0.15	180	Liquefaction	Ross et al. (24)
Alaska	1964	8.3	Quartz Creek	70	Sandy gravel	0	≈25	40–80	100	≈0.12	180	No liquefaction	Ross et al. (24)

TABLE 2 – LANDSLIDES DURING EARTHQUAKES DUE TO SOIL LIQUEFACTION

(After Seed, 1967)

Date	Earthquake	Magnitude	Location of slide	Epicentral distance, in miles	Type of structure	Soil type	Reference
1920	Kansu Province	–	Kansu Province	–	Loess slopes	Loess	Close and McCormick
1923	Kwanto (Tokyo)	8.2	Yokohama area	40	Coastal hillsides	–	Wakimizu, Horigam
			Tokyo area	60	Coastal hillsides	–	
1925	Santa Barbara	6.3	Santa Barbara	7	Earth dam	Silty sand	
1928	Chile	8.3	El Teniente	100	Tailings dam	Mining waste	Dobry, Lomnitz
1933	Long Beach	6.3	Long Beach	20	Highway fills	Fills over marshland on shore roads.	Wood, Richter, Hodgson
			Newport Beach	3	Highway fills		
1934	Bihar Nepal	8.4	Sitamarhi to Purnea	0 to 80	Road and railway fills	Fluvial sediments, including sands	Roy, Richter
			Motihari	70	Lake banks	Alluvium—sand lenses	
1935	India (now West Pakistan)	7.6	Quetta	20 to 40	River banks	Alluvium—uncertain gradation	West, Richter
1940	El Centro	7.0	All-American Canal	6	Canal banks	Levees and foundations of deltaic sands.	Ross (personal communication)
			Alamo Canal	7 to 25	Canal banks	Levees and foundations of deltaic sands.	
			Solfatara Canal	25 to 30	Canal banks	Levees and foundations of deltaic sands.	
			Brawley	20	Road and railway fills	Deltaic and fluvial sands	
1941	Garm	–	–	–	Loess slopes	Loess	Gubin
1943	Faizabad	–	–	–	Loess slopes	Loess	Gubin
1948	Fukui	7.2	Fukui plain	0 to 15	Levees, river banks, road and railway fills.	Aeolian sands, beach sands, fluvial sands and silts.	Tsuya, Collins and Foster, Butler et al.
1949	Chait	7.5	Surchob and Yasman River valleys	5 to 25	Loess slopes	Loess	Gubin
1950	Imperial Valley	5.4	Calipatria area	1 to 5	Canal banks	Deltaic and aeolian sands.	Wood and Heck
1954	Anchorage	6.7	Rabbit Creek	20 to 40	Embankment	Fill on sand	Hansen
1957	San Francisco	5.3	Lake Merced	8	Lake banks	Aeolian and beach sands.	Chan
1959	Jaltipan	6.5	Coatzacoalcos	20	River banks, waterfront fill	Fine sandy silt, uniform and loose.	Diaz de Cossio, Marsal
			Minatitlau-Coatzacoalcos highway	20 to 30	Road and bridge approach fills	Fill over marshland	
1960	Chile	8.4	Rinihue	140	River banks	Fluvial and glacial sands	Duke and Leeds, Lee (personal communication)
					Highway and railway fills	Foundations of fluvial and glacial gravels, sands, silts.	
			Puerto Montt	240	Coastal terraces	Glacio-fluvial deposits.	
					Sea walls and quay walls	Fill mainly sands to silty sands, loose.	
			Valdivia	125	River banks	Fluvial Sediments.	
1964	Alaska	8.3	Anchorage	70	Coastal bluffs	Sand layers and lenses in clay deposit.	Shannon and Wilson
			Valdez	40	Coastal delta	Silty sands and gravel, ($N \approx 15$)	Coulter and Miglaccio
			Seward	90	Coastal delta	–	
			Kenai Lake	80	Lake deltas	Deltaic sandy gravels, some sand lenses	McCulloch
1964	Niigata	7.3	Niigata area	35	Earth banks	Fluvial sand ($N < 15$)	Yamada, Yokomura, Kawakami and Yoda
1965	Chile	7.2	El Cobre	≈ 25	Tailings dam	Mining waste	Dobry
			La Patagua	≈ 9	Tailings dam	Mining waste	
			Hierro Viejo	≈ 16	Tailings dam	Mining waste	
			Los Maquis	≈ 8	Tailings dam	Mining waste	
			El Cerrado	≈ 18	Tailings dam	Mining waste	
1965	Seattle	6.7	Capitol Lake Blvd., Olympia	38	Road causeway	Sand/gravel fill over lake and tidal sediment	Ross (personal communication)
			Union Pacific at Tumwater	38	Railway on benched slope	Cut/fill slope in outwash sands.	
			Suquamish	26	Coastal bluff	Till over fine sand and silt strata.	
			Port Orchard	18	Waterfront fill	Sand over beach sand and bay mud	
			E. Mercer Way, Mercer Island	10	Roadways on benched slopes	Sand on tills and outwash sands.	
			Edmonds	29	Dumped fill on slope	Sandy till and refuse on till slope	
			Foster golf course, Duwamish	10	River terrace	Fluvial sands and silts.	
			Victor	24	Highway fill	Sand fill at toe of coastal bluff.	
1966	Parkfield	5.5	Cholame Creek north of Cholame	17	Stream banks	Fluvial sediments, sand strata or lenses.	Ross (personal communication)

TABLE 3 —Summary of Measured Seismic-Induced Settlements in Granular Soils

(After Lee and Albaisa, 1974)

Brief explanation of problem (1)	Laboratory or field (2)	Saturated or dry (3)	Accompanied by liquefaction (4)	Measured settlements, as a percentage (5)	Reference (6)
Cyclic simple shear tests	laboratory	dry	—	0.5	Seed and Silver, Youd
Shaking table rigid box, variable confining pressure, shaking continued beyond liquefaction	laboratory	saturated	yes	6	Yoshimi
Shaking table, rigid box	laboratory	dry and saturated	no	<0.25	Whitman
Field observations of ground settlement from controlled test blasting	field	saturated	yes no	<3 >0.5	Ivanov
Tohnankai earthquake, Japan, 1944, Naguya, 8 m–16 m of loose saturated sand	field	saturated	yes	5 (possibly less)	Kishida
Fukui earthquake, Japan, 1948, Maruoka, 6 m–8 m of loose saturated sand	field	saturated	yes	4–5	Kishida

TABLE 3 —*Continued*

(1)	(2)	(3)	(4)	(5)	(6)
Alaska earthquake 1964, 468 ft of alluvium—Homer split.	field	saturated	unknown	0.5	Grantz
Tokachioki earthquake, Japan, 1967, Hachinone, 20 loose sand	field	saturated	probably some	0.5-2	Ohsaki
5 m very loose moist sand backfill	field	saturated	probably yes	10	
San Fernando, Calif. Earthquake, 1971, Joseph Jensen Filtration Plant, up to 10 ft of loose to medium dense granular alluvium	field	saturated	yes	2	Dixon unpublished

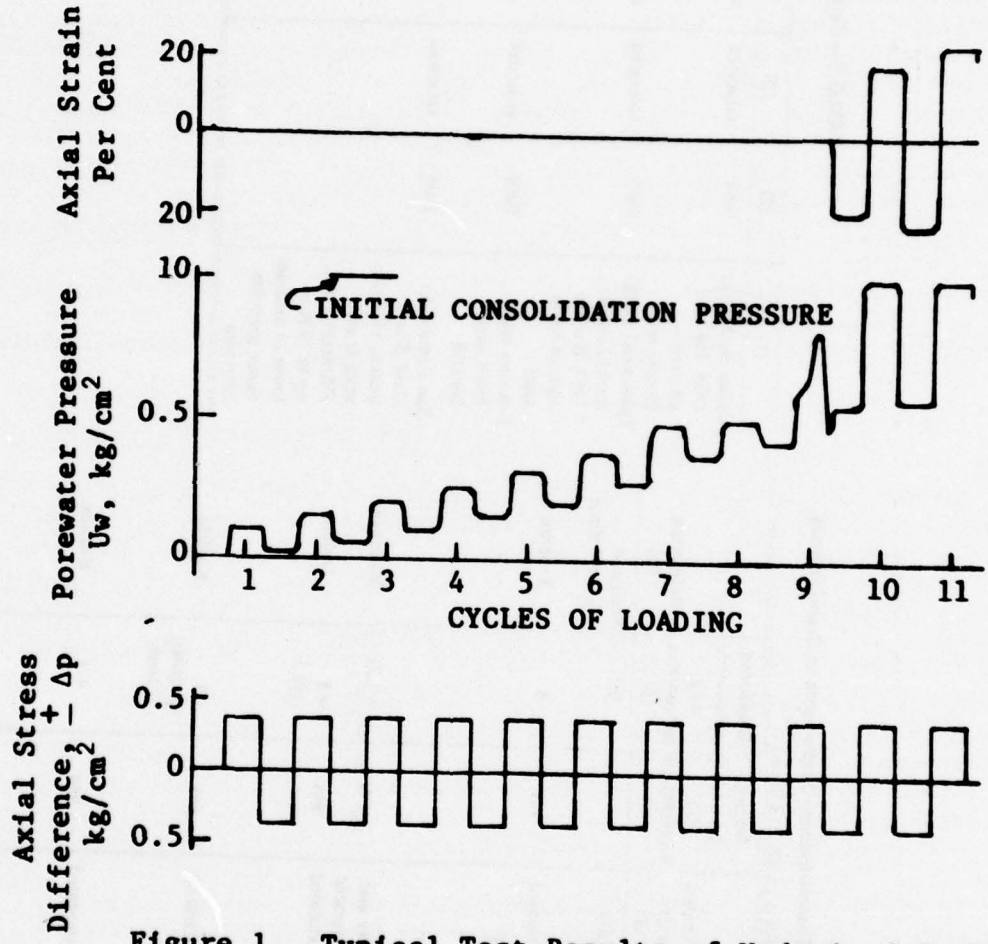


Figure 1. Typical Test Results of Undrained Cyclic Triaxial Test on Loose Saturated Sand (after Seed and Lee, 1966).

Other factors constant, the higher the relative density, the lower the liquefaction potential (Seed and Idriss, 1971).

3. Initial Effective Stress.

Other factors constant, the higher the initial effective stress, the lower the liquefaction potential (Lee and Fitton, 1969). The effect was shown in the field during the Niigata earthquake with soil under a 9-foot fill remaining stable, but similar soils surrounding the fill liquefied extensively (Seed and Idriss, 1967).

4. Intensity of Ground Shaking.

Other factors constant, the higher the intensity of ground shaking (accelerations or stress changes), the higher the liquefaction potential (Seed and Idriss, 1971).

5. Duration of Ground Shaking.

Other factors constant, the longer the duration (i.e., more strain cycles), the higher the liquefaction potential (Seed and Idriss, 1971). One large stress increase or many smaller cyclic stress increases can cause liquefaction under the right conditions.

6. Initial Shear Stress.

Other factors constant, liquefaction will be induced more easily under level ground conditions than in sloping zones of a deposit (Seed, 1967).

7. Pore-Water Pressure.

Liquefaction can only persist as long as high excess pore-water pressures persist in a soil. Therefore, the permeability of the saturated soil and the soils above and below it are important to the duration of liquefaction.

B. EVALUATING SOIL LIQUEFACTION POTENTIAL

It is apparent that any method for evaluating liquefaction potential should take the forementioned significant factors into account. Accordingly, Seed and Idriss (1971) proposed a general method for evaluating liquefaction potential from earthquakes. However, it is not known that all the above or if other factors are important for blast-induced liquefaction. The intensity of ground shock may be the most important factor causing close-in blast-induced liquefaction. Close-in, the stresses are so large that the soil fails on the first stress cycle. Far-out, the stress increase is smaller and requires more stress cycles to cause failure or liquefaction.

C. LABORATORY TESTS

The cyclic stability of sands, as determined by the cyclic triaxial

strength test, has been studied in detail during the past 10 years (Finn, Pickering and Bransby, 1971; Lee and Seed, 1967; Seed and Lee, 1966; Seed and Peacock, 1971). Ladd (1974 and 1977) discusses the effects of various specimen preparation methods on the cyclic behavior of reconstituted sands.

Laboratory triaxial tests are run on representative samples of in-situ soils. When a sample of saturated sand is subjected to stress controlled cyclic loading conditions as shown in Figure 1, it remains stable for some number of cycles, though the pore-water pressure progressively builds up. Suddenly the sample loses all its strength and undergoes large deformations when the pore-water pressure equals the applied confining pressure.

Although stress cycles from earthquakes (and blast loadings) are non-uniform, laboratory tests are generally run with uniform stress cycles. Figure 2 shows the effect of various nonuniform stress cycles on pore-water pressure. The significance of the order of stress cycles is apparent. For time history A, the initial large cycles result in a rapid increase of the volumetric slip strains and pore-water pressure. The reverse effect occurs with time history B. Figure 3 shows the effect of initial effective vertical stress on pore-water pressure increase. The effect of the initial effective vertical stress on the pore-water pressure--initial effective vertical stress ratio--is small.

For convenience, laboratory triaxial tests are normally run at a frequency of about one hertz. The behavior of sands has been shown to be independent of frequency in the range of 0.2-2-hertz (Martin, Finn and Seed, 1974).

D. ANALYSIS OF LABORATORY DATA

The laboratory data are usually presented in the form of the ratio of the applied cyclic stress to the effective overburden pressure versus the number of stress cycles required to develop liquefaction at various relative densities (see Figures 4 and 5).

E. ANALYSIS OF LIQUEFACTION POTENTIAL

A comparison of the cyclic stresses induced in the field with the cyclic stresses required to develop liquefaction in the laboratory (Figure 4), permits an evaluation of the factor of safety against liquefaction. While this method of analyzing liquefaction from earthquakes has been primarily developed by H. Bolton Seed and his colleagues at the University of California at Berkeley, many others have made significant contributions.

First, a dynamic response analysis is run from the knowledge of the soil properties of the system and the time history of the motions to compute the time history of accelerations, displacements, stresses and strains at any point in the system. To determine the liquefaction potential of the sand, it is necessary to determine if these stress variations will induce liquefaction. Using the information obtained from the cyclic triaxial testings, the number of field stress cycles and the equivalent average stress developed over these cycles is entered into Figure 4 for various depths to see if liquefaction will

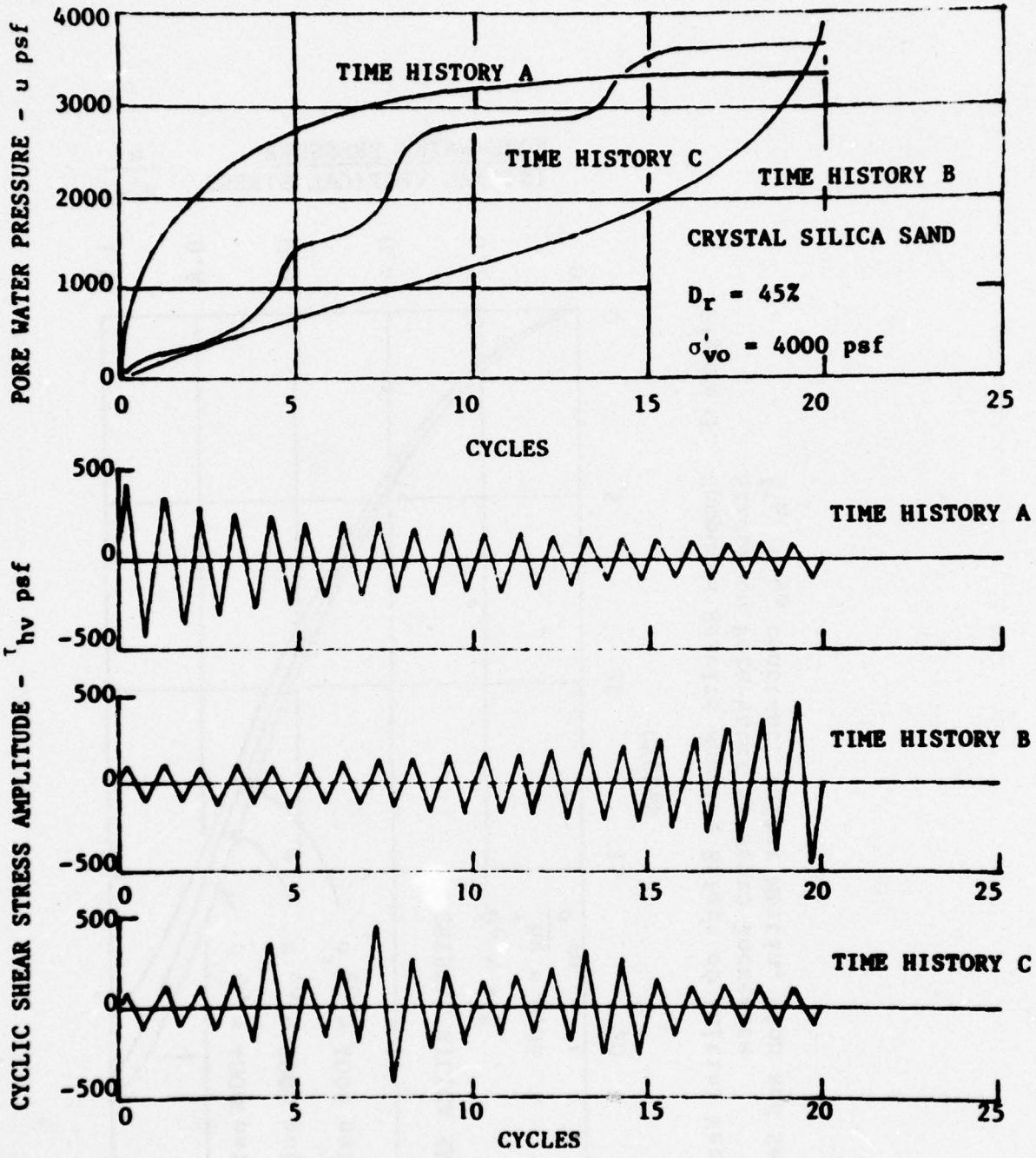


Figure 2. Computed Results Showing Effect of Non-Uniform Shear Stress Cycles on Pore-Water Pressure (after Martin, Finn and Seed, 1974).

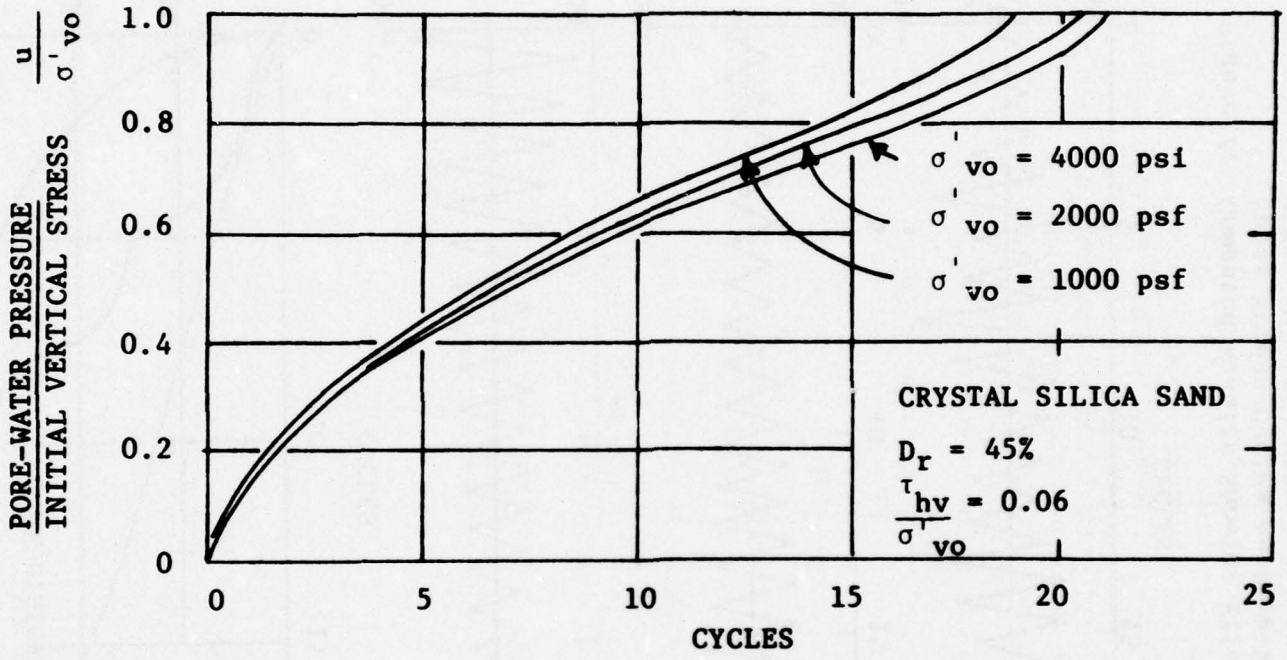


Figure 3. Computed Results Showing Effect of Initial Vertical Stress on Pore-Water Pressure Increases (τ_{hv}/σ'_{vo} constant) (after Martin, Finn and Seed, 1974).

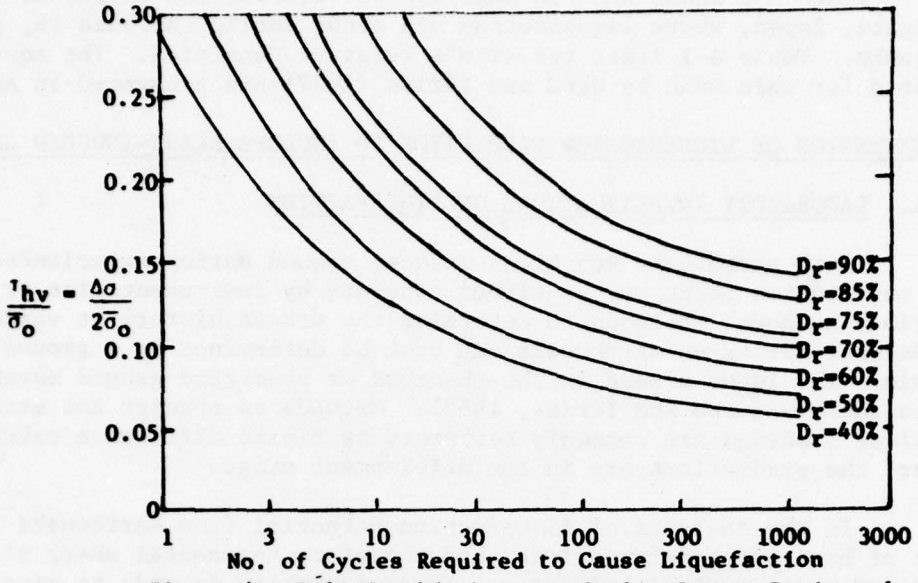


Figure 4. Relationship between Cyclic Stress Ratio and Number of Cycles Required to Cause Liquefaction for Simple Shear Tests on Medium Sand at Different Relative Densities.

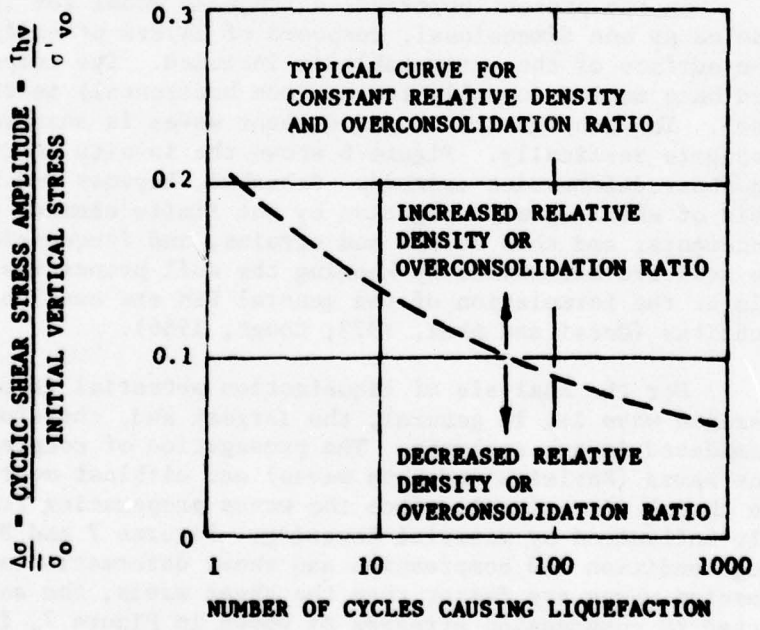


Figure 5. Method of Expressing Stress Conditions Causing Liquefaction in Cyclic Simple Shear Tests (after Martin, Finn and Seed, 1974).

occur. Figure A-2 shows such an analysis of liquefaction potential at a site at Niigata, Japan, where liquefaction did occur during the June 16, 1964, earthquake. Table A-1 lists the site's relative densities. The results presented for this sand by Seed and Idriss (1967) are presented in Appendix A.

IV. EXTENSION OF LIQUEFACTION PREDICTION TO INCLUDE BLAST-INDUCED GROUND SHOCK

A. LABORATORY INVESTIGATIONS OF LIQUEFACTION

Both earthquake and blast-induced ground motion experienced at a given observation point may be either recorded by instrumentation or predicted by various methods. Methods to determine the stress history at various depths in a deposit during an earthquake can best be determined by a ground response analysis. The input needed is the observed or predicted ground movements and soil parameters (Seed and Idriss, 1967). Methods to predict the stress history from blast loadings are commonly performed by finite difference calculations; however, the predictions are in the development stage.

In the analysis of liquefaction potential from earthquake loadings, the effect of horizontal deformations, and therefore horizontal shear stresses, is considered to control liquefaction. This assumption is made to simplify calculations and is based on the observation that during earthquakes, vertical accelerations are generally smaller than horizontal accelerations. In general, it is the shear wave which causes the peak accelerations in soil (Murphy, Weaver and Lamers, 1970).

In the present numerical earthquake model for liquefaction, the deposit is modeled as one dimensional, composed of layers of soils with various properties, and the surface of the water table is included. The component of the earthquake induced base motion (usually the maximum horizontal) is treated in a shear wave submodel. The propagation of plane shear waves is assumed one dimensional and to propagate vertically. Figure 6 shows the in-situ loading condition and the simple shear deformation assumed. Schnabel, Laysmer and Seed (1972) discuss the analysis of shear wave propagation by the finite element method (FEM). Nodal displacements, and thus stress and strains, and frequencies at various points in the soil are determined by knowing the soil properties and base movement. Details of the formulation of the general FEM are available in several recent publications (Desai and Abel, 1972; Cough, 1966).

For the analysis of liquefaction potential from blast loadings, the compression wave is, in general, the largest and, therefore, important and must be considered in any analysis. The propagation of compression waves, shear waves, surface waves (Rayleigh and Love waves) and airblast must be modeled as two (often three) dimensional, since the waves propagating from a point source are heavily influenced by material layering. Figures 7 and 8 show the in-situ loading condition and compression and shear deformation assumed. Since the compression waves are faster than the shear waves, the soil at depth is first subjected to compression stresses as shown in Figure 7, followed by shear stresses as shown in Figure 8. For near-surface areas, the soil may also be subjected to shock loading from surface waves and airblast shock. Near to the crater, the airblast is usually traveling faster than the compression wave in the soil, so the soil is loaded in the vertical direction from the airblast loading before

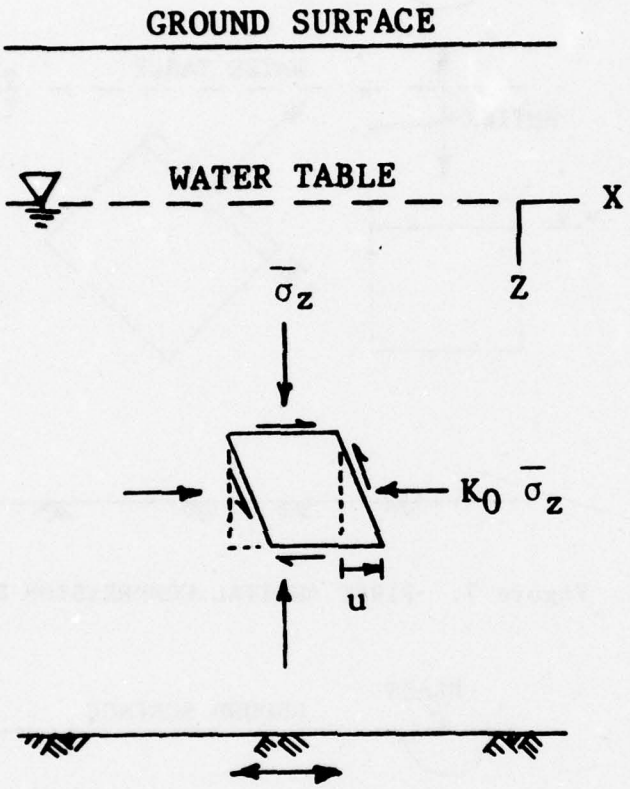


Figure 6. In-Situ Loading Condition and Simple Shear Deformation (after Liou, Streeter and Richart, 1977).

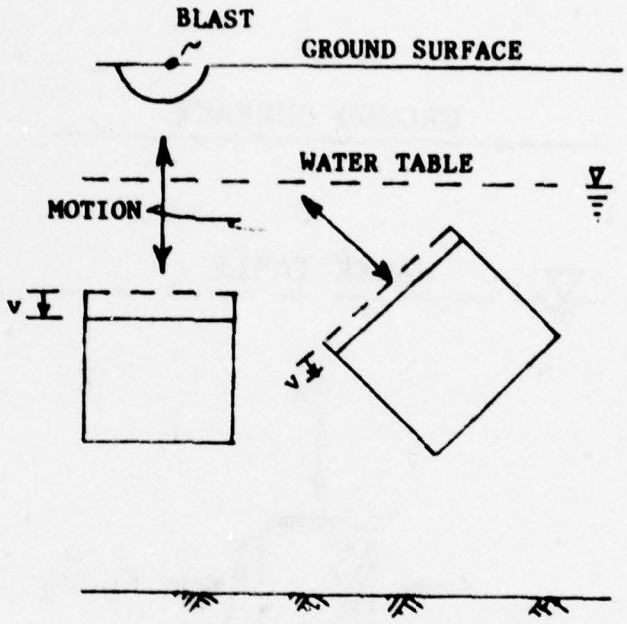


Figure 7. FIRST ARRIVAL COMPRESSION DEFORMATION

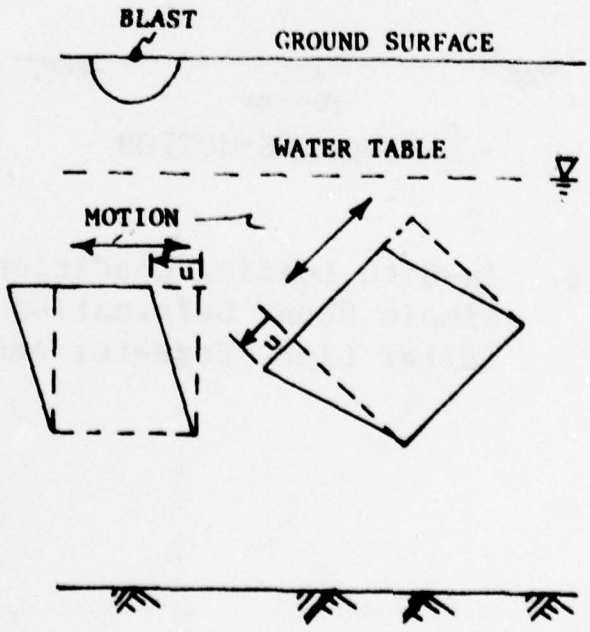


Figure 8. Simple Shear Deformation

the direct-induced ground compression wave arrives. The greatest effect of the airblast is in the near-surface layers close to the blast. The airblast-induced vertical loadings may be larger than the horizontal propagating ground compression wave loading for the near-surface layers. At greater depths, the effect of the directly coupled motion becomes larger.

The airblast (overpressure) is caused by the sudden release of energy from the explosive, heating the air into extremely hot gases which expand rapidly and generate a shock wave. This causes a sudden increase in pressure. The front of the blast wave travels rapidly away from the explosion as a front of highly compressed air. The velocity of the blast front, the peak pressure and the air density in the front decrease with increasing distance. At some distance, labeled "OR" on Figure 9, the ground compression wave outruns the airblast front. Past this point, the direct-induced ground compression wave is the first arrival. Since the compression wave is usually the largest in blast loadings, it may be possible to predict liquefaction by analyzing just the effects of the compression (first arrival) wave. As shown in Figure 2, the effect of smaller stress changes following large stress changes is small (i.e., the large stress changes account for most of the pore-water pressure increases).

In the area sufficiently far away from the crater where the soil behaves elastically (Figure 10), the use of dynamically loaded triaxial tests should be sufficient to predict the liquefaction potential. Data needed would be the compressive stress changes (possibly also the shear stress changes) and the number of cycles that the soil would be subjected to. This is an area of needed research. Along with laboratory tests on representative field samples at field confining pressures in question, an analysis could be made following procedures used in analyzing liquefaction by earthquakes described earlier in this paper by using cyclic compressive stress instead of cyclic shear stresses. For the triaxial test:

$$\tau_{max} = \frac{\sigma_1 - \sigma_3}{2} \qquad \text{EQ (1)}$$

where σ_1 = maximum principal stress

σ_3 = minimum principal stress

τ_{max} = maximum shear stress

Either the cyclic compressive stress could be converted to shear stress by EQ 1, or vise versa. However, the higher frequencies produced by blasts along with the short duration (as compared to earthquakes) may affect the results obtained unless accounted for or tested at such frequencies and duration. Research is needed to find the effect of higher frequencies and short duration on liquefaction.

An example of predicting liquefaction by shock loading follows: Assuming that the frequency has little effect on the results (which may not be the case), assume a blast occurred at a site with soil conditions similar to those shown in Appendix A, Figure A-2 and Table A-1, will the soil liquefy in the elastic zone at a depth of 35 feet? Let's also assume the following:

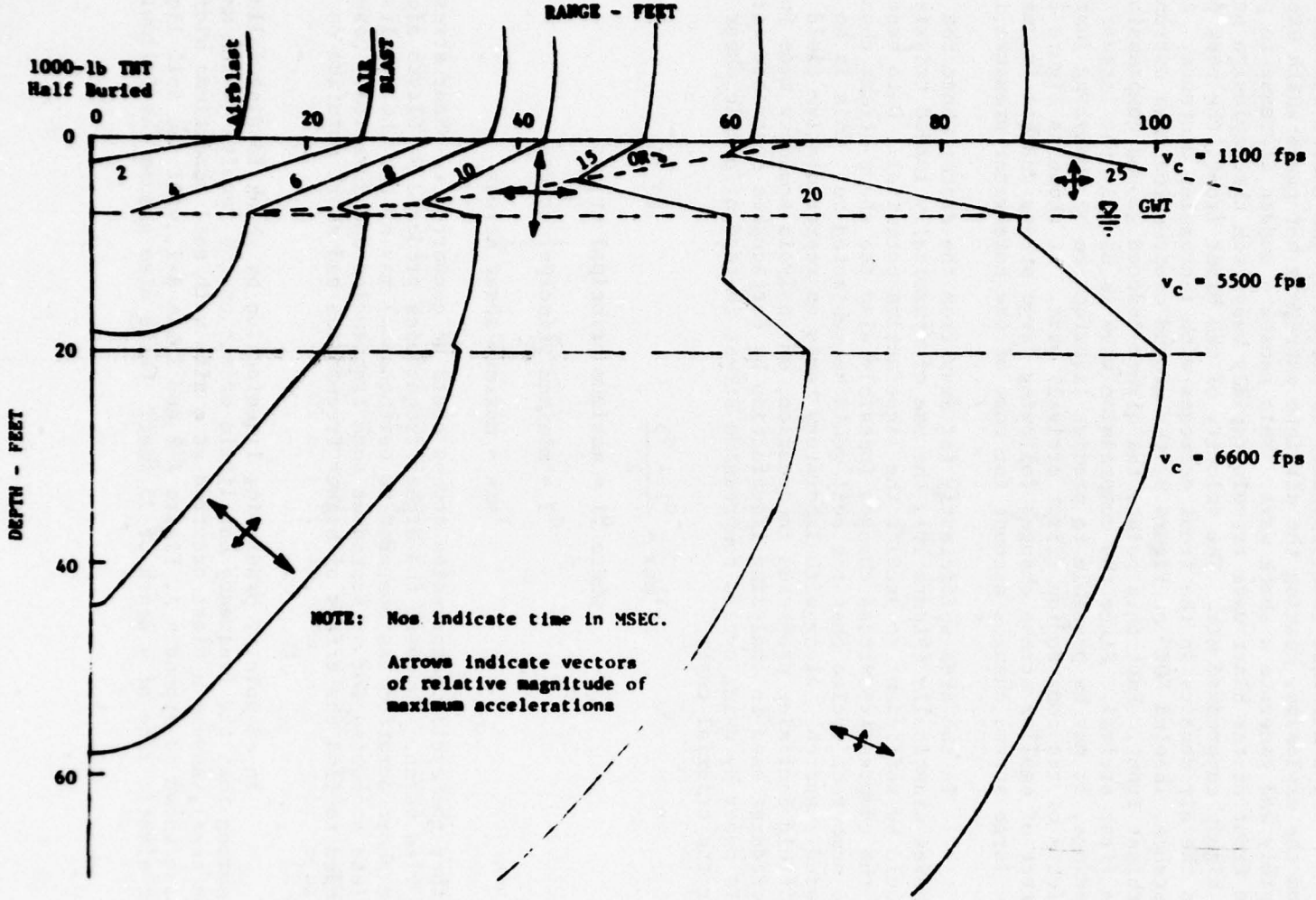


Figure 9. Airblast and Direct-Indiced Time of First Arrival Contours and Relative Magnitude of Maximum Accelerations

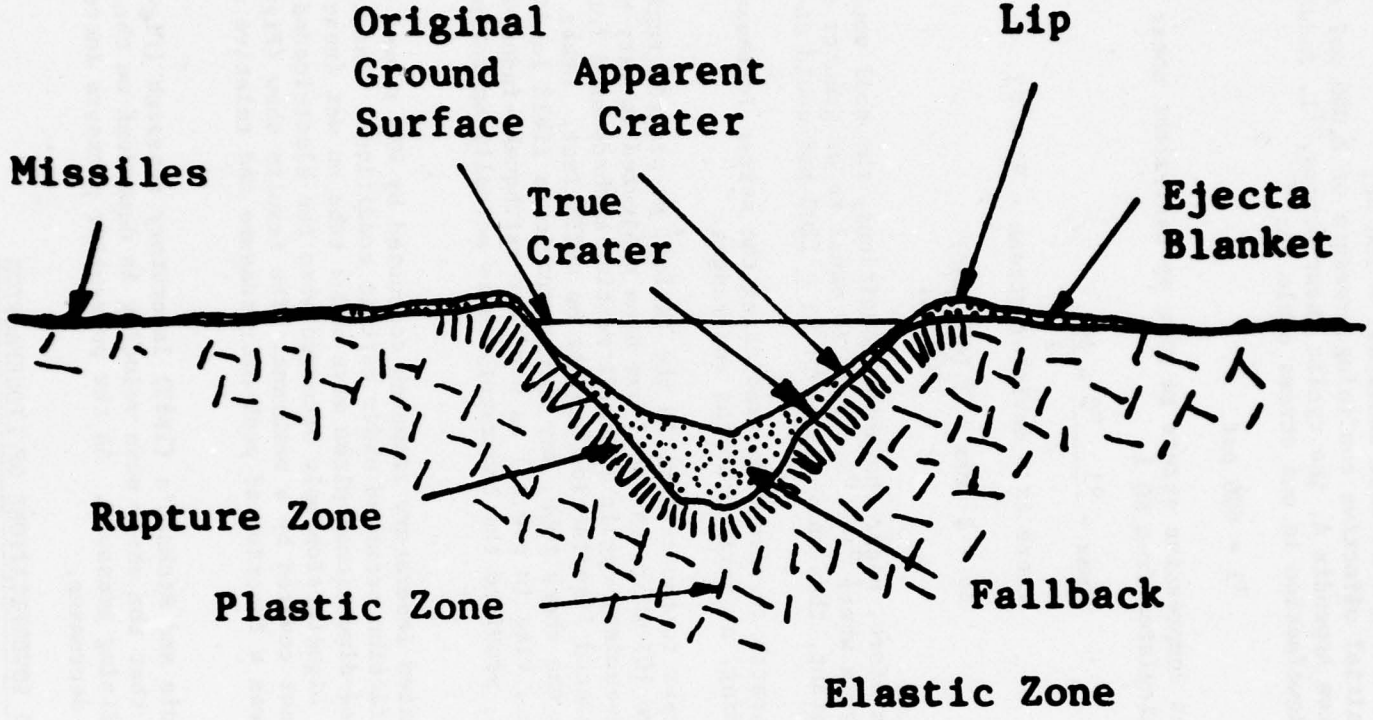


Figure 10. Idealized Crater Profile

Relative density of 40 percent
Bouyount unit weight of soil below GWT = 50 pcf
Unit weight of soil above GWT = 100 pcf
Initial effective confining pressure of 2,000 psf at 35 feet
From Appendix A, the cyclic shear stress, τ_1, inducing liquefaction in one stress cycle is:

$$\tau_1 = 600 \text{ psf}$$

The compressive stress to give an equivalent shear stress can be calculated from EQ 1.

$$\tau_{max} = \frac{\sigma_1 - \sigma_3}{2} = \frac{\Delta\sigma}{2}$$

where $\Delta\sigma$ = deviator stress = $\sigma_1 - \sigma_3$

$$\Delta\sigma = 2\ \tau_{max} = 2\ (600 \text{ psf})$$
$$= 1200 \text{ psf}$$

Therefore, under the above conditions, the soil would liquefy under one stress cycle where $\sigma_1 - \sigma_3$ stress is equal to or greater than 1200 psf. If σ_3 is constant, then an increase of $\sigma_1 \geq 1200$ psf would cause liquefaction.

Research is needed on predicting the stress increase in a soil, subject to shock loading, at various depths and ranges.

Closer to the crater, in the failed, or plastic region surrounding the crater (figure 10) where the soil has been subjected to very high stress values and high frequencies, cyclic triaxial testing methods used for predicting earthquake-induced liquefaction may not be sufficient. Other laboratory equipment, such as the shock tube, may more approximate field loadings. The same analysis (i.e., rise in p.w.p.) as used for earthquake-induced liquefaction may be sufficient, provided the laboratory tests actually approximate the field loadings.

Limited laboratory research conducted by WES showed that airblast-induced liquefaction occurred under certain conditions. The tests were conducted in a one-dimensional plane wave shock tube on wet (nearly saturated) loose sands. Liquefaction only occurred when the blast-loaded top surface of the sand was not covered by a membrane. The results show (Figure 11) that liquefaction was a function of peak overpressure and relative density (Perry, 1972).

Hardin and Richart's (1963) laboratory research (Figures 12 and 13) on sand shows that the shear wave velocity is dependent on the void ratio and effective confining pressure. As the pore-water pressure increases, the shear wave velocity decreases.

B. FIELD INVESTIGATIONS OF LIQUEFACTION

Investigations of blast-induced liquefaction have been reported. Studies by Lyman (1942) and Prugh (1963) showed that blasting was an effective

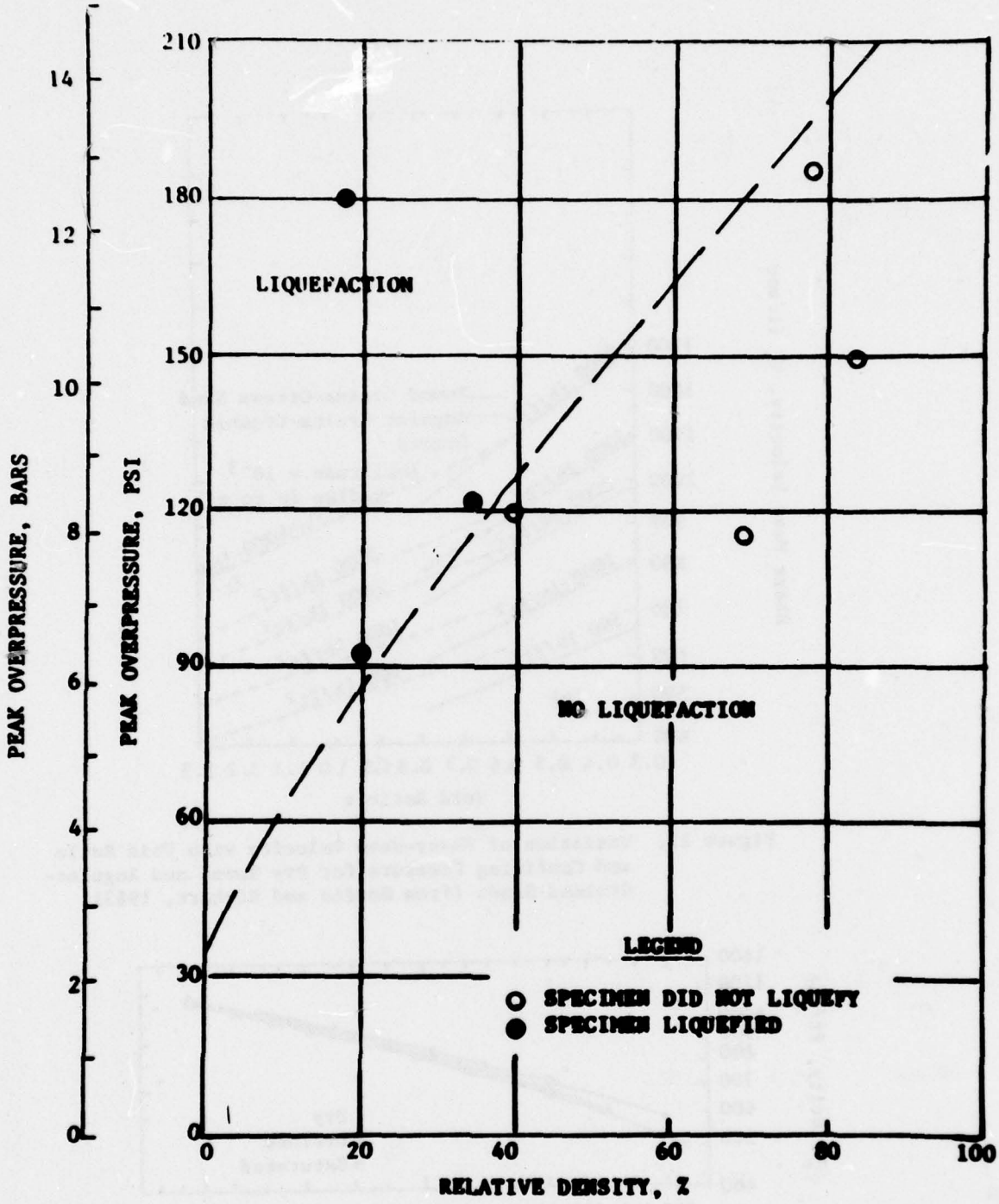


Figure 11. Liquefaction as a Function of Peak Overpressure and Relative Density for Both Wet and Dry Specimens Without Membrane (after Perry, 1972).

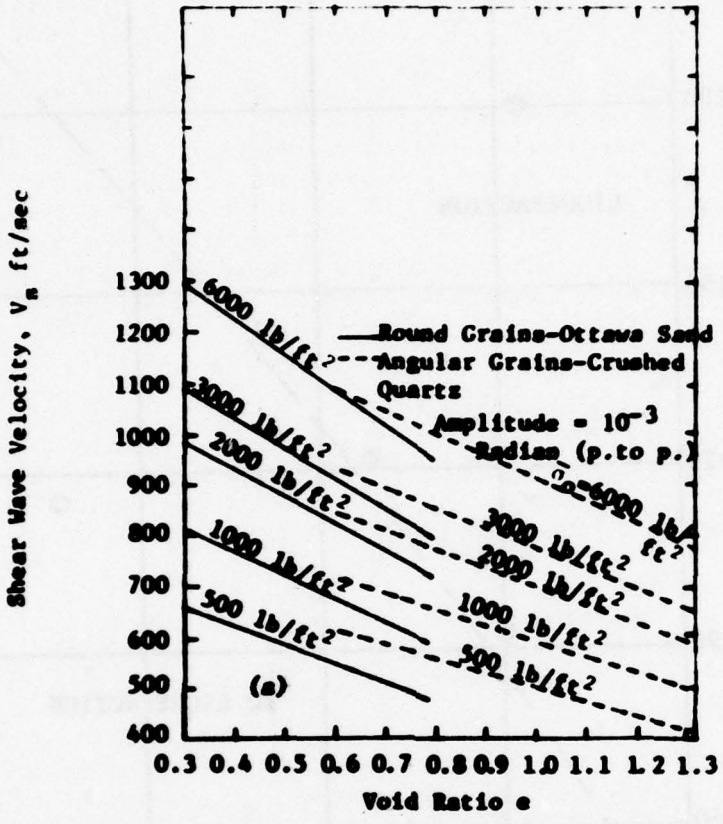


Figure 12. Variation of Shear-Wave Velocity with Void Ratio and Confining Pressure for Dry Round and Angular-Grained Sands (from Hardin and Richart, 1963).

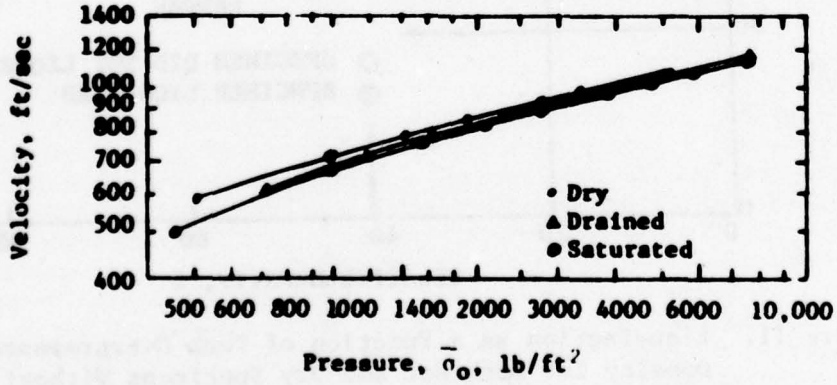


Figure 13. Variation of Shear-Wave Velocity with Confining Pressure for a Specimen of Ottawa Sand in the Dry, Saturated, and Drained Conditions (Test No. 18. e = 0.55 - 0.54) (from Hardin and Richart, 1963).

way to compact loose sands. Kummeneje and Eide (1961) used controlled blasting in determining whether submarine slopes might be susceptible to flow slides caused by earthquakes. Florin and Ivanov (1961) studied liquefaction and compaction of loose saturated sands by blasting. Their results showed that the ability to be liquefied depended upon the initial void ratio, the amount of energy introduced by the blast and the confining pressure. They concluded that a surcharge can be used as a method for reducing sand liquefaction. Perry (1972) reports a study where wet sand-filled test pits, with relative densities from 6 to 69 percent, located at the 50 psi peak airblast (overpressure) contour of a 100-ton high explosive field test did not liquefy. The laboratory study successfully predicted that liquefaction should not have occurred at this overpressure level. No tests at predicted levels of overpressure to cause liquefaction were reported.

Several references (Puchkov, 1962; Florin and Ivanov, 1961) indicate that the USSR has analytical and laboratory and field tests on soil property changes from blasts. The research effort has been with saturated sand deposits. They have developed a standard field test for liquefaction where a 5-kilogram charge of "ammonite" is placed at a depth of 4.5 meters. The liquefaction potential is determined by the ground settlements after the blast. An average ground surface settlement of 8-10 cm over a 5-meter radius indicates liquefaction. They feel the significant factors of blast-induced soil liquefaction are:

1. Soil type (sand).

2. Height of the water table and depth of the layer (initial effective overburden stress).

3. Porosity (relative density).

4. Peak particle velocity--a particle velocity of 6-10 cm/sec induced liquefaction in saturated loose sands located near the surface.

These factors are similar to those discussed earlier for earthquake-induced liquefaction.

For several years, the US Air Force and the Army have been involved in programs to monitor explosion phenomena. Various indirect evidence indicates that liquefaction is likely to have occurred at some sites. These include the following:

1. Anomalous ground movements involving low frequency oscillatory ground motions have been recorded in saturated soils (Pre DICE THROW, DIAL PACK).

2. Sand boils and/or water spouts, both within and outside the crater have been reported in the following tests: Pre DICE THROW, PRAIRIE FLAT, DIAL PACK, SNOW BALL and the KOA nuclear explosion.

3. Excessive pore-water pressures have been recorded by peizometers at DIAL PACK.

4. Settlement of the area around the crater has been reported at DIAL PACK.

5. Crater depth was less than expected, and the bottom of the craters were flat at Pre DICE THROW, PRAIRIE FLAT, DIAL PACK and SNOW BALL sites.

Figure 14 shows the geologic profile and relative densities of the Pre DICE THROW site. Figure 15 shows the wave pattern produced by the shock. Of special interest is the anomalously large amplitude wave of late arrival. The far-field low-frequency motion has been identified as the theoretically predicted fundamental Rayleigh mode. Also observed was a marked change in the ground motion, from a high frequency to a low frequency. As was the case for the 1964 Niigata, Japan, earthquake, this marked change may have occurred at the onset of liquefaction. The close-in low-frequency motion (dubbed the "X-wave") is attributed to the failure and liquefaction of the sands located beneath ground zero (Figure 16).

Figure 17 gives the near-surface horizontal accelerations versus horizontal range for a typical 100-ton TNT event. Note that accelerations measure in excess of 1,000 g's near-in, to 1 g at 400 feet out, to 0.16 g at a distance of 800 feet. For a 100-ton TNT event, the near-surface horizontal accelerations within 800 feet would be stronger than ever recorded for any earthquake (Table 1).

Note that the soil profile and relative densities are similar to the profile of the heavy damage zone, caused by liquefaction of sands by the Niigata earthquake (0.16 g max) on June 19, 1964, as shown in Appendix A, Figure A-2.

For DIAL PACK, Langley, Smith and Pfefferle (1972) report on an experiment to determine the effects of a large (500-ton TNT) blast loading on in-situ soil. The soil profile contained layers of sands, silts and clays with the original depth to the water table of about 22 feet (Figure 18). The pre-blast relative densities of the cohesionless soils in the upper thirty feet ranged from 50 to 80 percent. The upper 30 feet of the soil were monitored from core holes extending from 120 feet to 2,700 feet from ground zero. Before and for a month after the blast, core samples for laboratory testing and field measurements (pore-water pressure, GWT elevation and blow counts) were taken from a number of core holes.

The pore-water pressure data was acquired from well points and open drill holes. Twenty minutes after the blast, a geyser was observed outside the crater, 270 feet from ground zero (300 psi overpressure). The geyser originated at a pre-drilled instrumentation hole. Springs also flowed from cracks at ranges of 270 feet and greater, and flowed through the first 8 to 10 hours. A water well, located at 180 feet from ground zero and opened at a depth of 65 feet below the surface, also flowed during the early post-shot time period. The pre-shot water level had been about 22 feet. Inside the crater, springs developed at about twenty minutes after the blast and flowed for at least a day and a half. The flowing water brought sand to the surface in the form of sand boils. The first pore-water pressure measurement, taken at about three hours after the blast, showed an increase in pressure over the pre-blast pressure.

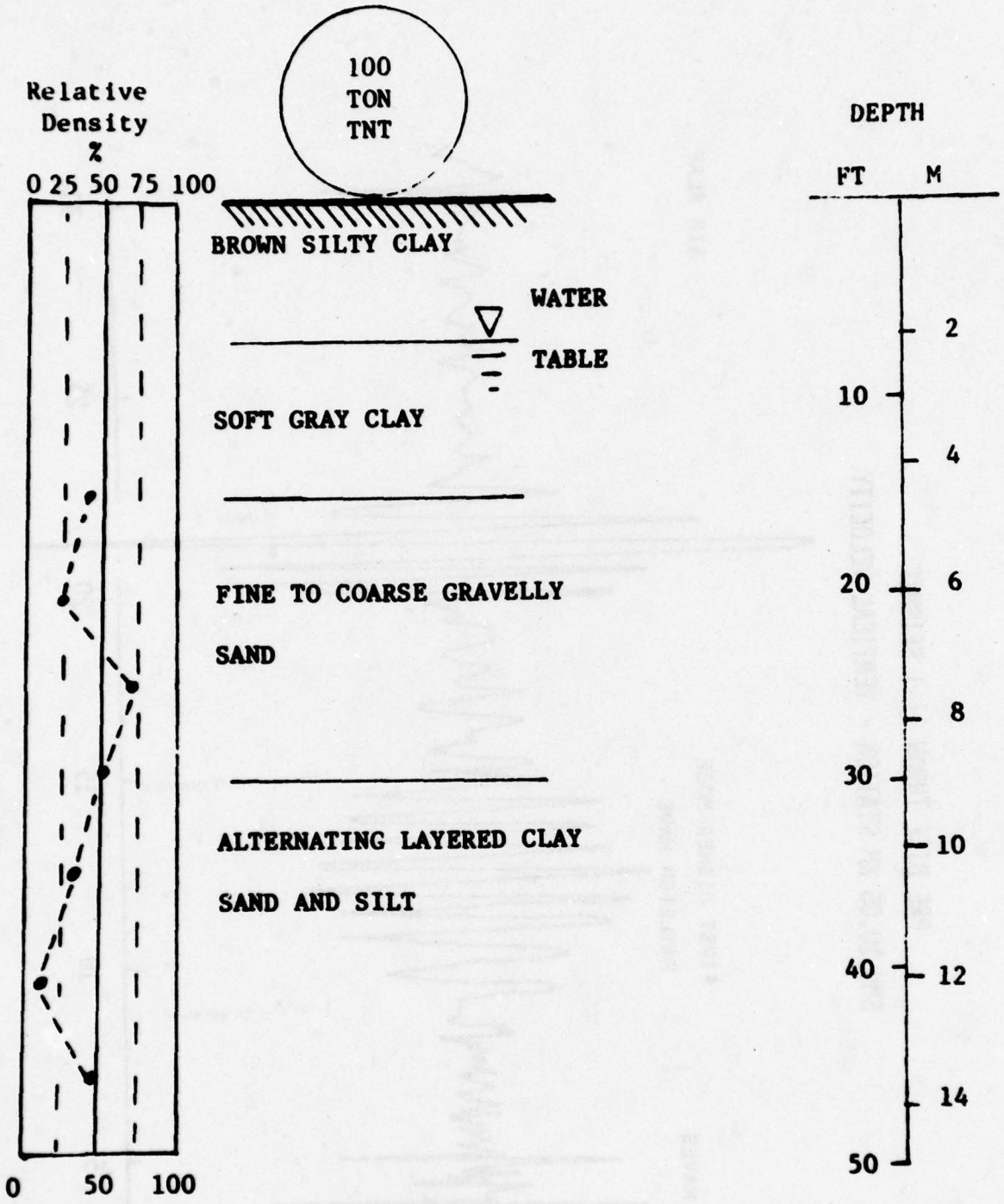


Figure 14. Pre-DICE THROW II Geologic Profile.

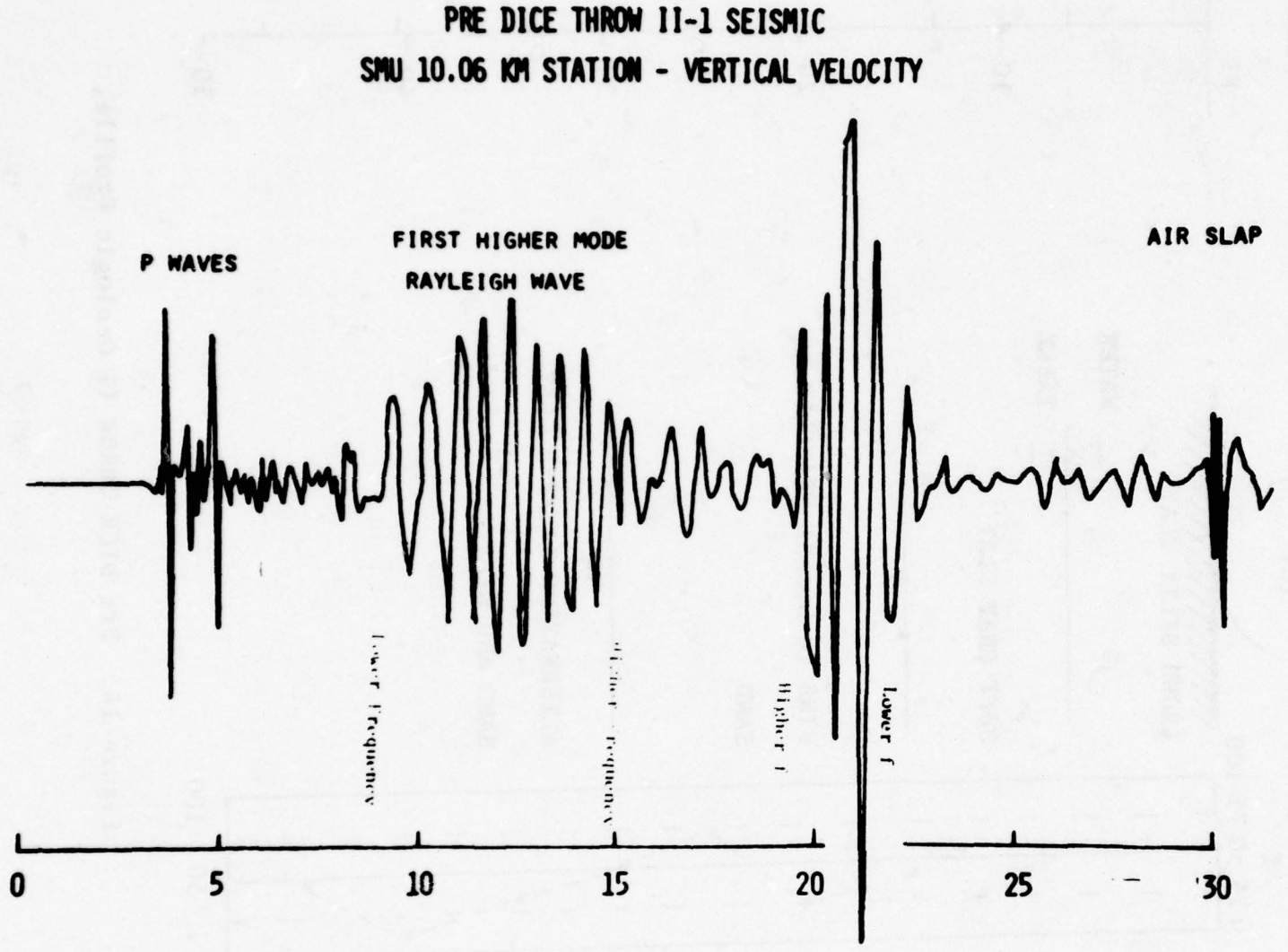
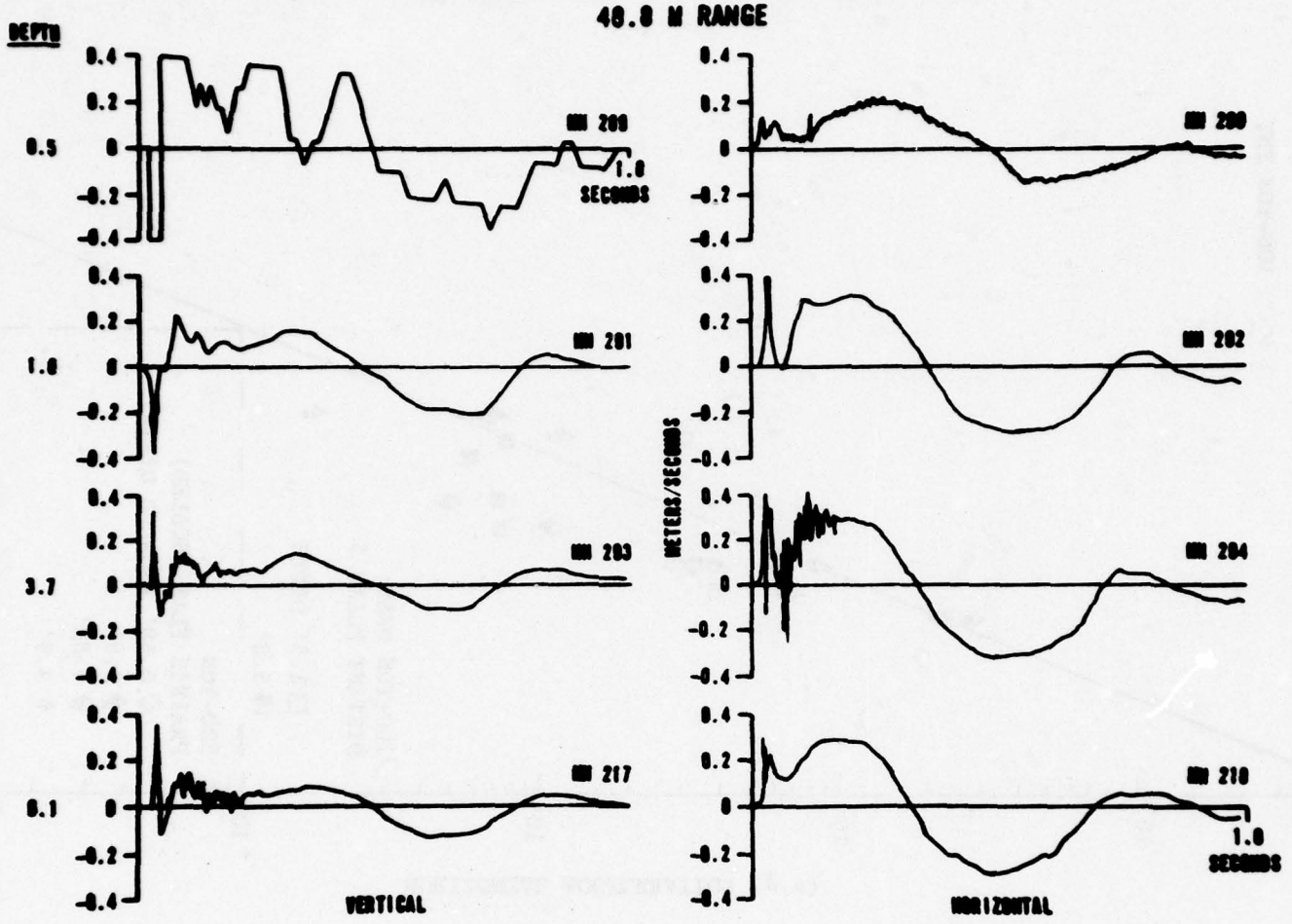


Figure 15. PRE-DICE THROW II Vertical Velocity Plot

Figure 16. PRE DICE THROW II-1 PARTICLE VELOCITIES
40.8 M RANGE



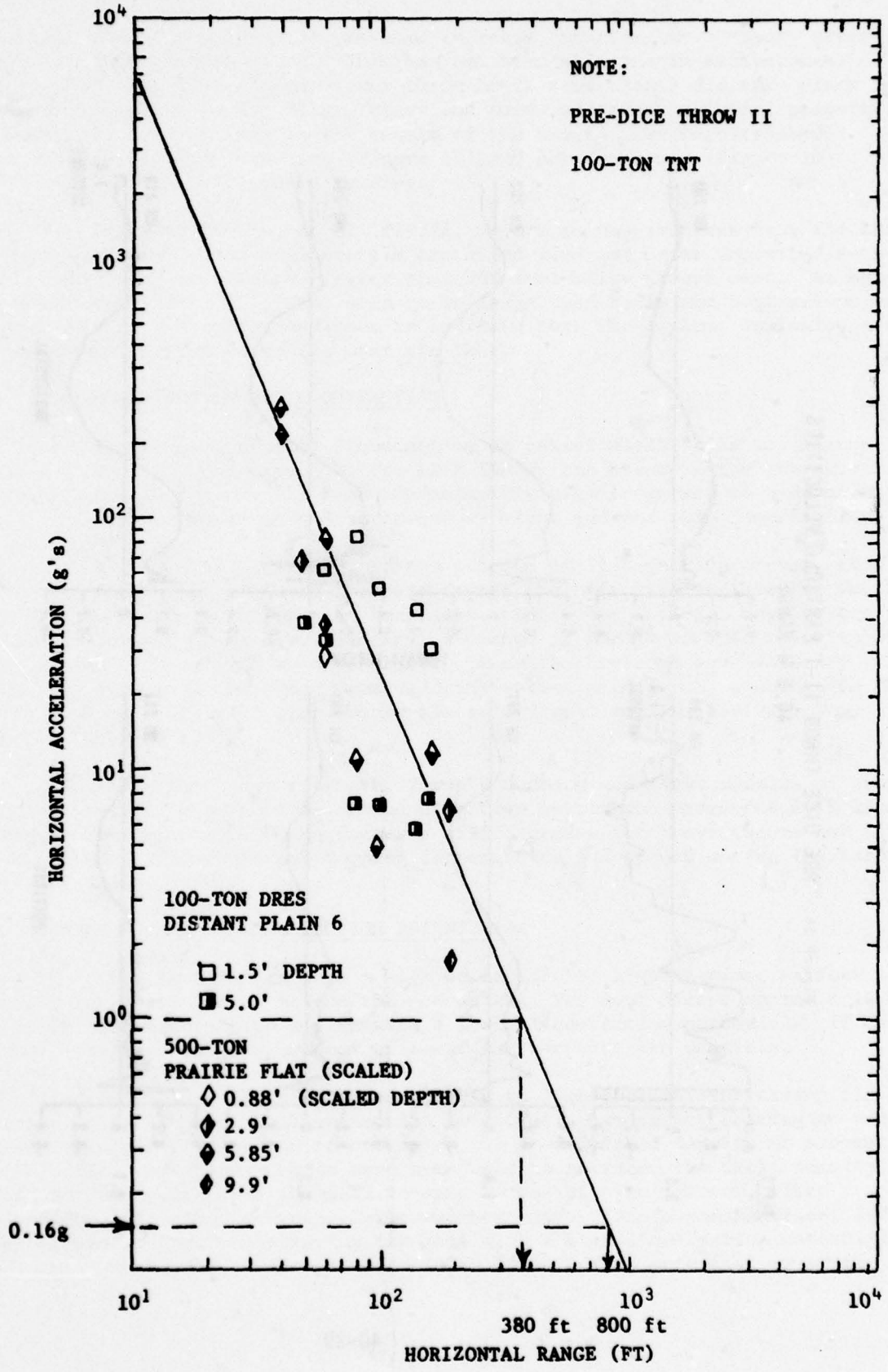


Figure 17. Horizontal Acceleration Versus Horizontal Range, Tangent Above Events

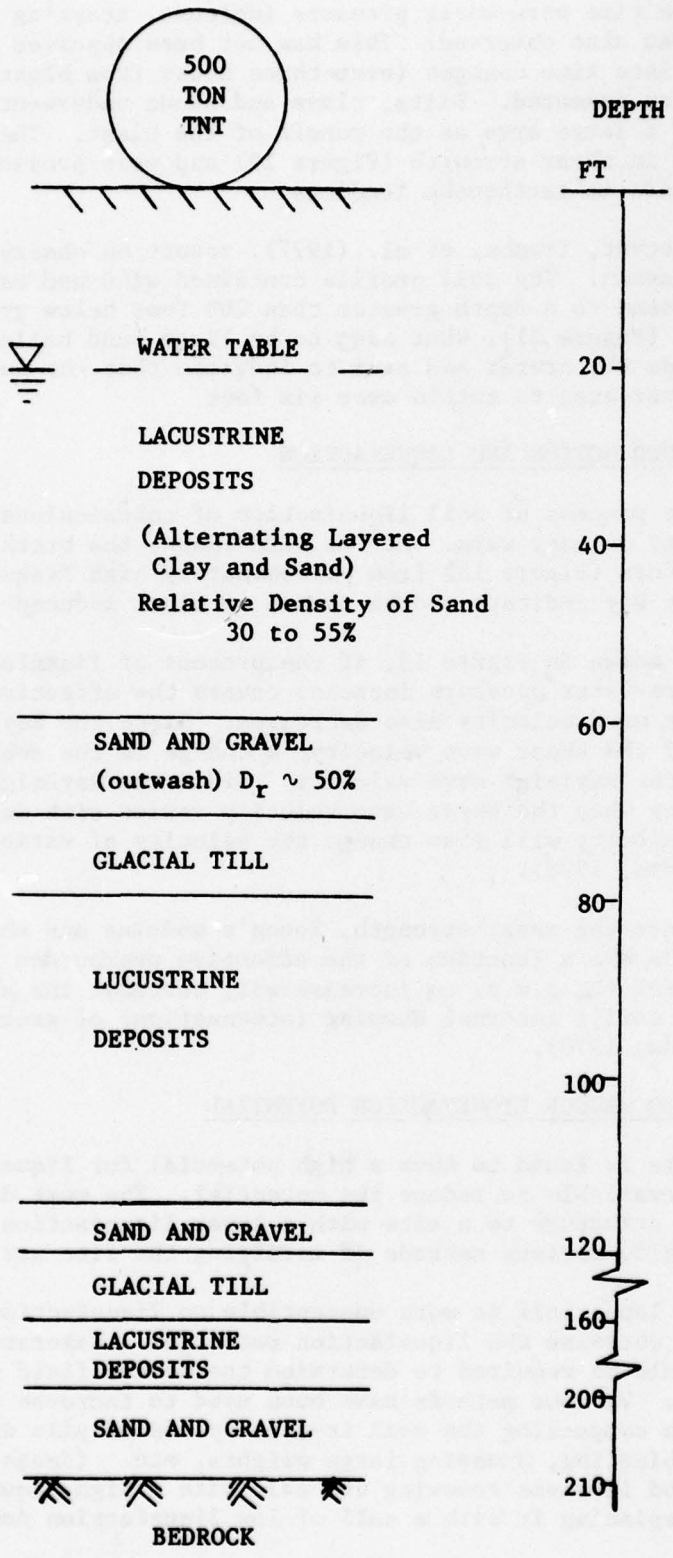


Figure 18. DIAL PACK Geologic Profile.

However, late time pore-water pressure increase, starting at 50 hours after the blast, was also observed. This has not been observed in earthquakes. Substantial late time changes (over three hours from blast) did take place in the parameters measured. Silts, clays and sands underwent material property changes over a large area as the result of the blast. The results showed that changes in shear strength (Figure 19) and pore pressure (Figure 20) followed trends in earthquake loadings.

Ristvet, Tremba, et al. (1977), report on observations from the KOA nuclear explosion. The soil profile contained wind and water deposited saturated coral sand to a depth greater than 200 feet below ground zero. As shown in the photo (Figure 21), what seem to be large sand boils and depressions were formed outside the crater and seem to indicate that the nuclear explosion caused the near-crater area to settle over six feet.

C. GROUND MOTION AND LIQUEFACTION

The process of soil liquefaction of cohesionless soils may change ground motions in many ways. At Pre DICE THROW, the break in the characteristic seismic waveform (Figure 15) from predominately high frequency to predominately low frequency may indicate and be caused by blast induced soil liquefaction.

As shown in Figure 13, if the process of liquefaction occurs, the resulting pore-water pressure increase causes the effective stresses to decrease and the shear wave velocity also decreases. Since the Rayleigh wave velocity is a function of the shear wave velocity, a change in the shear wave velocity will also change the Rayleigh wave velocity. Since the Rayleigh wave velocity varies with frequency when the shear wave velocity varies with depth, a change in the shear wave velocity will also change the velocity of various Rayleigh wave lengths (Dobrin, 1976).

Since the shear strength, Young's modulus and shear modulus of cohesionless soils are a function of the effective overburden pressure, soil liquefaction causing the p.w.p. to increase will decrease the above values and also decrease the soil's internal damping (attenuation) of ground motion (Richard, Hall and Woods, 1970).

V. METHODS TO REDUCE LIQUEFACTION POTENTIAL

If a site is found to have a high potential for liquefaction, various methods are available to reduce the potential. The most direct approach is to relocate the structure to a site with a lower liquefaction potential. If this is not feasible, various methods of modifying the site are possible.

Since a loose soil is more susceptible to liquefaction, increasing its density will decrease the liquefaction potential. Laboratory testing at various densities would be required to determine the needed field density to prevent liquefaction. Various methods have been used to increase the field density. These include compacting the soil in-situ by use of pile drivers, vibrofloatation, blasting, dropping large weights, etc. (Janes and Anderson, 1976). Another method involves removing the soil with a high liquefaction potential and simply replacing it with a soil of low liquefaction potential or putting

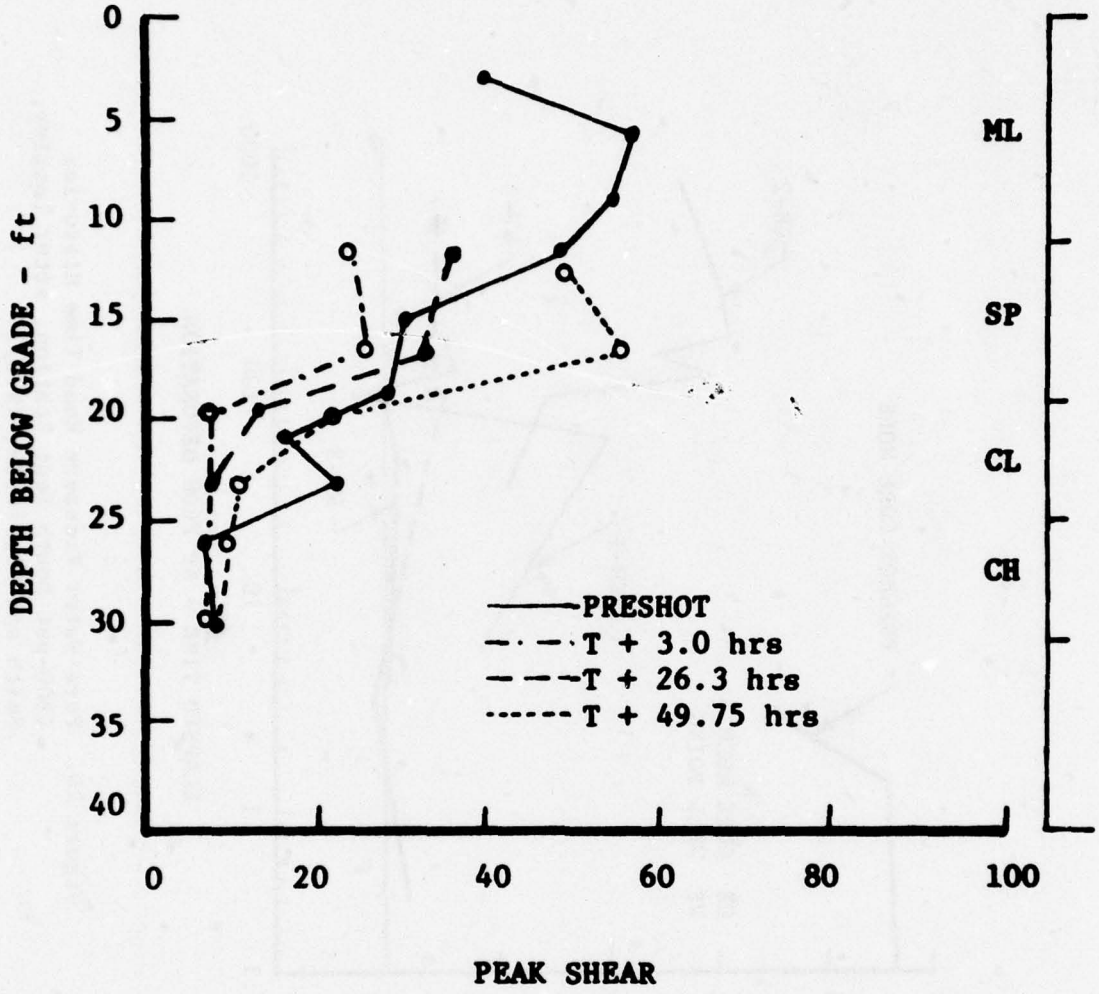


Figure 19. Shear Strength Comparisons (300-psi Location, after Langley, Smith and Pfefferle, 1972).

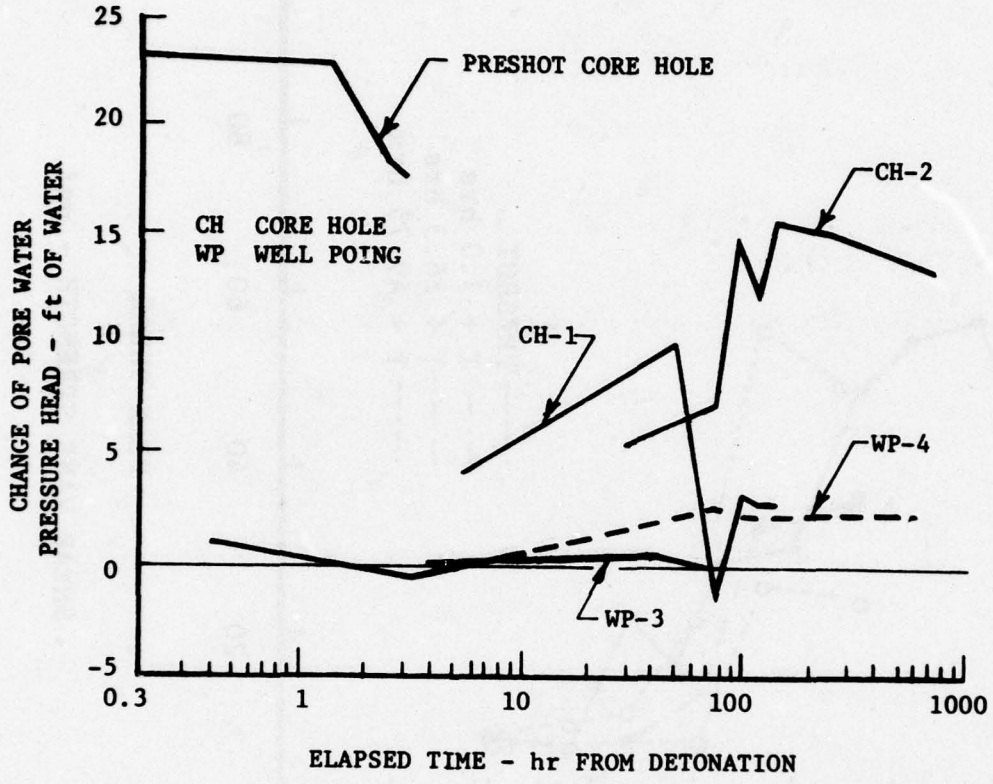


Figure 20. Pore-Water Pressure Head Time Histories (300-psi South Test Station, after Langley, Smith and Pfefferle, 1972).

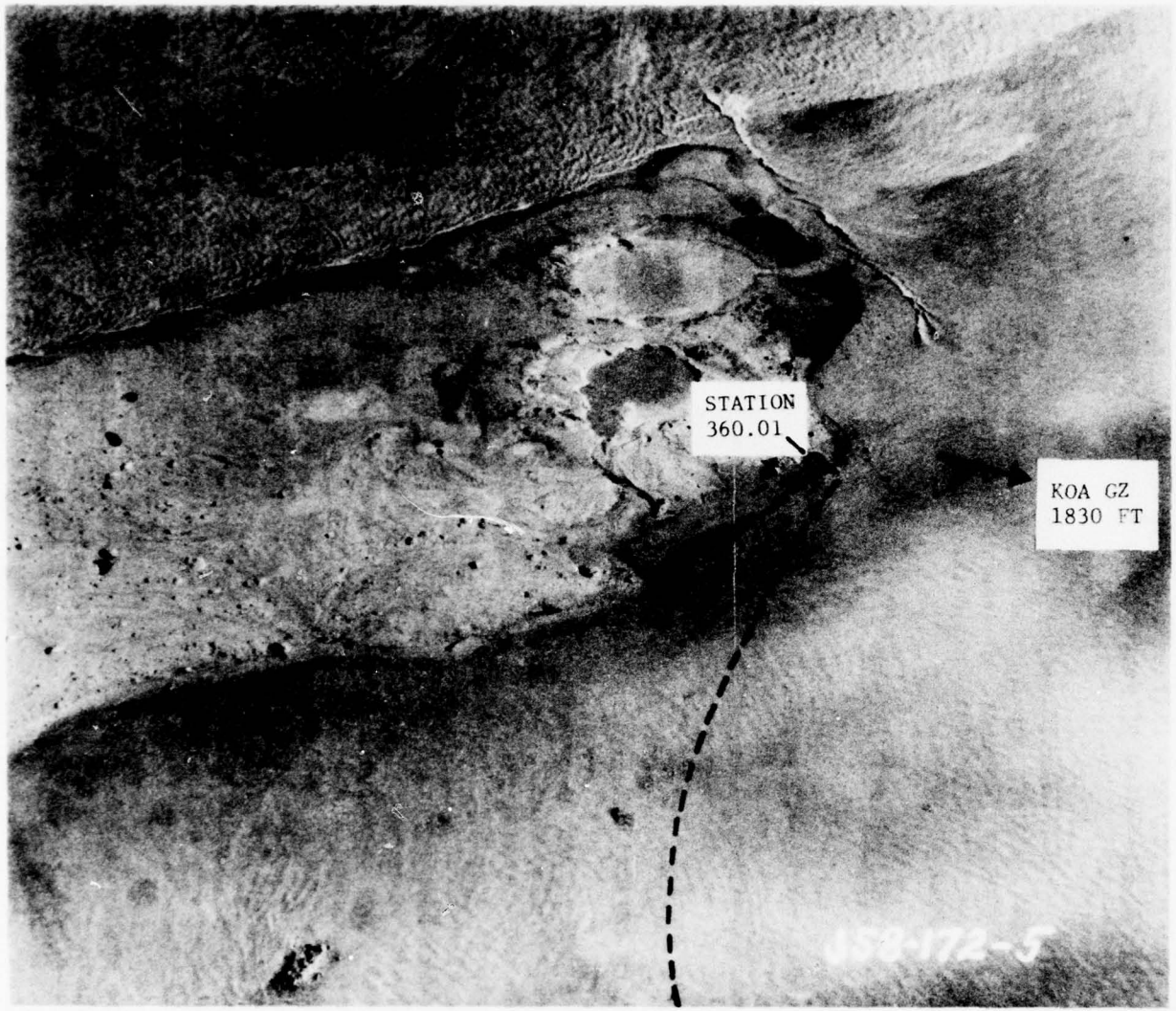


Figure 2J. **Possible Sand Boils and Depressions Which May Indicate Explosion-Induced Liquefaction of the Sand at the KOA Nuclear Explosion, Eniwetok Atoll, 1958.** NOTE: Aerial Post-KOA Detonation, 14 May 1958 (D+1). Station 360.01 sank ~ 6.7 feet. Looking Southwest.

the original soil back in at a higher density.

Modification of the soil by use of chemicals and grouting has also been used. Various methods to increase the effective stress on the soil have been used to decrease the liquefaction potential. These include lowering the ground water level and/or placing a fill over and around the site. Seed and Booker (1977) discuss stabilization of potentially liquefiable sand deposits using gravel drains.

If the soil with a high liquefaction potential is located near the surface, it may be possible to place the foundation at a depth where the soil would not be expected to liquefy. However, the use of long piles to accomplish this requires extensive investigations since the piles may buckle if the soil around them liquefies (Peck, 1977).

VI. CONCLUSIONS AND RECOMMENDATIONS

It has been shown that certain soil types under certain conditions have liquefied under earthquake and blast loadings. Detailed study is needed to determine which soil types and which conditions lead to a high blast-induced liquefaction potential. A detailed research program should be established to conduct theoretical, laboratory and field experiments on various soil types, densities and water levels. This program should include the effects of blasts on soil properties, pore-water pressures and ground motions. Both small scale and major high explosive tests are recommended.

Methods are needed to predict the possibility and extent of blast-induced liquefaction. The possibility of structural foundation failure from soil liquefaction and/or major damage to structures from liquefaction induced landslides should be studied. Relationships for saturated soil between particle velocity or stress changes, soil types, initial relative densities, initial effective overburden stresses vs liquefaction potential or pore-water pressure increase should be studied. Laboratory tests should include dynamic shear, vibration and shock tube tests on various soils. Field test should at least include ground motion, shear strength, relative densities and pore-water pressure measurements at various depths, times and locations. Especially at locations close to ground zero, it is recommended that measurements of the above properties also include data from much greater depths than at DIAL PACK. Future experiments should also include data at earlier times. Shear wave velocity measurements at various depths and locations should be taken pre-blast and continued after the blast.

Studies should be aimed at finding the major factors leading to blast-induced liquefaction. This information would assist in improving prediction techniques critical to the design and assessment of Air Force strategic missile systems.

REFERENCES

1. Casagrande, A., "Characteristics of Cohesionless Soils Affecting the Stability of Slopes and Earth Fills," Journal of the Boston Society of Civil Engineers, January 1936.

2. Clough, R.W., "The Finite Element Method in Structural Mechanics," Stress Analysis, O.C. Zienkiewicz and G.S. Hollister, eds., John Wiley and Sons, Ltd., London, England, 1966.

3. Corps of Engineers, "Report on the Slide of a Portion of the Upstream Face at Fort Peck Dam," Corps of Engineers, US Department of the Army, US Government Printing Office, Washington, D.C., July 1939.

4. Costantino, C.J., Wachowski, A. and Barnwell, U.L., "Finite Element Solution for Wave Propagation in Layered Media Caused by a Nuclear Detonation," Proc. Inter. Sym. on Wave Propagation and Dynamic Properties of Earth Materials, University of New Mexico, August 1967.

5. Davisson, M.T., "Static and Dynamic Behavior of a Playa Silt in 1-D Compassion," AFWL, Kirtland AFB, NM, Tech. Doc. Rep. #RTD TDR-63-3078, September 1963.

6. Desai, C.S., and Abel J.F., "Introduction of the Finite Element Method," Van Nostrand Reinhold Publishing Co., New York, NY, 1972.

7. Dobrin, M.B., Intro. to Geophysical Prospecting, 3rd Ed., McGraw Hill, 1976.

8. Finn, W.D.L., Pickering, D.J. and Bransby, P.L., "Sand Liquefaction in Triaxial and Simple Shear Tests," Journal of the Soil Mechanics and Foundations Division, ASCE, Vol. 97, No. SM4, April 1971.

9. Florin, V.A. and Ivanov, P.L., "Liquefaction of Saturated Sandy Soils," Proc. 5, Int. Conf. Soil Mechanics and Foundation Engineering, Vol. I, 1961.

10. Gibbs, H.J. and Holtz, W.G., "Research on Determining the Density of Sand by Spoon Penetration Test," Proceedings, Fourth International Conference on Soil Mechanics and Foundations Engineering, Vol. 1, 1957.

11. Hadala, P.F., "Effect of Constitutive Properties of Earth Media on Outrunning Ground Shock from Large Explosions," Waterways Experiment Station, TR S-73-6, August 1973.

12. Harkrider, D.G., "Surface Waves in Multilayered Elastic Media, Part II," Bull. Seism. Soc. Am., 60, 1970.

13. Janes, H.W. and Anderson, R.D., "Massive Compaction of Granular Soil - How We Stand," Proc. ASCE Annual Convention and Exposition, Philadelphia, 1976.

14. Japan Natl. Committee on Earthquake Engrg., "Niigata Earthquake of 1964," Proceedings, 3rd World Conf. on Earthquake Engrg., Auckland, New Zealand, January 1965.

15. Kummeneje, D., and Eide, O., "Investigation of Loose Sand Deposits by Blasting," Proc. 5th ICSMFE, Vol. 1, 1961.

16. Ladd, R.S., "Specimen Preparation and Liquefaction of Sands," Journal of the Geotechnical Engineering Division, ASCE, Vol. 100, No. GT10, October 1974.

17. Ladd, R.S., "Specimen Preparation and Cyclic Stability of Sands," Journal of the Geotechnical Engineering Division, ASCE, Vol. 103, No. GT6, June 1977.

18. Langley, N.P., Smith, C.R. and Pfefferle, W., "Dial Pack Event - Soil Pore Pressure and Shear Strength Test," Aerospace Corporation Report No. TOR - 0172 (S2970-20)-1, February 1972.

19. Lee, K.L., and Albaisee, A., "Earthquake Induced Settlements in Saturated Sands," Journal of the Geotechnical Engineering Division, ASCE, Vol. 100, No. GT4, April 1974.

20. Lee, K.L., and Fitton, J.A., "Factors Affecting the Cyclic Loading Strength of Soil," Special Technical Publication No. 450, ASTM, 1969.

21. Lee, K.L. and Seed, H.B., "Cyclic Stresses Causing Liquefaction of Sand," Journal of the Soil Mechanics and Foundations Division, ASCE, Vol. 93, No. SM1, January 1967.

22. Leet, L.D., "Earth Motion from the Atomic Bomb Test," American Scientist, 34, 198-211, 1946.

23. Lyman, A.K.B., "Compaction of Cohesionless Foundation Soils by Explosives," Trans. ASCE, Vol. 107, 1942.

24. Martin, G.R., Finn, W.D.L. and Seed, H.B., "Fundamentals of Liquefaction Under Cyclic Loading," Soil Mechanics Series #23, University of British Columbia, Vancover, Canada, February 1974.

25. Middlebrooks, T.A., "Fort Peck Slide," Transactions, ASCE, Vol. 107, Part 1, 1942.

26. Murphy, J.R., Weaver, N.L. and Lamers, G.B., "An Analysis of the Applicability of Existing Analytic Models for the Description of Observed Seismic Amplification Effects," Environmental Research Corp., Nevada Operations, US Atomic Energy Commission, Contract AT (29-2)-1163, September 1970.

27. Peck, R.B., "Pitfalls of Overconservation in Geotechnical Engineering," Civil Engineering - ASCE, February 1977.

28. Reinke, R.R., "Ground Motion Study of Pre DICE THROW," Ph.D. Thesis, Southern Methodist University, 1977 (in prep.).

29. Perry, E.B., "Movement of Variable - Density Inclusions in Wet Sand Under Blast Loading," US Army Engineer Waterways Experiment Station, Misc. Paper S-72-37, September 1972.

30. Ristvet, B.L., Tremba, E.L., et al., "Geologic and Geophysical Investigations of the Eniwetok Nuclear Craters," AFWL, Kirtland AFB, NM, Tech. Rep. No. AFWL-TR-77-XXX, 1977 (in prep.).

31. Prugh, B.J., "Densification of Soils by Explosive Vibration," J. Constr. Div. Proc. ASCE, Vol. 89, No. CO1, 1963.

32. Puchkov, S.V., "Correlation Between the Velocity of Seismic Oscillations of Particles and the Liquefaction Phenomenon of Water-Saturated Sand," Issue No. 6 of Problems of Engineering Seismology, Study No. 21, 1962.

33. Ross, G.A., Seed, H.B. and Migliaccio, R.R., "Bridge Foundations in Alaska Earthquake," Journal of the Soil Mechanics and Foundations Division, ASCE, Vol. 95, No. SM4, July 1969.

34. Schnabel, P.B., Lysmer, J. and Seed, H.B., "SHAKE: A Computer Program for Earthquake Response Analysis of Horizontally Layered Sites," Report No. EERC 72-12, Earthquake Engineering Research Center, University of California, Berkeley, California, 1972.

35. Seed, H.B., "Landslides During Earthquakes Due to Soil Liquefaction," Terzaghi Lecture, presented at the May 8-12, 1967, ASCE National Meeting on Structural Engineering, held at Seattle, Washington; Reprinted in Terzaghi Lectures, 1963-1972, ASCE, 1974.

36. Seed, H.B. and Booker, J.R., "Stabilization of Potentially Liquefiable Sand Deposits Using Gravel Drains," Journal of the Geotechnical Engineering Division, ASCE, Vol. 103, No. GT7, July 1977.

37. Seed, H.B. and Idriss, I.M., "Analysis of Soil Liquefaction: Niigata Earthquake," Journal of the Soil Mechanics and Foundations Division, ASCE, Vol. 93, No. SM3, May 1967.

38. Seed, H.B. and Idriss, I.M., "Simplified Procedure for Evaluating Soil Liquefaction Potential," Journal of the Soil Mechanics and Foundations Division, ASCE, Vol. 97, No. SM9, September 1971.

39. Seed, H.B. and Lee, K.L., "Liquefaction of Saturated Sands During Cyclic Loading, "Journal of the Soil Mechanics and Foundation Division, ASCE, Vol. 92, No. SM6, November 1966.

40. Seed, H.B., Martin, P.P. and Lysmer, J., "Pore-Water Pressure Changes During Soil Liquefaction," Journal of the Geotechnical Engineering Division, ASCE, Vol. 102, No. GT4, April 1976.

41. Seed, H.B., Peacock, W.H., "Sand Liquefaction Under Cyclic Loading Simple Shear Conditions," Journal of the Soil Mechanics and Foundations Division, ASCE, May 1968.

42. Seed, H.B. and Peacock, W.H., "Applicability of Laboratory Test Procedures for Measuring Soil Liquefaction Characteristics Under Cyclic Loading," Earthquake Engineering Research Center, Report No. EERC 70-8, November 1970.

43. Seed, H.B. and Peacock, W.H., "Procedures for Measuring Soil Liquefaction Characteristics," Journal of the Soil Mechanics and Foundations Division, ASCE, Vol. 97, No. SM8, August 1971.

44. Sowers, G.B. and Sowers, G.F., Introductory Soil Mechanics and Foundations, 3rd Ed, MacMillian, New York, 1970.

45. Taylor, D.W. and Whitman, R.V., The Behavior of Soils Under Dynamic Loadings - 3, Final Report on Lab Studies, Aug., MIT, Dept. Civil Eng. Soil Mechanics Lab, 1954.

46. Terzaghi, K. and Peck, R.B., Soil Mechanics in Engineering Practice, 2nd Ed, John Wiley and Sons, New York, 1967.

47. Waterways Experiment Station (WES), "Investigation of the Liquefaction Potential at the W.G. Huxtable Pumping Plant Site," US Army Engineer Waterways Experiment Station, NTIS No. AD-A025497, April 1976.

48. Yoshimi, Y., "An Experimental Study of Liquefaction of Saturated Soils," Japanese Society of Soil Mechanics and Foundation Engineering, Vol VII, No. 2, March 1967.

49. Melzer, L.S., "DICE THROW Seismic Measurements," Vol 2 of the proc. of the DICE THROW Symposium, Defense Nuclear Agency, June 1977.

APPENDIX A

RESULTS OF TESTS ON NIIGATA, JAPAN, SAND

Seed and Idriss (1967)

1. "At a relative density of 40 percent and under an initial effective confining pressure of 2,000 psf, the cyclic shear stress, τ_N, inducing liquefaction in different number of stress cycles, N is as follows:

   $N = 1 \qquad \tau_1 = 600$ psf

   $N = 10 \qquad \tau_{10} = 400$ psf

   $N = 100 \qquad \tau_{100} = 260$ psf

2. "Other factors being the same, the cyclic stress required to induce liquefaction is directly proportional to the initial effective confining pressure.

3. "Other factors being the same, the cyclic stress required to induce liquefaction is directly proportional to the relative density of the sand."

From the above, for a given sand under an effective overburden pressure of $\bar{\sigma}_o$, and having an initial relative density of D_r percent, the cyclic stress, N, required to cause liquefaction in N cycles will be:

$$\tau_N = A_N (\bar{\sigma}_o \times D_r) \qquad \text{EQ (A-1)}$$

where

A = constant, dependent on soil type and found from laboratory dynamic triaxial tests.

Applying the results above to the sand under an initial relative density of D_r percent, an effective overburden pressure of $\bar{\sigma}_o$, the cyclic shear stress, τ_{10}, required to cause liquefaction in 10 cycles will be:

$$\tau_{10} = 400 \text{ psf} = A_{10} (2{,}000 \text{ psf} \times 40)$$

$$A_{10} = \frac{400}{2{,}000 \times 40} = 0.005$$

for $\bar{\sigma} = 330$ psf and $D = 45\%$

$$\tau_{10} = 0.005 (330 \times 45)$$

$$= 75 \text{ psf}$$

For the soil condition shown in Figure A-2 and Table A-1, values of uniform

cyclic shear stress causing liquefaction in N cycles, τ_N, computed by Equation A-1 and listed in Table A-2, are plotted on Figure A-2.

TABLE A-1.--RELATIVE DENSITY OF SAND IN HEAVY DAMAGE AREA
NIIGATA EARTHQUAKE, June 1964.
(after Seed and Idriss, 1967)

Depth, in feet	Effective Overburden Pressure, in pounds per square foot	Penetration Resistance, in blows per foot	Relative Density, as a percentage		
			Terzaghi and Peck	Gibbs and Holtz	Average
0	0	6	25	65	45
10	680	7	27	60	44
20	1180	7	27	52	39
30	1680	12	40	61	50
40	2180	25	58	80	69
50	2680	32	68	82	75
60	3180	39	74	86	80
70	3680	43	79	86	83

TABLE A-2.--CYCLIC SHEAR STRESSES NEEDED TO CAUSE LIQUEFACTION
IN THE HEAVY DAMAGE AREA

Depth, in feet	Effective Overburden Pressure, in pounds per square foot	Relative Density, as a percentage	Cyclic Shear Stress Required to Cause Liquefaction in N Cycles, in pounds per square foot		
			N = 1	N = 10	N = 100
3	330	45	110	75	50
10	680	44	220	150	100
20	1,180	39	350	231	150
30	1,680	50	630	420	270
40	2,180	69	1,130	750	490
50	2,680	75	1,510	1,000	650
60	3,180	80	1,910	1,270	830
70	3,680	83	2,290	1,520	990

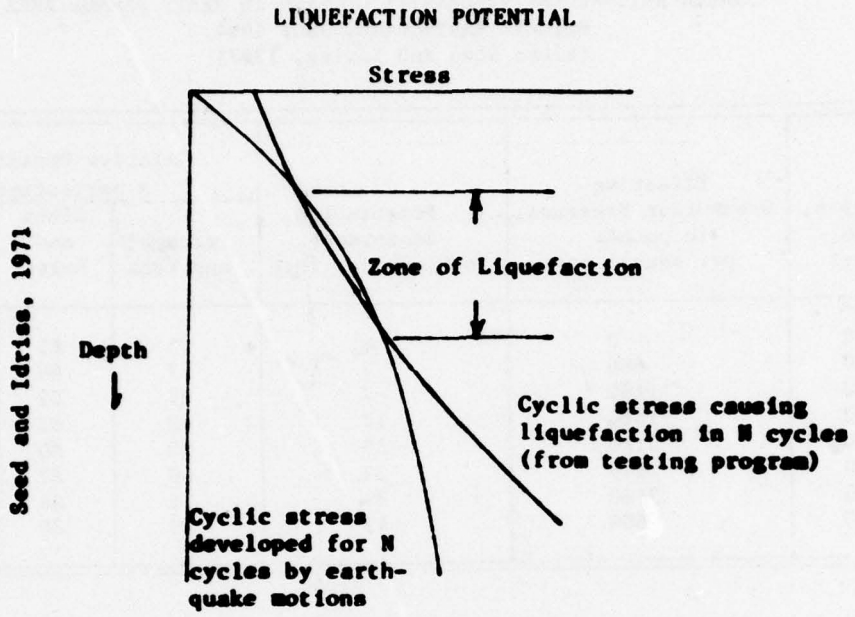


Figure A-1. Method of Evaluating Liquefaction Potential

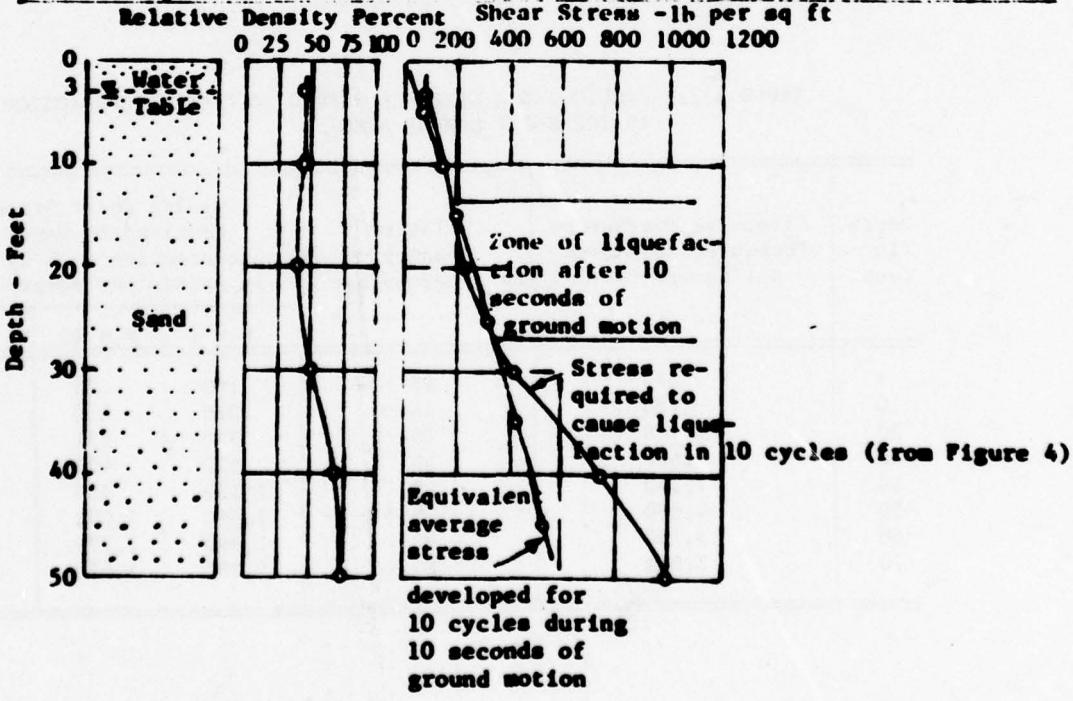


Figure A-2. Analysis of Liquefaction Potential--Heavy Damage Zone--Niigata Earthquake, June 1964 (after Seed and Idriss, 1967).

APPENDIX B

DETERMINING FIELD RELATIVE DENSITIES

Ideally, field densities are determined by measuring the density in place by recovering undisturbed samples. However, due to sampling problems below the ground water table, the field relative densities are usually determined from the Standard Penetration Test (SPT). First introduced in 1902 by Col Charles R. Gow, the SPT has become a widely accepted method to sample soils. The SPT consists of measuring, in terms of blows per foot, the resistance of the soil to the penetration of a standard split spoon driven by the free-fall of a 140-pound weight dropped 30 inches. Various empirical relationships to convert the number of blows per foot to relative density (D_r) have been proposed. Terzaghi and Peck (1967) suggested the relationship shown in Figure B-1. Gibbs and Holtz (1957) proposed that the relationship is also depending on the effective overburden pressure at the depth of the test as shown in Figure B-2. A field study of the applicability of these correlations indicates that the field relative densities fall somewhere between the two (Gibbs and Holtz, 1957). It has generally been established that the SPT has fairly reliable application to granular, noncohesive soils (i.e., sands), provided careful field testing procedures are followed and the above relationships are used. If maximum and minimum densities are determined in the laboratory from disturbed samples recovered from the SPT split spoon sampler, the relative density can be converted to approximate field dry unit weights using the relationship:

$$D_r = \frac{e_{max} - e_f}{e_{max} - e_{min}} (100) = \frac{(\gamma_{max})}{\gamma_f} \frac{(\gamma_f - \gamma_{min})}{(\gamma_{max} - \gamma_{min})} (100) \qquad \text{EQ (2)}$$

D_r = 0% for soil in its loosest state.

D_r = 100% for soil in its densest state.

e_{max} = void ratio of soil in loosest state.

e_{min} = void ratio of soil in densest state.

e_f = void ratio of soil in the field.

γ_{max} = dry unit weight of soil in densest state.

γ_{min} = dry unit weight of soil in loosest state.

γ_f = field dry unit weight.

Relative Density of Sand		
Penetration Resistance N (blows/ft)	Relative Density	D_r %
0-4	Very loose	0-50
4-10	Loose	0-50
10-30	Medium	50-70
30-50	Dense	70-90
> 50	Very dense	90-100

Figure B-1. Terzaghi and Peck (1967) and Sowers and Sowers (1970) Relationships Between Standard Penetration Resistance and Relative Density.

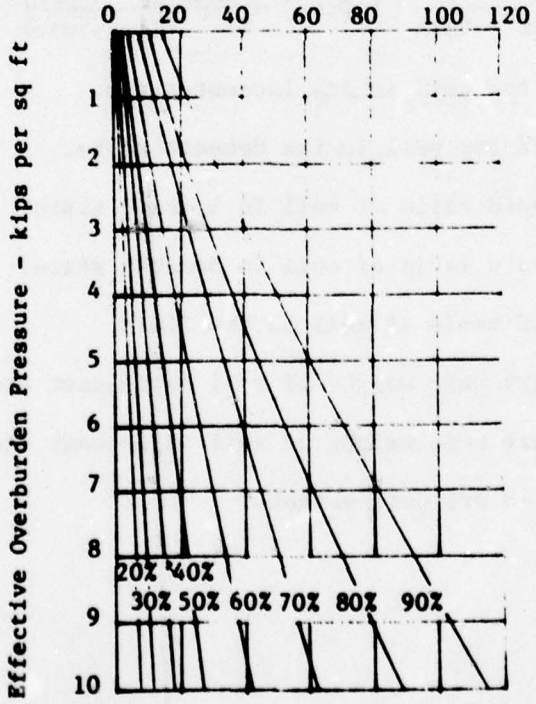


Figure B-2. Relationship Between Standard Penetration Resistance, Relative Density and Effective Overburden Pressure (after Gibbs and Holtz, 1957).

1977 USAF-ASEE SUMMER FACULTY RESEARCH PROGRAM
sponsored by
THE AIR FORCE OFFICE SCIENTIFIC RESEARCH
conducted by
AUBURN UNIVERSITY AND OHIO STATE UNIVERSITY

PARTICIPANT'S FINAL REPORT

DOUBLE RESONANCE APPARATUS FOR RELAXATION STUDIES OF HF IN HIGH VIBRATIONAL STATES

Prepared by:	Richard L. Redington, PhD
Academic Rank:	Professor
Department and University:	Department of Chemistry Texas Tech University
Assignment:	
(Air Force Base)	Kirtland Air Force Base
(Laboratory)	Air Force Weapons Laboratory
(Division)	Advanced Laser Technology Division
(Branch)	Chemical Laser Branch
USAF Research Colleague:	Leroy Wilson, PhD
Date:	August 19, 1977
Contract Number:	F44620-75-C-0031

DOUBLE RESONANCE APPARATUS FOR RELAXATION STUDIES OF HF IN HIGH VIBRATIONAL STATES

by

Richard L. Redington

ABSTRACT

Computational models of HF chemical laser systems require knowledge of the rate constants for collisional energy transfers by HF in highly excited vibrational states as input data. Likewise, a knowledge of line profiles for excited state transitions is essential for accurate theoretical analysis. In this report the status of an experimental program intended to obtain information for highly excited states of HF and DF using double resonance techniques is described. The pump light pulse is provided by a dye laser and the cw probe beam by a diode laser. The diode laser has been used to measure line profiles of the R(6) and R(10) lines of the fundamental vibration of DF. Pressure broadening by N_2, O_2, H_2, D_2, Ar, He, and SF_6 was observed.

ACKNOWLEDGEMENT

I am grateful to USAF/ASEE for the award of a summer faculty research fellowship and to Fred O'Brien for his concern and thoughtfulness in administering the summer program. I wish to express appreciation to my research colleagues Leroy Wilson and Bill Heath, and to Steve Davis, Ben Gross, Colin Hackett, Nick Pchelkin, and particularly, to Don Vonderhaar for helpfulness extended on various occasions during the summer.

INTRODUCTION

Calculations intended to describe laser action by HF or other laser systems are based on differential equations describing the time dependence of the populations of the various molecular energy levels. These interconnected rate equations are made as comprehensive as possible after considering the feasibility for solving them and the availability of experimental input information. Complete treatments require input information for radiative and nonradiative (e.g. collisional) energy transfer processes. The relative energy level positions for all states of interest for HF and DF are well known but only a few rate constants for collisional energy transfers involving highly excited vibrational states have been measured and there is no experimental data concerning line profiles or absorption coefficients for transitions arising from highly excited states. It is experimentally very difficult to study high energy states because of their normally low populations and rapid relaxation rates, however, the results of both computations and experiments point out the necessity for obtaining comprehensive knowledge of the properties of these states for the HF and DF molecules. The significance of the breakdown of initially assumed simplifications is presently becoming apparent. For example, the computed laser performance changes markedly when different line profiles are used for different excited state transitions[1]. As a second example, assuming harmonic oscillator behavior for vibration-to-translation energy transfer leads to contradictory interpretations for the various types of relaxation data that are available and to much smaller V-T transfer rates than are suggested by the data when the harmonic oscillator requirement is relaxed.[2] The present research is concerned with experimental methods for measuring the energy relaxation rates of highly excited HF and DF molecules.

OBJECTIVES

The original summer research objective was to measure a set of relaxation rate constants for HF vapor using a double resonance

apparatus. However, upon arrival in the laboratory and assessment of the project, which was in a "standby" mode in June, the research objective had to be changed. Major equipment was at hand but some items essential to performing double resonance experiments were unavailable, as it has turned out, for the entire summer fellowship period. Therefore, the research objectives have been to assemble and to test the system insofar as allowable by time and equipment limitations, to use the equipment to obtain alternative original research data (pressure broadened DF lines), and to become generally familiar with the research being performed on HF/DF laser systems for possible use in future work.

THE DOUBLE RESONANCE EXPERIMENT

Computational models for several HF chemical laser systems are discussed by Hough[1], Emanuel[3], Pummer[4], Hall[5], and authors that they cite. The equation for optical gain between two energy levels, which determines whether lasing action can occur, is based on the population densities of the two states and on the profile of the optical transition that connects them. The line profile is needed to take into account effects that broaden the transition, such as molecular translations and intermolecular collisions. The equation for the population of any energy level contains terms for population shifts into and out of the level arising from spontaneous and induced radiative transitions and from intermolecular collisions. The collisional processes are generally described using linear rate coefficients to couple every pair of energy states. Many of these coefficients must be assumed to be zero for lack of another value.

It is clear from the laser gain equations that careful spectroscopic experiments provide the data required for the computational investigations of chemical lasers. The energy levels and transition frequencies for all states of interest for HF and DF are accurately known[6-11], therefore,

the necessary research is based on accurate intensity measurements. When energy level populations are changing the time dependence of the absorption or emission measurements is related to the relaxation rate constants. Intensities measured as a function of wavelength across the band or line yields the line profile. Relaxation rates[12-23] and band profiles[24-30] have been reported for the lowest vibrational states of HF but few[18-20] measurements involving the states with $v \geq 3$ have been performed. It is possible to study these properties using double resonance techniques, whereby two transitions are simultaneously tuned by lasers of the experimental apparatus. Double resonance methods are well established[31-33], however, only two groups report results of energy relaxation measurements on HF using this technique[21-23].

The basic experiment is shown in the energy level diagram of Figure 1. The v = 0 energy levels of HF are normally the only thermally populated levels and an intense laser pulse, the pump, is used to excite molecules from a ground vibrational level $E_{0,J}$ to an excited vibrational energy level $E_{v',J'}$. The second laser provides a weak cw "probe" beam to monitor the population of level $E_{v',J'}$. The probe laser is tuned to resonance with an allowed transition originating from level $E_{v',J''}$, and its intensity is monitored as a function of time. The population of state $E_{v',J'}$ changes because of collisional and radiant energy transfers. The collisional energy transfers populate adjacent high energy states $E_{v'',J''}$ and the population of these states are also monitored in separate experiments using the weak cw probe laser. It may be experimentally difficult to tune the pump and probe laser beams to the two transition frequencies being examined if both laser line widths are very narrow because a narrow pulse beam will vibrationally excite only those molecules under the Doppler profile of the molecular absorption line that are in resonance with the narrow pulse. Exactly these same molecules must be in resonance with the probe beam and jitter of either pump or probe laser can result in failure of the experiment. Previous double resonance experiments[21-23] on HF circumvented the frequency matching problem by using HF lasers as pump and probe. The present

experiment uses a high intensity dye laser as the pump and a low intensity semiconductor diode laser as the probe. Both of these lasers are tunable, but even after line narrowing of the dye laser, its bandwidth will be wider than the HF absorption lines and therefore all velocity components contributing to the HF absorption line will be excited. The diode laser has a linewidth far narrower than the Doppler profile of any HF line and therefore it probes only a small fraction of the excited molecules. It is sometimes difficult to locate stable absorption lines arising from ground state transitions using the diode laser spectrometer and a major problem of the present research is to tune the diode laser probe beam to the weak, transient lines that arise from the high vibrational excitations. This problem is discussed below.

In addition to laser linewidths, the temporal behavior of the pump pulse is important in the double resonance epxeriments. The probe laser should be cw (continuous wave), at least over the duration of the relaxation phenomena of interest. The pump laser pulse should ideally be of subnanosecond or picosecond duration, much shorter than the relaxation phenomena of interest. In fact, however, the present dye laser pulse has a rise time of about 100 nsec and an overall duration of about 350 nsec. This long falloff or tail creates a problem because the rotational relaxation process of HF occur on a timescale only slightly longer than this for the low vibrational states[21-23], and therefore the rotational relaxation is already in progress during the lifetime of the pump laser pulse. The pump pulse duration can be shortened with the help of an electro-optic crystal used as a shutter.

Conceptually the double resonance experiment is very simple and the rise and decay of population in each excited state energy level can be cataloged as phenomenological data. However, extraction of the desired state-to-state relaxation rate constants is a complex matter, particularly for high vibrational excitations, because of the

many simultaneous processes that enter into the relaxation behavior of each energy level. The defining rate equations are strongly coupled and more attention must be given to the process of extracting rate constants from the observed kinetic data. One approach used by Javan and his colleagues[19] for the study of vibrational relaxation in high vibrational states of HF required the simultaneous excitation (i.e. laser pumping) of each vibrational state below the one of interest in order to mimic a high temperature Boltzmann distribution. Even after this approach to uncouple the kinetic equations, approximations had to be made in order to extract rate constants. The first step in the present project is simply to demonstrate the feasibility of the apparatus for use in double resonance experiments; the second step should be to consider means to uncouple the kinetic equations arising in the high energy states. These methods might involve simultaneous pumping of several levels as performed by Javan et al., shortening the timescales involved to subnanosecond duration, using well defined molecular beam samples, or other experimental ploys designed to limit the number of molecular energy states that can contribute to the observed experimental results.

Semiconductor diode lasers have a very narrow linewidth and are useful for the study of absorption line profiles[34,35]. It is intended that the probe laser be tuned to a single frequency for the double resonance kinetic measurements, but it may also be possible to obtain the desired excited state line profiles by a rapid scanning of the diode laser frequency across the absorption line. This possibility has recently been demonstrated for the case of carbon monoxide excited in a shock tube[36]. The short lifetimes of vibrationally excited HF will require a slightly more rapid sweep rate of the diode laser than was used for CO, or else a longer pump pulse of uniform intensity in order to create a sufficiently long "steady state" condition.

THE DOUBLE RESONANCE APPARATUS

The block diagram of the apparatus is given in Figure 2. The pump laser (A) is a Phase-R Model DL-1100 coaxial-flashlamp excited dye laser. The suitability of this laser as a pump for the present experiments must be evaluated in terms of its pulse energy and its pulse bandwidth, duration and shape, tunability, and reproducibility.

The company specifications for the laser with fresh rhodamine 6G dye are for an output energy of 0.25 J/pulse. This value is for flat mirrors with no added optical components. As a starting point, it is 5000 times larger than the HF pulses used in reference 23 to pump the harmonic oscillator allowed fundamental of HF. In addition to the reduced molecular absorption coefficients for transitions with $\Delta v = 4$ or 5 and the reduced energy provided by most other dyes, this factor of 5000 is reduced by adding the necessary line narrowing and pulse shaping optical components to the laser cavity. The pulse energy cannot be measured at present because there is no meter (e.g. a Scientech Pulse Calorimeter) available in the laboratory, but poor energies were observed because of dye deterioration. Stored dyes should be refrigerated and the circulator for the lasing dye solution should be provided with a cooler to lower the dye temperature to at least 20° C.

The laser line can be narrowed to approximately 2 Å using two intracavity prisms that are presently available. However, narrow linewidths cannot be measured without a Fabry-Perot interferometer[37]. The nominal 2 Å bandwidth corresponds to about 6 cm^{-1} (using 6000 Å as a reference point) compared with an HF line width of about 0.02 cm^{-1}. It is clear that most of the laser pulse energy will bypass the HF molecule unless the laser line is narrowed much further. A balance must therefore be sought between the pulse energy lost through narrowing the

laser line to more nearly match the HF absorption line and energy lost because it bypasses the HF molecule. This optimisation study was not possible now because of a lack of equipment.

The dye laser linewidth can be narrowed to a few hundredths of a wavenumber with the help of a Lyot filter[38,39]. A Lyot filter was purchased with the laser (although it had to be returned to the company for repair and still needs a final crystal polishing and, moreover, cannot presently be used efficiently because the accompanying polarizer is too small and should be replaced). Alternatively, laser lines narrower than 2 Å can be obtained by introducing additional intracavity prisms[40]. The Lyot filter, a birefringent crystal, can be used for one of two purposes: line narrowing or as an electro-optic shutter to shape the output laser pulse. At present, it is felt that the line narrowing application will be the more important. It is possible to obtain extra-cavity electro-optic shutters triggered by the dye laser.

The experience obtained using this dye laser, unfortunately with deteriorated dyes, plus considerations such as those above and general reading, suggest that tuning the laser to the HF frequenty will be easy but that the energy and the pulse reproducibility may turn out to be inadequate. The pulse duration is somewhat longer than desirable considering the HF rotational relaxation times expected for the excited states[21-23], and energy is lost in shortening or chopping the pulse. This generally pessimistic view of the pumping efficiency should be experimentally tested by initially probing transitions from the ground state of the sample molecules, rather than those from excited states. This is because there is no difficulty in tuning the probe laser to ground state lines and a population decrease in ground state levels due to successful pumping should be easily detected. This is probably the best way to optimize tuning of the pump laser to the desired molecular transition.

Returning to Figure 2, the pump laser beam is transferred to the sample cell (B) via a sapphire based beam splitter that will reflect most of the visible pump pulse and transmit the near infrared probe beam. This beam splitter is not yet available in the laboratory but is on order from Valtec Corporation. The beamsplitter is needed in order to make the pump and probe beams collinear, a necessity when rapid relaxation processes are to be studied.

The sample cell (B) is a Wilks Scientific Corporation 40 meter multiple reflection (White) cell. It has gold coated mirrors, nickle interior plating, and CaF_2 window-lenses. It is found that DF disappears rapidly (in minutes) in the cell in spite of its intended inertness to HF and DF, although after the initial "conditioning" exposures to DF it is possible to observe R(6) of DF in the cell at a 10.5 meter pathlength for several hours. Of course, part of the DF disappearance must be due to hydrogen-deuterium exchange with the cell walls. The optical quality of the cell diminished after the initial introductions of DF. It has become difficult to obtain pathlengths longer than about 20 meters whereas the 40.5 meter path was easily obtained originally. The present experience using DF with this cell parallels that reported in the literature for HF. It will be necessary to use a flow system in order to control and to have accurate knowledge of the pressures of HF or DF in the cell.

The pumping laser pulses are reflected off a second beam splitter when they leave the absorption cell and they can be passed, if desired, into a spectrograph, interferometer, or pulse energy calorimeter for analysis. Of these instruments, the spectrograph is the only one presently available.

The probe laser beam is generated by a semiconductor diode laser. This is mounted on the cold head of a low temperature, closed cycle

helium refrigerator and forms the source unit of the Laser Analytics Model LS-3 diode laser spectrometer (D). The laser beam, one inch in diameter, is passed through the sapphire based beam splitter into the sample absoprtion cell. After transmitting the absorption cell the beam re-enters the spectrometer and is ultimately detected by an InSb photovoltaic detector manufactured by the Santa Barbara Research Center. The detector is cooled with liquid nitrogen and its preamplified signal is displayed in a Tektronix Model 7904 oscilloscope. The response time of the detector is not given and this should be measured to verify that it is fast enough for the rotational relaxation studies. The response time of the Au:Ge detector used in the previously published studies of Hinchen and Hobbs[23] was about 2 nsec.

The two presently available diode lasers nominally cover the spectral range 3024 - 3131 cm^{-1}, which severely limits the transitions that are available for study. The R(6) - R(11) lines of the DF fundamental are accessible and several R-branch lines with similar J values are accessible for HF with the lower v = 4 and v = 5. The HF lines cannot be studied without pumping and this cannot be done now. On the other hand, a pressure broadening study of the fundamental DF lines was performed. These DF lines and/or similar R-branch lines of HCl can be conveniently studied using the available diode lasers. These ground state probed transitions will be useful for testing both the pump and probe laser performance when the double resonance experiments are initiated.

The performance of the diode lasers was disappointing in that they usually showed simultaneous laser emissions from several modes too close together to be separated using slit width and lens adjustments or using laser current and temperature adjustments. The background curves varied as a function of time as the weaker contributing modes would turn on or off. The mode structure was also sometimes affected by the optical path, changing upon insertion of the etalon, the 15 cm calibration cell,

or on changing the number of reflections in the long-path absorption cell. The optimisation adjustment process is very tedious. One possible reason for the poor mode performance may be the presence of a 3 Hz mechanical oscillation associated with the operation of the refrigerator cold head. A vibration-eliminating laser mounting is presently on order from Laser Analytics that will, hopefully, alleviate this problem.

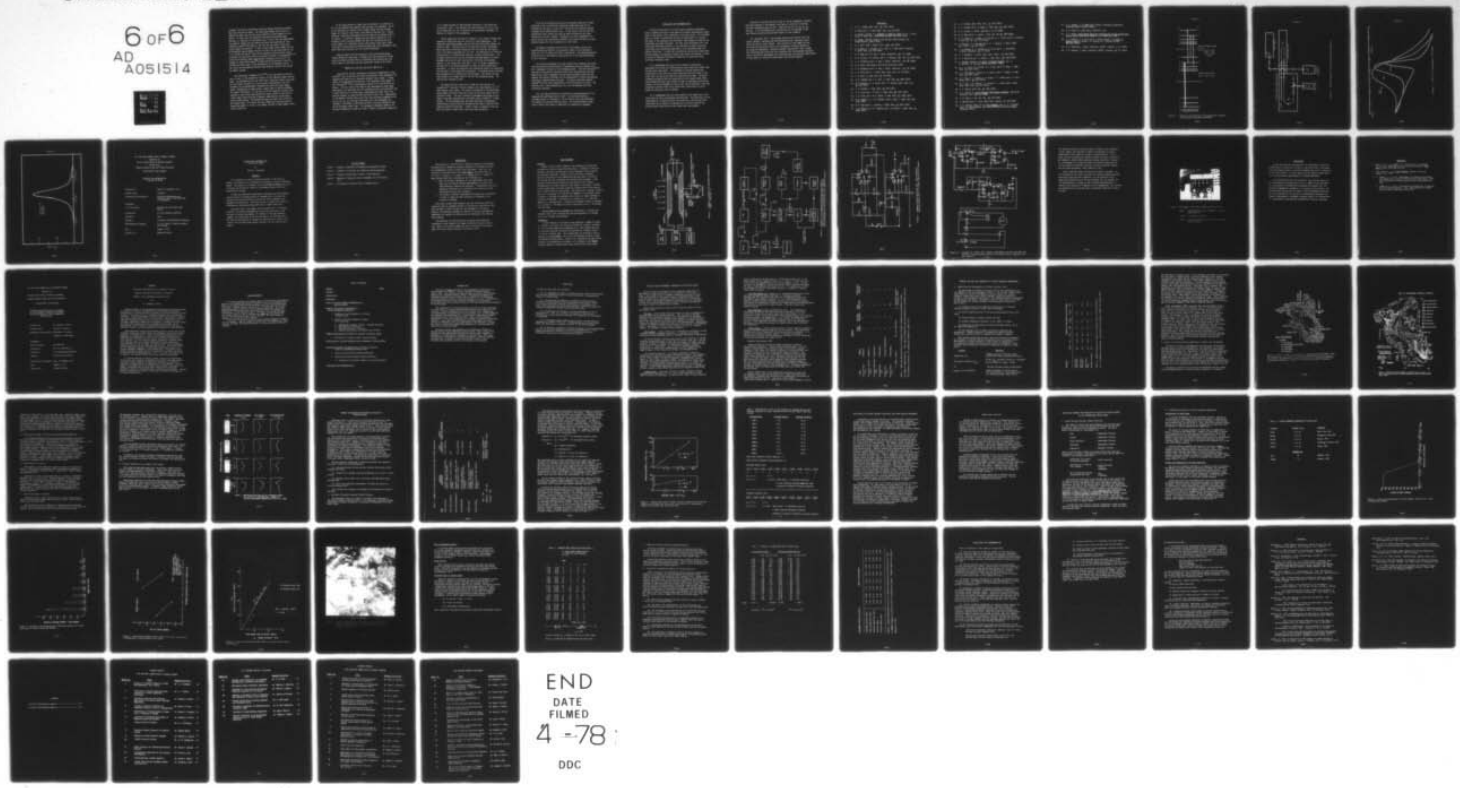
The sensitivity of the diode laser spectrometer using the present diodes was unimpressive, for example, intense absorption lines of CH_4 contained in the 15 cm cell at a pressure of 1 torr could not be detected. Of course, the CH_4 lines were easily observed using the long path cell.

As seen in Figure 2, the diode laser beam can be diverted by a beam splitter (presently on order) to block (E), which represents an HF or DF gain cell. This is intended to respond when the diode laser frequency is in resonance with one of the gain cell spectral transitions. The gain cell is the originally intended device to calibrate the diode laser to the HF or DF frequencies being probed. A difficulty is that only 19 lines have been observed from the parent laser[41], as it stands, and that these all originate from v = 2 or v = 1 states in the case of HF. Transitions arising from v = 4 or 5 states are needed for the present experiments and modifications of both laser design and gaseous input are needed in attempting to generate and to characterize laser emissions from these high vibrational excitations. In addition, an appropriate spectrograph for examining HF laser lines has not been available in the laboratory in recent weeks.

An alternative method for locating and tuning the probe diode laser to desired transitions rests on the capability to rapidly scan the laser injection current (and thereby the laser frequency) of the diode spectrometer. While line profile studies require a spectral sweep that is rapid in comparison with the sample lifetime, a simple line search procedure can

AD-A051 514 AUBURN UNIV ALA SCHOOL OF ENGINEERING F/G 5/2
1977 USAF-ASEE SUMMER FACULTY RESEARCH PROGRAM. VOLUME II.(U)
SEP 77 J F O'BRIEN F44620-75-C-0031
UNCLASSIFIED AFOSR-TR-78-0349 NL

6 OF 6
AD
A051514



END
DATE
FILMED
4-78
DDC

tolerate line profile distortions caused by energy relaxation processes that occur during the sweep. The diode spectrometer has a built-in, repetitive sweep rate of 8 kHz using injection current sweeps of up to 200 ma. An input jack for applying an externally generated sweep function, as required in the present case, is built into the spectrometer. The spectral region used to observe the shock tube generated CO line referred to above[36] was swept in 100 μsec and the author states that faster sweeps are possible. If the 3 micron diode lasers needed for the HF absorption region behave similarly to the 5 micron diode used for CO, it is likely that the HF lines can be located by rapid spectral scans. Estimated line positions can be calculated to tenths of a wavenumber[6,7,10] using the accurately known spectroscopic constants of HF and DF, and methane or other stable gases[42] provide precise calibration lines for setting the diode laser to the estimated HF or DF frequency values. If the levels can be pumped efficiently the probed HF and DF lines should be readily located.

The vibrational lifetimes of HF[12-20] are on the order of 100 μsec more or less, so the chances for success at the indicated sweep rate are good. The determination of the fixed laser injection current to be used for the kinetic studies (i.e. the current corresponding to the line maximum) can be determined by interpolation using the preset sweep range. Bracketting of peaks within a sweep range is easily performed for stable transitions: in the case of DF the injection current corresponding to the narrow band maximum was readily found in the limit of "zero" sweep range using the triangular sweep mode and successively smaller sweep ranges. The bracketting does not need to be carried to zero sweep range. Of course, the usual method for locating accurate absoprtion maxima is to use a slow sweep, the 400 Hz beam chopper, and a lock-in amplifier.

If the sweep method for probe laser calibration is successful it will be considerably more general than the gain cell approach. Any HF or DF transition of interest can be probed rather than the limited number of P-branch lines likely to be found in the gain cell. Double resonance relaxation experiments would not need to be limited to HF or DF samples. In addition, temperature and pressure induced HF or DF frequency shifts occuring between the gain cell conditions and the actual sample cell conditions may be sufficiently large that a small line search and optimisation procedure might need to be performed in any event when using the gain cell as initial calibration.

Assuming highly efficient pumping so that the excited energy states become well populated, it appears that the diode laser system yields excellent possibilities for obtaining rate constant and line profile data in the highly excited vibrational states of HF and DF.

PROFILES OF THE R(6) and R(10) LINES OF DF

Line profiles contain information concerning intermolecular interactions[43], and in the case of DF they are essential input parameters for computational models of an important chemical laser system. A large number of studies reporting profiles of HF absorption lines appear in the literature[24-30] but corresponding studies of DF line profiles are absent. The very narrow line width of the semiconductor diode laser beam makes it an excellent tool for examining narrow line profiles[44] and a Laser Analytics LS-3 diode laser spectrometer has been used in the present research to study the R(6) and R(10) lines of DF. Observations of the Doppler limited lines and of the lines pressure broadened by He, Ar, H_2, D_2, N_2, O_2, and SF_6 at pressures up to one atmosphere are reported. The choice of the R(6) and R(10) lines was dictated in part by the available diode laser. The strongest J-dependent behavior for pressure broadening is shown for lower J values; the present values are

in a J range expected to show monotonic decrease in line width with increasing J value. This behavior has been observed for the HF lines and is predicted, but not in quantitative experimental agreement, by theories of spectral line broadening.

The DF sample was purified by freezing it with liquid nitrogen and pumping off impurities that are volatile at that temperature. The sample was maintained between -60 and -25°C when extracting samples for spectral study. A Wilks Scientific Corporation 40 meter pathlength White type multi-reflection absorption cell was used for the studies with a 10.5 meter pathlength for all runs. The absorption cell had gold plated mirrors, a nickle plated interior, and CaF_2 window-lenses. The DF sample pressure could not be accurately measured because of sample decomposition and cell wall interactions (including H/D exchange). However, it was always much less than 1 torr, as further suggested by the need for a 10.5 meter pathlength in order to obtain appreciable absorption. At these low pressures self-broadening effects are negligible and the vapor is not extensively associated. The broadening gas pressures were measured using a Wallace and Tiernan gauge. The vacuum line was steel except for a copper lead-in line for the broadening gases. The spectra were recorded at 24°C.

The R(6) and R(10) lines occur at 3041.375 and 3103.561 cm^{-1}, respectively[11], and each line was studied in an approximately 0.7 cm^{-1} wide spectral scan region. The spectral background in the experiments often showed variations from scan to scan as the laser output was not perfectly stable. The laser injection currents were converted to wave number using data obtained with a Ge etalon with a 0.0497 cm^{-1} fringe spacing. The raw transmittance data were converted to absorption coefficients by digitizing the recorded curves using a Tektronix 4051 graphics system and digitizer. Figure 3 shows an example of the raw data and Figure 4 shows these lines after data conversion.

Since the DF pressures could not be accurately measured in these experiments the true molecular absorption coefficients may not be obtained and the data is useful for line profile and pressure induced frequency shift determinations only. At the time of this writing the quantitative data conversions have not been finished and the error limitations are still unknown. Therefore, the final paragraphs will merely outline the anticipated treatment to be given the data in a more detailed manuscript to be prepared at a later time.

The Doppler broadened R(6) and R(10) lines appear to have the expected Gaussian profiles, with spectral widths at half maximum of about 0.01 cm^{-1} for R(6) and R(10), respectively. The expected Gaussian profiles will be confirmed by testing the fit of the observed profiles to this function.

The pressure broadened lines show significantly enhanced band wings and profiles have been obtained at intermediate pressures between zero and 1 atmosphere for most of the broadening gases. The Voigt function[43,45] describes line profiles containing significant contributions from both Doppler and Lorentz broadening and the Voigt parameter connecting the Doppler and Lorentz halfwidths will be determined by fitting the observed profiles to computed Voigt functions. A recently published computer program[46] for the rapid computation of this function will be used. The profiles with 1 atm broadening gas will also be compared with pure Lorentzian functions.

The line shape parameters extracted from the measurements will be compared with published results on HF. The available theories, reviewed briefly in reference 1, will be used to calculate halfwidths for comparison with the observed values. The seven broadening cases cover a fairly wide range of conditions for theoretical treatment.

CONCLUSIONS AND RECOMMENDATIONS

It should be possible to initiate double resonance experiments using a tunable dye laser as the pump and a tunable semiconductor diode laser as the probe in this laboratory in the near future. All equipment that is critical to performing the initial experiments will soon be available in the laboratory and additional items needed to optimize the experiments have been indicated. The pump laser performance will very likely need optimization before it can successfully pump the desired transitions, but exploratory experiments can be performed under the present conditions. In addition to optimizing the dye laser band width and pulse shape, the detector response time should be measured in order to assure an adequate instrumental capability for measuring rapid rotational relaxation rates.

It is recommended that the initial, primarily exploratory, experiments be carried out probing ground state transitions rather than excited state transitions. The advantage of probing ground state transitions is that they have large intensities and are stable so the diode laser can easily be tuned into resonance with them. The double resonance procedures that are appropriate to the tunable diode probe laser/tunable dye pump laser system can then be developed using strong signals, and the performance of both lasers can be evaluated. With the presently available diode laser ground state transitions of the DF and/or HCl molecules can be examined.

It is recommended that the rapid spectral scan capability of the diode laser be fully investigated and exploited. The objectives of this study would be to obtain accurate line profiles of the excited state transitions and to develop a procedure for initially locating the excited state transitions with the diode laser spectrometer.

Profiles of the R(6) and R(10) lines of the DF fundamental vibration have been measured in the Doppler limit and as a function of pressure for seven broadening gases as 24°C. These are He, Ar, H_2, D_2, N_2, O_2, and SF_6. It is anticipated that a manuscript will be prepared in the near future containing the analyzed results of this research.

On a personal level, I have become familiar with the HF laser and energy transfer literature and have gained practical laboratory experience with several laser systems. Every activity of the summer was new to me and the cumulative results are considered a valuable addition to my scientific background. Research problems concerning HF laser systems and associated with extracting rate constants from the observed relaxation data, line profile measurement and interpretations, and possible applications of dye lasers for relaxation measurements have become apparent.

References

1. J. J. T. Hough, Appl. Opt., 16, 2297 (1977).

2. N. Cohen and J. F. Bott, Appl. Opt., 15, 28 (1976).

3. G. Emanuel, Chapter 8 in Handbook of Chemical Lasers, R. W. F. Gross and J. F. Bott, Eds., John Wiley and Sons, New York (1976).

4. H. Pummer, Technical Report from the Max Plank Institute for Plasma Physics, (March 1976).

5. R. J. Hall, IEEE J. Quant. Elect. Q-12, 453 (1976).

6. D. E. Mann, B. A. Thrush, D. R. Lide, J. J. Ball and N. Acquista, J. Chem. Phys., 34, 420 (1961).

7. D. U. Webb and K. N. Rao, J. Molec. Spectrosc., 28, 121 (1969).

8. R. W. Talley, H. M. Kaylor, and A. H. Nielsen, Phys. Rev. 77, 529 (1950).

9. E. S. Fishburne and K. N. Rao, J. Molec. Spectrosc., 19, 290 (1966).

10. W. B. Heath, PhD Thesis, Ohio State University (1975).

11. R. N. Spanbauer and K. N. Rao, J. Molec. Spectrosc., 16, 100 (1965).

12. J. R. Airey and S. F. Fried, Chem. Phys. Lett., 8, 23 (1971).

13. J. F. Bott, J. Chem. Phys. 57, 96 (1972).

14. R. R. Stephens and T. A. Cool, J. Chem. Phys. 56, 5863 (1972).

15. R. M. Osgood, Jr., A. Javan, and P. B. Sackett, Appl. Phys. Lett. 20, 469 (1972).

16. J. J. Hinchen, J. Chem. Phys. 59, 233 (1973).

17. R. A. Lucht and T. A. Cool, J. Chem. Phys. 60, 1026 (1974).

18. J. R. Airey and I. W. M. Smith, J. Chem. Phys. 57, 1669 (1972).

19. R. M. Osgood, Jr., P. B. Sackett, and A. Javan, J. Chem. Phys. 60, 1464 (1974).

20. M. A. Kwok and R. L. Wilkins, J. Chem. Phys. 63, 2453 (1975).

21. L. M. Peterson, G. H. Lindquist and C. B. Arnold, J. Chem. Phys. 61, 3480 (1974).

22. J. J. Hinchen, Appl. Phys. Lett., 27, 672 (1975).

23. J. J. Hinchen and R. H. Hobbs, J. Chem. Phys. 65, 2732 (1976).

24. G. A. Kuipers, J. Molec. Spectrosc., 2, 75 (1958).

25. B. M. Shaw and R. J. Lovell, J. Opt. Soc. Am. 59, 1598 (1969).

26. W. F. Herget, W. E. Deeds, N. M. Gailar, R. J. Lovell and A. H. Nielsen, J. Opt. Soc. Am., 53, 1113 (1962).

27. P. Varanasi, S. K. Sarangi and G. D. T. Tejwani, J. Quant. Spect. Rad. Transf., 12, 857 (1972).

28. T. A. Wiggins, N. C. Griffen, E. M. Arlin and D. L. Kerstetter, J. Molec. Spectrosc. 36, 77 (1970).

29. R. E. Meredith, J. Quant. Spect. Rad. Transf., 12, 485 (1972).

30. R. E. Meredith and F. G. Smith, J. Chem. Phys., 60, 3388 (1974).

31. K. Shimoda, Chapter 3 in Topics in Applied Physics, Vol. 2, H. Walther, Ed. Springer-Verlag, New York, (1976).

32. R. C. L. Yuan, J. M. Preses, G. W. Flynn, and A. M. Ronn, J. Chem. Phys. 59, 6128 (1973).

33. J. I. Steinfeld, I. Burak, D. G. Sutton, and A. V. Nowak, J. Chem. Phys. 52, 5421 (1970).

34. R. S. Eng, P. L. Kelley, A. R. Calawa, T. C. Harman and K. W. Nill, Molec. Phys., 28, 653 (1974).

35. R. S. Eng, A. R. Calawa, T. C. Harmon, P. L. Kelley and A. Javan, Appl. Phys. Lett. 21, 303 (1972).

36. R. K. Hanson, Appl. Opt. 16, 1479 (1977).

37. H. G. Heard, Ed. Laser Parameter Measurements Handbook, John Wiley and Sons, Inc., New York (1968).

38. J. W. Evans, J. Opt. Soc. Am., 39, 229 (1949).

39. H. Walther and J. L. Hall, Appl. Phys. Letters, 17, 239 (1970).

40. F. P. Schafer, Chapt. B3 in Laser Handbook, Vol. 1, F. T. Arecchi and E. O. Schulz-Dubois, Eds., North Holland Publishing Company, Amsterdam (1972).

41. D. J. Spencer, J. A. Beggs and H. Mirels, Aerospace Corporation Technical Report TR-0077 (2940)-4.

42. D. R. Lide, Jr., Laser Focus, Feb 1977, p 53.

43. S. S. Penner, Quantitative Molecular Spectroscopy and Gas Emissivities, Addison-Wesley Publishing Comapny, Inc., Reading PA (1959).

44. E. D. Hinkley, K. W. Nill and F. A. Blum, Chapter 2 in Topics in Applied Physics, Volume 2, H. Walther, Ed., Springer-Verlag, New York (1976).

45. B. H. Armstrong, J. Quant. Spectrosc. Radiat. Transfer, 7, 61 (1967).

46. S. R. Drayson, J. Quant. Spectrosc. Radiat. Transfer, 16, 611 (1976).

Figure 1

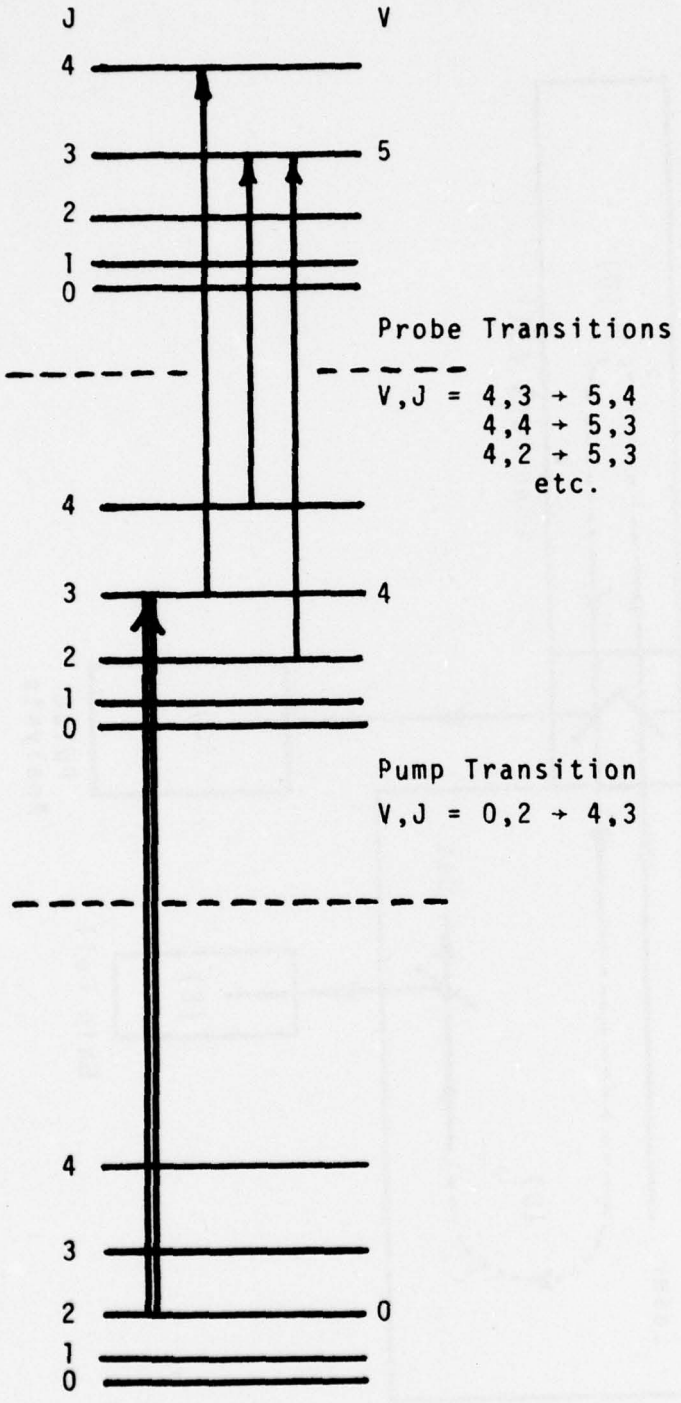


Figure 1. Possible Transitions for Relaxation Studies Using Double Resonance Methods

Figure 2

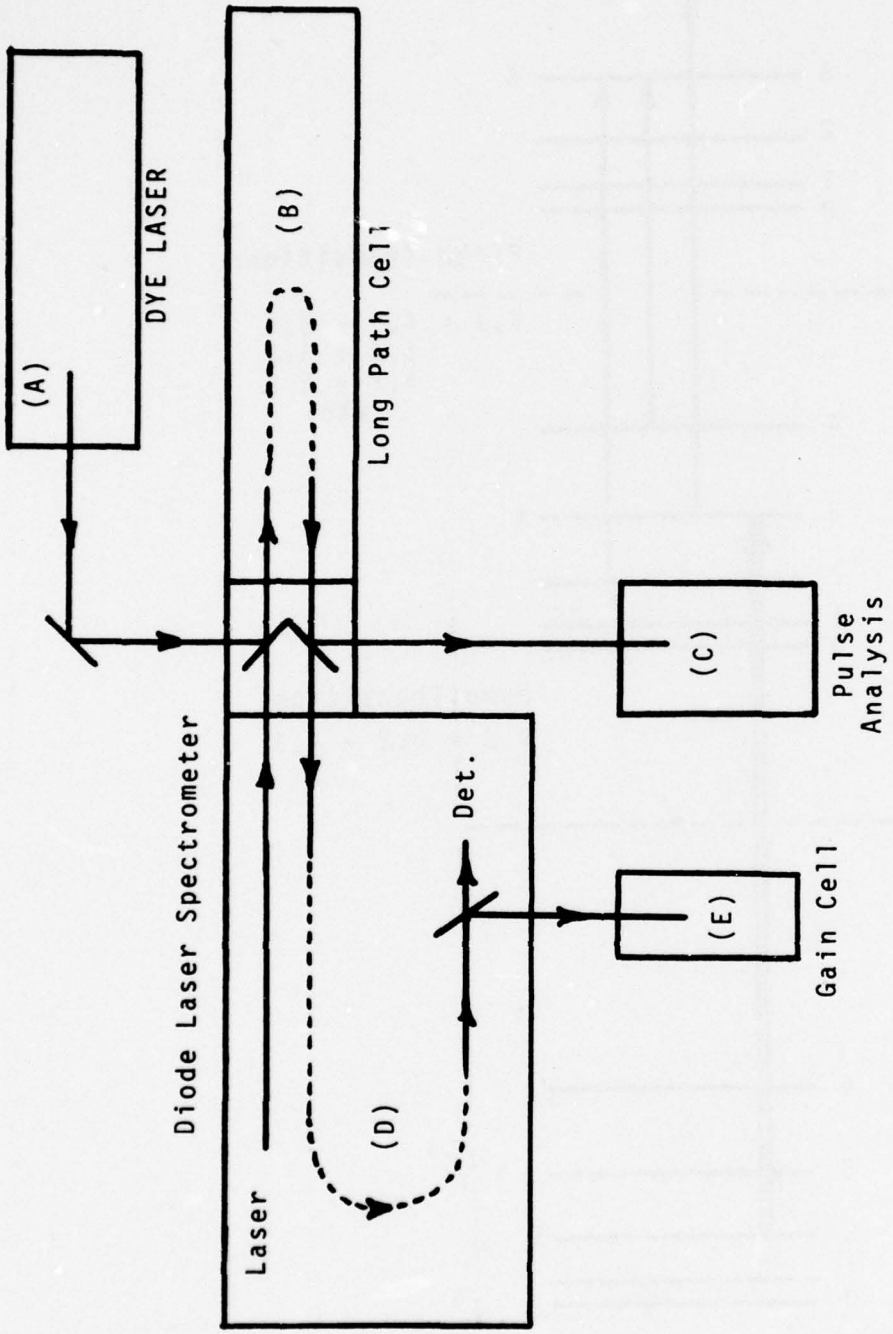


Figure 2. Block Diagram of Double Resonance Apparatus

Figure 3

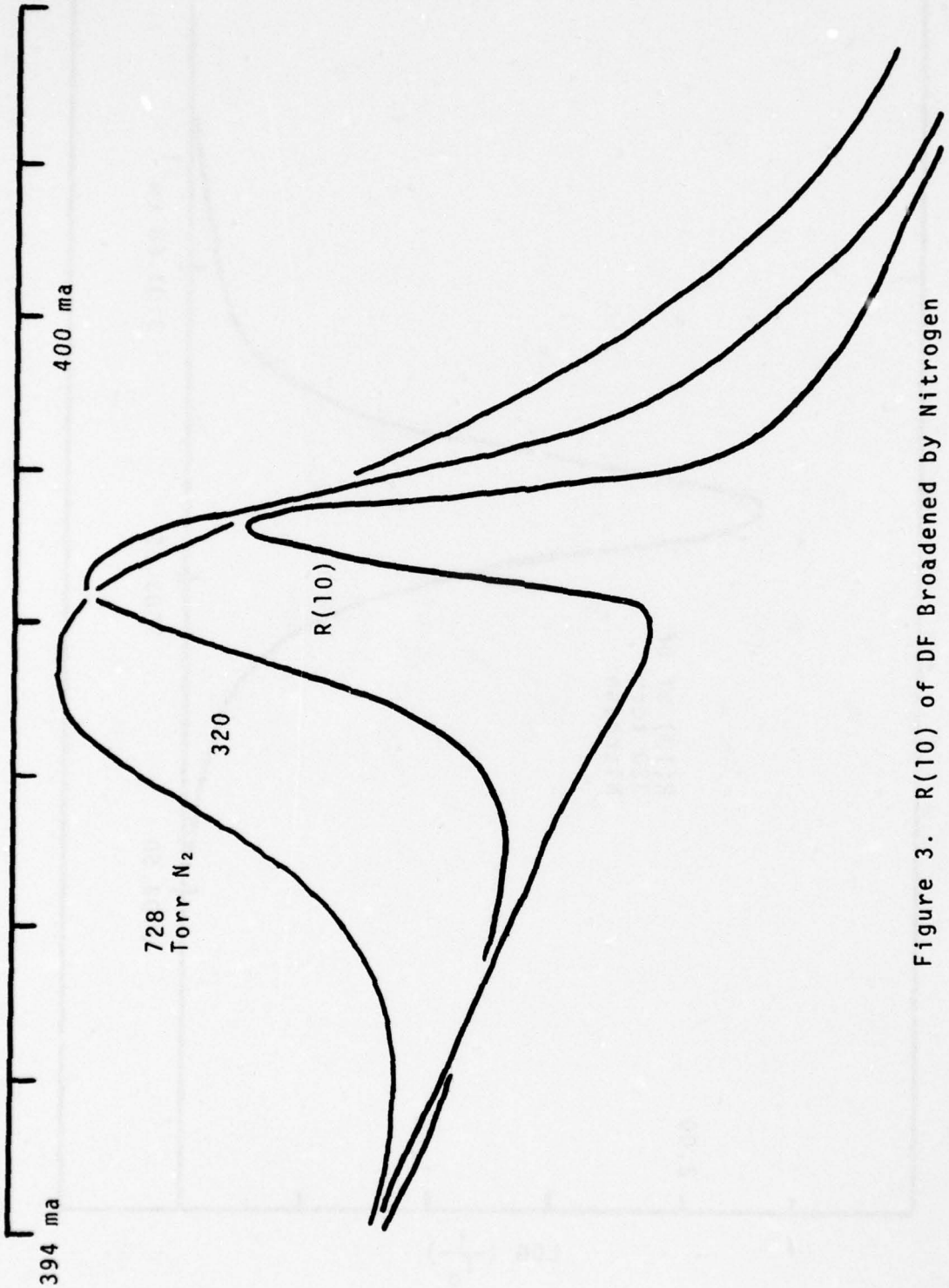
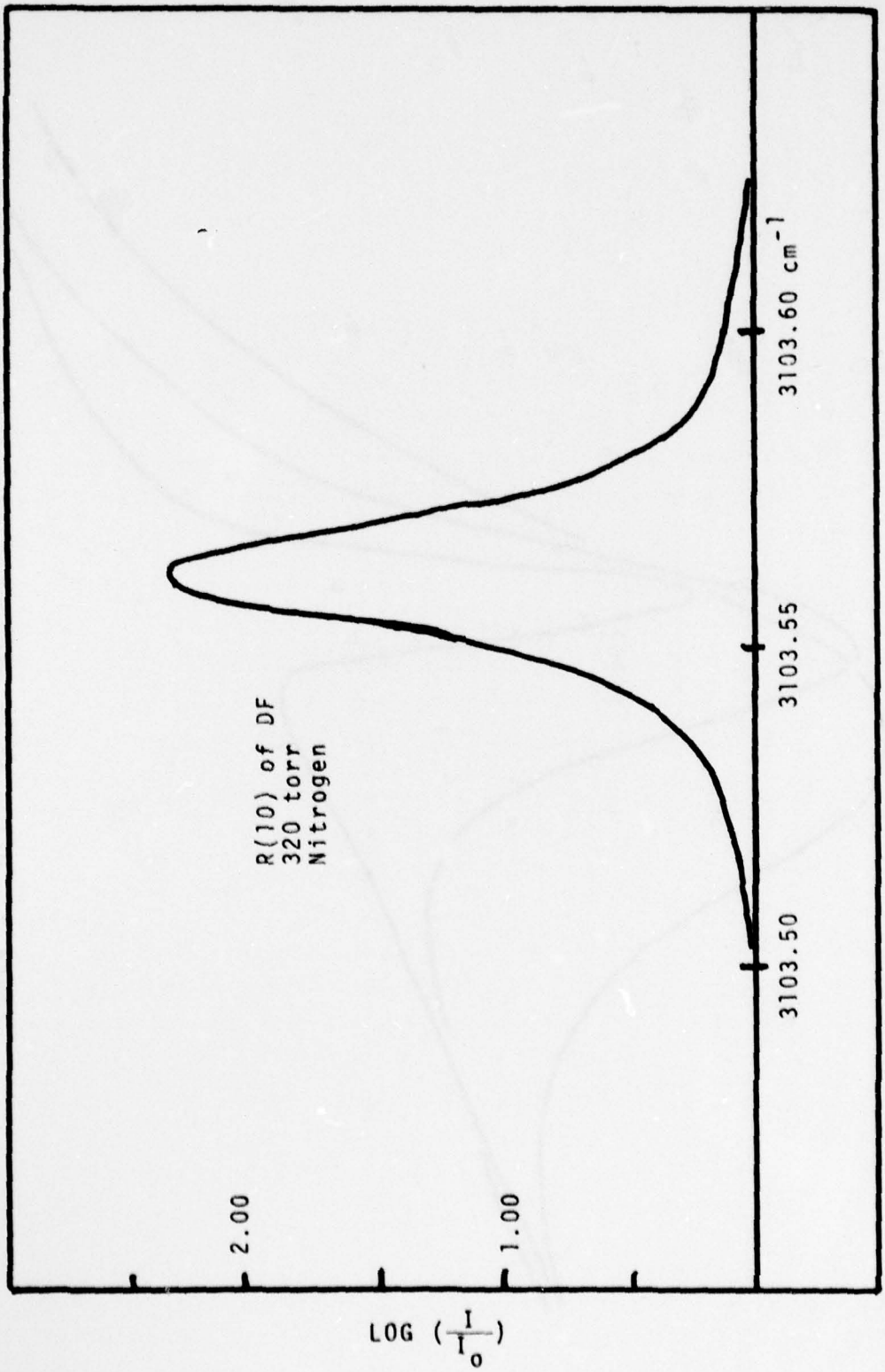


Figure 3. R(10) of DF Broadened by Nitrogen

Figure 4


R(10) of DF
320 torr
Nitrogen
3103.50
3103.55
3103.60 cm^{-1}
1.00
2.00
LOG ($\frac{I}{I_o}$)

1977 USAF-ASEE SUMMER FACULTY RESEARCH PROGRAM

sponsored by

THE AIR FORCE OFFICE SCIENTIFIC RESEARCH

conducted by

AUBURN UNIVERSITY AND OHIO STATE UNIVERSITY

PARTICIPANT'S FINAL REPORT

ELECTRON-ION RECOMBINATION IN LASER GAS MIXES

Prepared by:	Harold D. Southward, Ph.D
Academic Rank:	Professor
Department and University:	Electrical Engineering and Computer Science, The University of New Mexico
Assignment:	
(Air Force Base)	Kirtland Air Force Base, New Mexico
(Laboratory)	Air Force Weapons Laboraoty
(Division)	Laser
(Branch)	Electrical Lasers/Advanced Technolgy
USAF Research Colleague:	Lt. Col. Peter D. Tannin and Major Tom W. Meyer
Date:	August 5, 1977
Contract No.:	F44620-75-C-0031

ELECTRON-ION RECOMBINATION IN LASER GAS MIXES

by

Harold D. Southward

ABSTRACT

It is important to have an accurate estimate of the electron density for prediction of performance and scaling of electric discharge lasers. The purpose is to measure the electron/ion recombination rate as a function of gas mixture, electric field/number density (E/N) and characteristic energy.

To this end prospective measurement techniques were investigated, various pieces of existing pieces of equipment were interfaced and necessary electronic/electrical control and firing equipment were designed and constructed. One objective was to remove criticisms of techniques in obtaining previous data and to expand these data.

The major work of the summer period consisted of: (1) finding a method of accurately determining cathode fall potential so that E/N may be reliably determined; (2) redesign of the gas discharge chamber; (3) interfacing of the electron gun to its envelope and to the control electronics; (4) design and construction of control electronics; (5) providing high voltage isolation for the electron gun supply.

LIST OF FIGURES

Figure 1. Diagram of Apparatus For Measuring Recombination Rates.

Figure 2. Schematic of Electron Gun Timing and Firing Apparatus.

Figure 3. Diagram of Main Pulser and Sync. Pulse Generator.

Figure 4. Diagram of Timing and Control Equipment for the Electron Gun.

Figure 5. Photograph of Electron Gear for Timing Control

INTRODUCTION

The objective of this work is to consider prospective measurement techniques and to design and assemble apparatus to determine electron-ion recombination rates in various laser gas mixes. This is a continuation of work reported in the Laser Digest, Fall 1976, AFWL TR-77-15 by T. W. Meyer, J. D. Hines, P. D. Tannen and R. E. Jenigan.[1] Major points which form a setting for the following are:

1. Most of the major components for the experiments were available, but for various reasons they needed to be interfaced, some mechanical redesign was necessary. Considerable electronic design and fabrication for controlling the electron gun and obtaining data were also necessary.
2. Criticisms of previous experimental techniques were considered in order to remove as many objections as possible in the process of redesign.

This report places heavy emphasis upon the electronic/electrical timing and control equipment because of the positive contribution that this may make to those who may use this equipment in the future. Further, the mechanical changes are obvious to any user and physical dimensions and assembly are obvious and are obtainable from existing shop drawings.

Unfortunately the time period did not permit the taking and processing of data; however the summer period did bring the project very close to its research phase and due to location of the participant, this phase should continue in the Fall of 1977.

WORK PERFORMED

Overview:

Figure 1 shows a basic diagram of the apparatus for measuring recombination rates as taken from Reference 1. Although it does not represent the exact configuration of the equipment it does indicate the essential functions. Probes P_1 and P_2 are used to measure electric potentials in the plasma which are then used to calculate the cathode fall and ultimately the electric field strength. Total current is measured and a button current gives a more accurate determination of current density at the center of the anode. Further, a pulse transformer is placed around the cathode lead of the electron gun to monitor electron gun current. The cathode of a tetrode electron gun is at a potential of (-)150 kV with respect to the cathode, shown in Figure 1, and must be supplied with 60 cycle a-c power through an isolation transformer. The electron is held off by a 0 - 160 volt negative d-c voltage source. Electron gun filament current is supplied by a variable 0 - 30 ampere d-c source controlled by an 0 - 60 seconds interval timer.

Special apparatus was designed and constructed to initiate the filament timer, fire a positive voltage grid modulator at a preset time and to trigger oscilloscopes.

Discussion:

A block diagram of the electron gun apparatus is shown in Figure 2. Briefly, the pulser (at laboratory potential) creates a variable 0.1 to 10 second square pulse beginning at t_o. The leading edge (t_o) of the pulse subscript initiates the electron gun filament current to run for a present time. The falling edge (t_1) provides a time to initate all oscilloscopes and to fire the electron gun with a model 214 Hewelett-Packard pulser. Figure 3 is a diagram of the main pulser and sync. pulse generator and Figure 4 is a diagram of the Schmitt trigger, modulator trigger pulser and interval timer reset pulser.

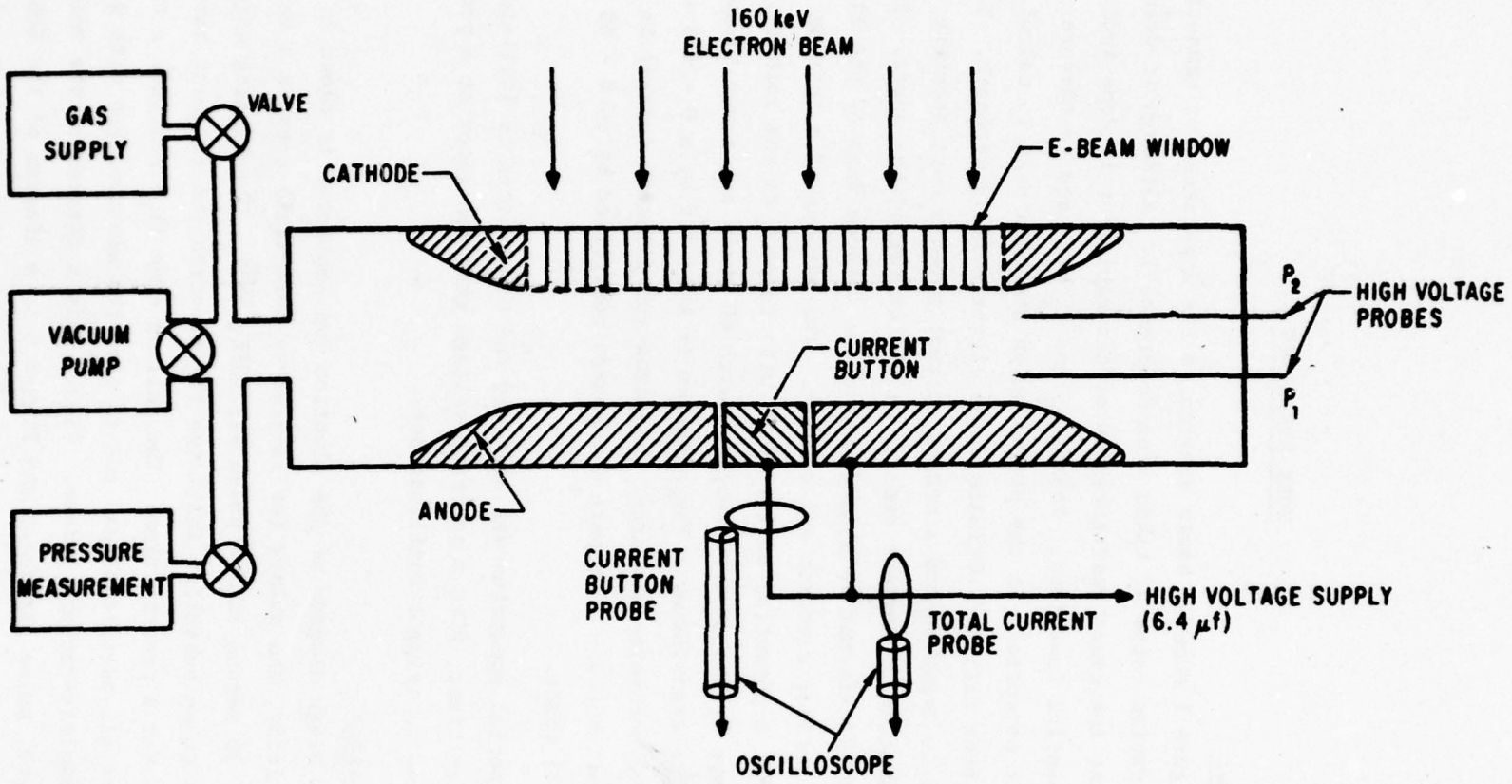


Figure 1. DIAGRAM OF APPARATUS FOR MEASURING RECOMBINATION RATES. (From Ref. 1.)

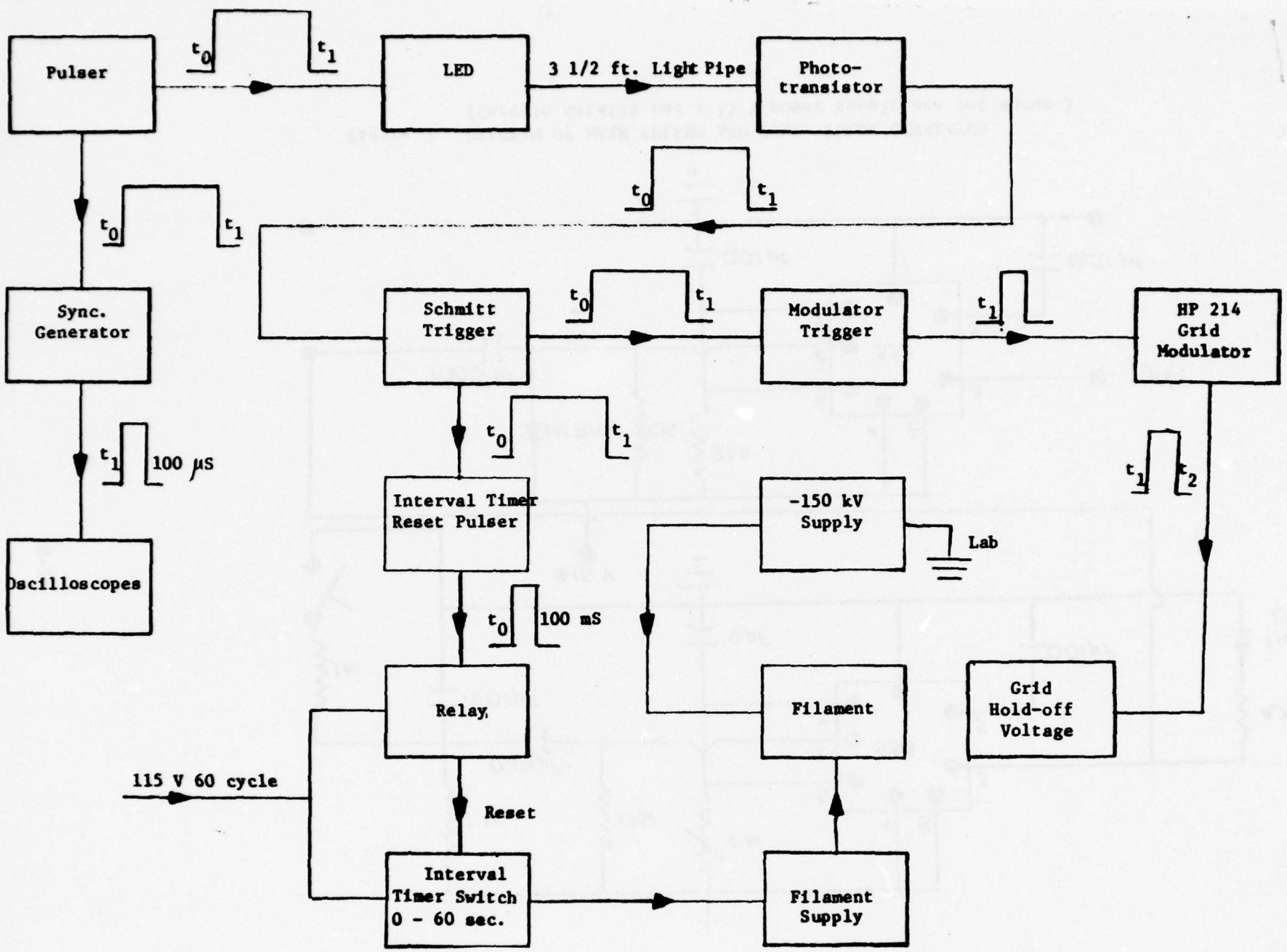


Figure 2. SCHEMATIC OF ELECTRON GUN TIMING AND FIRING APPARATUS. (Times t_1 and t_2 are variable and other fall times are fixed and adequate for the application, but somewhat arbitrary.)

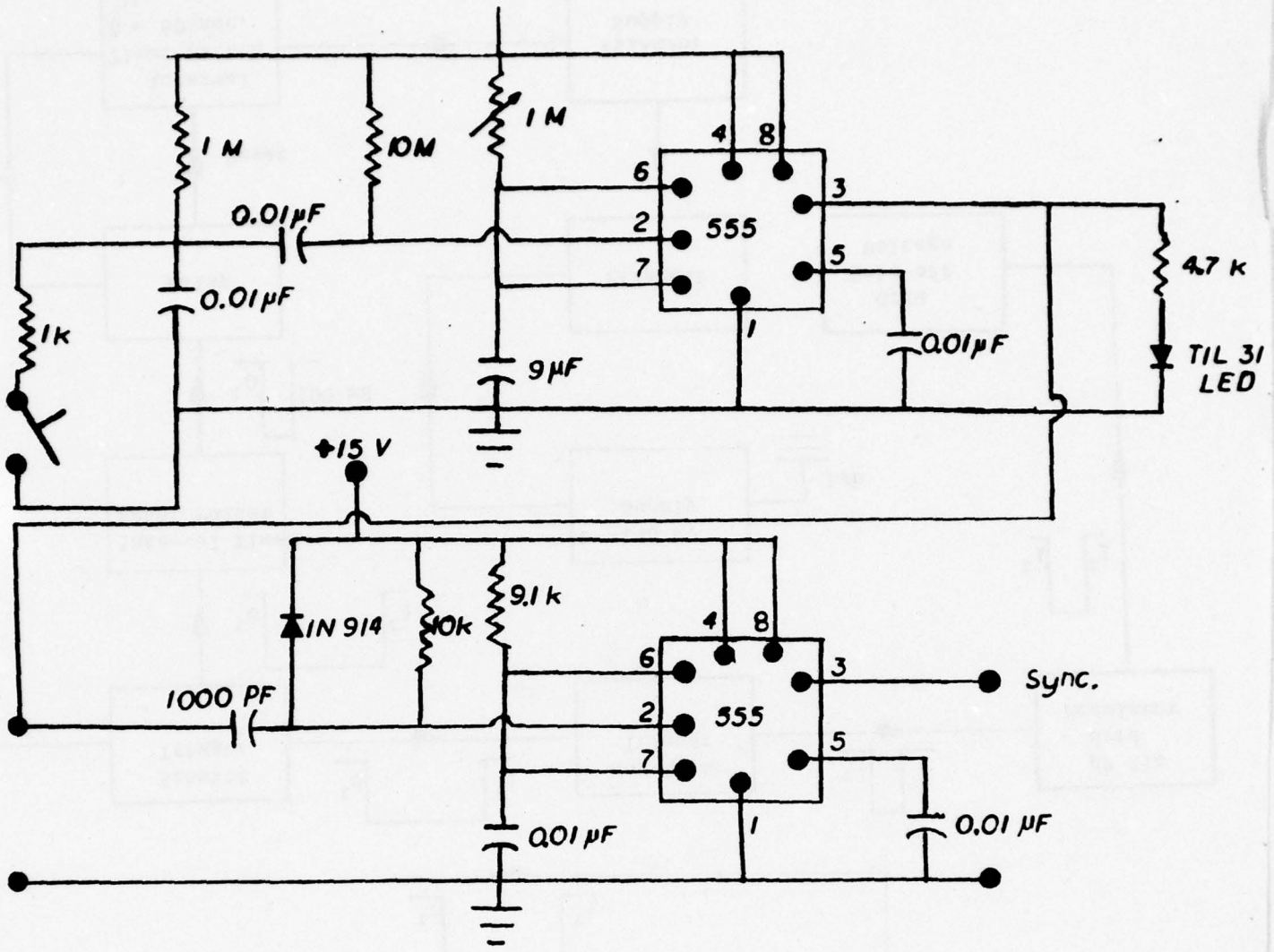


Figure 3. DIAGRAM OF MAIN PULSER AND SYNC. PULSE GENERATOR.
(Certain details and a 15 V power supply are not shown.)

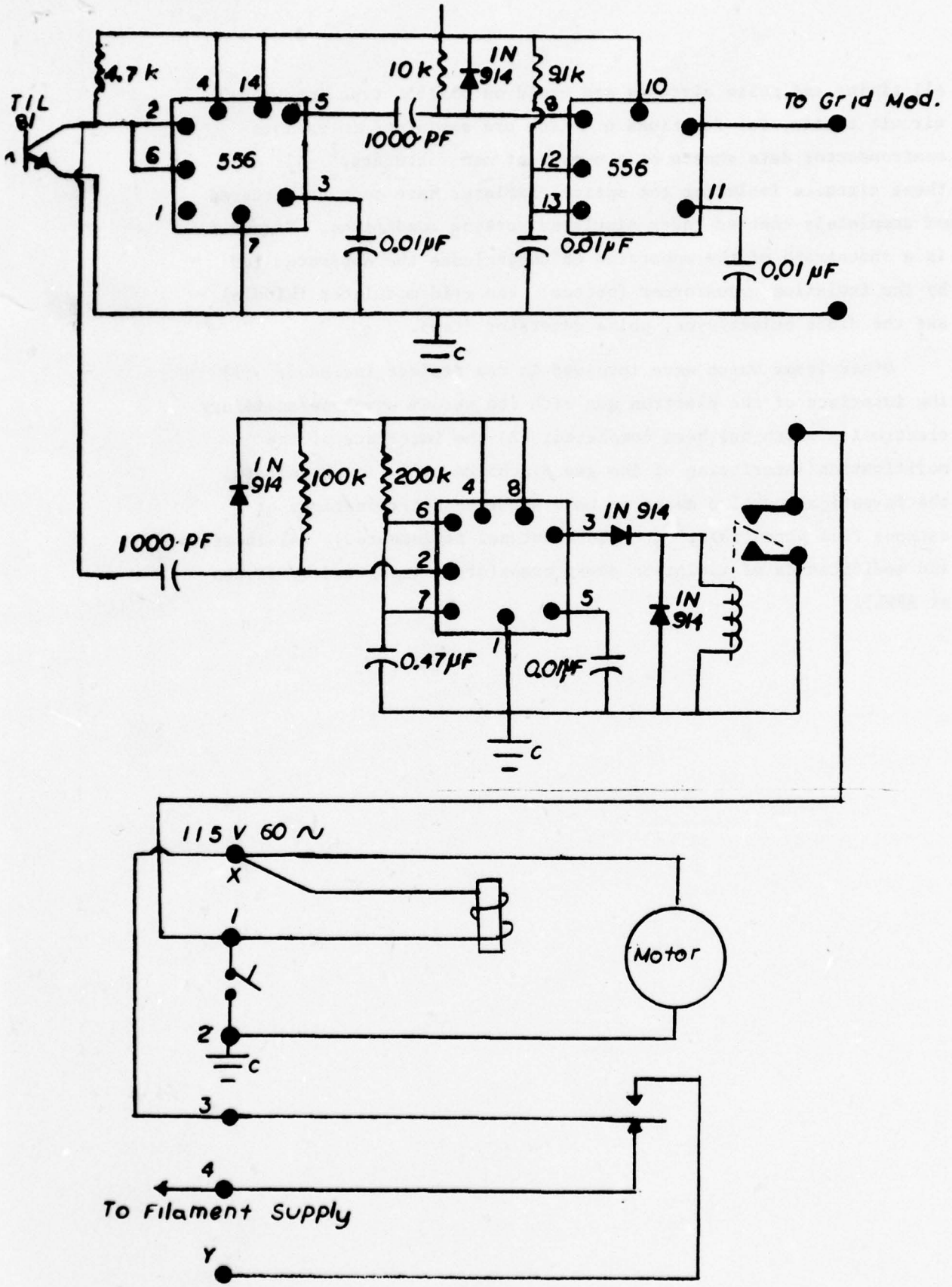


Figure 4. DIAGRAM OF TIMING AND CONTROL EQUIPMENT FOR THE ELECTRON GUN. (Certain miscellaneous details and three power supplies are not shown.)

All timing and pulse circuits are based on 555/556 type integrated circuit timers, the functions of which are explained in various semiconductor data sheets by a number of manufacturers.[2] All of these circuits including the optical isolater have been constructed and completely checked under simulated working conditions. Figure 5 is a photograph of the apparatus which includes the apparatus fed by the isolation transformer (bottom), the grid modulator (middle) and the diode pulser/sync. pulse generator (top).

Other items which were involved in the project included: (1) the interface of the electron gun with its vacuum envelope/ancillary electronics which has been completed; (2) the interface of the modification/interfacing of the gas discharge cell (in shops); (3) the investigation of a means to make accurate determinations of cathode fall potentials;[3] (complete but not implemented), (4) location and modification of isolation power transformer (modified by others at AFWL).

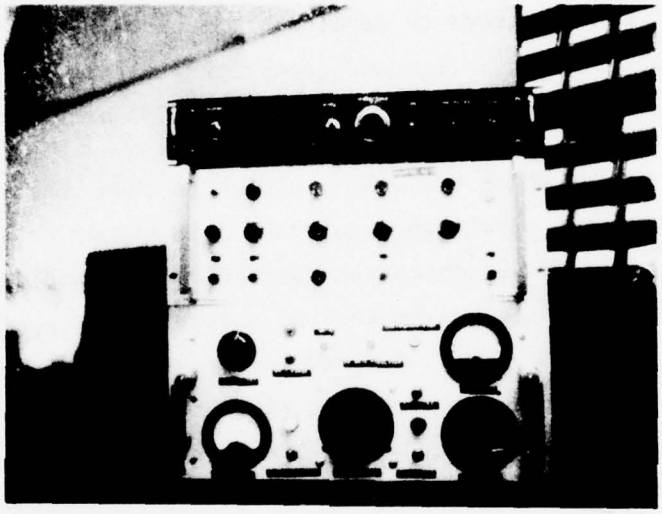


Figure 5. PHOTOGRAPH OF ELECTRONIC GEAR FOR TIMING CONTROL.

Lower : Equipment pertaining to Figure 4 including power supplies.

Middle: H-P Model 214 pulser.

UPPER : Equipment pertaining to Figure 3 including power supplies.

CONCLUSIONS

We may conclude that the apparatus for performing ion-electron recombination of gases will be ready to take data within a few weeks. (The participant intends to continue following this work to completion in the Fall of 1977.) It would appear that the research phase which is to follow would be appropriate for an AFOSR mini grant.

Some topics which could be included in this research phase are: (1) obtaining gas discharge decay data in a number of gas mixtures; (2) calculation of recombination parameters and cathode fall; (3) plotting recombination parameters as a function of gas mixture, E/N, characteristic energy with due regard to any contaminants which may be in the mixture; (4) calculation of characteristic energies from numerical approaches to Boltzmann transport theory; (5) consideration of contaminants by spectroscopic examination of the gas discharge.

REFERENCES

1. Meyer, T. H., J. D. Hines, P. D. Tannen, and R. E. Jernigan. "Electron-Ion Recombination Rates In Laser Gas Mixes," Laser Digest, Fall, 1976, AFWL TR-77-15.

2. Jung, Walter G., I. C. Timer Cookbook, Howard W. Sons and Company, Inc., 1977.

3. a. Ganley, J. T., et al, "Measurement of Potential Distribution and Cathode Fall In Electron-Beam-Sustained Discharges," 1976, IEEE Conference On Plasma Science, Austin, Texas, May 24-26, 1976.

   b. Leland, W. T., et al, "Calculation of Cathode Fall In Electron Beam Sustained Discharges," 1976, IEEE Conference On Plasma Science, Austin, Texas, May 24-26, 1976.

1977 USAF-ASEE SUMMER FACULTY RESEARCH PROGRAM

sponsored by

THE AIR FORCE OFFICE SCIENTIFIC RESEARCH

AUBURN UNIVERSITY AND OHIO STATE UNIVERSITY

PARTICIPANT'S FINAL REPORT

THE NATURE AND PREDICTION OF SECONDARY CALCIUM CARBONATE CEMENTATION (CALICHE) IN ALLUVIAL BASINS OF THE SOUTHWESTERN UNITED STATES

Prepared by:	Dr. Stephen G. Wells
Academic Rank:	Assistant Professor
Department and Univesity:	Department of Geology
	University of New Mexico

Assignment:	
(Air Force Base)	Kirtland AFB
(Laboratory)	Air Force Weapons Lab
(Division)	Civil Engineering Research
(Branch)	Facility Survivability
USAF Research Colleague:	Capt. Al Schenker, M.S.
Date:	August 9, 1977
Contract No.:	F44620-75-C-0031

ABSTRACT

The Nature and Prediction of Secondary Calcium Carbonate Cementation (Caliche) in Alluvial Basins of the Southwestern United States

by

Dr. Stephen G. Wells

Alluvial basins in the southwestern United States are being assessed for potential siting of the Multiple Aim Point Missile System (MX). Accumulation of calcium carbonate (caliche) in the soil horizons and upper portion of the basin fill is a secondary alteration due to weathering processes. Caliche development in alluvial materials change the physical and chemical properties of the in situ material. Specifically, calcium carbonate cementation binds clastic material into large grain sizes, increases compressive strength of the material, increases the bulk density, and reduces the infiltration rate of downward percolating waters. Consequently, these changes in engineering characteristics may pose a potential hazard to the construction and survivability of the MX system.

These properties change with different types of caliche and calcium carbonate content, and caliche types vary throughout the alluvial basins; therefore, the prediction of caliche occurrence and properties will be essential for siting the MX. Areas of the Southwest which have the following characteristics are most likely to have well-indurated and thick caliche: (a) old alluvial material composed of carbonate and/or basic igneous rocks, (b) alluvium downwind from playas which have concentrations of $CaCO_3$ or $CaSO_4$, (c) material that is coarse grained and poorly sorted, and (d) older alluvium or soils. Areas least likely to have appreciable amounts of $CaCO_3$ cementation may be young, fine grained sediments composed of acid igneous rocks. The depth to these caliche horizons is proportional to the amount of rainfall, and may be predicted by the following equation: $Dca = 1.63 (Pm - 0.45)$ where Dca is depth to the caliche, and Pm is the mean annual precipitation.

In certain portions of alluvial basins, erosion has removed most of the upper soil horizons and exposed the caliche to the near-surface. Satellite imagery (Landsat) is useful for detecting the caliche by variations in image density and morphology of the landscape. Caliche reduces the erodibility of the landscape which causes a decrease in the number of drainage lines per unit area, preservation of multiple geomorphic surfaces, and modification of channel characteristics. Alluvial material cemented with caliche is subjected to excessive flooding due to minimal infiltration.

ACKNOWLEDGEMENTS

The author expresses his sincere thanks to the Facility Survivability Branch, Civil Engineering Research Division of the Air Force Weapons Lab, KAFB for providing facilities and assistance, and for the interest given to my work. Special thanks is given to Lt. Col Frank Leech of the Civil Engineering Research Division for his sincere cooperation. This study benefited from discussions and time shared with Capt. Lou Karably, Mr. Steve Melzer, Lt Col Jim Neal, and Lt. Jim Shinn. The author expresses his sincere thanks to Capt Al Schenker for suggesting the project and for his time and ideas related to this research. Mr. Steve Cooper is thanked for his help with the computers.

The author is grateful to the Air Force Systems Command for support of this research. Special thanks are given to Dr. Art Guenther, Mr. Fred O'Brien, the ASEE, and Auburn University for their assistance during this research.

TABLE OF CONTENTS

Chapter — Page

ABSTRACT

INTRODUCTION

OBJECTIVES

TYPES OF CALCIUM CARBONATE CEMENTATION IN ALLUVIAL BASINS

CHEMICAL AND PHYSICAL PROPERITES OF CALCIUM CARBONATE CEMENTATION

1. Composition and Geochemistry of Caliche in Desert Soils

2. Effect of Calcium Carbonate on Desert Soil Properties

   A. Compressive Strength of $CaCO_3$ - cemented materials
   B. Bulk Densities of Caliche
   C. Infiltration Rates of Caliche
   D. Property Variations in the Desert Soil Profile

TERRAIN ASSOCIATIONS AND EFFECTS OF CALICHE IN ALLUVIAL BASINS

1. Influence of Caliche on Desert Fluvial Systems

APPLICATIONS OF CALICHE PROPERTIES AND OCCURRENCE TO THE MX SYSTEM

QUALITATIVE METHODS FOR PREDICTION OF CALICHE IN ALLUVIAL BASINS IN SOUTHWESTERN UNITED STATES

1. Buried Calcium Carbonate Cemented Materials

2. Subaerial Calcium Carbonate Cemented Materials

   A. Evaluation of Satellite Imagery for Caliche Detection

CONCLUSIONS AND RECOMMENDATIONS

INTRODUCTION

The Basin and Range province of the southwestern United States is being assessed for potential siting of Multiple Aim Point Missile System (MX). This province is characterized by isolated, block-faulted mountains and intervening desert plains. The geologic processes and resulting characteristics of these alluvial basins are of significant concern if effective siting of these MX systems is to occur. Specifically, the sedimentologic nature and surficial processes of the potential basins sites may pose a potential hazard to the construction and survivability of the MX system.

The accumulation of calcium carbonate (caliche) in clastic materials of these basins is a common secondary-weathering process related to arid climates. Caliche development will have an impact on the engineering and sedimentologic characteristics of the alluvial fill. Caliche indurates the previously unconsolidated fill, increasing the compressive strength and binding clasts into larger particles. Thus, calcium carbonate cementation of the alluvial deposits may increase the possible ejecta-size material. Large ejecta blocks derived from nuclear impact craters on caliche may adversely affect the performance of the MX system. Caliche may also adversely affect engineering properties of alluvial materials which will host the MX System

Caliche occurrence and properties are considerably variable in alluvial basins of the southwestern United States. Thus, siting of MX Systems may risk engineering and geologic hazard unless a method is developed for predicting the occurrence of caliche types. This study concentrates on near-surface carbonate cementation. However, cemented horizons exist at depths in basin alluvium and a study of their occurrence and properties are not in the scope of this project.

OBJECTIVES

The goals of this study are fivefold:

(1) To determine the types of caliche that will affect the MX System and how their properties relate to the survivability, and engineering aspects of the MX system.

(2) To illustrate the general, or regional, characteristics of caliche in alluvial basins of the southwestern United States. These characteristics include; chemical constituents and variables which affect $CaCO_3$ precipitation in alluvial materials, engineering properties related to compressive strength and infiltration rates.

(3) To delineate the effects of caliche development on terrain characteristics. That is, to answer the question: how does the induration of clastic materials influence the erodibility and morphology of landforms?

(4) To determine those variables which control calcium carbonate cementation in alluvial basin fill. Understanding these variables will permit the delineation of regions favorable to caliche development.

(5) To develop a conceptual (qualitative) model for caliche development based on the interrelationships of variables determined above. This conceptual model will provide a basis for further work which may successfully evolve into a useful quantitative model.

TYPES OF CALCIUM CARBONATE CEMENTATION IN ALLUVIAL BASINS

Six major types of secondary calcium carbonate cementation are described by Lattman (1973,1975) and are adopted for use in this study. The various types of carbonate cementation are given in Table 1 and described below. The caliche types are differentiated on the basis of variations in morphology, physical properties, vertical and lateral extent. Variations in chemical constituents are not considered a factor for caliche classification; however, varying concentrations of $CaCO_3$ do affect the properties of caliche.

Detailed descriptions of these caliche types are given by Cooley and others (1973):

"Caliche. In this report the term caliche is used to encompass all secondary deposits of calcium carbonate. The term caliche has been commonly used to designate deposits of calcium carbonate by pedogenic processes. However, in the present study, deposits of calcium carbonate due to what are believed to be other than pedogenic processes have been found, and these play an important role in the investigation. Additionally, caliches of pedogenic origin are transitional with caliches of nonpedogenic origin. Therefore, it is felt best to here use caliche as a general term for all secondary calcium carbonate deposits.

Soil Caliche. A soil caliche is an accumulation of secondary calcium carbonate formed by pedogenic processes. It consists of two major transitional types depending mainly on thickness and degree of development:

(1) Calcic horizon. As here used, this is a soil horizon of calcium carbonate accumulation which is more than six inches thick, has a calcium carbonate equivalent content of more than 15 percent, by weight, and has at least 5 percent, by volume, of identifiable secondary carbonates (Soil Survey Staff, p. 3-38, 1967). If a horizon of secondary carbonate accumulation is indurated or cemented such that dry fragments do not slake in water, it is a petrocalcic horizon, as discussed below.

(2) Petrocalcic horizon. A laterally continuous, cemented or indurated calcic horizon is called a petrocalcic horizon. Dry fragments do not slake in water and noncapillary pores are plugged (Soil Survey Staff, p. 3-40, 1967). It may be capped by a laminar layer, and its structure may be either massive or platy. This horizon is often called calcrete. The term K-fabric has been used by Gile, et al. (1965), for petrocalcic horizons meeting certain qualifications as to fabric and content. In this report petrocalcic horizon will be used to subsume the K-fabric concept as the distinctions will not be required in this study.

Laminar Layer. This layer consists of thinly laminated calcium carbonate which contains few or no coarse clasts and which is found under a variety of conditions. It may occur as a more or less continuous

cap on a petrocalcic horizon where it is believed by some to be a late stage feature of soil formation (Gile, et al., 1965). It may also occur on any relatively impermeable surface such as bedrock or clay. It may be found, not uncommonly, locally coating the sides of gullies and washes and also in discontinuous thin layers on clay. It is generally of very low permeability which is maintained because of a tendency to rapidly cement small fractures.

Gully-Bed Cementation (Lattman, L.H., unplublished manuscript, 1972). Gully-bed cementation, here called GBC, is a massive, generally nonlaminated, well cemented layer found on, or immediately beneath the bed loads of many gullies and washes. It is of low permeability and commonly includes boulders, pebbles, and sand that were earlier bedload. Such layers are discontinuous laterally but otherwise may be indistinguishable from petrocalcic horizons or laminar layers. They may include some laminar horizons.

Case Hardening (Lattman and Simonberg, 1971). Case hardening is cementation of alluvial and colluvial material exposed in very steep to vertical slopes, such as gully sides and terrace risers. It is believed to be due to thin-film surface water causing solution of silt-sized calcareous material and redeposition. It is locally extremely hard and of low permeability, depending upon age and sorting of the cemented material. Older exposures are better cemented, and in any one exposures the poorer the sorting (the greater the range in grain size) the better the cementation.

Caliche Rubble. Caliche rubble consists of loose, generally irregular pieces of calcium carbonate lying loose on the surface. Such rubble may locally cover up to 75 percent of the surface in the area studied. It is believed to be derived from two sources: 1) mechanical breakup of laminar layers and near surface petrocalcic horizons; and 2) by seperation of coating from pebbles and larger clasts."

(Adapted from Lattman, 1973)

These six types of caliche are ranked according to selected characteristics in Table 1. These characteristics include: (1) areal extent or distribution in an alluvial basin, (2) relative thickness compared to other types, (3) lateral continuity of caliche horizon, and (4) depth to the top of the caliche horizon below the surface. The ranking is designed such that 1 represents caliches with the greatest areal extent, thickness, etc. and 6 represent caliches with the least values. Of these six types, calcic and petrocalcic horizons are the most significant, and both form by pedogenic (soil-forming) processes. That is, calcic and petrocalcic horizons have the highest ranking in the four characteristics, and more importantly, are the most continuous caliches in alluvial basins of the southwestern U.S. Gully-bed cementation and laminar layers are discontinuous although they occur widely over alluvial basins.

Reeves (1976) offers a well-summarized description of other ways to classify caliche than the one given above. These classifications are primarily concerned with describing local morphologic characteristics rather than regional features. Gile et al (1966) present a classification scheme that is regional but only includes pedogenic caliche.

TYPE	ORIGIN	RANKING			
		AREAL EXTENT	RELATIVE THICKNESS	AREAL CONTINUITY	DEPTH BELOW SURFACE
Calcic Horizon (ca)	Pedogenic	1	1	1	1
Petrocalcic Horizon (Pca)	Pedogenic	2	3	2	2
Gully-Bed Cementation (gbc)	Nonpedogenic	4	4	5	4
Case-Hardening (ch)	Nonpedogenic	3	2	3	5
Laminar Layer (LL)	Pedogenic/Nonpedogenic	V	6	4	3
Caliche Rubble (cr)	Nonpedogenic	V	5	NA	6

V = highly variable NA = not applicable 1 - represents greatest 6 - represents least

Table 1. Types and Characteristics of Secondary Carbonate Cementation and Ranking of Types According to Characteristics. This table is generalized and representative of secondary $CaCO_3$ in the Southwest; therefore, the ranking may change at a given site.

CHEMICAL AND PHYSICAL PROPERTIES OF CALCIUM CARBONATE CEMENTATION

1. Composition and Geochemistry of Caliche in Desert Soils

The mineralogy of caliche at selected sites in the southwestern U.S. are compared to the world averages in Table 2. The two most common chemical constituents of caliche in southwestern alluvial basins are calcium carbonate ($CaCO_3$) and silica (SiO_2); commonly, ninety-five percent of caliche is calcium carbonate and silica. The remaining chemical constituents are MgO, Al_2O_3, and Fe_2O_3. Of primary concern to this study is the origin and accumulation of calcium carbonate in unconsolidated alluvium and desert soils.

In a detailed study of the chemical characteristics of caliches sampled throughout the world, Goudie (1972) concluded:

(a) Microcrystalline calcite is the major mineralogical form of the $CaCO_3$.

(b) Silica content is usually greater than 10%.

(c) Dolomite (magnesium carbonate) is not common to caliche.

(d) Gypsum may be concentrated in high percentages locally, but is not regionally significant.

(e) Clay minerals occur in small fractions as sepiolite and palygorskite. Chemical analyses are planned for samples collected during this research and will be compared with Goudie's findings.

Many physical properties of desert soils and alluvium are dependent on the amount of calcium carbonate accumulation (to be discussed later). The addition of calcium carbonate to desert soils is influenced by the solubility of $CaCO_3$ and factors which affect the solubility. Those variables which increase or decrease the solubility of $CaCO_3$ are listed below:

Variable	Influence
Temperature (T)	Higher values of T decrease $CaCO_3$ solubility; $CaCO_3$ precipitation occurs.
CO_2 Partial Pressure (P_{CO_2})	Lower P_{CO_2} decreases solubility, increased precipitation of $CaCO_3$ occurs.
PH	Increase PH causes $CaCO_3$ precipitation
percent clay in material	$CaCO_3$ formation in the presence of of clay results in a more soluble form of calcium carbonate than calcite.

Location	Chemical Constituent in Percentage						
	$CaCO_3$	CaO	SiO_2	MgO	Al_2O_3	Fe_2O_3	CO_2
World Mean Comparison	79.3	42.6	12.3	3.1	2.1	2.0	---
High Plains New Mexico	81.3	45.6	14.3	0.3	1.0	0.7	35.7
High Plains Texas	71.8	40.2	22.3	0.1	0.4	0.4	31.6
Southern Arizona	78.3	---	-----	---	---	---	---

Table 2: Chemical Analyzes of Caliche at selected sites in the Southwestern U.S. as compared to world mean. Data taken from Aristarian (1969) and Goudie (1972).

The influence of temperature on calcium carbonate solubility is illustrated by recent work of Lattman (1975). Alluvium composed of basic igneous rock detritus has higher diurnal temperatures as compared to alluvium composed of acid igneous detritus. Under higher temperatures the $CaCO_3$ is less soluble and may precipitate. Alluvium composed of basic igneous detritus have higher temperatures which favors precipitation of $CaCO_3$ more readily than acid igneous detritus. Additional data to support this hypothesis is available from thermal IR imagery studies of acid and basic igneous bedrock. Well developed caliche is quite common to basalt flows but is not well developed on rocks of granitic composition. IR imagery illustrates that diurnal temperatures on basalt flows are higher than on more acidic rocks. Additionally, cracks and fissures in the basalt act as blackbody cavities and radiate heat through the night. Such conditions are favorable for calcium carbonate precipitation, and may explain why: (1) thick caliches are commonly found on basic igneous rocks and detritus, and (2) calcium carbonate filled veins in basaltic bedrock.

Olsen and Watanabe (1959) cautioned that the relationship of P_{CO_2} to calcite solubility doesn't necessarily apply to calcareous soils. Their research illustrated that calcium carbonate was more soluble in soils than pure calcite under constant P_{CO_2}. The precipitation of $CaCO_3$ in clayey alluvium results in a more soluble form of $CaCO_3$ than calcite. The presence of clay in a medium also resulted in higher concentrations of Ca^{++} and HCO_3^- and higher values of pH (Olsen and Watanabe, 1959). The exact form of the calcium carbonate in the soil is unknown, but less stable forms of $CaCO_3$ (such as vaterite) are known to occur in the presence of Mg^{++}, Ca^{++}, and organic matter. More soluble phases of calcium carbonate in the presence of clay may explain, in part, the lower $CaCO_3$ accumulations in nongravelly materials as described by Gile et al (1966). More soluble $CaCO_3$ can be carried down further in the soil profile and can be disseminated over a greater vertical distance. Thus, longer time periods are necessary for nongravelly (fine-grained) materials to develop thick calcium carbonate horizons. Note that fine grained material includes very fine sand and smaller diameters; whereas, coarse grained material includes fine sand and larger diameters.

2. Effect of Calcium Carbonate Cementation on Desert Soil Properties

Caliche is a natural cementing agent in desert soils and alluvium. The major effect of caliche development is the induration of previously unconsolidated alluvium and binding clasts into particle sized larger than the in situ grain size. The amount of calcium carbonate accumulation and induration increases with time. Thus, older desert soils, given the proper conditions, will be better cemented by calcium carbonate than younger desert soils. This relationship is shown in Figures 1 and 2, which illustrate soil-geomorphic relationships in southwestern Arizona. The soils with calcium carbonate accumulation, calciorthids and paleorthids, occur closest to the mountain front on the highest and oldest alluvial fan surfaces, or on the coarse-grained alluvial fan deposits. (Figure 1 and 2)

The physical properties of soils and unconsolidated alluvium change with increasing amounts of calcium carbonate; therefore, the physical

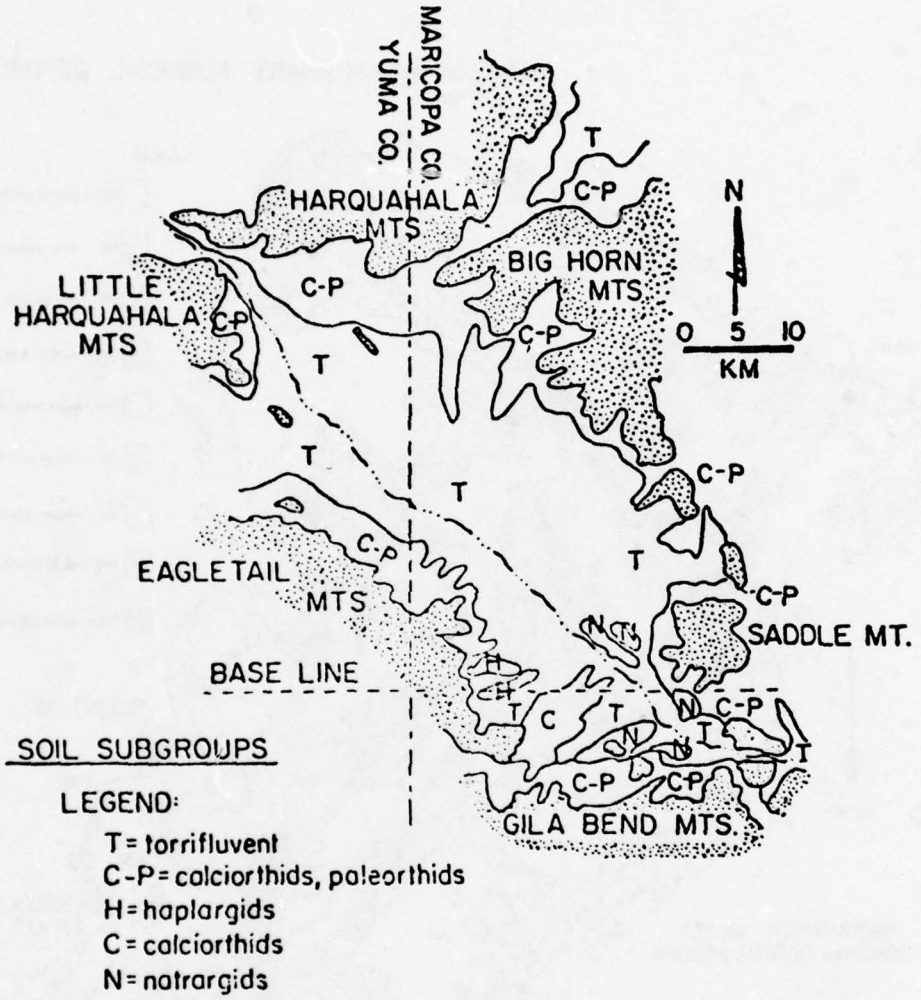


Figure 1. Soils of a typical alluvial basin in Southwestern Arizona (Wells, 1976), Soil nomenclature: torrifluvent = young poorly developed soils in hot alluvium, calciorthids, and paleorthids = desert soils with calcium carbonate accumulation; haplargids and natrargids = alkaline or saline soils with argillic B horizon.

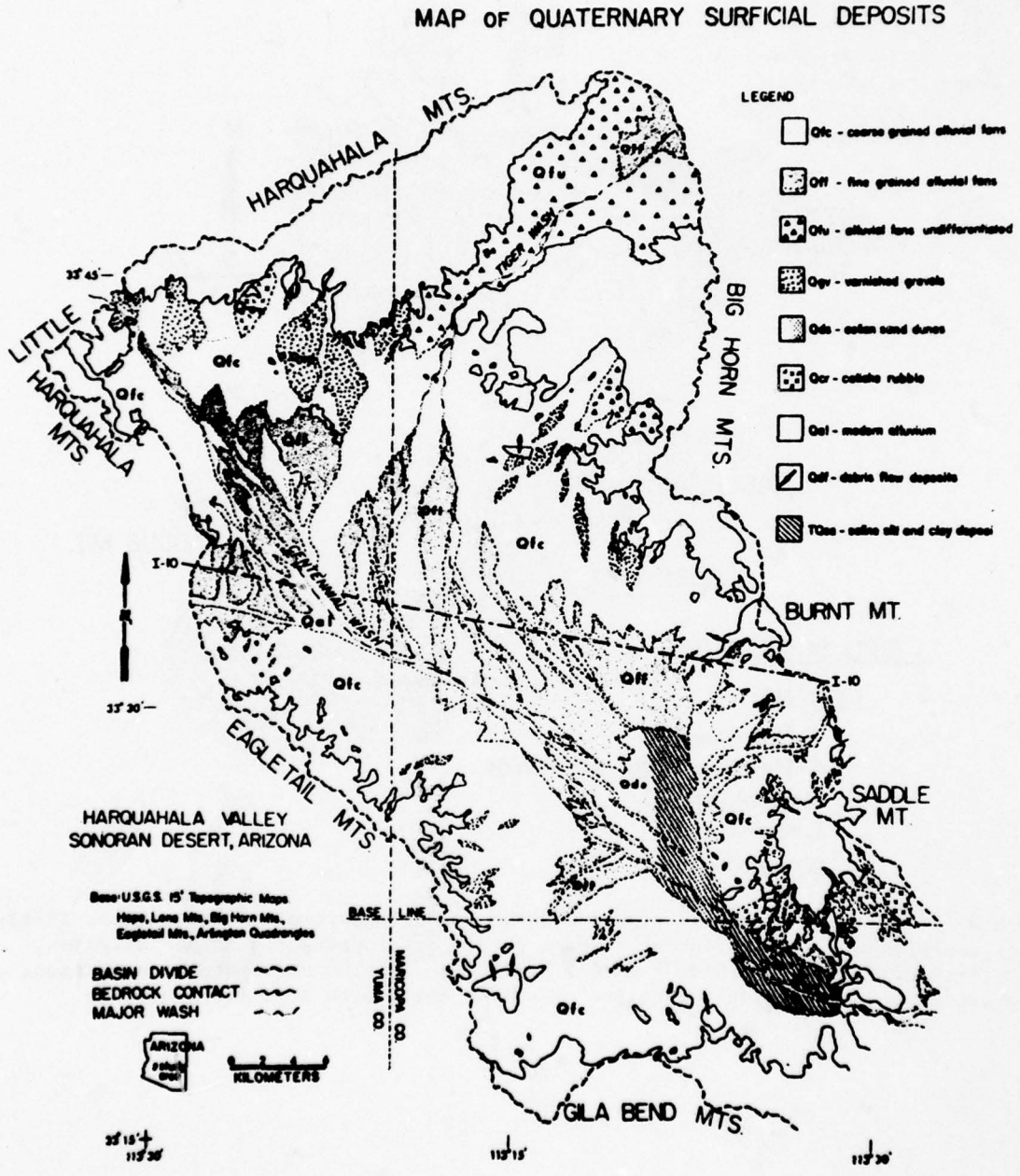


Figure 2. Quaternary surficial deposits in alluvial basin of Arizona. Note that 1 meter thick petrocalcic horizons underlie the caliche rubble deposits. (Wells, 1976).

properties of the soils will vary with their age. Commonly younger soils, such as torrifluvents, are poorly indurated with slight $CaCO_3$ cementation. These soils commonly occur in the axial portions of the desert basins of the Southwest (Fig. 1). Well-indurated and well-cemented paleorthids are older soils and occur marginal to the mountain fronts (Fig. 1). The complex relationship between these soil types is illustrated in Figure and causes of soil boundaries in arid regions is discussed by Gile (1974). It is important to understand that the amount of $CaCO_3$ cementation and the soil properties vary spatially (across desert basins) as well as with time.

A. Compressive Strength of Calcium Carbonate Cemented Materials

Gile (1961) determined that the compressive strength of soils (both air dry and moist) increases logarithmically with increasing calcium carbonate content according to the equation: Log Y = 2.10 + 0.18X where r = 0.78 Y = compressive strength, X = percent carbonate, r = Correlation coefficient at the 1% level. Compressive strength measurements by Gile ranged from 85 to 7880 psi on air dried samples and from 3 to 5430 psi on moist samples. The mean values of the compressive strength for non-indurated, air dried samples is 12 times the mean of indurated caliche. Additionally, moist-compressive strength of petrocalcic horizons average approximately 8 times higher than air-dried calcic, or poorly indurated, horizons. Laminar layers, which have the highest relative percent of calcium carbonate compared to other caliche types, have compressive strengths similar to concrete (Gile, 1961).

B. Bulk Densities of Caliche

Measurements of bulk densities, specific gravity of caliches are sparse. Gile (1961) and Netterberg (1971) have made measurements for caliches in New Mexico and South Africa, respectively. Their results are discussed below:

The range in values of bulk densities for caliche in southeastern New Mexico is 1.3 to 2.2 g/cm^3. The bulk density of soils increases linearly with increasing calcium carbonate content according to the equation: Y = 1.57 + 0.0037 X, where r = 0.58, Y = bulk density, X = carbonate content, r = correlations coefficient at the 1% level. Highest bulk densities are associated with petrocalcic horizons and laminar layers. In South Africa, bulk densities are higher and approximate the values of specific gravity for combined silica and calcium carbonate.

C. Infiltration Rates of Caliche

Detailed studies of water infiltration on caliche horizons have been conducted by Gile (1961) and Cooley et al (1973). Their data and results are discussed below.

The infiltration rate of desert soils decreases with increasing calcium carbonate content and induration. Older soils with well developed caliche, such as paleorthids, have the lowest infiltration rates.

Non-pedogenic caliches, such as gully-bed cementation, will have very low infiltrations too. Laminar layers are essentially impervious zones as their hydraulic conductivities average 1.23×10^{-5} in/min. Fractured caliche horizons would increase the permeability. However, field observations indicate that fracturing of caliche is limited to banks near incised gullies and washes, and that fractures are commonly re-cemented with laminar layer-type material. The permeability of the desert soil is also related to the depth of burial of the caliche horizon as well as how well it is indurated. Infiltration rates are slightly higher for caliches in moister climates as the caliche occurs at greater depths (Fig 8). Additionally, infiltration rates on desert surfaces covered with caliche rubble may be slightly higher in that the upper few centimeters are composed of fragmented caliche and silt. However, caliche will serve as a barrier to downward percolating water, and such barriers result in increased runoff.

The relationship between infiltration rates and the amount of calcium carbonate content has been quantitatively evaluated by Gile (1961). He found the following relation: Log Y = 0.78 - 0.02X, where r = -0.080 Y = infiltration rate, X = percent carbonate, r = correlation coefficent at 1% level.

In summary, the two major variables influencing infiltration rates are calcium carbonate content and depth of caliche in the soil profile. The lower the content and deeper the horizon, the higher the infilitration rate.

D. Property Variations in the Desert Soil Profile

The properties mentioned above will vary within a single profile and with stages of carbonate development. These variations in the soil profile are diagrammatically illustrated in Figure 3. Note that the oldest soils have the greatest variation of properties within the profile. Older soils with more carbonate content have greater compressive strengths and bulk densities and low infiltration rates.

Engineering properties of soils have been discussed by Reeves (1976). Reeves concluded that older soils will have lower values of Linear Shrinkage, Plasticity Index, soluble salt and water absorption than younger soils due increased $CaCO_3$ content. In general, these properties should behave similar to the infiltration rate with increasing depth in the soil (Fig. 3)

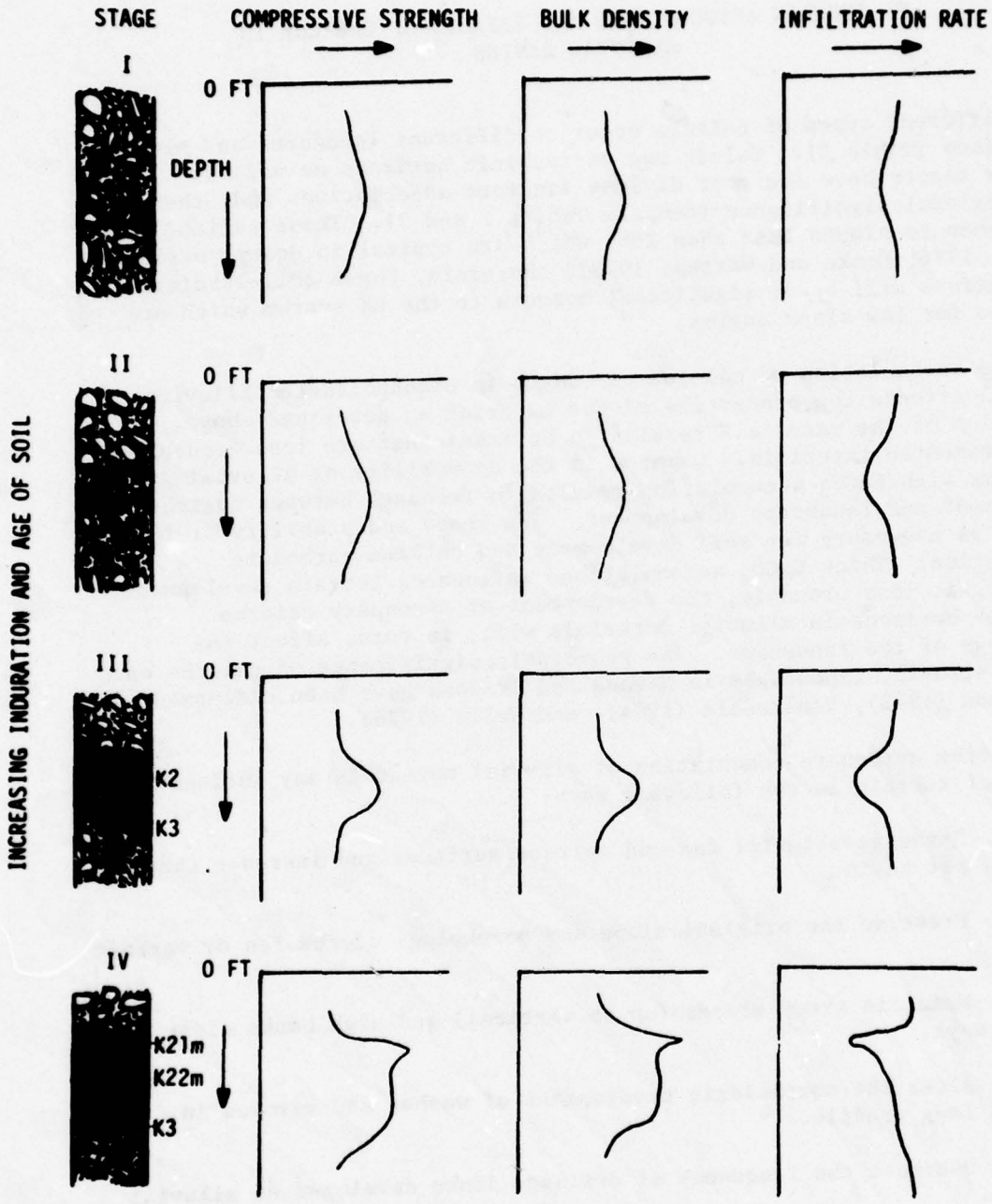


Figure 3. Generalized Variations of Soil Properties Within Soil Profiles of Different Ages. STAGES I-IV Carbonate Development Adapted from Gile et al., 1966

TERRAIN ASSOCIATIONS AND EFFECTS OF CALICHE IN ALLUVIAL BASINS

Different types of caliche occur on different landforms and slope conditions (Table 3). Calcic and petrocalcic horizons as well as laminar layers have the most diverse landform associations and, therefore, have regional significance (Compare Tables 1 and 3). These caliche types are common to slopes less than 10^{o}, which are typical in desert basins (Wells, 1976; Cooke and Warren, 1973); therefore, these soil-landform associations will be of significant concern to the MX system which are designed for low slope angles.

The accumulation of calcium carbonate in unconsolidated alluvium and soil affects the properties of the material as described above. Induration of the materials results in horizons that are less erodable than uncemented materials. Changes in the erodibility of alluvial landforms with $CaCO_3$ accumulation results in feedback between caliche development and landscape development. The shape and stability of the terrain is necessary for soil development and calcium carbonate accumulation. Thick $CaCO_3$ accumulations influences terrain development by making it less erodable, the development of secondary calcium carbonate horizons in alluvial materials will, in turn, affect the morphology of the landscape. The geomorphic significance of caliche on desert, alluvial landscapes in Nevada and Arizona have been discussed by Lattman (1973), VanArsdale (1974), and Wells (1976).

Calcium carbonate cementation of alluvial materials may influence the desert terrain in the following ways:

(1) Preserve alluvial fan and terrace surfaces and increase their frequency per basin.

(2) Preserve the original slope and morphology of the fan or terrace surface.

(3) Maintain steep slopes (up to vertical) and high banks along drainage ways.

(4) Alter the morphologic development of washes and arroyos in cross and long profile.

(5) Decrease the frequency of drainage lines developed on alluvial materials.

1. Influence of Caliche on Desert Fluvial Systems

The geomorphic effects of caliche on alluvial fan morphology is described in detail by Lattman (1973). The influence of calcium carbonate sementation on washes and gullies is described by VanArsdale (1974) and Wells (1976).

Table 3. Summary of Terrain Characteristics and Types of $CaCO_3$ Cementation.

TYPE	LANDFORM ASSOCIATION	SLOPE ASSOCIATION*	RANKING IMPACT ON LANDSCAPE+
Calcic Horizon	Alluvial fan, terrace floodplans, playas, piedmont, pediment	Low to Moderate	5
Petrocalcic Horizon	Alluvial fan, terrace, piedmont, peidment	Low	1
Gully-Bed Cementation	Ephemeral washes (beds and lower banks), gullies or rills	Low to Moderate	3
Case-Hardening	Any surface exposure of unconsolidated alluvium or colluvium	Low to Extreme	2
Laminar Layer	Alluvial fan, terrace piedmont, pediment, hillslopes (colluvial or bedrock)	Low to Extreme	4
Caliche Rubble	Abandon alluvial fan surfaces, terraces	Low	6

*Low: $>10^{o}$

Moderate: $>10^{o}$ $>30^{o}$

Extreme: $>30^{o}$

+ Influence or feedback of caliche on landscape development in desert basins

The hydraulic geometry and channel patterns of washes are controlled by caliche horizons that are exposed at the surface. Channels flowing on caliche horizons, and whose banks are composed of uncemented alluvium, will have high width-depth ratios. Additionally, these streams may be braided and/or highly sinuous. Washes incised into caliche, and whose banks are cemented, will have lower width-depth ratios. In these reaches channel infiltration is minimal. Consequently, the discharge of streams which drain areas of caliche should be higher. To test this hypothesis, computed discharge (based on flood marks rather actual flow) is plotted against the drainage area above a given cross-section where discharge measurements were obtained (Fig. 4). Computed discharge and drainage area are related to each other by a power function, and equations describing this relationship are:

Equation 1: $Q_c = 10.4\ A_d^{0.72}$ for watersheds without caliche

Equation 2: $Q_c = 25\ A_d^{0.36}$ for watersheds with caliche

where,

Q_c = computed discharge

A_d = drainage area

r = 0.990 at 5 % level for Equation 1

r = 0.983 at 5 % level for Equation 2

The logarithmic plots of these variables and the regression equations indicate that drainage basins with caliche have higher computed discharges at selected cross-sections than those basins without caliche. The lower slope of the line on the logarithmic plot of discharge and area in basins with caliche rubble indicates that basins larger than 10 km^2 would have lower discharges than basins without caliche rubble. An explanation of this relationship is that drainage basins with caliche rubble are not larger than 10 km^2 in the Harquahala Valley; therefore basins above this size follow the relationship: $Q_c = 10.4\ A_d^{.72}$.

In the reaches confined by the caliche horizons channel sinuosity decreases and straight channel segments occur. After the wash or gully has incised through the cemented horizon, infiltration increases, the width-depth ratio increases, and channel sinuosity increases.

Alluvial fan surfaces, which are heavily cemented and display calcic and petrocalcic horizons as well as laminar layers, promote excessive surface runoff as overland flow (Cooley et al, 1973). In such regions, the drainage texture, or the drainage density and drainage frequency, should be affected by this increase in overland flow. Specifically, fluvial systems developed on caliche should have a coarser texture (fewer surface streams). The Mann-Whitney U is used to test the relationship between drainage density and drainage frequency of watersheds with and without caliche. Results of this statistical test are given in Table 4. It can be seen that drainage density is not statistically different at the 5 % level in basins with and without caliche. However, drainage frequency is statistically different for these two basin types. Drainage basins with caliche have low values of drainage frequency, and are usually less than 16 (Table 4).

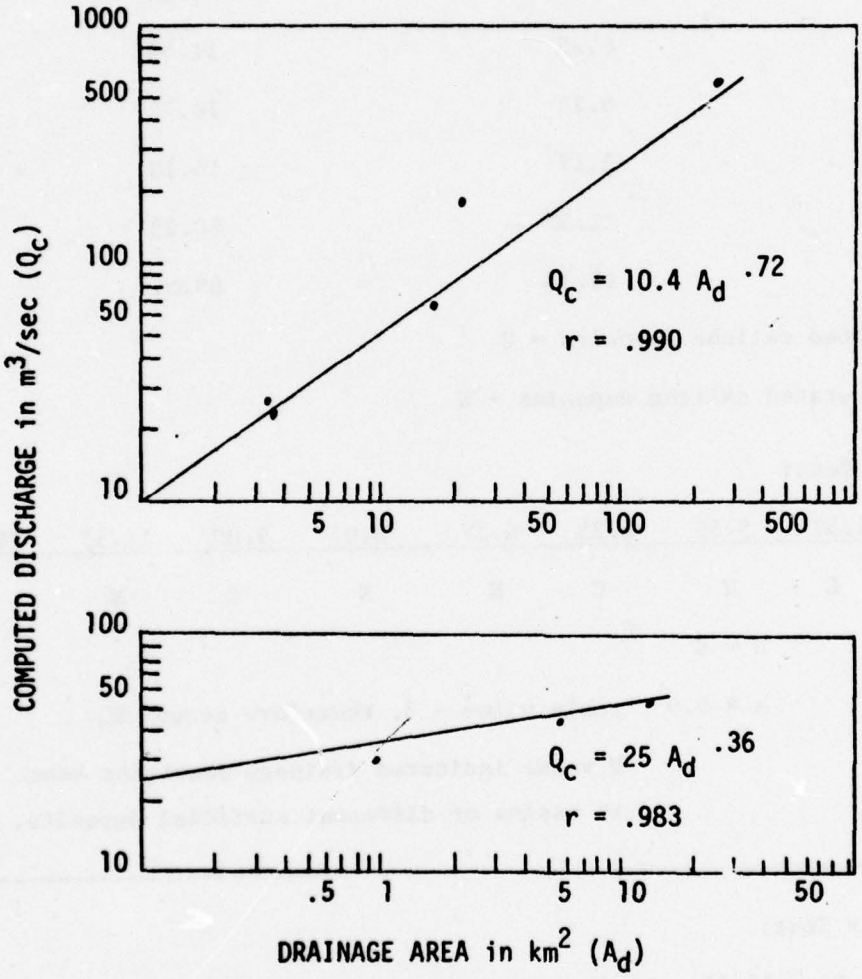


Figure 4. Computed discharge of desert stream at selected cross-section compared to drainage area above that cross-section for weathersides without (A) and with (B) caliche horizons.

Table 4. Mann-Whitney U Test for Relationship of Drainage Denisty and Drainage Frequency of Desert Drainage Basins with and without indurated caliche

Drainage Basin	Drainage Density	Drainage Frequency
IMQ-C	5.35	16.14
IMQ-D	8.01	23.35
CPQ-A	4.57	11.11
CPQ-B	3.40	4.16
CPQ-C	9.00	23.30
CPQ-D	6.25	11.54
BHMQ-A	6.27	16.72
BHMQ-B	3.17	16.10
EMQ-A	11.57	50.23
EMQ-B	19.33	69.57

basin with indurated caliche deposits = C

basin without indurated caliche deposits = N

Drainage Denisty Test:

3.17	3.40	4.57	5.35	6.25	6.27	8.01	9.00	11.57	19.33
N	C	C	N	C	N	N	C	N	N

n_2 = C = 4 U = 8

n_1 = N = 6 α = 0.05 table value - 3, therefore accept H_o.

U value indicated drainage densities same in basins of different surficial deposits.

Drainage Frequency Test:

4.16	11.11	11.54	16.10	16.14	16.72	23.30	23.35	50.23	69.57
C	C	C	N	N	N	C	N	N	N

n_2 = C = 4 U = 3

n_1 = N = 6 α = 0.05 table value - 3, therefore reject H_o.

U value indicates drainage frequency different in basins of different surficial deposits.

APPLICATION OF CALICHE STUDIES TO MULTIPLE AIM POINT MISSILE SYSTEM(MX)

Cementation of alluvial material in SW United States valleys affects siting of MX missile systems in two ways: its influence on Nuclear Weapons Effects (NWE), and on construction of facilities. Since alluvial valleys are so varied in the types and sizes of alluvium filling them, the prediction of the occurrence of cementation and subsequent understanding of their response to an NWE environment will greatly enhance the survivability of a system.

As regards NWE, better knowledge of caliche occurrence, as well as its areal extent, abundance or lack of, and distribution with depth will aid in predicting (1) crater size, (2) amount and size of ejecta, and (3) the shock propagation that radiates out from the detonation point. All three effects need to be better understood to design the MX system to a stated level of survivability. For example, loose, uncemented alluvium would yield a larger crater than in alluvium that was massively cemented for a total sequence in the crater region and approaching rock characteristics. Caliche cemented alluvium produces a more competent media for cratering which results in reduced ejecta, according to a proportionality factor in relation to a smaller crater size associated with more massive cementation. Massive cementation also influences the size of ejecta that will occur. Loose, minimally indurated alluvium will produce ejecta no larger than the in-situ size materials. With caliche cementing the material together, ejecta size will increase dramatically, especially with the best cemented mateiral, material approaching concrete with large aggregate as a matrix. (Note that a buried cemented layer under loose alluvium acts differently than would a massively cemented section as described previously.) A buried massively cemented alluvial layer will influence the aspect ration, (Ra/Da) ratio of [apparent crater radius/depth of apparent crater], of cratering when it imposes an impedance mismatch between the loose alluvium and cemented alluvium interface. If loose alluvium overlies an old massively cemented zone, the cratering mechanism will tend to bottom out at the resistant layer, and the aspect ratio may be expected to increase with a corresponding increase in the amount of ejecta.

Another NWE effect that is of concern is the attenuation of ground shock propagation. In loose medium, the bulk density is low, as compared with highly indurated caliche bearing alluvium. As the overall density and competency of the alluvium increases so does its ability to transmit strong motion seismic shock waves to greater distances. Peak particle velocity, scaled peak displacement, and scaled peak acceleration may all be expected to be higher for highly indurated alluvium than uncemented "loose" material, Crawford et al., 1974. Depending on the types of seismic signal that may be propagated through the alluvium, controlled by cementation, a strategic facility will need to be designed to survive varying degrees and modes of seismic wave velocity acceleration, frequency and amplitude.

Engineering Properties

Besides the NWE concerns of caliche, the engineering properties of alluvium altered by cementation is important. The initial cost of constructing an MX facility will depend to a large extent on the ease of excavation for a foundation or, in the case of the trench concept, a 14' wide by 20' deep x 11 mi trench. An increase of caliche cementing the alluvium will make excavation more difficult and time-consuming which will drive cost up substantially.

Once the facility is built, there will be an overburden of soil, one to two feet thick. If an area has extensive cementation in situ then there is reason to be concerned that once the overburden is backfilled over and around the structure that re-cementation of the soil will take place rapidly. This could degrade the egress ability of the missile substantially (the missile container must break through the roof of the tunnel and overburden for egress) since a cemented soil would be much more difficult to punch through than to loose backfilled soil.

Calcium carbonate cementation of the soil alluvium will also influence the hazards of flooding. A loose soil will readily infiltrate run-off water while soils that have pedogenic cement will resist infiltration (Figure 3) and increase the likelyhood of flooding. Another non-pedogenic carbonate cement, gully bed cementation is another form of cement that lines the gully beds of washes and prevents infiltration of flood waters. Therefore where gully bed cementation is prevelant, as in parts of Nevada, flood waters from the mountains can be channeled far down the slopes and endanger a structure housing strategic missiles.

For the most part caliche cementation of alluvium can only complicate the problems associated with MX structures. This is true both in NWE and the engineering properties.

QUALITATIVE METHODS FOR PREDICTION OF CALICHE IN ALLUVIAL BASINS OF THE SOUTHWESTERN UNITED STATES

1. Buried Calcium Carbonate Cemented Material

Six types of caliche have been delineated and discussed above. Of these six types, calcic and petrocalcic horizons are the most significant, and both form by pedogenic processes. The major factors influencing soil development are:

Time	- Independent Variable
Climate	- Independent Variable
Parent Materials	- Independent Variable
Topography	- Independent Variable
Vegetation	- Dependent Variable

Work by Gile and others (1961) and Lattman (1973) have found that development of caliche is influenced by three basic factors which are related to the variables given above:

Composition and texture of alluvial materials	- parent materials
Availibility of $CaCO_3$ as fine sediment	- parent materials climate topography
Age of geomorphic surface developed on alluvium	- time topography

Field results during this study indicate that a high availibility of $CaCO_3$ fines does not always result in the presence of caliche. In alluvium of similar composition and texture and similar $CaCO_3$ source conditions, one side of the Tularosa Basin, New Mexico had cementation while the other did not show cementation. Either the age of the surfaces are dramatically different, or another variable is influencing the processes of $CaCO_3$ accumulation. It is suggested that stability of the geomorphic surface, or rates of erosion and aggradation, is also important to calcium carbonate accumulation. Unless the surface remains stable for a long enough period for soil development, calcic and petrocalcic horizons will not develop. This factor is not important to the development of non-pedogenic caliches such as gully-bed cementation and certain types of laminar layers.

Of these four basic factors, specific conditions in each one exist which are favorable for calcium carbonate cementation. These conditions are discussed below:

A. Conditions Favorable to Calcium Carbonate Cementation

Availability of $CaCO_3$ Fines

It is well documented that well developed carbonate horizons in soil profiles are developed on alluvium consisting of a $CaCO_3$-source or the $CaCO_3$ has been transported by eolian processes to the alluvium and re-worked into the soil profile. Thus, areas with calcium carbonate sources in the bedrock, which can be re-worked into eolian fines, are susceptible to $CaCO_3$ accumulation and cementation.

The amount of calcium carbonate in eolian dust is summarized in Table 5 for the US and Middle East. Samples of eolian sand collected on the downwind side of an active playa are analyzed for grain size distribution and acid-soluble materials (Figures 5 and 6). In this medium to fine sand, the coarser fraction of the grain size distribution had the largest concentrations of acid-soluble materials (calcium carbonate) (Fig. 6). Nearly 55% of the grains with diameters of 9.52 mm were acid-soluble materials.

Alluvial material downwind from sources of $CaCO_3$ are commonly the most heavily cemented (Lattman, 1971; Purcell, 1973). Additionally, studies in Arizona indicate similar results where alluvial fans downwind from calcerous sand dunes are heavily cemented (Fig 2). (Wells, 1976). An additional source of calcium carbonate cementation related to external sources (as opposed to in situ) is rainfall. Goudie (1973) summarized the Ca^{++} content in rainwater, and concentrations ranged from 0.7 to 63.6.

Texture and Composition of Alluvial Materials

The size and sorting of alluvium is an important factor controlling the degree of calcium carbonate cementation (Lattman, 1971 and 1973). Coarser grained material have better developed caliche layers. It is noted that $CaCO_3$ accumulates more readily on larger clasts, although the detailed mechanics are not fully understood. Additionally, poorly sorted materials have better caliche development as there is less pore space, or void space, to fill with calcium carbonate.

Lattman has found that the composition of the alluvial materials is another important factor controlling the degree of cementation. Obviously, clastic materials composed of limestone and other types of carbonate are readily dissolved and $CaCO_3$ is re-precipitated as caliche. However, in both Arizona and Nevada, materials composed of basic igneous rocks have the highest degree of cementation. In addition to the effects of temperature on calcium carbonate precipitation (See section above), Lattman has suggested that the release of calcium from weathering of calcic feldspars is another factor. The decrease in calcium oxide in various weathered basic igneous rocks suggests this process may be valid (Fig. 7).

Table 5. CALCIUM CARBONATE PERCENTAGE OF EOLIAN DUST

LOCATION	PERCENT $CaCO_3$	REFERENCE
Texas	5 to 20	Warn & Cox, 1951
Kansas	Up to 6	Swineford & Frye, 1951
Nevada	25 to 27	Kaplan, 1973
Israel	5 to 30	Ginzbourg & Yaalon, 1963
Sahara	1 to 16	Junge, 1958
	PERCENT CaO	
Iowa	∿2	Bennett, 1939
Kansas	∿3	Bennett, 1939

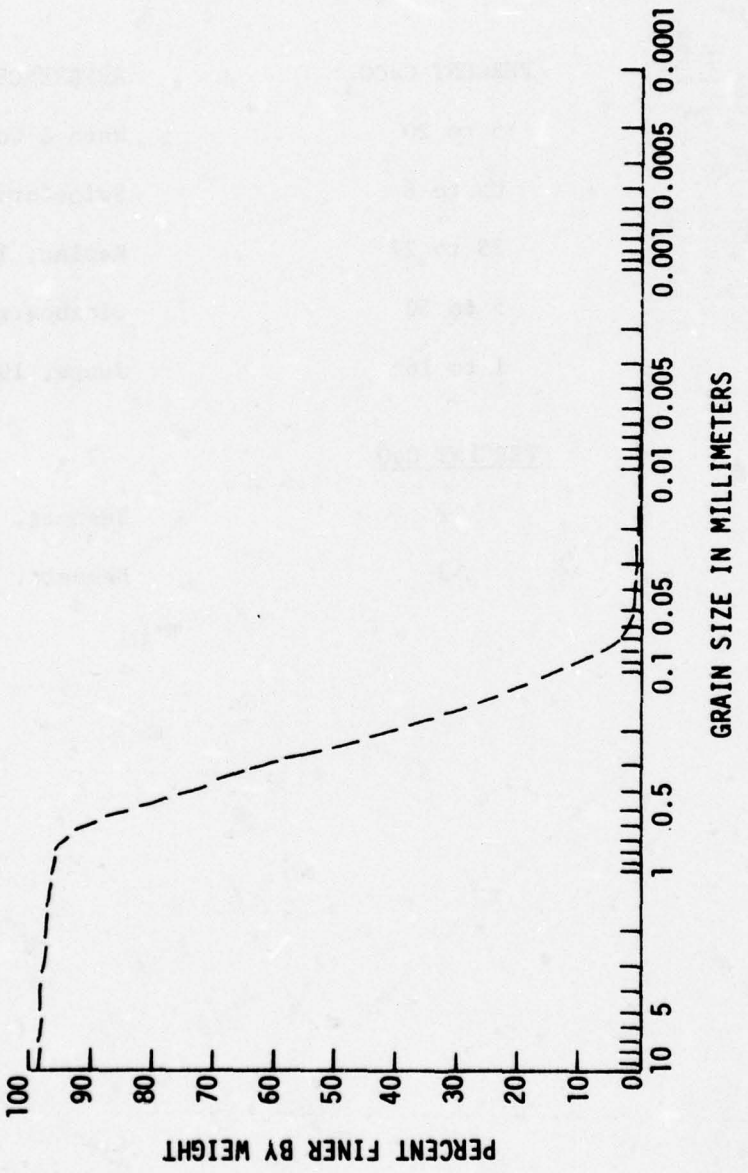


Figure 5. Grain size distrubition of eolian sediment derived from a playa in Southeastern Nevada.

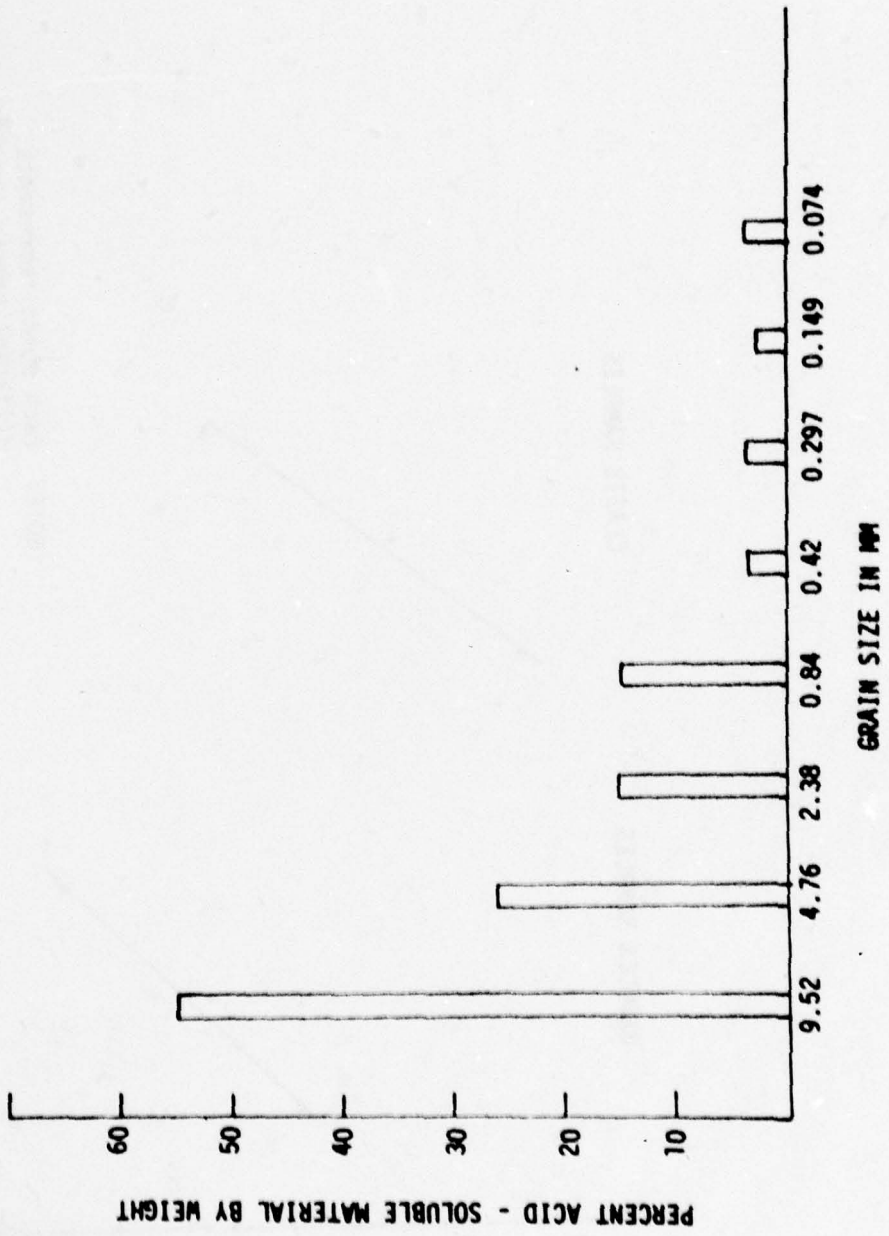


Figure 6. Histogram illustrating percent acid-soluble material in various grain sizes of eolian transported sediment.

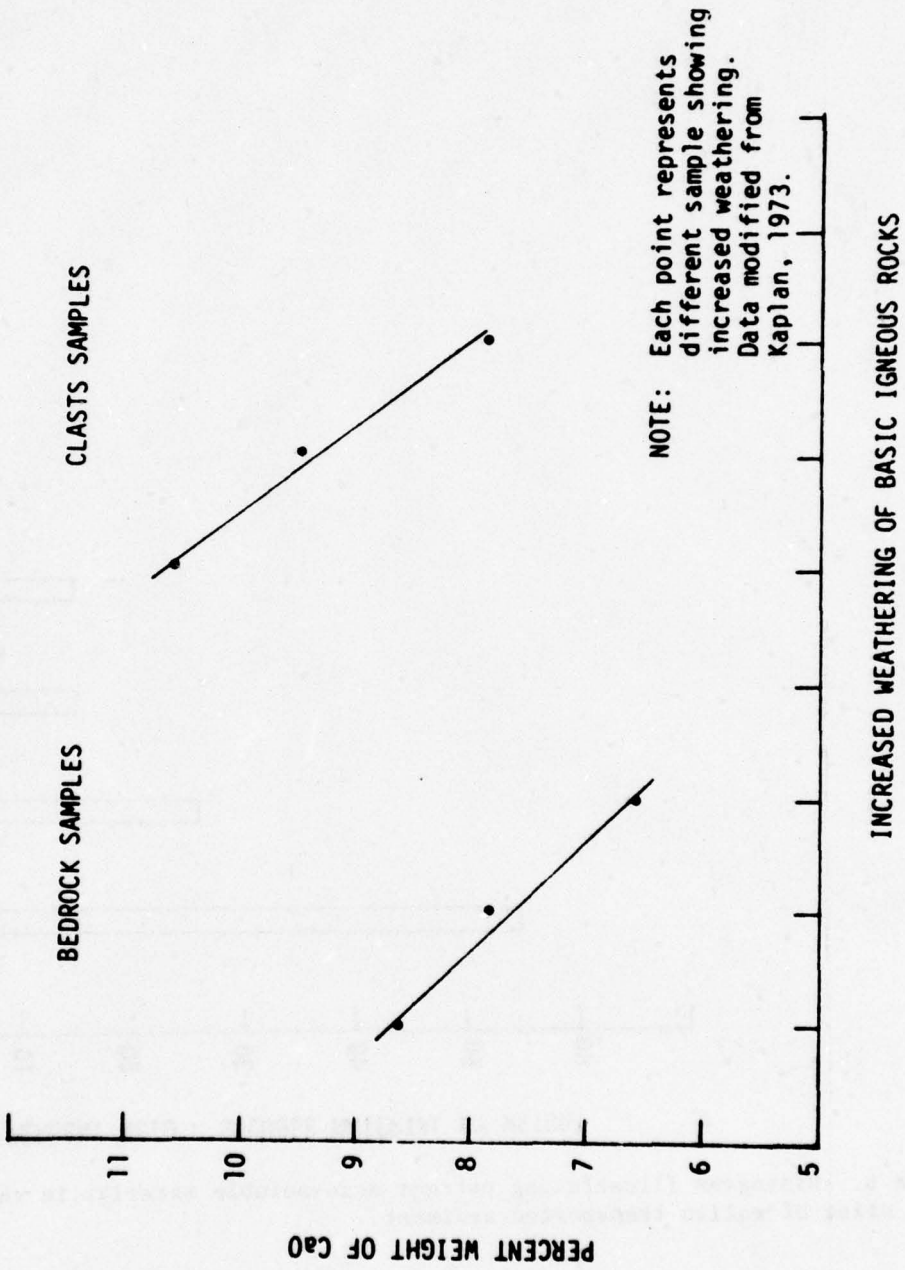


Figure 7. Relationship between percent weight of CaO and various stages of weathering on andesite bedrock and clasts.

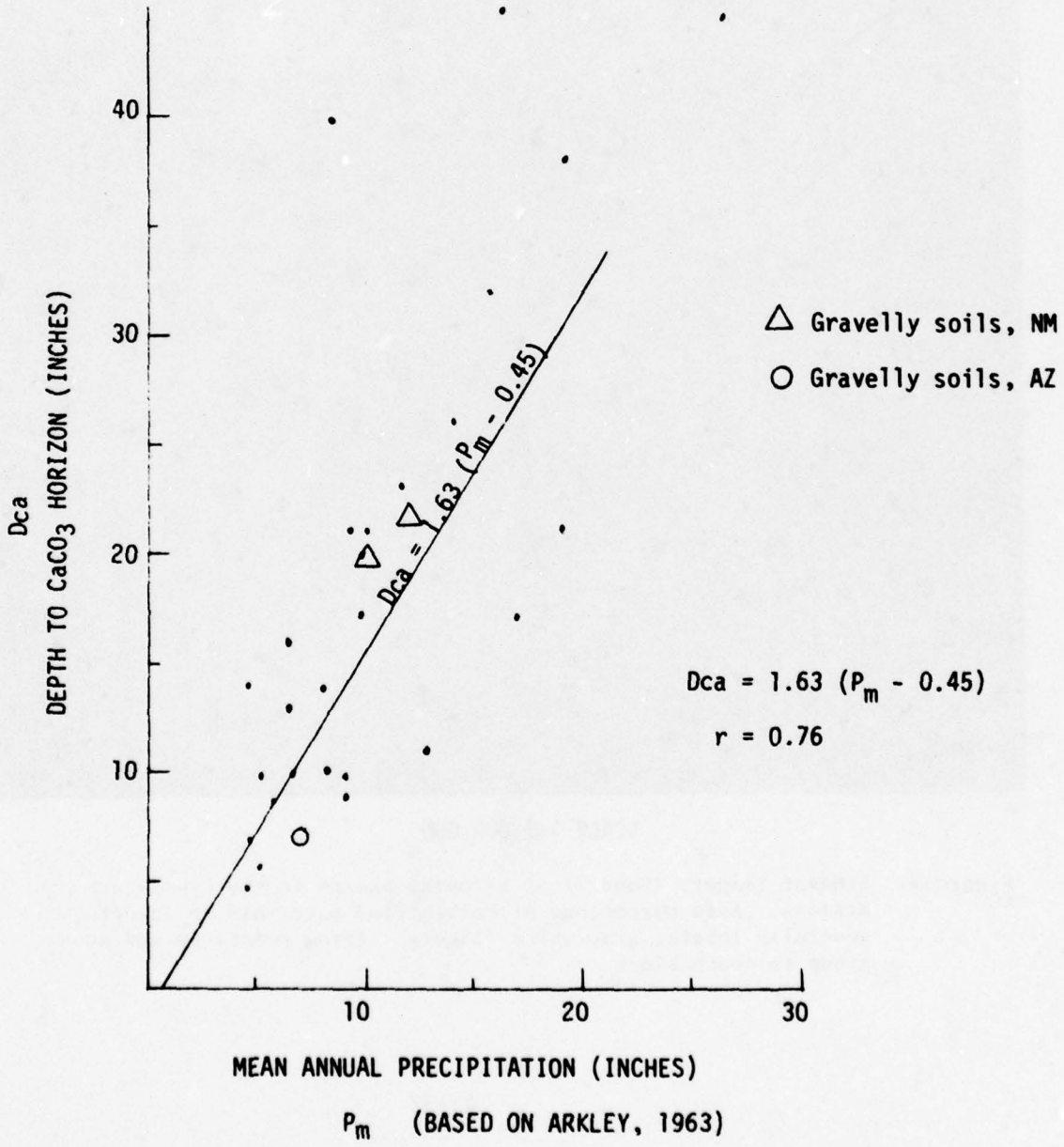
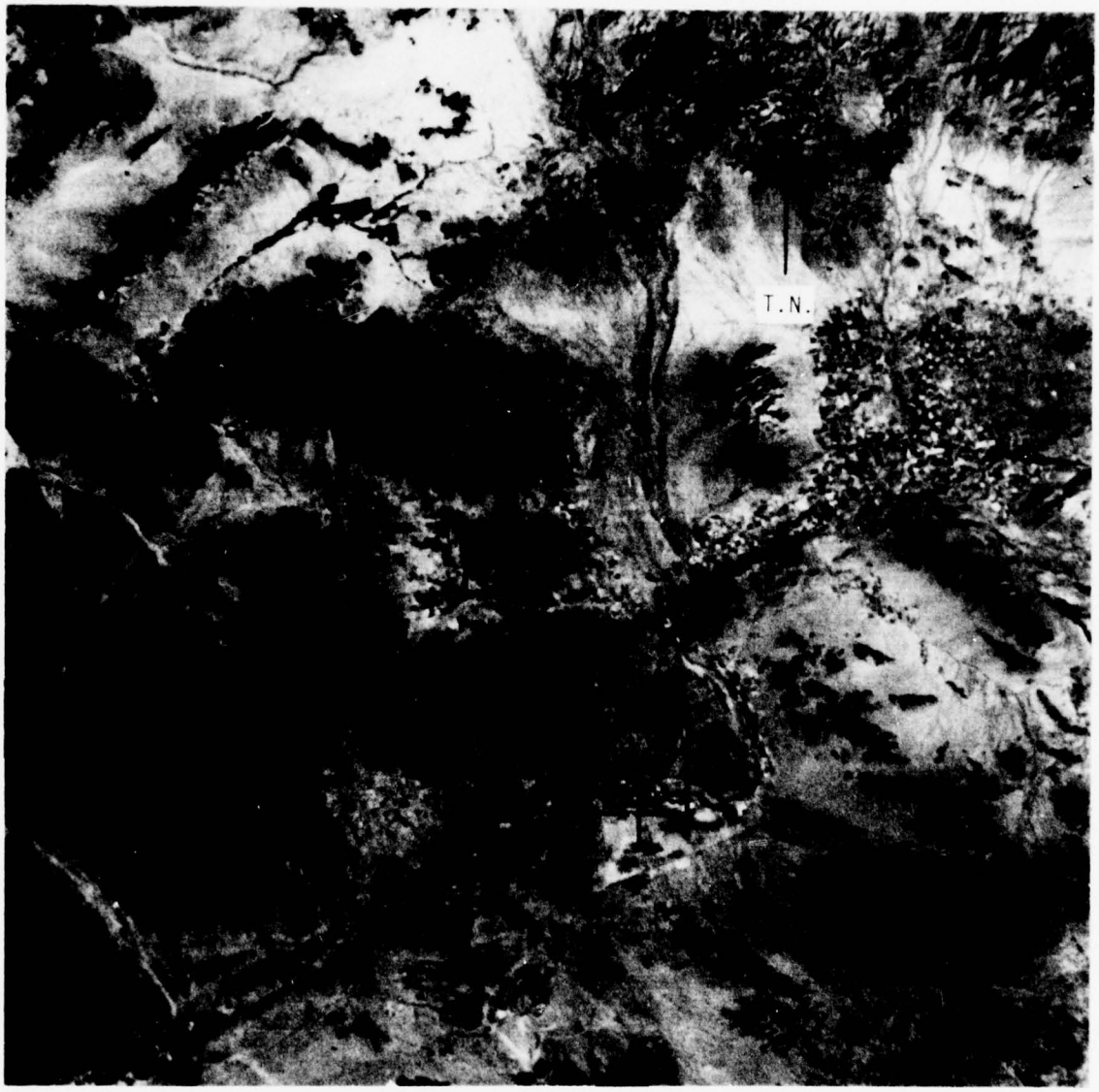


Figure 8. Linear relationship between depth to caliche and mean annual precipitation.



SCALE 1:1,000,000

Figure 9. Landsat imagery (Band 7) of alluvial basins in southwestern Arizona. Note morphology of calichified materials in inserts, generally lobate, gray-white fingers. Arrow points to one such group in south block.

Age of Geomorphic Surface

It has been shown in the previous discussions that the degree of calcium carbonate cementation increases with age; therefore, no further discussion is included. However, Lattman (1975) warns that not all caliche cements older alluvial materials. Non-pedogenic caliches, such as laminar layers, may form on relatively recent topographic surfaces.

Other Factors

Both in Nevada and in Arizona, thick and well-indurated caliche is found associated with gypsiferous deposits (Lattman, 1975; Wells, 1976). Conversion of gypsum to calcium carbonate by sulphate-reducing bacteria has been documented by lab experiments (Lattman and Lauffenberger, 1974).

Predictability of Caliche Depth

Under the conditions described both soil and non-pedogenic caliche may develop. However, to ascertain how deep in the soil calcic or petrocalcic horizons develop, the depth of leaching rainfall relationship found by Arkley (1963) can be utilized. For buried caliches a significant correlation has been found between depth to the soil-caliche (Dca) and mean annual precipitation (Pm) (Table 6). Arkley found that with increasing moisture, the calcium carbonate would be carried deeper through the soil profile, as the depth of leaching increases. A linear equation developed by Arkley appears to be a quantitative tool to detect depth to caliche in the soil;

$$Dca = 1.63 (Pm - 0.45) \quad r = 0.76$$

Dca = depth to caliche

Pm = mean annual precipitation

Data collected in New Mexico and Arizona follows this relationship (Fig 8).

TABLE 6. SPEARMAN RANK CORRELATION COEFFECIENT, r_s

X = MEAN ANNUAL PRECIPITATION
Y = DEPTH TO $CaCO_3$ HORIZON
N = 24

		RANK			
X	Y	X	Y	d_i	d_i^2
5.09	5.68	3	1	2	4
4.67	6.81	2	2	0	0
5.68	8.68	5	3	2	4
5.10	9.82	4	6	-2	4
6.67	9.91	8	7	1	1
8.09	10.01	10	8	2	4
9.02	9.82	12	5	7	49
8.98	8.86	11	4	7	49
12.67	10.94	18	9	9	81
7.93	13.85	9	11	-2	4
6.33	12.96	7	10	-3	9
4.49	13.99	1	12	-11	121
6.30	15.99	6	13	-7	49
9.63	17.12	14	14	0	0
16.84	17.13	22	15	7	49
9.75	19.98	15	16	-1	1
9.17	21.12	13	18	-5	25
9.95	21.09	16	17	-1	1
18.89	21.19	23	19	4	16
11.60	23.09	17	20	-3	9
13.91	26.02	19	21	-2	4
15.57	32.00	20	22	-2	4
18.95	38.07	24	23	1	1
16.11	45.21	21	24	-3	9

TOTAL $d_i^2 = 498$

$$r_s = 1 - \frac{[6\Sigma d_i^2]}{N^3 - N} \quad \text{then } r_s = 1 - \left[\frac{2988}{(13824-24)}\right] = 1 - .22$$

$$r_s = 0.78$$

Critical values of r_s, where N = 24, at $\alpha = 0.01$: 0.485

Thus $r_s > 0.485$ and is significant at the 0.01 level.

2. Subaerial Calcium Carbonate Cemented Materials

Erosional processes in alluvial basins may expose previously buried caliche horizons. Caliche horizons on such erosional surfaces may be subjected to mechanical breakup and may develop a thin layer of caliche rubble and silt. Since caliche is white to light buff in color, alluvial material containing caliche should have lighter tones.

Caliche when exposed to the surface has a dramatic effect on the landscape morphology as described above. Both of these variables, light-tonal appearance and geomorphic effect, enhance the use of satellite, or airborne, imagery for caliche detection.

A. Evaluation of Satellite Imagery for Caliche Detection

Recent studies of the southwestern United States have found aerial imagery to be a useful tool for identifying calichified alluvial surfaces in Nevada basins (Lattman, 1971; Lenhart, 1974). Lenhart (1974) used two techniques, the ration and contrast methods, to quantitatively evaluate the differences in the density of calichified and non-calichified alluvial surfaces. He found the contrast method to be the optimum technique to separate these fan surfaces, Wells (1976), using a modified contrast method, evaluated density differences among various types of surficial deposits in desert basins of Arizona. The Arizona study differs from the Nevada study, in that multiple frames were used in Nevada as compared to single frame in Arizona. Additionally, both black and white MSS Band 7 and color infrared composites of Bands 4,5, and 7 were used for the Arizona study as compared to the black and white Band 7 in Nevada.

The results of the imagery study for Arizona are given in Tables 7 and 8, and are described below:

(1) The mean of the image density for both calichified and non-calichified surfaces are nearly the same, 0.67 and 0.69 respectively.

(2) The variance of the image density for calichified surfaces is greater (7.2×10^{-3}) than for non-calichified surfaces (3.6×10^{-3}). These results support the work in Nevada by Lenhart.

(3) Calichified surfaces are not statistically different from uncemented coarse grained alluvial fans. Lenhard (1974) was able to separate these deposits on fan surfaces in Nevada.

(4) Calichified surfaces can be differentiated statistically based on image densities from fine grained alluvial fans and varnished gravels.

(5) The morphology of exposed caliche on satellite imagery is characteristically similar in Nevada and Arizona. Calichified surfaces appear as light-toned, finger-like ridges (Fig 9).

Table 7. Variance of Image Densities, Arizona Study.

Calichified Surface			Non-Calichified Surface		
	$x,-\bar{x}$	$(x,-\bar{x})^2 \times 10^3$		$x,-\bar{x}$	$(x,-\bar{x})^2 \times 10^3$
0.63	-.04	1.6	0.66	-0.03	0.9
0.65	-.02	0.4	0.65	- .04	1.6
0.60	-.07	4.9	0.66	- .03	0.9
0.75	.08	6.4	0.75	.06	3.6
0.89	.22	48.4	0.63	- .06	3.6
0.67	0.00	0	0.67	- .02	0.4
0.93	.26	67.6	0.61	- .08	6.4
0.63	-.04	1.6	0.68	- .01	0.1
0.63	-.04	1.6	0.81	0.12	14.4
0.65	-.02	0.4	0.71	.02	0.4
0.67	0	0	0.94	.15	22.5
0.68	.01	0.1	0.72	.03	0.9
0.59	-.08	6.4	0.61	- .08	6.4
0.64	-.03	0.9	0.60	- .09	8.1
0.63	-.04	1.6	0.67	- .02	0.4
0.65	-.02	.4	0.73	.04	1.6
0.75	.08	6.4	0.71	.02	0.4
0.61	-.06	3.6	0.63	- .06	3.6
0.63	-.04	1.6	0.72	.03	0.9
0.68	.01	0.1	0.66	- .03	0.9
0.67	0	0	0.70	.01	0.1
0.64	-.03	0.9	0.70	.01	0.1
0.59	-.08	6.4	0.65	- .04	1.6
Mean: $\bar{X}$=.67		Σ=172.2	$\bar{X}$=.69		Σ 86.5

Variance: $\sigma^2 = 7.2 \times 10^{-3}$ $\sigma^2 = 3.6 \times 10^{-3}$

QUATERNARY SURFICIAL DEPOSIT	DENSITY MEASUREMENTS							
Varnished gravels (Qgv)	0.67	0.69	0.71	0.65	0.64	0.68	0.64	0.61
Fine grained fans (Qff)	0.43	0.39	0.40	0.34	0.37	0.38	0.38	0.31
Coarse grained fans (Qfc)	0.49	0.42	0.44	0.37	0.35	0.47	0.56	0.45
Alluvium (Qal)	0.19	0.27	0.30	0.43	0.30	0.48	0.30	0.28
Caliche rubble (Qcr)	0.45	0.50	0.34	0.33	0.35	0.33	0.37	0.63

Table 8. Density measurements from color composite transparencies of MSS Bands 4,5, and 7 of LANDSAT imagery of alluvial valley in southwestern Arizona. LANDSAT imagery was taken on February 2, 1973.

CONCLUSIONS AND RECOMMENDATIONS

Major conclusions of this study are listed below:

(1) Six major types of caliche are typical to alluvial basins of which calcic and petrocalcic cementation are the most significant. These two carbonate types are soil-caliches and pedogenic processes are therefore significant. Calcic and petrocalcic horizons have the greatest distribution, thickest horizons, and greatest lateral continuity of all six types.

(2) Calcium carbonate and silica are the two most predominant chemical constituents in caliche. Concentration of calcium carbonate is the greatest factor affecting the physical properties of caliche. The concentration of calcium carbonate is influenced by its solubility. Temperature, CO_2 partial pressure, pH, and the presence of clay influence $CaCO_3$ solubility. More soluble phases of calcium carbonate occur in soils than calcite in the presence of clays.

(3) Calcium carbonate cementation is unevenly distributed across alluvial basins. The degree of induration and concentration of caliche is highly variable but commonly the well-indurated caliches occur nearest the mountain front.

(4) Compressive strength of caliche increases logarithmically with increasing carbonate content. Bulk density increases linearly with increasing calcium carbonate content. Infiltration rates decrease with increasing calcium carbonate content. Petrocalcic horizons and laminar layers have the highest compressive strengths and bulk densities and the lowest infiltration rates. These properties not only vary with the distribution of caliche type, but also vary with age of the soil and depth in the soil profile.

(5) Calcium carbonate cementation of alluvial material reduces its erodibility and controls landscape develop. Alluvial basins which display well-developed cementation have multiple fan and terrace surfaces. Case-hardening cements the banks of streams, and gully-bed cementation cements their floors. These and other types of $CaCO_3$ cement reduce the width of channel and increase its depth, and lower channel sinuosity. Infiltration is minimal on caliches resulting in excessive runoff and flooding in regions adjacent caliche. Caliche does not affect the length of stream channels per area (drainage density) but reduce the number of stream channels per area (drainage frequency).

(6) The following conditions are those most favorable for caliche development; areas having these conditions will have well-developed caliche:

(a) Alluvial materials composed of carbonate clasts or clasts derived from basic igneous rocks.

(b) Alluvial materials situated near a source for fine grained $CaCO_3$, such as playas, floodplains, etc.

(c) Alluvium adjacent to or overlying gypsiferous deposits.

(d) Coarse, poorly sorted alluvium with low void space.

(e) Older alluvium or older geomorphic surfaces on which $CaCO_3$ can accumulate with time.

(f) Stable geomorphic surfaces which are not subjected to accelerated erosion and deposition.

(7) Depth to caliche horizons in soil horizons can be predicted by the equation: Dca = 1.63 (Pm-0.45) where Dca is the depth to the caliche horizon and Pm is the mean annual precipitation. The more rainfall then the farther the $CaCO_3$ can be carried down through the soil profile.

(8) Caliches that are shallowly buried or exposed at the surface can be detected by densities contrasts on satellite imagery. Caliche has high variances of image density. Additionally, caliche affects the morphology of the landscape and this may be useful for its detection. Commonly, near-surface caliche areas have drainage densities less than 16 km/km^2. In addition caliche preserves fan surfaces in the shape of finger-like ridges which are light toned.

Recommended Future Work:

It is obvious from the results above that only the most general factors influencing caliche development has been delineated. Although the 4 major factors influencing caliche provide a qualitative approach to predicting areas with $CaCO_3$ cementation, the mechanics, dynamics and chemical behavior of cementation in the field are not fully understood. For example, what is the relative importance of the following variables in controlling atmospheric (eolian) CaCO3 fines?

Particle size of wind blown detritus
Soil erodibility
Surface roughness
Mean annual wind velocity
Length of source area parallel to prevailing wind

All these variables may not be important, but their relative importance has yet been resolved. Thus, the following research procedures are those that would provide detailed process data on caliche development, and such data could be used for a quantitative model

(1) Establish a remote monitoring, or instrumentation system to measure:

(a) Rate of $CaCO_3$ deposition

(b) Wind Velocity and direction

(c) Rainfall amount and intensity, duration of surface wetting

(d) Temperature of surface and up to a depth of 6 inches

(2) Establish these instrumentation station in 3 areas of varying cementation and in 4 areas without cementation.

(3) Conduct laboratory experiments on rates of carbonate cementation under controlled conditions. One could vary composition of material, texture of sampled alluvium, duration amd amount of wetting.

(4) Conducted detailed field studies on caliche characteristics, including variations in thickness, calcium carbonate content, horizontal and vertical relationships between petrocalcic and calcic horizons, textural characteristics, and compositional characteristics.

(5) Use of multi-variant statistics to develop a quantitative model for determining most significant process-variables controlling cementation and for developing a quantitative model to predict not only occurrence but physical properties. Chemical studies will provide data on $CaCO_3$ solubility and content which controls major engineering properties.

REFERENCES

Aristarain, L., 1970, Chemical Analyses of Caliche Profiles from the High Plains, New Mexico: Jour. Geology V. 78, p. 201-212.

Arkley, R.J., 1963, Calculation of Carbonate and a Water Movement in Soil from Climatic Data: Soil Sci. V. 96, p. 239-248.

Cooke, R.U. and Warren A., 1973, Geomorphology in Deserts., Univ. of Calif. Press, Los Angeles, 374 pp.

Cooley, R.L., G.W. Fiero, Jr., L. H. Lattman and A.L. Mindling, 1973, Influence of surface and near-surface caliche distribution on infiltration characteristics and flooding, Las Vegas area, Nevada: Center for Water Resource Research, Desert Research. Inst. Proj. Rept. 21, 41 p.

Crawford, R.E., Higgins, C.J., and Boltmann, E.H., 1974, The Air Force Manaual for Design and Analysis of Hardened Structures: AFWL-TR-74-102, 1118 p.

Gile, L.H., 1961, A Classification of Ca horizons in soils of a desert region, Dona Ana County, New Mexico: Soil Sci. Soc. America Proc. V. 25, p. 52-61.

, 1974, Causes of Soil Boundaries in an Arid Region: I. Age and Parent Materials. Soil Sci Soc. Am Proc. Vol 39, p. 316-330

, F.F. Peterson and R.B. Grossman, 1965a, The K horizon: A Master Soil Horizon of Carbonate Accumulation: Soil Science, V. 99, p. 74-82.

Goudie A.S., 1972, The Chemistry of World Calcrete Deposits: Jou. Geology, V. 80, p. 449-463

, 1973, Duricrusts in Tropical and Subtropical Landscapes Clarendon Press, Oxford, England, 174 p.

Kaplan, A.E. 1973, The Geomorphology of McCullough Alluvial Fan, Clark County, Nevada: Unpubl. MS Thesis, Univ. of Cincinnati, 69 p.

Lattman, L.H., 1971, Geomorphology of the East Flank of the Spring Mts., Nevada: Air Force Cambridge Research Laboratories, Rept. AFCRL-71-0326, 89 p.

, 1973, Calcium Carbonate Cementation of Alluvial Fans, in southern Nevada; Geol. Soc. America Bull., V. 84, p. 3013-3028.

, Sandra K. Lauffenburger, 1974, Proposed role of Gypsum in the Formation of Caliche: Zeit. Geomorph. V. 20, p. 140-149.

, 1975, Factors Affecting Development and Optional Photomapping Technique of Calcium Carbonate Cementation of Arid Region Sediment: US Army Research Office, Rept. DA-ARO-D-31-124-71-6-137, 25 p.

Lenhart, R., 1974, An Evaluation of ERTS Imagery for Remote Sensing of Alluvial Fans in Nevada: Unpubl. MS Thesis, Univ. of Cincinnati, 69 p.

Netterberg, F., 1971, Calcrete in Road Construction: Natl. Inst. Road Research Full., 10, 73 p.

Purcell, C.W. Jr., 1973, Eolian Transport: A Process Supplying Carbonate Material for Caliche Formation: Unpubl. MS Thesis, Univ. of Cincinnati, 66 p.

Olson, S.R. and F.S. Watanbe, 1959, Solubility of Calcium Carbonate in Calcareous Soils: Soil Sci, V. 88, p. 123-129

Reeves, C.C., Jr., 1976, Caliche: Estacado Books, Lubbock, Texas, 233 p.

Van Arsdale, R., 1974, The Influence of Caliche on the Geometry of Arroyos near Buckeye, Arizona: Unpubl. MS Thesis, Univ. of Cincinnati, 69 p.

Wells, S.G., 1976, A Study of Surficial Processes and Geomorphic History of a basin the Sonoran Desert, Southwestern Arizona; Unpubl. PHD Dissertation; Univ. of Cincinnati, 328 p.

APPENDIX

Listing of 1975 Research Reports---------- A-1

Listing of 1976 Research Reports---------- A-3

RESEARCH REPORTS

1975 USAF/ASEE SUMMER FACULTY RESEARCH PROGRAM

Report No.	Title	Research Associate	
1	Design of a Subsonic Combustion Tunnel and Expermental Test Program	Dr. L. I. Boehman	39
2	The Effect of Cobalt Hydroxide Coprecipitation in Nickel Hydroxide Electrodes	Dr. J. T. Maloy	40
3	Overload Protection and Filtering Requirements for Phase Control Voltage Regulators	Dr. Thomas A. Stuart	41
4	A Study on Numerical Methods for Computing Transonic Flows in Turbomachines	Dr. Shu-Yi S. Wang	42
5	An Analysis of Varying Material Properties: A Measure of Damage	Dr. Donald C. Stouffer	43
6	Continuous Performance Measurement of Manually Controlled Systems	Dr. Richard A. Miller	44
7	Digital Autopilot Design	Dr. J. F. Delansky	45
8	Transient Thermal Analysis of External Stores	Dr. Dupree Maples	46
9	Analysis of Missle Control Systems	Dr. Michael E. Warren	47
10	Digital Autopilot Design	Dr. J. N. Youngblood	48
11	Ohmic Contacts for Transferred Electron Devices	Dr. Bruce P. Johnson	49
12	A Navigation Algorithm for the Low-Cost GPS Receiver	Dr. Philip S. Noe	50
13	Electro-Optical Tracker Analysis	Dr. Jerry W. Rogers	51
14	A Real Time Terminal Guidance Simulation Facility	Dr. Richard J. Wolf	52

1975 RESEARCH REPORTS (continued)

Report No.	Title	Research Associate	
15	Fatigue Crack Propagation in Laminated and Monolithic Aluminum Alloy Panels	Dr. J. A. Alic	53
16	RPV Ground Impact Attenuator Simulation	Dr. Charles E. Nuckolls	54
17	A Method for Investigating the Angular Vibration Response of a Structure	Dr. Philip C. Rymers	55
18	Analysis of Inherent Errors in Asynchronous Redundant Digital Flight Controls	Dr. Charles Slivinsky	56
19	Pattern Recognition Techniques Applied to Flat-Bottom Holes	Dr. J. Kent Bryan	57
20	Ultrasonic Techniques for Nondestructive Evaluation (NDE)	Dr. M. Paul Hagelberg	58
21	Fracture of Graphite/Epoxy Composites	Dr. Don H. Morris	59
22	Optical Properties of Europium-Doped Pottasium Chloride Laser Window Materials	Dr. Thomas G. Stoebe	60

RESEARCH REPORTS

1976 USAF/ASEE SUMMER FACULTY RESEARCH PROGRAM

Report No.	Title	Research Associates
1	A Near Field Model for Dissolved Oxygen and Other Water Quality Parameters	Dr. Barry A. Benedict
2	Ecological Considerations for Development of a Water Quality Assessment Model	Dr. Lloyd C. Fitzpatrick
3	Dynamic Responses of Aircraft Shelters	Dr. Fang-Hui-Chou
4	A Sensitivity Study of Noisemap Power Offset Profiles (DSELs)	Dr. D. K. Holger
5	Determination of Unloaded and Loaded Pavement Profiles Used for Prediction of Dynamic Response of Aircraft	Dr. William H. Highter
6	Wind Tunnel Experiment Program for Aerodynamics of Missiles at High Angle of Attack	Dr. William L. Oberkampf
7	Analysis of Millimeter Wave Signatures of Snow and Ice	Dr. Irene K. Petroff
8	Configuration Specifications for a Digital Guided Weapon Flight Control Module	Dr. C. W. Caldwell
9	Sensor and Navigation System Processing Requirements for Digital Guided Missiles	Dr. Robert A. Higgins
10	Interpretation of Laser Velocimeter Measurements in Transonic Turbulent Boundary Layers	Dr. William G. Tiederman
11	Methods to Quantify Constituents in Binary Component Cryodeposits	Dr. Kent F. Palmer
12	Engine Test Cell Acoustics	Dr. G. T. Patterson
13	High Angle of Attack Support Interference	Dr. Robert C. Nelson
14	Development of a Nested Virtual Machine, Data-Structure Oriented Software Design Methodology and Procedure for its Evaluation	Dr. M. M. Drossman
15	Real-World Limitations of Radar Signatures for Target Identification	Dr. Robert D. Strattan
16	Confidence Intervals for Life Cycle Cost Analysis	Dr. H. A. Wiebe

Report No.	Title	Research Associates
17	Computer Aided Decision of Special Monopole and Dipole Antennas	Dr. Shreedhar G. Lele
18	Satellite Based Remote Probing of Atmospheric Visibility: A Bibliography of Relevant Literature	Dr. George C. Sherman
19	Analysis of Spectroscopic Data for Trace Gases in the Earth's Atmosphere	Dr. Louise Gray Young
20	Potential Technology Breakthroughs in Next Generation Radars	Dr. John Spragins
21	Pilot Transfer Function Identification	Dr. Bruce K. Colburn
22	Modeling of Eye Level Blood Pressure and Flow as a Function of G_z	Dr. James J. Freeman
23	Effect of Radiofrequency Radiation (RFR) on Performance and Retention of a Delayed Response Task	Dr. Carole D. Hansult
24	Time-Resolved Fluorescence of the $a^3II_0^+$ State of BrCL	Dr. John J. Wright
25	Dynamic Response of an Aboveground Arch Subjected to a Blast Load	Dr. David Y. L. Wang
26	Optical Fiber Explosion-Initiation System	Dr. Donald A. Smith
27	Density and Temperature Dependence Studies of the Thallium Mercury Excimer System	Dr. P. W. Chan
28	Signal Processing for Optics Progress as of July 1, 1976	Dr. Craig S. Sims
29	Syntheses and Decomposition Mechanisms of New Nitroaliphatic and Polycyclic Triazoline Compounds	Dr. William D. Closson
30	Electrode Erosion in Pulsed Plasma Thrusters	Dr. D. D. Chesak
31	Preparation of Solid Propellant Burning Rate Modifiers	Dr. Amos J. Leffler
32	Electrochemical Studies in Anhydrous Liquid Hydrazine	Dr. John R. Dodd
33	The Transfer Effectiveness of Platform Motion and Field of View in Training Selected UPT Maneuvers	Dr. Edward D. McDowell